

Fermilab-FN-0713

PHYSICS OF INTENSITY DEPENDENT BEAM INSTABILITIES

K. Y. Ng

Fermi National Accelerator Laboratory, P.O. Box 500, Batavia, IL 60510*

US Particle Accelerator School
Sponsored by UCLA
Long Beach, CA
January 14-25, 2002

These lectures are available at www-ap.fnal.gov/ng/uspas02/
Errata will be posted there
Please sent comments and errors to ng@fnal.gov

*Operated by the Universities Research Association, Inc., under contract with the U.S. Department of Energy.

This is a revised edition of the lecture notes, *Physics of Collective Beam Instabilities*, given at the US Particle Accelerator School, SUNY Stony Brook, New York, June 5-16, 2000. Many new additions have been made and many errors corrected.

K.Y. Ng
December 28, 2001

Contents

1 WAKES AND IMPEDANCES	1-1
1.1 Wake Fields	1-1
1.2 Two Appromixations	1-3
1.3 Panofsky-Wenzel Theorem	1-4
1.4 Cylindrically Symmetric Chamber	1-6
1.5 Coupling Impedances	1-12
1.6 Exercises	1-23
2 LONGITUDINAL PHASE SPACE	2-1
2.1 Momentum Compaction	2-1
2.2 Equations of Motion	2-4
2.3 Vlasov Equation	2-11
2.4 Coasting Beams	2-12
2.5 Exercises	2-14
3 POTENTIAL-WELL DISTORTION	3-1
3.1 Static Solution	3-1
3.2 Reactive Force	3-2
3.3 Haissinski Equation	3-5

3.4	Elliptical Phase-Space Distribution	3-8
3.5	Synchrotron Tune Shift	3-11
3.6	Potential-Well Distortion Compensation	3-13
3.6.1	Ferrite Insertion	3-15
3.7	Exercises	3-20
4	BETATRON TUNE SHIFTS	4-1
4.1	Static Transverse Forces	4-1
4.1.1	Electric Image Forces	4-3
4.1.2	Magnetic Image Forces	4-5
4.1.3	Space charge Self-Forces	4-9
4.2	Tune Shift for a Beam	4-15
4.2.1	Image Formation	4-15
4.2.2	Coasting Beams	4-16
4.2.3	Bunched Beams	4-18
4.3	Other Vacuum Chamber Geometries	4-20
4.3.1	Circular Vacuum Chamber	4-20
4.3.2	Elliptical Vacuum Chamber	4-22
4.3.3	Rectangular Vacuum Chamber	4-25
4.3.4	Closed Yoke	4-27
4.4	Connection with Impedance	4-29
4.5	More about Wake Functions	4-31
4.6	Exercises	4-34
5	ENVELOPE EQUATION	5-1

5.1	The Integer Resonance	5-1
5.2	The K-V Equation	5-4
5.2.1	One Dimension	5-7
5.2.2	Two Dimensions	5-9
5.3	Collective Oscillations of Beams	5-12
5.3.1	One Dimension	5-12
5.3.2	Two Dimensions	5-16
5.4	Simulations	5-19
5.4.1	One Dimension	5-19
5.4.2	Two Dimensions	5-21
5.5	Application to Synchrotrons	5-22
5.6	Exercises	5-24
6	LONGITUDINAL MICROWAVE INSTABILITY FOR PROTONS	6-1
6.1	Keil-Schnell Criterion	6-1
6.1.1	Dispersion Relation	6-4
6.1.2	Stability Curve	6-8
6.1.3	Landau Damping	6-11
6.1.4	Self-Bunching	6-12
6.1.5	Overshoot	6-15
6.2	Observation and Cure	6-15
6.3	Ferrite Insertion and Instability	6-19
6.3.1	Microwave Instability	6-19
6.3.2	Cause of Instability	6-22
6.3.3	Heating the Ferrite	6-26

6.3.4	Application at the PSR	6-31
6.4	Exercises	6-36
7	LONGITUDINAL MICROWAVE INSTABILITY FOR ELECTRONS	7-1
7.1	Bunch Modes	7-1
7.2	Mode Mixing	7-6
7.3	Bunch Lengthening and Scaling Law	7-10
7.4	Sawtooth Instability	7-14
7.5	Exercises	7-22
8	BEAM LOADING AND ROBINSON'S STABILITY	8-1
8.1	Equivalent Circuit	8-2
8.2	Beam Loading in an Accelerator Ring	8-6
8.2.1	Steady-State Compensation	8-9
8.3	Robinson's Stability Criteria	8-13
8.3.1	Phase Stability at Low Intensity	8-13
8.3.2	Phase Stability at High Intensity	8-15
8.3.3	Robinson's Damping	8-18
8.4	Transient Beam Loading	8-20
8.4.1	Fundamental Theorem of Beam Loading	8-21
8.4.2	From Transient to Steady State	8-23
8.4.3	Transient Beam Loading of a Bunch	8-27
8.4.4	Transient Compensation	8-36
8.5	Examples	8-42
8.5.1	Fermilab Main Ring	8-42

8.5.2	Fermilab Booster	8-43
8.5.3	Fermilab Main Injector	8-45
8.5.4	Proposed Prebooster	8-47
8.6	Exercises	8-56
9	LONGITUDINAL COUPLED-BUNCH INSTABILITIES	9-1
9.1	Sacherer's Integral Equation	9-1
9.1.1	Synchrotron Tune Shift	9-6
9.1.2	Water Bag Model	9-8
9.1.3	Robinson's Instability	9-8
9.2	Time Domain	9-12
9.3	Observation and Cures	9-20
9.3.1	Higher-Harmonic Cavity	9-23
9.3.2	Passive Landau Cavity	9-26
9.3.3	Rf Voltage Modulation	9-36
9.3.4	Uneven Fill	9-39
9.4	Exercises	9-51
10	TRANSVERSE INSTABILITIES	10-1
10.1	Transverse Focusing and Transverse Wake	10-1
10.2	Separation of Transverse and Longitudinal Motions	10-2
10.3	Sacherer's Integral Equation	10-4
10.4	Solution of Sacherer's Integral Equations	10-7
10.5	Sacherer's Sinusoidal Modes	10-10
10.6	Chromaticity Frequency Shift	10-12

10.7 Exercises	10-17
11 TRANSVERSE COUPLED BUNCH INSTABILITIES 11-1	
11.1 Resistive Wall	11-1
11.2 Narrow Resonances	11-5
11.3 Exercises	11-8
12 HEAD-TAIL INSTABILITIES 12-1	
12.1 Transverse Head-Tail	12-1
12.2 Longitudinal Head-Tail	12-4
12.3 Exercises	12-14
13 MODE COUPLING 13-1	
13.1 Transverse	13-1
13.2 Space Charge and Mode Coupling	13-6
13.3 Longitudinal	13-11
13.4 High Energy Accelerators	13-15
13.5 Exercises	13-19
14 LANDAU DAMPING 14-1	
14.1 Harmonic Beam Response	14-2
14.2 Shock Response	14-5
14.3 Landau Damping	14-10
14.4 Transverse Bunched Beam Instabilities	14-13
14.5 Longitudinal Bunched Beam Instabilities	14-18
14.6 Transverse Unbunched Beam Instabilities	14-20
14.7 Longitudinal Unbunched Beam Instabilities	14-24

14.8 Beam Transfer Function and Impedance Measurements	14-28
14.9 Exercises	14-33
15 BEAM BREAKUP	15-1
15.1 Two-Particle Model	15-2
15.2 Long Bunch	15-5
15.2.1 Balakin-Novokhatsky-Smirnov Damping	15-6
15.2.2 Autophasing	15-9
15.3 Linac	15-13
15.3.1 Adiabatic Damping	15-13
15.3.2 Detuned Cavity Structure	15-14
15.3.3 Multi-Bunch Breakup	15-19
15.3.4 Analytic Treatment	15-22
15.3.5 Amount of Energy Chirp	15-27
15.4 Misaligned Linac	15-34
15.5 Exercises	15-43
16 TRANSITION AND SPACE CHARGE MISMATCH	16-1
16.1 Equations of Motion	16-2
16.2 Nonadiabatic Time	16-3
16.3 Bunch Shape at Transition	16-4
16.4 More Sophisticated Approximation	16-7
16.4.1 Adiabatic Region	16-7
16.4.2 Nonadiabatic Region	16-12
16.5 Space Charge Mismatch	16-17

16.5.1 Mathematical Formulation	16-19
16.6 Transition Jump	16-23
16.7 Exercises	16-25
17 NEGATIVE-MASS INSTABILITY 17-1	
17.1 Growth at Cutoff	17-2
17.1.1 Simple Model	17-2
17.1.2 Shortcomings	17-8
17.2 Schottky-Noise Model	17-11
17.2.1 Comparison of Growths at Cutoff and High Frequencies	17-23
17.2.2 Difficulties in Simulation	17-25
17.3 Self-Bunching Model	17-29
17.4 Exercise	17-32
18 INSTABILITY OF ISOCHRONOUS RINGS 18-1	
18.1 Higher-Order Momentum Compaction	18-2
18.2 η_1 -Dominated Bucket	18-5
18.3 η_2 -Dominated Bucket	18-9
18.4 Microwave Instability Near Transition	18-11
18.4.1 Analytic Solutions	18-11
18.4.2 Bunched Beam Simulations	18-13
18.4.3 Coasting Beam Simulations	18-19
18.5 Exercises	18-24
19 TWO-STREAM INSTABILITY 19-1	
19.1 Introduction	19-1

19.2 Trapped Electrons	19-1
19.2.1 Single-Electron Mechanics	19-4
19.2.2 Centroid-Oscillation Instability	19-8
19.2.3 Production of Electrons	19-17
19.2.4 Electron Bounce Frequency	19-20
19.2.5 Discussion and Conclusion	19-21
19.3 Fast Beam-Ion Instability	19-23
19.3.1 The Linear Theory	19-23
19.3.2 Spectrum of Electron Beam	19-31
19.3.3 Possible Cures	19-32
19.3.4 Applications	19-32
19.4 Exercises	19-49

Chapter 1

WAKES AND IMPEDANCES

1.1 Wake Fields

A positively charged particle at rest has static electric field going out radially in all directions. In motion with velocity v , magnetic field is generated. As the particle velocity approaches c , the velocity of light, the electric and magnetic fields are pancake-like, the electric field is radial and magnetic field azimuthal (the Liénard-Wiechert fields) with an open angle of about $1/\gamma$, where $\gamma = \sqrt{1 - v^2/c^2}$. It is interesting to point out that no matter how far away, this pancake is always perpendicular to the path of motion. In other words, the fields move with the test particle without any lagging behind as illustrated in Fig. 1.1. Such a field pattern is, of course, the steady-state solution of the problem.

When placed inside a perfectly conducting beam pipe, the pancake of fields is trimmed by the beam pipe. A ring of negative charges will be formed on the walls of the beam pipe where the electric field ends, and these image charges will travel at the same pace with the particle, creating the so-called *image current*. If the wall of the beam pipe is not perfectly conducting or contains discontinuities, the movement of the image charges will be slowed down, thus leaving electromagnetic fields behind. For example, when coming across a cavity, the image current will flow into the walls of the cavity, exciting fields trapped inside the cavity. These fields left behind by the particle are called *wake fields*, which are important because they influence the motion of the particles that follow.

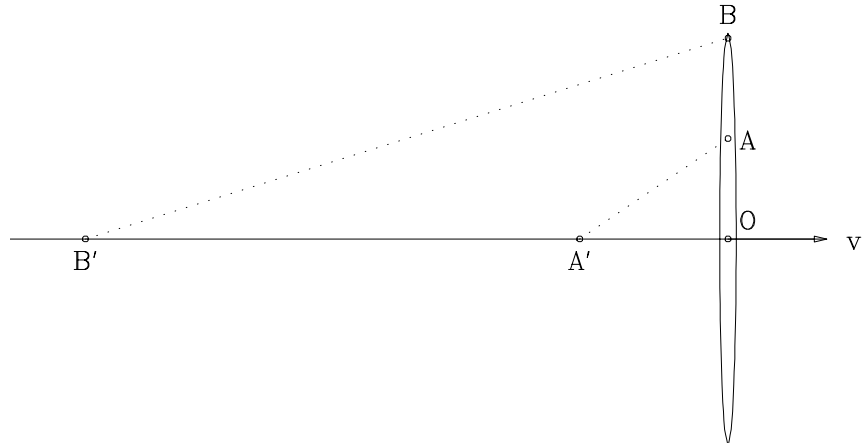


Figure 1.1: Schematic drawing of pan-cake electromagnetic fields emitted by an ultra-relativistic particle traveling with velocity v . The pan-cake is always perpendicular to the path of the particle and travels in pace with the particle no matter how far away the fields are from the particle. There is no violation of causality because fields at points A and B come from the particle at different locations. Fields from A are from A' at a time OA'/v ago, while fields at B from point B' at a time OB'/v ago.

In addition to the wake fields, the electromagnetic fields seen by the beam particle consist of also the external fields from the magnets, rf, etc. The electric field \vec{E} and magnetic flux density \vec{B} can be written as

$$(\vec{E}, \vec{B})_{\text{seen by particles}} = (\vec{E}, \vec{B})_{\text{external, from magnets, rf, etc.}} + (\vec{E}, \vec{B})_{\text{wake fields}} \quad (1.1)$$

where

$$(\vec{E}, \vec{B})_{\text{wake fields}} \left\{ \begin{array}{l} \propto \text{beam intensity} \\ \ll (\vec{E}, \vec{B})_{\text{external}} \end{array} \right.$$

Note that the last restriction, which is certainly not true in plasma physics, allows wake fields to be treated as perturbation. This perturbation, however, will break down when potential-well distortion is large. In that case, the potential-well distortion has to be included into the non-perturbative part. What we need to compute are the wake fields at a distance z behind the source particle and their effects on the test or witness particles that make up the beam. The computation of the wake fields is nontrivial. So approximations are required.

1.2 Two Approximations

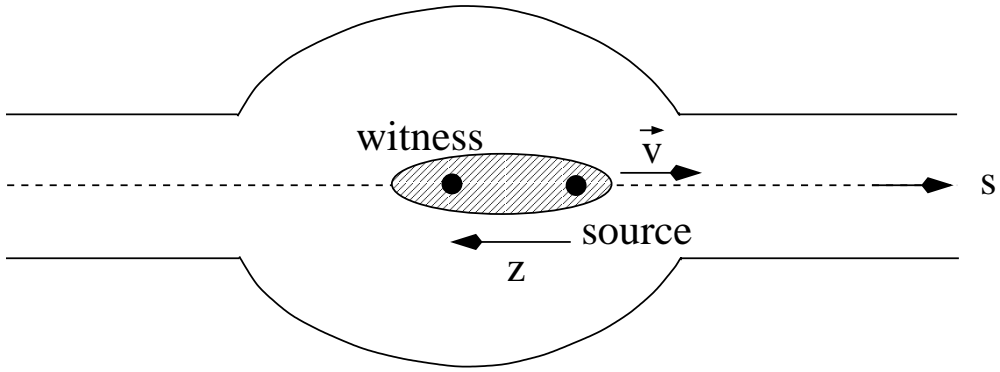


Figure 1.2: Schematic drawing of a witness particle at a distance z behind some source particle in a beam. Both particles are traveling along the direction s with velocity \vec{v} .

At high energies, the particle beam is rigid and the following two approximations apply:^{*}

(1) **The rigid beam approximation**, which says that the beam traverses the discontinuity of the vacuum chamber rigidly and the wake field perturbation does not affect the motion of the beam during the traversal of the discontinuity. This is a good approximation even in the presence of synchrotron oscillations, because the longitudinal distance between two beam particles changes negligibly in a revolution turn relative to the circumference of the accelerator ring. This implies that the distance z of the test particle behind some source particle as shown in Fig. 1.2 does not change.

(2) **The impulse approximation**. Although the test particle carrying a charge q sees a wake force \vec{F} coming from (\vec{E}, \vec{B}) , what it cares is the impulse

$$\Delta \vec{p} = \int_{-\infty}^{\infty} dt \vec{F} = \int_{-\infty}^{\infty} dt q(\vec{E} + \vec{v} \times \vec{B}) \quad (1.2)$$

as it completes the traversal through the discontinuity at its fixed velocity \vec{v} . Note that MKS units have been used in Eq. (1.2) and will be adopted throughout the rest of the lectures. We will therefore be coming across the electric permittivity of free space $\epsilon_0 = 10^7/(4\pi c^2)$ farads/m and the magnetic permeability of free space $\mu_0 =$

^{*}This approach to the Panofsky-Wenzel Theorem was presented by A.W. Chao at the OCPA Accelerator School, Hsinchu, Taiwan, August 3-12, 1998.

$4\pi \times 10^{-7}$ henry/m. These two quantities are related to the free-space impedance Z_0 and velocity of light c by

$$\begin{aligned} Z_0 &= \sqrt{\frac{\mu_0}{\epsilon_0}} = 2.99792458 \times 40\pi = 376.730313 \text{ Ohms ,} \\ c &= \frac{1}{\sqrt{\mu_0\epsilon_0}} = 2.99792458 \times 10^8 \text{ m/s .} \end{aligned} \quad (1.3)$$

Both \vec{E} , \vec{B} , and \vec{F} are difficult to compute even at high beam energies. However, the impulse $\Delta\vec{p}$ has great simplifying properties through the Panofsky-Wenzel (P-W) theorem, which forms the basis of wake potentials and impedances.

1.3 Panofsky-Wenzel Theorem

Maxwell equations for a particle in the beam are:

$$\left\{ \begin{array}{ll} \vec{\nabla} \cdot \vec{E} = \frac{\rho}{\epsilon_0} & \text{Gauss's law for electric charge,} \\ \vec{\nabla} \times \vec{B} - \frac{1}{c^2} \frac{\partial \vec{E}}{\partial t} = \mu_0 \beta c \rho \hat{s} & \text{Ampere's law,} \\ \vec{\nabla} \cdot \vec{B} = 0 & \text{Gauss's law for magnetic charge,} \\ \vec{\nabla} \times \vec{E} + \frac{\partial \vec{B}}{\partial t} = 0 & \text{Faraday's \& Lenz law.} \end{array} \right. \quad (1.4)$$

We have replaced the current density with $\vec{j} = \beta c \rho \hat{s}$ where ρ is the charge density of the beam. The beam particle velocity $|\vec{v}| = \beta c$ will be treated as a constant, which is the result of the rigid-beam approximation, and is certainly true at high energies when $\beta \approx 1$. Note that we have been denoting the s -axis as the direction of motion of the beam, while reserving z as the distance the witness particle is *ahead* the source particle. For a circular ring, the s -axis constitutes the axis of symmetry of the vacuum chamber. Together with the transverse coordinates x and y , they form an instantaneous right-handed Cartesian coordinate system. Thus, the above wake fields \vec{E} and \vec{B} as well as wake force \vec{F} are function of x, y, s, t . From the rigid beam approximation, the location of the test particle, s , is not independent, but is related to t by $s = z + \beta ct$, where z is regarded as time-independent and the location of the source particle is given by $s_{\text{source}} = \beta ct$. Since we are looking at the field behind a source, z is negative.

The Lorentz force on the test particle of charge q is $\vec{F} = q(\vec{E} + \beta c \hat{s} \times \vec{B})$. Here the rigid-beam approximation has also been used by requiring that the test particle has the same velocity as all other beam particles. It follows that

$$\vec{\nabla} \cdot \vec{F} = \frac{q\rho}{\epsilon_0 \gamma^2} - \frac{q\beta}{c} \frac{\partial E_s}{\partial t}, \quad (1.5)$$

$$\vec{\nabla} \times \vec{F} = -q \left(\frac{\partial}{\partial t} + \beta c \frac{\partial}{\partial s} \right) \vec{B} . \quad (1.6)$$

We are only interested in the impulse

$$\Delta \vec{p}(x, y, z) = \int_{-\infty}^{\infty} dt \vec{F}(x, y, z + \beta c t, t); \quad (1.7)$$

i.e., the integration of \vec{F} along a rigid path with z being held fixed. Applying the curl to both sides,

we obtain for the right side,

$$\begin{aligned} \text{Right Side} &= -q \int_{-\infty}^{\infty} dt \left[\left(\frac{\partial}{\partial t} + \beta c \frac{\partial}{\partial s} \right) \vec{B}(x, y, s, t) \right]_{s=z+\beta ct} \\ &= -q \int_{-\infty}^{\infty} dt \frac{d\vec{B}}{dt} = -q \vec{B}(x, y, z + \beta ct, t) \Big|_{t=-\infty}^{\infty} = 0 . \end{aligned} \quad (1.9)$$

We therefore arrive at relation

$$\vec{\nabla} \times \Delta \vec{p} = 0 , \quad (1.10)$$

which is the P-W theorem. It is important to note that so far no boundary conditions have been imposed. The P-W theorem is valid for any boundaries! The only needed inputs are the two approximations: the rigid-bunch approximation and the impulse approximation. The P-W theorem even does not require $\beta = 1$. It just requires $\beta \approx 1$ so that β can remain constant. Thus, the P-W theorem is very general.

The P-W theorem can be decomposed into a component parallel to the \hat{s} and one perpendicular to \hat{s} . The decomposition is obtained by taking dot product and cross product of \hat{s} with Eq. (1.10):

$$\vec{\nabla} \cdot (\hat{s} \times \Delta \vec{p}) = 0 , \quad (1.11)$$

$$\frac{\partial}{\partial z} \Delta \vec{p}_\perp = \vec{\nabla}_\perp \Delta p_s . \quad (1.12)$$

Equation (1.11) says something about the transverse components of $\Delta \vec{p}$, which becomes, in Cartesian coordinates,

$$\frac{\partial \Delta p_x}{\partial y} = \frac{\partial \Delta p_y}{\partial x} . \quad (1.13)$$

On the other hand, Eq. (1.12) relates $\Delta \vec{p}_\perp$ and $\Delta \vec{p}_z$, that the transverse gradient of the longitudinal impulse is equal to the longitudinal gradient of the transverse impulse. Thus, the P-W theorem strongly constraints the components of $\Delta \vec{p}$.

There is an important supplement to the P-W theorem, which states:

$$\beta = 1 \longrightarrow \vec{\nabla}_\perp \cdot \Delta \vec{p}_\perp = 0 . \quad (1.14)$$

Proof:

$$\begin{aligned} \vec{\nabla} \cdot \Delta \vec{p} &= \int_{-\infty}^{\infty} dt \left[\vec{\nabla} \cdot \vec{F}(x, y, s, t) \right]_{s=z+ct} = -\frac{q}{c} \int_{-\infty}^{\infty} dt \left[\frac{\partial E_s}{\partial t} \right]_{s=z+ct} \\ &= q \int_{-\infty}^{\infty} dt \left[\frac{\partial E_s}{\partial s} \right]_{s=z+ct} = \frac{\partial}{\partial z} \Delta p_s , \end{aligned}$$

where we have used the fact that the longitudinal component of the wake force is independent of the magnetic flux density. For the second last step, use has been made of

$$\frac{\partial}{\partial t} E_s(s, t) = \frac{d}{dt} E_s(s, t) - \frac{ds}{dt} \frac{\partial}{\partial s} E_s(s, t) . \quad (1.15)$$

It is important to note that $4\pi q\rho/\gamma^2$, the space charge term of $\vec{\nabla} \cdot \vec{F}$ in Eq. (1.6) has been omitted because $\beta = 1$.

1.4 Cylindrically Symmetric Chamber

When the beam of cylindrical cross section is inside a cylindrically symmetric vacuum chamber, naturally cylindrical coordinates will be used. Some differential operators in the cylindrical coordinates are listed in Table 1.16. The P-W theorem, Eq. (1.10), and the supplemental theorem, Eq. (1.14), become [2]

Table 1.1: Differential operators in the cylindrical coordinates. Here \vec{A} is a vector and Φ is a scalar.

$\vec{\nabla} \cdot \vec{A} = \frac{1}{r} \frac{\partial}{\partial r} (r A_r) + \frac{1}{r} \frac{\partial A_\theta}{\partial \theta} + \frac{\partial A_s}{\partial s} ,$ $\vec{\nabla} \times \vec{A} = \hat{r} \left(\frac{1}{r} \frac{\partial A_\theta}{\partial s} - \frac{\partial A_\theta}{\partial s} \right) + \hat{\theta} \left(\frac{\partial A_r}{\partial s} - \frac{\partial A_s}{\partial r} \right) + \hat{s} \left(\frac{1}{r} \frac{\partial (r A_\theta)}{\partial r} - \frac{1}{r} \frac{\partial A_r}{\partial \theta} \right) ,$ $\nabla^2 \Phi = \frac{1}{r} \frac{\partial}{\partial r} \left(r \frac{\partial \Phi}{\partial r} \right) + \frac{1}{r^2} \frac{\partial^2 \Phi}{\partial \theta^2} + \frac{\partial^2 \Phi}{\partial s^2} .$

$$\left\{ \begin{array}{lcl} \frac{\partial}{\partial r} (r \Delta p_\theta) & = & \frac{\partial}{\partial \theta} \Delta p_r , \\ \frac{\partial}{\partial z} \Delta p_r & = & \frac{\partial}{\partial r} \Delta p_s , \\ \frac{\partial}{\partial z} \Delta p_\theta & = & \frac{1}{r} \frac{\partial}{\partial \theta} \Delta p_s , \\ \frac{\partial}{\partial r} (r \Delta p_r) & = & -\frac{\partial}{\partial \theta} \Delta p_\theta \quad (\beta = 1) . \end{array} \right. \quad (1.16)$$

Now, this set equations for $\Delta \vec{p}$ becomes surprisingly simple. It does not contain any source terms and is completely independent of boundaries, which can be conductors, resistive wall, dielectric, or even plasma. This result solely arises from the Maxwell equations plus the two approximations.

There is no loss of generality by letting $\Delta p_z \sim \cos m\theta$ with $m \geq 0$. Then, we get

$$\Delta p_s = \Delta \tilde{p}_s \cos m\theta \quad \rightarrow \quad \Delta p_r = \Delta \tilde{p}_r \cos m\theta \quad \text{and} \quad \Delta p_\theta = \Delta \tilde{p}_\theta \sin m\theta , \quad (1.17)$$

where $\Delta \tilde{p}_s$, $\Delta \tilde{p}_r$, and $\Delta \tilde{p}_\theta$ are θ -independent. The set of equations for $\Delta \vec{p}$ becomes

$$\left\{ \begin{array}{lcl} \frac{\partial}{\partial r} (r \Delta \tilde{p}_\theta) & = & -m \Delta \tilde{p}_r , \\ \frac{\partial}{\partial z} \Delta \tilde{p}_r & = & \frac{\partial}{\partial r} \Delta \tilde{p}_s , \\ \frac{\partial}{\partial z} \Delta \tilde{p}_\theta & = & -\frac{m}{r} \Delta \tilde{p}_s , \\ \frac{\partial}{\partial r} (r \Delta \tilde{p}_r) & = & -m \Delta \tilde{p}_\theta \quad (\beta = 1) . \end{array} \right. \quad (1.18)$$

From the first and last equations, we must have, for $m = 0$,

$$\Delta\tilde{p}_\theta = 0 \quad \text{and} \quad \Delta\tilde{p}_\theta = 0 , \quad (1.19)$$

otherwise they will be proportional to r^{-1} which is singular at $r = 0$. From the same two equations, we get, for $m \neq 0$,

$$\frac{\partial}{\partial r} \left[r \frac{\partial}{\partial r} (r \Delta\tilde{p}_r) \right] = m^2 \Delta\tilde{p}_r , \quad (1.20)$$

and therefore

$$\Delta p_r(r, \theta, z) \sim r^{m-1} \cos m\theta . \quad (1.21)$$

Now the whole solution can be written as, for all $m \geq 0$,

$$\begin{cases} v\Delta\vec{p}_\perp = -qI_m W_m(z) mr^{m-1} (\hat{r} \cos m\theta - \hat{\theta} \sin m\theta) , \\ v\Delta p_s = -qI_m W'_m(z) r^m \cos m\theta . \end{cases} \quad (1.22)$$

In above, $W_m(z)$ is called the *transverse wake function of azimuthal m* and $W'_m(z)$ the *longitudinal wake function of azimuthal m* . They are related because of the P-W theorem. The wake functions are functions of one variable z only, and are the only remaining unknown. They must be solved with boundary conditions. Recall that the complicated Maxwell-Vlasov equation that involves \vec{E} , \vec{B} , and sources has been reduced drastically to solving just for W_m .

More comments about Eq. (1.22) are in order. The original solution in the top line of Eq. (1.22) was for $m \neq 0$ only. However, we can always define a $W_0(z)$ which is the anti-derivative of $W'_0(z)$ so that the solution holds for all m . Although $W_0(z)$ has no physical meaning, yet it will be helpful in discussions below. In Eq. (1.22), q is the charge of the test particle and I_m is the electric m th multipole of the source particle. For a source particle of charge e at an offset a from the axis of the cylindrical beam pipe, $I_m = ea^m$. Thus, W'_m has the dimension of force per charge square per length^(2m-1) or Volts/Coulomb/m^{2m}, while W_m has the dimension of force per charge square per length^{2m} or Volts/Coulomb/m^{2m-1}. The negative signs on the right sides arise just from a convention. For example, we want the longitudinal wake $W'm(z)$ to be positive when the impulse acting on the test particle is decelerating.

Recall that we have been looking at the wake force on a particle traveling at $s = z+vt$ behind a source particle traveling at $s = vt$. Thus $z < 0$. When $v \rightarrow c$, causality has to

be imposed that $W_m(z) = 0$ when $z > 0$. For our discussions below, we will continue to use v instead of c in most places, because we would like to derive stability conditions and growth rates also for machines that are not ultra-relativistic. However, strict causality will be imposed as if the velocity is c .

Immediately behind a source particle, the test particle should receive a retarding force, otherwise a particle will continue to gain energy as it is traveling down the vacuum chamber in direction violation of the conservation of energy. This implies that $W'_m(z) > 0$ when $|z|$ is small, recalling that the $W'_m(z)$ is defined in Eq. (1.22) with a negative sign on the right side. This is illustrated in Fig. 1.3. It will be proved later in Chapter 7.5 that

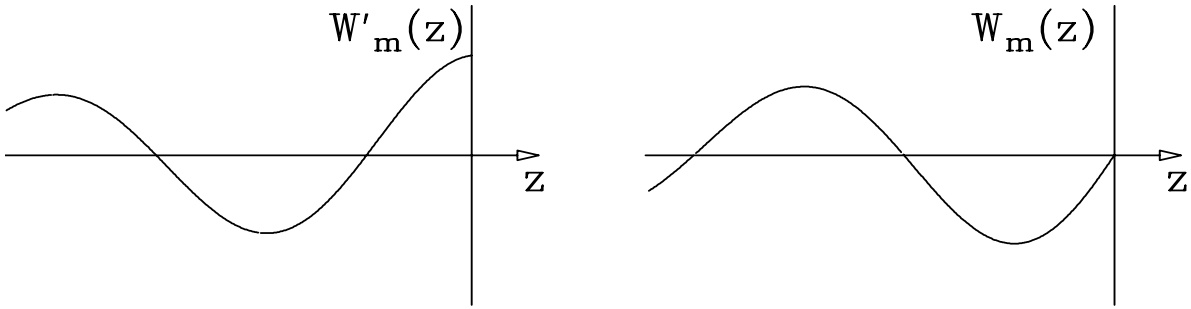


Figure 1.3: The longitudinal wake $W'_m(z)$ vanishes when $z > 0$ and is positive definite when $|z|$ is small. The transverse wake $W_m(z)$ starts out from zero and goes negative as $|z|$ increases.

a particle sees half of its own wake. For the transverse wake $W_m(z)$, it starts out from zero[†] and goes negative as $|z|$ increases, as required by the P-W theorem. Thus, when the source particle is deflected, a transverse wake force is created in the direction that it will deflect particles immediately following in the *same* direction of the deflection of the source. Again, special attention should be paid to the negative sign on the right side of the definition of $W_m(z)$ in Eq. (1.22). The transverse wake W_m vanishes at $z = 0$ implies that a particle will not see its own transverse wake at all. This leads to the important conclusion that a shorter bunch will be preferred if the transverse wake dominates, and a longer bunch will be preferred if the longitudinal wake dominates.

When $m = 0$ or the monopole, we have $\Delta p_\perp = 0$ while Δp_s is independent of (r, θ) and depends only on z . Thus, particles in a thin transverse slice of the beam will see

[†]Although it can not be proved that $W_m(0) = 0$, however, most wakes do have this property.

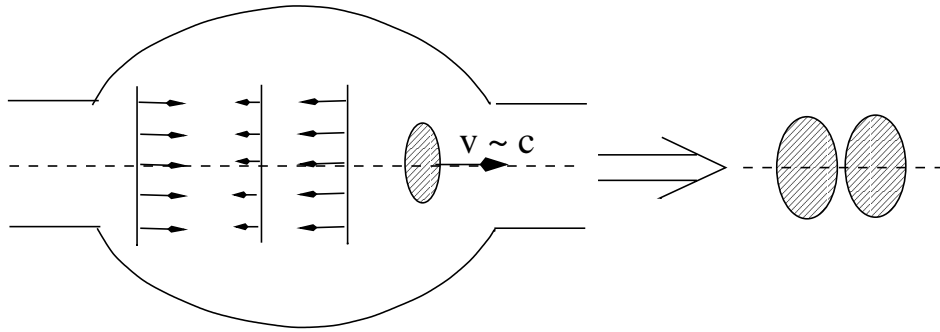


Figure 1.4: All particles in a vertical slice of the beam see exactly the same monopole wake impulse ($m = 0$) from the source according to the slice position z behind the source. This longitudinal variation of impulse effect on the slices can lead to longitudinal microwave instability.

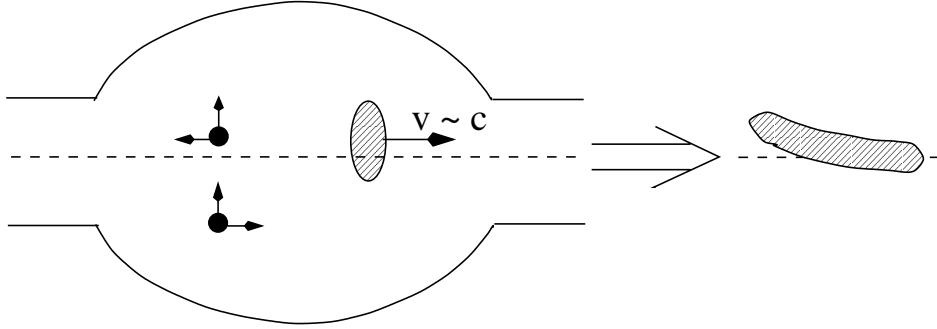


Figure 1.5: Kicks for all the particles in the slice from the dipole wake impulse also have the same magnitude; however, the longitudinal kicks point to forward or backward direction depending on whether the particles are above or below the axis of symmetry.

the same impulse in the s -direction according to the dependence of W'_0 on z , as shown in Fig. 1.4. This impulse can lead to self-bunching or microwave instability.

For $m = 1$, we have from Eq. (1.22) that Δp_{\perp} is independent of (r, θ) but depends on z only. All particles in a vertical slice of the beam suffer exactly the same vertical kick from the dipole wake impulse ($m = 1$) which depends only on how far the slice is behind the dipole source, as is shown in Fig. 1.5. Such an impulse can lead to the tilting of the tail of the bunch into a banana shape; it can also cause beam breakup. On the other hand, the dipole longitudinal impulse Δp_s ($m = 1$) is proportional to the offset in the x -direction.

For the sake of convenience, many authors do not like to work with a negative z for the particles that are following. There is another convention that $W_m(z) = 0$ when $z < 0$. This does not change the physics and the direction of the wake forces will not be changed. Thus, instead of Fig. 1.3, we have Fig. 1.6 instead. A price has to be paid

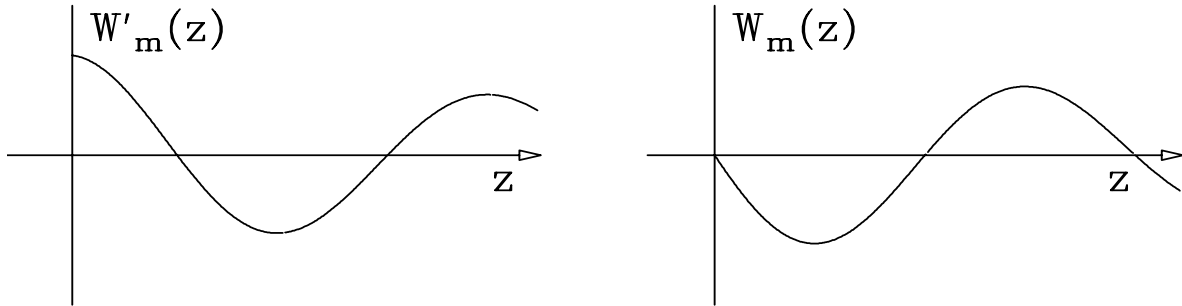


Figure 1.6: This is a different convention that the wake functions $W_m(z)$ vanish when $z < 0$. Since the physics is the same, the wake functions are the same as in Fig. 1.3 and just the direction of z has been changed. In this convention, the interpretation $W'_m(z) \equiv -\frac{d}{dz}W_m(z)$ is required.

for this convention. We must interpret the connection between the longitudinal and transverse wakes as

$$W'_m(z) \equiv -\frac{d}{dz}W_m(z) . \quad (1.23)$$

This convention will be used for the rest of the lectures.[‡] Fortunately, we will not be using Eq. (1.23) much below, because most longitudinal instabilities are driven dominantly by the monopole longitudinal wake W'_0 and most transverse instabilities are driven dominantly by the dipole transverse wake W_1 .

[‡]The readers should be aware of yet another convention in the literature that the wake functions $W_m(z)$ and $W'_m(z)$ are defined in Eq. (1.22) *without* the negative signs on the right sides. As a result, the wake functions will have just the opposite signs of what are depicted in Fig. 1.6.

1.5 Coupling Impedances

Beam particles form a current, of which the component with frequency $\omega/(2\pi)$ is[§] $I(s, t) = \hat{I}e^{-i\omega(t-s/v)}$, where \hat{I} may be complex. This current component at location s and time t will be affected by the wake of the preceding beam particles that pass the point s at time $t-z/v$ with the charge element $I(s, t-z/v)dz/v$. The total *accelerating* voltage seen (or energy gained per unit test charge) will be

$$V(s, t) = - \int_{-\infty}^{\infty} \hat{I}e^{-i\omega[t-(s+z)/v]} W'_0(z) \frac{dz}{v} = -I(s, t) \int_{-\infty}^{\infty} e^{i\omega z/v} W'_0(z) \frac{dz}{v}. \quad (1.24)$$

Thus, we can identify the *longitudinal coupling impedance* of the vacuum chamber as

$$Z_0^{\parallel}(\omega) = \int_{-\infty}^{\infty} e^{i\omega z/v} W'_0(z) \frac{dz}{v}. \quad (1.25)$$

This definition is the same as the ordinary impedance in a circuit. However, we have here much more than in a circuit because the current distribution can possess higher multiples.

When the current is displaced transversely by a from the axis of symmetry of the beam pipe, the *deflecting* transverse force acting on a current particle is obtained by summing the charge element $I(s, t-z/v)dz/v$ passing s at time $t-z/v$,

$$\langle F_1^{\perp}(s, t) \rangle = -\frac{qa}{\ell} \int_{-\infty}^{\infty} \hat{I}e^{-i\omega[t-(s+z)/v]} W_1(z) \frac{dz}{v} = -\frac{qa}{\ell} I(s, t) \int_{-\infty}^{\infty} e^{i\omega z/v} W_1(z) \frac{dz}{v}, \quad (1.26)$$

where $\langle F_1^{\perp}(s, t) \rangle$ is the transverse force averaged over a length ℓ covering the discontinuity of the vacuum chamber, and is therefore equal to $v\Delta p_{\perp}/\ell$, with Δp_{\perp} being the transverse impulse studied in the previous sections. For an accelerator ring or storage ring, this length is taken to be the ring circumference C . We identify the *transverse coupling impedance* of the vacuum chamber as

$$Z_1^{\perp}(\omega) = \frac{i}{\beta} \int_{-\infty}^{\infty} e^{i\omega z/v} W_1(z) \frac{dz}{v}. \quad (1.27)$$

[§]We are going to use the physicist convention (except in Chapter 7.5) of denoting the frequency dependence by $e^{-i\omega t}$, which leads to the results that the capacitive impedance is positive imaginary while the inductive impedance is negative imaginary. The opposite is true in the engineering convention of $e^{j\omega t}$.

In both Eqs. (1.24) and (1.26), the lower limits of integration have been extended to $-\infty$, because the wake functions vanish when $z < 0$. From Eq. (1.26), it is evident that we can also compute the transverse impedance by integrating the wake force averaged over one turn according to

$$Z_1^\perp(\omega) = -\frac{i}{q\beta I_0 a} \int_0^C F_1^\perp(s, t) ds , \quad (1.28)$$

where Ia represents the dipole source current. Since $\Re Z_1^\perp(\omega) > 0$ implies an energy loss, the force leads the displacement Ia by $\frac{\pi}{2}$, and hence the factor $-i$ in Eq. (1.28). The Lorentz factor $\beta = v/c$ is a convention.

Inversely, the wake functions can be written in terms of the impedances:

$$W_m(z) = -\frac{i\beta}{2\pi} \int_{-\infty}^{\infty} Z_m^\perp(\omega) e^{-i\omega z/v} d\omega , \quad (1.29)$$

$$W'_m(z) = \frac{1}{2\pi} \int_{-\infty}^{\infty} Z_m^\parallel(\omega) e^{-i\omega z/v} d\omega , \quad (1.30)$$

where the path of integration in both cases is above all the singularities of the impedances so as to guarantee causality.

Note that the longitudinal impedance is mostly the monopole ($m = 0$) impedance and the transverse impedance is mostly the dipole ($m = 1$) impedance, if the beam pipe cross section is close to circular and the particle path is close to the pipe axis. They have the dimensions of Ohms and Ohms/length, respectively. The impedances have the following properties:

$$1. \quad Z_0^\parallel(-\omega) = [Z_0^\parallel(\omega)]^* \quad \text{and} \quad Z_1^\perp(-\omega) = -[Z_1^\perp(\omega)]^* . \quad (1.31)$$

$$2. \quad Z_0^\parallel(\omega) \text{ and } Z_1^\perp(\omega) \text{ are analytic with poles only in the lower half } \omega\text{-plane.} \quad (1.32)$$

$$3. \quad Z_m^\parallel(\omega) = \frac{\omega}{c} Z_m^\perp(\omega) , \quad (1.33)$$

for cylindrical geometry and each azimuthal harmonic including $m = 0$.

$$4. \quad \Re Z_0^\parallel(\omega) \geq 0 \quad \text{and} \quad \Re Z_1^\perp(\omega) \geq 0 \quad \text{when } \omega > 0 , \quad (1.34)$$

if the beam pipe has the same entrance cross section and exit cross section.

$$5. \quad \int_0^\infty d\omega \Im Z_m^\perp(\omega) = 0 , \quad \text{and} \quad \int_0^\infty d\omega \frac{\Im Z_m^\parallel(\omega)}{\omega} = 0 . \quad (1.35)$$

The first follows because the wake functions are real, the second from the causality of the wake functions, and the third from the Panofsky-Wenzel theorem [1] between transverse and longitudinal electromagnetic forces. $\Re Z_m^{\parallel}(\omega) \geq 0$ is the result of the fact that the total energy of a particle or a bunch cannot be increased after passing through a section of the vacuum chamber where there is no accelerating external forces, while $\Re Z_m^{\perp}(\omega) \geq 0$ when $\omega > 0$ follows from the Panofsky-Wenzel theorem. The fifth property follows from the assumption that $W_m(0) = 0$.

For a pure resistance R , the longitudinal wake is $W'_0(z) = R\delta(z/v)$. At low frequencies, the wall of the beam pipe is inductive. This wake function is $W'_0(z) = L\delta'(z/v)$, where L is the inductance.

For a nonrelativistic beam of radius a inside a circular beam pipe of radius b , the longitudinal space charge impedance for $m = 0$ is**

$$Z_0^{\parallel}(\omega) = i \frac{\omega}{\omega_0} \frac{Z_0}{2\gamma^2\beta} \left(1 + 2 \ln \frac{b}{a} \right), \quad (1.36)$$

where $Z_0 = \sqrt{\mu_0/\epsilon_0} \approx 377 \Omega$ is the impedance of free space, μ_0 and ϵ_0 are, respectively, the magnetic permeability and electric permittivity of free space, $\omega_0/(2\pi)$ is the revolution frequency of the beam particle with Lorentz factors γ and β . Although this impedance is capacitive, however, it appears in the form of a negative inductance. The corresponding wake function is

$$W'_0(z) = -\delta'(z/v) \frac{1}{\omega_0} \frac{Z_0}{2\gamma^2\beta} \left(1 + 2 \ln \frac{b}{a} \right). \quad (1.37)$$

The $m = 1$ transverse space charge impedance for a length ℓ of the circular beam pipe is

$$Z_1^{\perp}(\omega) = i \frac{Z_0\ell}{2\pi\gamma^2\beta^2} \left[\frac{1}{a^2} - \frac{1}{b^2} \right], \quad (1.38)$$

and the corresponding transverse wake function is

$$W_1(z) = \frac{Z_0c\ell}{2\pi\gamma^2} \left[\frac{1}{a^2} - \frac{1}{b^2} \right] \delta(z). \quad (1.39)$$

An important impedance is that of a resonant cavity. Near the resonant frequency $\omega_r/(2\pi)$, the m th multipole longitudinal impedances can be derived from a *RLC*-parallel

**This expression will be derived in Chapter 3. Here, the space charge force is seen by beam particles at the beam axis. If the force is averaged over the cross section of the beam with a uniform transverse cross section, the first term in the brackets becomes $\frac{1}{2}$ instead of 1.

circuit:

$$Z_m^{\parallel}(\omega) = \frac{R_{ms}}{1 + iQ \left(\frac{\omega_r}{\omega} - \frac{\omega}{\omega_r} \right)}, \quad (1.40)$$

where the resonant angular frequency is $\omega = (L_m C_m)^{-1/2}$ and quality factor is $Q = R_{ms} \sqrt{C_m / L_m}$. Here, for the m th multipole, the shunt impedance R_{ms} is in Ohms/m^{2m}, the inductance in henry/m^{2m}, and the capacitance in farad-m^{2m}. The transverse impedance can now be obtained from the P-W theorem of Eq. (1.33):

$$Z_m^{\perp}(\omega) = \frac{c}{\omega} \frac{R_{ms}}{1 + iQ \left(\frac{\omega_r}{\omega} - \frac{\omega}{\omega_r} \right)}. \quad (1.41)$$

Another example is the longitudinal impedance for a length ℓ of the resistive beam pipe:

$$Z_0^{\parallel}(\omega) = [1 - i \operatorname{sgn}(\omega)] \frac{\ell}{2\pi b \sigma_c \delta_{\text{skin}}}, \quad (1.42)$$

where b is the radius of the cylindrical beam pipe, σ_c is the conductivity of the pipe wall,

$$\delta_{\text{skin}} = \sqrt{\frac{2c}{Z_0 \mu_r \sigma_c |\omega|}}, \quad (1.43)$$

is the skin depth at frequency $\omega/(2\pi)$, and μ_r is the relative magnetic permeability of the pipe wall. The transverse impedance is

$$Z_1^{\perp}(\omega) = [1 - i \operatorname{sgn}(\omega)] \frac{\ell c}{\pi \omega b^3 \sigma_c \delta_{\text{skin}}}, \quad (1.44)$$

and is related to the longitudinal impedance by

$$Z_1^{\perp}(\omega) = \frac{2c}{b^2 \omega} Z_0^{\parallel}(\omega). \quad (1.45)$$

The above relation has been used very often to estimate the transverse impedance from the longitudinal. However, we should be aware that this relation holds only for resistive impedances of a cylindrical beam pipe. The monopole longitudinal impedance and the dipole transverse impedance belong to different azimuthals; therefore they should not be related. An example that violates Eq. (1.45) is the longitudinal and transverse space charge impedances stated in Eqs. (1.36) and (1.38).

More expressions for impedances resulting from various types of discontinuity in the vacuum chamber are reprinted from the *Handbook of Accelerator Physics and Engineering* [3] in the following pages.

3.2.5 Explicit Expressions of Impedances and Wake Functions

K.Y. Ng, FNAL

References

- [1] A.W. Chao, Physics of Collective Beam Instabilities in High Energy Accelerators, Wiley (1993) ch.2
- [2] K.Y. Ng, PA 23 (1988) 93
- [3] S.A. Heifets, G. Sabbi, SLAC/AP-104 (1996)
- [4] E. Keil, B. Zotter, PA 3 (1972) 11; K.Y. Ng, Fermilab Report FN-389 (1981)
- [5] S.S. Kurennoy, PR E55 (1997) 3529; S.S. Kurennoy, R.L. Gluckstern, *ibid* (1997) 3533
- [6] S.S. Kurennoy, G.V. Stupakov, PA 45 (1994) 95
- [7] A.M. Sessler, unpublished citation in E. Keil, NIM 100 (1972) 419; L.A. Veinshtein, Sov. Phys. JETP 17 (1963) 709; D. Brandt, B. Zotter, CERN-ISR/TH/82-13 (1982)
- [8] C.C. Johnson, Field and Wave Electrodynamics, McGraw-Hill, Ch.6
- [9] G. Nassibian, F. Sacherer, NIM 59 (1971) 21; G. Nassibian, CERN/PS 84-25 (BR) (1984); CERN 85-68 (BR) (1986)
- [10] M. Sands, SLAC note PEP-253 (1977); H.A. Bethe, PR 66 (1944) 163
- [11] S.S. Kurennoy, PA 39 (1992) 1; PA 50 (1995) 167; R.L. Gluckstern, PRA 46, 1106, 1110 (1992); S.S. Kurennoy, R.L. Gluckstern, G.V. Stupakov, PR E52 (1995) 4354
- [12] A. Fedotov, PhD Thesis, U. Maryland (1997)
- [15] R. Gluckstern, PR D39 (1989) 2773, 2780; G. Stupakov, PAC 95 3303, K. Yokoya and K. Bane, PAC 99, p.1725
- [16] A. Novokhatski, A. Mosnier, PAC 97, p.1661
- [17] K.L.F. Bane, A. Novokhatski, SLAC Report AP-117 (1999)
- [18] K.Y. Ng and R. Warnock, PAC 89 798, PR D40 (1989) 231
- [19] T.S. Wang, AIP Conf. Proc. 448, (1998) p.286
- [20] T.S. Wang and R. Gluckstern, PAC 99, p.2876
- [13] G.V. Stupakov, SLAC-PUB-7908 (1998), submitted to PR Special Topics
- [14] S.A. Heifets, PRD 40 (1989) 3097; S.A. Heifets, S.A. Kheifets, Rev. Mod. Phys. 63 (1990) 631

General Remarks and Notations:

W'_m denotes m th azimuthal longitudinal wake function as a function of distance z for $z < 0$. When $z > 0$, $W'_m(z) = 0$ and $W'_m(0) = \lim_{z \rightarrow 0^-} W'_m(z)$. Similar for transverse wake W_m .

The m th azimuthal longitudinal impedance $Z_m(\omega) = \int e^{-i\omega z/v} W_m^{\parallel}(z) dz/v$ is related to the transverse impedance of the same azimuthal $Z_m^{\perp}(\omega) = \int e^{-i\omega z/v} W_m^{\perp}(z) dz/(\beta v)$ by $Z_m^{\parallel} = (\omega/c)Z_m^{\perp}$ (valid when $m \neq 0$). In many cases, $\beta = v/c$ has been set to 1.

Unless otherwise stated, round beam pipe of radius b is assumed. $C = 2\pi R$ is the ring circumference and n is the revolution harmonic. $Z_0 \approx 377 \Omega$ is the free-space impedance. ϵ_0 and μ_0 are the free-space dielectric constant and magnetic permeability.

Description	Impedances	Wakes
<u>Space-charge:</u> [1] beam radius a in a length L of perfectly conducting beam pipe of radius b .	$Z_0^{\parallel} = i \frac{Z_0 L}{2C\beta\gamma^2} \left[1 + 2 \ln \frac{b}{a} \right]$ $Z_{m \neq 0}^{\perp} = i \frac{Z_0 L}{2\pi\beta^2\gamma^2 m} \left[\frac{1}{a^{2m}} - \frac{1}{b^{2m}} \right]$	$W'_0 = \frac{Z_0 c L}{4\pi\gamma^2} \left[1 + 2 \ln \frac{b}{a} \right] \delta'(z)$ $W_{m \neq 0} = \frac{Z_0 c L}{2\pi\gamma^2 m} \left[\frac{1}{a^{2m}} - \frac{1}{b^{2m}} \right] \delta(z)$
<u>Resistive Wall:</u> [1] pipe length L , wall thickness t , conductivity σ_c , skin depth δ_{skin} . For $t \gg \delta_{\text{skin}}$ and $b/\chi \gg z \approx c/ \omega \gg b\chi^{1/3}$.	$\frac{Z_m^{\parallel}}{L} = \frac{\omega}{c} \frac{Z_m^{\perp}}{L} = \frac{Z_0 c / (\pi b^{2m})}{[1 + \text{sgn}(\omega)i](1 + \delta_{m0})bc\sqrt{\frac{\sigma_c Z_0 c}{2 \omega }} - \frac{ib^2\omega}{m+1} + \frac{imc^2}{\omega}}$ $t \gg \delta_{\text{skin}} = \sqrt{2c/(\omega Z_0\sigma_c)}$, $ \omega \gg c\chi/b$, $\chi = 1/(Z_0\sigma_c b)$	
For $t \ll \delta_{\text{skin}}$ or very low freq., and $b/\chi \gg z \approx c/ \omega \gg \sqrt{bt}$.	$Z_m^{\parallel} = \frac{\omega}{c} Z_m^{\perp}$ $Z_m^{\perp} = \frac{1 - \text{sgn}(\omega)i}{1 + \delta_{m0}} \frac{L}{\pi\sigma_c\delta_{\text{skin}}b^{2m+1}}$	$W_m = -\frac{c}{\pi b^{2m+1}(1 + \delta_{m0})} \sqrt{\frac{Z_0}{\pi\sigma_c}} \frac{L}{ z ^{1/2}}$ $W'_m = -\frac{c}{2\pi b^{2m+1}(1 + \delta_{m0})} \sqrt{\frac{Z_0}{\pi\sigma_c}} \frac{L}{ z ^{3/2}}$
A pair of strip-line BPM's: [2] length L , angle each subtending to pipe axis ϕ_0 , forming transmission lines of characteristic impedance Z_c with pipe.	$Z_0^{\parallel} = 2Z_c \left[\frac{\phi_0}{2\pi} \right]^2 \left[2 \sin^2 \frac{\omega L}{c} - i \sin \frac{2\omega L}{c} \right]$ $Z_1^{\perp} = \left[\frac{Z_0^{\parallel}}{\omega} \right]_{\text{pair}} \frac{c}{b^2} \left[\frac{4}{\phi_0} \right]^2 \sin^2 \frac{\phi_0}{2}$	$W'_0 = 2Z_c c \left[\frac{\phi_0}{2\pi} \right]^2 [\delta(z) - \delta(z+2L)]$ $W_1 = \frac{8Z_c c}{\pi^2 b^2} \sin^2 \frac{\phi_0}{2} [H(z) - H(z+2L)]$
The strip-lines are assumed to terminate with impedance Z_c at the upstream end.		
<u>Heifets inductive impedance:</u> [3] low freq. pure inductance \mathcal{L} . Z_0^{\parallel} rolls off as $\omega^{-1/2}$.	$Z_0^{\parallel} = -\frac{i\omega\mathcal{L}}{(1 - i\omega a/c)^{3/2}}$ $\longrightarrow -i\omega\mathcal{L}$ as $a \rightarrow 0$	$W'_0 = \frac{c^2\mathcal{L}}{a\sqrt{\pi a z}} \left[1 + \frac{2z}{a} \right] e^{z/a}$ $\longrightarrow c^2\mathcal{L}\delta'(z)$ as $a \rightarrow 0$
Pill-box cavity at low freq.: length g , radial depth $h+b$, where $g \leq h \ll b$ [6].	$Z_0^{\parallel} = -i \frac{\omega Z_0}{2\pi cb} \left[gh - \frac{g^2}{2\pi} \right]$ $Z_1^{\perp} = -i \frac{Z_0}{\pi b^3} \left[gh - \frac{g^2}{2\pi} \right]$	$W'_0 = -\frac{Z_0 c}{2\pi b} \left[gh - \frac{g^2}{2\pi} \right] \delta'(z)$ $W_1 = -\frac{Z_0 c}{\pi b^3} \left[gh - \frac{g^2}{2\pi} \right] \delta(z)$

Description	Impedances	Wakes
Pill-box cavity at low freq.: length g , radial depth $h + b$, where $h \ll g \ll b$ [6].	$Z_0^{\parallel} = -i\frac{\omega Z_0 h^2}{\pi^2 cb} \left[\ln \frac{2\pi g}{h} + \frac{1}{2} \right]$ $Z_1^{\perp} = -i\frac{2Z_0 h^2}{\pi^2 b^3} \left[\ln \frac{2\pi g}{h} + \frac{1}{2} \right]$	$W'_0 = -\frac{Z_0 ch^2}{\pi^2 b} \left[\ln \frac{2\pi g}{h} + \frac{1}{2} \right] \delta'(z)$ $W_1 = -\frac{2Z_0 ch^2}{\pi^2 b^3} \left[\ln \frac{2\pi g}{h} + \frac{1}{2} \right] \delta(z)$
Pill-box cavity: length g , radial depth d . At freq. $\omega \gg c/b$, diffraction model applies [1].	$Z_m^{\parallel} = \frac{[1 + \text{sgn}(\omega)i]Z_0}{(1+\delta_{m0})\pi^{3/2}b^{2m+1}} \sqrt{\frac{cg}{ \omega }}$ $Z_m^{\parallel} = \frac{\omega}{c} Z_m^{\perp}$	$W_m = -\frac{2Z_0 c \sqrt{2g}}{(1+\delta_{m0})\pi^{2b^{2m+1}}} z ^{1/2}$ $W'_m = \frac{Z_0 c \sqrt{2g}}{(1+\delta_{m0})\pi^{2b^{2m+1}}} z ^{-1/2}$
Optical model: [7] A series of cavities of periodic length L . Each cavity has width g , high Q resonances of freq. $\omega_n/(2\pi)$ and loss factor $k_n^{(m)}$ for azimuthal mode m . Formulas for computation of W'_m . $\text{erfc}(x)$ is the complementary error function.	$\text{Re}Z_m^{\parallel} = \sum_{n=1}^N \pi k_n^{(m)} \delta(\omega - \omega_n) + \frac{2\pi C_{\text{sv}} G(\bar{\nu}) F(\nu)}{(1+\delta_{m0}) b^{2m}} H(\omega - \omega_N)$ $W'_m = \sum_{n=1}^N 2k_n^{(m)} \cos \frac{\omega_n z}{c} + \frac{2C_{\text{sv}} G(\bar{\nu})}{(1+\delta_{m0}) b^{2m}} \int_{\omega_N}^{\infty} d\omega F(\nu) \cos \frac{\omega z}{c}$ where $C_{\text{sv}} = 2Z_0 j_{m1}^2 / (\pi^2 \zeta^2 \beta) \approx 650 \Omega$ for $m = 0$ and 1650Ω for $m = 1$, j_{m1} is first zero of Bessel function J_m , $\zeta = 0.8237$. $G(\bar{\nu}) = \bar{\nu}^2 K_1^2(\bar{\nu})$, $F(\nu) = \frac{\sqrt{\nu}+1}{(\nu+2\sqrt{\nu}+2)^2}$, $\bar{\nu} = \frac{\omega b}{\beta \gamma c}$, $\nu = \frac{\omega}{\omega_{\text{sv}}} = \frac{4b^2 \omega}{\zeta^2 c \sqrt{gL}}$ $\int_{\hat{\omega}}^{\infty} d\omega F(\nu) \cos \frac{\omega z}{c} = \omega_{\text{sv}} \tilde{F}_0(z/c) - \int_0^{\hat{\omega}} d\omega F(\nu) \cos \frac{\omega z}{c}$ $\tilde{F}_0(x) = \int_0^{\infty} d\omega F(\nu) \cos \omega x = \frac{\pi}{4} (1 + 4x) e^{2x} \text{erfc}(\sqrt{2x}) - \sqrt{\frac{\pi x}{2}}$	
Resonator model for the m th azimuthal, with shunt imp. $R_s^{(m)}$, resonant freq. $\omega_r/(2\pi)$, quality factor Q [1].	$Z_m^{\parallel} = \frac{R_s^{(m)}}{1 + iQ(\omega_r/\omega - \omega/\omega_r)}$ $Z_m^{\perp} = \frac{c}{\omega} \frac{R_s^{(m)}}{1 + iQ(\omega_r/\omega - \omega/\omega_r)}$	$W_m = \frac{R_s^{(m)} c \omega_r}{Q \bar{\omega}_r} e^{\alpha z/c} \sin \frac{\bar{\omega}_r z}{c}$ where $\alpha = \omega_r/(2Q)$ $\bar{\omega}_r = \sqrt{ \omega_r^2 - \alpha^2 }$
Res. freq. $\omega_{mnp}/(2\pi)$ and shunt impedance $(R_s)_{mnp}$ of a pill-box cavity for n th radial and p th longitudinal modes. Radial depth d and length g . x_{mn} is n th zero of Bessel function J_m [8].	$\frac{\omega_{mnp}^2}{c^2} = \frac{x_{mn}^2}{d^2} + \frac{p^2 \pi^2}{g^2}$ $\left[\frac{R_s}{Q} \right]_{0np} = \frac{Z_0}{x_{0n}^2 J_0'^2(x_{0n})} \frac{8c}{\pi g \omega_{0np}}$ $\left[\frac{R_s}{Q} \right]_{1np} = \frac{Z_0}{J_1'^2(x_{1n})} \frac{2c^2}{\pi g d^2 \omega_{1np}^2}$	$\begin{cases} \sin^2 \frac{g \omega_{0np}}{2\beta c} \times \frac{1}{1 + \delta_{0p}} & p \text{ even} \\ \cos^2 \frac{g \omega_{0np}}{2\beta c} & p \text{ odd} \end{cases}$ $\begin{cases} \sin^2 \frac{g \omega_{1np}}{2\beta c} & p \neq 1 \text{ and even} \\ \cos^2 \frac{g \omega_{1np}}{2\beta c} & p \text{ odd} \end{cases}$

Description	Impedances	Wakes
Low-freq. response of a <u>pill-box cavity</u> : [4] length g , radial depth d . When $g \gg 2(d-b)$, replace g by $(d-b)$. Here, $S = d/b$.	$Z_0^{\parallel} = -i \frac{Z_0 g}{2\pi R} \ln S$ $Z_1^{\perp} = -i \frac{Z_0 g}{\pi b^2} \frac{S^2 - 1}{S^2 + 1}$	$W'_0 = -\frac{Z_0 c g}{2\pi} \ln S \delta'(z)$ $W_1 = -\frac{Z_0 c g}{\pi b^2} \frac{S^2 - 1}{S^2 + 1} \delta(z)$
Effect will be one half for a step in the beam pipe from radius b to radius d , or vice versa, when $g \gg 2(d-b)$.		
Iris of half elliptical cross section at low freq.: width $2a$, maximum protruding length h [5].	$Z_0^{\parallel} = -i \frac{\omega Z_0 h^2}{4cb}$ $Z_1^{\perp} = -i \frac{Z_0 h^2}{2b^3}$	$W'_0 = -\frac{Z_0 c h^2}{4b} \delta'(z)$ $W_1 = -\frac{Z_0 c h^2}{2b^3} \delta(z)$
Pipe transition at low freq.: tapering angle θ , transition height h . γ is Euler's constant and ψ is the psi-function [6].	$Z_0^{\parallel} = \frac{\omega b^2 Z_1^{\perp}}{2c} = -i \frac{\omega Z_0 h^2}{2\pi^2 cb} \left\{ \ln \left[\frac{b\theta}{h} - 2\theta \cot \theta \right] + \frac{3}{2}\gamma - \psi \left(\frac{\theta}{\pi} \right) - \frac{\pi}{2} \cot \theta - \frac{\pi}{2\theta} \right\}$ $W'_0 = - \left \frac{Z_0^{\parallel}}{\omega} \right c^2 \delta'(z), \quad W_1 = - \left Z_1^{\perp} \right c \delta(z), \quad h \cot \theta \ll b$	
Pipe transition at low frequencies with transition height $h \ll b$ [6].	$Z_0^{\parallel} = \frac{\omega b^2}{2c} Z_1^{\perp} = -i \frac{\omega Z_0 h^2}{2\pi^2 cb} \left(\ln \frac{2\pi b}{h} + \frac{1}{2} \right)$ $W'_0 = - \left \frac{Z_0^{\parallel}}{\omega} \right c^2 \delta'(z), \quad W_1 = - \left Z_1^{\perp} \right c \delta(z)$	
Kicker with window-frame magnet [9]: width a , height b , length L , beam offset x_0 horizontally, and all image current carried by conducting current plates.	$Z_0^{\parallel} = \frac{\omega^2 \mu_0^2 L^2 x_0^2}{4a^2 Z_k}$ $Z_1^{\perp} = \frac{c\omega \mu_0^2 L^2}{4a^2 Z_k}$	$W'_0 = -\frac{c^3 \mu_0^2 L^2 x_0^2}{4a^2 Z_k} \delta''_0(z)$ $W_1 = -\frac{c^3 \mu_0^2 L^2}{4a^2 Z_k} \delta'(z)$
$Z_k = -i\omega\mathcal{L} + Z_g$ with $\mathcal{L} \approx \mu_0 b L/a$ the inductance of the windings and Z_g the impedance of the generator and the cable. If the kicker is of C-type magnet, x_0 in Z_0^{\parallel} should be replaced by $(x_0 + b)$.		
Traveling-wave kicker with characteristic impedance Z_c for the cable, and a window magnet of width a , height b , and length L [9].	$Z_0^{\parallel} = \frac{Z_c}{4} \left[2 \sin^2 \frac{\theta}{2} - i(\theta - \sin \theta) \right], \quad Z_1^{\perp} = \frac{Z_c L}{4ab} \left[\frac{1 - \cos \theta}{\theta} - i \left(1 - \frac{\sin \theta}{\theta} \right) \right]$ $W'_0 = \frac{Z_c c}{4} \left[\delta(z) - \delta \left(z - \frac{Lc}{v} \right) - \frac{Lc}{v} \delta'(z) \right]$ $W_1 = \frac{Z_c v}{4ab} \left[H(z) - H \left(z - \frac{Lc}{v} \right) - \frac{Lc}{v} \delta(z) \right]$ $\theta = \omega L/v$ denotes the electrical length of the kicker windings and $v = Z_{cac}/(Z_0 b)$ is the matched transmission-line phase velocity of the capacitance-loaded windings.	
Bethe's electric and magnetic moments of a hole of radius a in beam pipe wall [10].	Electric and magnetic dipole moments when wavelength $\gg a$: $\vec{d} = -\frac{2\epsilon_0}{3} a^3 \vec{E}, \quad \vec{m} = -\frac{4}{3\mu_0} a^3 \vec{B}$ \vec{E} and \vec{B} are electric and magnetic flux density at hole when hole is absent. This is a diffraction solution for a thin-wall pipe.	

Description	Impedances	Wakes
Small obstacle [5, 11] on beam pipe, size \ll pipe radius, freq. below cutoff. α_e and α_m are electric polarizability and magnetic susceptibility of the obstacle.	$Z_0^{\parallel} = -i \frac{\omega Z_0}{c} \frac{\alpha_e + \alpha_m}{4\pi^2 b^2}$ $Z_1^{\perp} = -i \frac{Z_0(\alpha_e + \alpha_m)}{\pi^2 b^4} \cos \Delta\varphi$	$W'_0 = -Z_0 c \frac{\alpha_e + \alpha_m}{4\pi^2 b^2} \delta'(z)$ $W_1 = -Z_0 c \frac{\alpha_e + \alpha_m}{\pi^2 b^4} \cos \Delta\varphi \delta(z)$
$\Delta\varphi$ is the azimuthal angle between the obstacle and the direction concerning Z_1^{\perp} and W_1 .		
Polarizabilities for various geometry: beam pipe radius is b and wall thickness is t .		
Elliptical hole: major and minor radii are a and d . $K(m)$ and $E(m)$ are complete elliptical functions of the first and second kind, with $m = 1 - m_1$ and $m_1 = (d/a)^2$. For long ellipse \perp beam, major axis $a \ll b$, beam pipe radius, because the curvature of the beam pipe has been neglected here [12].	$\alpha_e + \alpha_m = \begin{cases} \frac{\pi a^3 m_1^2 [K(m) - E(m)]}{3E(m)[E(m) - m_1 K(m)]} & \xrightarrow[m \rightarrow 1]{\text{m} \rightarrow 1} \begin{cases} \frac{\pi d^4 [\ln(4a/d) - 1]}{3a} & \parallel \text{beam} \\ \frac{\pi a^3}{3[\ln(4a/d) - 1]} & \perp \text{beam} \end{cases} \\ \frac{\pi a^3 [E(m) - m_1 K(m)]}{3[K(m) - E(m)]} & \xrightarrow[\text{long ellipse}]{\text{long ellipse}} \begin{cases} \frac{\pi a^3}{3[\ln(4a/d) - 1]} & \perp \text{beam} \end{cases} \end{cases}$ $\alpha_e + \alpha_m \xrightarrow[m \rightarrow 0]{\text{circular}} \frac{2a^3}{3}$ circular hole $a = d \ll b$ Above are for $t \ll a$, $\times 0.56$ (circular) or $\times 0.59$ (long ellipse) when $t \geq a$. For higher frequency correction, add to $\alpha_e + \alpha_m$ the extra term, $+ \frac{2\pi a^3}{3} \left[\frac{11\omega^2 a^2}{30c^2} \right]$ circular, $\begin{cases} -\frac{\pi ad^2}{3} \left[\frac{\omega^2 a^2}{5c^2} \right] & \parallel \text{beam} \\ +\frac{2\pi a^3}{3} \left[\frac{2\omega^2 a^2}{5c^2 [\ln(4a/d) - 1]} \right] & \perp \text{beam} \end{cases}$ long ellipse	
Rectangular slot: length L , width w .	$\alpha_e + \alpha_m = w^3 (0.1814 - 0.0344w/L)$	$t \ll a$, $\times 0.59$ when $t \geq a$
Rounded-end slot: length L , width w .	$\alpha_e + \alpha_m = w^3 (0.1334 - 0.0500w/L)$	$t \ll a$, $\times 0.59$ when $t \geq a$
Annular-ring-shaped cut: inner and outer radii a and $d = a + w$ with $w \ll d$.	$\alpha_e + \alpha_m = \frac{\pi^2 d^2 a}{2 \ln(32d/w) - 4} - \frac{\pi^2 w^2 (a + d)}{16}$ $t \ll d$ $\alpha_e + \alpha_m = \pi d^2 w - \frac{1}{2} w^2 (a + d)$ $t \geq d$	
Half ellipsoidal protrusion with semi axes h radially, a longitudinally, and d azimuthally. ${}_2F_1$ is the hypergeometric function.	$\alpha_e + \alpha_m = 2\pi ahd \left[\frac{1}{I_b} + \frac{1}{I_c - 3} \right]$ $I_b = {}_2F_1\left(1, 1; \frac{5}{2}; 1 - \frac{h^2}{a^2}\right)$, $I_c = {}_2F_1\left(1, \frac{1}{2}; \frac{5}{2}; 1 - \frac{a^2}{h^2}\right)$, if $a = d$ $\alpha_e + \alpha_m = \pi a^3$ if $a = d = h$, $\frac{2\pi h^3}{3[\ln(2h/a) - 1]}$ if $a = d \ll h$ $\alpha_e + \alpha_m = \frac{8h^3}{3} \left[1 + \left(\frac{4}{\pi} - \frac{\pi}{4} \right) \frac{a}{h} \right]$ if $a \ll h = d$ $\alpha_e + \alpha_m = \frac{8\pi h^4}{3a} \left[\ln \frac{2a}{h} - 1 \right]$ if $a \gg h = d$	

<p>Array of pill-boxes, box spacing L, each with gap width g, beam pipe radius b. Gluckstern-Yokoya-Bane formula [15] at high freq. to order $(kg)^{-1}$:</p>	<p>For each cavity of length L with $k = \omega/c$,</p> $Z_0^{\parallel} = \frac{iZ_0L}{\pi kb^2} \left\{ 1 + [1 + i \operatorname{sgn}(k)] \frac{\alpha L}{b} \sqrt{\frac{\pi}{ k g}} \right\}^{-1}$ <p>with $k = \omega/c$. $\alpha = 1$ when $g/L \ll 1$ and $\alpha = \alpha_1 = 0.4648$ when $g/L = 1$, the limiting case of infinitely thin irises. In general, with $\Upsilon = g/L$, $\alpha(\Upsilon) = 1 - \alpha_1 \Upsilon^{1/2} - (1 - 2\alpha_1)\Upsilon + \mathcal{O}(\Upsilon^{3/2})$.</p>
<p>The above pill-box array with radial depth d generates a single-frequency resonance impedance at $\omega_r = c \left(\frac{2L}{bgd} \right)^{1/2}$ [16, 17].</p>	$Z_0^{\parallel} = \frac{Z_0cL}{2\pi b^2} \sum_{\omega'=\pm\omega_r} \left[\pi\delta(\omega-\omega') + \frac{i}{\omega-\omega'} \right]$ $Z_1^{\perp} = \frac{2cL}{b^2\omega} Z_0^{\parallel}$ $W_0'(z) = \frac{Z_0cL}{\pi b^2} \cos \frac{\omega_r z}{c}$ $W_1(z) = \frac{2Z_0L}{\pi b^4\omega_r} \sin \frac{\omega_r z}{c}$ <p>The corresponding resonator per pill box has $\frac{R_s^{(0)}\omega_r}{Q} = \frac{Z_0cL}{\pi b^2}$.</p>
<p>Smooth toroidal b and $R = \frac{1}{2}(a+b)$. As the Lorentz factor $\gamma \rightarrow \infty$, (ultra-relativistic beam), a <u>curvature contribution</u> remains for the longitudinal impedance [18].</p>	<p>Valid from zero frequency up to just below synchronous resonant modes, i.e., $0 < \nu < \sqrt{R/h}$ with $\nu = \omega h/c$,</p> $\frac{Z_0^{\parallel}}{n} = iZ_0 \left(\frac{h}{\pi R} \right)^2 \left\{ \left[1 - e^{-2\pi(b-R)/h} - e^{-2\pi(R-a)/h} \right] \left[1 - 3 \left(\frac{\nu}{\pi} \right)^2 \right] \right.$ $\left. + 0.05179 - 0.01355 \left(\frac{\nu}{\pi} \right)^2 \right\} + \rho$ $\approx iZ_0 \left(\frac{h}{\pi R} \right)^2 \left[A - 3B \left(\frac{\nu}{\pi} \right)^2 \right].$ <p>where ρ is quadratic in ν. As $(b-a)/h$ increases, ρ vanishes exponentially and $A \approx B \approx 1$. In general, $A/B \approx 1$ implying $\operatorname{Im}Z_0^{\parallel}$ changes sign (a node) near $\nu = \pi/\sqrt{3}$.</p>
<p>Rf cage: beam of radius a surrounded by a cylindrical cage or array of N wires of radius ρ_w, length L at radial distance r_w from beam center. Wire filling factor is $f_w = N\rho_w/(\pi r_w)$. Formulas are valid at low frequencies, $0 < n < R/r_w$ and $N \gg 1$.</p>	$\frac{Z_0^{\parallel}}{n} = \frac{iZ_0L}{4\pi R\beta\gamma^2} \left[1 + 2 \ln \frac{r_w}{a} + C_{\parallel} \right], \quad Z_1^{\perp} = \frac{iZ_0L}{2\pi\beta^2\gamma^2} \left[\frac{1}{a^2} - \frac{1 - C_{\perp}}{r_w^2} \right]$ <p>Without metallic beam pipe outside wire array or cage [19],</p> $C_{\parallel} = -\frac{2 \ln(nr_w/R) \ln(\pi f_w)}{N \ln(nr_w/R) + \ln(\pi f_w)}, \quad C_{\perp} = -\frac{2 \ln(\pi f_w)}{N - 2 \ln(\pi f_w)}$ <p>With infinitely conducting metallic beam pipe, radius $b > r_w$ [20],</p> $C_{\parallel} = 2 \ln \frac{b}{r_w} - \frac{2N[\ln(b/r_w)]^2}{N \ln(b/r_w) - \ln(\pi f_w) + \ln[1 - (r_w/b)^{2N}]}$ $C_{\perp} = \frac{[1 - (r_w/b)^2][(r_w/b)^2 + (b/r_w)^2]\{\ln[1 - (r_w/b)^{2N}] - 2 \ln(\pi f_w)\}}{N[1 - (r_w/b)^2] + [(r_w/b)^2 + (b/r_w)^2] \ln[1 - (r_w/b)^{2N}] - 2 \ln(\pi f_w)}$ <p>A ceramic layer between the wires and metallic beam pipe has negligible effect on the impedances.</p>

<p>Wall roughness [13] 1-D axisymmetric bump, $h(z)$ or 2-D bump $h(z, \theta)$. Valid for low frequency $k = \omega/c \ll (\text{bump length or width})^{-1}$, $h \ll b$, pipe radius, and $\nabla h \ll 1$.</p>	<p>1-D: $Z_0^{\parallel} = -\frac{2ikZ_0}{b} \int_0^{\infty} \kappa \tilde{h}(\kappa) ^2 d\kappa$ with spectrum $\tilde{h}(k) = \frac{1}{2\pi} \int_{-\infty}^{\infty} h(z) e^{-ikz} dz$</p> <p>2-D: $Z_0^{\parallel} = -\frac{4ikZ_0}{b} \sum_{m=-\infty}^{\infty} \int_{-\infty}^{\infty} \frac{\kappa^2}{\sqrt{\kappa^2 + m^2/b^2}} \tilde{h}_m(\kappa) ^2 d\kappa$ with spectrum $\tilde{h}_m(k) = \frac{1}{(2\pi)^2} \int_0^{2\pi} d\theta \int_{-\infty}^{\infty} dz h(z, \theta) e^{-ikz-im\theta}$</p>
Heifets and Kheifets formulas for tapered steps and tapered cavity at high frequencies [14].	
<p>Taper in from radius h to b ($< h$), out from radius b to h; tapering angle α. Tapering inefficient for a bunch of rms length σ, if $2(h-b) \tan \alpha \gg \sigma$. All formulas here and below are valid for <i>positive</i> $k = \omega/c$ only.</p>	$\text{Re}Z_0^{\parallel} = \pm \frac{Z_0}{2\pi} \ln \frac{h}{b} + (Z_0^{\parallel})_{\text{step}}, \quad \text{Re}Z_1^{\perp} = \pm \frac{Z_0 b}{4\pi} \left(\frac{1}{b^2} - \frac{1}{h^2} \right) + (Z_1^{\perp})_{\text{step}}$ $(Z_0^{\parallel})_{\text{step}} = \frac{Z_0}{2\pi} \ln \frac{h}{b}, \quad \tan \alpha > \frac{h-b}{kb^2}, \quad (Z_0^{\parallel})_{\text{step}} = \frac{Z_0}{4} kb \tan \alpha, \quad \tan \alpha \ll \frac{1}{kb}$ $(Z_1^{\perp})_{\text{step}} = \frac{Z_0}{4\pi b} \left[1 - \frac{1}{(1+kb)^2} {}_2F_1 \left(1, \frac{3}{2}, 3, \frac{4bh}{(b+h)^2} \right) \right], \quad \tan \alpha > \frac{h-b}{kb^2}, \quad kb \gg 1$ $(Z_1^{\perp})_{\text{step}} = \frac{Z_0 b}{4\pi} \left(\frac{1}{b^2} - \frac{1}{h^2} \right), \quad \tan \alpha > \frac{h-b}{kb^2}, \quad kb \gg 1, \quad h \gg b$ $(Z_1^{\perp})_{\text{step}} = \frac{Z_0}{16b} (kb)^3 \tan \alpha, \quad \tan \alpha \ll \frac{1}{kb}$
<p>Pill-box cavity: total length g, radial depth h without taper. Tapering angle α on both sides, $g \gg h$.</p>	$Z_0^{\parallel} = \begin{cases} \frac{(1+i)Z_0}{2\pi b} \sqrt{\frac{g}{k\pi}} & g \ll kb^2 \\ -i \frac{Z_0}{\pi} \ln \frac{h}{b} & g \gg kb^2 \end{cases}$ $\text{Re}Z_0^{\parallel} = 2(Z_0^{\parallel})_{\text{step}}, \quad \text{Re}Z_0^{\perp} = 2(Z_0^{\perp})_{\text{step}} \quad \text{as given above}$

1.6 Exercises

- 1.1. Prove the properties of the impedances in Eqs. (1.31)-(1.34).
- 1.2. Using a *RLC*-parallel circuit, derive the longitudinal impedance in Eq. (1.40) by identifying $R_{0s} = R$, $\omega_r = 1/\sqrt{LC}$, and $Q = R\sqrt{C/L}$. Then show that the wake function is $W'_0 = 0$ for $z < 0$, and for $z > 0$,

$$W'_0(z) = \frac{\omega_r R_{0s}}{Q} e^{-\alpha z/v} \left[\cos \frac{\bar{\omega} z}{v} - \frac{\alpha}{\bar{\omega}} \sin \frac{\bar{\omega} z}{v} \right], \quad (1.46)$$

with $\alpha = \omega_r/(2Q)$ and $\bar{\omega} = \sqrt{\omega_r^2 - \alpha^2}$. Similarly, show that

$$W_1(z) = -\frac{R_{1s} v \omega_r}{Q \bar{\omega}_r} e^{-\alpha z/v} \sin \frac{\bar{\omega} z}{v}, \quad (1.47)$$

for $z > 0$ and zero otherwise.

- 1.3. Show that the wake functions corresponding to the longitudinal resistive wall impedance of Eq. (1.42) and the transverse resistive wall impedance of Eq. (1.44) for a length ℓ are, respectively,

$$W'_0(z) = -\frac{\beta^{3/2} c \ell}{4\pi b z^{3/2}} \sqrt{\frac{Z_0 \mu_r}{\pi \sigma_c}}, \quad (1.48)$$

$$W_1(z) = -\frac{\beta^{3/2} c \ell}{\pi b^3 z^{1/2}} \sqrt{\frac{Z_0 \mu_r}{\pi \sigma_c}}, \quad (1.49)$$

where b is the beam pipe radius, σ_c is the conductivity and μ_r the relative magnetic permeability of the beam pipe walls. The above are only approximates and are valid for $b\chi^{1/3} \ll z \ll b/\chi$, where $\chi = 1/(b\sigma_c Z_0)$. When $z \ll b\chi^{1/3}$, $W'_0(z)$ should have the proper positive sign.

Bibliography

- [1] W.K.H. Panofsky and W.A. Wenzel, Rev. Sci. Instr. **27**, 967 (1956).
- [2] A.W. Chao, *Physics of Collective Beam Instabilities in High Energy Accelerators*, John Wiley & Sons, 1993, p. 251.
- [3] *Handbook of Accelerator Physics and Engineering*, Ed. A.W. Chao and M. Tigner, 1999, World Scientific.

Chapter 2

LONGITUDINAL PHASE SPACE

2.1 Momentum Compaction

A bunch of charged particles has a spread of energy because of many reasons, for example, random quantum excitation which changes the energy of the particles randomly (for electrons and ultra-high energy protons only), intrabeam scattering which is just Coulomb scattering among the particles, Touschek scattering [1] which is large-angle Coulomb scattering which converts the transverse momentum of a particle into longitudinal, and, most important of all, a means to counter collective instabilities through Landau damping. In an accelerator ring or storage ring, particles with different energies have different closed orbits, their lengths are given by

$$C = C_0 [1 + \alpha_0 \delta + \mathcal{O}(\delta^2)] , \quad (2.1)$$

where δ is the fractional spread in momentum and C_0 is the orbit length of the so-called *on-momentum* particle. The proportionality constant α_0 is called the *momentum-compaction factor* of the accelerator ring. The fraction momentum spread is related to the lowest order fractional energy spread $\Delta E/E_0$ by

$$\delta = \frac{\Delta p}{p_0} \approx \frac{1}{\beta_0^2} \frac{\Delta E}{E_0} . \quad (2.2)$$

where p_0 , E_0 , and $v_0 = \beta_0 c$ are the momentum, energy, and longitudinal velocity of the on-momentum particle. The momentum-compaction factors of most accelerators and

storage rings have the property that $\alpha_0 > 0$, implying that particles with larger energy will travel along longer closed orbits with more radial excursions. A longer closed orbit may imply relatively longer revolution period T . On the other hand, a higher energy particle travels with higher velocity v and the period of revolution will be relatively shorter. The result is a slip in revolution time ΔT (either positive or negative) every turn with respect to the on-momentum particle. The particles inside the bunch will therefore spread out longitudinally and the bunch will disintegrate unless there is some longitudinal focusing force like the rf voltage. Since $T = C/v$, a *slip factor* η can be defined by

$$\frac{\Delta T}{T_0} = \frac{\Delta C}{C_0} - \frac{\Delta v}{v_0} \equiv \eta\delta , \quad (2.3)$$

where T_0 is the revolution period of the on-momentum particle. Thus, to the lowest order in the fractional momentum spread, we have

$$\eta = \alpha_0 - \frac{1}{\gamma_0^2} , \quad (2.4)$$

where $E_0 = \gamma_0 mc^2$ and m is the rest mass of the particle. Higher orders of the slip factor will be given in Chapter 18.

For most electron rings and high energy proton rings, the particle velocity v is extremely close to c , the velocity of light, so that the revolution-time slip is dominated by the increase in orbit length. We therefore have $\eta \approx \alpha_0$ and we call the operation *above the transition energy*. For low-energy hadron rings, the velocity term may dominate making $\eta < 0$ and we say the operation is *below the transition energy*, implying that the velocity change of an off-momentum particle is more important than the change in orbit length. The higher-momentum particle, having a larger velocity, will complete a revolution turn in less time than the on-momentum particle, resulting in a forward slip. Obviously, transition occurs when the velocity change is just as important as the change in orbit length, or $\eta = 0$. The transition energy is defined as $E_t = \gamma_t mc^2$ and $\gamma_t = \alpha_0^{-1/2}$. There are also rings, like the 1.2 GeV CERN Low Energy Antiproton Ring (LEAR) and many newly designed ones [2] that have negative momentum-compaction factors or $\alpha_0 < 0$. In these rings, lower momentum particles have longer closed orbits or larger radial excursions than higher momentum particles. Negative momentum compaction implies an imaginary γ_t and the slip factor will always be negative, indicating that the ring will be always below transition. Some believe that such rings will be more stable against collective instabilities [3]. Design and study of negative momentum compaction rings have been an active branch of research in accelerator physics lately [4].

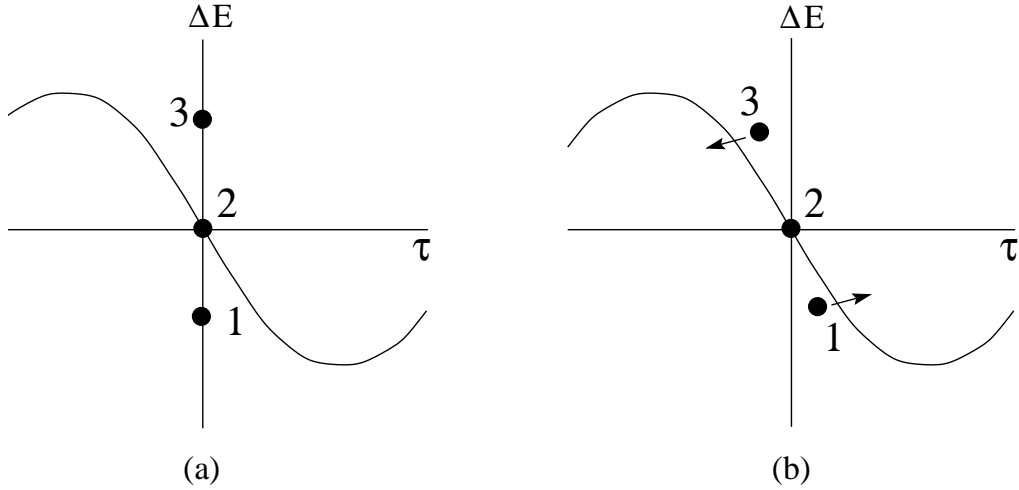


Figure 2.1: Three particles are shown in the longitudinal phase planes. (a) Initially, they are all at the rf phase of 180° and do not gain or lose any energy. (b) One turn later, the on-momentum particle, denoted by 2, arrives with the same phase of 180° without any change in energy. The particle with lower energy, denoted by 1, arrives earlier and gains energy from the positive part of the rf voltage wave at phase $< 180^\circ$. The particle with higher energy, denoted by 3, arrives late and loses energy because it sees the rf voltage wave at phase $> 180^\circ$.

In order to have the particles bunched, a longitudinal focusing force will be required. This is done by the introduction of rf cavities. Consider three particles arriving in the first turn at exactly the same time at a cavity gap, where the rf sinusoidal gap voltage wave is at 180° , as shown in Fig. 2.1a. All three particles are seeing zero rf voltage and are not gaining any energy from the rf wave. The drawing of the rf voltage wave implies that the rf voltage at the cavity gap was positive a short time ago and will be negative a short time later. Assume that the ring is above transition or $\eta > 0$. One turn later, the on-momentum particle, denoted by 2 in the figure, arrives at the cavity gap at exactly the time when the rf sinusoidal voltage curve is again at 180° and gains no energy. At this moment, the positions of the three particles and the rf wave are shown in Fig. 2.1b. The lower energy particle, denoted by 1, arrives at the gap earlier by τ_1 , which we call *time slip*. It sees the positive part of the rf voltage and gains energy. For the second turn, it arrives at the gap earlier by $\tau_1 + \tau_2$, where $\tau_2 < \tau_1$ because the particle energy has been raised in the second passage. This particle will continue to gain energy from the rf every turn and its turn-by-turn additional time slip diminishes. Eventually, this

particle will have an energy higher than the on-momentum particle and starts to arrive at the cavity gap later turn after turn, or its turn-by-turn time slip becomes negative. Similar conclusion can be drawn for the particle, denoted by 3 in the figure, that has initial energy higher than the on-momentum particle. With the rf voltage wave, the off-momentum particles will oscillate around the on-momentum particle and continue to form a bunch. In reality, the particles lose an amount of energy U_s every turn due to synchrotron radiation. This is compensated by shifting the rf phase slightly from 180° to $\phi_s = \sin^{-1}(U_s/V_{\text{rf}})$, where V_{rf} is the rf voltage (the peak value of the rf wave), so that the on-momentum particle will see the rf voltage at the phase ϕ_s when traversing the cavity gap. This particle is also called the *synchronous* particle.

2.2 Equations of Motion

To measure the charge distribution in a bunch, we choose a fixed reference point s_0 along the ring and put a detector there. A particle in a bunch is characterized longitudinally by τ , the time it arrives at s_0 ahead of the synchronous particle. We record the amount of charge arriving when the time advance is between τ and $\tau + d\tau$. The result is $e\rho(\tau)d\tau$, where $\rho(\tau)$ is a measure of the particle distribution* and e is the particle charge. The actual linear particle density per unit length is $\lambda(\tau) = \rho(\tau)/v$, where v is the velocity of the synchronous particle. Note that this charge distribution is measured at a fixed point but at different times. Therefore, it is *not* a periodic function of τ . In one turn, the change in time advance is

$$\Delta\tau = -\eta T_0 \delta . \quad (2.5)$$

The negative sign comes about because the period of a higher-momentum particle is larger above transition ($\eta > 0$) and therefore its time of arrival slips. During that turn, the energy gained by the particle relative to the synchronous particle is

$$\Delta E = eV_{\text{rf}}(\sin \phi - \sin \phi_s) - [U(\delta) - U_s] + C\langle F_0^{\parallel} \rangle - C_0\langle F_{0s}^{\parallel} \rangle , \quad (2.6)$$

where the subscript s stands for synchronous particle. The first term on the right is the sinusoidal rf voltage and the second term is the radiation energy. The third is the average wake force defined in the previous section due to all beam particles ahead; it can therefore be written as, according to Fig. 2.2,

*Note the change in notation. In Chapter 1, ρ represents charge density. From here on, ρ represents particle number density so that $\int \rho(\tau)d\tau = N_b$ the total number of particles in the bunch. The charge density becomes $e\rho$.

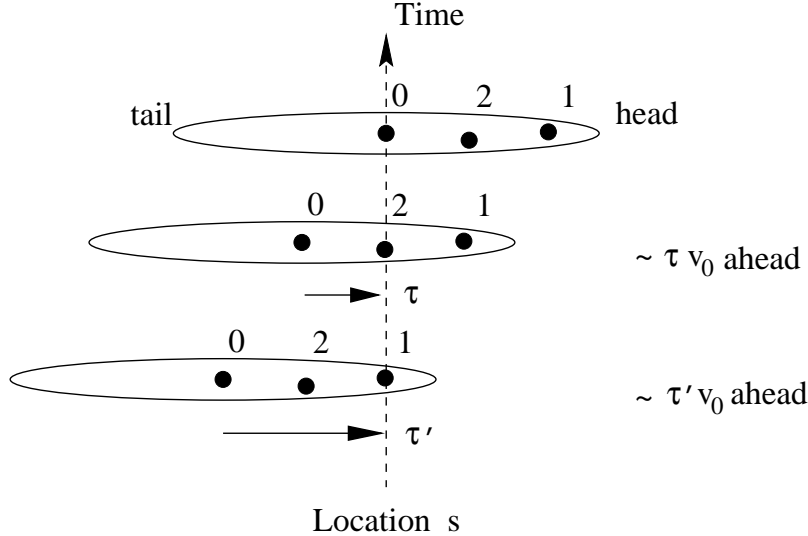


Figure 2.2: Top: the synchronous particle 0 arriving at the location s at the ring. Middle: test particle 2 arriving at s with a time advance τ and seeing the wake left by source particle 1 (bottom) arriving at s with a time advance τ' . Thus test particle is $z \sim v_0(\tau' - \tau)$ behind source particle. The total wake force acting on test particle 2 is the superposition of the wake forces contributed by all particles in the bunch with time advances $\tau' \geq \tau$.

$$\langle F_0^{\parallel}(\tau) \rangle = -\frac{e^2}{C} \int_{\tau}^{\infty} d\tau' \rho(\tau') W'_0(\tau' - \tau) . \quad (2.7)$$

Notice that we have written, for convenience, the wake function as a function of time advance $(\tau' - \tau)$ instead of distance $z \sim v_0(\tau' - \tau)$, with v_0 denoting the velocity of the synchronous particle. There is an approximation here because the particles inside the bunch travel with slightly different velocity. The error, which is less than $\tau_L \Delta v$, is small, where τ_L is the total bunch length in time and Δv is the maximum velocity spread in the bunch. This is actually the rigid-bunch approximation. In the same approximation, we do not distinguish between C and C_0 , the path length of an off-momentum particle and that of the synchronous particle. The signs in Eq. (2.7) and in front of $\langle F_0^{\parallel}(\tau) \rangle$ in Eq. (2.6) can be checked by seeing whether there is an energy loss when substituting the wake of, for example, a real resistance $W'_0(\tau) = R\delta(\tau)$. The synchronous phase ϕ_s in Eq. (2.6) is a parameter chosen to balance the energy loss in a storage ring, or to accomplish a designed rate of increase of energy in an accelerator. The average wake force acting on the synchronous particle, $\langle F_{0s}^{\parallel} \rangle$, can be obtained from Eq. (2.7) by letting $\tau = 0$.

The two equations of motion are related because the momentum spread is related to the energy spread by $\delta = \Delta E / (\beta_0^2 E_0)$, and the rf phase seen is related to the time advance,

$$\phi - \phi_s = -h\omega_0\tau , \quad (2.8)$$

where $\omega_0/(2\pi) = 1/T_0$ is the revolution frequency of the ring for the synchronous particle and h is the rf harmonic, which is the number of oscillations the rf wave makes during one revolution period. The negative sign on the right side of Eq. (2.8) comes about because when the particle arrives earlier or $\tau > 0$, it sees a rf phase *earlier* than the synchronous phase ϕ_s (see Fig. 2.1). Writing as *discrete* differential equations, they become

$$\frac{d\tau}{dn} = -\frac{\eta T_0}{\beta_0^2} \frac{\Delta E}{E_0} , \quad (2.9)$$

$$\frac{d\Delta E}{dn} = eV_{\text{rf}}[\sin(\phi_s - h\omega_0\tau) - \sin \phi_s] - [U(\delta) - U_s] + C_0 \left(\langle F_0^{\parallel} \rangle - \langle F_{0s}^{\parallel} \rangle \right) . \quad (2.10)$$

To simplify future mathematical derivations, a continuous independent variable is needed instead of the discrete turn number n . Time is not a good variable here because particles with different energies complete one revolution turn in different time intervals. Even for one particle, its energy oscillates with synchrotron motion and so is the time for consecutive revolution turns. We choose instead s , the distance measured along the closed orbit of the synchronous particle, because the increase in s per revolution turn is always the length of the closed orbit[†] C_0 of the synchronous particle, regardless of the momentum offset of the beam particle under consideration. This transition from discrete turn number n to the continuum is a good approximation, because in reality it takes a particle many (~ 50 to 100 in electron rings and ~ 200 to 1000 in proton rings) revolution turns to complete a synchrotron oscillation, and it takes the beam a large number of turns for an instability to develop.

With τ and ΔE as the canonical variables[‡], the equations of motion for a particle in a small bunch become

$$\frac{d\tau}{ds} = -\frac{\eta}{v_0 \beta_0^2 E_0} \Delta E , \quad (2.11)$$

$$\frac{d\Delta E}{ds} = \frac{eV_{\text{rf}}}{C_0} \left[\sin(\phi_s - h\omega_0\tau) - \sin \phi_s \right] - \frac{U(\Delta E) - U_s}{C_0} + \langle F_0^{\parallel}(\tau, s) \rangle - \langle F_{0s}^{\parallel}(s) \rangle . \quad (2.12)$$

[†]In subsequent chapters, the subscript ‘0’ in C_0 , E_0 , v_0 , β_0 , γ_0 , etc for the synchronous particle may be omitted in order to simplify the notation.

[‡]This set of canonical variables should not be used if the accelerator is ramping. Instead the set τ/ω_0 and $\Delta E/\omega_0$ is preferred

Although one may also use $t = s/v_0$ as the independent variable, we want to emphasize that this t is the time describing the synchronous particle and is *not* the time variable for an off-energy particle. Thus, the independent variable s is quite different from the time variable.

Let us first neglect the wake potential and also the small difference between the energy lost by the off-momentum particle $U(\delta)$ and the energy lost by the on-momentum particle U_s . For small amplitude oscillations, the two equations combine to give

$$\frac{d^2\tau}{ds^2} - \frac{2\pi\eta heV_{rf}\cos\phi_s}{C_0^2\beta_0^2E_0}\tau = 0. \quad (2.13)$$

Therefore, the bunch particles are oscillating with the angular frequency $\omega_{s0} = \nu_{s0}\omega_0$, where

$$\nu_{s0} = \sqrt{-\frac{\eta heV_{rf}\cos\phi_s}{2\pi\beta_0^2E_0}} \quad (2.14)$$

is called the *synchrotron tune* or the number of synchrotron oscillations a particle makes in one revolution turn, and $\omega_{s0} = \nu_{s0}\omega_0$ the *synchrotron angular frequency*. The subscript “0” indicates that these are the *unperturbed* small-amplitude values or with the wake potential turned off. The negative sign inside the square root implies that ϕ_s should be near 180° in the second quadrant above transition ($\eta > 0$), but near 0° in the first quadrant below transition ($\eta < 0$). Synchrotron motion is slow and the synchrotron tune is usually of the order of 0.001 to 0.01. When the oscillation amplitude becomes larger, the rf sine wave cannot be linearized. The focusing force is smaller and the synchrotron tune ν_s for maximum phase excursion $\hat{\phi}$ will become smaller as is shown in Fig. 2.3 according to

$$\nu_s(\hat{\phi}) = \frac{\pi\nu_{s0}}{2K(\sin\frac{1}{2}\hat{\phi})}, \quad (2.15)$$

where

$$K(x) = \int_0^{\pi/2} \frac{du}{\sqrt{1-x^2\sin^2 u}} \quad (2.16)$$

is the complete elliptic integral of the first kind. This prediction has been verified experimentally at the Indiana University Cyclotron Facility (IUCF) Cooler Ring [5]. In the small-amplitude approximation, we have $\nu_s(\hat{\phi}) = \nu_{s0}\left(1 - \frac{1}{12}\hat{\phi}^2\right)$. In other words, there will be a spread in the synchrotron tune among the particles in the bunch, which will be very essential to the Landau damping of the collective instabilities to be discussed later. As the oscillation amplitude continues to increase, a point will be reached when

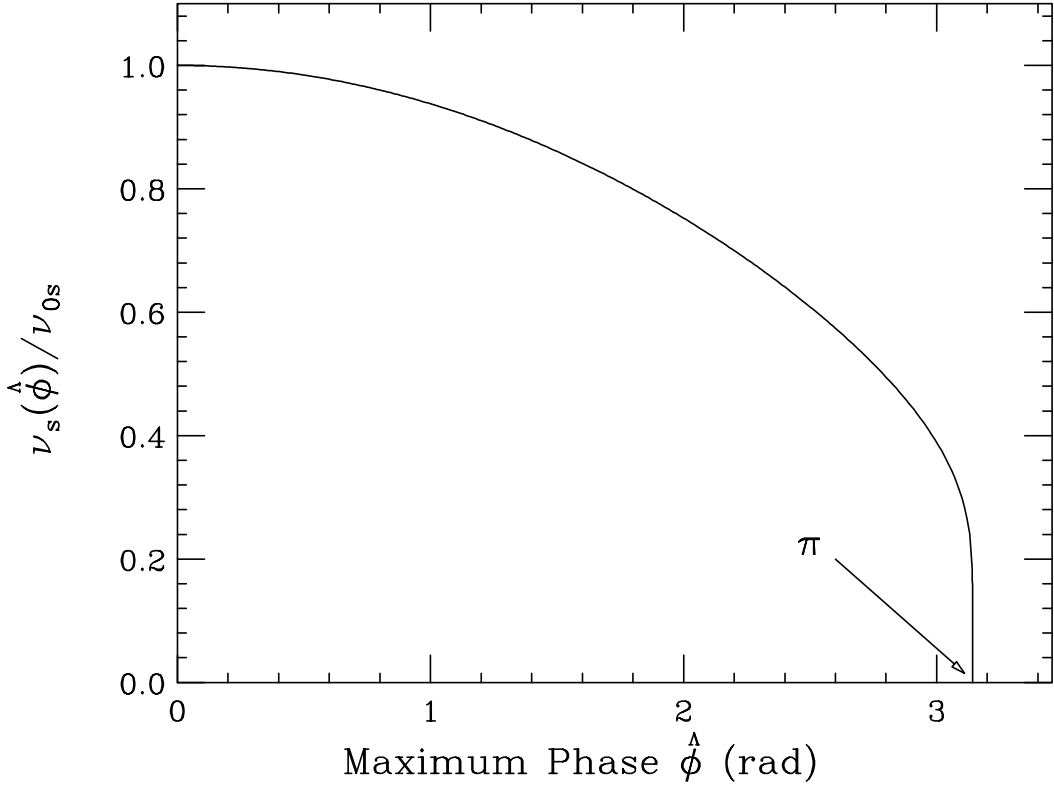


Figure 2.3: Plot showing the synchrotron frequency decreasing to zero at the edge of the rf bucket.

there is no more focusing provided by the rf voltage anymore. This boundary in the τ - ΔE phase space provides the maximum possible bunch area allowed and is called the *rf bucket* holding the bunch. Any particle that goes outside the bucket will be lost. The equation of motion is, in fact, exactly that of a pendulum, whose frequency of oscillation decreases with amplitude. If we start the pendulum motion at its rest position with too large a kinetic energy, the pendulum will no longer be in oscillatory motion. It will wrap around the point of support performing librations instead. This critical angular amplitude of the pendulum is $\pm\pi$, exactly the same for the rf bucket. Figure 2.4 illustrates some stationary buckets (when the synchronous phase $\phi_s = 180^\circ$ above transition) and moving or accelerating buckets (when ϕ_s is between 90° and 180°). The figure also shows the trajectories of libration outside the buckets. The horizontal axis is the rf phase (instead of the time advance used in Fig. 2.1); the trajectories

therefore move clockwise (instead of counter-clockwise in Fig. 2.1).

If the radiation energy is neglected, the two equations of motion are derivable from the Hamiltonian

$$H = -\frac{\eta}{2v_0\beta_0^2E_0}(\Delta E)^2 - \frac{eV_{\text{rf}}}{C_0h\omega_0} \left[\cos(\phi_s - h\omega_0\tau) - \cos \phi_s - h\omega_0\tau \sin \phi_s \right] + V(\tau) , \quad (2.17)$$

with the aid of the Hamiltonian equations

$$\begin{cases} \frac{d\tau}{ds} = \frac{\partial H}{\partial \Delta E} , \\ \frac{d\Delta E}{ds} = -\frac{\partial H}{\partial \tau} . \end{cases} \quad (2.18)$$

The potential of the wake force is given by

$$V(\tau) = \frac{e^2}{C_0} \int_0^\tau d\tau'' \left[\int_{-\infty}^\infty d\tau' \rho(\tau') W'_0(\tau' - \tau'') - \int_{-\infty}^\infty d\tau' \rho(\tau') W'_0(\tau') \right] . \quad (2.19)$$

The second term in the squared brackets comes from $\langle F_{0s}^{\parallel} \rangle$, the energy lost by the synchronous particle due to the wake potential of the vacuum chamber. In Eq. (2.17), the $\cos \phi_s$ term is added to adjust the rf potential to zero for synchronous particles ($\tau = 0$). For small-amplitude oscillations, the Hamiltonian simplifies to

$$H = -\frac{\eta}{2v_0\beta_0^2E_0}(\Delta E)^2 - \frac{\omega_{s0}^2\beta_0^2E_0}{2\eta v_0}\tau^2 + V(\tau) , \quad (2.20)$$

where $\omega_{s0} = \nu_{s0}\omega_0$, the synchrotron angular frequency for small amplitudes, is given by Eq. (2.14).

In an electron ring, synchrotron radiation may provide damping to many collective instabilities. Because this damping force is dissipative in nature, strictly speaking a Hamiltonian formalism does not apply. However, the synchrotron radiation damping time is usually very much longer than the synchrotron period. The fast growing instabilities will evolve to their full extent before the damping mechanism becomes materialized. Here, we are interested mostly in studying those instabilities that grow within one radiation damping time of the ring. For a time period much less than the radiation damping time, radiation can be neglected and the Hamiltonian formalism therefore applies.

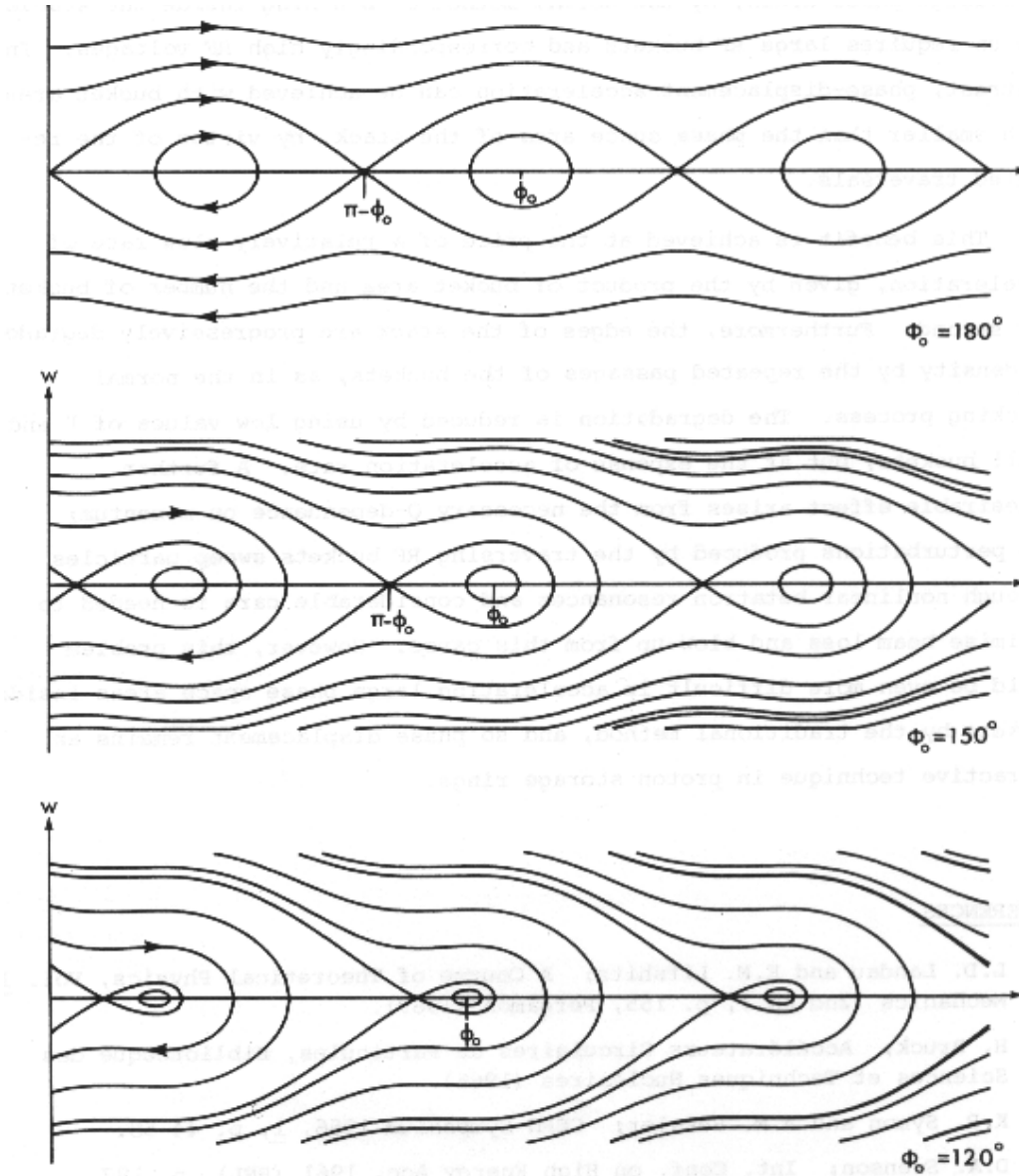


Figure 2.4: The trajectories in the longitudinal phase space above the transition energy. Top plot shows the stationary buckets when the synchronous phase $\phi_0 = 180^\circ$. Middle and lower plots show the moving or accelerating buckets when the synchronous phases are, respectively, $\phi_0 = 150^\circ$ and 120° . The moving buckets shrink when the synchronous phase decreases from 180° towards 90° . Notice that the horizontal axis is the rf phase (instead of arrival time in Fig. 2.1); the directions of the trajectories are therefore clockwise above transition.

2.3 Vlasov Equation

We would like to study the evolution of a bunch that contains, say, 10^{12} particles. The Hamiltonian in Eq. (2.17) has to be modified to include 10^{12} sets of canonical variables in order to fully describe the bunch. The description of the motion of a collection of 10^{12} particles is known as the *particle approach*, and is often tackled in the time domain. However, what are of interest to us are the collective behaviors of the bunch like the motion of its centroid, the evolution of the particle distribution, etc. In other words, we are studying here the evolution of various modes of motion of these collective variables. For 10^{12} particles, there are 10^{12} modes of motion. However, we will never be interested in those modes whose wavelengths are of the order of the separation between two adjacent particles inside the bunch, because they correspond to motions of very high frequencies, and those motions are microscopic in nature. What we would like to study are the macroscopic modes of the bunch, or those having wavelengths of the same order as the length of the bunch or the radius of the vacuum chamber. Sometimes, we may even want to study modes with wavelengths one tenth or one hundredth of the bunch length or beam pipe radius, but definitely not down to the microscopic size like the distance between two neighboring beam particles. In other words, we go to the frequency domain and look at the different modes of motion of oscillation of the bunch as a whole. Our interest is on those few modes that have the lowest frequencies or longest wavelengths. This direction of study is known as the *mode approach*.

When collisions are neglected, the basic mathematical tool for the mode approach is the Vlasov equation or the Liouville theorem [6]. It states that if we follow the motion of a representative particle in the longitudinal or τ - ΔE phase space, the density of particles in its neighborhood is constant. In other words, the distribution of particles $\psi(\tau, \Delta E; s)$ moves in the longitudinal phase space like an incompressible fluid. Mathematically, the Vlasov equation reads

$$\frac{d\psi}{ds} = \frac{\partial\psi}{\partial s} + \frac{d\tau}{ds} \frac{\partial\psi}{\partial\tau} + \frac{d\Delta E}{ds} \frac{\partial\psi}{\partial\Delta E} = 0 . \quad (2.21)$$

In terms of the Hamiltonian, it becomes

$$\frac{\partial\psi}{\partial s} + [\psi, H] = 0 , \quad (2.22)$$

where $[,]$ denotes the Poisson bracket. Here, the time of early arrival τ and the energy offset ΔE are the set of canonical variables chosen. The Poisson bracket is therefore

$$[\psi, H] = \frac{\partial\psi}{\partial\tau} \frac{\partial H}{\partial\Delta E} - \frac{\partial\psi}{\partial\Delta E} \frac{\partial H}{\partial\tau} . \quad (2.23)$$

Together with the Hamiltonian equations of Eq. (2.18), Eq. (2.21) is reproduced.

If radiation is included in the discussion, one must extend the Vlasov equation to the Fokker-Planck equation [7]

$$\frac{d\psi}{ds} = A \frac{\partial}{\partial \Delta E} (\Delta E \psi) + \frac{D}{2} \frac{\partial^2 \psi}{\partial \Delta E^2}, \quad (2.24)$$

where A and D are related, respectively, to the damping and diffusion coefficients.

2.4 Coasting Beams

A coasting beam is not bunched. There is no rf voltage and therefore no synchrotron oscillation. Thus, there is no synchronous particle. For the longitudinal position, we can make reference with respect to a designated point in the accelerator ring. For the energy offset, we can make reference with respect to the average energy change for all the on-momentum particles. Here, we cannot talk about bunch modes. Instead, the linear density of an excitation of the beam can be described much better by an harmonic wave,

$$f_1(\theta, t) \sim e^{in\theta - \Omega t}, \quad (2.25)$$

where θ is the azimuthal angle around the ring measured from a point of reference, n is a revolution harmonic or n modulations of the longitudinal linear density when viewed from the top of the accelerator ring at a fixed time t , and Ω is the angular velocity of the wave. The harmonic $n = 0$ should be excluded because it will violate charge conservation since the integral of f_1 over the whole ring does not vanish when $n = 0$. The excitation of Eq. (2.25) is a *snapshot* view, similar to taking a picture of the beam above the accelerator ring. Thus the linear density is a periodic function of θ with period 2π . The linear density can therefore be expanded as a Fourier series and the excitation $f_1(s, t)$ is just a Fourier component. To describe a beam particle, we use the canonical variable z and ΔE , where $z = R\theta$ with $R = C_0/(2\pi)$ being the mean radius of the on-momentum closed orbit. Here, z is just the longitudinal distance ahead of the point of reference at time t and ΔE is the energy offset. Since we are using snapshot description, the real time t can be used as the continuous independent variable. The equations of motion are

$$\frac{dz}{dt} = -\frac{\eta \Delta E}{v_0 \beta_0^2 E_0}, \quad (2.26)$$

$$\frac{d\Delta E}{dt} = -\frac{U - U_s}{T_0} + v_0 \langle F_0^\parallel(z, t) \rangle - v_0 \langle F_{0s}^\parallel(t) \rangle, \quad (2.27)$$

where v_0 and T_0 are, respectively, the velocity and revolution period of the on-momentum particle, $\langle F_0^{\parallel}(z, t) \rangle$ is the average longitudinal wake force acting on the beam particle under consideration and $\langle F_{0s}^{\parallel}(t) \rangle$ is the average of the average longitudinal wake force acting on all the on-momentum particles. The subtraction of $\langle F_{0s}^{\parallel}(t) \rangle$ is necessary, because sometimes the average wake force may have a dc resistive term and we do not want to include it in our discussion since it is usually compensated, for example, by a dc gap voltage. Otherwise, the beam will continue to lose energy and will not be able to stay inside the vacuum chamber.

When synchrotron radiation is neglected, the equations of motion can be derived from the Hamiltonian

$$H = -\frac{\eta\Delta E}{2v_0\beta_0^2E_0} + \int_0^z \left[\langle F_0^{\parallel}(z', t) \rangle - \langle F_{0s}^{\parallel}(t) \rangle \right] v_0 dz' . \quad (2.28)$$

For the beam distribution $\psi(z, \Delta E; t)$ in the longitudinal phase space, the Vlasov equation becomes

$$\frac{\partial\psi}{\partial t} + \frac{dz}{dt} \frac{\partial\psi}{\partial z} + \frac{d\Delta E}{dt} \frac{\partial\psi}{\partial\Delta E} = 0 , \quad (2.29)$$

where dz/dt and $d\Delta E/dt$ are given by the equations of motion. It is important to realize that dz/dt is *not* the longitudinal velocity v of the particle having energy offset ΔE . Instead, it represents the phase slip (in length) per revolution period T_0 .

2.5 Exercises

- 2.1. The Hamiltonian of Eq. (2.17) describes motion in the longitudinal phase space, when the wake potential $V(\tau)$ is not included. With the effects of the wake potential neglected, find the fixed points of the Hamiltonian above and below transition, and determine whether they are stable or not. The separatrices are the contours of fixed Hamiltonian values that pass through the unstable fixed points. They separate the region of libration motion from rotation motion[§]. Plot the separatrices.
- 2.2. The canonical variables τ_0 and ΔE_0 evaluated at ‘time’ $s = 0$ become τ_1 and ΔE_1 at an infinitesimal time Δs later according to

$$\tau_1 = \tau_0 + \frac{\partial H}{\partial \Delta E_0} \Delta s, \quad \Delta E_1 = \Delta E_0 - \frac{\partial H}{\partial \tau_0} \Delta s. \quad (2.30)$$

Consider the small phase-space area element $d\tau_0 d\Delta E_0 = J d\tau_1 d\Delta E_1$. Show that the Jacobian $J = 1$ to the first order in Δs , implying that the area surrounding a given number of particles does not change in time, which is Liouville Theorem. It is possible to prove $J = 1$ to all orders in Δs using canonical transformation. See, for example, H. Goldstein, *Classical Mechanics*, Addison-Wesley, Chapter 8-3.

- 2.3. Starting from the Hamiltonian in Eq. (2.17) with the synchronous phase $\phi_s = 0$ or π but in the absence of the wake potential, derive the synchrotron tune, Eq. (2.3), of a particle having an rf phase amplitude $\hat{\phi}$. Repeat the derivation for any arbitrary synchronous phase.

[§]Libration implies periodic motion in the phase space, similar to a sine wave going from $-\infty$ to $+\infty$. Rotation motion in phase space implies to-and-fro oscillatory motion.

Bibliography

- [1] C. Bernardine, *et al*, Phys. Rev. Lett. **10**, 407 (1963).
- [2] *JHP Accelerator Design Study Report*, KEK Report 97-16, JHF-97-10, 1997; K.Y. Ng, D. Trbojevic, and S.Y. Lee, Proceedings of 1991 IEEE Particle Accelerator Conference, San Francisco, 1991, Ed. Lizama (IEEE, New York, 1991), pp. 159; C. Ankenbrandt, *et al*, Phys. Rev. ST Accel. Beams 1, 081001 (1999).
- [3] S.X. Fang, K. Oide, K. Yokoya, B. Chen, J.Q. Wang, Proceedings of 1995 Particle Accelerator Conference, Dallas, pp. 3064.
- [4] S.Y. Lee, K.Y. Ng, and D. Trbojevic, Phys. Rev. **E4**, 3040 (1993); S.Y. Lee, K.Y. Ng, and D. Trbojevic, Fermilab Internal Report FN-595, 1992.
- [5] H. Huang, et al., Phys. Rev. **E48**, 4678 (1993).
- [6] A.A. Vlasov, J. Phys. USSR **9**, 25 (1945).
- [7] H. Risken, *The Fokker-Planck Equation*, 2nd Edition, Springer-Verlag, N.Y., 1989.

Chapter 3

POTENTIAL-WELL DISTORTION

3.1 Static Solution

The wake potential affects the particle bunch in two ways. Static perturbation changes the shape of the bunch, while time-dependent perturbation can lead to instability of the bunch. This is analogous to quantum mechanics, where time-independent perturbation shifts the energy levels while time-dependent perturbation causes transition. In this chapter, we are going to study stationary bunch distributions, or distributions influenced by the time-independent perturbation of the wake potential. This alteration of bunch distribution is called *potential-well distortion*.

From the Vlasov equation depicted in Eq. (2.21), it is evident that the solution for the stationary particle distribution $\psi(\tau, \Delta E)$ in the longitudinal phase space must satisfy

$$[\psi, H] = 0 , \quad (3.1)$$

or it is sufficient that ψ is a function of the Hamiltonian,

$$\psi = \psi(H) . \quad (3.2)$$

Recall that the Hamiltonian of a particle with small amplitude synchrotron oscillations is

$$H = -\frac{\eta}{2v\beta^2 E_0} (\Delta E)^2 - \frac{\omega_{s0}^2 \beta^2 E_0}{2\eta v} \tau^2 + V(\tau) , \quad (3.3)$$

which describes the motion of a beam particle in the potential well

$$U(\tau) = -\frac{\omega_{s0}^2 \beta^2 E_0}{2\eta v} \tau^2 + V(\tau) , \quad (3.4)$$

where ΔE and τ are the energy offset and time advance of the beam particle, while the synchronous particle has energy E_0 , velocity* $v = \beta c$, bare synchrotron angular frequency ω_{s0} , and slip factor η . Here, the potential-well contributed by the wake function is [Eqs. (2.7), (2.12), and (2.18)],

$$V(\tau) = \frac{e^2}{C_0} \int_0^\tau d\tau'' \int_{\tau''}^\infty d\tau' \rho(\tau') W'_0(\tau' - \tau'') , \quad (3.5)$$

where C_0 is the length of the designed closed orbit, W'_0 is the longitudinal monopole wake function, and $\rho(\tau)$ is the linear particle density under the influence of the wake. When the effects of the wake potential is removed, this is just a parabolic potential well. In the presence of the wake potential, the potential well is distorted and the distribution of the beam particle in the longitudinal phase space is therefore modified. As will be seen below, a purely reactive wake potential, meaning that the coupling impedance is either inductive or capacitive, will modify the parabolic potential in such a way that the potential well remains symmetric. Correspondingly, the distorted particle distribution will also be head-tail symmetric, assuming that the original particle distribution in the rf potential along is symmetric. A wake potential with a resistive component, however, will affect the symmetry of the parabolic potential well so that the bunch distribution will no longer be head-tail symmetric.

3.2 Reactive Force

Consider a particle beam with linear density $\rho(s, t)$ traveling in the positive s direction with velocity v inside a cylindrical beam pipe of radius b with infinitely-conducting walls. The axis of the beam coincides with the axis of the beam pipe. The beam is assumed to be rigid; therefore $\rho = \rho(s - vt)$. We also assume at this moment that the beam is uniformly distributed transversely within a radius a which does not vary longitudinally. We are interested in the longitudinal electric field E_s seen by the beam particles at the axis of the beam. To compute that we invoke Faraday's law,

$$\vec{\nabla} \times \vec{E} = -\frac{\partial}{\partial t} \vec{B} , \quad (3.6)$$

*Here, we drop the subscript "0" for v and β for the sake of convenience.

or in the integral form,

$$\oint \vec{E} \cdot d\ell = -\frac{\partial}{\partial t} \oint \vec{B} \cdot d\vec{A} . \quad (3.7)$$

In above, the closed path of integration of the electric field \vec{E} is along two radii of the beam pipe at s and $s + ds$ together with two length elements at the beam axis and the wall of the beam pipe, as illustrated in Fig. 3.1. The area of integration of the magnetic

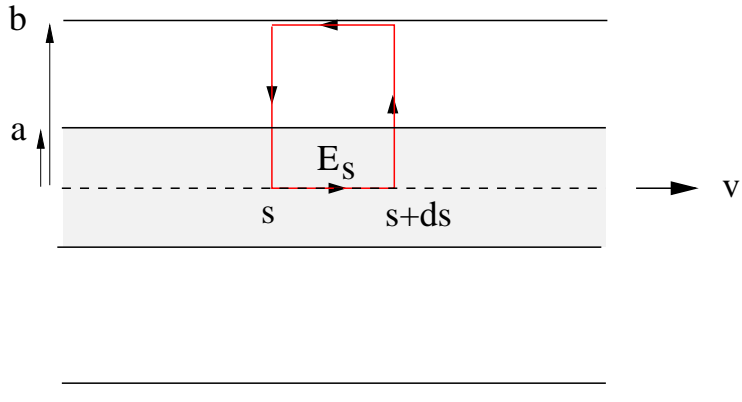


Figure 3.1: (color) Derivation of the space charge longitudinal electric field E_s experienced by a beam particle in a beam of radius a in an infinitely conducting beam pipe of radius b .

flux density \vec{B} is the area enclosed by the closed path. Now, the left side of Eq. (3.7) becomes

$$\text{L. S.} = E_s ds + \frac{e\rho(s+ds-vt)}{2\pi\epsilon_0} \left[\int_0^a \frac{r dr}{a^2} + \int_a^b \frac{dr}{r} \right] - \frac{e\rho(s-vt)}{2\pi\epsilon_0} \left[\int_0^a \frac{r dr}{a^2} + \int_a^b \frac{dr}{r} \right] , \quad (3.8)$$

while the right side

$$\text{R. S.} = -\frac{\partial}{\partial t} \frac{\mu_0 e \rho(s-vt)v}{2\pi} \left[\int_0^a \frac{r dr}{a^2} + \int_a^b \frac{dr}{r} \right] ds . \quad (3.9)$$

Assumption has been made that the open angle $1/\gamma$ of the radial electric field is small compared with the distance ℓ over which the linear density changes appreciably, or $b/\gamma \ll \ell$. Here, $\gamma = E_0/(mc^2)$ and m is the rest mass of the beam particle. In terms of the squared-bracketed expressions in Eqs. (3.8) and (3.9), we can define

$$g_0 = 2 \left[\int_0^a \frac{r dr}{a^2} + \int_a^b \frac{dr}{r} \right] = 1 + 2 \ln \frac{b}{a} , \quad (3.10)$$

which is a geometric factor depending on the geometry of the beam and the beam pipe, and it will deviate from Eq. (3.10) if we relax, for example, the restriction of the transverse uniformity of the particle distribution. Combining the above, we arrive at

$$E_s + \frac{eg_0}{4\pi\epsilon_0} \frac{\partial\rho}{\partial s} = v^2 \frac{e\mu_0 g_0}{4\pi} \frac{\partial\rho}{\partial s}, \quad (3.11)$$

or

$$E_s = -\frac{eg_0}{4\pi\epsilon_0\gamma^2} \frac{\partial\rho}{\partial s}, \quad (3.12)$$

which is the space charge force experienced by a particle in a beam. In the reduction from Eq. (3.10) to Eq. (3.12), use has been made of the relation $\epsilon_0\mu_0 = c^{-2}$.

The first application is a longitudinal harmonic wave

$$\rho_1(s, t) \propto e^{i(ns/R - \Omega t)}, \quad (3.13)$$

perturbing a coasting beam of uniform linear density ρ_0 , where n is a revolution harmonic, R is the radius of the accelerator ring, and Ω is the frequency of the wave. It will be shown in Chapter 6 that $\Omega \approx n\omega_0 = nv/R$; the difference comes from the perturbation of the coupling impedance. Thus, ρ_1 is roughly a function of $s - vt$. Substitution into Eq. (3.12) results in the voltage

$$V = -E_s C_0 = \frac{ineZ_0cg_0}{2\gamma^2} \rho_1 \quad (3.14)$$

seen by a beam particle per accelerator turn. The perturbing wave constitutes a perturbing current $I_1 = e\rho_1 v$. Therefore, the space charge impedance per harmonic seen is

$$\left. \frac{Z_0^{\parallel}}{n} \right|_{\text{sp ch}} = \frac{iZ_0g_0}{2\gamma^2\beta}, \quad (3.15)$$

which is to be compared with Eq. (1.36). From Eq. (3.12), the space charge force experienced by a beam particle at position s and time t becomes

$$F(s, t) = \frac{ie^2v}{2\pi} \left. \frac{Z_0^{\parallel}}{n} \right|_{\text{sp ch}} \frac{\partial\rho(s, t)}{\partial s}. \quad (3.16)$$

Since an inductive impedance can be viewed as a negative space charge impedance, we can write the force due to a general reactive impedance as

$$F(s, t) = \frac{ie^2v}{2\pi} \left. \frac{Z_0^{\parallel}}{n} \right|_{\text{reactive}} \frac{\partial\rho(s, t)}{\partial s}. \quad (3.17)$$

When the position of the beam particle is measured in terms of time advanced τ ahead of the synchronous particle, the particle linear distribution $\lambda(\tau, t)$, which is normalized to the total number of beam particles, is related to $\rho(s, t)$ by

$$\rho(s, t)ds = \lambda(\tau, t)d\tau \quad \text{or} \quad \frac{\partial\rho(s, t)}{\partial s} = \frac{1}{v^2} \frac{\partial\lambda(\tau, t)}{\partial\tau} . \quad (3.18)$$

The reactive force exerted on a beam particle becomes

$$F(\tau, t) = \frac{ie^2}{2\pi v} \frac{Z_0^{\parallel}}{n} \left|_{\text{reactive}} \right. \frac{\partial\lambda(\tau, t)}{\partial\tau} . \quad (3.19)$$

Of course, the above expression can also be obtained by substituting the reactive wake function

$$W'_0(\tau) = \delta'(\tau) \left[\frac{i}{\omega_0} \frac{Z_0^{\parallel}}{n} \right]_{\text{reactive}} \quad (3.20)$$

directly into Eq. (2.7).

The second application is on potential-well distortion. For a bunch, the head has a negative slope or $\partial\lambda/\partial\tau < 0$, while the tail has a positive slope or $\partial\lambda/\partial\tau > 0$. For a space charge impedance, the head of the bunch is therefore accelerated and gains energy, while the tail decelerated and loses energy. Below transition, the head arrives earlier after one turn while the tail arrives later, resulting in the spreading out of the bunch. The space charge force therefore distorts the rf potential by counteracting the rf focusing force. On the other hand, an inductive force enhances the rf focusing. The opposite is true above transition.

3.3 Haissinski Equation

For an electron bunch, because of the random quantum radiation and excitation, the stationary distribution should have a Gaussian distribution in ΔE , or

$$\psi(\tau, \Delta E) = \frac{1}{\sqrt{2\pi}\sigma_E} \exp\left(-\frac{\Delta E^2}{2\sigma_E^2}\right) \rho(\tau) , \quad (3.21)$$

where σ_E is the rms beam energy spread determined by synchrotron radiation. Noting Eq. (3.2) and the Hamiltonian in Eq. (3.3), we must have

$$\psi(\tau, \Delta E) \propto \exp\left(\frac{v\beta^2 E_0}{\eta\sigma_E^2} H\right) . \quad (3.22)$$

The linear density or distribution $\rho(\tau)$ is obtained by an integration over ΔE . Since Hamiltonian H depends on $\rho(\tau)$ [see, for example, Eqs. (2.19) and (2.20)], we finally arrive at a self-consistent equation for the linear density,

$$\rho(\tau) = \rho(0) \exp \left[- \left(\frac{\omega_{s0} \beta^2 E_0}{\eta \sigma_E} \right)^2 \frac{\tau^2}{2} + \frac{e^2 \beta^2 E_0}{\eta T_0 \sigma_E^2} \int_0^\tau d\tau'' \int_{\tau''}^\infty d\tau' \rho(\tau') W'_0(\tau' - \tau'') \right]. \quad (3.23)$$

This is called the *Haissinski equation* [1], where the constant $\rho(0)$ is obtained by normalizing to the total number of particles in the bunch:

$$\int d\tau \rho(\tau) = N. \quad (3.24)$$

The solution will give a linear distribution that deviates from the Gaussian form, and we call this *potential-well distortion*. Since the rf voltage is modified, the angular synchrotron frequency also changes from ω_{s0} to the perturbed incoherent ω_s accordingly.

For a purely resistive impedance $Z_0^{\parallel}(\omega) = R_s$ with the wake function $W'_0(z) = R_s \delta(z/v)$, the equation can be solved analytically giving the solution [3]

$$\rho(\tau) = \frac{\sqrt{2/\pi} e^{-\tau^2/(2\sigma_\tau^2)}}{\alpha_R \sigma_\tau \{ \coth(\alpha_R N/2) - \text{erf}[\tau/(\sqrt{2}\sigma_\tau)] \}}, \quad (3.25)$$

where

$$\sigma_\tau = \frac{|\eta| \sigma_E}{\beta^2 \omega_{s0} E_0}, \quad \alpha_R = \frac{e^2 \beta^2 E_0 R_s}{\eta T_0 \sigma_E^2}, \quad (3.26)$$

and

$$\text{erf}(x) = \frac{2}{\sqrt{\pi}} \int_0^x e^{-t^2} dt \quad (3.27)$$

is the error function. For a weak beam with $|\alpha_R|N \lesssim 1$, the peak beam density occurs at

$$\tau = \frac{\alpha_R N}{\sqrt{2\pi}} \sigma_\tau. \quad (3.28)$$

This peak moves forward above transition ($\alpha_R > 0$) and backward below transition ($\alpha_R < 0$) as the beam intensity increases. This effect comes from the parasitic loss of the beam particle which is largest at the peak of the linear density $\rho(\tau)$ and smallest at the two ends. Those particles losing energy will arrive earlier/later than the synchronous particle in time above/below transition and the distribution will therefore lean forward/backward. Such bunch profiles are plotted in Fig. 3.2 for $\alpha_R N = -10, -5, 0$,

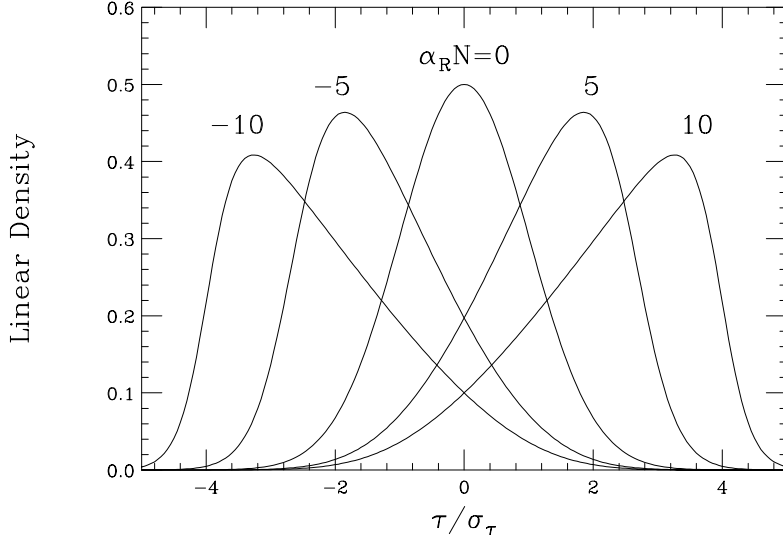


Figure 3.2: Plot of bunch profiles between $\pm 5 \sigma$ s for $\alpha_R N = -10, -5, 0, 5$, and 10 , according to the solution of the Haissinski equation when the impedance is purely resistive. These profiles are normalized to $\sigma_\tau \sqrt{\pi/2}$ when integrated over τ . It is evident that the profile leans forward above transition ($\alpha_R > 0$) and backward below transition ($\alpha_R < 0$).

5, and 10. In the plots, the linear densities are normalized to $\sigma_\tau \sqrt{\pi/2}$ when integrated over τ .

When the longitudinal impedance is purely inductive, $W'_0(z) = L\delta'(z/v)$, the double integrals can be performed and the Haissinski equation becomes

$$\rho(\tau) = ke^{-\tau^2/(2\sigma_\tau^2) - \alpha_L \rho(\tau)}, \quad (3.29)$$

where k is a positive constant and $\alpha_L = e^2 \beta^2 E_0 L / (\eta T_0 \sigma_E^2)$. The above can be rewritten as

$$\rho(\tau) e^{\alpha_L \rho(\tau)} = ke^{-\tau^2/(2\sigma_\tau^2)}. \quad (3.30)$$

The right side is an even function of τ and so must be the left side, $\rho e^{\alpha_L \rho}$. Thus, it appears that the distorted distribution ρ is also an even function of τ . The linear distribution will remain left-right symmetric. Thus, the reactive part of the impedance will either lengthen or shorten the bunch, while the resistive part will cause the bunch to lean forward or backward. When $|\alpha_L|N \lesssim 1$, we can iterate,

$$\rho \approx ke^{-\tau^2/(2\sigma_\tau^2)} \left(1 - k\alpha_L e^{-\tau^2/(2\sigma_\tau^2)} \right). \quad (3.31)$$

Without the impedance term, k in Eq. (3.29) represents the particle density at the center of the bunch. Now for $\alpha_L > 0$, Eq. (3.31) says that effectively k becomes smaller. In other words, the distribution spreads out, or the effective rms bunch length becomes larger than σ_τ . This is the situation of either a repulsive inductive impedance force above transition or a repulsive capacitive force ($L < 0$) below transition. On the other hand, for an attractive inductive force below transition or an attractive capacitive force above transition, $\alpha_L < 0$. The bunch will be shortened.

For a general wake function, the Haissinski equation can only be solved numerically. The equation, however, can be cast into the more convenient form (Exercise 3.2)

$$\rho(\tau) = \xi \exp \left[- \left(\frac{\omega_{s0} \beta^2 E_0}{\eta \sigma_E} \right)^2 \frac{\tau^2}{2} - \frac{e^2 \beta^2 E_0}{\eta T_0 \sigma_E^2} \int_0^\infty d\tau' \rho(\tau + \tau') \int_0^{\tau'} d\tau'' W'_0(\tau'') \right]. \quad (3.32)$$

Notice that $\rho(\tau)$ on the left side only depends on the ρ on the right side evaluated in front of τ . We can therefore solve for ρ at successive slices of the bunch by assigning zero or some arbitrary value to ρ at the very first slice (the head) and some value to the constant ξ . The value of ξ is varied until the proper normalization of ρ is obtained.

The longitudinal wake potential of the damping rings at the SLAC Linear Collider (SLC) has been calculated carefully. Using it as input, the Haissinski equation is solved numerically at various beam intensities. The results are shown as solid curves in Fig. 3.3 along with the actual measurements. The agreement has been very satisfactory [2].

3.4 Elliptical Phase-Space Distribution

An easier way to compute the bunch length distorted by the reactive impedance is to consider the elliptical phase-space distribution

$$\psi(\tau, \Delta E) = \frac{3N|\eta|\sqrt{\kappa}}{2\pi\beta^2\omega_{s0}E_0\hat{\tau}_0^3} \sqrt{\hat{\tau}_0^2 - \left(\frac{\eta}{\beta^2\omega_{s0}E_0} \right)^2 \Delta E^2 - \kappa\tau^2} \quad (3.33)$$

for an electron bunch, where $\hat{\tau}_0$ is the unperturbed half bunch length (in time advance). The distribution vanishes when the expression inside the square root of Eq. (3.33) becomes negative. The maximum half energy spread $\widehat{\Delta E}$ derived from Eq. (3.33),

$$\widehat{\Delta E} = \frac{\beta^2\omega_{s0}E_0\hat{\tau}_0}{|\eta|}, \quad (3.34)$$

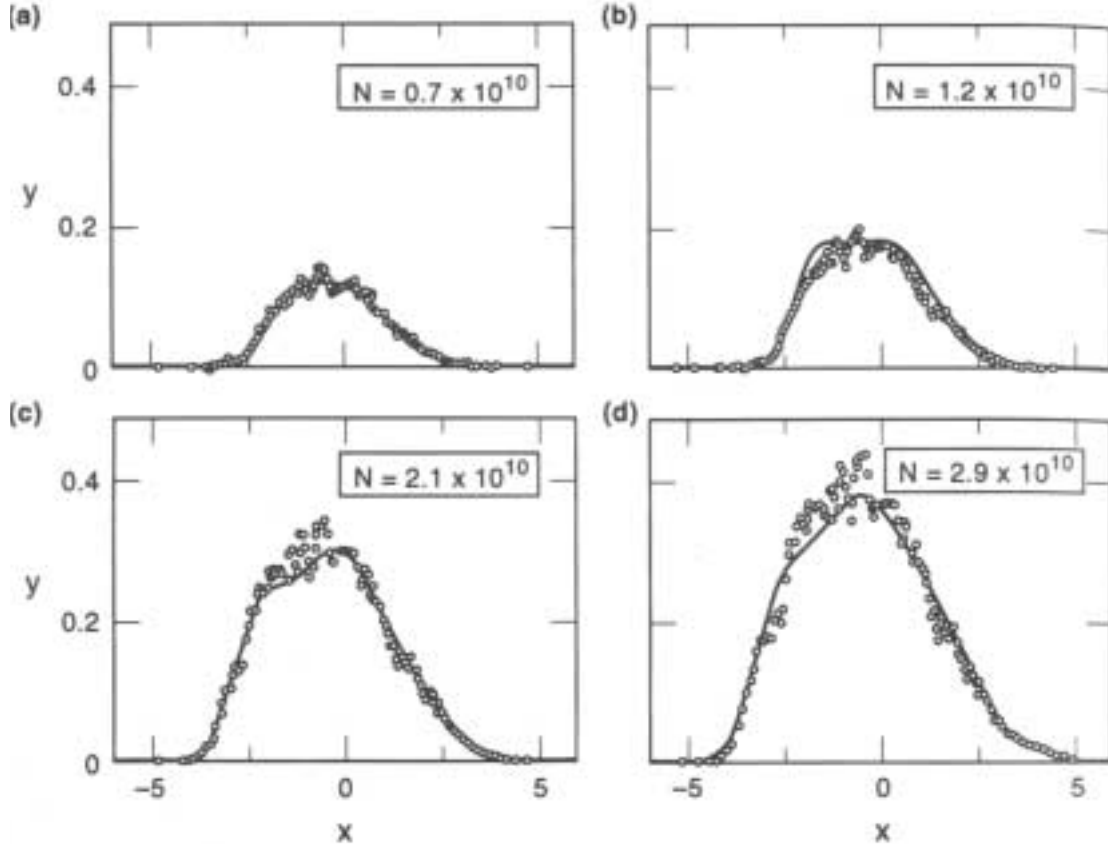


Figure 3.3: Potential-well distortion of bunch shape for various beam intensities for the SLAC SLC damping ring. Solid curves are solution of the Haissinski equation and open circles are measurements. The horizontal axis is in units of unperturbed rms bunch length σ_{z0} , while the vertical scale gives $y = 4\pi e\rho(z)/[V'_{\text{rf}}(0)\sigma_{z0}]$. The beam is going to the left.

is exactly that given by the phase equation (2.11). The maximum half energy spread is a constant determined by synchrotron radiation, while the half width of the bunch derived from Eq. (3.33),

$$\hat{\tau} = \frac{\hat{\tau}_0}{\sqrt{\kappa}} \quad (3.35)$$

is determined by the parameter κ . This distribution when integrated over ΔE gives the normalized parabolic linear distribution

$$\rho(\tau) = \frac{3N\sqrt{\kappa}}{4\hat{\tau}_0^3} (\hat{\tau}_0^2 - \kappa\tau^2) . \quad (3.36)$$

With the reactive wake function $W'_0(z) = L\delta'(z/v)$, the Hamiltonian of Eq. (2.20) can therefore be written as a quadratic in ΔE and τ :

$$H = -\frac{\eta}{2v\beta^2 E_0}(\Delta E)^2 - \frac{\omega_{s0}^2 \beta^2 E_0}{2\eta v} \tau^2 - \frac{e^2 L}{C_0} \rho(\tau). \quad (3.37)$$

Substituting for the linear density $\rho(\tau)$, the Hamiltonian becomes

$$H = \frac{\omega_{s0}^2 \beta^2 E_0}{2\eta v} \left[-\left(\frac{\eta}{\beta^2 \omega_{s0} E_0} \right)^2 \Delta E^2 - \tau^2 (1 - D\kappa^{3/2}) \right], \quad (3.38)$$

where

$$D = \frac{3e^2 N \eta v L}{2\omega_{s0}^2 \beta^2 E_0 C_0 \hat{\tau}_0^3}, \quad (3.39)$$

and the constant term involving $\hat{\tau}_0$ has been dropped. To be self-consistent, the expression of ψ in Eq. (3.33) must be a function of the Hamiltonian. Comparing Eq. (3.33) with Eq. (3.38), we arrive at

$$\kappa = 1 - D\kappa^{3/2} \quad (3.40)$$

or

$$\left(\frac{\hat{\tau}}{\hat{\tau}_0} \right)^3 = \left(\frac{\hat{\tau}}{\hat{\tau}_0} \right) + D. \quad (3.41)$$

This cubic can be solved by iteration. First we put $\hat{\tau}/\hat{\tau}_0 = 1$ on the right side. If $D > 0$, we find $\hat{\tau}/\hat{\tau}_0 > 1$ or the bunch is lengthened. If $D < 0$, it is shortened. The former corresponds to either an inductive force above transition or a capacitive force below transition. The latter corresponds to either an inductive force below transition or a capacitive force above transition. This is illustrated in the first row of Fig. 3.4, where we notice that the energy spread of the bunch is unchanged for various types of perturbation.

For a proton bunch, the energy spread is also modified but the bunch area remains constant. The phase-space distribution has to be rewritten as

$$\psi(\tau, \Delta E) = \frac{3N|\eta|}{2\pi\beta^2\omega_{s0}E_0\hat{\tau}_0^3} \sqrt{\hat{\tau}_0^2 - \frac{1}{\kappa} \left(\frac{\eta}{\beta^2\omega_{s0}E_0} \right)^2 \Delta E^2 - \kappa\tau^2}. \quad (3.42)$$

Now we have (Exercise 3.6)

$$\hat{\tau} = \frac{\hat{\tau}_0}{\sqrt{\kappa}} \quad \text{and} \quad \widehat{\Delta E} = \sqrt{\kappa} \widehat{\Delta E}_0. \quad (3.43)$$

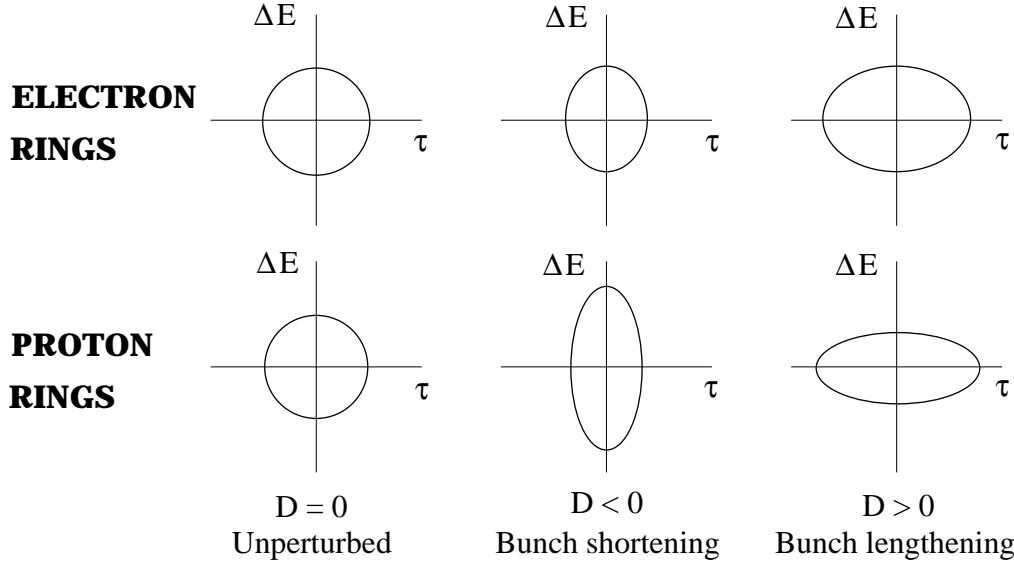


Figure 3.4: Potential well distortion of the bunch shape in the longitudinal phase space. $D > 0$ corresponds to either an inductive perturbation above transition or a capacitive perturbation below transition, while $D < 0$ implies either an inductive perturbation below transition or a capacitive perturbation above transition. Top row is for electron rings where the energy spread remains constant as a result of radiation damping. Bottom row is for proton rings where the bunch area is constant.

Again comparing with the Hamiltonian, we arrive at the quartic equation

$$\left(\frac{\hat{\tau}}{\hat{\tau}_0}\right)^4 = 1 + D \left(\frac{\hat{\tau}}{\hat{\tau}_0}\right). \quad (3.44)$$

This is illustrated in the bottom row of Fig. 3.4.

3.5 Synchrotron Tune Shift

When the potential well is distorted, the frequency of oscillation will be changed also. For an elliptical bunch distribution in the longitudinal phase space, the synchrotron oscillation frequency shift can be easily extracted from the Hamiltonian in Eq. (3.38). We get

$$\left(\frac{\omega_s}{\omega_{s0}}\right)^2 = \left(1 + \frac{\Delta\omega_s}{\omega_{s0}}\right)^2 = 1 - D\kappa^{3/2}. \quad (3.45)$$

As a first approximation, the synchrotron frequency shift $\Delta\omega_s$ or synchrotron tune shift $\Delta\nu_s$ is given by

$$\frac{\Delta\omega_s}{\omega_{s0}} = \frac{\Delta\nu_s}{\nu_{s0}} \approx -\frac{D}{2} = -\frac{3e^2 N \eta v L}{4\omega_{s0}^2 \beta^2 E_0 C_0 \hat{\tau}_0^3}, \quad (3.46)$$

where $\omega_{s0}/(2\pi)$ is the *bare* or *unperturbed* synchrotron frequency and $\nu_{s0} = \omega_{s0}/\omega_0$ is the *bare* or *unperturbed* synchrotron tune. We see that an inductive vacuum chamber will lower/increase the synchrotron tune above/below transition. For the longitudinal space charge self-force, the synchrotron tune will be shifted upward/downward above/below transition. Notice that this is the tune shift for an individual particle and is called the *incoherent* tune shift.

For a more general bunch distribution and a more general impedance, we resort to the equations of motion [Eqs. (2.11) and (2.12)], from which we obtain

$$\frac{d^2\tau}{ds^2} + \frac{\nu_{s0}^2}{R^2} \tau = -\frac{\eta}{v\beta^2 E_0} \left[\langle F_0^\parallel(\tau, s) \rangle - \langle F_0^\parallel(0, s) \rangle \right]. \quad (3.47)$$

The wake force on the right side is

$$\langle F_0^\parallel(\tau, s) \rangle - \langle F_0^\parallel(0, s) \rangle = -\frac{e^2}{C_0} \int_{-\infty}^{\infty} d\tau' \rho(\tau', s) \left[W'_0(\tau' - \tau) - W'_0(\tau') \right]. \quad (3.48)$$

To obtain the synchrotron tune shift in the dipole mode, we linearize the wake force, or

$$\langle F_0^\parallel(\tau, s) \rangle - \langle F_0^\parallel(0, s) \rangle = \left[\frac{e^2}{C_0} \int_{-\infty}^{\infty} d\tau' \rho(\tau', s) W''_0(\tau') \right] \tau. \quad (3.49)$$

The synchrotron tune shift can therefore be read out easily as

$$\frac{\Delta\nu_s}{\nu_{s0}} = \frac{e^2 \eta R}{4\pi \nu_{s0}^2 v \beta^2 E_0} \int_{-\infty}^{\infty} d\tau' \rho(\tau', s) W''_0(\tau'). \quad (3.50)$$

As a check, let us substitute for the inductive wake potential $W'_0(\tau) = L\delta'(\tau)$. The integral can be performed to get

$$\frac{\Delta\nu_s}{\nu_{s0}} = \frac{e^2 \eta R L}{4\pi \nu_{s0}^2 v \beta^2 E_0} \left. \frac{\partial^2 \rho}{\partial \tau^2} \right|_{\tau=0}. \quad (3.51)$$

If we substitute for the parabolic bunch distribution of Eq. (3.36), we get back the tune shift result obtained in Eq. (3.46).

If we average Eq. (3.47) over all the beam particles, we obtain the equation of motion of the center-of-mass of the bunch and we can compute the *coherent* synchrotron tune

shift of the bunch due to potential-well distortion. However, there is another contribution to this coherent tune shift from the dynamic part of the perturbation which we are going into later (see Sec. 9.1.1 below). This dynamic contribution will cancel the potential-well contribution, resulting in no coherent synchrotron tune shift in the dipole mode when the bunch intensity is weak and the wake is no longer than the bunch spacing. Physically, this dipole mode is a rigid rotation of the bunch in the longitudinal phase space. The wake field pattern, and therefore the potential-well distortion, moves with the bunch. Thus, the motion of the bunch as a whole is not affected by the wake field at all. On the other hand, the picture for incoherent motion is about a beam particle moving inside the bunch with the bunch center at rest. An individual particle can therefore sample a variation of the wake field while executing synchrotron oscillation. Thus, to demonstrate the effect of space charge impedance or inductive impedance, the coherent quadrupole mode of the synchrotron oscillation should be measured. If the incoherent synchrotron tune is desired, a Schottky scan of the beam is necessary.

3.6 Potential-Well Distortion Compensation

Potential-well distortion can often be a serious problem in the operation of an accelerator or storage ring. If the distortion opposes the rf bunching, a much larger rf voltage and hence rf power will be required to counteract the distortion. Even when such a higher compensating rf voltage is available, the rf bucket may have been so much distorted that its useful area has very much been reduced. An example is the Los Alamos Proton Storage Ring (PSR), which stores an intense proton beam at the kinetic energy of 797 MeV. The ring has a transition gamma of $\gamma_t = 3.1$, implying that the operation of the ring is below transition. The longitudinal space charge force is therefore repulsive in nature and tends to lengthen the bunch. This longitudinal repulsive force will counteract the rf bunching force. We will study how serious the potential-well distortion is and a possible way to cure the problem.

The PSR has a circumference of 90.2 m. It receives chopped proton beams from a linac cumulatively in 1000 to 2000 turns. The beam is bunched by an rf buncher to the desired length and is then extracted for experimental use. The rf buncher is of rf harmonic $h = 1$, or there is only one bunch. The revolution frequency and the rf frequency are both 2.796 MHz. A typical store consists of a bunch consisting of 3.2×10^{13} protons, of half length $\hat{\tau} = 133.5$ ns, occupying roughly two third of ring, and a half

energy spread of $\widehat{\Delta E}/E_0 = 0.005$. If space charge is neglected, to keep such a bunch matched to the rf bucket, the synchrotron tune is

$$\nu_{s0} = \frac{|\eta| \widehat{\Delta E}_0}{\omega_0 \beta^2 E_0 \hat{\tau}} = 0.000402 , \quad (3.52)$$

and the required rf voltage is

$$V_{rf} = \frac{2\pi\beta^2 E_0 \nu_{s0}^2}{e|\eta|h} = 6.60 \text{ kV} . \quad (3.53)$$

Now let us estimate the space charge effect [4]. The 95% (or full) normalized transverse emittance is $50 \times 10^{-6} \pi \text{m}$. From this and the ring lattice, the g_0 factor has been estimated to be

$$g_0 = 1 + 2 \ln \frac{b}{a} \approx 3.0 , \quad (3.54)$$

where a is the beam radius and b is the beam pipe radius. The longitudinal space charge impedance is therefore

$$\left(\frac{Z_0^{\parallel}}{n} \right)_{spch} = i \frac{Z_0 g_0}{2\gamma^2 \beta} \approx i 196 \Omega . \quad (3.55)$$

According to Eq. (3.19), a particle with an arrival time τ ahead of the synchronous particle sees an electric field

$$E_{s spch} = -\frac{e}{2\pi\beta c} \left| \frac{Z_0^{\parallel}}{n} \right|_{spch} \frac{d\lambda}{d\tau} , \quad (3.56)$$

where $\lambda(\tau)$ is the linear particle density of the bunch and is normalized to the number of particles in the bunch by integrating over τ . This electric field comes from the longitudinal space charge effect and is in the direction of the motion of the bunch. It is positive in the head half of the bunch ($\tau > 0$) and negative in the tail half ($\tau < 0$). It is therefore repulsive. Assume a parabolic distribution,

$$\lambda(\tau) = \frac{3N}{4\hat{\tau}} \left(1 - \frac{\tau^2}{\hat{\tau}^2} \right) , \quad (3.57)$$

so that the electric field becomes linear in τ . The particle will gain in a turn the potential

$$V_{spch} = E_{s spch} C_0 = \frac{3eN}{2\omega_0 \hat{\tau}^2} \left| \frac{Z_0^{\parallel}}{n} \right|_{spch} \frac{\tau}{\hat{\tau}} = 4.82 \frac{\tau}{\hat{\tau}} \text{ kV} , \quad (3.58)$$

according to its position in the bunch. This potential is of roughly the same size as the rf voltage required if there is no space charge. Thus, in the presence of space charge, we need to increase V_{rf} from 6.60 kV to approximately $6.60 + 4.82 = 11.42$ kV; nearly 42% of the rf voltage has been spent to counteract the space charge force. One must realize that the rf buncher at PSR was capable to deliver only 12 kV in 1997. Although the rf buncher has been upgraded to about 18 kV, there is also a goal to increase the beam intensity to 5×10^{13} protons as well. It is important to point out that rf compensation to space charge can never be exact. The rf force is sinusoidal while the space charge force is linear if the linear distribution is parabolic. Although the space charge force may become sinusoidal-like if the unperturbed linear beam distribution is Gaussian, the frequency content is still very different from the rf focusing force.

3.6.1 Ferrite Insertion

It has been proposed that if ferrite rings (also called cores) are installed inside the vacuum chamber, the proton beam will see an extra inductive impedance from the ferrite, and hopefully this inductive impedance will cancel the capacitive space charge impedance of the beam [5, 6]. Toshiba M₄C_{21A} ferrite rings are used, each having an inside diameter $d_i = 12.7$ cm, outside diameter $d_o = 20.3$ cm, and thickness $t = 2.54$ cm. The relative magnetic permeability is $\mu' \approx 70$ at the PSR rotation frequency, 2.796 MHz. With n_f ferrite rings stacked together, the impedance per harmonic is

$$\frac{Z_0^{\parallel}}{n_{\text{ferrite}}} = -i \frac{Z_0 \omega_0 t n_f}{2\pi c} \mu' \ln \frac{d_o}{d_i} = 2.93 n_f \Omega . \quad (3.59)$$

Thus, to cancel a space charge impedance per harmonic of $\sim 300 \Omega$, about $n_f = 102$ will be needed. Three ferrite inserts were assembled. Each consisted of a stainless-steel pill-box cavity having an inner diameter of 20.3 cm and inner length of 75.5 cm, so that 30 ferrite cores could be packed inside. To prevent charge buildup on the inner surface of the cores, each of the cores were treated with a very thin ($1 \text{ M}\Omega$ per square) conductive coating (Heraeus R8261) baked on the inner and outer surface. Additional radial conducting ‘spokes’ were added to provide conductivity from the inner surface to the outer wall of the chamber. Solenoidal wiring was wound outside the stainless steel container so that the magnetic permeability of the ferrite could be controlled.

Two such ferrite tuners or inserts were installed in the PSR in 1997. To study space charge compensation caused by the installed inductance, two experiments, using different

bunch lengths, were completed. The designated charge configurations were injected into the PSR and the longitudinal profiles (bunch length and shape) were observed, digitized, and recorded using signals from a wide-band wall current monitor at the end of each 625- μ s injection period. The experiments were performed for two bunch lengths: ~ 50 ns (half length) with 4.0×10^{12} particles and ~ 150 ns (half length) with 1.2×10^{13} . The rf voltage was set to 7 kV in both cases. The resulting waveforms are compared with detailed particle tracking simulations in Fig. 3.5 for the two bunch lengths. The solid curve in the top left plot represents the bunch shape with the full effect of the inserted inductance (zero bias). The dotted curve corresponds to data with the effect of the inductance diminished by 900-A dc bias. The difference of peak heights is about 16%. Simulations performed with assumed injection momentum spread $\Delta p/p = 0.08\%$ are shown in the top right plot. They predict an rms bunch length of 19 ns, but increasing to 22 ns when the ferrite bias current is raised to 900 A with the inductance reduced to 34% of its unbiased value. We see that the experiment measurements are consistent with the simulation predictions. Similar conclusion can be drawn for the long-bunch-length situation shown in bottom plots of Fig. 3.5. We see that bunch lengths have been reduced with the ferrite insertion, indicating that the space charge impedance has been cancelled to a certain extent.

It is unfortunate that the change in synchrotron frequency could not be measured to give another demonstration of the cancellation of space charge. This is mainly due to the slow synchrotron oscillation in the PSR. During the whole accumulation and storage time, the beam particles usually make less than one synchrotron oscillation. A similar space charge compensation experiment had also been performed at the KEK PS Main Ring, but with a much lower intensity of 2 to 9×10^{11} protons per bunch [7]. The beam kinetic energy was 500 MeV with a space charge impedance $Z_0^{\parallel}/n = i310 \Omega$. Instead of ferrite, the inductor inserts or tuners were loaded with a Met-Glass-like material called Finemet. Since the coherent synchrotron frequency in the dipole mode is not affected by space charge, the coherent frequency of the quadrupole synchrotron oscillation was measured instead as a function of bunch intensity. The inductor tuners were not equipped with biased current coil to control the permeability of the Finemet. In order to alleviate the effect of the Finemet when required, mechanical copper shorts were installed across the inductor tuners instead. As shown in Fig. 3.6, with several inductor tuners installed, the coherent frequency was less dependent on intensity without the mechanical shorts than with the mechanical shorts, indicating that the space charge force had been partially cancelled by the Finemet cores.

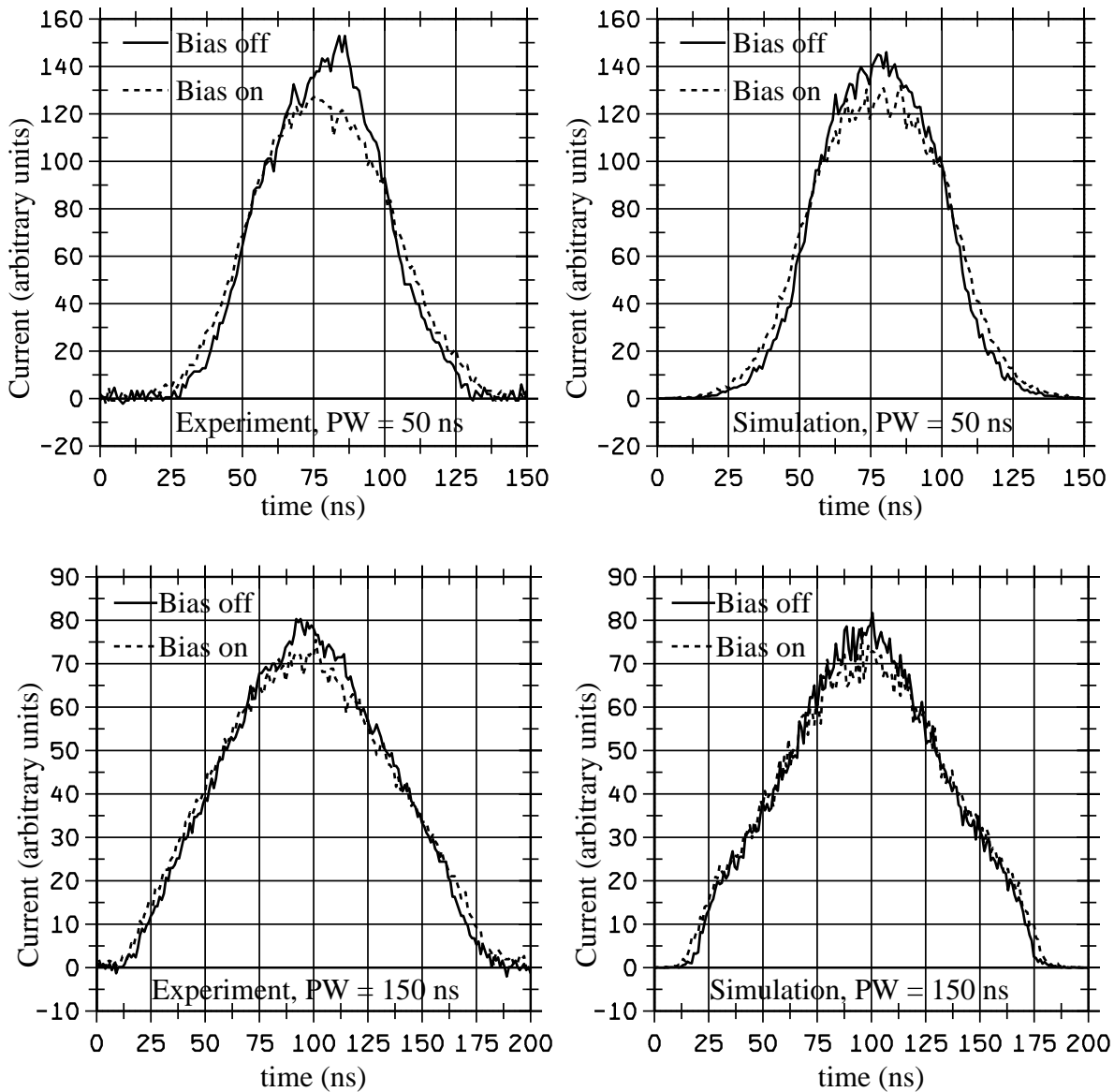


Figure 3.5: Measured (left) and simulated (right) pulse shapes after $625 \mu\text{s}$, for injected pattern widths of 50 ns with 4.0×10^{12} protons (bottom) and 150 ns with 1.2×10^{13} protons. In both cases, $V_{\text{rf}} = 7.5 \text{ kV}$. Solid: no bias, dotted: 900-A bias or a reduction of μ' by factor or 34%.

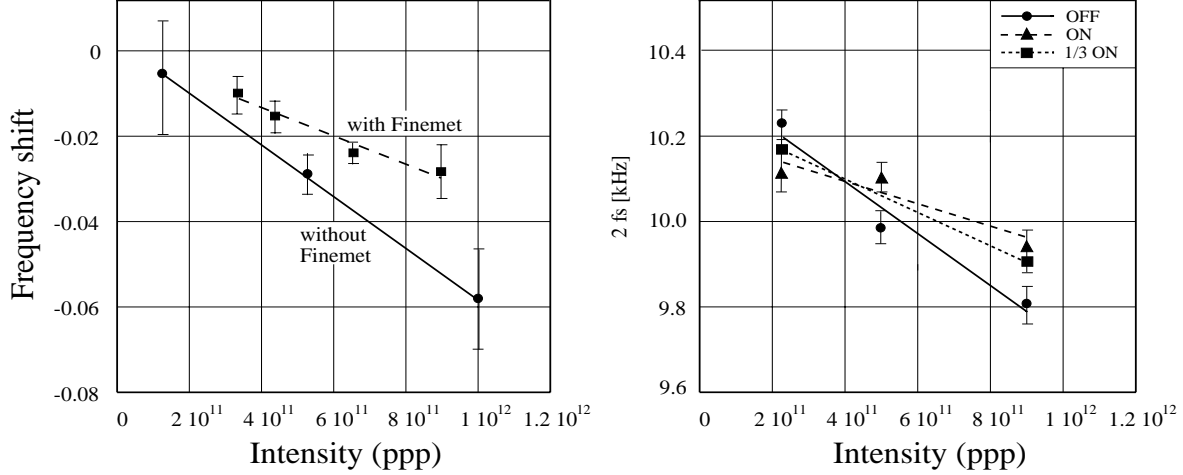


Figure 3.6: Left: Measured frequency shifts of the quadrupole oscillations versus beam intensity at KEK with and without Finemet insertion. Right: New KEK results of quadrupole oscillation frequency versus beam intensity with Finemet tuners off, $\frac{1}{3}$ on, and off.

The second experiment at the PSR is to measure the onset of vertical instability using a short-stripline beam-position monitor. With a 3.0×10^{13} proton beam stored, the rf voltage was lowered until vertical instability was registered. This signal comes about when the rf bucket is not large enough to hold the bunch so that some protons spill out into the bunch gap. These protons in the gap trap electrons preventing them to be cleared and causing a transverse e-p instability. Many previous performance points (blue squares) are plotted in Fig. 3.7 as the required buncher voltage versus beam intensity. The historical performance is roughly represented by the dashed line. The results of this experiment are indicated by red triangles. It was found that less buncher voltage was required to sustain the beam in the presence of the inductor inserts. For example, at the highest intensity that could be reached during the experiment, 3×10^{10} protons in the beam, only 6.9 kV was required, which amounted to a $\sim 60\%$ reduction of what had previously been necessary to maintain stability. This result indicates that the space charge impedance has been compensated to a certain extent by the ferrite cores installed in the vacuum chamber. Thus, less rf voltage will be required to bunch the proton beam. At the same time, it was found that the bunch gap was the cleanest ever observed.

This experiment, however, has far from being perfect. First, there are only a few points measured (the red triangles in Fig. 3.7); the indication is therefore not very convincing. Second, the bunch lengthening when the solenoidal bias was turned on had

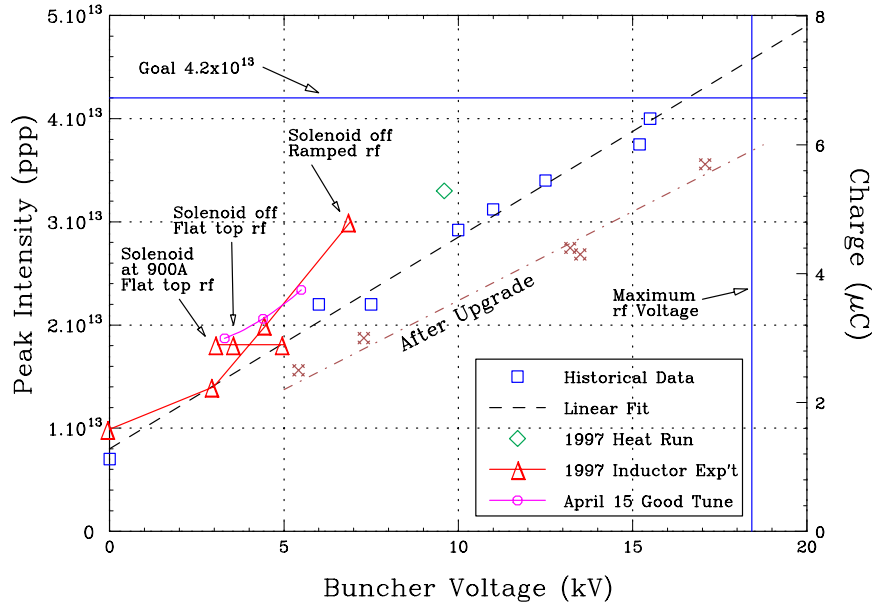


Figure 3.7: The performance of the PSR: the required buncher voltage plotted against the intensity of the beam. The dashed line shows roughly the historical performance before upgrade. The red triangles are results of the experiment discussed here. For example, with the ferrite insertion without solenoidal bias, only 6.9 kV is required to hold a bunch containing 3×10^{13} protons, which is about $\frac{1}{3}$ less than the historical value.

only been minimal and not spectacular (see Fig. 3.5), leaving behind the question of the efficiency about the inserts—how much space charge had actually been compensated. Third and worst of all, a longitudinal instability had been observed, although at the intensity of 3.2×10^{13} protons, this instability had been small and appeared to be tolerable. Because of these and other reasons, the ferrite inserts were removed during the upgrade. After the upgrade, when the machine was turned on, however, the performance was very poor as is indicated by the dot-dashed line in Fig. 3.7. In order to improve the performance, the inductor inserts were once again installed. But with the upgraded beam intensity, the small longitudinal instability had become so intense that the beam profiles became heavily distorted and there was a considerable of beam loss. This instability together with its eventual cure will be discussed in detail in Sec. 6.3.

3.7 Exercises

- 3.1. Show that the geometric factor defined Eq. (3.10) for the longitudinal space charge impedance becomes

$$g_0 = \frac{1}{2} + 2 \ln \frac{b}{a} , \quad (3.60)$$

when the longitudinal electric field opposing the beam is averaged over all the beam particles. In above, b is the radius of the beam pipe and a is the transverse radius of the beam.

- 3.2. Transform the Haissinski equation (3.23) according to the following:

(1) Notice that the integral over τ'' can be rewritten as

$$\int_0^\tau d\tau'' \rightarrow - \int_\tau^\infty d\tau'' + \text{constant} , \quad (3.61)$$

where the constant can be absorbed into the normalization constant $\rho(0)$ which we rename by ξ .

(2) The integration in the τ' - τ'' space is in the 0° to 45° quadrant between the lines $\tau'' = \tau$ and $\tau'' = \tau'$. Translate the τ' and τ'' axes so that the region of integration is now between the τ' -axis and the 45° line $\tau'' = \tau'$.

(3) Integrate over τ'' first from 0 to τ' ; then integrate over τ' .

(4) Change the variable τ'' to $\tau' - \tau''$. Now the Haissinski equation takes the more convenient form of Eq. (3.32), or

$$\rho(\tau) = \xi \exp \left[- \left(\frac{\omega_{s0} \beta^2 E_0}{\eta \sigma_E} \right)^2 \frac{\tau^2}{2} - \frac{e^2 \beta^2 E_0}{\eta T_0 \sigma_E^2} \int_0^\infty d\tau' \rho(\tau + \tau') \int_0^{\tau'} d\tau'' W'_0(\tau'') \right] . \quad (3.62)$$

- 3.3. The bunch in the Fermilab Tevatron contains $N = 2.7 \times 10^{11}$ protons and has a designed half length of $\hat{\tau} = 2.75$ ns. The ring main radius is $R = 1$ km and the slip factor is $\eta = 0.0028$ at the incident energy of $E_0 = 150$ GeV. The rf harmonic is $h = 1113$ and the rf voltage is $V_{rf} = 1.0$ MV. Assume a broadband impedance centered at $\omega_r/(2\pi) \approx 3$ GHz, quality factor $Q = 1$, and shunt impedance $R_s = 250$ kΩ.

(1) Show that the frequencies that the bunch samples are much less than the resonant frequency of the broadband, so that the asymmetric beam distortion driven by $\Re Z_0^\parallel$ can be neglected.

- (2) Using only the inductive part of the impedance at low frequencies, compute from Eq. (3.44) the equilibrium bunch length as a result of potential-well distortion.
- (3) Electron bunches are usually very short. If an electron bunch of rms bunch length 2 cm is put into the Tevatron, show that its spectrum will sample the resonant peak of $\Re Z_0^{\parallel}$ and may suffer asymmetric distortion. Compute the asymmetric factor $\alpha_R N$ given by Eq. (3.25) and determine whether the asymmetry is large or not.
- 3.4. From Eq. (3.41) for an electron bunch, show that there are two solutions for the perturbed bunch length due to distortion by a capacitive impedance when $-2/3^{3/2} < D < 0$. Which one is physical? When $D < -2/3^{3/2}$, there is no solution. At this critical situation, the bunch shortening ratio is $3^{-1/2}$.

Hint: Transform Eq. (3.41) to

$$4x^3 - 3x = \frac{3^{3/2}}{2}D \quad (3.63)$$

and substitute for $x = \sin \theta$. What is the right side in terms of θ ?

- 3.5. When the coupling impedance is purely resistive,
- (1) derive the potential-well distorted linear distribution, Eq. (3.25).
 - (2) Show that when the intensity of the bunch is weak, the peak of the distribution is given by Eq. (3.28).

Hint: Transform the Haissinski equation to a differential equation,

$$\rho' + \frac{\tau}{\sigma_{\tau}^2} \rho - \alpha_R \rho^2 = 0 . \quad (3.64)$$

Solve the equation and determine $\rho(0)$.

- 3.6. Starting from Eq. (3.42), filling in the missing steps, derive the quartic equation (3.44) for the proton half bunch length under the influence of a purely reactive longitudinal impedance.

Bibliography

- [1] J. Haissinski, Nuovo Cimento **18B**, 72 (1973).
- [2] K.L.F. Bane and R.D. Ruth, Proc. IEEE Conf. Part. Accel., Chicago, 1989, p.789.
- [3] A.G. Ruggiero, IEEE Trans. Nucl. Sci. **NS-24**, 1205 (1977).
- [4] K.Y. Ng and Z. Qian, *Instabilities and Space-Charge Effects of the High-Intensity Proton Driver*, Fermilab Report FN-659, 1997, AIP Conference Proceedings 435, Workshop on Physics at the First Muon Collider and at the Front End of the Muon Collider, Ed. S. Geer and R. Raja, Batavia, IL, Nov. 6-9, 1997, p. 841.
- [5] J.E. Griffin, K.Y. Ng, Z.B. Qian, and D. Wildman, Fermilab Report FN-661, 1997.
- [6] Plum, M.A., Fitzgerald, D.H., Langenbrunner, J., Macek, R.J., Merrill, F.E., Neri, F., Thiessen, H.A., Walstrom, P.L., Griffin, J.E., Ng, K.Y., Qian, Z.B., Wildman, D., and Prichard, B.A. Jr., *Phys. Rev. ST Accel. Beams*, **2**, 064201 (1999).
- [7] Koba, K., Machida, S., and Mori, Y., KEK Note, 1997 (unpublished); Koba, K., these proceedings; Koba, K., *et al*, *Phys. Sci. Instr.*, **70**, 2988 (1999).

Chapter 4

BETATRON TUNE SHIFTS

4.1 Static Transverse Forces

The vertical motion of a beam particle inside a beam obeys the equation of motion

$$\frac{dp_y}{dt} = F_{\text{ext}}(y) + F_{\text{beam}}(y, \bar{y}) , \quad (4.1)$$

where $p_y = \gamma mdy/dt$ is the vertical momentum of the particle and m its rest mass*. Since we want to study the motion of small vertical displacement y , the Lorentz factor γ can therefore be taken out of the derivative. Here, $F_{\text{ext}}(y)$ is the force due to the magnets outside the vacuum chamber and gives rise to betatron oscillations, while $F_{\text{beam}}(y, \bar{y})$ is the force coming from the electromagnetic fields of the beam on the particle at y and the beam vertical center at \bar{y} . For example, with quadrupole focusing,

$$F_{\text{ext}}(y) = \frac{B'_y}{B\rho} y , \quad (4.2)$$

where $B'_y = dB_y/dx$ is the gradient of the quadrupole magnetic flux density and $B\rho$ the rigidity of the beam. For the sake of simplicity, this focusing can be assumed to be uniform along the accelerator ring; we can therefore make the replacement

$$\langle F_{\text{ext}}(y) \rangle \longrightarrow -(\nu_0^V \omega_0)^2 y , \quad (4.3)$$

*Here, we concentrate on the transverse motion of the beam particles and ignore their momentum offsets and synchrotron motion. Thus, the revolution period of every particle at every turn is the same. This allows us to use the real time t as the independent variable.

where ν_0^V is the number of vertical oscillations the particle makes in a turn or what we usually call the *bare* vertical betatron tune, while $\omega_0/(2\pi)$ is the revolution frequency. Notice that the average of the external force is proportional to the impulse in one accelerator turn. Now the transverse equation of motion becomes

$$\frac{d^2y}{ds^2} + \frac{(\nu_0^V)^2}{R^2} y = \frac{\langle F_{\text{beam}}(y, \bar{y}) \rangle}{\gamma m v^2}, \quad (4.4)$$

where R is the average radius of the ring. In above, the rigid-bunch and impulse approximations have been applied to the F_{beam} , and we have replaced d/dt by vd/ds with $v = \beta c$ being the velocity of the beam, c the velocity of light, and s the distance measured along the longitudinal path in the ring. In this chapter, we are going to study the steady-state effects of the transverse wake potential on the beam. Therefore, there is no explicit time dependency in $\langle F_{\text{beam}} \rangle$. As will be shown below, the steady-state effects of the wake potential contribute to betatron tune shifts, while the time-dependent effects may excite instabilities.

Since we are interested only in small amount of motion in the vertical direction, the beam force can be Taylor expanded to obtain

$$\frac{d^2y}{ds^2} + \frac{(\nu_0^V)^2}{R^2} y = \frac{1}{\gamma m v^2} \left(\frac{\partial \langle F_{\text{beam}} \rangle}{\partial y} \Big|_{\bar{y}=0} y + \frac{\partial \langle F_{\text{beam}} \rangle}{\partial \bar{y}} \Big|_{y=0} \bar{y} \right), \quad (4.5)$$

The first term on the right side is proportional to the vertical displacement of the witness particle; it therefore constitutes a shift of the vertical betatron tune ν_0^V to become ν_{incoh}^V . When the shift is small[†], we write $(\nu_{\text{incoh}}^V)^2 = (\nu_0^V)^2 + 2\nu_0^V \Delta\nu_{\text{incoh}}^V$ with

$$\Delta\nu_{\text{incoh}}^V = -\frac{R^2}{2\nu_0^V \gamma m v^2} \frac{\partial \langle F_{\text{beam}} \rangle}{\partial y} \Big|_{\bar{y}=0}. \quad (4.6)$$

Since this shift affects an individual beam particle, $\Delta\nu_{\text{incoh}}^V$ is called the vertical *incoherent tune shift*. Thus, the incoherent tune shift can be computed by setting $\bar{y} = 0$ or without any displacement of the center of the whole beam.

Let us come back to Eq. (4.5), the transverse equation of motion. We can write one such equation for each beam particle. Perform an average by adding up these equations and dividing by the total number of beam particles. The result is

$$\frac{d^2\bar{y}}{ds^2} + \frac{(\nu_0^V)^2}{R^2} \bar{y} = \frac{1}{\gamma m v^2} \left(\frac{\partial \langle F_{\text{beam}} \rangle}{\partial y} \Big|_{\bar{y}=0} \bar{y} + \frac{\partial \langle F_{\text{beam}} \rangle}{\partial \bar{y}} \Big|_{y=0} \bar{y} \right). \quad (4.7)$$

[†]When the tune shift is large $\Delta\nu_{\text{incoh}}^V$ on the left side of Eq. (4.6) should be replaced by $\Delta(\nu^V)^2_{\text{incoh}}/(2\nu_0^V)$. The same applies to Eqs. (4.8), (4.13), (4.16), (4.19), etc.

This equation describes the vertical motion of the center of the beam, or the *coherent motion* of the beam, which is just a simple harmonic motion. The vertical betatron tune of the center of the beam, or the *coherent* vertical betatron tune of the beam, is now $\nu_{\text{coh}}^V = \nu_0^V + \Delta\nu_{\text{coh}}^V$. When the perturbation is small, the coherent tune shift becomes

$$\Delta\nu_{\text{coh}}^V = -\frac{R^2}{2\nu_0^V \gamma mv^2} \left(\frac{\partial \langle F_{\text{beam}} \rangle}{\partial y} \Big|_{\bar{y}=0} + \frac{\partial \langle F_{\text{beam}} \rangle}{\partial \bar{y}} \Big|_{y=0} \right). \quad (4.8)$$

Because we keep only the linear terms of the Taylor expansion in Eq. (4.5), we have included only the dipole parts of the wake force. As a result, these tune shifts should be called dipole coherent tune shift and dipole incoherent tune shift.

Let us assume here that the vacuum chamber is completely smooth and infinitely conducting. Then the force on a beam particle from the beam comes from only two sources: (1) electromagnetic interaction of the beam particle with all other beam particles in the beam, which we call *self-force*, (2) reflection of electromagnetic fields from the walls of the vacuum chamber, which we call *image forces*.

4.1.1 Electric Image Forces

The image forces certainly depends on the geometry of the vacuum chamber. Let us consider the simple case when the vacuum chamber consists of two infinite horizontal plates at location $y = \pm h$ as illustrated in Fig. 4.1. The beam of say positive charges is displaced by \bar{y}_1 vertically and the witness particle is at y_1 . We wish to consider the electric force on the witness particle coming from reflection by the top and bottom walls of the vacuum chamber. In order that the horizontal electric field at the top wall vanishes, there must be an image of the beam with negative charges at position $y = 2h - \bar{y}_1$ or at a distance $2h - \bar{y}_1 - y_1$ from the witness particle. In order that the horizontal electric field at the bottom wall vanishes, this image will have another image of positive charges from the bottom wall at $y = -(4h - \bar{y}_1)$ or $4h - \bar{y}_1 + y_1$ from the witness particle. This secondary image will have a third image of negative charges from the top wall, a 4th image of positive charges from the bottom wall, etc.

Similarly, the beam has an image of negative charges first from the bottom wall at $y = -(2h + \bar{y}_1)$ or $2h + \bar{y}_1 + y_1$ from the witness particle. This image will form another image of positive charges through the top wall with positive charges at $y = 4h + \bar{y}_1$ or $4h + \bar{y}_1 - y_1$ from the witness particle, etc. Summing up, the vertical electric field acting

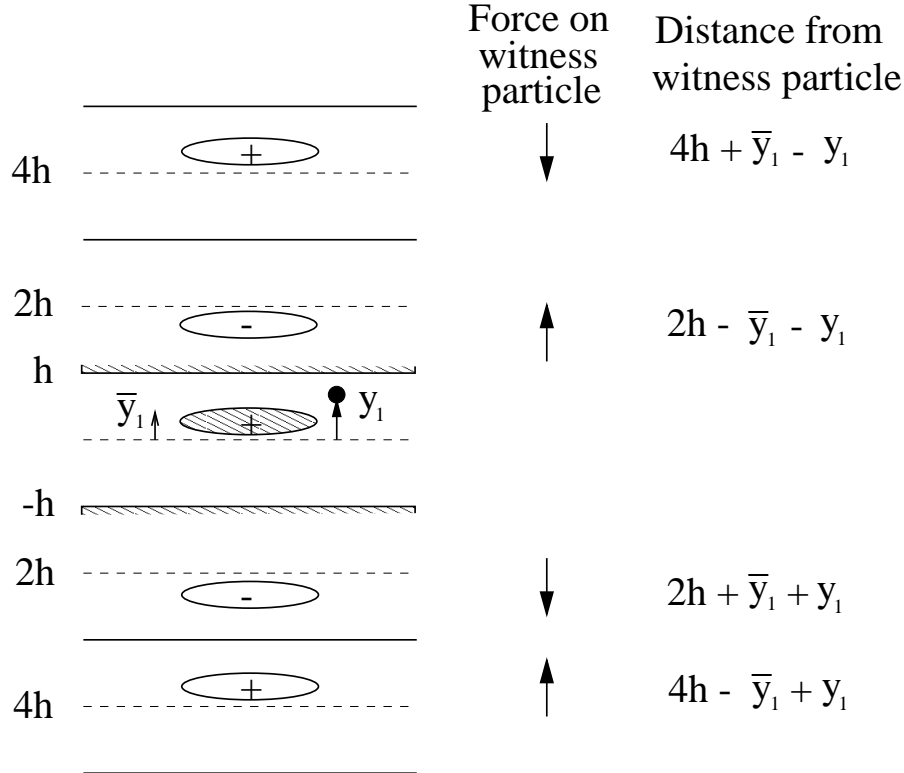


Figure 4.1: Illustration showing the electric forces from the images of a beam, off centered vertically by \bar{y}_1 , acting on a witness particle at location y_1 inside the beam between two infinite horizontal conducting parallel plates separated vertically by distance $2h$.

on the witness particle is, according to Gauss's law in the cylindrical coordinates,

$$E_y = \frac{e\lambda}{2\pi\epsilon_0} \left[+ \frac{1}{2h - \bar{y}_1 - y_1} - \frac{1}{2h + \bar{y}_1 + y_1} + \frac{1}{6h - \bar{y}_1 - y_1} - \frac{1}{6h + \bar{y}_1 + y_1} + \dots - \frac{1}{4h + \bar{y}_1 - y_1} + \frac{1}{4h - \bar{y}_1 + y_1} - \frac{1}{8h - \bar{y}_1 - y_1} + \frac{1}{8h + \bar{y}_1 + y_1} + \dots \right], \quad (4.9)$$

where λ is the linear particle density per unit length along the ring. Every two adjacent terms are grouped together giving

$$E_y = \frac{e\lambda}{2\pi\epsilon_0} \left[+ \frac{2(\bar{y}_1 + y_1)}{(2h)^2 - (\bar{y}_1 + y_1)^2} + \frac{2(\bar{y}_1 + y_1)}{(6h)^2 - (\bar{y}_1 + y_1)^2} + \dots + \frac{2(\bar{y}_1 - y_1)}{(4h)^2 - (\bar{y}_1 - y_1)^2} + \frac{2(\bar{y}_1 - y_1)}{(8h)^2 - (\bar{y}_1 - y_1)^2} + \dots \right]. \quad (4.10)$$

Since we consider only small vertical motion, only terms linear in $\bar{y}_1 + y_1$ and $\bar{y}_1 - y_1$ are kept leading to

$$\begin{aligned} E_y &= \frac{e\lambda}{\pi\epsilon_0 h^2} \left[(\bar{y}_1 + y_1) \left(\frac{1}{2^2} + \frac{1}{6^2} + \frac{1}{10^2} + \dots \right) + (\bar{y}_1 - y_1) \left(\frac{1}{4^2} + \frac{1}{8^2} + \frac{1}{12^2} + \dots \right) \right] \\ &= \frac{e\lambda}{\pi\epsilon_0 h^2} \left[(\bar{y}_1 + y_1) \frac{\pi^2}{32} + (\bar{y}_1 - y_1) \frac{\pi^2}{96} \right]. \end{aligned} \quad (4.11)$$

In the literature, there is a standard way to write these image contributions following the work of Laslett [1, 2, 3]:

$$E_y = \frac{e\lambda}{\pi\epsilon_0} \frac{\epsilon_1^V}{h^2} y_1 \quad \text{and} \quad \frac{e\lambda}{\pi\epsilon_0} \frac{\xi_1^V}{h^2} \bar{y}_1, \quad (4.12)$$

where ϵ_1^V and ξ_1^V are called, respectively, the incoherent and coherent *electric image coefficients*. For the situation of two parallel plates, we have $\epsilon_1^V = \pi^2/48$ and $\xi_1^V = \pi^2/16$. Attention should be paid that in deriving the coherent image coefficient, y_1 has been replaced by \bar{y}_1 in Eq. (4.9) or (4.10) or (4.11). According to Eqs. (4.6) and (4.8), the coherent and incoherent vertical tune shifts due to electric images are:

$$\Delta\nu_{\text{incoh}}^V = -\frac{Nr_0R}{\pi\gamma\beta^2\nu_0^V} \frac{\epsilon_1^V}{h^2} \quad \text{and} \quad \Delta\nu_{\text{coh}}^V = -\frac{Nr_0R}{\pi\gamma\beta^2\nu_0^V} \frac{\xi_1^V}{h^2}, \quad (4.13)$$

where we have replaced the linear particle density by $\lambda = N/(2\pi R)$ with N being the total number of particles in the beam, and introduced the classical radius of the particle $r_0 = e^2/(4\pi\epsilon_0 mc^2)$.

Notice that there is a negative sign in front of each of the tune shift expressions in Eq. (4.13). This implies that a positive image coefficient will contribute a downward shifting to the betatron tune.

4.1.2 Magnetic Image Forces

Unlike the electric field that cannot penetrate the metallic vacuum chamber at any frequency, the effect of the magnetic field is more complex. The magnet field has an ac component and a dc component. The ac component has its component parallel to the wall of the vacuum chamber converted into eddy current. In other words, the ac magnetic field *cannot* penetrate the wall of the vacuum chamber. There the boundary condition is $B_\perp = 0$, or the magnetic flux density B is parallel to the wall of the vacuum

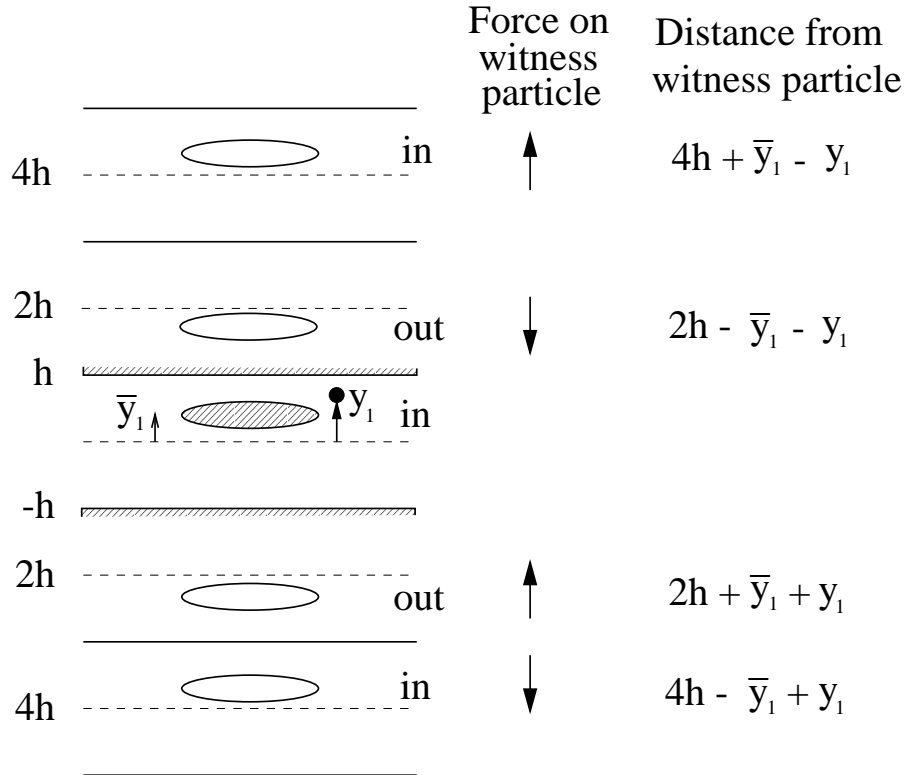


Figure 4.2: Illustration showing the magnetic forces from the images of a beam, off centered vertically by \bar{y}_1 , acting on a witness current at location y_1 inside the beam between two infinite horizontal conducting parallel plates separated vertically by distance $2h$. The normal components of the non-penetrating magnetic fields vanish at the plates. The beam or image currents flowing into or out of the paper are labeled “in” or “out”.

chamber. To accomplish this, the first image from a boundary wall gives an image current that flows in the opposite direction to that the beam. The total force from these magnetic images acting on the witness charge current at position y_1 is illustrated in Fig. 4.2 and is expressed as

$$\frac{F_y^{\text{mag}}}{e} = -\frac{e\mu_0\lambda v^2}{2\pi} \left[+\frac{1}{2h-\bar{y}_1-y_1} - \frac{1}{2h+\bar{y}_1+y_1} + \frac{1}{6h-\bar{y}_1-y_1} - \frac{1}{6h+\bar{y}_1+y_1} + \dots - \frac{1}{4h+\bar{y}_1-y_1} + \frac{1}{4h-\bar{y}_1+y_1} - \frac{1}{8h-\bar{y}_1-y_1} + \frac{1}{8h+\bar{y}_1+y_1} + \dots \right]. \quad (4.14)$$

There is the factor v^2 outside the square brackets on the right side. One v comes from the source beam current and the other v comes from the Lorentz force. It is interesting to see that the factor outside the square brackets is equal to $-e\lambda\beta^2/(2\pi\epsilon_0)$. Thus, the force due to the ac magnetic images are equal to the force due to the electric images multiplied by the factor $-\beta^2$. This leads to

$$\frac{F_y^{\text{mag}}}{e} = -\frac{e\lambda\beta^2}{2\pi\epsilon_0 h^2} \left[(\bar{y}_1 + y_1) \frac{\pi^2}{32} + (\bar{y}_1 - y_1) \frac{\pi^2}{96} \right]. \quad (4.15)$$

Following Eq. (4.13), tune shifts due to ac magnetic images can be expressed as terms of the former electric image coefficients ϵ_1^V and ξ_1^V :

$$\Delta\nu_{\text{incoh}}^V = \frac{Nr_0R}{\pi\gamma\nu_0^V} \frac{\epsilon_1^V}{h^2} \quad \text{and} \quad \Delta\nu_{\text{coh}}^V = \frac{Nr_0R}{\pi\gamma\nu_0^V} \frac{\xi_1^V}{h^2}. \quad (4.16)$$

There is always a dc part of the magnetic field that can penetrate the wall of the beam pipe and lands on the pole faces of the magnet as if the vacuum chamber were not there. The boundary condition on the magnet pole faces is now B_\perp continuous and $B_\parallel = 0$. In order to accommodate this, all the image currents must flow in exactly the same direction of the source beam, as illustrated in Fig. 4.3. The force on the witness particle is now

$$\begin{aligned} \frac{F_y^{\text{mag}}}{e} = & \frac{e\mu_0\lambda v^2}{2\pi} \left[+ \frac{1}{2g - \bar{y}_1 - y_1} - \frac{1}{2g + \bar{y}_1 + y_1} + \frac{1}{6g - \bar{y}_1 - y_1} - \frac{1}{6g + \bar{y}_1 + y_1} + \dots \right. \\ & \left. + \frac{1}{4g + \bar{y}_1 - y_1} - \frac{1}{4g - \bar{y}_1 + y_1} + \frac{1}{8g - \bar{y}_1 - y_1} - \frac{1}{8g + \bar{y}_1 + y_1} + \dots \right], \end{aligned} \quad (4.17)$$

where the magnetic pole faces are at $y = \pm g$ or the magnets have a vertical gap $2g$ between the poles faces. It is important to note the slight difference between Eqs. (4.14) and (4.17). Here we obtain

$$\frac{F_y^{\text{mag}}}{e} = +\frac{e\lambda\beta^2}{2\pi\epsilon_0 g^2} \left[(\bar{y}_1 + y_1) \frac{\pi^2}{32} - (\bar{y}_1 - y_1) \frac{\pi^2}{96} \right], \quad (4.18)$$

as compared to Eq. (4.15). Following Laslett, we write the tune shifts due to dc magnetic images as

$$\Delta\nu_{\text{incoh}}^V = -\frac{Nr_0R}{\pi\gamma\nu_0^V} \frac{\epsilon_2^V}{g^2} \quad \text{and} \quad \Delta\nu_{\text{coh}}^V = -\frac{Nr_0R}{\pi\gamma\nu_0^V} \frac{\xi_2^V}{g^2}, \quad (4.19)$$

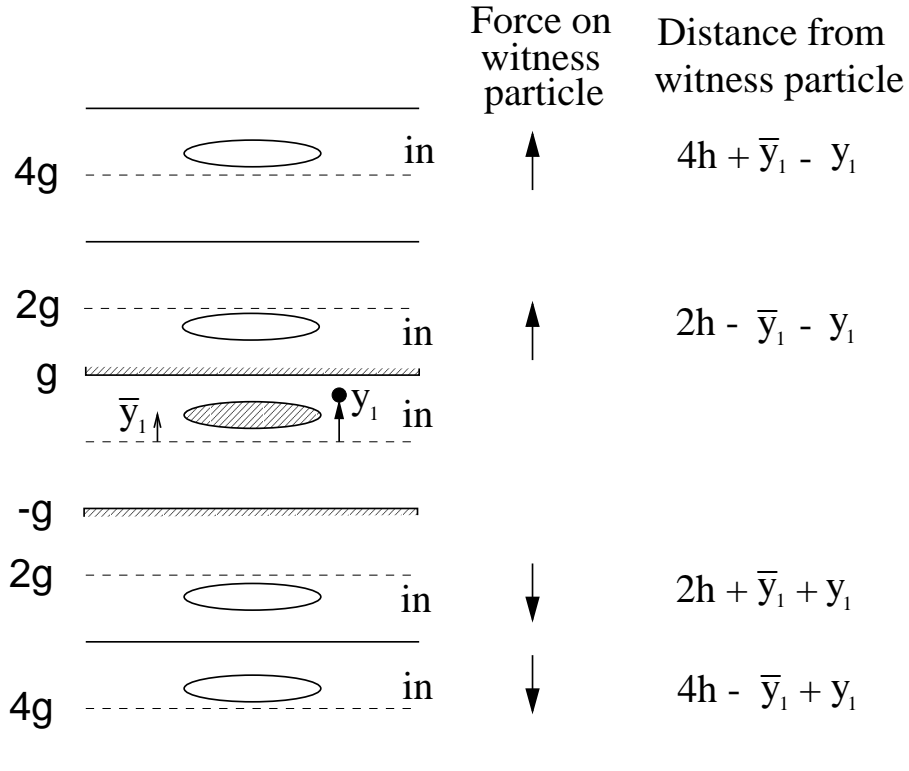


Figure 4.3: Illustration showing the magnetic forces from the images of a beam, off centered vertically by \bar{y}_1 , acting on a witness current at location y_1 inside the beam between two infinite horizontal parallel pole faces separated vertically by distance $2g$. The parallel components of the penetrating magnetic fields vanish at the pole faces. Here, the beam and all image currents flow into the paper.

where ϵ_2^V and ξ_2^V are called, respectively, the vertical incoherent and coherent dc *magnetic image coefficients*. For the special case of two parallel plates, they assume the values $\epsilon_2^V = \pi^2/24$ and $\xi_2^V = \pi^2/16$.

There is also a set of horizontal image coefficients: ϵ_1^H , ϵ_2^H , ξ_1^H , and ξ_2^H . Because the image forces acting on the witness particle come directly from the individual images, the electric field and magnetic flux density from the images at the location of the witness particle satisfy source-free Gauss's law, or $\vec{\nabla} \cdot \vec{E} = 0$ and $\vec{\nabla} \cdot \vec{B} = 0$. We therefore always have

$$\epsilon_1^H = -\epsilon_1^V \quad \text{and} \quad \epsilon_2^H = -\epsilon_2^V. \quad (4.20)$$

On the other hand, there is no definite relationship between the horizontal and vertical

coherent electric image coefficients. In the special case of two parallel plates, it is obvious that $\xi_1^H = 0$ and $\xi_2^H = 0$, which is the result of translational invariance. For a beam pipe with circular cross section or square cross section, $\epsilon_1^H = 0$ and $\epsilon_2^H = 0$ because of symmetry between the horizontal and vertical.

It is important to point out that electric and magnetic image coefficients are always defined with reference to the square of the *half vertical* vacuum chamber h or the square of the *half vertical* magnetic pole gap g , independent of whether we are talking about the vertical or horizontal tune shifts. For the example of a rectangular beam pipe of half height h and half width w , only h^2 will enter into the denominators but never w^2 , such as in Eqs. (4.13), (4.16), or (4.19). In the same way, for an elliptical beam pipe of vertical radius b and horizontal radius a , the image coefficients will be defined with reference to $h = b$ but not a . It is because of such a dedicated reference that the relations in Eq. (4.20) hold.

4.1.3 Space charge Self-Forces

The interaction of a beam particle with other beam particles in the beam depends on the transverse distribution of the beam. Let us first consider a uniformly distributed coasting beam of circular cross section and radius a . The witness particle at $y = y_1 \leq a$ sees, in the y -direction, an electric force[‡]

$$F_y^{\text{elect}} = \frac{e^2 \lambda}{2\pi\epsilon_0 a^2} (y_1 - \bar{y}_1) , \quad (4.21)$$

and a magnetic force

$$F_y^{\text{mag}} = -\frac{e^2 \mu_0 \lambda v^2}{2\pi a^2} (y_1 - \bar{y}_1) = -\frac{e^2 \lambda \beta^2}{2\pi\epsilon_0 a^2} (y_1 - \bar{y}_1) , \quad (4.22)$$

or a total force of

$$F_y = \frac{e^2 \lambda}{2\pi\epsilon_0 \gamma^2 a^2} (y_1 - \bar{y}_1) . \quad (4.23)$$

where \bar{y}_1 is vertical position of the center of the beam. This self-force is a space charge force. According to Eq. (4.6), this self-force leads to a space charge tune shift of

$$\Delta\nu_{\text{spch coh}}^{V,H} = -\frac{Nr_0 R}{2\pi\gamma^3 \beta^2 a^2 \nu_0^{V,H}} . \quad (4.24)$$

[‡]The vertical electric and magnetic forces in Eqs. (4.21) and (4.22) are true for any particle at a vertical distance $y = y_1 \leq a$ above the center of the beam and are independent of the particle horizontal position.

It is clear from Eq. (4.23) that the coherent space charge tune shifts in both transverse directions are zero. This is understandable, because the center of the beam does not see its own space charge force. We can also define the self-field or space charge coefficients in the vertical and horizontal directions, $\epsilon_{\text{spch}}^{V,H} = \frac{1}{2}$, such that

$$\Delta\nu_{\text{spch incoh}}^{V,H} = -\frac{Nr_0R}{\pi\gamma^3\beta^2\nu_0^{V,H}}\frac{\epsilon_{\text{spch}}^{V,H}}{a^2}. \quad (4.25)$$

The space charge coefficients take care of the transverse shape of the beam and how the beam particles are distributed.

Now consider a beam with uniform transverse distribution but elliptical cross section with vertical and horizontal radii a_V and a_H . In defining the space charge coefficients, we follow the same convention of the Laslett image coefficients that the a^2 in the denominator of Eq. (4.25) is always a_V^2 , independent of whether we are referring to the vertical or horizontal space charge tune shift. The vertical and horizontal space charge coefficients are then (Exercise 4.3)

$$\epsilon_{\text{spch}}^V = \frac{a_V}{a_V + a_H} \quad \text{and} \quad \epsilon_{\text{spch}}^H = \frac{a_V^2}{a_H(a_V + a_H)}. \quad (4.26)$$

These coefficients become $\frac{1}{2}$ when $a_V = a_H$ as expected.

We can also express the incoherent space charge tune shift in term of the normalized emittance of the beam

$$\epsilon_N^{V,H} = \gamma\beta \frac{a_{V,H}^2}{\langle\beta_{V,H}\rangle}, \quad (4.27)$$

where $\langle\beta_{V,H}\rangle$ is the average vertical/horizontal betatron function of the ring, which is roughly equal to $R/\nu_0^{V,H}$. Then, we have

$$\Delta\nu_{\text{spch incoh}}^{V,H} = -\frac{Nr_0}{\pi\gamma^2\beta\sqrt{\epsilon_N^{V,H}}\left(\sqrt{\epsilon_N^{V,H}} + \sqrt{\epsilon_N^{H,V}\langle\beta_{H,V}\rangle/\langle\beta_{V,H}\rangle}\right)B}. \quad (4.28)$$

In the above, we have also introduced the single-bucket bunching factor B to take care of the fact the the beam may be longitudinally bunched. The single-bucket bunching factor is defined as

$$B = \frac{I_{\text{av}}}{I_{\text{pk}}}, \quad (4.29)$$

where I_{av} and I_{pk} are, respectively, the current of a bunch averaged over a *single* rf bucket and its peak current, or the average current to the peak current assuming that all the buckets are filled.

We can also consider a beam with cylindrical cross section but with transverse bi-Gaussian distribution,

$$f(x, y) = \frac{\lambda}{2\pi\sigma^2} e^{-(x^2+y^2)/(2\sigma^2)} , \quad (4.30)$$

where σ is the rms transverse spread of the beam and $\lambda = N/(2\pi R)$ is the linear density. A particle at $y = y_1$ vertically above the center of the beam sees an electric force in the y direction,

$$F_y^{\text{elect}} = \frac{e^2}{2\pi\epsilon_0 y_1} \frac{\lambda}{\sigma^2} \int_0^{y_1} e^{-r^2/(2\sigma^2)} r dr = \frac{e^2 \lambda}{2\pi\epsilon_0 y_1} \left[1 - e^{-y_1^2/(2\sigma^2)} \right] . \quad (4.31)$$

For small offset, $y_1 \ll \sigma$, we have

$$F_y^{\text{elect}} = \frac{e^2 \lambda}{4\pi\epsilon_0 \sigma^2} y_1 . \quad (4.32)$$

The magnetic force is the same but multiplied by $-\beta^2$. The incoherent space charge tune shift is therefore

$$\Delta\nu_{\text{spch incoh}}^{V,H} = -\frac{Nr_0R}{4\pi\gamma^3\beta^2\sigma^2\nu_0^{V,H}} . \quad (4.33)$$

Here, we can define the 95% normalized transverse emittance $\epsilon_{N95}^{V,H}$ of the beam which encloses 95% of the beam particles. This corresponds to a radius r_{95} given by

$$\frac{1}{2\pi\sigma^2} \int_0^{r_{95}} e^{-r^2/(2\sigma^2)} 2\pi r dr = 95\% , \quad (4.34)$$

which gives $r_{95} \approx \sqrt{6}\sigma$. Thus

$$\epsilon_{N95}^{V,H} = \gamma\beta \frac{r_{95}^2}{\langle\beta_{V,H}\rangle} \approx \gamma\beta \frac{6\sigma^2}{\langle\beta_{V,H}\rangle} . \quad (4.35)$$

The space charge tune shift becomes

$$\Delta\nu_{\text{spch incoh}}^{V,H} = -\frac{3Nr_0}{2\pi\gamma^2\beta\epsilon_{N95}^{V,H}B} . \quad (4.36)$$

In general, if the beam has an elliptical cross section with vertical/horizontal rms beam size $\sigma_{V,H}$, the space charge coefficients for a particular beam particle can be represented by

$$\epsilon_{\text{spch}}^V = \frac{f\sigma_V}{\sigma_V + \sigma_H} \quad \text{and} \quad \epsilon_{\text{spch}}^H = \frac{f\sigma_V^2}{\sigma_H(\sigma_V + \sigma_H)} , \quad (4.37)$$

where the form factor f comes about because each particle in a transverse slice of the beam receives different tune shifts. For the bi-Gaussian distribution, if we consider only the particles at the center of the beam where the tune shifts are largest, $f = 3$. Thus the tune shift is three times as large as the tune shift for a uniform distribution in Eq. (4.28). This is because particles are mostly concentrated near the bunch center in a bi-Gaussian distribution and the linear particle density at the bunch center is therefore much larger. However, the tune shift for those particles with transverse offsets will be much smaller. If we make a rough model by assuming those particles within one sigma of the beam core to have the maximum tune shift while those outside do not experience any space charge force, we obtain some sort of average for the particles in the cross sectional slice, $f = 3(1 - e^{-1/2}) = 1.180$, which is only slightly larger than that for a uniformly distributed beam.

It is important to point out that what we really care for is the spread in space charge tune shift among the particles inside the beam, but not so much the maximum space charge tune shift, because the latter can be corrected by changing the bare tune of the machine. For a distribution of finite extent, the space charge tune spread is always less than the maximum space charge tune spread, which occurs at the center of the beam for most distributions. For a transverse bi-Gaussian distribution that extend to infinity, the space charge tune shift of a particle infinitely far away from the beam axis is zero, and therefore the space charge tune spread is equal to the maximum space charge tune shift. However, these particles are excluded from a realistic distribution which has a finite extent and this makes the space charge tune spread less than the maximum tune shift. When the bi-Gaussian distribution is truncated more and more (by including only those particles closer and closer to the beam center), the space charge tune spread becomes smaller and smaller while the maximum space charge tune shift remains unchanged. For a round beam, with bi-Gaussian distribution, $\sigma_r = \sigma_H = \sigma_V$ and maximum excursion r , the form factor $f(r/\sigma_r)$ in Eq. (4.37) for betatron amplitude r is found to be

$$\frac{f(r/\sigma_r)}{3} = \frac{8\sigma_r^2}{\pi r^2} \int_0^{\pi/2} \left[1 - \exp \left(-\frac{r^2}{2\sigma_r^2} \sin^2 \theta \right) \right] d\theta = \sum_{n=1}^{\infty} \frac{(2n)!}{2(n!)^3} \left(-\frac{r^2}{8\sigma_r^2} \right)^{n-1}, \quad (4.38)$$

which is depicted in Fig. 4.4. Consider a beam with a bi-Gaussian distribution truncated at $2.5\sigma_r$, we see that the particles at the edge of the beam have a space charge tune shift $\sim 40\%$ of the maximum space charge tune shift. Thus the space charge tune spread is equal to $\sim 60\%$ the maximum space charge tune shift. On the other hand, for the uniform transverse distribution, the space charge tune shift is amplitude independent and the spread is zero exactly.

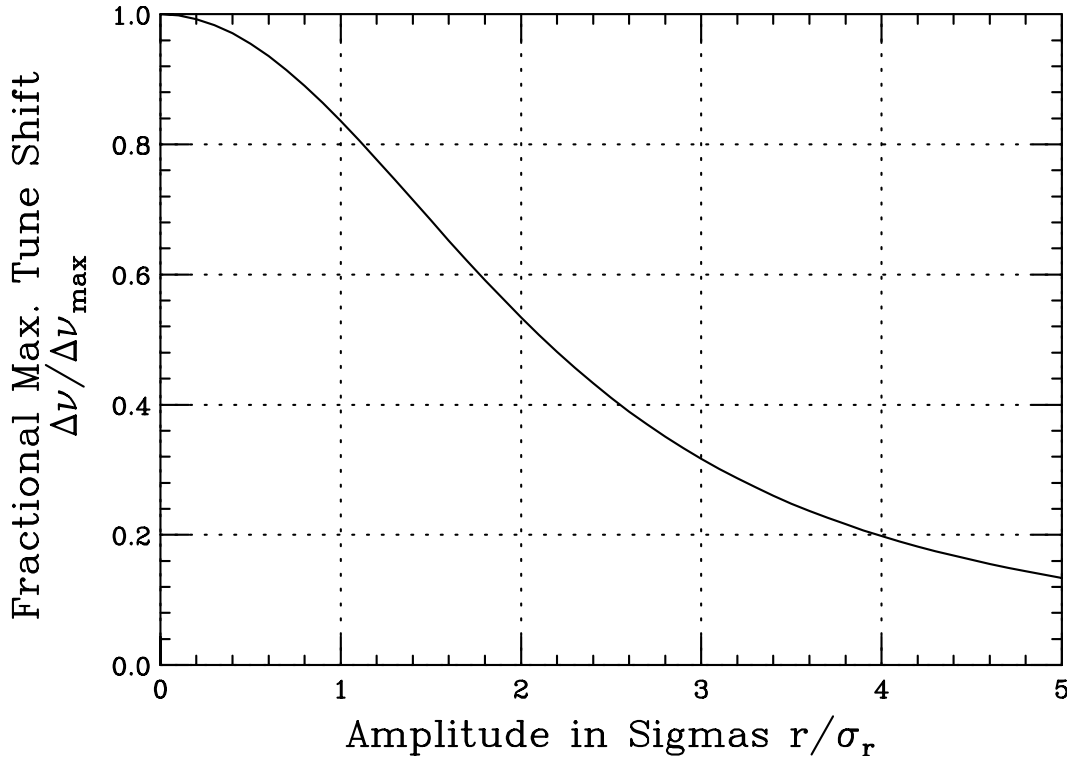


Figure 4.4: Plot of space charge tune shift of a particle with betatron amplitude r as a fraction of the maximum space charge tune shift of a bi-Gaussian distributed round beam with rms beam size σ_r .

We now understand that the space charge self-force of a bunch acting on the individual beam particles constitutes vertical and horizontal tune spreads. Usually, people say that large incoherent space charge tune spreads will encompass a lot of parametric resonances in the ν^V - ν^H tune space and lead to instability. For this reason, the beam intensities in low-energy synchrotrons are limited by the horizontal and vertical space charge tune spreads. The common rule of thumb is that incoherent self-field tune spreads should not exceed ~ 0.40 . At the same time, the widths of important stopbands should also be minimized by corrections made to the ring lattice. However, these self-field tune spreads at injection have never been well-measured beam parameters. It is difficult to measure because low-energy rings are usually ramped very rapidly. Thus, the self-field tune spreads diminish very quickly as the energy of the beam increases. Most low-energy rings that have large space charge tune spreads are ramped by resonators. To measure the self-field tune spreads, we must disconnect the magnet winding currents from the resonator so as to provide a longer interval for which the beam energy does not change.

This is not always possible, because the beam will generally become unstable if it is allowed to stay at such low energy for a long time. If the condition is available, however, the tune spreads can be measured by a technique called rf knockout. A narrow band rf signal is used to excite the beam. Those particles with the correct tune resonate with the driving signal and are lost. Since only a small fraction of the beam resonates, this resonating frequency of rf signal corresponds to the incoherent tune of the beam. Another way is to perform a Schottky scan which shows the tunes of individual particles. The coherent tune shifts can be measured by the same rf knockout method. If the exciting rf signal hits a coherent tune, the whole beam will be lost.

As we shall see in Chapter 5 that it is the *coherent* rather than the *incoherent* tune shifts that determine the instability of a beam. In fact, this is quite reasonable. When the bunch is oscillating at an integer coherent tune, we have the usual integer resonance. This leads to an instability because all particles are performing betatron oscillations with a tune component that is at an integer. The whole beam will become unstable. Although the dipole coherent space charge tune shift vanishes because the beam moves rigidly, there are other coherent motion of the beam, for example when the beam size oscillates without the beam center being moved. Some of these modes will be derived after introducing the envelope equation.

One may argue that if the incoherent tune spread covers an integer or half-integer resonance, *a small amount* of particles are hitting the resonance, and this small amount of the beam will be unstable. It will be shown in Chapter 5 that even this statement is incorrect, because the space charge self-force vanishes when the incoherent motion of the beam particles hit a resonance. Then why should we study the incoherent space charge tune shift if the resonances have nothing to do with incoherent motion? The answer is: the higher-multipole coherent space charge tune shifts depend on the incoherent space charge tune shift. Thus, if the incoherent space charge tune shift can be controlled, say by blowing up the transverse beam size, the higher-multipole coherent space charge tune shifts will become smaller also. In this way, a higher intensity beam will be possible before hitting the parametric resonances.

4.2 Tune Shift for a Beam

In this section, we want to derive the general expressions of incoherent and coherent tune shifts for a beam, unbunched or bunched, in terms of Laslett image coefficients and the self-force coefficients. These expressions are complicated by the fact that the magnetic field may or may not penetrate the vacuum chamber.

4.2.1 Image Formation

Let us recall how images of the beam are formed, in the walls of the vacuum chamber? or in the magnetic pole faces? For the electric field, because the parallel component vanishes on the walls of the vacuum chamber which we assume to be infinitely conducting, images will always be formed in the walls of the vacuum chamber. We therefore say that electric field is always *non-penetrating*. In this discussion, *penetrating* or *non-penetrating* always implies penetrating or non-penetrating the vacuum chamber.

The magnetic field is quite different. All low-frequency magnetic field will penetrate the vacuum chamber and form images in the magnet pole faces. If no magnet pole faces are present, we assume that magnetic field will go to infinity and will no longer affect the test particle. All high-frequency magnetic field will not penetrate the vacuum chamber and form images in the walls of the vacuum chamber.

Before proceeding further, there is an important rule that is worth mentioning. For images in the wall of the vacuum chamber, we use the *electric* image coefficient $\epsilon_1^{V,H}$ or $\xi_1^{V,H}$, depending on whether it is incoherent or coherent. The electric image coefficients are used not only for electric images but also for magnetic images. The only difference is that, for magnetic images, we use $-\beta^2 \epsilon_1^{V,H}$ or $-\beta^2 \xi_1^{V,H}$. This is because the actual contribution of magnetic field from the images in the walls of the vacuum chamber is exactly the same as the electric field. The factor β^2 comes about because we need a factor of β from the magnetic part of the Lorentz force and another factor of β from the source which is the beam current. The negative sign comes about because the magnetic force on a beam is always in opposite direction to the electric force. As for images formed in the magnet pole faces, they can only be magnetic images, because electric field cannot penetrate the vacuum chamber. Their contributions will be $\beta^2 \epsilon_2^{V,H}$ or $\beta^2 \xi_2^{V,H}$, respectively, when the tune shifts are incoherent or coherent. Here we have the same factor of β^2 . However, there is *no negative sign*, which is just a convention.

In other words, one may consider the negative sign to have been absorbed into the definition of $\beta^2 \epsilon_2^{V,H}$ or $\beta^2 \xi_2^{V,H}$. We can also say that electric image coefficients are for images in the walls of the vacuum chamber independent of whether the effect is electric or magnetic, while magnetic image coefficients are for images in the magnet pole faces. All these considerations are summarized in Table 4.1, where we also separate the coherent tune shift in Eq. (4.8) into two parts: the dc part $\partial \langle F_{\text{beam}} \rangle / \partial y|_{\bar{y}=0}$ when the beam is stationary and the ac part $\partial \langle F_{\text{beam}} \rangle / \partial \bar{y}|_{y=0}$ when the beam is oscillating.

Table 4.1: Relation of each component of the beam force to the image coefficients with images formed in the vacuum chamber or magnetic pole faces.

Beam force components	Images in vacuum chamber		Comments
	electric	magnetic	
$\frac{\partial \langle F_{\text{beam}} \rangle}{\partial y} \Big _{\bar{y}=0}$	$\frac{\epsilon_1^{V,H}}{h^2}$	$-\beta^2 \frac{\epsilon_1^{V,H}}{h^2}$	$\beta^2 \frac{\epsilon_2^{V,H}}{g^2}$ incoherent dc coherent
$\frac{\partial \langle F_{\text{beam}} \rangle}{\partial y} \Big _{\bar{y}=0} + \frac{\partial \langle F_{\text{beam}} \rangle}{\partial \bar{y}} \Big _{y=0}$	$\frac{\xi_1^{V,H}}{h^2}$	$-\beta^2 \frac{\xi_1^{V,H}}{h^2}$	$\beta^2 \frac{\xi_2^{V,H}}{g^2}$ coherent
$\frac{\partial \langle F_{\text{beam}} \rangle}{\partial y} \Big _{y=0}$		$-\beta^2 \frac{\xi_1^{V,H} - \epsilon_1^{V,H}}{h^2}$	$\beta^2 \frac{\xi_2^{V,H} - \epsilon_2^{V,H}}{g^2}$ ac coherent

4.2.2 Coasting Beams

Now we are ready to express the tune shifts in terms of image coefficients. First, let us study the simpler case of a coasting beam, where the only ac magnetic field comes from betatron oscillations. The frequency will be low when the betatron tune is close to an integer and the magnetic field may be penetrating. On the other hand, the frequency will be high when the betatron tune is close to a half integer and the magnetic field may be non-penetrating. The incoherent tune shifts are:

$$\Delta \nu_{\text{incoh}}^{V,H} = -\frac{Nr_0R}{\pi\gamma\beta^2\nu_0^{V,H}} \left[\frac{\epsilon_1^{V,H}}{h^2} + \mathcal{F}\beta^2 \frac{\epsilon_2^{V,H}}{g^2} + (1-\beta^2) \frac{\epsilon_{\text{spch}}^{V,H}}{a_V^2} \right]. \quad (4.39)$$

\uparrow \uparrow \uparrow
 electric image magnetic image self-field, $(1-\beta^2)$ gives
 in vacuum chamber in magnet poles balance between \vec{E} and \vec{H}

Here, the first term comes from the electric images in the vacuum chamber since electric field is always non-penetrating and therefore the incoherent electric image coefficient $\epsilon_1^{V,H}/h^2$. The second term comes the magnetic images in the magnet pole faces and therefore the incoherent magnetic image coefficient $\epsilon_2^{V,H}$ together with the factor β^2 in front and g^2 in the denominator. The factor \mathcal{F} represents the fraction of the ring circumference where the beam is sandwiched between magnetic pole faces. As stated before, the incoherent beam force comes from the images of the beam center which is not displaced or $\bar{y} = 0$. These images are not moving and the beam force is therefore static or dc, and the magnetic field is therefore landing on the magnet pole faces. The last term is just the space charge contribution, where the 1 denotes the electric part and $-\beta^2$ the magnetic part.

For the coherent tune shifts of a coasting beam, if the magnetic field is penetrating, we just have simply,

$$\Delta\nu_{\text{coh}}^{V,H} = -\frac{Nr_0R}{\pi\gamma\beta^2\nu_0^{V,H}} \left[\frac{\xi_1^{V,H}}{h^2} + \mathcal{F}\beta^2 \frac{\xi_2^{V,H}}{g^2} \right],$$

\uparrow \uparrow
 electric image magnetic image
 in vacuum chamber in magnet poles

(4.40)

where all the magnetic field penetrates the vacuum chamber and forms images in the magnet pole faces. Note that there is no space charge term because the center of the beam does not see the self-force among beam particles.

When the magnetic field is non-penetrating, we have instead

$$\Delta\nu_{\text{coh}}^{V,H} = -\frac{Nr_0R}{\pi\gamma\beta^2\nu_0^{V,H}} \left[\frac{\xi_1^{V,H}}{h^2} + \mathcal{F}\beta^2 \frac{\epsilon_2^{V,H}}{g^2} - \beta^2 \frac{\xi_1^{V,H} - \epsilon_1^{V,H}}{h^2} \right].$$

\uparrow \uparrow \uparrow
 electric image magnetic image ac magnetic image
 in vacuum chamber in magnet poles in vacuum chamber

(4.41)

To understand this expression, recall the magnetic part of beam force on the right side of Eq. (4.5). The ac magnetic field comes from the betatron oscillation of the whole beam and has its source from the second term on the right side only, since we require a moving beam center or $\bar{y} \neq 0$. According to Table 4.1, the contribution is therefore $-\beta^2(\xi_1^{V,H} - \epsilon_1^{V,H})/h^2$. The dc part of the coherent magnet beam force is the first term on the right side of Eq. (4.5). Since this dc field produces images in the magnet pole faces,

we have therefore the second term of Eq. (4.41). The first term comes from the electric component of the coherent beam force. After re-arrangement, the coherent tune shift with penetrating fields reads

$$\Delta\nu_{\text{coh}}^{V,H} = -\frac{Nr_0R}{\pi\gamma\beta^2\nu_0^{V,H}} \left[\frac{(1-\beta^2)\xi_1^{V,H}}{h^2} + \beta^2\frac{\epsilon_1^{V,H}}{h^2} + \mathcal{F}\beta^2\frac{\epsilon_2^{V,H}}{g^2} \right]. \quad (4.42)$$

4.2.3 Bunched Beams

For bunched beam, we would like to compute the maximum tune shifts when the beam current is at its local maximum. We therefore divide by the bunching factor B suitably so that the bunch intensity will be properly enhanced. Notice that ac magnetic field now comes from two sources: transverse betatron oscillation of the bunch and longitudinal or axial bunching of the beam. Although both effects are ac, their frequencies are in general very different. The frequency of transverse betatron oscillation is $(n-\nu_0^{V,H})\omega_0/(2\pi)$, where n is the revolution harmonic closest to the tune. These frequencies are therefore only fractions of the revolution frequency. On the other hand, the axial bunch frequency is a $h\omega_0/(2\pi)$ with h the rf harmonic, which is often many times revolution frequency. For this reason, it is reasonable to consider the ac magnetic fields arising from axial bunching *always non-penetrating*, while the ac magnetic fields arising from betatron oscillation sometimes non-penetrating and sometimes penetrating.

In the expressions below, we try also to include the effect of trapped particles that carry charges of the opposite sign. Take a proton beam, for example, electrons can be trapped, giving a neutralization coefficient χ_e , which is defined as the ratio of the total number of trapped electrons to the total number of protons. (For antiproton beam, the particles trapped are positively charged ions.) The trapped electrons will not travel longitudinally. Therefore, they only affect the electric force but not the magnetic force. In other words, for electric contributions, we replace 1 by $(1 - \chi_e)$.

The incoherent tune shift for a bunched beam is expressed as

$$\Delta\nu_{\text{incoh}}^{V,H} = -\frac{Nr_0R}{\pi\gamma\beta^2\nu_0^{V,H}} \left[\frac{1-\chi_e}{B} \frac{\epsilon_1^{V,H}}{h^2} + \mathcal{F}\beta^2 \frac{\epsilon_2^{V,H}}{g^2} - \beta^2 \left(\frac{1}{B} - 1 \right) \frac{\epsilon_1^{V,H}}{h^2} + (1-\chi_e-\beta^2) \frac{\epsilon_{\text{spch}}^{V,H}}{a_V^2} \right]. \quad (4.43)$$

↑	↑	↑	↑
electric image in vacuum chamber	magnetic image in magnet poles	ac magnetic image from axial bunching	self-field

The second term represents magnetic fields of a stationary beam and its images and

therefore the usual incoherent magnetic image coefficient $\epsilon_2^{V,H}$, which describes dc magnetic fields penetrating the vacuum chamber and landing at the magnet poles. Here, there is no division by the bunching factor B , because we are talking about the dc fields coming from the *average* beam current.

The third term is for the ac magnetic fields generated from axial bunching and a division by B is therefore necessary. Since the ac magnetic fields are non-penetrating, their contribution is the same as that of the incoherent electric field and therefore the factor $-\beta^2\epsilon_1^{V,H}$. We must remember that there is a dc part that lands on the magnet pole faces which we have considered already and must not be included here again. For this reason, we need to replace B^{-1} by $B^{-1} - 1$. The accuracy of this term can be inferred by noticing its disappearance when we let $B \rightarrow 1$, or the bunched beam becomes totally unbunched. After re-arrangement, this incoherent tune shift becomes

$$\Delta\nu_{\text{incoh}}^{V,H} = -\frac{Nr_0R}{\pi\gamma\beta^2\nu_0^{V,H}} \left[\left(\frac{1-\chi_e-\beta^2}{B} + \beta^2 \right) \frac{\epsilon_1^{V,H}}{h^2} + \mathcal{F}\beta^2 \frac{\epsilon_2^{V,H}}{g^2} + (1-\chi_e-\beta^2) \frac{\epsilon_{\text{spch}}^{V,H}}{a_V^2} \right]. \quad (4.44)$$

For coherent motion with penetrating magnetic fields from betatron oscillation, we have

$$\Delta\nu_{\text{coh}}^{V,H} = -\frac{Nr_0R}{\pi\gamma\beta^2\nu_0^{V,H}} \left[\frac{1-\chi_e}{B} \frac{\xi_1^{V,H}}{h^2} + \mathcal{F}\beta^2 \frac{\xi_2^{V,H}}{g^2} - \beta^2 \left(\frac{1}{B} - 1 \right) \frac{\xi_1^{V,H}}{h^2} \right]. \quad (4.45)$$

$$\begin{array}{ccc} \uparrow & \uparrow & \uparrow \\ \text{electric image} & \text{magnetic image} & \text{ac magnetic image} \\ \text{in vacuum chamber} & \text{in magnet poles} & \text{from axial bunching} \end{array}$$

where the third term is contributed by the magnetic field of bunching frequencies, which cannot penetrate the vacuum chamber. The magnetic fields divide into the dc part and the ac part in exactly the same way as Eq. (4.43), the expression for incoherent tune shift. Because we are talking about coherent tune shifts, the coefficients $\epsilon_2^{V,H}$ and $\epsilon_1^{V,H}$ are replaced, respectively by $\xi_2^{V,H}$ and $\xi_1^{V,H}$. After re-arrangement, the coherent tune shifts with penetrating magnetic fields from betatron oscillation becomes

$$\Delta\nu_{\text{coh}}^{V,H} = -\frac{Nr_0R}{\pi\gamma\beta^2\nu_0^{V,H}} \left[\left(\frac{1-\chi_e-\beta^2}{B} + \beta^2 \right) \frac{\xi_1^{V,H}}{h^2} + \mathcal{F}\beta^2 \frac{\xi_2^{V,H}}{g^2} \right]. \quad (4.46)$$

Finally, we come to ac magnetic fields that are non-penetrating coming from both

axial bunching and betatron oscillation. The coherent tune shifts are

$$\Delta\nu_{\text{coh}}^{V,H} = -\frac{Nr_0R}{\pi\gamma\beta^2\nu_0^{V,H}} \left[\frac{1-\chi_e}{B} \frac{\xi_1^{V,H}}{h^2} + \mathcal{F}\beta^2 \frac{\epsilon_2^{V,H}}{g^2} - \beta^2 \frac{\xi_1^{V,H} - \epsilon_1^{V,H}}{h^2} - \beta^2 \left(\frac{1}{B} - 1 \right) \frac{\xi_1^{V,H}}{h^2} \right]. \quad (4.47)$$

↑ ↑ ↑ ↑
 electric image magnetic image ac magnetic image ac magnetic image
 in vacuum chamber in magnet poles from transverse from axial bunching
 motion

Here, the axial bunching parts are very exactly the same as in Eq. (4.45) because they describe exactly the same ac magnetic fields coming from axial bunching. As for the dc magnetic fields, the contribution in Eq. (4.45) comes from both terms of the beam force on the right side of Eq. (4.5) and contributes the coefficient $\xi_2^{V,H}$. Here the dc magnetic fields come from only the first term of the beam force and contribute $\epsilon_1^{V,H}$ instead, for exactly the same reason as in Eq. (4.39). The part of the second term that comes from betatron oscillation of the beam gives rise to the second last term of Eq. (4.47), for exactly the same reason as in Eq. (4.39). After re-arrangement, this coherent tune shift takes the form

$$\Delta\nu_{\text{coh}}^{V,H} = -\frac{Nr_0R}{\pi\gamma\beta^2\nu_0^{V,H}} \left[\frac{1-\chi_e - \beta^2}{B} \frac{\xi_1^{V,H}}{h^2} + \mathcal{F}\beta^2 \frac{\epsilon_2^{V,H}}{g^2} + \beta^2 \frac{\epsilon_1^{V,H}}{h^2} \right]. \quad (4.48)$$

4.3 Other Vacuum Chamber Geometries

The electric and magnetic image coefficients have been computed for other geometries of the vacuum chamber: circular cross section, elliptical cross section [2, 3, 4], and rectangular cross section [5], and even with the beam off-centered. The computations for the rectangular and elliptical cross sections involve one or more than one conformal mappings and the results are given in terms of elliptical functions.

4.3.1 Circular Vacuum Chamber

The situation of circular cross section with an on-center beam is rather simple. Consider a line charge of linear density λ_1 at location $x = 0$ and $y = \bar{y}_1$ inside the cylindric beam pipe of radius b with infinitely conducting walls. We place an image line charge of linear density λ_2 at location $x = 0$ and $y = \bar{y}_2$ as shown in left plot of Fig. 4.5.

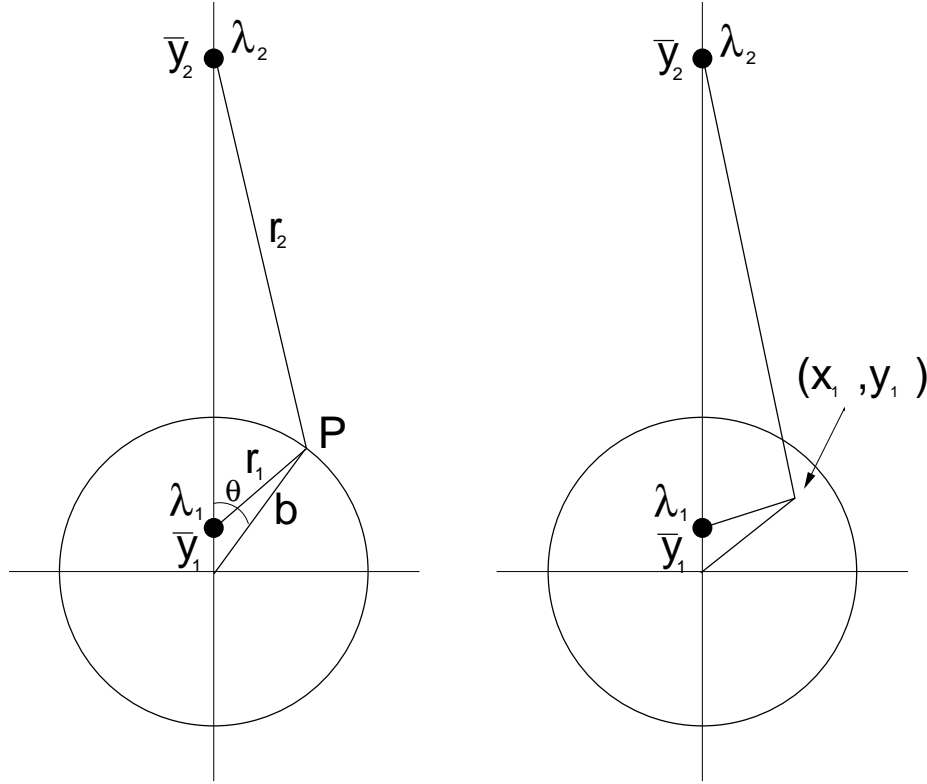


Figure 4.5: Left plot illustrates a line charge density λ_1 inside a cylindrical beam pipe offset vertically by \bar{y}_1 . There is an image line charge density λ_2 at \bar{y}_2 such that the electric potential vanishes at every point P at the beam pipe. Right plot shows the combined electric force acting on a witness line charge at (x_1, y_1) .

The electric potential at point P on a chamber wall at an angle θ is given by

$$V_P = -\frac{e\lambda_1}{2\pi\epsilon_0} \ln r_1 - \frac{e\lambda_2}{2\pi\epsilon_0} \ln r_2 , \quad (4.49)$$

where

$$\begin{cases} r_1^2 = \bar{y}_1^2 + b^2 - 2\bar{y}_1 b \cos \theta , \\ r_2^2 = \bar{y}_2^2 + b^2 - 2\bar{y}_2 b \cos \theta . \end{cases} \quad (4.50)$$

Two assertions are made:

$$\bar{y}_2 = \frac{b^2}{\bar{y}_1} \quad \text{and} \quad \lambda_2 = -\lambda_1 . \quad (4.51)$$

We obtain from the first assertion that $r_2^2 = r_1^2(b^2/\bar{y}_1^2)$. Then the second assertion ensures that the electric potential V_P vanishes aside from a constant for any point on the wall of the cylindrical vacuum chamber.

To compute the image force, place a witness line charge at $x = x_1$ and $y = y_1$, as illustrated in the right plot of Fig. 4.5. The electric force exerted on the witness charge by the image has the y component

$$\frac{F_y^{\text{elec}}}{e} = \frac{e\lambda_1}{2\pi\epsilon_0} \frac{\frac{b^2}{\bar{y}_1} - y_1}{x_1^2 + \left(\frac{b^2}{\bar{y}_1} - y_1\right)^2} \rightarrow \frac{e\lambda_1}{2\pi\epsilon_0} \frac{\bar{y}_1}{b^2}, \quad (4.52)$$

where in the last step only terms linear in y_1 and \bar{y}_1 are retained. According to Eq. (4.13),

$$\Delta\nu_{\text{incoh}}^V = -\frac{Nr_0R}{\pi\gamma\beta^2\nu_0^V} \frac{\epsilon_1^V}{b^2} \quad \text{and} \quad \Delta\nu_{\text{coh}}^V = -\frac{Nr_0R}{\pi\gamma\beta^2\nu_0^V} \frac{\xi_1^V}{b^2}, \quad (4.53)$$

we immediately obtain the incoherent and coherent electric image coefficients for a circular beam pipe:

$$\epsilon_1^V = 0 \quad \text{and} \quad \xi_1^V = \frac{1}{2}. \quad (4.54)$$

Because of the cylindrical symmetry, we also have

$$\epsilon_1^H = 0 \quad \text{and} \quad \xi_1^H = \frac{1}{2}. \quad (4.55)$$

It is not surprising to see the incoherent electric image coefficients vanish. This is because at the point of observation of the witness charge, $\vec{\nabla} \cdot \vec{E} = 0$, leading to $\epsilon_1^V + \epsilon_1^H = 0$.

4.3.2 Elliptical Vacuum Chamber

4.3.2.1 Off-centered Beam

The elliptical cross section of the vacuum chamber has *half width* w and *half height* $h < w$. They are also known as the major and minor radii. The focal points are on the horizontal axis at distance $\varepsilon = \sqrt{w^2 - h^2}$ from the center. Consider a line beam on the horizontal axis at distance x from the center. The image coefficients can be obtained by performing two conformal mappings [2, 3, 4]. The derivations are rather involved. Here, we only present the results. When the beam is inside the focal points[†] or $0 < x < \varepsilon$,

$$\epsilon_1^V = -\epsilon_1^H = \frac{h^2}{12W^2} \left[A \left(\frac{2K}{\pi \operatorname{cn} dn} \right)^2 + \frac{6Kk'^2 x \operatorname{sn}}{\pi W \operatorname{cn} dn} - \frac{4\varepsilon^2 + 5x^2}{2W^2} \right], \quad (4.56)$$

[†]These expressions are presented from Eqs. (74) to (76) in Ref. [3]. The expression following Eq. (74) is incorrect that the factor $(1 + k^2 + k^4)$ in the middle term should have been $(1 + 2k^2 + k^4)$. The first factor in Eq. (76) after the opening square bracket, $(1 - k^2 S^2)$, should have been $(1 - k^2 S^4)$.

$$\xi_1^V = \frac{h^2}{4W^2} \left[\left(\frac{2K \operatorname{dn}}{\pi \operatorname{cn}} \right)^2 + \frac{2Kk'^2 x \operatorname{sn}}{\pi W \operatorname{cn} \operatorname{dn}} - \frac{\varepsilon^2 + x^2}{W^2} \right], \quad (4.57)$$

$$\xi_1^H = -\frac{h^2}{4W^2} \left[(1 - k^2 \operatorname{sn}^4) \left(\frac{2Kk'}{\pi \operatorname{cn} \operatorname{dn}} \right)^2 + \frac{2Kk'^2 x \operatorname{sn}}{\pi W \operatorname{cn} \operatorname{dn}} - \frac{\varepsilon^2 + x^2}{W^2} \right], \quad (4.58)$$

where

$$A = (2 - k^2) - \frac{1}{2}(1 + k^2)^2 \operatorname{sn}^2 - k^2(1 - 2k^2) \operatorname{sn}^4, \quad (4.59)$$

and

$$W^2 = \varepsilon^2 - x^2 = w^2 - h^2 - x^2. \quad (4.60)$$

The arguments of the Jacobian elliptic functions sn , cn , dn are

$$\left(\frac{2K(k)}{\pi} \sin^{-1}(x/\varepsilon), k \right), \quad (4.61)$$

where $K = K(k)$ is the complete elliptical function of the first kind and k is called the *modulus*[‡]. The complementary modulus k' is given by

$$k' = \sqrt{1 - k^2}. \quad (4.62)$$

We first compute the *nome*, defined as

$$q = \exp \left[-\frac{\pi K'(k)}{K(k)} \right], \quad (4.63)$$

using the expression

$$q = \frac{w - h}{w + h}, \quad (4.64)$$

then the complementary modulus k' using[§]

$$k'^{\frac{1}{2}} = \frac{1 + 2 \sum_{s=1}^{\infty} (-1)^s q^{s^2}}{1 + 2 \sum_{s=1}^{\infty} q^{s^2}}, \quad (4.65)$$

and finally the modulus k through Eq. (4.62).

[‡]Some authors also define the *parameter* $m = k^2$ and the *complementary parameter* $m' = k'^2 = 1 - m$.

[§]This formula was stated wrongly in Eq. (6) of Ref. [5].

Notice that each term in Eqs. (4.56), (4.57), and (4.58) becomes singular when the beam approaches the focal points of the elliptic cross section. However, the singularities cancel each other in each expression to arrive at a finite value as $x \rightarrow \varepsilon$. For this reason double precision must be used in evaluating these expressions. Right at the focal points the image coefficients become[¶]

$$\epsilon_1^V = -\epsilon_1^H = \frac{h^2}{360\varepsilon^2} \left[(1 - 16k^2 + k^4) \left(\frac{2K}{\pi} \right)^4 + 10(1 + k^2) \left(\frac{2K}{\pi} \right)^2 - 11 \right], \quad (4.66)$$

$$\xi_1^V = \frac{h^2}{180\varepsilon^2} \left[(2 + 13k^2 + 2k^4) \left(\frac{2K}{\pi} \right)^4 + 5(1 + k^2) \left(\frac{2K}{\pi} \right)^2 - 7 \right], \quad (4.67)$$

$$\xi_1^H = \frac{-h^2}{180\varepsilon^2} \left[2(1 - 16k^2 + k^4) \left(\frac{2K}{\pi} \right)^4 + 5(1 + k^2) \left(\frac{2K}{\pi} \right)^2 - 7 \right]. \quad (4.68)$$

When the beam is outside the focal points or $x > \varepsilon$, the image coefficients assume the form^{||}

$$\epsilon_1^V = -\epsilon_1^H = \frac{h^2}{12W^2} \left[B_1 \left(\frac{2K}{\pi \operatorname{sn} \operatorname{cn}} \right)^2 + \frac{6Kx \operatorname{dn}}{\pi W \operatorname{sn} \operatorname{cn}} - \frac{4\varepsilon^2 + 5x^2}{2W^2} \right], \quad (4.69)$$

$$\xi_1^V = \frac{h^2}{4W^2} \left[\left(\frac{2K \operatorname{cn}}{\pi \operatorname{sn}} \right)^2 + \frac{2Kx \operatorname{dn}}{\pi W \operatorname{sn} \operatorname{cn}} - \frac{\varepsilon^2 + x^2}{W^2} \right], \quad (4.70)$$

$$\xi_1^H = -\frac{h^2}{4W^2} \left[B_2 \left(\frac{2K}{\pi \operatorname{sn} \operatorname{cn}} \right)^2 + \frac{2Kx \operatorname{dn}}{\pi W \operatorname{sn} \operatorname{cn}} - \frac{\varepsilon^2 + x^2}{W^2} \right], \quad (4.71)$$

where

$$B_1 = \frac{3}{2} - \frac{1}{2}(8 - k'^2) \operatorname{sn}^2 + (1 + k'^2) \operatorname{sn}^4, \quad B_2 = 1 - 2 \operatorname{sn}^2 + k'^2 \operatorname{sn}^4. \quad (4.72)$$

Unlike the situation when the beam is inside the focal points, here

$$W^2 = x^2 - \varepsilon^2 = x^2 - w^2 + h^2, \quad (4.73)$$

[¶]in Ref. [3], in Appendix D(f), the first term of ξ_1^V was $(2 - 13k^2 + 2k^4)$ which has a wrong sign preceding $13k^2$ as compared with our Eq. (4.67). In Ref. [4], Table II, Part (c), the expression for ϵ_1 when $x = \varepsilon$, has an overall incorrect sign.

^{||}In Ref. [3], Appendix D(e), the expressions for ϵ_1^V , ξ_1^V , and ξ_1^H all have negative signs in front of the middle terms inside the square brackets. They should be all positive as given by Eqs. (4.69), (4.70), and (4.71). The expression for B_1 in Ref. [3] has the typo that S in the second term on the right side should have been S^2 .

and the Jacobian elliptic functions sn , cn , and dn have arguments

$$\left(\frac{2K(k)}{\pi} \cosh^{-1}(x/\varepsilon), k' \right) . \quad (4.74)$$

However, the nome q , modulus k , and complementary modulus k' are the same as given by Eqs. (4.64), (4.62), and (4.65).

4.3.2.2 Centered Beam

When the beam is right at the center of the vacuum chamber, $x = 0$. The arguments of the elliptic functions in Eq. (4.61) simplify to $(0, k)$ and we have $\text{sn} = 0$, $\text{cn} = \text{dn} = 1$. The expressions for the image coefficients in Eqs. (4.56), (4.57), and (4.58) simplify readily to

$$\epsilon_1^V = -\epsilon_1^H = \frac{h^2}{12\varepsilon^2} \left[(1 + k'^2) \left(\frac{2K}{\pi} \right)^2 - 2 \right] , \quad (4.75)$$

$$\xi_1^V = \frac{h^2}{4\varepsilon^2} \left[\left(\frac{2K}{\pi} \right)^2 - 1 \right] , \quad (4.76)$$

$$\xi_1^H = \frac{h^2}{4\varepsilon^2} \left[1 - \left(\frac{2Kk'}{\pi} \right)^2 \right] . \quad (4.77)$$

4.3.3 Rectangular Vacuum Chamber

4.3.3.1 Off-Centered Beam

To conform with the elliptical beam pipe, let h and w be, respectively, the *half height* and *half width* of the rectangular cross section**. When the beam is on the horizontal axis but with fractional offset g (or at distance gw from the center), the image coefficients are††

$$\epsilon_1^V = -\epsilon_1^H = \frac{K^2(k)}{4} \left[\frac{k'^4 \text{sn}^2 \text{cn}^2}{2 \text{dn}^2} - \frac{k'^2(1 - 2 \text{sn}^2)}{3} - \frac{\text{dn}^2(3 - 4 \text{sn}^2 + 4 \text{sn}^4)}{6 \text{sn}^2 \text{cn}^2} \right] , \quad (4.78)$$

**Note that in Ref. [5], h and w are the *full height* and *full width* of the rectangular cross section.

††Equation (4.78) was reported in Eq. (53) of Ref. [5] with a wrong sign in front of sn_{10}^4 inside the last term in the curly brackets.

$$\xi_1^V = \frac{K^2(k)}{4} \frac{k'^4 \operatorname{sn}^2 \operatorname{cn}^2}{\operatorname{dn}^2}, \quad (4.79)$$

$$\xi_1^H = \frac{K^2(k)}{4} \left[k'^2 (1 - 2 \operatorname{sn}^2) + \frac{\operatorname{dn}^2}{\operatorname{sn}^2 \operatorname{cn}^2} \right]. \quad (4.80)$$

The arguments of the elliptic functions sn , cn , dn are

$$\left(\frac{K(k)y_0}{h}, k' \right) = \left(\frac{K(k)w}{h}(1-g), k' \right), \quad (4.81)$$

where $y_0 = (1-g)w$ is the position of the beam measured from one vertical wall of the vacuum chamber, and $K(k)$ is the complete elliptical function of the first kind.

Here, the nome is computed according to

$$q = e^{-2\pi w/h}, \quad (4.82)$$

which is quite different from the one used in Eq. (4.64) for the elliptical beam pipe. Next, the complementary modulus k' can be computed from Eq. (4.65), from which the modulus k can be obtained via Eq. (4.62).

4.3.3.2 Centered Beam

For a centered beam, $g = 0$, the arguments of the elliptical functions become

$$\left(\frac{K(k)w}{h}, k' \right) = \left(\frac{1}{2} K'(k), k' \right) = \left(\frac{1}{2} K(k'), k' \right). \quad (4.83)$$

Notice that the periods of sn , cn , dn with modulus k' are $4K(k')$. The elliptical functions simplify to [6]

$$\operatorname{sn}\left(\frac{1}{2}K(k'), k'\right) = \frac{1}{\sqrt{1+k}}, \quad \operatorname{cn}\left(\frac{1}{2}K(k'), k'\right) = \frac{\sqrt{k}}{\sqrt{1+k}}, \quad \operatorname{dn}\left(\frac{1}{2}K(k'), k'\right) = \sqrt{k}. \quad (4.84)$$

The electric image coefficients simplify to

$$\epsilon_1^V = -\epsilon_1^H = \frac{K^2(k)}{12} (1 - 6k + k^2), \quad (4.85)$$

$$\xi_1^V = \frac{K^2(k)}{4} (1 - k)^2, \quad (4.86)$$

$$\xi_1^H = K^2(k) k, \quad (4.87)$$

which involve only the complete elliptical function of the first kind.

4.3.3.3 Comments

1. Since q decreases exponentially as w/h increases, very accurate value of k' can be computed with Eq. (4.65). For example, even for $1 \geq w/h \geq 0.2$, 14-figure accuracy can be readily obtained for k' and also k^2 afterward using Eq. (4.62), when the summations are extended to $s = 5$. In fact, for centered beam, there is no need to go to $w/h < 1$, because we can interchange the role of w and h .
2. When $w/k > 1$, q becomes very small and k' is very close to 1. (For example, $k^2 = 2.9437 \times 10^{-3}$, 5.5796×10^{-5} and 1.0420×10^{-7} , respectively, when $w/h = 1$, 2 and 3.) Equation (4.62) can no longer give accurate result for k . To preserve accuracy, we must expand k^2 as power series in q with the aid of Eqs. (4.62) and (4.65):

$$k^2 = 16q(1 - 8q + 44q^2 - 192q^3 + 718q^4 - 2400q^5 + 7352q^6 - 20992q^7 + 56549q^8 - \dots) , \quad (4.88)$$

from which 14-figure accuracy can be obtained when $w/k \geq 1$.

3. Because $k^2 \ll 1$ when $w/h > 1$, Eqs. (4.85), (4.86), and (4.87) can be viewed as expansions from values for the infinite horizontal plates. In fact, with

$$K(k) = \frac{\pi}{2} \left[1 + \frac{1}{4}k^2 + \frac{9}{64}k^4 + \mathcal{O}(k^6) \right] , \quad (4.89)$$

we can write

$$\epsilon_1^V = -\epsilon_1^H = \frac{\pi^2}{48} \left[1 - 6k + \frac{3}{2}k^2 - 3k^3 + \frac{27}{32}k^4 - \frac{33}{16}k^5 + \mathcal{O}(k^6) \right] , \quad (4.90)$$

$$\xi_1^V = \frac{\pi^2}{16} \left[1 - 2k + \frac{3}{2}k^2 - k^3 + \frac{27}{32}k^4 - \frac{11}{16}k^5 + \mathcal{O}(k^6) \right] , \quad (4.91)$$

$$\xi_1^H = \frac{\pi^2}{4} k \left[1 + \frac{1}{2}k^2 + \frac{11}{32}k^4 + \mathcal{O}(k^6) \right] . \quad (4.92)$$

4.3.4 Closed Yoke

Mathematically, it is impossible to compute the magnetic image coefficients for a closed cylindrical iron yoke that has infinite relative permeability. In fact, no solution exists

for a closed iron yoke of any geometry. This is because Ampere's law requires

$$\oint \vec{H} \cdot d\ell = I . \quad (4.93)$$

For a beam of current I , the component of magnetic field \vec{H} along the inner surface of the iron yoke is therefore nonzero. Thus, the magnetic flux density \vec{B} inside the yoke becomes infinite. Speaking in the reverse order, if the magnetic flux density inside the yoke is finite, the magnetic field \vec{H} along the inner surface must vanish. From Ampere's law, one gets $I = 0$, or no current is allowed to flow through the yoke.

For a normal-temperature magnet, we like to operate in the linear region of the B - H hysteresis curve, for example at Point N in Fig. 4.6, in order to take advantage of

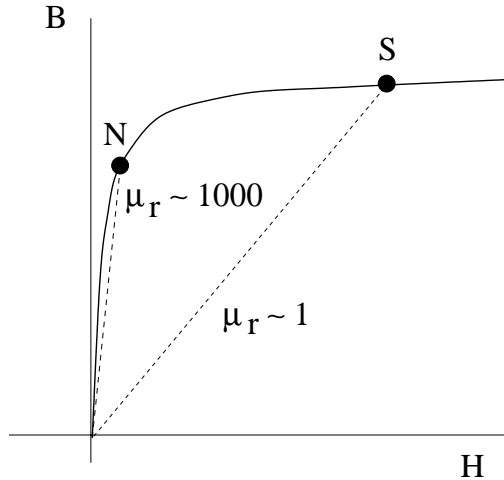


Figure 4.6: B - H hysteresis plot showing the operation of normal temperature magnet at Point N where the relative magnetic permeability μ_r is large. The operation of superconducting magnet is at Point S where the iron yoke is at saturation and $\mu_r \approx 1$.

the large relative magnetic permeability, $\mu_r \sim 1000$. Then, most of the magnetic flux density across the pole gap is supplied by μ_r and only a few percents come from the winding current. Such operation limits the magnetic flux density to $B_{\max} \sim 1.8$ T. This explains why the iron yoke is mostly made up of two pieces glued together with some medium. In that case, \vec{H} will only be large in the medium but relatively small inside the yoke and a much larger beam current will be allowed.

The story for superconducting magnets is quite different. Here, the magnetic flux density is mostly supplied by the high winding current, while the iron yoke is always

saturated. The operation point in the hysteresis curve is now at S of Fig. 4.6 in the large H region where the local slope is 1. Thus the relative permeability μ_r becomes close to 1 and is very much less than the linear region of the hysteresis curve. If a closed iron yoke is used, the maximum beam current allowed by Ampere's law becomes $\mu_r \sim 1000$ times larger at operation point S than at operation point N .

When the relative permeability is finite, the Laplace equation can still be solved using the image method, provided there is sufficient symmetry in the geometry. Readers with interest are referred to, for example, the book by Binns and Lawrenson [7].

In Table 4.2, we tabulate the self-field coefficients for uniformly charged beams and image coefficients for centroid beams [8].

4.4 Connection with Impedance

In Eq. (4.5), the term proportional to y on the right side is absorbed into the betatron tune shift so that ν_0^V becomes ν_V . The equation becomes

$$\frac{d^2y}{ds^2} + \frac{(\nu_V)^2}{R^2}y = \frac{1}{\gamma m v^2} \left. \frac{\partial \langle F_{\text{beam}}(y, \bar{y}) \rangle}{\partial \bar{y}} \right|_{y=0} \bar{y} . \quad (4.94)$$

The coherent force on the right is related to the transverse wake function and therefore the transverse impedance. The connection can be easily made using Eq. (1.28), which says

$$\left. \frac{\partial \langle F_{\text{beam}}(y, \bar{y}) \rangle}{\partial \bar{y}} \right|_{y=0} \bar{y} = \frac{ie Z_1^\perp \beta I \bar{y}}{C} = \frac{ie^2 Z_1^\perp \beta^2 c \lambda \bar{y}}{C} . \quad (4.95)$$

On the other hand, in Eq. (4.12), according to the definition of the image coefficient,

$$e E^V(y, \bar{y})|_{y=0} = \frac{e^2 \lambda Z_0 c}{\pi} \frac{\xi_1^V - \epsilon_1^V}{h^2} \bar{y} . \quad (4.96)$$

As a result, we obtain

$$Z_1^\perp = -i \frac{Z_0 C}{\pi \gamma^2 \beta^2} \frac{\xi_1^V - \epsilon_1^V}{h^2} . \quad (4.97)$$

For a circular beam pipe, $\xi_1^V = \frac{1}{2}$ and $\epsilon_1^V = 0$. This is just exactly the second half of the transverse space charge impedance in Eq. (1.38). Thus, the transverse space charge impedance can be interpreted as the summation of two parts: the part proportional

Table 4.2: Self-field coefficients for uniformly charged beam and image coefficients for centered beam.

Coeff.	Circular	Elliptical	Rectangular	Parallel Plates
ϵ_{spch}^V	$\frac{1}{2}$	$\frac{a_V}{a_H + a_V}$		
ϵ_{spch}^H	$\frac{1}{2}$	$\frac{a_V^2}{a_H(a_H + a_V)}$		
ϵ_1^V	0	$\frac{h^2}{12\varepsilon^2} \left[(1+k'^2) \left(\frac{2K}{\pi} \right)^2 - 2 \right]$	$\frac{K^2(k)}{12} (1 - 6k + k^2)$	$\frac{\pi^2}{48}$
ϵ_1^H	0	$\frac{-h^2}{12\varepsilon^2} \left[(1+k'^2) \left(\frac{2K}{\pi} \right)^2 - 2 \right]$	$\frac{-K^2(k)}{12} (1 - 6k + k^2)$	$-\frac{\pi^2}{48}$
ϵ_2^V	*	*	*	$\frac{\pi^2}{24}$
ϵ_2^H	*	*	*	$-\frac{\pi^2}{24}$
ξ_1^V	$\frac{1}{2}$	$\frac{h^2}{4\varepsilon^2} \left[\left(\frac{2K}{\pi} \right)^2 - 1 \right]$	$\frac{K^2(k)}{4} (1 - k)^2$	$\frac{\pi^2}{16}$
ξ_1^H	$\frac{1}{2}$	$\frac{h^2}{4\varepsilon^2} \left[1 - \left(\frac{2Kk'}{\pi} \right)^2 \right]$	$K^2(k)k$	0
ξ_2^V	*	*	*	$\frac{\pi^2}{16}$
ξ_2^H	*	*	*	0

* ϵ_2 and ξ_2 for closed magnetic boundary (e.g., circular, elliptic, or rectangular) cannot be calculated when the relative permeability $\mu_r \rightarrow \infty$, since the induced magnetic field would not permit a charged beam to pass through because the field energy would become infinite. Closed magnetic yokes are used in superconducting magnets, but there the coefficients $\epsilon_2 = \xi_2 \rightarrow 0$, since the magnetic material is driven completely into saturation ($\mu_r \rightarrow 1$).

$K(k)$ is the complete elliptic integral of the first kind. k is determined from $(w-h)/(w+h) = \exp(-\pi K'/K)$ for the elliptical cross section but $w/h = K'/(2K)$ for the rectangular cross section, where w and h are the half width and half height, with $\varepsilon = \sqrt{w^2 - h^2}$, and $K' = K(k')$ with $k' = \sqrt{1 - k^2}$.

to a^{-2} is the self-field contribution and the part proportional to b^{-2} is the wall image contribution. We can therefore rewrite the expression in a more general form

$$Z_1^{V,H} = i \frac{Z_0 C}{\pi \gamma^2 \beta^2} \left[\frac{\epsilon_{\text{spch}}^{V,H}}{a_V^2} - \frac{\xi_1^{V,H} - \epsilon_1^{V,H}}{h^2} \right], \quad (4.98)$$

where h is the half height of the vacuum chamber.

It is important to distinguish the difference between the force generating the coherent tune shift and the force generating the transverse impedance. The former involves the ξ_1 coefficient while the later involves $\xi_1 - \epsilon_1$. The coherent tune shift is the result of all forces acting on the center of the beam \bar{y} , while the transverse impedance comes from the force generated by the center motion of the beam on an individual particle. In other words,

$$\begin{aligned} \Delta\nu &\propto \frac{\partial \langle F_{\text{beam}}(y, \bar{y}) \rangle}{\partial y} \Big|_{y=0} + \frac{\partial \langle F_{\text{beam}}(y, \bar{y}) \rangle}{\partial \bar{y}} \Big|_{y=0}, \\ Z_1^\perp &\propto \frac{\partial \langle F_{\text{beam}}(y, \bar{y}) \rangle}{\partial \bar{y}} \Big|_{y=0}. \end{aligned} \quad (4.99)$$

Thus, the results can be very different. Take the example of a beam between two infinite conducting planes. Because of horizontal translational invariance, the horizontal force acting at the center of the beam vanishes independent of whether the beam is moving horizontally or vertically. The horizontal coherent tune shift therefore vanishes. However, the horizontal motion of the center of mass of the beam does provide a horizontal force on an individual particle, which may not be moving with the center of mass. That individual particle will therefore see a nonvanishing transverse impedance.

4.5 More about Wake Functions

Most of the time the vacuum chamber is not cylindrical in shape. Thus, the expansion into circular harmonics in Sec. 1.4 cannot be performed. Here, we want to emphasize that it is always completely valid to expand \vec{E} and \vec{B} into circular harmonics. However, when the boundary conditions are applied, \vec{E} and \vec{B} of different circular harmonics will be mixed together, and so are the wake functions W_m for different m 's. In other words, equations corresponding to an individual m are not independent, thus rendering the expansion useless. For this reason, we need to give slightly different definitions for the wake functions when there is no cylindrical symmetry.

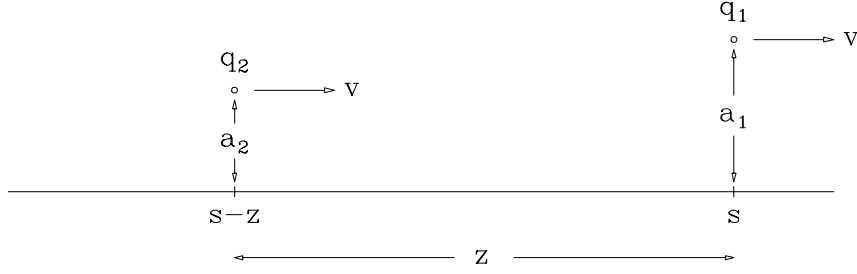


Figure 4.7: Test particle with charge q_1 at an offset of a_1 from the designated path leaves wake fields to the witness particle with charge q_2 at an offset of a_2 at a distance z behind.

Consider a test particle carrying charge q_1 traveling with velocity v longitudinally along a designated path in a vacuum chamber. A witness particle of charge q_2 at a distance z behind along the same path sees a longitudinal force F_0^{\parallel} and a transverse force F_0^{\perp} due to the wake fields of the test particle. In general, these forces depend also on the location s of the test particle along the beam pipe. However, when we apply the impulse approximation, these forces are integrated over s for a long length ℓ of the beam pipe and become functions of z only. For a circular machine, ℓ is taken as the circumference C . Unlike the situation of traveling along the symmetry axis of a cylindrical beam pipe, here there is always an average transverse force $\langle F_0^{\perp} \rangle$. This transverse force comes mostly from the images in the walls of the vacuum chamber. It should be weak in general and can therefore be incorporated into the betatron tunes as tune shifts in the way discussed above in Sec. 4.1.

The *longitudinal wake function* is defined as

$$W'_0(z) = -\frac{\langle F_0^{\parallel} \rangle \ell}{q_1 q_2}, \quad (4.100)$$

where $\langle F_0^{\parallel} \rangle \ell$ denotes the longitudinal integrated wake force or impulse.

If the path of the source particle is displaced transversely by a_1 from the designated path as in Fig. 4.7, the witness particle displaced by a_2 at a distance z behind will see a longitudinal force F_1^{\parallel} and a transverse force F_1^{\perp} . The *transverse wake function* is now defined by

$$W_1(z) = -\lim_{a_1, a_2 \rightarrow 0} \frac{(\langle F_1^{\perp} \rangle - \langle F_0^{\perp} \rangle) \ell}{a_1 q_1 q_2}, \quad (4.101)$$

where the transverse force along the designated path $\langle F_0^{\perp} \rangle$ has been subtracted away

because it has been taken care of already as tune shifts. Defined in this way, $W'_0(z)$ and $W_1(z)$ will be the same as the $m = 0$ longitudinal wake function and the $m = 1$ transverse wake function defined in Chapter 1.

4.6 Exercises

4.1. Consider a beam with bi-parabolic or semi-circular distribution

$$\rho(r) = \frac{2e\lambda}{\pi\hat{r}^2} \left(1 - \frac{r^2}{\hat{r}^2}\right), \quad (4.102)$$

where \hat{r} is the radial extent of the beam and λ is the linear particle density.

- (1) Compute the self-field or space charge incoherent tune shift at the center of the beam where it is maximal and show that the space charge coefficient defined in Eq. (4.25) is $\epsilon_{\text{spch}} = 1$.
- (2) Explain how one can understand that ϵ_{spch} for this distribution is in between $\epsilon_{\text{spch}} = \frac{1}{2}$ for uniform distribution and $\epsilon_{\text{spch}} \approx \frac{3}{2}$ for bi-Gaussian distribution.

4.2. The horizontal betatron tune shift due to a quadrupole gradient error $\Delta k(s) = \Delta B'_V/(B\rho)$ at location s along the accelerator ring is

$$\Delta\nu_{\beta_H} = \frac{1}{4\pi} \int_0^C \beta_H(s) \Delta k(s) ds, \quad (4.103)$$

where β_H is the betatron function, C is the circumference of the ring, $\Delta B'_V$ is the vertical quadrupole gradient error, and $(B\rho)$ is the magnetic rigidity. Consider the space charge self-force as a quadrupole gradient error, derive, using the above formula, the incoherent dipole space charge tune shift, Eq. (4.24), inside a beam of uniform transverse distribution.

4.3. Consider a beam with elliptic cross section and uniform particle distribution.

- (1) Show that the electric potential

$$V(x, y) = -\frac{e\lambda}{2\pi\epsilon_0} \frac{1}{a_H + a_V} \left(\frac{x^2}{a_H} + \frac{y^2}{a_V}\right) \quad (4.104)$$

for $x^2/a_H^2 + y^2/a_V^2 < 1$ and 0 otherwise, satisfies the Laplace equation

$$\nabla^2 V(x, y) = -\frac{e\lambda}{\pi\epsilon_0 a_H a_V}, \quad (4.105)$$

where λ is the linear particle density of the beam.

- (2) Show that inside the beam, the transverse electric fields are

$$E_x = \frac{e\lambda}{\pi\epsilon_0} \frac{x}{a_H(a_H + a_V)}$$

$$E_x = \frac{e\lambda}{\pi\epsilon_0} \frac{y}{a_V(a_H + a_V)} \quad (4.106)$$

(3) Comparing with the electric field components inside a cylindrically symmetric beam of radius a , show that the space charge tune shift coefficients, defined in Eq. (4.25), inside this beam of elliptic cross section are

$$\epsilon_{\text{spch}}^H = \frac{a_V^2}{a_H(a_H + a_V)} \quad \text{and} \quad \epsilon_{\text{spch}}^V = \frac{a_V}{a_H + a_V} . \quad (4.107)$$

4.4. We are going to derive the electric potential $V(x, y, z)$ for a 3-dimensional charge distribution,

$$\rho(x, y, z) = \frac{eN}{(2\pi)^{3/2}\sigma_x\sigma_y\sigma_z} \exp\left[-\frac{x^2}{2\sigma_x^2} - \frac{y^2}{2\sigma_y^2} - \frac{z^2}{2\sigma_z^2}\right] , \quad (4.108)$$

following the method of Takayama [9], where N is the total number of particles.

(1) Show that the Green function of the Laplace equation can be written as

$$G(\vec{r}, \vec{\xi}) = \frac{1}{4\pi|\vec{r} - \vec{\xi}|} = \frac{1}{2\pi^{3/2}} \int_0^\infty dq e^{-|\vec{r} - \vec{\xi}|^2 q^2} . \quad (4.109)$$

In other words, $G(\vec{r}, \vec{\xi})$ satisfies

$$\nabla^2 G(\vec{r}, \vec{\xi}) = -\delta(\vec{r} - \vec{\xi}) . \quad (4.110)$$

(2) Changing the variable of integration to $t = q^{-2}$, show that the electric potential can be written as

$$V(x, y, z) = \frac{1}{4\pi^{3/2}\epsilon_0} \int_0^\infty \frac{dt}{t^{3/2}} \int_{-\infty}^\infty d\vec{\xi} \rho(\vec{\xi}) e^{-|\vec{r} - \vec{\xi}|^2/t} . \quad (4.111)$$

(3) With ρ given by Eq. (4.108), derive the electric potential

$$V(x, y, z) = \frac{eN}{4\pi^{3/2}\epsilon_0} \int_0^\infty dt \frac{\exp\left[-\frac{x^2}{(2\sigma_x^2+t)} - \frac{y^2}{(2\sigma_y^2+t)} - \frac{z^2}{(2\sigma_z^2+t)}\right]}{\sqrt{(2\sigma_x^2+t)(2\sigma_y^2+t)(2\sigma_z^2+t)}} . \quad (4.112)$$

4.5. Consider a beam with bi-Gaussian transverse charge distribution,

$$\rho(x, y) = \frac{e\lambda}{2\pi\sigma_x\sigma_y} \exp\left(-\frac{x^2}{2\sigma_x^2} - \frac{y^2}{2\sigma_y^2}\right) , \quad (4.113)$$

where σ_x and σ_y are the rms width and height, and λ is the linear particle density.

(1) From Eq. (4.112), show that the electric potential is

$$V(x, y) = \frac{e\lambda}{4\pi\epsilon_0} \int_0^\infty dt \frac{\exp\left[-\frac{x^2}{(2\sigma_x^2+t)} - \frac{y^2}{(2\sigma_y^2+t)}\right]}{\sqrt{(2\sigma_x^2+t)(2\sigma_y^2+t)}}. \quad (4.114)$$

(2) Show that the transverse electric fields are

$$E_x = \frac{e\lambda x}{4\pi\epsilon_0} \int_0^\infty dt \frac{\exp\left[-\frac{x^2}{(2\sigma_x^2+t)} - \frac{y^2}{(2\sigma_y^2+t)}\right]}{(2\sigma_x^2+t)\sqrt{(2\sigma_x^2+t)(2\sigma_y^2+t)}},$$

$$E_y \rightarrow E_x \quad \text{with } x \rightarrow y, \quad y \rightarrow x. \quad (4.115)$$

(3) The self-field or space charge tune shifts are at their maxima at the center of the beam, or $x \rightarrow 0$ and $y \rightarrow 0$. Show that they are given by Eq (4.33) with

$$\begin{aligned} \sigma^2 &\rightarrow \frac{\sigma_x(\sigma_x + \sigma_y)}{2} \quad \text{for } \Delta\nu_{\text{spch coh}}^H \\ \sigma^2 &\rightarrow \frac{\sigma_y(\sigma_x + \sigma_y)}{2} \quad \text{for } \Delta\nu_{\text{spch coh}}^V. \end{aligned} \quad (4.116)$$

4.6. Derive the lowest order space charge self-force coefficient ϵ_{spch} of a particle with betatron amplitude r inside a cylindrical symmetric coasting beam with transverse bi-Gaussian distribution.

Answer: $\epsilon_{\text{spch}} = \frac{1}{2}f(r/\sigma_r)$ where σ_r is the rms beam radius and the form factor $f(r/\sigma_r)$ is given by Eq. (4.38).

Bibliography

- [1] L.J. Laslett, Proceedings of 1963 summer Study on Storage Rings, BNL-Report 7534, p. 324; L.J. Laslett and L. Resegotti, Proceedings of VIth Int. Conf. on High Energy Accelerators, Cambridge, MA, 1967, p. 150.
- [2] B. Zotter, CERN Reports ISR-TH/72-8 (1972); IST-TH/74-38 (1974); ISR-TH/75-17 (1975); Proceedings of VIth National particle Accelerator Conf., Washington DC, 1974 (IEEE, 1975).
- [3] B. Zotter, Nucl. Instru. Meth. **129**, 377 (1975).
- [4] B. Zotter, CERN Report ISR-TH/74-11 (1974).
- [5] K.Y. Ng, Particle Accelerators **16**, 63 (1984).
- [6] See, for example, Table 16.5, p.571 of Abramowitz and Stegun, Handbook of Mathematical Functions, Dover, 1965.
- [7] K.J. Binns and P.J. Lawrenson, *Analysis and Computation of Electric and Magnetic Field Problems*, 2nd Ed., Pergamon Press, 1973.
- [8] G. Guignard, CERN 77-10 (1977).
- [9] K. Takayama, Lett. Al Nuovo Cimento **34**, 190 (1982).

Chapter 5

ENVELOPE EQUATION

We often read that when the linear part of the space charge force is added to the linear equation of motion, it produces an incoherent tune shift, which if large enough can place individual particles onto low-order betatron resonant lines resulting in an instability. This picture, although appealing, is very misleading. In fact, the resonant driving force drives the beam to resonance only when the *coherent* space charge tune shift lands the coherent betatron tune of the beam onto the resonance lines. We are going to show that resonant driving force of any order will *not* affect an individual particle when the space charge force shifts its betatron tune onto the resonance line of that order.

5.1 The Integer Resonance

In this section, we are going to study the effects on beam particles under the influence of errors in the dipoles. We will find that although the beam center is able to see the force from the dipole errors, it will not see the self-fields from the beam particles. On the other hand, a single particle sees the self-fields and has its betatron tunes shifted. However, a single particle oscillating at an integer tune will be not be driven by the dipole-error force. We shall follow a discussion by Baartman [1].

The integer resonance is driven by errors in the dipoles around the accelerator ring. The transverse motion of a beam particle is governed by

$$\frac{d^2 X}{d\psi^2} + \nu_{0x}^2 X = F_{scx} + F_{ex}(\psi) \quad (5.1)$$

where

$$\psi = \int_0^s \frac{ds}{\nu_{0x} \beta_x(s)} \quad (5.2)$$

is the transverse Floquet phase which advances by 2π per turn, X is the normalized transverse offset (actual offset x divided by square root of the betatron function β_x), and ν_{0x} is the bare betatron tune. The *force** due to errors in dipoles in the x -direction is represented by $F_{ex}(\psi)$, which is periodic in ψ and is X independent. The space charge force F_{scx} , if linear, can be written as

$$F_{scx} = -2\nu_{0x} \Delta\nu_{sc}(X - \langle X \rangle) , \quad (5.3)$$

where $\langle X \rangle$ is the transverse offset of the center of charge of the beam and $\Delta\nu_{sc}$ is the incoherent space charge tune shift depicted in, for example, Eq. (4.24). The equation of motion becomes

$$\frac{d^2 X}{d\psi^2} + \nu_{0x}^2 X = -2\nu_{0x} \Delta\nu_{sc}(X - \langle X \rangle) + F_{ex}(\psi) . \quad (5.4)$$

Taking the average, we obtain the equation of motion for the center of the beam,

$$\frac{d^2 \langle X \rangle}{d\psi^2} + \nu_{0x}^2 \langle X \rangle = F_{ex}(\psi) . \quad (5.5)$$

The space charge term disappears, indicating that the motion of the center of charge is not affected by the space charge self-force. Physically, the beam transverse motion is rigid and therefore the center cannot see any change in the pattern of the space charge self-field. In other words, there is no coherent dipole space charge tune shift. However, we do see that the center of the beam is driven by the dipole force due to lattice error. The beam will be unstable if the coherent tune ν_{0x} , or just bare tune here, is equal to an integer. Another way of saying the same thing is that as the coherent tune approaches an integer, the closed-orbit distortion, being kicked in the same direction in every turn, increases without limit. To show this more clearly, let us write the n th-harmonic component of the periodic lattice-error force as $F_{ex}(\psi) = f_n e^{in\psi}$. The particular solution of Eq. (5.5) is

$$\langle X \rangle = \frac{f_n e^{in\psi}}{\nu_{0x}^2 - n^2} , \quad (5.6)$$

*Here F_{scx} and F_{ex} do not have the dimension of a force. They should be forces divided by appropriate variables. But for simplicity, we just call them forces.

which is indeed unstable when the $\nu_{0x} = n$.

The incoherent motion is obtained by subtracting Eq. (5.5) from Eq. (5.4),

$$\frac{d^2}{d\psi^2} (X - \langle X \rangle) + (\nu_{0x}^2 + 2\nu_{0x}\Delta\nu_{sc}) (X - \langle X \rangle) = 0 , \quad (5.7)$$

showing that an individual particle is making betatron motion about the center of the beam with the incoherent betatron tune $\nu_{incoh} = \nu_{0s} + \Delta\nu_{sc}$. It is important to notice that the incoherent equation of motion contains no driving terms for the integer resonance. Therefore, incoherent motion is not affected by dipole errors. This means that the incoherent tune can be equal to an integer with no adverse effects. It is worth re-emphasizing: A particle which is shifted by direct space charge to a tune of exactly an integer, turn by turn sees the same dipole errors at the same betatron phase, and yet is not even slightly affected compared with other particles which do not have an integer tune. This is not due to space charge stabilizing the resonance, as claimed by Ref. [2], because in this example of linear space charge, there is no incoherent tune spread to generate Landau damping. The correct answer is simply no driving term for incoherent motion.

This concept can be extended easily to any nonlinear space charge force. For the i th particle, the equation of motion is

$$\frac{d^2X_i}{d\psi^2} + \nu_{0x}^2 X_i = \sum_j' F_{ij} + F_{ex} , \quad (5.8)$$

where F_{ij} is the force of the j th particle acting on the i th particle, and \sum_j' implies a summation over j but with $j = i$ excluded. Thus, $\sum_j' F_{ij}$ is just the space charge force on the i th particle. We now take the average of Eq. (5.8) by summing over i , giving exactly Eq. (5.5) again. This result is obtained because of Newton's third law: $F_{ij} = -F_{ji}$ when $i \neq j$. Subtracting Eq. (5.5) from Eq. (5.8), we arrive at the incoherent equation

$$\frac{d^2}{d\psi^2} (X - \langle X \rangle) + \nu_{0x}^2 (X_i - \langle X \rangle) = \sum_j' F_{ij} . \quad (5.9)$$

Again, there is no dipole driving force for the equation of incoherent motion. The space charge self-force, being nonlinear, does not just reduce to a simple incoherent tune shift. The incoherent tune will be different for different particle depending on its amplitude and the transverse beam distribution. However, whatever the incoherent tune is, even at an integer, the individual particle will not be affected by the dipole lattice error at all.

5.2 The K-V Equation

Now let us come to the errors in the quadrupoles. This force, denoted by $XF(\psi)$ is responsible for the half-integer resonance. Sometimes it is also called the linear error force, because quadrupoles are linear elements of the accelerator lattice. The equation of transverse motion for a particle is

$$\frac{d^2 X}{d\psi^2} + \nu_{0x}^2 X = -2\nu_{0x}\Delta\nu_{sc}(X - \langle X \rangle) + XF(\psi), \quad (5.10)$$

where a linear space charge force $-2\nu_{0x}\Delta\nu_{sc}(X - \langle X \rangle)$ has been assumed. Coherent motion is obtained by averaging Eq. (5.10),

$$\frac{d^2 \langle X \rangle}{d\psi^2} + \nu_{0x}^2 \langle X \rangle = \langle X \rangle F(\psi), \quad (5.11)$$

and the difference gives the incoherent motion

$$\frac{d^2}{d\psi^2} (X - \langle X \rangle) + (\nu_{0x}^2 + 2\nu_{0x}\Delta\nu_{sc}) (X - \langle X \rangle) = (X - \langle X \rangle) F(\psi). \quad (5.12)$$

It appears in Eq. (5.12) that the incoherent motion is driven by the quadrupole-error force so that the particle will experience an instability at the half integer. This conclusion is incorrect, although there is nothing wrong with the derivation from Eqs. (5.10) to (5.12). A quadrupole in the lattice will change the size of the particle beam and so will the quadrupole-error force. The incoherent space charge tune shift depends on the beam size, which is a function of the quadrupole error force $XF(\psi)$. Actually, the effect of the quadrupole-error force inside the incoherent space charge tune shift just cancels the quadrupole-error force on the right side of Eq. (5.12), leaving behind an incoherent motion not affected by the quadrupole-error force. To demonstrate this, we need to study the equation of motion governing the beam size or beam envelope.

The dipole coherent tune shifts are zero because the beam center does not experience any variation of the forces between beam particles, when the beam is executing rigid dipole oscillations as a whole. Thus, the space charge forces do not affect the restoring force of rigid oscillation and therefore do not affect the dipole coherent tunes. However, there are other collective modes of oscillation in a beam. Examples are the breathing mode, where the transverse beam size expands and contract without the beam center being moved, and the mode when the breathing in the two transverse directions are 180°

out of phase. The restoring forces of these modes of oscillation do depend on the forces between the beam particles. Thus, their frequencies of oscillation are affected by the space charge forces. To study these modes, we need to resort to the equations of motion governing the beam envelope.

The envelope equation was first derived by Kapchinsky and Vladimirskey [3] for a coasting beam with uniform charge density and elliptical cross section. Later it was generalized by Sacherer [4] to include any distribution when the beam envelope \hat{x} is replaced by the rms beam size $\tilde{x} = \sqrt{\langle x^2 \rangle}$ of the beam. We are going to follow Sacherer's approach.

Consider an ensemble of particles that obey the single-particle equations

$$\begin{aligned} x' &= p_x , \\ p'_x &= F_x(x, s) , \end{aligned} \tag{5.13}$$

where x is the transverse offset, p is the canonical momentum, and the prime denotes derivative with respect to time s , the distance along the designed orbit of the accelerator. The total force[†] in the x -direction,

$$F_x(x, s) = F_{scx} + F_{extx} , \tag{5.14}$$

includes the space charge self-force F_{scx} and the external force F_{extx} . Averaging over the particle distribution $f(x, p, s)$, we obtain the equations of motion for the center of the beam:

$$\begin{aligned} \langle x \rangle' &= \langle p_x \rangle , \\ \langle p_x \rangle' &= \langle F_x(x, s) \rangle = \langle F_{extx} \rangle . \end{aligned} \tag{5.15}$$

where the last equation follows from $\langle F_{scx} \rangle = 0$ because of Newton's third law. Note that the order of the averaging and differentiation with respect to s is immaterial and can be interchanged if one wishes. For a linear machine, for example with only dipoles and quadrupoles in the ring, the external force is linear. We can write $F_{extx} = K_x(s)x$, and the equation of motion governing the center of the beam becomes

$$\langle x \rangle'' + K_x(s)\langle x \rangle = 0 , \tag{5.16}$$

which involves only first moments and is independent of the space charge force or the detailed form of the beam distribution.

[†]We call them forces, although $F_x(x, s)$, F_{scx} , and F_{extx} do not have the dimension of a force. Note that they have different dimension from the forces introduced in Eq. (5.1).

The second moments satisfy the equations

$$\begin{aligned}\langle x^2 \rangle' &= 2 \langle xx' \rangle = 2 \langle xp_x \rangle , \\ \langle xp_x \rangle' &= \langle x' p_x \rangle + \langle xp'_x \rangle = \langle p_x^2 \rangle - K_x(s) \langle x^2 \rangle + \langle x F_{scx} \rangle , \\ \langle p_x^2 \rangle' &= 2 \langle pp'_x \rangle = -2K_x(s) \langle xp_x \rangle + 2 \langle p_x F_{scx} \rangle .\end{aligned}\quad (5.17)$$

Notice that this set of equations is not closed because $\langle x F_{scx} \rangle$ and $\langle p F_{scx} \rangle$ are usually functions of the higher moments like $\langle x^n \rangle$, $\langle x^n p_x \rangle$, etc. As will be demonstrated below, if the self-force is derived from the free-space Poisson equation, $\langle x F_{scx} \rangle$ depends mainly on the second moments and very little, if at all, on the higher moments.

Let us introduce the rms emittance

$$E_x = \sqrt{\langle x^2 \rangle \langle p_x^2 \rangle - \langle xp_x \rangle^2} . \quad (5.18)$$

Using the rate of change in the second moments in Eq. (5.17), the rate of change of the rms emittance along the accelerator is

$$E'_x = \frac{\langle xp_x \rangle \langle x F_{scx} \rangle - \langle x^2 \rangle \langle p_x F_{scx} \rangle}{E_x} . \quad (5.19)$$

Thus, the rms emittance is an invariant provided that the space charge force is linear, or when it can be written as $F_{scx} = \epsilon(s)(x - \langle x \rangle)$. However, if we assume that the rms emittance is either time invariant or its time dependency is known *a priori*, $\langle p_x^2 \rangle$ can be expressed in terms of $\langle x^2 \rangle$, $\langle xp_x \rangle$, and E_x . Then, the first two equations in Eq. (5.17) form a closed set, and they can be combined to give

$$\tilde{x}'' + K(s)\tilde{x} - \frac{E_x^2}{\tilde{x}^3} - \frac{\langle x F_{scx} \rangle}{\tilde{x}} = 0 , \quad (5.20)$$

where $\tilde{x} = \sqrt{\langle x^2 \rangle}$ is the rms beam size.

The space charge term has an interesting interpretation. If we define the linear part of the space charge force F_{scx} as $\varepsilon(s)x$, where $\varepsilon(s)$ is determined by minimizing at a fixed time

$$D = \int [\varepsilon(s)x - F_{scx}]^2 n(x, s) dx , \quad (5.21)$$

where the linear distribution is

$$n(x, s) = \int f(x, p, s) dp , \quad (5.22)$$

and the phase-space distribution is $f(x, p_x, s)$, then we obtain

$$\varepsilon(s)x = \frac{\langle xF_{sc}x \rangle}{\tilde{x}^2}x . \quad (5.23)$$

In other words, the rms envelope equation depends only on the linear part of the space charge force determined by least square.

Finally, let us express the envelope equation in terms of the static electric field \mathcal{E}_x of the space charge self-force in the x -direction and put back all the missing factors. The envelope equation in the mks units now reads

$$\tilde{x}'' + K(s)\tilde{x} - \frac{E_x^2}{\tilde{x}^3} - \frac{e}{m\gamma^3\beta^2c^2} \frac{\langle x\mathcal{E}_x \rangle}{\tilde{x}} = 0 , \quad (5.24)$$

where m is the mass of the beam particles. In the denominator, we have the Lorentz factor $\gamma\beta^2$ because of Newton's second law and the other γ^2 because of the presence of the magnetic field of the beam in the laboratory frame, as demonstrated in Eqs. (4.23) and (4.24).

5.2.1 One Dimension

Consider a very long beam traveling in the z -direction with very wide width in the y -direction. The situation can be approximated by a one-dimensional beam having space charge self-force only in the x -direction and we assume that its distribution is symmetric with respect to the $x = 0$ plane. The static electric field \mathcal{E}_x in the x -direction is given by Poisson equation

$$\frac{\partial \mathcal{E}_x}{\partial x} = \frac{e}{\epsilon_0} n(x, s) , \quad (5.25)$$

from which

$$\mathcal{E}_x = \frac{e}{\epsilon_0} \int_0^x n(x', s) dx' . \quad (5.26)$$

Here, $n(x, s)$ is the particle distribution per unit volume. Therefore, when integrated over x from $-\infty$ to $+\infty$, it is normalized to σ , the particle density per unit area in the y - z plane. Since the electric field is proportional to the fraction of particles it encloses between $\pm x$, we must have $\mathcal{E}_x \propto 1/\tilde{x}$. Thus,

$$\frac{\langle x\mathcal{E}_x \rangle}{\tilde{x}} = \frac{e}{\epsilon_0} \frac{\int_{-\infty}^{\infty} x \frac{n(x)}{\sigma} dx \int_0^x n(x') dx'}{\left[\int_{-\infty}^{\infty} x^2 \frac{n(x)}{\sigma} dx \right]^{1/2}} = \frac{e\sigma}{2\epsilon_0} \varrho , \quad (5.27)$$

where we have defined the dimensionless parameter

$$\varrho = \frac{2 \int_{-\infty}^{\infty} x h(x) dx \int_0^x h(x') dx'}{\left[\int_{-\infty}^{\infty} x^2 h(x) dx \right]^{1/2}}. \quad (5.28)$$

We have introduced a new distribution function $h(x) = n(x)/\sigma$ so that σ , the particle number per unit area in the y - z plane, is factored out and $h(x)$ is normalized to unity. It is important to point out that while ϱ is dimensionless, $h(x)$ can be scaled to anything that is convenient. For example, in a uniform distribution, we can choose the edges as ± 1 , and in a Gaussian distribution, we can choose the rms spread as 1. Substituting in Eq. (5.24), the one dimensional envelope equation now becomes

$$\tilde{x}'' + K(s)\tilde{x} - \frac{E_x^2}{\tilde{x}^3} - \frac{2\pi r_0 \sigma}{\gamma^3 \beta^2} \varrho = 0, \quad (5.29)$$

where $r_0 = e^2/(4\pi\epsilon_0 mc^2)$ is the classical radius of the beam particles. Table 5.1 shows the values of ϱ for four distributions. We see that for a wide range of distributions that are likely to be encountered, the variation of ϱ is less than 2.3%. Thus the one dimension rms envelope equation will be accurately described by Eq. (5.29) with $\varrho = 1/\sqrt{3}$.

Table 5.1: The values of the dimensionless parameter ϱ for a wide range of distributions. They are all close to $1/\sqrt{3}$.

Distribution	$h(x)$	$\sqrt{3}\varrho$
Uniform	$\begin{cases} \frac{1}{2} & x \leq 1 \\ 0 & x > 1 \end{cases}$	1.000
Parabolic	$\begin{cases} \frac{3}{4}(1-x^2) & x \leq 1 \\ 0 & x > 1 \end{cases}$	0.996
Gaussian	$\frac{1}{\sqrt{2\pi}}e^{-x^2/2}$	0.977
Hollow	$\frac{1}{\sqrt{2\pi}}x^2e^{-x^2/2}$	0.987

For a uniform distribution in one dimension, the half widths of the beam is $\hat{x} = \sqrt{3}\tilde{x}$. The full emittance is $\epsilon_x = 3E_x$, since we also have $\hat{p}_x = \sqrt{3}\sqrt{\langle p_x^2 \rangle}$. The envelope equation

for the half beam width in one dimension becomes

$$\hat{x}'' + K(s)\hat{x} - \frac{\epsilon_x^2}{\hat{x}^3} - \frac{2\pi r_0 \sigma}{\gamma^3 \beta^2} = 0 , \quad (5.30)$$

where $\varrho = 1/\sqrt{3}$ has been substituted.

5.2.2 Two Dimensions

With the absence of cross-correlations and coupling terms, the rms envelope equations in the two transverse directions are given by Eq. (5.24) and the two space charge terms $\langle xF_{scx} \rangle$ and $\langle yF_{scy} \rangle$ depend on the particle distribution. It will be shown below that $\langle xF_{scx} \rangle$ and $\langle yF_{scy} \rangle$ depend only on second moments if the distribution has the elliptical symmetry

$$n(x, y, s) = n\left(\frac{x^2}{a^2} + \frac{y^2}{b^2}, s\right) , \quad (5.31)$$

which when integrated over x and y gives the linear particle density λ . Corresponding to this distribution, the static electric field in the x -direction at a fixed location s is given by

$$\mathcal{E}_x = \frac{eabx}{2\epsilon_0} \int_0^\infty \frac{n(T)}{a^2 + u} \frac{du}{D(u)} , \quad (5.32)$$

where

$$D(u) = \sqrt{(a^2 + u)(b^2 + u)} \quad (5.33)$$

and

$$T = \frac{x^2}{a^2 + u} + \frac{y^2}{b^2 + u} . \quad (5.34)$$

The validity of Eq. (5.32) can be verified by computing the divergence of the electric field. We get

$$\frac{\partial \mathcal{E}_x}{\partial x} = \frac{eab}{2\epsilon_0} \int_0^\infty \frac{du}{D(u)} \left[\frac{n(T)}{a^2 + u} + \frac{2x^2 n'(T)}{(a^2 + u)^2} \right] . \quad (5.35)$$

Changing variable of integration from u to T ,

$$dT = - \left[\frac{x^2}{(a^2 + u)^2} + \frac{y^2}{(b^2 + u)^2} \right] du \quad (5.36)$$

and noting that

$$\frac{d \ln D(u)}{du} = \frac{1}{2} \left(\frac{1}{a^2 + u} + \frac{1}{b^2 + u} \right) , \quad (5.37)$$

we arrive at

$$\vec{\nabla} \cdot \vec{\mathcal{E}} = \frac{eab}{2\epsilon_0} \left[\int_0^\infty \frac{du}{D(u)} 2n(T) \frac{d \ln D(u)}{du} - \int_{u=0}^{u=\infty} dT \frac{2n'(T)}{D(u)} \right] , \quad (5.38)$$

The variable in the first integral can now be easily changed from u to T , and we obtain

$$\begin{aligned} \vec{\nabla} \cdot \vec{\mathcal{E}} &= \frac{eab}{\epsilon_0} \int_{u=0}^{u=\infty} dT \left[\frac{n(T)}{D^2} \frac{dD}{dT} - \frac{n'(T)}{D} \right] \\ &= -\frac{eab}{\epsilon_0} \int_{u=0}^{u=\infty} dT \frac{d}{dT} \left[\frac{n}{D} \right] = \frac{e}{\epsilon_0} n \left(\frac{x^2}{a^2} + \frac{y^2}{b^2} \right) , \end{aligned} \quad (5.39)$$

as required by Gauss's law. In passing, we give also the electric potential

$$\Phi(x, y) = -\frac{eab}{4\epsilon_0} \int_0^\infty \frac{du}{D(u)} \int_0^T dT' n(T') . \quad (5.40)$$

Now we are ready to compute $\langle x\mathcal{E}_x \rangle$ and $\langle y\mathcal{E}_y \rangle$. By definition,

$$\langle x\mathcal{E}_x \rangle = \frac{eab}{2\epsilon_0 \lambda} \int_0^\infty \frac{du}{D(u)} \int_{-\infty}^\infty \frac{x^2 dx}{a^2 + u} \int_{-\infty}^\infty dy n(T) n \left(\frac{x^2}{a^2} + \frac{y^2}{b^2} \right) . \quad (5.41)$$

This suggests the change of variables x and y to the circular coordinates r and θ ,

$$r \cos \theta = \frac{x}{\sqrt{a^2 + u}} , \quad r \sin \theta = \frac{y}{\sqrt{b^2 + u}} \rightarrow \frac{dx dy}{D(u)} = r dr d\theta . \quad (5.42)$$

We also let

$$r'^2 = \frac{x^2}{a^2} + \frac{y^2}{b^2} = r^2 \left[\frac{a^2 + u}{a^2} \cos^2 \theta + \frac{b^2 + u}{b^2} \sin^2 \theta \right] . \quad (5.43)$$

The integration variable u is now changed to r' with

$$2r' dr' = \frac{r^2}{a^2 b^2} (a^2 \sin^2 \theta + b^2 \cos^2 \theta) du , \quad (5.44)$$

with the integration limits u from 0 to ∞ changed to r to ∞ . All these changes convert Eq. (5.41) to

$$\langle x\mathcal{E}_x \rangle = \frac{ea^3 b^2}{2\pi\epsilon_0 \lambda (a+b)} \int_0^\infty n(r^2) 2\pi r dr \int_r^\infty n(r'^2) 2\pi r' dr' , \quad (5.45)$$

where the integration over θ has been performed with the help of

$$\int_0^{2\pi} \frac{\cos^2 \theta}{a^2 \sin^2 \theta + b^2 \cos^2 \theta} d\theta = \frac{2\pi}{b(a+b)} . \quad (5.46)$$

Note that the variables r and r' carry no dimension. With the new defined function

$$Q(r) = ab \int_0^r n(r'^2) 2\pi r' dr' \quad \text{with} \quad Q(\infty) = \lambda , \quad (5.47)$$

Eq. (5.45) can be integrated to give

$$\langle x\mathcal{E}_x \rangle = \frac{ea}{2\pi\epsilon_0\lambda(a+b)} \int_0^\infty dr \frac{dQ(r)}{dr} [\lambda - Q(r)] = \frac{ea\lambda}{4\pi\epsilon_0(a+b)} . \quad (5.48)$$

Since $\tilde{x} = \sqrt{\langle x^2 \rangle} \propto a$ and $\tilde{y} = \sqrt{\langle y^2 \rangle} \propto b$, we obtain the final rms envelope equation in two dimension:

$$\begin{aligned} \tilde{x}'' + K_x(s)\tilde{x} - \frac{E_x^2}{\tilde{x}^3} - \frac{r_0\lambda}{\gamma^3\beta^2} \frac{1}{\tilde{x} + \tilde{y}} &= 0 , \\ \tilde{y}'' + K_y(s)\tilde{y} - \frac{E_y^2}{\tilde{y}^3} - \frac{r_0\lambda}{\gamma^3\beta^2} \frac{1}{\tilde{x} + \tilde{y}} &= 0 . \end{aligned} \quad (5.49)$$

For a uniform distribution with elliptical symmetry in two dimensions, the half widths of the beam are $\hat{x} = 2\tilde{x}$ and $\hat{y} = 2\tilde{y}$. The emittance is $\epsilon_{x,y} = 4E_{x,y}$, since we also have $\hat{p}_{x,y} = 2\sqrt{\langle p_{x,y} \rangle}$. The envelope equation becomes

$$\begin{aligned} \hat{x}'' + K_x(s)\hat{x} - \frac{\epsilon_x^2}{\hat{x}^3} - \frac{4r_0\lambda}{\gamma^3\beta^2} \frac{1}{\hat{x} + \hat{y}} &= 0 , \\ \hat{y}'' + K_y(s)\hat{y} - \frac{\epsilon_y^2}{\hat{y}^3} - \frac{4r_0\lambda}{\gamma^3\beta^2} \frac{1}{\hat{x} + \hat{y}} &= 0 . \end{aligned} \quad (5.50)$$

These are just the well-known K-V equations. However, the rms envelope equations depicted in Eq. (5.49) are not restricted to the uniform K-V distribution and are valid for any distribution with elliptical symmetry.

Two comments are in order. First, the distribution with elliptical symmetry, represented by Eq. (5.31), is a very general distribution. Nearly all practical beam distributions fall into this category. Therefore, Sacherer's conclusion that $\langle x\mathcal{E}_x \rangle$ in Eq. (5.48) does not involve moment higher than second order is remarkable. Second, the rate of change of the beam emittance E_x , Eq. (5.19), depends on both $\langle x\mathcal{E}_x \rangle$ and $\langle p_x\mathcal{E}_x \rangle$, and will vanish if both of them do not involve moments higher than second order. Unfortunately, $\langle p_x\mathcal{E}_x \rangle$ does depend on moments of the beam which is higher than second order. As a result, the emittance introduced in Eq. (5.18) is time dependent and this renders the rms envelope equations not a closed system. The set of rms envelope equations is only closed when the distribution is uniform. It can be shown that the rate of increase of emittance is just proportional to the energy of the part of the space charge self-field that is nonlinear [5, 6, 7].

5.3 Collective Oscillations of Beams

5.3.1 One Dimension

The one-dimension envelope equation for uniform beam, Eq. (5.29), contains the external focusing term $K_x(s)$, which includes both the ideal quadrupole focusing force and the gradient errors. We first eliminate the rapidly varying part of $K_x(s)$ from the envelope equation by introducing the Floquet phase advance ψ_x , which increases by 2π each revolution turn,

$$\psi_x = \int_0^s \frac{ds}{\nu_{0x}\beta_x(s)} , \quad (5.51)$$

where ν_{0x} is the bare tune and β_x is the betatron function defined in the absence of the space charge self-force. Next introduce the dimensionless half beam size

$$\hat{X} = \frac{\hat{x}}{\sqrt{\epsilon_x\beta_x}} , \quad (5.52)$$

where the full emittance ϵ_x , defined via Eq. (5.18),

$$\epsilon_x = 3\sqrt{\langle x^2 \rangle \langle p_x^2 \rangle - \langle xp_x \rangle^2} , \quad (5.53)$$

is a constant of motion because the distribution is now uniform and the space charge force is therefore linear [see Eq. (5.19)]. The envelope equation for a uniform beam in one dimension now becomes (Exercise 5.1)

$$\frac{d^2\hat{X}}{d\psi_x^2} + \nu_{0x}^2\hat{X} - \frac{\nu_{0x}^2}{\hat{X}^3} - \frac{2\pi r_0\sigma}{\gamma^3\beta^2} \frac{\nu_{0x}^2\beta_x^{3/2}}{\sqrt{\epsilon_x}} = 0 . \quad (5.54)$$

The last term on the right side depends on s through the betatron function β_x . Because β_x is periodic in s or the phase advance ψ_x , we can expand it as a Fourier series. The oscillatory part is x independent and is therefore similar to the force due to dipole errors which we have studied earlier in Sec. 5.1. Since it will drive only integer resonance and we are interested in half-integer resonance only in this section, this oscillatory part is discarded. The non-oscillatory part is related to the incoherent space charge tune shift $\Delta\nu_{scx}$, or (Exercise 5.2)

$$2\nu_{0x}\Delta\nu_{scx} = -\frac{2\pi r_0\sigma}{\gamma^3\beta^2} \frac{\nu_{0x}^2\bar{\beta}_x^{3/2}}{\sqrt{\epsilon_x}} , \quad (5.55)$$

where $\bar{\beta}_x$ is the betatron function averaged over the Floquet phase ψ and is equal to R/ν_{0x} , with R being the radius of the accelerator ring. In terms of $\Delta\nu_{scx}$, the one-dimension envelope equation now takes the simple form[‡]

$$\frac{d^2\hat{X}}{d\psi_x^2} + (\nu_{0x}^2 + 2\nu_{0x}\Delta\nu_s \cos n\psi_x) \hat{X} - \frac{\nu_{0x}^2}{\hat{X}^3} + 2\nu_{0x}\Delta\nu_{scx} = 0 , \quad (5.56)$$

where we have included the part in $K(s)$ that corresponds to quadrupole gradient errors as a force possessing n th harmonic and total stopband width $\Delta\nu_s$.

When space charge is absent, the *static* solution (s or ψ_x independent) of the envelope equation is just $\hat{X} = 1$. Here, *static* is just mathematically true for the normalized beam size \hat{X} . In fact, this solution is not physically static, because it corresponds to the beam size

$$\hat{x} = \sqrt{\epsilon_x \beta_x} , \quad (5.57)$$

and β_x is a function of s . We can also see how the normalization process simplifies the analysis of the envelope equation. The solution in Eq. (5.57) says nothing more than the fact that $\sqrt{\beta_x}$ is the beam radius when the beam is *matched* to the lattice. In fact, the envelope equation, Eq. (5.29), before normalizing, is the equation satisfied by $\sqrt{\beta_x}$.

In the presence of space charge, the ‘static’ solution becomes

$$\hat{X} = 1 + \xi_x , \quad (5.58)$$

which can be solved as a power series in

$$\Delta_x = \frac{\Delta\nu_{scx}}{\nu_{0x}} . \quad (5.59)$$

We obtain

$$\xi_x = -\frac{\Delta_x}{2} + \frac{3\Delta_x^2}{8} + \mathcal{O}(\Delta_x^3) . \quad (5.60)$$

Since $\Delta\nu_{scx} < 0$, the beam size is therefore larger due to the repulsive nature of the space charge force. This can be viewed as an increase in the betatron function due to space charge by

$$\beta_x \longrightarrow \frac{\beta_x \nu_{0x}}{\nu_{0x} + \Delta\nu_{scx}} . \quad (5.61)$$

[‡]The incoherent space charge tune shift is negative. Many authors prefer to denote $\Delta\nu_{scx}$ as the absolute value of the tune shift. In that convention, the sign in the last term on the right side of Eq. (5.56) will be positive instead.

Now we are ready to solve the envelope equation around the ‘static’ solution, for which we let

$$\hat{X} = 1 + \xi_x + \delta_x(\psi_x) . \quad (5.62)$$

Here, δ_x represents the amplitude of oscillation of the beam width about the equilibrium value $1 + \xi_x$. We only need δ_x to be infinitesimal. Therefore, we perform the power series expansion according to

$$\delta_x \ll \xi_x \ll 1 , \quad (5.63)$$

and keep only the first order in δ_x . We also require only an infinitesimal driving force, because this is what it needs to drive a particle into instability. Thus, we will consider the width of the stopband $\Delta\nu_s/\nu_{0x}$ to be of the same order as δ_x . This consideration leads to the equation

$$\frac{d^2\delta_x}{d\psi_x^2} + (4\nu_{0x}^2 + 6\nu_{0x}\Delta\nu_{scx})\delta_x = -2\nu_{0x}\Delta\nu_s \cos n\psi_x . \quad (5.64)$$

Thus the beam envelope oscillates with the natural coherent tune $2(\nu_{0x} + \frac{3}{4}\Delta\nu_{scx})$, and resonance occurs when

$$n^2 = 4\nu_{0x}^2 + 6\nu_{0x}\Delta\nu_{scx} \quad \text{or} \quad \frac{n}{2} \approx \nu_{0x} - \frac{3}{4}|\Delta\nu_{scx}| = \nu_{x \text{ incoh}} + \frac{1}{4}|\Delta\nu_{scx}| . \quad (5.65)$$

The incoherent tune $\nu_{x \text{ incoh}} = \nu_{0x} + \Delta\nu_{scx}$ can therefore be depressed beyond the half-integer $\frac{n}{2}$ by $\frac{1}{4}|\Delta\nu_{scx}|$, a quarter of the incoherent tune shift before hitting the resonance as is illustrated in Fig. 5.1. Solution of Eq. (5.64) gives

$$\hat{X} = 1 - \frac{\Delta\nu_{scx}}{2\nu_{0x}} - \frac{2\nu_{0x}\Delta\nu_s \cos n\psi_x}{4\nu_{0x}^2 + 6\nu_{0x}\Delta\nu_{scx} - n^2} , \quad (5.66)$$

where only the lowest order of $\Delta\nu_{scx}/\nu_{0x}$ has been included. Clearly, this solution reflects the resonance depicted in Eq. (5.65), although the solution is perturbative and is not valid near the resonance. We also see the beam envelope oscillate and that represents a quadrupole breathing mode, which is a coherent mode or collective mode because all beam particles have to participate collectively to produce this pattern of motion. This is in contrast to the incoherent motion, where a single beam particle executes betatron oscillations regardless of what the rest are doing.

Now we are in the position to study whether the force due to quadrupole errors will drive a single particle unstable at the half-integer resonance. Let us return to Eq. (5.12), the equation of motion of a single particle, which we rewrite as

$$\frac{d^2X}{d\psi_x^2} + (\nu_{0x}^2 + 2\nu_{0x}\Delta\nu_s \cos n\psi_x) X + 2\nu_{0x}\Delta\nu_{scx} \frac{X}{\hat{X}} = 0 . \quad (5.67)$$

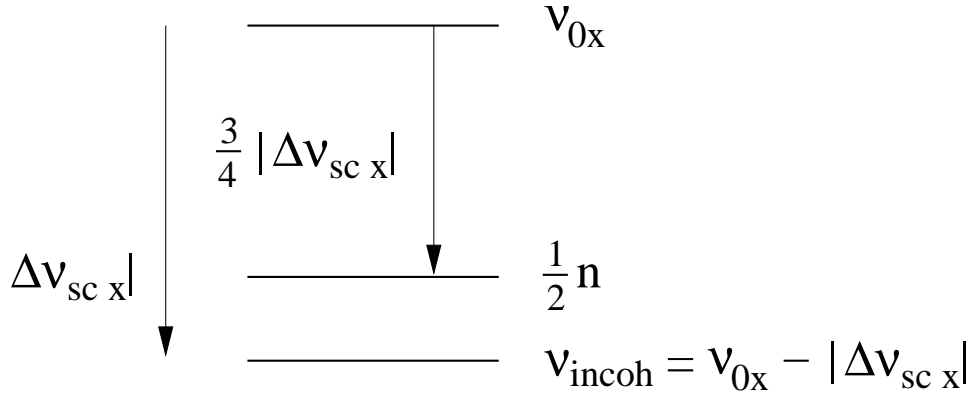


Figure 5.1: Plot showing that the incoherent tune of a one-dimensional beam, $\nu_{\text{incoh}} = \nu_{0x} - |\Delta\nu_{scx}|$, can be depressed to pass the half-integer $\frac{1}{2}n$ before the coherent quadrupole tune $\nu_{0x} - \frac{3}{4}|\Delta\nu_{scx}|$ reaches the half-integer instability.

where X and \hat{X} are, respectively, the x -coordinate of the particle and the beam half width normalized by $\sqrt{\beta_x \epsilon_x}$. $\Delta\nu_{scx}$, as given by Eq. (5.55), is the commonly quoted incoherent space charge tune shift without consideration of the beam being driven by the gradient errors of the quadrupole. The correct incoherent space charge tune shift is actually given by $\Delta\nu_{scx}/\hat{X}$ (see Exercise 5.2). Since we are not interested in the rigid motion of the beam, the beam center $\langle X \rangle$ can be set to zero. When the perturbative solution \hat{X} of the beam envelope in Eq. (5.66) is substituted, Eq. (5.67) becomes

$$\frac{d^2 X}{d\psi_x^2} + (\nu_{0x} + \Delta\nu_{scx})^2 X + 2\nu_{0x}\Delta\nu_s \cos n\psi_x \left[1 + \frac{2\nu_{0x}\Delta\nu_{scx}}{4\nu_{0x}^2 + 6\nu_{0x}\Delta\nu_{scx} - n^2} \right] X = 0 . \quad (5.68)$$

where the non-resonant free oscillations have not been included. At the particle intensity which shifts the betatron tune to half-integer, namely $\nu_{0x} + \Delta\nu_{scx} = n/2$, the two terms inside the square brackets cancel, and the single-particle equation of motion reduces to

$$\frac{d^2 X}{d\psi_x^2} + \left(\frac{n}{2}\right)^2 X = 0 . \quad (5.69)$$

We see that when the incoherent tune of a particle is shifted to half-integer, the driving force due to gradient errors cancels exactly. Thus, no resonance occurs for the particle.

The above proof appears to be overly approximated[§]. The reader can pursue this proof to another order of the incoherent tune shift.

[§]The more accurate condition for envelope instability is $\nu_{0x}^2 - \frac{3}{2}|\nu_{0x}\Delta\nu_{scx}| = \left(\frac{n}{2}\right)^2$. So the more accurate condition for “incoherent resonance” is $\nu_{0x}^2 - 2|\nu_{0x}\Delta\nu_{scx}| = \left(\frac{n}{2}\right)^2$. Use of these conditions make the driving term vanish to a more accurate degree.

5.3.2 Two Dimensions

Similar to the one-dimensional case, we normalize the two-dimensional envelope equations with uniformly distributed elliptic cross section in the same way by introducing the phase advances

$$\psi_x = \int_0^s \frac{ds}{\nu_{0x}\beta_x(s)} \quad \text{and} \quad \psi_y = \int_0^s \frac{ds}{\nu_{0y}\beta_y(s)}, \quad (5.70)$$

and the dimensionless half beam radii

$$\hat{X} = \frac{\hat{x}}{\sqrt{\epsilon_x\beta_x}} \quad \text{and} \quad \hat{Y} = \frac{\hat{y}}{\sqrt{\epsilon_y\beta_y}}, \quad (5.71)$$

where ν_{0x} and ν_{0y} are the bare tunes and β_x and β_y are the betatron functions in the x and y directions, respectively, defined in the absence of the space charge self-force. Equation (5.50) that governs the motion of the beam radii becomes

$$\begin{aligned} \frac{d^2\hat{X}}{d\psi_x^2} + (\nu_{0x}^2 + 2\nu_{0x}\Delta\nu_{scx} \cos n_x \psi_x) \hat{X} - \frac{\nu_{0x}^2}{\hat{X}^3} + 2\nu_{0x}\Delta\nu_{scx} \frac{a+b}{a\hat{X}+b\hat{Y}} &= 0, \\ \frac{d^2\hat{Y}}{d\psi_y^2} + (\nu_{0y}^2 + 2\nu_{0y}\Delta\nu_{scy} \cos n_y \psi_y) \hat{Y} - \frac{\nu_{0y}^2}{\hat{Y}^3} + 2\nu_{0y}\Delta\nu_{scy} \frac{a+b}{a\hat{X}+b\hat{Y}} &= 0, \end{aligned} \quad (5.72)$$

where $a = \sqrt{\epsilon_x\beta_x}$ and $b = \sqrt{\epsilon_y\beta_y}$ are the beam radii defined through the average betatron functions $\bar{\beta}_x$ and $\bar{\beta}_y$,

$$\Delta\nu_{scx} = -\frac{2\lambda r_0 R^2}{\gamma^3 \beta^2 \nu_{0x} a(a+b)} \quad \text{and} \quad \Delta\nu_{scy} = -\frac{2\lambda r_0 R^2}{\gamma^3 \beta^2 \nu_{0y} b(a+b)} \quad (5.73)$$

are the incoherent space charge tune shifts. We have also included the forces due to gradient errors at harmonics n_x and n_y .

We first solve for the *static* beam radii

$$\hat{X} = 1 + \xi_x \quad \text{and} \quad \hat{Y} = 1 + \xi_y \quad (5.74)$$

in terms of the incoherent tune shifts

$$\Delta_x = \frac{\Delta\nu_{scx}}{\nu_{0x}} \quad \text{and} \quad \Delta_y = \frac{\Delta\nu_{scy}}{\nu_{0y}}. \quad (5.75)$$

Up to second order, we get

$$\xi_x = -\frac{\Delta_x}{2} + \frac{\Delta_x^2}{4} - \frac{\Delta_x \Delta_y}{8} \quad \text{and} \quad \xi_y = -\frac{\Delta_y}{2} + \frac{\Delta_y^2}{4} - \frac{\Delta_x \Delta_y}{8}. \quad (5.76)$$

Next, the infinitesimal displacements δ_x and δ_y are included:

$$\hat{X} = 1 + \xi_x + \delta_x \quad \text{and} \quad \hat{Y} = 1 + \xi_y + \delta_y . \quad (5.77)$$

The derivation becomes very lengthy and uninteresting. For the sake of simplicity, we study the special case of a round beam with $a = b$ and obtain the equations for small amplitude oscillation:

$$\frac{d^2\delta_x}{d\psi_x^2} + (4 + 5\Delta_x) \nu_{0x}^2 \delta_x - \nu_{0x}^2 \Delta_x \delta_y = -2\nu_{0x}^2 \Delta \nu_{scx} \cos n_x \psi_x , \quad (5.78)$$

$$\frac{d^2\delta_y}{d\psi_y^2} + (4 + 5\Delta_y) \nu_{0y}^2 \delta_y - \nu_{0y}^2 \Delta_y \delta_x = -2\nu_{0y}^2 \Delta \nu_{syc} \cos n_y \psi_y . \quad (5.79)$$

This is just a set of driven coupled simple-harmonic oscillators. For a round beam, we expect the incoherent space charge tune shifts in the two transverse directions to be equal. The eigenvalues ν can be found by solving the eigenvalues of the matrix

$$\begin{pmatrix} 4\nu_{0x}^2 + 5\nu_{0x}\Delta \nu_{scx} & -\nu_{0x}\Delta \nu_{scx} \\ -\nu_{0x}\Delta \nu_{scx} & 4\nu_{0y}^2 + 5\nu_{0y}\Delta \nu_{scx} \end{pmatrix} , \quad (5.80)$$

from which we get

$$\nu^2 = 2(\nu_{0x}^2 + \nu_{0y}^2) + 5\nu_{0x}\Delta \nu_{scx} \pm \sqrt{4(\nu_{0x}^2 - \nu_{0y}^2)^2 + (\nu_{0x}\Delta \nu_{scx})^2} . \quad (5.81)$$

When the two bare tunes are close so that $|\nu_{0x} - \nu_{0y}| \ll |\nu_{0x}\Delta \nu_{scx}|$, the two coherent tunes are

$$\nu^2 = \begin{cases} 4\bar{\nu}^2 - 4|\nu_{0x}\Delta \nu_{scx}| \\ 4\bar{\nu}^2 - 6|\nu_{0x}\Delta \nu_{scx}| \end{cases} \quad \text{or} \quad \nu \approx \begin{cases} 2\left(\bar{\nu} - \frac{1}{2}|\Delta \nu_{scx}|\right) \\ 2\left(\bar{\nu} - \frac{3}{4}|\Delta \nu_{scx}|\right) \end{cases} , \quad (5.82)$$

where $2\bar{\nu}^2 = \nu_{0x}^2 + \nu_{0y}^2$. This represents that the two transverse directions are tightly coupled. The eigenfunctions are $\sim (\delta_x + \delta_y)$ for the upper solution and $\sim (\delta_x - \delta_y)$ for the lower solution. Thus, the upper solution is the symmetric breathing mode where the oscillations are in phase in both transverse directions and the tune is $\bar{\nu} - \frac{1}{2}|\Delta \nu_{scx}|$. The lower solution is the antisymmetric mode where the beam envelope oscillates out of phase in the two transverse directions with tune $\bar{\nu} - \frac{3}{4}|\Delta \nu_{scx}|$.

If the tune split is large so that $|\nu_{0x} - \nu_{0y}| \gg |\nu_{0x}\Delta\nu_{scx}|$, the oscillations in the two transverse directions are almost uncoupled. The envelope oscillations in the two transverse directions are just two independent oscillators. The two coherent tunes are

$$\nu^2 = \begin{cases} 4\nu_{0x}^2 - 5|\nu_{0x}\Delta\nu_{scx}| \\ 4\nu_{0y}^2 - 5|\nu_{0x}\Delta\nu_{scx}| \end{cases} \quad \text{or} \quad \nu \approx \begin{cases} 2\left(\nu_{0x} - \frac{5}{8}|\Delta\nu_{scx}|\right) \\ 2\left(\nu_{0y} - \frac{5}{8}|\Delta\nu_{scy}|\right) \end{cases}. \quad (5.83)$$

Let us come back to the situation of no tune split. Suppose that the bare tunes $\nu_{0x} \sim \nu_{0y} \sim \bar{\nu}$ are $\Delta\nu$ above a half-integer or integer. We try to increase the beam intensity. and the incoherent tune shift $|\Delta\nu_{scx}|$ increases accordingly. We will first meet with the condition $\frac{3}{4}|\Delta\nu_{scx}| = \Delta\nu$ and the antisymmetric mode becomes unstable. However, the incoherent tune, $\nu_{0x} - |\Delta\nu_{scx}|$ has passed the half integer already by a factor of $\frac{4}{3}$. The symmetric mode will meet with the half-integer and become unstable much later when $|\Delta\nu_{scx}| = 2\Delta\nu$.

Similar to the one-dimensional case, the oscillatory solutions for the envelope radii can be solved. When substituted back into the single-particle equations of motion, we can verify that the driving force vanishes when the incoherent equations are at half integers, showing that the incoherent motion of individual particles can have their tunes right at half-integers without instability.

Other distributions can be analyzed in the same way. Notice that, for a round beam, the space charge tune shift $\Delta\nu_{scx}$ in the last term of Eq. (5.72) is

$$\Delta\nu_{scx} = -\frac{Nr_0}{2\pi\gamma^3\beta^2\epsilon} = -\frac{Nr_0}{8\pi\gamma^3\beta^2\epsilon_{rms}}, \quad (5.84)$$

where $N = 2\pi R\lambda$ is the total number of particles in the beam, ϵ is the full emittance of the uniform distributed beam and ϵ_{rms} is the rms emittance. Now rewrite Eq. (5.84) as

$$\Delta\nu_{scx} = \frac{1}{2} \left[-\frac{Nr_0}{4\pi\gamma^3\beta^2\epsilon_{rms}} \right], \quad (5.85)$$

where the square-bracketed term is the maximum incoherent space charge tune shift of a bi-Gaussian distributed round beam. Thus what we need to remember is that the factor $\Delta\nu_{scx}$ in the envelope equation represents one half of the maximum incoherent space charge tune shift for bi-Gaussian distribution. We mentioned before that for the

case of strong coupling, the tune depression of the antisymmetric mode is $\frac{3}{4}|\Delta\nu_{scx}|$ and the incoherent tune shift can exceed that needed for coincidence with a half integer resonance by a factor of $\frac{4}{3}$. Now for the case of the bi-Gaussian distribution, the tune depression of this mode becomes $\frac{3}{4} \times \frac{1}{2}$ of the maximum incoherent space charge tune shift for the bi-Gaussian distributed beam, and therefore the incoherent tune can exceed that needed for coincidence with a half-integer resonance by as much as a factor of $\frac{8}{3}$. For this reason, we define a parameter G , such that Eq. (5.84) can be written as

$$\Delta\nu_{scx} = \frac{1}{G} \left[\begin{array}{l} \text{max incoherent} \\ \text{sp ch tune shift} \end{array} \right]. \quad (5.86)$$

Then, the incoherent space charge tune shift for the distribution considered will exceed the tune depression of a particular collective quadrupole mode G times better than if the distribution is uniform.

If we neglect the time dependency of the emittances, the rms envelope equations, Eq. (5.49), say that the space charge effects of all beams are the same if they have the same rms widths and emittances. These beams are called *equivalent* beams. For example, an *equivalent uniform beam* implies that the beam has the same rms dimensions as a uniform beam.

5.4 Simulations

5.4.1 One Dimension

Baartman [1] performed simulations with up to 50,000 particles according to the equation of motion:

$$x'' + \nu_0^2 x = \alpha x^{m-1} \cos(n\theta) + F_{sc}. \quad (5.87)$$

Here, the driving force leads to resonances whenever the tune ν satisfies $m\nu = n$. The space charge self-force F_{sc} on a particular particle in the simulations is simply equal to an intensity parameter multiplied by the difference between the number of particles to its left and to its right.

For a sextupole force ($m = 3$) and bare tune equals $\nu_0 = 2.45$, the relevant resonance is at $n/m = 7/3 = 2.3333$. We expect to see the beam in resonance when the coherent tune $\nu_{coh} = \nu_0 - C_{33}|\Delta\nu_{sc}| = 7/3$, where $\Delta\nu_{sc}$ is the incoherent space charge tune shift

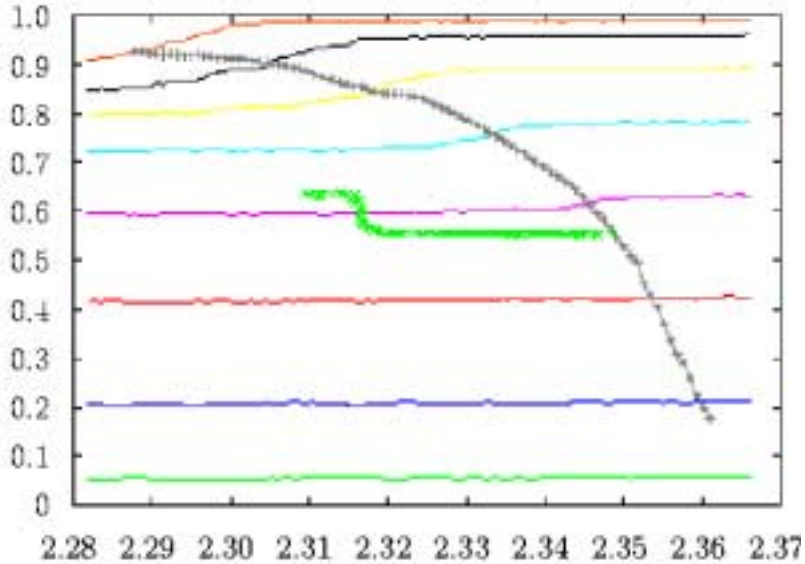


Figure 5.2: (color) Plot of the rms size (thick curve at center) of the simulated one-dimensional beam of Gaussian distribution as a function of the incoherent tune, which is used here as a measure of the beam intensity. Obviously, there is no effect on the beam when the incoherent tune crosses the $7/3$ resonance. But the rms beam size increases very suddenly when the incoherent tune reaches 2.3167 corresponding to the $7/3$ resonance of the coherent tune. See text for the other curves.

and $C_{33} = 7/8$ by solving the envelope equation in one dimension. This corresponds to an incoherent space charge tune shift of $|\Delta\nu_{sc}| = (2.45 - 2.333)/C_{33} = 0.1334$ or the incoherent tune of $2.45 - 0.1334 = 2.3167$. The simulations were performed for a beam with transverse Gaussian distribution. The results are plotted in Fig. 5.2 as the fraction of particles inside a given betatron amplitude versus the incoherent tune of the stationary beam of the same rms size. The incoherent tune is chosen because it serves as a measure of the beam intensity. Larger incoherent tune implies lower beam intensity. The thick curve in the center is the rms beam size. We clearly see that it passes the incoherent tune of $7/3$ with nothing happening. However, there is a sharp threshold at the expected incoherent tune 2.3167. This verifies the fact that it is the coherent tune but not the incoherent tune that determines the arrival of a resonance. The horizontal curves in the figure represent the fraction of particles inside a fixed emittance for the Gaussian distribution. They step downwards as particles are driven to larger amplitudes. The stepdown occurs when a horizontal curve meets the curve connecting the + symbols. These + symbol represent the emittance at which the

incoherent tune is on resonance. If we examine the figure more closely, we find that only those horizontal curves representing more than 50% of particles step downwards, and also the stepdowns are more appreciable only when the particle amplitude becomes larger. This phenomenon happens because of some halo particles residing at the very edge of the beam. They behave like a separate beam and feel the space charge force from the core of the beam as an external force. Since this is not the space charge self-force of the beam halo, our discussion of the irrelevance of the incoherent tune does not apply to these particles.

5.4.2 Two Dimensions

Machida [8] performed two-dimensional space charge simulations of the SSC Low Energy Booster by including quadrupole error forces. The horizontal bare tune was fixed at $\nu_{0x} = 11.87$ while the vertical bare tune ν_{0y} varied from 11.95 to 11.55. The maximum incoherent tune shift was kept fixed at $|\Delta\nu_{scy}| = 0.33$ with a half-integer stopband 0.02. The beam simulated had a bi-Gaussian distribution. The threshold for emittance growth was found to be roughly 11.63, when the incoherent tune had already passed the half-integer resonance of 11.50. An incoherent tune shift of 0.33 for a bi-Gaussian distributed beam is the same as an incoherent tune shift of $0.33/2=0.165$ of an equivalent uniform beam. According to Eq. (5.81), the incoherent tune shift of an equivalent uniform beam is 0.199, or $2 \times 0.199 = 0.398$ for a bi-Gaussian beam. If we include the stopband, meaning that the half-integer resonance will start at $11.50 + 0.02 = 11.52$, the incoherent tune shift of an equivalent uniform beam is 0.1687, or $2 \times 0.1687 = 0.337$ for a bi-Gaussian beam. The number is very close to the incoherent tune shift of the 0.33 input into the simulations.

In other two-dimensional simulations, Machida and Ikegami [9] also demonstrated that it was the *coherent* rather than the *incoherent* tune shifts that determine the instability of a beam. Some results are illustrated in Fig. 5.3. In the simulations, the horizontal coherent quadrupole tune hits the integer 13 when the beam intensity reaches ~ 15 A. We do see that the horizontal emittance increases rapidly around the beam intensity of 15 A. The vertical coherent quadrupole tune hits the integer 11 when the beam intensity is raised to around 13 to 15 A. Around those intensities, large increase in vertical emittance is evident in the plots. However, we do not see any growth of emittance when the coherent quadrupole tunes cross half integers. The simulations were performed using beams with the water-bag distribution, the K-V distribution, and the

parabolic distribution. As is seen in the plots, the results do not depend much on the beam distribution.

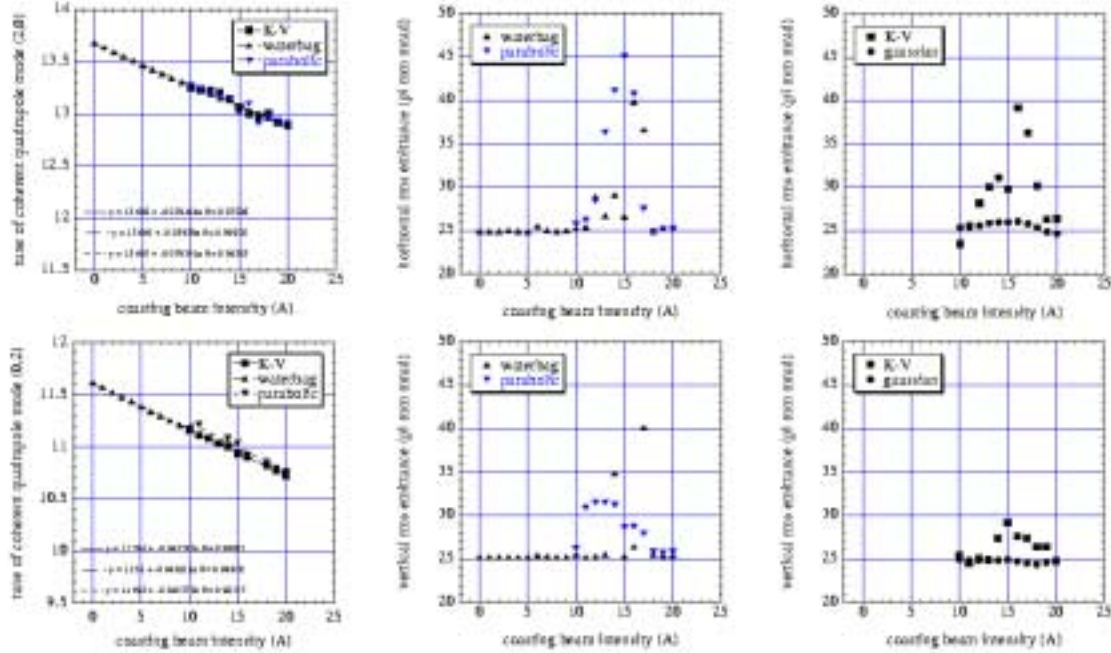


Figure 5.3: (color) Tune of coherent quadrupole mode (left) and rms emittance at 512 turns after injection (center and right) versus beam intensity. Upper figures show results in the horizontal plane while lower ones show results in the vertical plane. Rms emittance growth is observed when either the horizontal or vertical coherent quadrupole tune crosses an integer. (Reproduced from Ref. [9]).

5.5 Application to Synchrotrons

Let us apply what we have learned to some low-energy synchrotrons. For the Fermilab Booster with an injection energy of 400 MeV and round beam, the bare tunes derived from the lattice are $\nu_{0x} = 6.70$ and $\nu_{0y} = 6.80$. The nearest half-integer is 6.5. Thus, if the half-integer resonance arises from the incoherent motion of the beam particles, the largest incoherent space charge tune shift allowed will be $|\Delta\nu_{scx}| = 0.20$. If the resonance comes from one of the coherent quadrupole envelope modes hitting the half-integer, the largest incoherent space charge tune shift allowed becomes[¶] $|\Delta\nu_{scx}| = 0.296$

[¶]We can also make the rough estimate of assuming the two betatron bare tunes are equal, i.e., $\nu_{0x} \sim \nu_{0y} \sim 6.70$. Then the incoherent space charge tune shift according to Eq. (5.82) is $|\Delta\nu_{scx}| \sim$

or $|\Delta\nu_{scy}| = 0.291$. These numbers are obtained from the matrix of Eq. (5.80) by substituting $\frac{1}{2}\nu = 6.5$ for the eigentune and solving for $|\Delta\nu_{scx}|$. On the other hand, from the experimentally measured beam size, the calculated incoherent space charge tune shift is 0.40, which definitely exceeds the result from incoherent motion and agrees more or less with the result from the coherent mode. So far the estimation has been based on uniform distribution. If the distribution were bi-Gaussian, the largest incoherent space charge tune shift allowed would become $|\Delta\nu_{scx}| = 2 \times 0.296 = 0.592$ or $|\Delta\nu_{scy}| = 2 \times 0.291 = 0.582$ instead for particles at the center of the beam with small amplitude betatron oscillations.

Similar computations are performed for various low-energy synchrotrons, for which the beams are mostly round and the distribution uniform. The results are tabulated in Table 5.2. We see that for all the synchrotrons listed, the space charge tune shifts computed from experimentally measured beam sizes exceed those derived from incoherent particle motion and are close to those derived from the coherent modes.

Table 5.2: Estimated incoherent space charge tune shifts for various low-energy synchrotrons. The incoherent space charge tune shifts are derived from the experimentally measured beam size (3rd column), the assumption that the half-integer resonance comes from the incoherent motion of the beam particles (4th column), and the assumption that the half-integer resonance comes from a coherent envelope mode (5th column). We see that the values from experiments exceed those from incoherent motion and agree mostly with those from the coherent modes.

Synchrotron	Bare tunes ν_{0x}/ν_{0y}	$ \Delta\nu_{scx} / \Delta\nu_{scy} $		
		from experiment	from incoh motion	from coherent motion
KEK Booster	2.17/2.30	0.23	0.17	0.25/0.24
FNAL Booster	6.70/6.80	0.40	0.20	0.30/0.29
ISIS	3.70/4.20	0.40	0.20	0.31/0.27
AGS	8.75/8.75	0.58	0.25	0.33/0.33
AGS Booster	4.80/8.75	0.50	0.30	0.46/0.25
CERN PS	6.22/6.22	0.27	0.22	0.29/0.29
CERN PS-2	6.22/6.28	0.36	0.22	0.31/0.31

$|\Delta\nu_{scx}| \sim \frac{4}{3} \times 0.2 = 0.267$.

5.6 Exercises

- 5.1. Supply the missing steps in transforming the one-dimension envelope equation from Eq. (5.30) to the normalized form of Eq. (5.54). You may need the definition of the betatron function

$$\frac{\beta_x \beta''_x}{2} - \frac{\beta'_x}{4} + \beta_x^2 K_x(s) - 1 = 0 , \quad (5.88)$$

where the prime denotes derivative with respect to s , the distance along the accelerator ring, and $K_x(s)$ is the focusing strength of the external quadrupoles.

- 5.2. Show that the incoherent space charge tune shift $\Delta\nu_{scx}$ of a one-dimension beam uniformly distributed in the x direction and infinite in the y and s directions is given by

$$2\nu_{0x}\Delta\nu_{scx} = \frac{2\pi r_0 \sigma R^2}{\gamma^3 \beta^2 \hat{x}} , \quad (5.89)$$

where the beam has extent between $\pm\hat{x}$, σ is the particle density per unit area in the $y-s$ plane, r_0 is the classical particle radius, γ and β are the Lorentz parameters, and R is the mean radius of the accelerator ring.

- 5.3. Verify the expression for $\langle x\mathcal{E}_x \rangle$ given by Eq. (5.48) by computing this quantity for a round beam with (1) uniform distribution and (2) bi-Gaussian distribution.
- 5.4. Derive the incoherent space charge tune shifts for the various synchrotrons listed in the last column of Table 5.2 when the intensity of the beam having uniform distribution is increased so that the first coherent envelope mode reaches the half-integer resonance.

Bibliography

- [1] R. Baartman, *Betatron Resonances with Space Charge*, Proceedings of Int. Workshop on Emittance in Circular Accelerators Nov. 1994, KEK, Japan, KEK report 95-7, p.273; R. Baartman, *Betatron Resonances with Space Charge*, Proceedings of Workshop on Space Charge Physics in High Intensity Hadron Rings, p.73, Ed. Luccio, A.U., and Weng, W.T., (Shelter Island, New York, May 4-7, 1998).
- [2] W.T. Weng, *Space Charge Effects — Tune Shifts and Resonances*, AIP Conf. Proceedings **153** 1987, p.43..
- [3] I.M. Kapchinsky and V.V. Vladimirsksy, *Limitations of Proton Beam Current in a Strong Focusing Linenar Accelerator Associated with the Beam Space Charge*, Proc. Int. Conf. on High Energy Acc., CERN, 1959, p.274.
- [4] F. Sacherer, *RMS Envelope Equations with Space Charge*, IEEE Trans. Nucl. Sci. **NS-18**, (PAC 1971) 1105 (1971). See also the longer report of the same title in CERN-SI-Int.-DL/70-12, Nov., 1970.
- [5] P.M. Lapostolle, *Possible Emittance Increase Through Filamentation due to Space Charge*, IEEE Trans. Nucl. Sci. **NS-20**, Pac'71, 1101 (1971).
- [6] T.P. Wangler, K.R. Crandall, R.S. Mills, and M. Reiser, *Relation Between Field Energy and RMS Emittance in Intense Particle Beams*, Proc. Particle Accelerator Conference 1985, Vancouver, BC, p.2196.
- [7] I. Hoffmann, *Space Charge Dominated Beams Transport*, CERN Accelerator School for Advanced Accelerator Physics, Oxford, England, September 16027, 1985, p.327.
- [8] S. Machida, *Space Charge Effects in Low Energy Proton Synchrotrons*, Nucl. Inst. Meth. **A309**, 43 (1991).

- [9] S. Machida and M. Ikegami, *Simulation of Space Charge Effects in a Synchrotron*, Proceedings of Workshop on Space Charge Physics in High Intensity Hadron Rings, p.73, Ed. Luccio, A.U., and Weng, W.T., (Shelter Island, New York, May 4-7, 1998).

Chapter 6

LONGITUDINAL MICROWAVE INSTABILITY FOR PROTONS

6.1 Keil-Schnell Criterion

According to Eq. (2.10), a beam particle changes its energy per turn according to

$$\frac{d\Delta E}{dn} = eV_{\text{rf}}[\sin(\phi_s - h\omega_0\tau) - \sin\phi_s] - [U(\delta) - U_s] + C_0(\langle F_0^{\parallel} \rangle - \langle F_{0s}^{\parallel} \rangle) , \quad (6.1)$$

where the first two terms on the right represent, respectively, the rf focusing and radiation damping. The last term comes from the longitudinal wake potential [Eq. (2.7)]:

$$\langle F_0^{\parallel}(\tau) \rangle - \langle F_{0s}^{\parallel} \rangle = -\frac{e^2}{C_0} \left[\int_{-\infty}^{\infty} d\tau' \rho(\tau') W'_0(\tau' - \tau) - \int_{-\infty}^{\infty} d\tau' \rho(\tau') W'_0(\tau') \right] , \quad (6.2)$$

where $\rho(\tau)$ is the linear particle density of the beam for a particle that arrives τ earlier than the synchronous particle. For a purely inductive wake potential $W'_0(\tau) = L\delta'(\tau)$ ($\tau \geq 0$) with L being the inductance, the energy gained per turn becomes

$$\frac{d\Delta E}{dn} = e^2 L \rho'(\tau) + \dots , \quad (6.3)$$

where we have only displayed the contribution of the wake potential and assumed $\rho'(0) = 0$. Now consider a coasting beam with a very small momentum spread. If a small bump is developed along the beam and the vacuum chamber is inductive ($L > 0$), particles

at the front of the bump lose energy because $\rho'(\tau) < 0$, and particles at the rear of the bump gain energy because $\rho'(\tau) < 0$. Above transition ($\eta > 0$), particles at the front arrive earlier and particles at the rear arrive later. Thus the bump will be smoothed out, as illustrated in the left drawing in Fig. 6.1. The result will be the same if the beam sees a capacitive wake ($L < 0$) and is below transition. However, for capacitive wake above transition, particles at the front of the bump gain energy and will arrive later while those at the rear of the bump lose energy and will arrive earlier, thus enhancing the bump. The situation is the same for an inductive wake below transition. In other word, the situation is unstable against small nonuniformity in the linear distribution.

Below transition

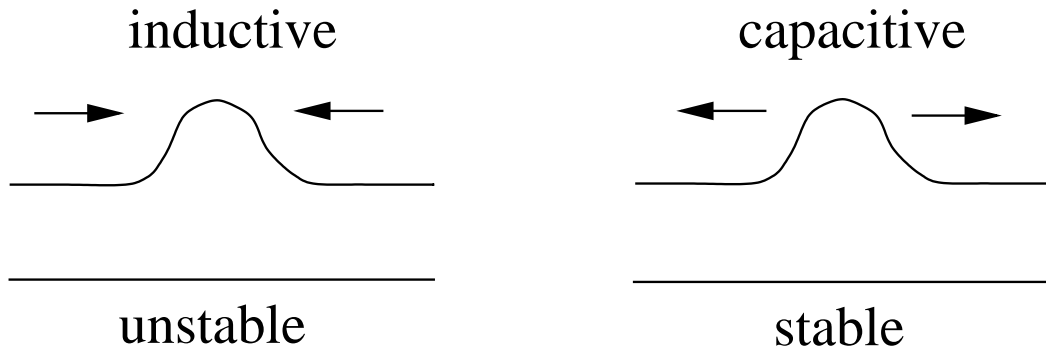


Figure 6.1: Below transition, a bump will be smoothed out under a capacitive force (right) and the beam will be stable against bump formation. However under an inductive force, the bump will continue to grow (left) and the beam will be unstable against small perturbations. Above transition, the opposite is true.

So far the momentum spread of particles in the beam has not been considered. In order for the bump to grow, the growth rate must be faster than phase-drifting rate coming from the momentum spread of the beam particles, otherwise the bump will be smeared. This damping process is called *Landau damping* [1]. The impedance driving the instability need not be purely reactive. It can be the real part of the impedance. Especially for a sharp bump, the driving frequency will be very high.

This same consideration can also be applied to a bunch provided that the growth must be faster than synchrotron frequency otherwise the bump will be smeared out. Needless to say, the size of the bump is much less than the length of the bunch. The driving impedance must therefore have a wavelength less than the length of the bunch.

This growth at high frequencies is called *microwave instability*. This discussion is very similar to that in Sec. 3.2. There, the concern is about the enhancement or partial cancellation of the rf focusing force at rf frequency; therefore an inductive force below transition or a capacitive force above transition is preferred to prevent bunch lengthening. Here, the concern is the evolution of a small bump at high frequencies. In order that a small bump will not grow, the opposite conclusion is obtained. In other words, to smooth out a bump, a capacitive force below transition or an inductive force above transition is preferred.

Because of the random quantum excitation in an electron bunch, there is a finite probability of having electrons jumping outside the bucket and getting lost. To increase the *quantum lifetime* of an electron bunch, a large rf bucket is necessary. Touschek scattering will also convert transverse momentum spread of electrons into longitudinal. In order that those electrons will not be lost, the rf bucket has to be large. For this reason, the bucket in an electron machine is in general very much larger than the size of the electron bunch, usually the height of the bucket is more than 10 times the rms energy spread of the bunch, in contrast with only about 3 times or less in proton machines. To achieve this, the rf voltage V_{rf} for an electron ring will be relatively much larger than that in a proton ring of the same energy. Another reason of a high V_{rf} in an electron machine is to compensate for the energy loss due to synchrotron radiation. For example, in the high-energy ring of PEP II storing 9 GeV electrons, $V_{\text{rf}} = 18.5$ MV is required. On the other hand, V_{rf} for the Fermilab Tevatron storing 1 TeV protons is only 2.16 MV. As a result, the synchrotron tunes for electron rings, $\nu_s \sim 0.01$, are usually an order of magnitude larger than those for proton rings, $\nu_s \sim 0.001$. For this reason, in the consideration of collective instabilities, the synchrotron period of the protons is sometimes much longer than the instability growth times. The wavelength of the perturbation or instability driving force is often of the same size as the radius or diameter of the vacuum chamber, which is usually much shorter than the length of a proton bunch. As a result, the proton bunches can be viewed locally as coasting beams in many instability considerations. Thus, each individual revolution harmonic can be considered as an independent mode. On the other hand, the electron bunch is mostly short, of the same size or even shorter than the diameter of the vacuum chamber. In other words, the electron bunch length can be of the same order or even shorter than the wavelength of the instability driving force. Therefore, for electron bunches, their bunch structure must be considered when studying their instabilities. Individual revolution harmonics are no longer independent and we need to study bunch modes instead.

6.1.1 Dispersion Relation

Let us first study the dispersion relation governing microwave instability of a proton beam [2]. Consider a coasting beam, with mean energy E_0 and mean velocity v_0 . The unperturbed phase-space distribution is*

$$\psi_0(\Delta E) = \frac{N}{C_0} f_0(\Delta E) , \quad (6.4)$$

where $\psi_0(\Delta E)$ is normalized to the number of particle N in the beam when integrated over the energy offset ΔE and distance s along the closed orbit of the on-momentum orbit. The energy spread distribution $f_0(\Delta E)$ is normalized to unity when integrated over ΔE . Since the linear distribution of a coasting beam is uniform, ψ_0 does not depend on the location s or the time t . The length of the beam is therefore equal to the circumference C_0 of the accelerator ring. Note that here we are using t as the independent variable, because we are using a snap-shot description. The variables s and ΔE are used to describe the beam in the longitudinal phase space.

This stationary distribution is perturbed by an infinitesimal longitudinal density wave ψ_1 which is position dependent and evolves in time. At time t , we postulate the ansatz

$$\psi_1(s, \Delta E, t) = \hat{\psi}_1(\Delta E) e^{ins/R - i\Omega t} , \quad (6.5)$$

where $R = C_0/(2\pi)$ is mean radius of the closed orbit of an on-momentum particle, and $\Omega/(2\pi)$ the collective frequency of oscillation to be determined. Here, n denotes the revolution harmonic and $n = 0$ must be excluded, otherwise charge conservation will be violated. Actually, this is a snap-shot description; therefore the linear density will be periodic in s . By ansatz, we mean a postulation of the solution which must be verified to be consistent later. In fact, Eq. (6.5) can be considered as just one term of a Fourier series expansion. In other words, our postulation is the independence of each revolution harmonic or the revolution harmonics are good eigennumbers. When integrated over ΔE , we get the perturbation line density at time t ,

$$\rho_1(s, t) = \hat{\rho}_1 e^{ins/R - i\Omega t} . \quad (6.6)$$

A test particle at the fixed location s monitors the perturbation wave passing through and experiences a wake force due to all beam particles that pass the location at an earlier

*The distribution in Eq. (6.4) can also be normalized to N by integration over ΔE and s/v_0 after the replacement of C_0 in the denominator by $T_0 = C_0/v_0$. In that case, dz should be replaced by dz/v_0 in Eq. (6.7), and v_0 should be deleted in Eqs. (6.8), (6.10), (6.11), and also the right side of Eqs. (6.8).

time. This force, averaged over the ring circumference, can be expressed as

$$\langle F_0^{\parallel}(s, t) \rangle = -\frac{e^2}{C} \int_0^\infty dz \rho_1(s, t-z/v_0) W'_0(z) = -\frac{e^2 v_0}{C_0} \rho_1(s, t) Z_0^{\parallel}(\Omega), \quad (6.7)$$

where $Z_0^{\parallel}(\Omega)$ is the longitudinal impedance of the vacuum chamber evaluated at the collective frequency. There is a similar force acting on the particle from the wake of the unperturbed beam distribution by replacing ρ_1 with the unperturbed ρ_0 in Eq. (6.7). But that force has no time dependency and is of no interest to us here. In fact, this force will give a modified steady-state Hamiltonian and will contribute to the a modification of the unperturbed particle distribution, which we call potential-well distortion. Notice that the impedance samples the coherent frequency of the perturbation and has no knowledge of the revolution harmonic dependency. This is because the impedance is located at a fixed point along the ring. However, as we shall see below, the coherent frequency Ω does contain a harmonic content.

The particle energy will be perturbed according to the equation of motion Eq. (6.1)

$$\frac{d\Delta E}{dt} = -\frac{e^2 v_0}{T_0} Z_0^{\parallel}(\Omega) \hat{\rho}_1 e^{ins/R-i\Omega t}, \quad (6.8)$$

where $T_0 = C_0/v_0$ is the revolution period of the on-momentum particles.

Now let us pull out the Vlasov equation in its first order,

$$\frac{\partial \psi_1}{\partial t} + \frac{\partial \psi_1}{\partial s} \frac{ds}{dt} + \frac{\partial \psi_0}{\partial \Delta E} \frac{d\Delta E}{dt} = 0. \quad (6.9)$$

Substitution leads to

$$-i(\Omega - n\omega)\psi_1 = \frac{e^2 v_0 Z_0^{\parallel}(\Omega)}{T_0} \frac{d\psi_0}{d\Delta E} \hat{\rho}_1 e^{ins/R-i\Omega t}, \quad (6.10)$$

where $\omega = v/R$ and v are, respectively, the angular revolution frequency and velocity of a beam particle with energy offset ΔE . Next we have

$$\psi_1(s, \Delta E, t) = \frac{ie^2 v_0 Z_0^{\parallel}(\Omega)}{T_0} \frac{d\psi_0}{d\Delta E} \frac{\hat{\rho}_1 e^{ins/R-i\Omega t}}{\Omega - n\omega}. \quad (6.11)$$

Integrate both sides over ΔE . From Eq. (6.6), the left side is just the perturbation linear density which cancels $\hat{\rho}_1$ and the exponential on the right side, leaving behind

$$1 = \frac{ie^2 N Z_0^{\parallel}}{T_0^2} \int \frac{f'_0(\Delta E)}{\Omega - n\omega} d\Delta E, \quad (6.12)$$

where the unperturbed distribution f_0 in Eq. (6.4) that is normalized to unity has been used, and the prime is derivative with respect to ΔE . An integration by part leads to the dispersion relation

$$1 = \frac{ieI_0\eta n Z_0^{\parallel}(\Omega)\omega_0^2}{2\pi\beta^2 E_0} \int \frac{f_0(\Delta E)}{(\Omega - n\omega)^2} d\Delta E , \quad (6.13)$$

where use has been made to the relation

$$\frac{d\omega}{d\Delta E} = -\frac{\eta\omega_0}{\beta^2 E_0} , \quad (6.14)$$

and $I_0 = eN/T_0$ is the mean current of the beam. The negative sign on the right side of Eq. (6.14) comes about because the revolution frequency decreases as energy increases above transition. An immediate conclusion of Eq. (6.13) is that our ansatz for ψ_1 in Eq. (6.5) is correct and all revolution harmonics are decoupled[†]. Equation (6.13) is called a dispersion relation because it provides the relation of the collective frequency Ω to the wave number n/R . This collective frequency is to be solved from the dispersion relation for each revolution harmonic. If Ω has an imaginary part that is positive, the solution reveals a growth and there is a collective instability.

If there is no energy spread, the collective frequency can be solved easily. The collective frequency of oscillation is

$$\Omega = n\omega_0 + \omega_0 \sqrt{\frac{eI_0\eta n^2}{2\pi\beta^2 E_0}} \sqrt{\left| \frac{i \operatorname{Re} Z_0^{\parallel}(\Omega)}{n} - \frac{\operatorname{Im} Z_0^{\parallel}(\Omega)}{n} \right|}_{\Omega \approx n\omega_0} , \quad (6.15)$$

of which the positive imaginary part is the growth rate. Writing it this way, the first square root is real above transition ($\eta > 0$), and there is no growth only when Z_0^{\parallel} is purely inductive,

$$\frac{\operatorname{Im} Z_0^{\parallel}(n\omega_0)}{n} < 0 , \quad (6.16)$$

as postulated at the beginning of this chapter. By the same token, the beam is stable below transition if the impedance is purely capacitive. For a low-energy machine, the space charge impedance per harmonic is frequency independent and rolls off only at very high frequencies. Therefore above transition, the growth rate is directly proportional to

[†]This is true when only the linear terms are included in the Vlasov equation. For the inclusion of the lowest nonlinear terms, see Refs. [10, 11].

n or frequency. This is the source of *negative-mass instability* for a proton machine just above transition. The terminology comes about because the space charge force appears to be attractive above transition in binding particles together to form clumps as if the mass of the particles is negative. From Eq. (6.15), we can define

$$\omega_G = \omega_0 \sqrt{-\frac{\eta ieI_0 n Z_0^{\parallel}}{2\pi i \beta^2 E_0}} \quad (6.17)$$

as the growth rate without damping due to energy spread. Close examination reveals some similarity of this definition with the expression of synchrotron angular frequency ω_s . We can therefore interpret ω_G as the synchrotron angular frequency inside a bucket created by the interaction of the beam current I_0 with the longitudinal coupling impedance Z_0^{\parallel} at the revolution harmonic n . The factor $-i$ takes care of the fact that the voltage created has to be 90° out of phase with the current so that a bucket can be formed.

Now let us consider a realistic beam that has an energy spread. Since ω is a function of the energy offset ΔE , define a revolution frequency distribution $g_0(\omega)$ for the unperturbed beam such that

$$g_0(\omega)d\omega = f_0(\Delta E)d\Delta E . \quad (6.18)$$

Substituting into Eq. (6.13) and integrating by part, we obtain

$$1 = -\frac{ieI_0\eta Z_0^{\parallel}(\Omega)\omega_0^2}{2\pi\beta^2 E_0} \int \frac{g'_0(\omega)}{\Omega - n\omega} d\omega . \quad (6.19)$$

Given the frequency distribution $g_0(\omega)$ of the unperturbed beam and the impedance Z_0^{\parallel} of the ring at roughly $n\omega_0$, the collective frequency Ω can be solved from the dispersion equation. For a given revolution harmonic n , there can be many solutions for Ω . However, we are only interested in those that have positive imaginary parts. This is because if there is one such unstable solution, the system will be unstable independent of how many stable solutions there are. However, there is a subtlety in dealing with solution on the edge of stability, that is, when Ω is real. The dispersion relation will blow up when $n\omega = \Omega$ during the integration. This subtlety can be resolved if the problem is formulated as an initial value problem, which we will discuss in Chapter 14 on Landau damping. It will be shown that the proper way to go around the subtlety is to make the replacement

$$\frac{\Omega}{n} \longrightarrow \frac{\Omega}{n} + i\epsilon , \quad (6.20)$$

where ϵ is an infinitesimal positive real number and the harmonic n is considered positive. In other words, the path of integration in the ω -plane always goes under the Ω/n pole as illustrated in Fig. 6.2.

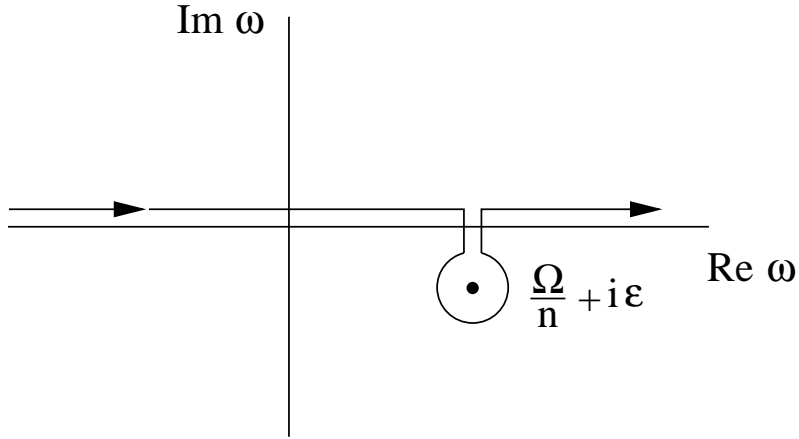


Figure 6.2: The path of integration in the dispersion relation must go below the Ω pole.

6.1.2 Stability Curve

For a Gaussian distribution, the integral in the dispersion relation is related to the complex error function, so that an analytic solution can be written down. For other distributions, one has to resort to numerical method. For a given growth rate or $\text{Im } \Omega$, we perform the integral for various values of $\text{Re } \Omega$ and read off $\text{Re } Z_0^{\parallel}$ and $\text{Im } Z_0^{\parallel}$ from the dispersion equation. Thus, we can plot a contour in the $\text{Re } Z_0^{\parallel}$ - $\text{Im } Z_0^{\parallel}$ plane corresponding to a certain growth rate. This plot for the Gaussian distribution below transition is shown in Fig. 6.3. What are plotted is the real part U' and imaginary part V' of

$$U' + iV' = \frac{eI_0\beta^2(Z_0^{\parallel}/n)}{|\eta|E_0(\Delta E/E)_{\text{FWHM}}^2} \quad (6.21)$$

at fixed growth rates. From outside to inside, the contours in the figure correspond to growth rates 0.5 to -0.5 in steps of -0.1 in units of HWHM of the frequency spread, where negative values imply damping. The contour corresponding to the stability threshold is drawn in dot-dashes and the area inside it is stable. Note that the positive V' -axis

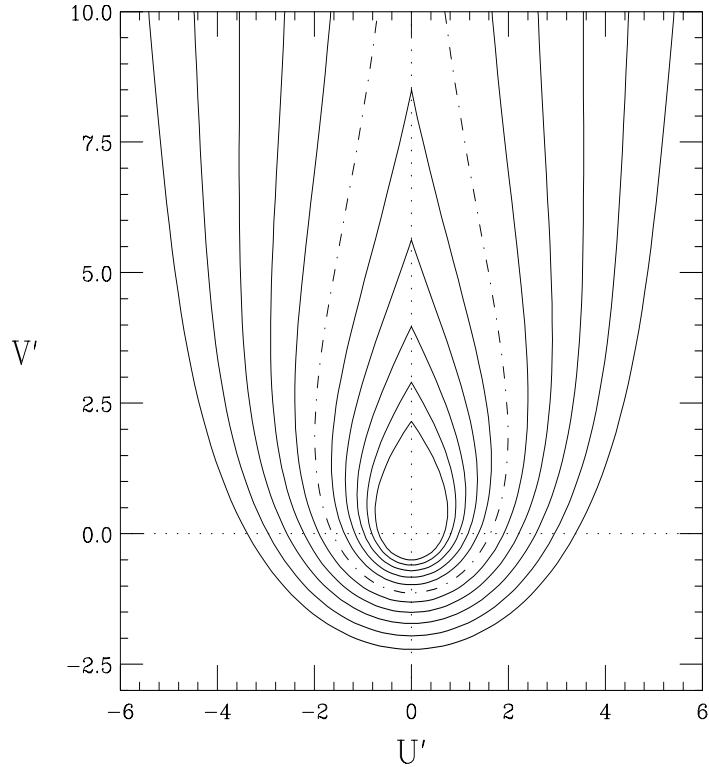


Figure 6.3: The growth contours for a Gaussian distribution in revolution frequency below transition. The abscissa U' and ordinate V' are, respectively, real and imaginary parts of $eI_0\beta^2(Z_0^{\parallel}/n)/[|\eta|E_0(\Delta E/E)^2_{\text{FWHM}}]$. From outside to inside, the contours correspond to growth rates 0.5 to -0.5 in steps of -0.1 in units of HWHM of the frequency spread, where negative values imply damping. The contour corresponding to the stability threshold is drawn in dot-dashes and the area inside it is stable.

is a cut and those damping contours continue into other Riemann sheets after passing through the cut. Therefore, for each (U', V') outside the stability region bounded by the dot-dashed curve, there can also be one or more stable solutions. However, since there is at least one unstable solution, this outside region is termed unstable.

Obviously, these contours depend on the distribution $g_0(\omega)$ assumed. In Fig. 6.4, we plot the stability contours for various frequency distributions below transition. They are for frequency distributions, from inside to outside, $f(x) = \frac{3}{4}(1-x^2)$, $\frac{8}{3\pi}(1-x^2)^{3/2}$, $\frac{15}{16}(1-x^2)^2$, $\frac{315}{32}(1-x^2)^4$, and $\frac{1}{\sqrt{2\pi}}e^{-x^2/2}$. The innermost one is the parabolic distribution with discontinuous density slopes at the edges and we see that the stability contour

curves towards the origin in the positive V' region. The contour next to it corresponds

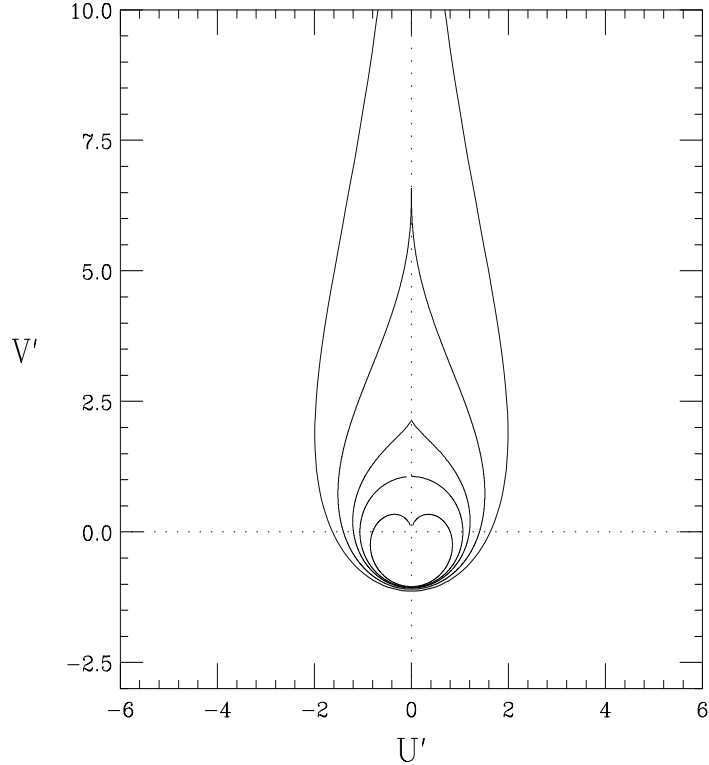


Figure 6.4: The stability contours for different frequency distribution below transition. The abscissa U' and ordinate V' are, respectively, real and imaginary parts of $eI_0\beta^2(Z_0^{\parallel}/n)/[|\eta|E_0(\Delta E/E)_{\text{FWHM}}^2]$. From inside to outside, they correspond to unperturbed revolution frequency distribution $f(x) = \frac{3}{4}(1-x^2)$, $\frac{8}{3\pi}(1-x^2)^{3/2}$, $\frac{15}{16}(1-x^2)^2$, $\frac{315}{32}(1-x^2)^4$, and $\frac{1}{\sqrt{2\pi}}e^{-x^2/2}$. Note that all contours cut the V' -axis at about -1 .

to continuous density slopes at the edges and it does not dip downward in the positive V' region. As the edges become smoother or with higher derivatives that are continuous, the contour shoots up higher in the upper half plane. For all distributions with a finite spread, the contours end with finite values at the positive V' -axis. For the Gaussian distribution which has infinite spread and continuous derivatives up to infinite orders, the contour will only approach the positive V' -axis without intersecting it.

We note in Fig. 6.4 that, regardless the form of distribution, all contours cut the negative V' -axis at ~ -1 . Therefore, it is reasonable to approximate the stability region by a unit circle in the U' - V' plane, so that a stability criterion can be written analytically.

This is the *Keil-Schnell criterion* which reads [3] (Exercise 6.1)

$$\left| \frac{Z_0^{\parallel}}{n} \right| < F \frac{|\eta| E_0}{e I_0 \beta^2} \left(\frac{\Delta E}{E_0} \right)_{\text{FWHM}}^2, \quad (6.22)$$

where F is a distribution-dependent form factor and is equal to the negative V' -intersection of the contour. For all the distributions discussed here, $F \approx 1$. (See Exercise 6.1 below).

For a bunch beam, if the disturbance has a wavelength much less than the bunch length, we can view the bunch locally as a coasting beam. Boussard [4] suggested to apply the same Keil-Schnell stability criterion to a bunch beam by replacing the coasting beam current I_0 with the peak current I_{peak} of the bunch. Krinsky and Wang [6] performed a vigorous derivation of the microwave stability limit for a bunch beam with a Gaussian energy spread and found the stability criterion

$$\left| \frac{Z_0^{\parallel}}{n} \right| < \frac{2\pi |\eta| E_0}{e I_{\text{peak}} \beta^2} \left(\frac{\Delta E}{E_0} \right)_{\text{rms}}^2. \quad (6.23)$$

Comparing with Eq. (6.22), the Krinsky-Wang criterion corresponds to the Keil-Schnell criterion with a form factor of $\pi/(4 \ln 2) = 1.133$, which is exactly the negative V' -intersect (see Exercise 6.1.) We want to point out that it is necessary for the Keil-Schnell criterion of Eq. (6.22) to be defined in terms of the *full width at half maximum* (FWHM) of the energy spread. Only such a reference will give a form factor that is close to unity for all reasonable distributions of the energy spread. This may be because the FWHM provides us with a more accurate measurement of the spread than the rms value. As an example, in terms of FWHM according to Eq. (6.22), the form factors for the Gaussian and the parabolic distributions are, respectively, and $F = \pi/(4 \ln 2) = 1.133$ and $F = \pi/3 = 1.0472$. Since $\Delta E_{\text{FWHM}} = 2\sqrt{2 \ln 2} \Delta E_{\text{rms}}$ for the Gaussian distribution and $\Delta E_{\text{FWHM}} = \sqrt{10} \Delta E_{\text{rms}}$ for parabolic distribution, if we express the stability criterion in terms of the rms energy spread as in Eq. (6.23), the form factors become $F = 1$ for the Gaussian distribution and $F = 5/3 = 1.67$ for parabolic the distribution.

6.1.3 Landau Damping

Keil-Schnell Criterion can be rearrange to read

$$n\omega_0 \sqrt{\frac{e|\eta||Z_0^{\parallel}/n|I_0}{2\pi\beta^2 E_0}} < n\omega_0 \sqrt{\frac{F}{2\pi}} \frac{|\eta|\Delta E|_{\text{FWHM}}}{\beta^2 E_0}. \quad (6.24)$$

The left side is the growth rate without damping as discussed in Eq. (6.17) with I_0 replaced by I_{peak} in the case of a bunch. The right side can therefore be considered as the Landau damping rate coming from energy spread or frequency spread. Stability is maintained if Landau damping is large enough. The theory of Landau damping is rather profound, for example, the exchange of energy between particles and waves, the mechanism of damping, the contour around the poles in Eq. (6.13), etc. These will be studied in detailed in Chapter 14. The readers are also referred to the papers by Landau and Jackson [1, 7], and also a very well-written chapter in Chao's book [2].

6.1.4 Self-Bunching

Neglecting the effect of the wake function, the Hamiltonian for particle motion can be written as

$$H = -\frac{\eta}{2v\beta^2 E_0}(\Delta E)^2 + \frac{eV_{\text{rf}}}{2\pi v h} \cos(h\omega_0\tau), \quad (6.25)$$

where the synchronous angle has been put to zero and the small-bunch approximation has been relaxed. It is easy to see that the height of the bucket is

$$\Delta E|_{\text{bucket}} = \sqrt{\frac{eE_0 V_{\text{rf}}}{\pi h |\eta|}}. \quad (6.26)$$

Keil-Schnell criterion can now be rearranged to read

$$\sqrt{\frac{eE_0 I_0 |Z_0^{\parallel}|}{\pi n |\eta|}} < \sqrt{\frac{F}{\pi \beta^2}} \Delta E|_{\text{FWHM}}. \quad (6.27)$$

Comparing with Eq. (6.26), the left side can be viewed as the height of a bucket created by an induced voltage $I_0 |Z_0^{\parallel}|$ while the right side roughly the half full energy spread of the beam. This induced voltage will bunch the beam just as an rf voltage does. If the self-bunched bucket height is less than the half full energy spread of the beam, the bunching effect will not be visible and beam remains coasting. Otherwise, the beam breaks up into bunchlets of harmonic n , and we call it unstable. This mechanism is known as *self-bunching*.

In fact, self-bunching is not so simple. The image current of the beam is rich in frequency components. For the component at the resonant frequency of the impedance, the voltage induced, called *beam loading voltage*, is in phase with the image current

or, more correctly, in opposite direction of the beam. Such voltage will not create any rf-like bucket at all, and therefore cannot produce self-bunching. Remember that when the beam is in the storage mode inside an accelerator ring, the rf voltage is at 90° to the beam current and the bucket created will be of maximum size—the so-called *stationary bucket* with synchronous angle $\phi_s = 0$ when the operation is below transition. As the synchronous angle ϕ_s increases, the angle between the rf voltage and the beam, or the *detuning angle* $\psi = \frac{\pi}{2} - \phi_s$, defined in Eq. (6.30) below, decreases and so is the bucket area—the so-called *moving bucket*. When the rf voltage is in phase with the beam, the synchronous angle $\phi_s = \frac{\pi}{2}$ and the bucket area shrinks to zero. In order for the beam image current to develop spontaneous self-bunching, the fields developed must be of such a phase and amplitude as to develop a real bucket of sufficient area to contain the beam. Although a small beam loading angle or a large synchronous angle will result in a small bucket area, however, as the beam frequency moves away too far from the resonance frequency, the beam loading voltage induced by the resonance impedance decreases also because the resonant impedance rolls off when the detuning is large. Consequently, there is a frequency deviation between the beam Fourier component and the resonance frequency at which the developed bucket area passes through a maximum. Some may argue that it is not the bucket area but the bucket height that sets the instability threshold, and the bucket height also goes through a maximum in between $\phi_s = 0$ and $\frac{\pi}{2}$. It is this bucket height that should enter into Eq. (6.26) for the stability criterion.

The impedance of a resonance is

$$Z_0^{\parallel}(\omega) = \frac{R_s}{1 - iQ \left(\frac{\omega}{\omega_r} - \frac{\omega_r}{\omega} \right)} , \quad (6.28)$$

where R_s is the shunt impedance, Q the quality factor, and ω_r the angular resonant frequency. When the frequency ω of the image current is close to the resonant frequency, we can write

$$Z_0^{\parallel}(\omega) \approx R_s \cos \psi e^{-i\psi} , \quad (6.29)$$

with the detuning angle defined as

$$\tan \psi = 2Q \frac{\omega_r - \omega}{\omega_r} . \quad (6.30)$$

Therefore, the beam loading voltage induced by the image current of frequency component ω will be proportional to $\cos \psi$ and at an angle ψ from the image current. Since $\psi = \frac{\pi}{2} - \phi_s$ and both the bucket area and height are proportional to the square root of

the voltage, we have,

$$\begin{aligned} \text{induced bucket area} &\propto \alpha(\Gamma)\sqrt{\Gamma}, \\ \text{induced bucket height} &\propto \beta(\Gamma)\sqrt{\Gamma}, \end{aligned} \quad (6.31)$$

where $\Gamma = \sin \phi_s = \cos \psi$. The parameter $\alpha(\Gamma)$ is the ratio of the moving bucket area to the stationary bucket area (when $\Gamma = 0$), and the parameter $\beta(\Gamma)$ is the ratio of the moving bucket height to the stationary bucket height [8]. The induced bucket area and bucket height plotted against Γ in Fig. 6.5. We see that the induced bucket area

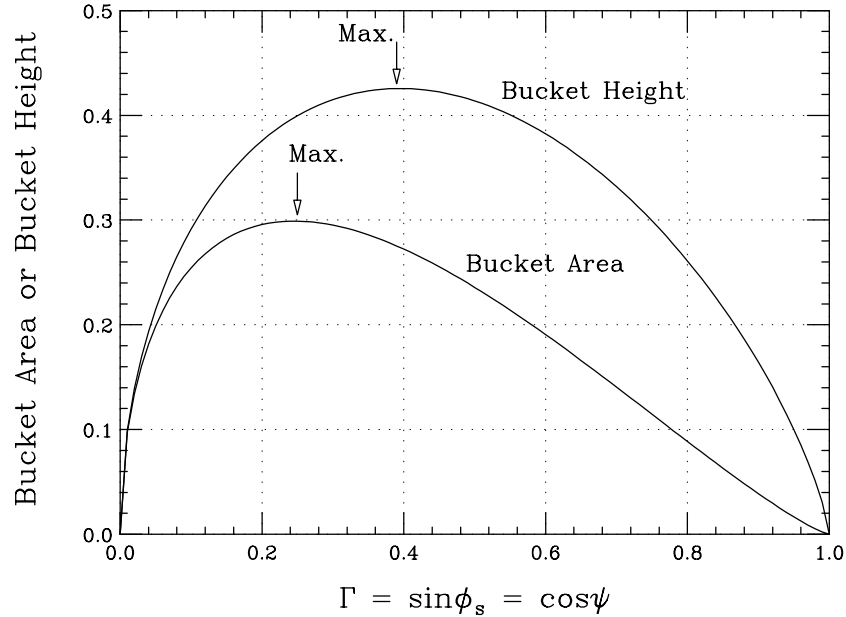


Figure 6.5: Plot showing the area and height of the bucket created by image current interacting with a resonant impedance. At a certain detuning ψ , describing the frequency offset of the image current Fourier component from the resonant frequency of the impedance, the induced bucket area or bucket height passes through a maximum. Self-bunching is most probable when the bucket area or bucket height is maximized.

has a maximum when $\Gamma = 0.25$ or the detuning angle $\psi = 76^\circ$, while the induced bucket height has a maximum when $\Gamma = 0.39$ or the detuning angle $\psi = 67^\circ$. From these results, the most probable frequency at which self-bunching takes place can be inferred.

There are two comments. First, our discussion above is for an accelerator operating below transition. The detuning angle is positive implying that the frequency shift is towards the inductive or low-frequency side of ω_r . When the accelerator is above

transition, the detuning will be towards the capacitive or high-frequency side of ω_r . This can be easily understood in a phasor-diagram description, which we will pursue in Chapter 7.5. The synchronous angle ϕ_s that we reference in this subsection is in fact the negative of the usual synchronous angle. This is because the beam loading voltage is essentially in the opposite direction of the beam current. Therefore the beam loading voltage will decelerate the beam instead of the usual acceleration by the rf voltage. However, the sign of ϕ_s does not affect the area or height of the induced bucket.

6.1.5 Overshoot

When the current is above the microwave threshold, the self-bunching concept tells us that there will be an increase in energy spread of the beam. The increase continues until it is large enough to stabilize the beam again according to the Keil-Schnell criterion. For a proton beam, experimental observation indicates that there will be an overshoot. Let $(\Delta E)_i$ be the initial energy spread which is below the threshold energy spread $(\Delta E)_{\text{th}}$ postulated by the Keil-Schnell criterion. The final energy spread $(\Delta E)_f$ was found to be given empirically by [9]

$$(\Delta E)_i (\Delta E)_f = (\Delta E)_{\text{th}}^2 . \quad (6.32)$$

Thus the final energy spread is always larger than the threshold energy spread. Overshoot formulas similar to but not exactly the same as Eq. (6.32) have been derived by Chin and Yokoya [10], and Bogacz and Ng [11]. For a bunch, the rf voltage introduces synchrotron oscillations. Thus, an increase in energy spread implies also eventual increase in bunch length. At the same time, the bunch area will be increased also.

The situation is quite different for electron bunches because of their short bunch lengths and the presence of radiation damping. This will be discussed in Chapter 7.

6.2 Observation and Cure

In order for a bunch to be microwave unstable, the growth rate has to be much faster than the synchrotron frequency. For the Fermilab Main Ring, the synchrotron period was typically about 100 to 200 turns or 2 to 4 ms. A naive way is to observe the microwave growth is to view the spectrum of the bunch over a large range of frequencies at a certain moment. However, the bunch spectrum produced by a network analyzer is usually via a

series of frequency filters of narrow width, starting from low frequencies and working its way towards high frequencies. This process is time consuming. As soon as the filtering reaches the frequencies concerned, typically a few GHz, the microwave growth may have been stabilized already through bunch dilution, and therefore no growth signals will be recorded. The correct way is to set the network analyzer at a narrow frequency span and look at the beam signal as a function of time. The frequency span is next set to an adjacent narrow frequency interval and the observation repeated until the frequency range of a few GHz has been covered. Besides, we must make sure that the network analyzer is capable of covering the high frequency of a few GHz for the microwave growth signals. The cable from the beam detector to the network analyzer must also be thick enough so that high-frequency attenuation is not a problem in signal propagation. Such an observation was made at the CERN Intersecting Storage Ring (ISR) which is a coasting beam machine. The network analyzer was set at zero span at 0.3 GHz. The beam current was at 55 mA. The signal observed from injection for 0.2 s is shown at the lower left corner of Fig. 6.6 in a linear scale. We see the signal rise sharply and decade very fast, implying an instability which saturates very soon. The beam current was next increased by steps to 190 mA and the observation repeated. We notice that with a higher beam current, the instability starts sooner and stays on longer. The center frequency of the network analyzer was next increased at the steps of 0.2 GHz and the observation repeated. The observation reveals an instability driven by a broadband impedance centering roughly at 1.2 GHz. Microwave instability can also be revealed in monitoring the longitudinal beam profiles, sometimes known as mountain ranges, via a wall resistance monitor. An example is shown in Fig. 6.8. From the ripples, the frequency of the driving impedance can be determined.

One way to produce microwave instability is to lower the rf voltage adiabatically. As the momentum spread of the bunch becomes lower than the Keil-Schnell criterion, microwave instability will develop. From the critical rf voltage, the momentum spread of the bunch can be computed and the impedance of the vacuum chamber driving the instability can be inferred. The rf voltage of the cavities in a proton synchrotron cannot be very much reduced, otherwise multi-pactoring will occur. The total voltage of the rf system can, however, be reduced by adjusting the phases between the cavities. For example, if the phase between two cavities is 180° , the voltages in these two cavities will be canceled. This is called paraphasing. For this reason, it is not possible to know the rf voltage exactly. Small errors in the paraphasing angles will bring about a large uncertainty in the tiny paraphased voltage. For this reason, the impedance determined

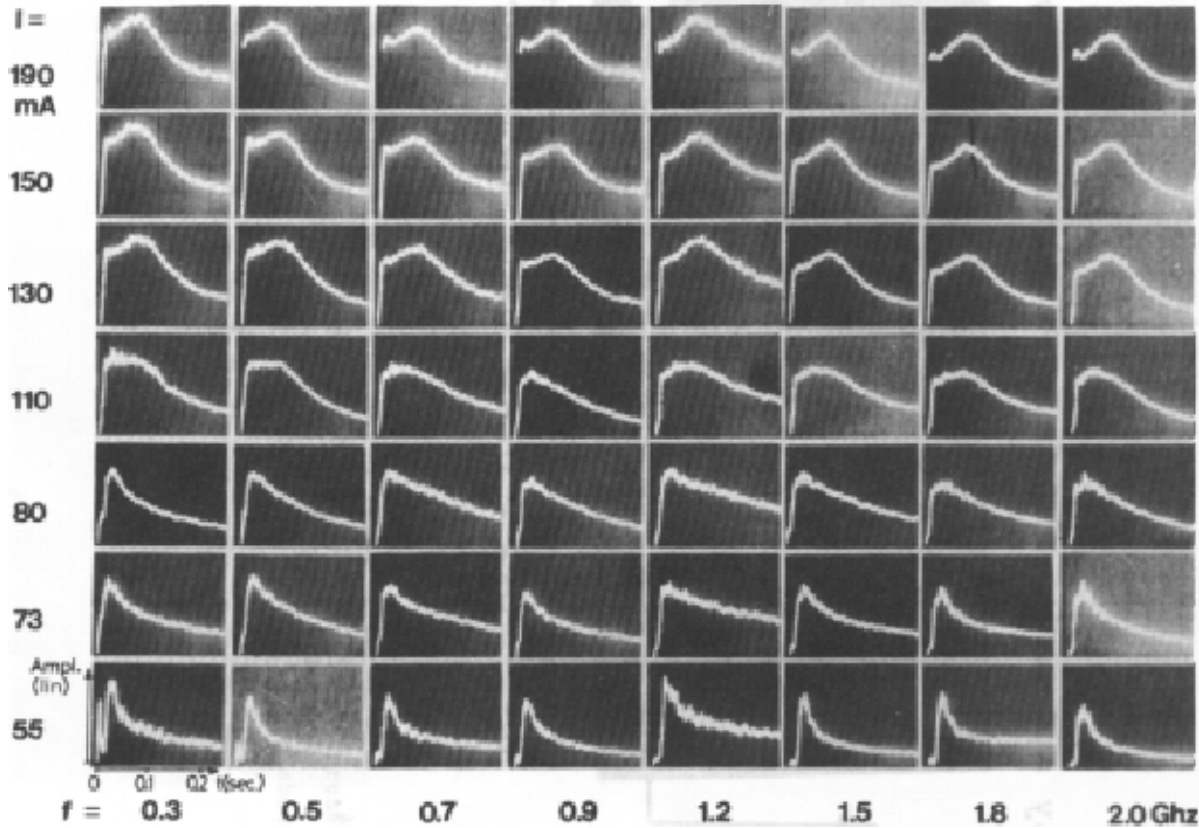


Figure 6.6: Pick-up signal after injection in the CERN ISR, for different observation frequencies but at zero span and different values of beam current. For high beam current, the signal grows before it decays.

by this method may not be accurate.

Another way to observe microwave instability is through debunching. The rf voltage is turned off abruptly and beam starts to debunch. During debunching, the local momentum spread decreases. When the latter is small enough, microwave instability occurs. From the time the instability starts, the impedance of the vacuum chamber can be inferred with the help of the Keil-Schnell criterion. In performing this experiment, the rf cavities must be shorted mechanically after the rf voltage is turned off. Otherwise, the beam will excite the cavities, a process called beam loading. The excited fields inside the cavities can bunch the beam developing high-frequency signals resembling signals of microwave instability. Such an experiment has been performed at the CERN Proton Synchrotron (CPS) and the observation is displayed in Fig. 6.7. The figure shows the time development at 2 ms per division. The top trace shows the rf

voltage which is turned off at 4 ms point. The network analyzer was set at a span from 1.5 to 1.8 GHz and the beam pick-up signal of the beam is shown in the lower trace. We see high-frequency beam signal start developing about 1 ms after the rf voltage is turned off. The signal grows for a few ms before it subsides. The shortcoming of this method of impedance measurement is the difficulty in determining the exact time when the microwave instability starts to develop. One must understand that the growth of the signal amplitude is exponential; therefore the very initial growth may not be visible.

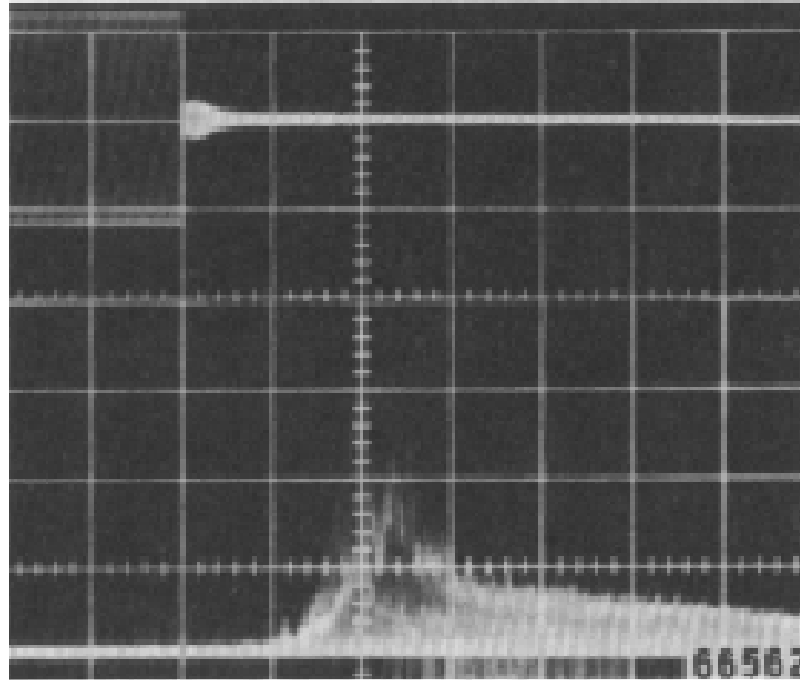


Figure 6.7: Microwave signal observed during debunching in the CERN CPS after the rf voltage (top trace) is turned off. The lower trace shows the beam signal at 1.5 to 1.8 GHz. The sweep is 2 ms per division.

Since microwave instability occurs so fast, it is not possible to use a damper system to cure it. One way to prevent the instability is to blow up the bunch so that the energy spread is large enough to provide the amount of Landau damping needed. Another way is to reduce the impedance budget of the ring by smoothing out the beam pipe discontinuities. For negative-mass instability driven by the space charge impedance just after transition, one can try to modify the ramp curve so that transition can be crossed faster. Of course, a γ_t -jump mechanism will be very helpful.

6.3 Ferrite Insertion and Instability

In Sec. 3.6, we discuss an experiment at the Los Alamos PSR where the space charge repulsive force is large compared with the available rf bunching force. Ferrite rings enclosed inside two pill-case cavities were installed into the vacuum chamber so that the beam would see an amount of inductive force from the ferrite, hoping that the space charge repelling force would be compensated. The experiment results show that this additional inductive force did cancel an appreciable amount of the space charge force of the intense proton beam to a certain extent. This is evident because the bunch lengths were shortened in the presence of the ferrite inserts with zero bias of the solenoidal current wound outside the ferrite tuners, and lengthened when the ferrite rings were biased. Also, the rf voltage required to keep the protons bunched to the required length had been lowered by about 1/3 in the presence of the ferrite insertion. At the same time the gap between successive proton beams was the cleanest ever seen, indicating that the rf buncher was able to keep the beam within the space charge distorted rf buckets so that no proton would leak out. However, the space charge compensation of the potential-well distortion had not been perfect. The ferrite insertion did lead to serious instability which we are going to discuss below.

6.3.1 Microwave Instability

The PSR was upgraded in 1998. The two previous ferrite tuners together with an additional one were installed in order to compensate for the space charge force of the higher intensity beam. However, an instability was observed [12]. With the rf buncher off, Fig. 6.8 shows the mountain-range plot of two consecutive turns of a chopped coasting beam accumulated for 125 μ s and stored for 500 μ s. The signals were recorded at a wide-band wall current monitor. The ripples at the beam profile indicate that a longitudinal microwave instability has occurred. The fast Fourier transform spectrum in Fig. 6.9 shows that the instability is driven at 72.7 MHz or the 26th revolution harmonic. The instability had also been observed in bunched beam. Ripples also show up at the rear half of a bunch, as recorded by a wall-gap monitor in Fig. 6.10. The top plots are two successive turns of a \sim 250 ns (full width) bunch. Apparently, the instability is tolerable because ripples do not distort the shape of the bunch by too much. However, the \sim 100 ns bunch on the lower plots is totally disastrous. The instability lengthens the bunch to almost 200 ns with very noticeable head-tail asymmetry.

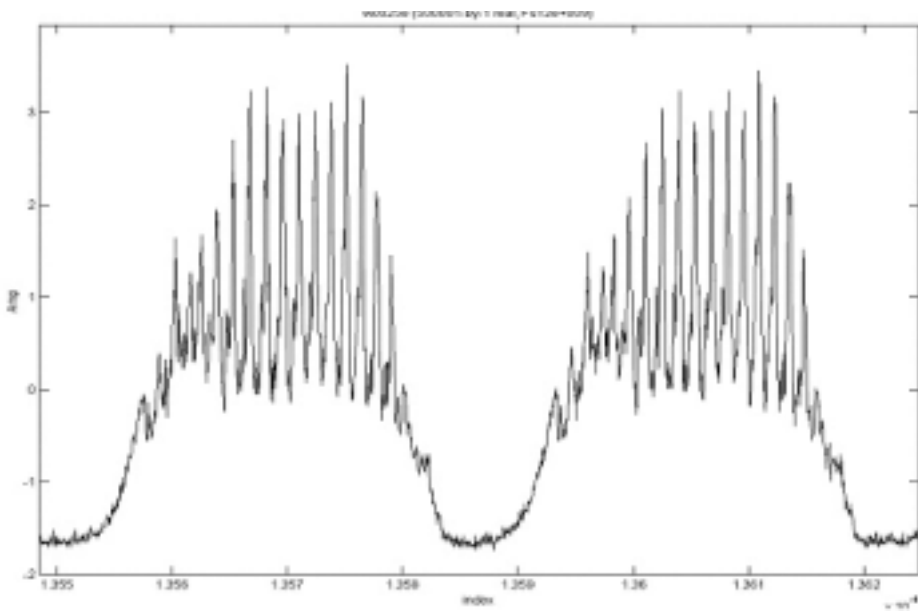


Figure 6.8: Beam profile of two consecutive turns of a chopped coasting beam recorded in a wall-gap monitor after storage of $\sim 500 \mu\text{s}$. The ripples show that a longitudinal microwave instability has occurred.

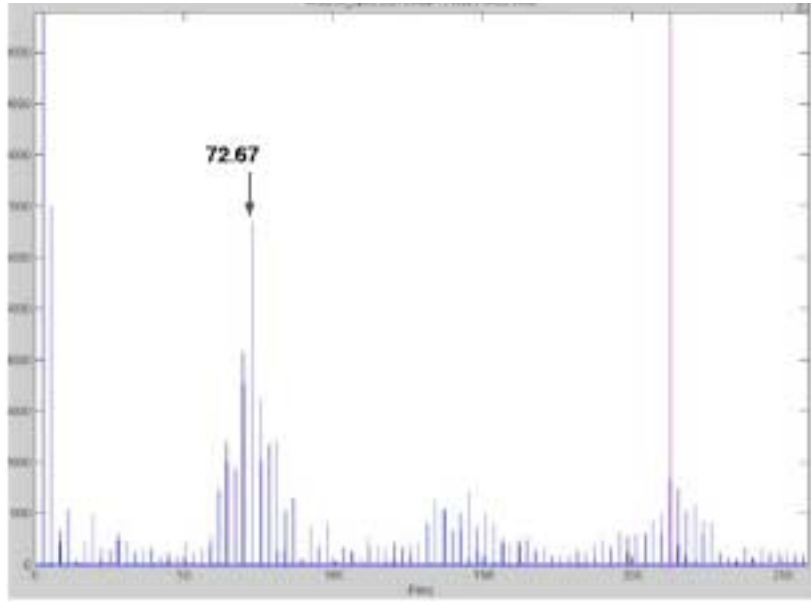


Figure 6.9: (color) Spectrum of the instability signal of the chopped beam in Fig. 6.8, showing the driving frequency is at 72.7 MHz.

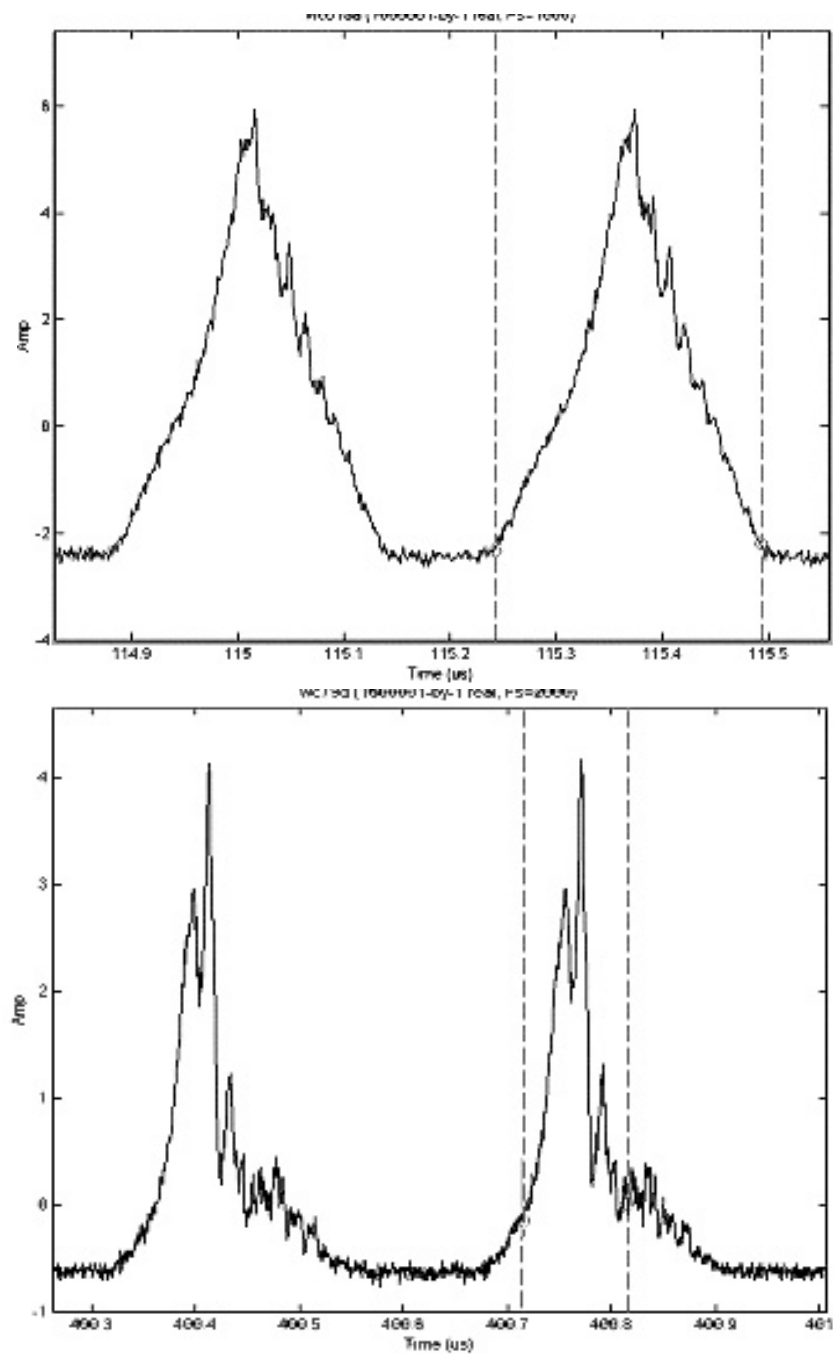


Figure 6.10: Instability perturbation on profiles of bunches with full width 250 ns (top) and 100 ns (bottom). The effect on the 250 ns bunch may be tolerable, but certainly not on the 100 ns bunch, which has lengthened almost to 200 ns.

6.3.2 Cause of Instability

In order to understand the reason behind the instability, let us first construct a simple model for the ferrite tuner. To incorporate loss, the relative permeability of the ferrite can be made complex[‡]: $\mu_s \rightarrow \mu'_s + i\mu''_s$. The impedance of a ferrite core of outer/inner diameter d_o/d_i and thickness t is therefore

$$Z_0^{\parallel} = -i(\mu'_s + i\mu''_s)\omega L_0 , \quad (6.33)$$

where $L_0 = \mu_0 t \ln(d_0/d_i)$ denotes the inductance of the ferrite if the relative permeability μ_s were unity. It is clear that μ'_s and μ''_s must be frequency-dependent. Their general behaviors are shown in Fig. 6.11. For the Toshiba M₄C₂₁A ferrite, μ'_s is roughly constant at ~ 50 to 70 at low frequencies and starts to roll off around $\omega_r/(2\pi) \sim 50$ MHz, while μ''_s , being nearly zero at low frequencies, reaches a maximum near $\omega_r/(2\pi)$. The simplest

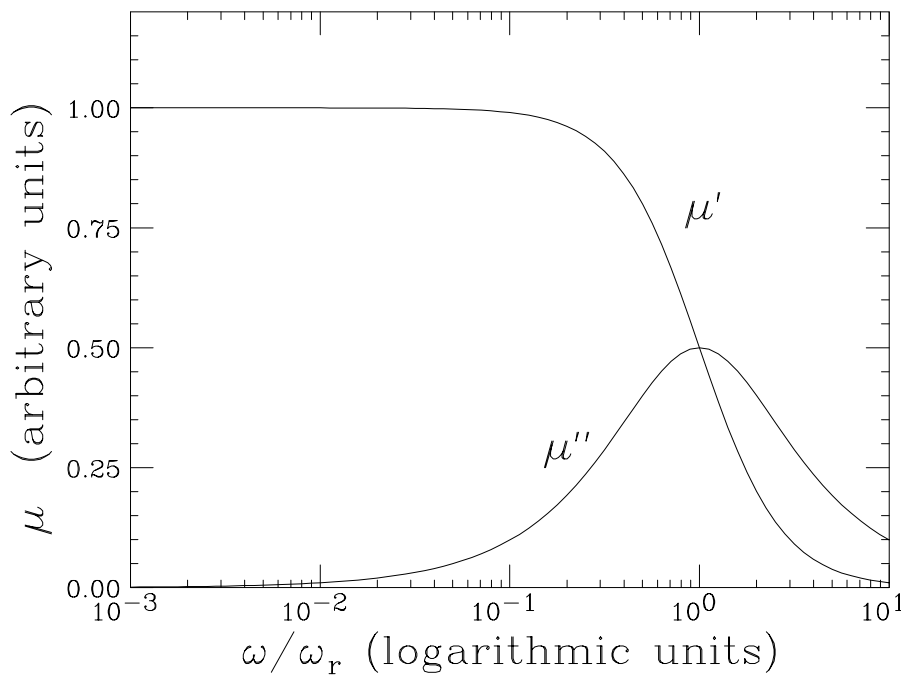


Figure 6.11: (color) Plot of μ' and μ'' as functions of frequency in the 2-parameter model. These are the typical properties of μ' and μ'' for most ferrites.

[‡]The subscript 's' signifies that the permeabilities are defined as if an inductor and a resistor are *in series*.

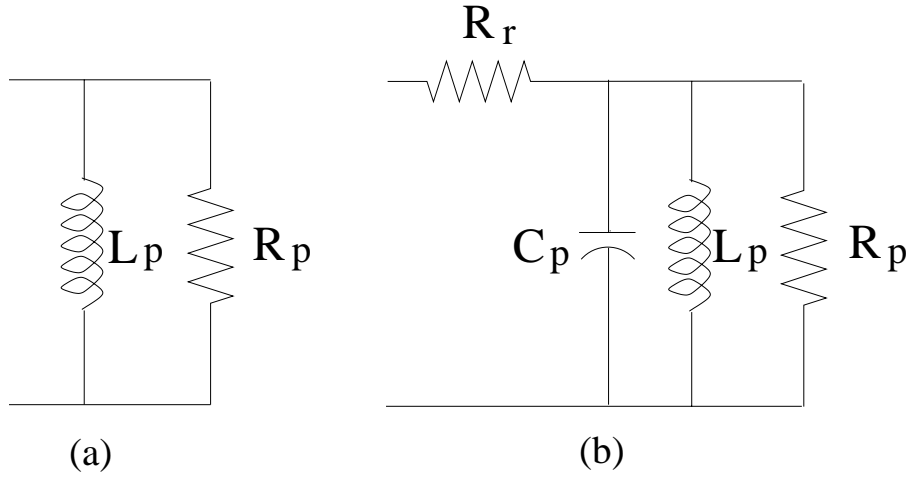


Figure 6.12: (a) Two-element model of ferrite. (b) Three-element model of ferrite cores enclosed in a pill-box cavity.

model for a piece of ferrite consists of an *ideal* inductance L_p and an *ideal* resistor R_p in parallel, as indicated in Fig. 6.12(a).

The impedance of the ferrite core is

$$Z_0^{\parallel}(\omega) = -i\omega L_p \frac{1 + i\omega/\omega_r}{1 + \omega^2/\omega_r^2}, \quad (6.34)$$

with a resonance at

$$\omega_r = \frac{R_p}{L_p}, \quad (6.35)$$

and

$$\mu'_s = \frac{L_p}{L_0} \frac{1}{1 + \omega^2/\omega_r^2}, \quad \mu''_s = \frac{L_p}{L_0} \frac{\omega/\omega_r}{1 + \omega^2/\omega_r^2}. \quad (6.36)$$

We see that the series μ'_s is relatively constant at low frequencies and starts to roll off when approaches ω_r , while μ''_s increases as ω at low frequencies and resonates at ω_r . The corresponding longitudinal wake potential is

$$W(\tau) = R_p [\delta(\tau) - \omega_r e^{-\omega_r \tau}]. \quad (6.37)$$

When the ferrite is biased, L_p decreases so that μ'_s decreases. In this model, this is accomplished by a rise in the resonant frequency ω_r . Actually, measurements show that

the resonant frequency of μ_s'' does increase when the ferrite is biased. Thus, this simple 2-parameter model gives a very reasonable description of the ferrite.

With the ferrite cores enclosed in a pill-box cavity, a 3-parameter broadband parallel- RLC resonance model, as indicated in Fig. 6.12(b), appears to be more appropriate for the ferrite tuner as a whole. Sometimes there may be an additional residual resistance R_r which we neglect for the time being. We have, for the inductive insert,

$$Z_0^{\parallel}(\omega) = \frac{R_p}{1 - iQ \left(\frac{\omega}{\omega_r} - \frac{\omega_r}{\omega} \right)}, \quad (6.38)$$

where the resonant frequency is $\omega_r = (L_p C_p)^{-1/2}$ and the quality factor is $Q = R_p \sqrt{C_p / L_p}$.

For a space charge dominated beam, the actual area of beam stability in the complex Z_0^{\parallel}/n -plane (or the traditional $U'-V'$ plane) is somewhat different from the commonly quoted Keil-Schnell estimation [3, 4]. In Fig. 6.13, the heart-shape solid curve, denoted by 1, is the threshold curve for parabolic distribution in momentum spread, where the momentum gradient is discontinuous at the ends of the spread. Instability develops and a smooth momentum gradient will result at the ends of the spread, changing the threshold curve to that of a distribution represented by 2, for example, $\frac{15}{16}(1 - \delta^2/\hat{\delta}^2)^2$, where δ is the fractional momentum spread and $\hat{\delta}$ the half momentum spread. Further smoothing of the momentum gradient at the ends of the spread to a Gaussian distribution will change the threshold curve to 3. On the other hand, the commonly known Keil-Schnell threshold is denoted by the circle of unit radius in dots. This is the reason why in many low-energy machines the Keil-Schnell limit has been significantly overcome by a factor of about 5 to 10 [5]. In this case, the space charge is almost the only source of the impedance, the real part of the impedance can be typically orders of magnitude smaller. As an example, if the impedance of the Los Alamos PSR is at Point A, the beam is within the microwave stable region if the momentum spread is Gaussian like, although it exceeds the Keil-Schnell limit. Now, if we compensate the space charge potential-well distortion by the ferrite inductance, the ferrite required will have an inductive impedance at low frequency equal to the negative value of the space charge impedance at A, for example, about -5.5 units according to Fig. 6.13. However, the ferrite also has a resistive impedance or $\Re Z_0^{\parallel}$ coming from μ_s'' . Although $\Re Z_0^{\parallel}/n$ is negligible at low frequencies (for example, the rf frequency of 2.796 MHz of the PSR), it reaches a peak value near $\omega_r/(2\pi)$ (about 50 to 80 MHz for the Toshiba M₄C_{21A} inside the pill-box container) with the peak value the same order of magnitude as the low-frequency $\Im Z_0^{\parallel}$. Actually,

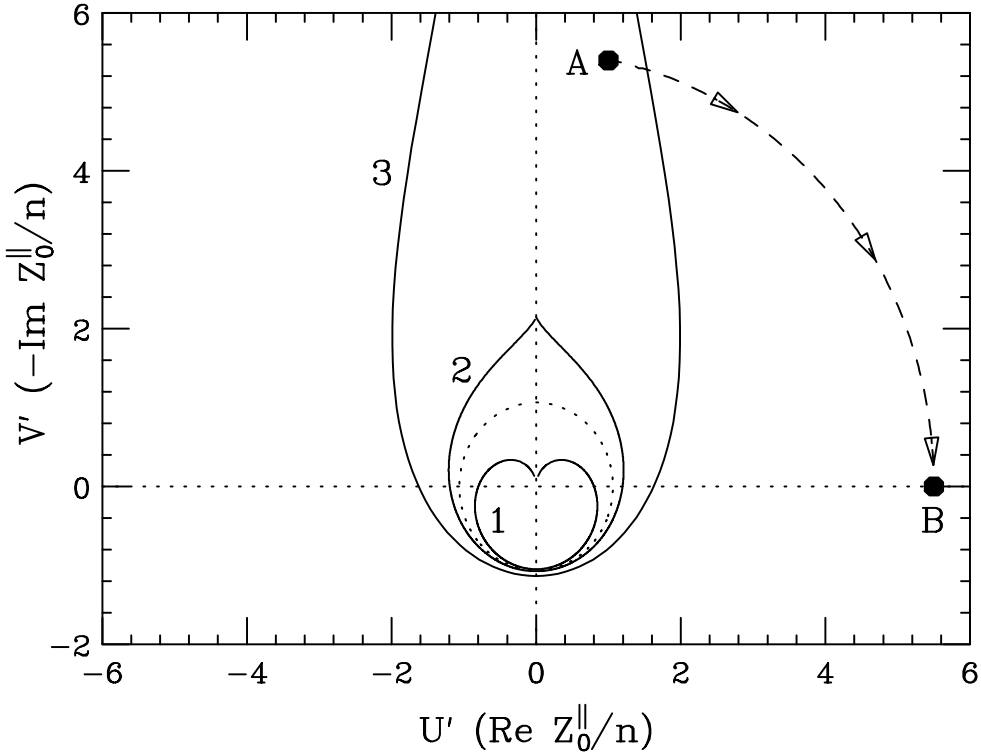


Figure 6.13: Microwave instability threshold curves in the complex Z_0^{\parallel} (or U' - V') plane, for (1) parabolic momentum distribution, (2) distribution with a continuous momentum gradient, and (3) Gaussian momentum distribution. The commonly quoted Keil-Schnell threshold criterion is denoted by the circle in dots. An intense space charge beam may have impedance at Point A outside the Keil-Schnell circle and is stable. A ferrite tuner compensating the space charge completely will have a resistive impedance roughly at Point B and is therefore unstable.

according to the *RLC* model discussed above, we get approximately

$$\frac{\text{Re } Z_0^{\parallel}/n|_{\text{pk}}}{\text{Im } Z_0^{\parallel}/n|_{\omega \rightarrow 0}} \approx \frac{Q^2 + Q + 1}{Q + 2} = \left\{ \begin{array}{ll} Q & \text{if } Q \gg 1 \\ 1 & \text{if } Q \sim 1 \\ \frac{1}{2} & \text{if } Q \ll 1 \end{array} \right\} \geq \frac{1}{2}. \quad (6.39)$$

The *RL* model gives the same impedance ratio of $\frac{1}{2}$ as the low- Q case of Eq.(6.39). Thus the ferrite will contribute a resistive impedance denoted roughly by Point B (~ 5.5 units) when $Q \sim 1$ or at least one half of it when $Q \ll 1$. This resistive impedance of the ferrite insert will certainly exceed the threshold curve and we believe that the longitudinal instability observed at the Los Alamos PSR is a result of this consideration. It follows

from here that such low-frequency compensation of an intense space charge induced potential-well distortion will result in the microwave instability at high frequencies, $\omega \simeq \omega_r$. The conclusion appears to be that strong space charge potential-well distortion can only be compensated by the ferrite inductance to some extent to ensure that the resistive part of the ferrite insertion is kept below the microwave instability threshold. However, Eq. (6.39) is only correct when the RLC circuit is composed of an *ideal* resistor, an *ideal* inductor, and an *ideal* capacitor. In reality, the ferrite cores are much more complicated. To represent the inductor insert, many of these elements are frequency dependent. Thus, if one chooses the right ferrite in the construction of the inductive insert, it is possible to have the ratio of $\Re Z_0^{\parallel}/n|_{\text{pk}}$ to $\Im Z_0^{\parallel}/n|_{\omega \rightarrow 0}$ much less than $\frac{1}{2}$. Such a ferrite will be the best candidate for space charge compensation.

6.3.3 Heating the Ferrite

One way to avoid the longitudinal microwave instability driven by the compensating ferrite is to choose a ferrite having the properties of high μ'_s at low frequencies and low loss[§] at high frequencies. Their ratio should be at least or larger than ~ 10 . Past experience indicates that when a piece of ferrite is heated up, μ'_s will increase and hopefully the loss at high frequencies will decrease, thus having exactly the same properties that we are looking for.

A measurement of the temperature dependency of the ferrite has been made on a ferrite insert similar to those manufactured for the PSR was used, but much shorter containing only several ferrite cores. A sinusoidal wave was introduced from one end of the ferrite tuner via an antenna while the transmitted wave was received with another antenna at the other end. What was measured was S_{21} , the forward transmission through the network (in this case cavity), or the attenuation of a passive network. The results are shown in Fig. 6.14 and reveal that the resonant loss peak drops by a factor of about 8 when the ferrite cores are heated from the room temperature of 23°C to 100°C.

A measurement of the permeability of the ferrite has also been made on a single Toshiba M₄C₂₁A ferrite core as a function of core temperature. To provide both a good electrical circuit path and a uniform core temperature, the core was encased in an aluminum test fixture before being placed on a hot plate. The top half of the test fixture

[§]Low loss does not imply low μ'' . Whenever ferrite is used, for example in the inductor insert, there will be inevitably capacitance involved. Thus low loss actually implies low R_p .

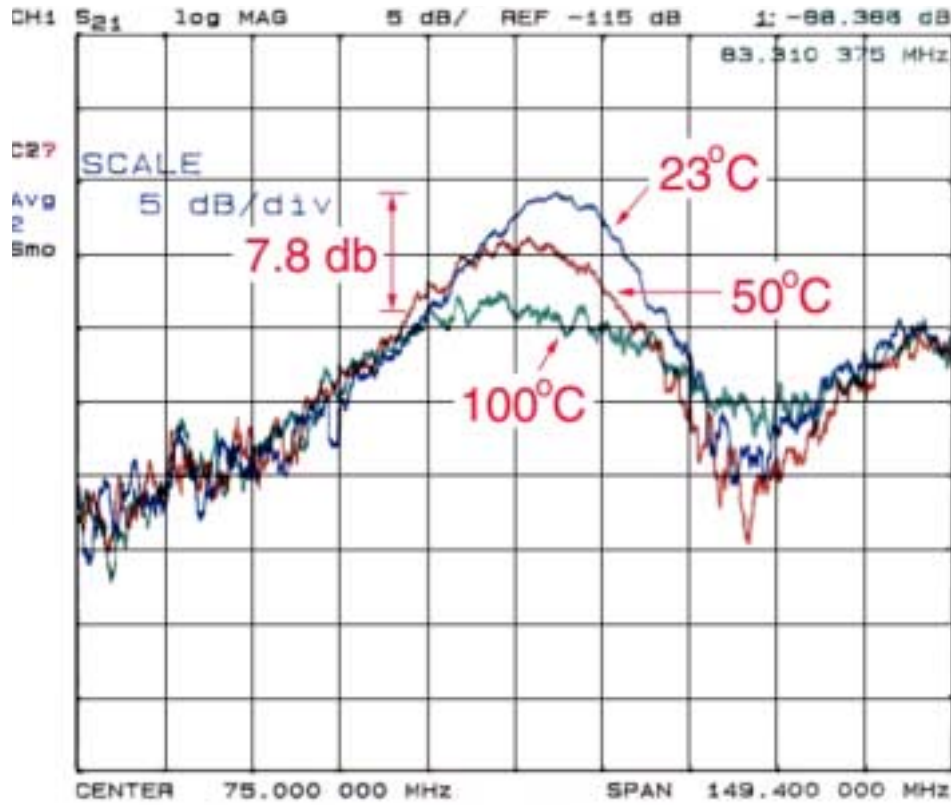


Figure 6.14: (color) An antenna at one end of the ferrite tuner sends out a sinusoidal wave to be picked up by another antenna at the other end of the tuner, and the loss is recorded. As the ferrite cores are heated from room temperature to 100°C, the loss has reduced by almost 8 times.

consisted of a machined aluminum disk, 9 in in diameter and 1.25 in thick. The inner section of the disk was machined out 0.005 in undersize to accommodate the ferrite core. The disk was then heated and the core was slipped into the disk. Upon cooling, the aluminum disk contracted and made a good thermal contact with one side and the outer edge of the ferrite core. The aluminum fixture and core were then flipped over onto a flat aluminum plate so that only the inner edge of the core was exposed. A good electrical connection between the aluminum disk and flat plate was made using strips of adhesive backed copper tape. The test fixture was placed on a hot plate and covered with two fire bricks. The test fixture was then heated to 175°C and allowed to cool slowly.

The impedance measurement was made by placing the probe of an HP4193A vector impedance meter directly across the inner edge of the ferrite core. Impedances were

measured from 10 MHz to 110 MHz in 10 MHz steps from 150°C to 25°C. The temperature of the core was monitored by a Fluke 80T-150U temperature probe inserted into a small hole in the aluminum disk portion of the test fixture.

In order to make an electrical model of the entire core and test fixture structure, it was necessary to obtain the equivalent parallel capacitance of the test set-up as depicted in Fig. 6.12(b). The capacitor C_p was determined by adding additional fixed 100 pf capacitors across the inner edge of the ferrite core and observing the change in the resonant frequency of the structure from 41 to 28 MHz, a frequency range in which the μ'_s of the ferrite is known to be relatively constant. In this manner, a capacitance of $C_p = 75$ pf was chosen to represent the equivalent parallel capacitance of the test circuit. There was also a series residual resistance of $R_r = 0.55 \Omega$ in the probe. This residual resistance introduces a large error at low frequencies (below ~ 10 Hz) when the resistive part of the RLC circuit is small. From the measurements of the input impedance, R_p and L_p were computed. From Eq. (6.36), the relative permeability, μ'_s and μ''_s were inferred. These are plotted in Figs. 6.15 and 6.16. We see that from 23°C to 150°C, μ'_s at low frequencies has almost been doubled, implying that the inductance L_p at low frequencies has been doubled according to Eq. (6.36). The loss component μ''_s also increases with temperature with its peak moves towards lower frequencies. This is obvious in the two-element model of a ferrite, because Eq. (6.36) says that the peak of μ''_s is proportional to L_p and independent of R_p .

There is always a capacitance accompanied the ferrite insert. For a pill-box enclosing a single ferrite core, the capacitance measured was $C_p = 75$ pF, which is not too different from the computed value of 93 pF where a relative dielectric $\epsilon_r = 13$ has been assumed for the ferrite. The real part of the impedance of the ferrite insert per ferrite core, $\Re Z_0^{\parallel}$, is shown in Fig. 6.17. The resonant peaks are actually represented by the element R_p in the RLC circuit. The measured values of R_p as a function of frequency and temperature is shown in Fig. 6.18. We see that R_p depends very much on frequency and exhibits resonant peaks, which diminishes and moves to lower frequencies as the temperature increases. Thus the loss at high frequencies has been very much reduced by heating the ferrite. For a coasting beam, the energy lost to the ferrite core is given by the area under each $\Re Z_0^{\parallel}$ curve. Although both R_p and L_p vary tremendously with temperature, we find out that this loss is in fact temperature independent within 10% from 23°C to 150°C. However, the impedance becomes broader and broader and the resonant frequency shifts lower as the temperature increases.

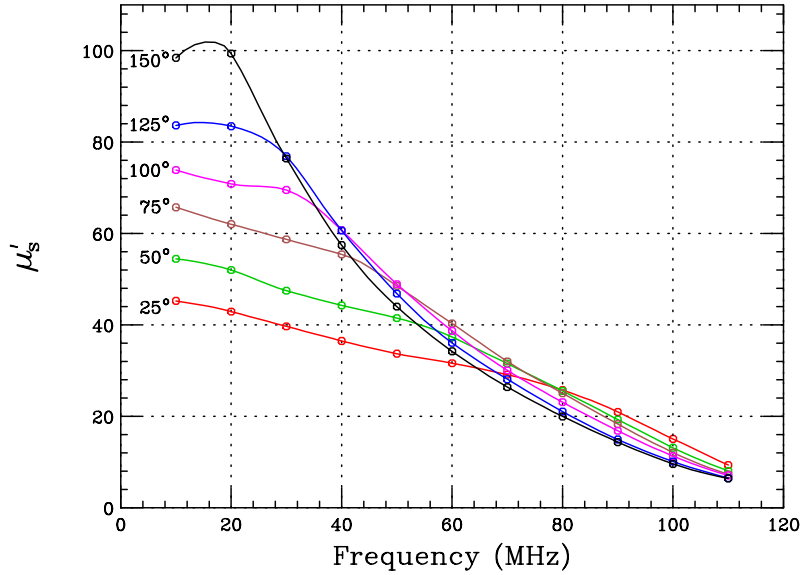


Figure 6.15: (color) Measured real part of the series magnetic permeability, μ'_s of a single Toshiba M₄C₂₁A ferrite core up to 110 MHz at 25°, 50, 75, 100, 125, and 150°C. Measured points are denoted by circles.

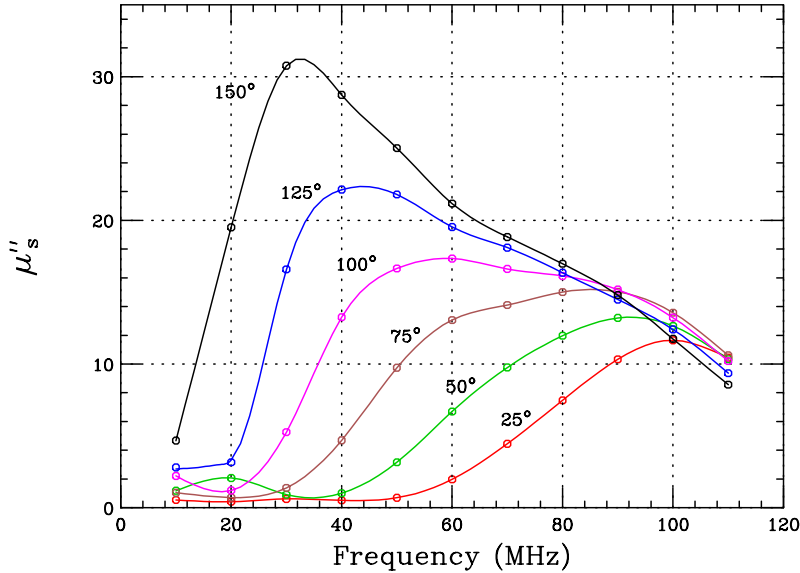


Figure 6.16: (color) Measured imaginary part of the series magnetic permeability, μ''_s of a single Toshiba M₄C₂₁A ferrite core up to 110 MHz at 25°, 50, 75, 100, 125, and 150°C. Measured points are denoted by circles.

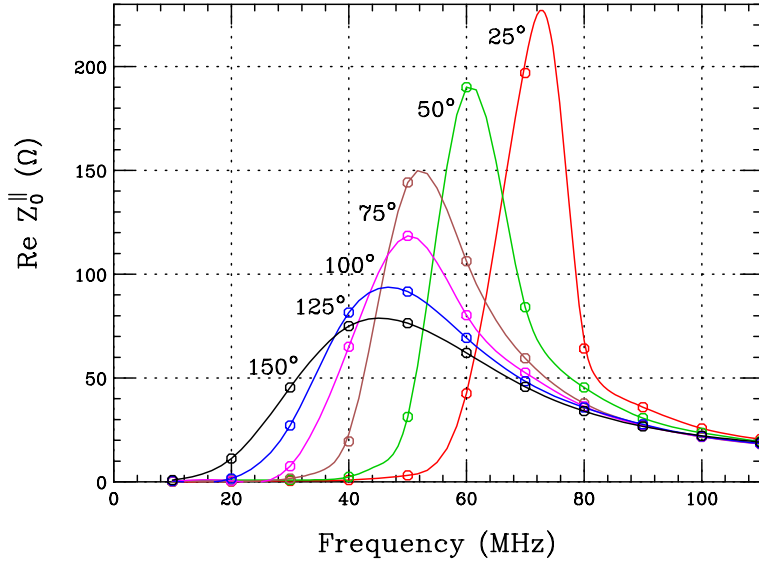


Figure 6.17: (color) Measured real part of the impedance of a single Toshiba M₄C₂₁A ferrite core inside an enclosing pill-box cavity up to 110 MHz at 25°, 50, 75, 100, 125, and 150°C. Measured points are denoted by circles.

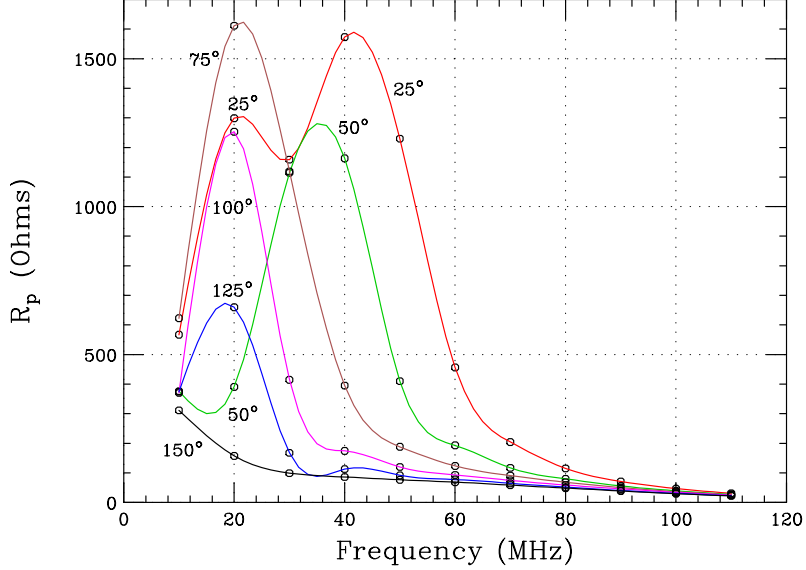


Figure 6.18: (color) Measured resistance of the resistor R_p in the RL model of the Toshiba M₄C₂₁A ferrite core or the RLC model of the inductor insert as functions of frequency at 25°, 50, 75, 100, 125, and 150°C. Measured points are denoted by circles.

The threshold microwave instability, depicted in Fig. 6.13, is determined by the impedance per unit PSR revolution harmonic, Z_0^{\parallel}/n , whose real and imaginary parts are shown, respectively, in Figs. 6.19 and 6.20. We now see that the resonant peak of $\Re Z_0^{\parallel}/n$ decreases with increasing temperature (except at 25°C). This explains why microwave instability can be alleviated by heating the ferrite cores.

The properties of the heated ferrite can be understood as follows. A piece of ferrite consists of domains with magnetization. The total magnetization is the vector sum of the magnetization of the domains. When the temperature increases, the domain magnetizations are freer to move. They tend to line up resulting in higher magnetic permeability μ'_s , which is what we have been observing. However, if the temperature becomes too high, the spins of individual atoms or molecules become random and the total magnetization will drop and reach zero at the Curie temperature.

6.3.4 Application at the PSR

Later in 1999 the solenoids of the ferrite inserts for PSR were removed, the outside of the inserts were wound with heating tapes, and two modules were reinstalled in the PSR. When the ferrite is heated to 130°C, the longitudinal microwave instability, seen in the in Fig. 6.21, disappears. The profile of the 100 ns bunch in the presence of the heated ferrite tuners, is no longer distorted and the bunch has not been lengthened. Further beam studies with the heated ferrites carried out during the remainder of 1999 demonstrated other benefits of the inductors without unmanageable operational impacts.

Two effects of the ferrite inserts are thought to contribute to improving the instability threshold possibly in two ways. One is the effect of a cleaner gap that will trap fewer electrons during gap passage. This will improve the threshold of transverse e-p coupled-centroid instability (Chapter-19). The other is the increased momentum spread from the removal of the space charge depression of the bucket height. This will increase Landau damping and improve the threshold of longitudinal microwave instability. The latter increase in momentum spread is illustrated in Fig. 6.22 which shows plots from ACCSIM simulations [14]. The simulations show the effect of longitudinal space charge on the rf bucket height and momentum spread for a beam of 7.3 $\mu\text{C}/\text{pulse}$ with 13 kV rf voltage. The left plot shows the bunch and the bucket without longitudinal space charge or the equivalent to full compensation by the inductive inserts. The right plot shows the bunch and bucket subject to the longitudinal space charge force. For this case, the

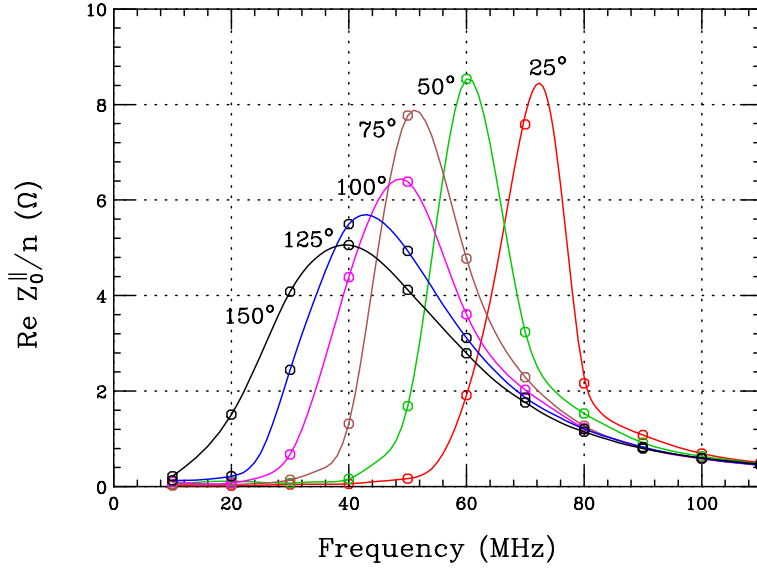


Figure 6.19: (color) Measured real part of the impedance per revolution harmonic of a single Toshiba M₄C₂₁A ferrite core inside an enclosing pill-box cavity up to 110 MHz at 25°, 50, 75, 100, 125, and 150°C. Measured points are denoted by circles.

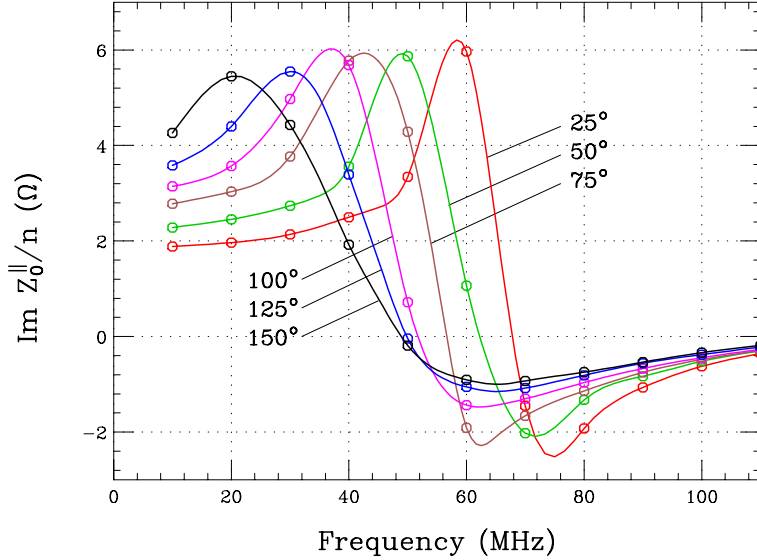


Figure 6.20: (color) Measured imaginary part of the impedance per revolution harmonic of a single Toshiba M₄C₂₁A ferrite core inside an enclosing pill-box cavity up to 110 MHz at 25°, 50, 75, 100, 125, and 150°C. Measured points are denoted by circles.

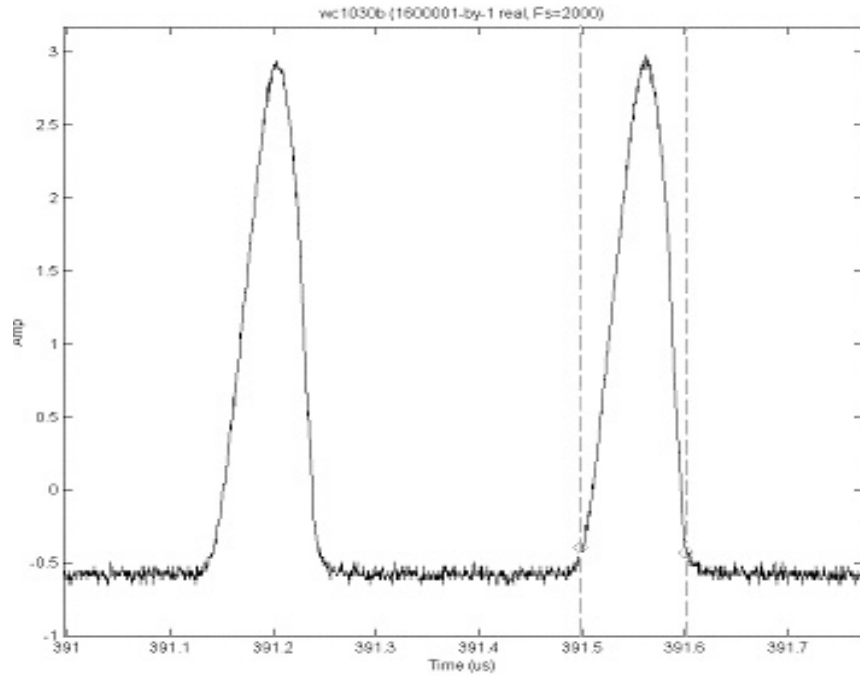


Figure 6.21: With two ferrite tuners installed and heated to 130°C, the instability ripples disappear from the profile of the 100 ns bunch.

space charge effect reduces the bucket height by $\sim 23\%$. In the absence of space charge, the bucket height scales by the square root of the rf voltage and would imply a reduction $\sim 41\%$ in rf voltage to reach the same bucket height as with space charge. This argument implies that with inductors a $\sim 41\%$ reduction in rf voltage would reach the same momentum spread as obtained in their absence. This is in reasonable agreement with the observed effect of $\sim 35\%$. Thus, it appears that Landau damping explains much of the effect of the ferrite inserts on the instability. With the increase in bucket height after the compensation of the space charge force by the inductive inserts, the bucket is able to hold the beam particles inside without leakage into the gap region. Thus, the ferrite inserts improve the thresholds of both the longitudinal microwave instability as well as the transverse two-stream coupled-centroid instability.

Comparable reductions in threshold curves have been obtained with other means of Landau damping such as the use of a skew quadrupole (coupled Landau damping), sextupoles and octupoles. It has also been observed that the effects of these (on the instability threshold) add with that of the inductors. An additional sextupole was installed in the upgrade. It is surprising that this sextupole has an important bearing

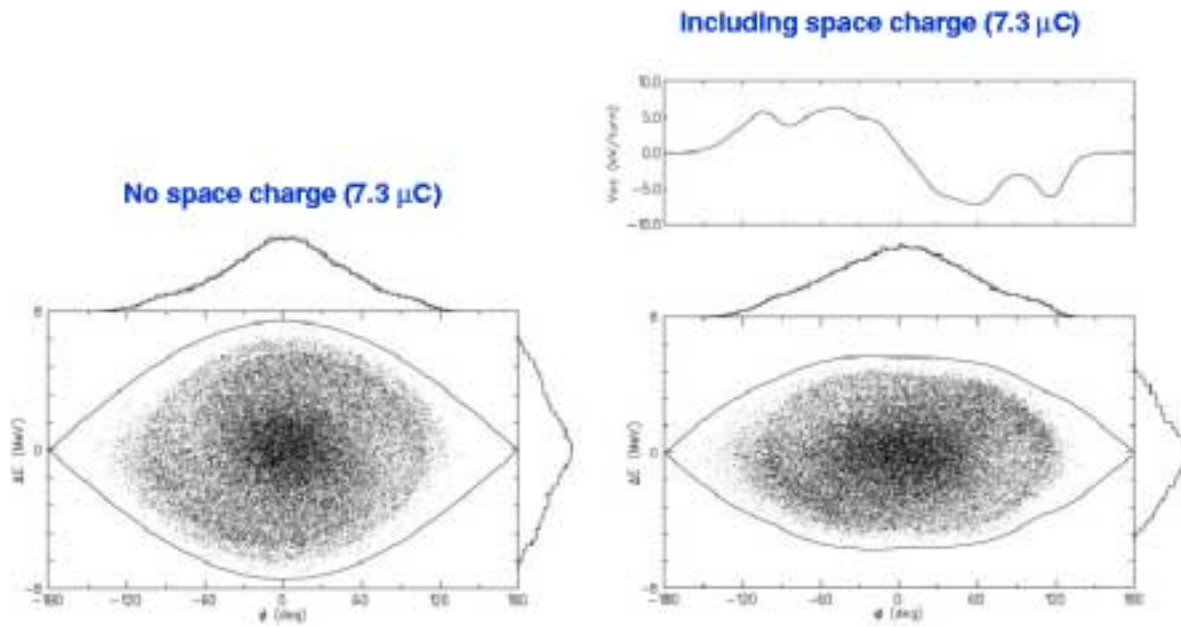


Figure 6.22: Simulation of a PSR bunch with an intensity of $7.3 \mu\text{C}$ at the buncher voltage of 13 kV using the code ACCSIM. The left plot is the result without space charge while the right plot is the result with space charge included. Notice that in the presence of space charge the bucket height is reduced by 24%, implying a cancellation of the rf voltage by 42%. The top curve on the right shows the space charge voltage per turn (proportional to the spatial derivative of the proton line density).

on the beam stability. Turning on this sextupole current to $+20 A$ and optimizing the former four sextupoles and two octupoles in the ring can help to improve the threshold curve by $\sim 25\%$ as is shown in Figure 6.23. It is understandable that the sextupoles and octupoles introduce tune spread which can provide Landau damping of the vertical coupled e-p instability once protons leak into the bunch gap and prevent the electrons from clearing. However, why just one sextupole has this much effect is not clear at all.

In late 1999 the combined effect of heated ferrites and a skew quad enabled us to accumulate and store at the PSR a record $9.7 \mu\text{C}/\text{pulse}$, which is all that the linac could deliver. For this demonstration, the accumulation time was $1225 \mu\text{s}$, the maximum obtainable at 1 Hz from the linac. The ferrite inserts were heated to 190°C , which over compensates longitudinal space charge by $\sim 50\%$. The rf buncher was at the maximum of 18 kV. In addition, the bunch width was stretched out to 305 ns, something never

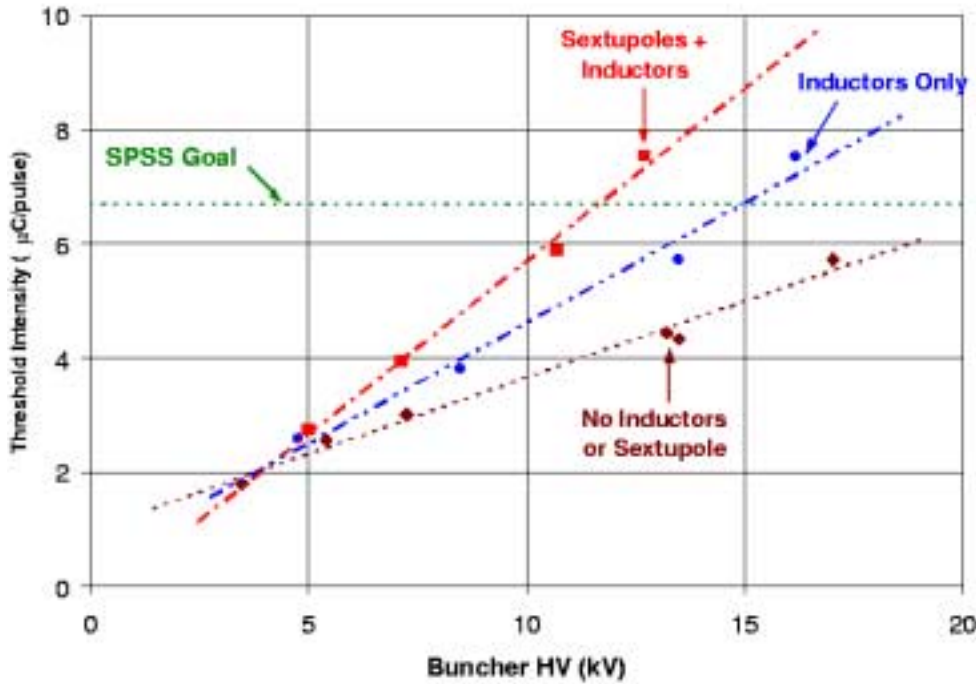


Figure 6.23: (color) After the upgrade, the PSR operating without the ferrite insert had a lower bunch intensity versus buncher voltage, depicted in dots, than the historical, depicted in dashes.

been accomplished before without reducing the threshold intensity. Beam losses were high ($\sim 5\%$), which would be prohibitive at 20 Hz. There was, no doubt, significant emittance growth that could be attributed to transverse space charge effects from the very high peak beam current of 82 A observed in this demonstration.

Engineered versions of the heated ferrites were installed in the fall of 2000 and have been used in production running ever since. A bunch length of 290 ns instead of the 250 has reduced the accumulation time accordingly thereby saving $\sim \$15k$ per month in linac power costs. At the present, the PSR with two heated-ferrite modules can operate stably at an intensity of $8 \mu\text{C}/\text{pulse}$ for low repetition rates (for beam studies and single pulse users). Thus, the peak intensity goal of the upgrade has been surpassed. The remaining challenge is to reduce beam losses so that routine operation at 20 Hz is possible with acceptable activation of the ring.

6.4 Exercises

- 6.1. The dispersion relation of Eq. (6.19) can be rewritten in a simpler form. let us measure revolution angular frequency in terms of $2S$, the FWHM spread, which is related to the FWHM energy spread by

$$2S \equiv \omega - \omega_0|_{\text{FWHM}} = -\frac{\eta\omega_0}{\beta^2} \frac{\Delta E}{E_0}|_{\text{FWHM}} . \quad (6.40)$$

We can then introduce a dimensionless reduced angular frequency x such that

$$n\omega - n\omega_0 = nxS \quad \text{and} \quad \Omega - n\omega_0 = nx_1 S , \quad (6.41)$$

where we have used the fact the the collective angular frequency Ω in Eq. (6.15) is close to $n\omega_0$. The frequency distribution function $g_0(\omega)$ is now transformed to a distribution $f(x)$ which is normalized to 1 when integrated over x . We have

$$\frac{dg_0(\omega)}{d\omega} d\omega = \frac{d f(x)}{dx} \frac{dx}{d\omega} dx = \frac{1}{S} \frac{d f(x)}{dx} dx . \quad (6.42)$$

- (a) Show that the dispersion relation (6.19) becomes

$$1 = -\frac{i2 \operatorname{sgn}(\eta)}{\pi} (U' + iV') \int \frac{f'(x)}{x_1 - x} dx , \quad (6.43)$$

where U' and V' are defined in Eq. (6.21).

- (b) When the beam current is just above threshold, the reduced collective angular frequency is written as $x_1 = x_{1R} + i\epsilon$ where x_{1R} is real and ϵ is an infinitesimal positive number. Show that the stability curve can be obtained from

$$1 = -\frac{i2 \operatorname{sgn}(\eta)}{\pi} (U' + iV') \left[\wp \int \frac{f'(x)}{x_{1R} - x} dx - i\pi f'(x_{1R}) \right] . \quad (6.44)$$

by varying x_{1R} , where \wp denotes the principal value of the integral.

- (c) show that the negative V' -intersect or the lowest point of the bell-shaped stability curve V'_{in} is given by

$$1 = -\frac{2 \operatorname{sgn}(\eta)V'_{\text{in}}}{\pi} \wp \int \frac{f'(x)}{x} dx . \quad (6.45)$$

In fact, the form factor in the Keil-Schnell criterion is given by $F = |V'_{\text{in}}|$.

- (d) The form factor F 's in the Keil Schnell criterion for various frequency distribution functions are listed in Table 6.1. Verify the results.

Table 6.1: Form factors in the Keil-Schnell criterion for various distributions. For the first four, the distributions reside only inside the region $|\Delta\omega| \leq \widehat{\Delta\omega}$. When normalized to the HWHM, the domain becomes $|x| \leq a$.

Frequency Distribution		Form Factor F
$g_0(\omega)$	$[\Delta\omega = \omega - \omega_0]$	
$\frac{3}{4\widehat{\Delta\omega}} \left(1 - \frac{\Delta\omega^2}{\widehat{\Delta\omega}^2}\right)$	$\frac{3}{4a} \left(1 - \frac{x^2}{a^2}\right)$	$a^2 = 2$ $\frac{\pi a^2}{6} = 1.0472$
$\frac{8}{3\pi\widehat{\Delta\omega}} \left(1 - \frac{\Delta\omega^2}{\widehat{\Delta\omega}^2}\right)^{3/2}$	$\frac{8}{3\pi a} \left(1 - \frac{x^2}{a^2}\right)^{3/2}$	$a^2 = \frac{1}{1 - 2^{-2/3}}$ $\frac{\pi a^2}{8} = 1.0612$
$\frac{15}{16\widehat{\Delta\omega}} \left(1 - \frac{\Delta\omega^2}{\widehat{\Delta\omega}^2}\right)^2$	$\frac{15}{16a} \left(1 - \frac{x^2}{a^2}\right)^2$	$a^2 = \frac{1}{1 - 2^{-1/2}}$ $\frac{\pi a^2}{10} = 1.0726$
$\frac{315}{256\widehat{\Delta\omega}} \left(1 - \frac{\Delta\omega^2}{\widehat{\Delta\omega}^2}\right)^4$	$\frac{315}{256a} \left(1 - \frac{x^2}{a^2}\right)^4$	$a^2 = \frac{1}{1 - 2^{-1/4}}$ $\frac{\pi a^2}{18} = 1.0970$
$\frac{1}{\sqrt{2\pi}\sigma} \exp\left(-\frac{\Delta\omega^2}{2\sigma^2}\right)$	$\frac{1}{\sqrt{2\pi}a} \exp\left(-\frac{x^2}{2a^2}\right)$	$a^2 = \frac{1}{2 \ln 2}$ $\frac{\pi a^2}{2} = 1.1331$

6.2. Using Eq. (6.44), plot the bell-shaped stability contours for the distributions listed in Table 6.1 as illustrated in Fig. 6.4.

6.3. Using Eq. (6.43), show that the constant-growth contours for the Gaussian distribution are given by

$$1 = \frac{i \operatorname{sgn}(\eta) 4 \ln 2}{\pi} (U' + iV') [1 + i\sqrt{\pi \ln 2} x_1 w(\sqrt{\ln 2} x_1)] , \quad (6.46)$$

where use has been made of the integral representation of the complex error function:

$$w(z) = \frac{i}{\pi} \int_{-\infty}^{\infty} \frac{e^{-t^2}}{z - t} dt \quad \text{for } \operatorname{Im} z > 0 . \quad (6.47)$$

Plot the contours in Fig. 6.3.

Bibliography

- [1] L.D. Landau, J. Phys. USSR **10**, 25 (1946);
- [2] A.W. Chao, *Physics of Collective Beam Instabilities in High Energy Accelerators*, John Wiley & Sons, 1993, p. 251.
- [3] E. Keil and W. Schnell, CERN Report TH-RF/69-48 (1969); V.K. Neil and A.M. Sessler, Rev. Sci. Instr. **36**, 429 (1965).
- [4] D. Boussard, CERN Report Lab II/RF/Int./75-2 (1975).
- [5] J. Bosser, C. Carli, M. Chanel, N. Madsen, S. Maury, D. Möhl, G. Tranquille, Nucl. Instrum. and Meth. **A441**, 1 (2000).
- [6] S. Krinsky and J.M. Wang, Particle Accelerators **17**, 109 (1985).
- [7] J.D. Jackson, Plasma Phys. **C1**, 171 (1960).
- [8] See for example, C. Bovet, et al., *A Selection of Formulae and Data Useful for the Design of A.G. Synchrotron*, CERN/MPS-SI/Int. DL/70/4, 23 April, 1970.
- [9] R.A. Dory, Thesis, MURA Report 654, 1962.
- [10] Y. Chin and K. Yokoya, Phys. Rev. **D28**, 2141 (1983).
- [11] S.A. Bogacz and K.Y. Ng, Phys. Rev. **D36**, 1538 (1987).
- [12] K.Y. Ng, J.E. Griffin, D. Wildman, M. Popovic, A. Browman, D. Fitzgerald, R. Macek, M. Plum, and T. Spickermann, *Recent Experience with Inductive Insert at PSR*, Proceedings of 2001 Particle Accelerator Conference, June 11-22, 2001, Chicago.

- [13] M. Popovic, private communication.
- [14] F.W. Jones, G.H. Mackenzie, and H. Schönauer, *Accsim — A program to Simulate the Accumulation of Intense Proton Beams*, Proceedings of the 14th International Conference on High Energy Accelerators, Particle Accelerators **31**, 199 (1990).

Chapter 7

LONGITUDINAL MICROWAVE INSTABILITY FOR ELECTRONS

7.1 Bunch Modes

In the previous chapter, microwave instability for a coasting beam was discussed. The theory can also be extended to a bunch provided that two criteria are satisfied: (1) the bunch is much longer than the wavelength of the perturbation and (2) the growth time is much shorter than a synchrotron oscillation period. These criteria are mostly satisfied by proton bunches, but not by electron bunches. Another theory of longitudinal instability is therefore necessary for electron bunches.

For electron bunches, the synchrotron period is usually much shorter than the collective instability growth times. Thus, synchrotron oscillation cannot be neglected in the study of longitudinal instability. The revolution harmonics can no longer be studied individually; they are no longer good eigennumbers. Here, we must study the different modes of oscillation inside a bunch.

Because the beam particles execute synchrotron oscillations, it is more convenient to use instead circular coordinates r, ϕ in the longitudinal phase space. We define the coordinates of a beam particle by

$$\begin{cases} \tau = r \cos \phi , \\ p_\tau = r \sin \phi = \frac{\eta \delta}{\omega_s} , \end{cases} \quad (7.1)$$

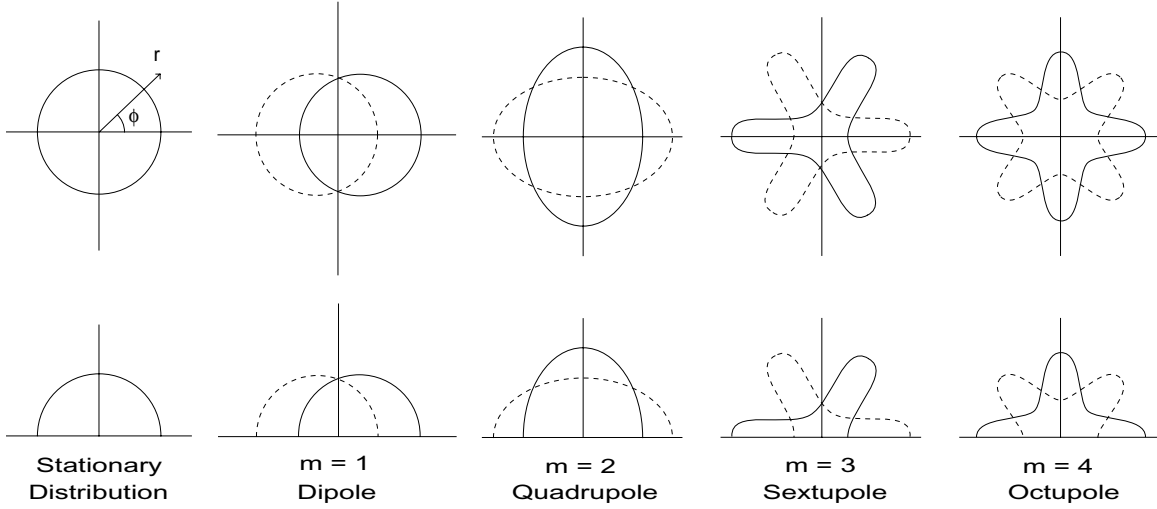


Figure 7.1: Azimuthal synchrotron modes of a bunch in the longitudinal phase space (top) and as linear density (bottom).

where τ is the time advance ahead of the synchronous particle and p_τ the conjugate momentum. A few azimuthal modes are shown in Fig. 7.1. One type of oscillation is azimuthal in ϕ , such as $\cos m\phi$. For example, $m = 1$ corresponds to a rigid dipole oscillation which we usually observe when the bunch is injected with a phase error. $m = 2$ corresponds to a quadrupole oscillation when there is a mismatch between the bunch and the rf bucket so that the oscillation appears to be twice as fast. The drawings show the motion of the bunch with the m th azimuthal mode. To obtain the m th azimuthal mode, the stationary distribution must be subtracted. For example, for the $m = 1$ mode with infinitesimal amplitude, after subtracting the stationary distribution we obtain a ring with positive charges on the right and negative charges on the left. The best description will be $\cos \phi$, and there are two nodes at $\phi = \pm\frac{\pi}{2}$. The $m = 2$ mode assumes the shape of $\cos 2\phi$ with 4 nodes at $\phi = \pm\frac{\pi}{4}$ and $\pm\frac{3\pi}{4}$. For the m th mode, the shape is $\cos m\phi$ with $2m$ nodes.

It is clear that to drive the higher azimuthal modes, *longitudinal impedance* of higher frequencies will be required. These modes can be understood mathematically if we follow a particle and record its time of arrival at a fixed location along the accelerator ring turn after turn. First assume a point particle. The signal recorded is

$$\text{signal} \propto \sum_{k=-\infty}^{\infty} \delta \left[s - kC_0 - v\hat{\tau} \cos \left(\frac{\omega_s s}{v} + \varphi \right) \right], \quad (7.2)$$

where ω_s is the angular synchrotron frequency, C_0 is the length of closed orbit of the synchronous particle whose velocity is v . For the particle under study, the turn number is denoted by k , the amplitude of synchrotron oscillation or the maximum time arrival ahead of the synchronous particle is $\hat{\tau}$, and the initial synchrotron phase is represented by φ . It is safe to substitute $s = kC_0$ inside the argument of cosine because the amplitude of synchrotron oscillation is very much smaller than the circumference of the ring. We get

$$\begin{aligned} \text{signal} &\propto \int_{-\infty}^{\infty} \frac{d\omega}{2\pi v} \sum_{k=-\infty}^{\infty} e^{-i[s-kC_0-\hat{\tau}v \cos(k\omega_s C_0/v+\varphi)]\omega/v} \\ &= \int_{-\infty}^{\infty} \frac{d\omega}{2\pi v} \sum_{k=-\infty}^{\infty} \sum_{m=-\infty}^{\infty} i^m J_m(\omega \hat{\tau}) e^{-i(s-kC_0)\omega/v} e^{-im(k\omega_s C_0/v+\varphi)}, \end{aligned} \quad (7.3)$$

where the mathematic formula for Bessel function,

$$e^{ix \cos \phi} = \sum_{m=-\infty}^{\infty} i^m J_m(x) e^{-im\phi} \quad (7.4)$$

has been used. The summation over k can be performed using the Poisson formula,

$$\frac{1}{2\pi} \sum_{k=-\infty}^{\infty} e^{ik\theta} = \sum_{p=-\infty}^{\infty} \delta(\theta - 2\pi p), \quad (7.5)$$

to obtain

$$\text{signal} \propto \int_{-\infty}^{\infty} \frac{d\omega}{C_0} \sum_{p=-\infty}^{\infty} \sum_{m=-\infty}^{\infty} i^m J_m [(p\omega_0 + m\omega_s)\hat{\tau}] \delta(\omega - p\omega_0 - m\omega_s) e^{-im\varphi} e^{-im\omega s/v}, \quad (7.6)$$

where $\omega_0/(2\pi) = v/C_0$ is the revolution frequency of the synchronous particle. Now we see all the azimuthal modes as sidebands of each harmonic line. The Bessel functions in the summation determines the amplitude of the sidebands. The synchrotron amplitude $\hat{\tau}$ is usually very much smaller than the revolution period. In this case, the lowest sideband $m = 1$ dominates. The revolution harmonics ($m = 0$) have roughly the same amplitude under the envelope of J_0 while the amplitudes of the $m = 1$ sidebands increase linearly with frequency under the envelope of J_1 . If $\hat{\tau}$ is getting larger, however, the higher order sidebands ($m > 1$) will be observed. The $m = 2$ sidebands can have larger amplitudes than the revolution harmonics ($m = 0$) and the $m = 1$ sidebands when J_2 assumes a maximum. This is illustrated in Fig. 7.2, where, for simplicity, only the positive frequency part has been shown.

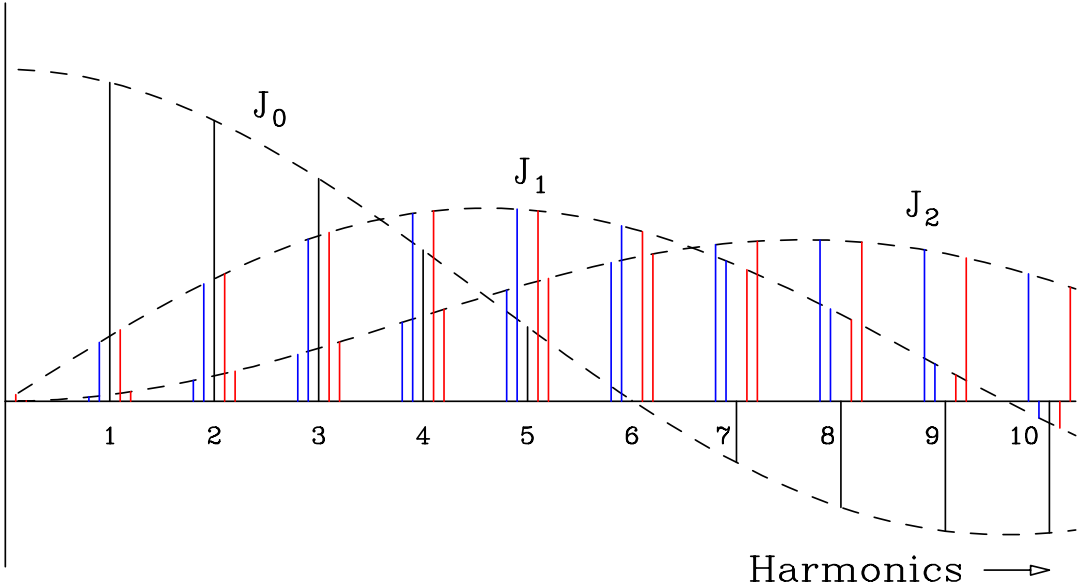


Figure 7.2: (color) Spectrum of a beam particle with synchrotron motion. Only the positive frequency is shown. The revolution harmonics ($m = 0$) are bounded by Bessel function of order zero, the first synchrotron sidebands ($m = 1$) are bounded by Bessel function of order one, and the second synchrotron sidebands ($m = 2$) are bounded by Bessel function of order two.

It is important to point out that the Bessel functions have nothing to do with the linear distribution of the bunch and here we are dealing with only a point bunch. The Bessel functions just reflect the synchrotron motion of the point bunch. If we wish to know the signal from a bunch of particles, we need to multiply Eq. (7.6) by the particle distribution $f(\varphi, \hat{\tau})$ in the synchrotron phase φ and the synchrotron oscillation amplitude $\hat{\tau}$ and integrate over φ and $\hat{\tau}$. For example, if $f(\varphi, \hat{\tau})$ is random in φ , the integral vanishes for all azimuthals except for $m = 0$, or just the revolution harmonics. This is understandable because the bunch is smooth azimuthally. The distribution must be nonuniform in the synchrotron phase before some azimuthal sidebands can be excited. We also see that the sidebands have zero width if they are excited, even if we are gathering signals from an ensemble of particles. The sidebands will be broadened, however, when the beam particles see the coupling impedance of the vacuum chamber.

Of course, to describe a bunch completely, there will also be radial modes, where the bunch oscillates with nodes at certain radii r . Let us concentrate on only one radial mode per azimuthal, the one that is most easily excited. At zero beam intensity, these modes are separated by the synchrotron frequency $\omega_s/(2\pi)$; for example, the m th mode

exhibits as a sideband $m\omega_s/(2\pi)$ away from a revolution harmonic line. This implies that at low intensities, the azimuthal modes are good eigenmodes. The radial eigenmodes, however, depend on the radial distribution of the unperturbed bunch. If the intensity of the bunch is increased, the spacings of the sidebands will change.

Here, we wish to study the collective motion of the bunch, implying that it will oscillate with a coherent frequency $\Omega/(2\pi)$. The time dependent part is written as

$$\sum_{p=-\infty}^{\infty} F_p e^{-i(p\omega_0 + \Omega)t}, \quad (7.7)$$

where F_p is some factor depending on p and $\omega_0/(2\pi)$ is the revolution frequency. Suppose that the synchrotron dipole mode is excited, we will have $\Omega \approx +\omega_s$, provided that the intensity of the bunch is not too large. Therefore, the spectrum of the bunch will consist of only *upper* synchrotron sidebands at a distance ω_s above the harmonic lines, as shown in the top plot of Fig. 7.3. Of course, not all the sidebands will be excited equally. The excitation will depend on the driving impedance and also the bunch shape. All these are grouped into the factor F_p . However, in an oscilloscope or network analyzer, we can see only *positive* frequencies. This is equivalent to folding the spectrum about the zero frequency point, the upper synchrotron sidebands corresponding to the negative harmonics will appear as lower synchrotron sidebands for the positive frequencies, or the lower plot of Fig. 7.3. When the driving impedance is a narrow resonance, we may have $\Omega \approx -\omega_s$ instead. Suppose the narrow resonance is at frequency $\omega_r = p\omega_0 - \omega_s$ with $p > 0$. Since $\Re Z_0^{\parallel}(\omega)$ is symmetric about $\omega = 0$, this narrow resonance is also driving the negative frequency $-\omega_r = p'\omega_0 + \omega_s$ where $p' = -p$, which is the upper sideband of a negative harmonic. In other words, because of the definite symmetries of $\Re Z_0^{\parallel}(\omega)$ and $\Im Z_0^{\parallel}(\omega)$ and also the spectrum of synchrotron motion in Eq. (7.6) about $\omega = 0$, it is possible for us to study only the half the sidebands, either the upper ($\Omega \approx \omega_s$) or ($\Omega \approx -\omega_s$) lower. Studying the upper sidebands alone will yield exactly the same results as studying the lower sidebands alone. For this reason, we can assume all the excited synchrotron sidebands to be only upper sidebands in the language of having both positive and negative frequencies. This analysis, however, is not correct for transverse collective motion, because the synchrotron sidebands are around the tune lines which are not symmetric about the zero-frequency point.

We would like to emphasize here that the spectrum of beam particles performing synchrotron motion is very different from the spectrum of the coherent motion of beam particles. In the former, Eq. (7.6), we see all the possible modes. However, in the latter,

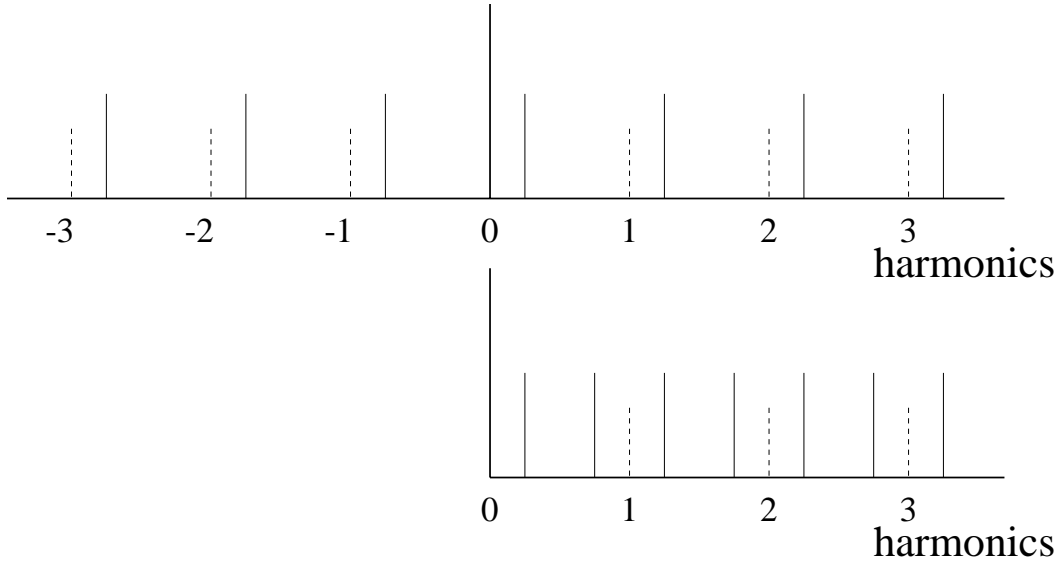


Figure 7.3: Top plot shows the synchrotron lines for both positive and negative revolution harmonics. The revolution harmonics are shown in dashes and the synchrotron *upper* sidebands in solid. Lower plot shows the negative-harmonic side folded onto the positive-harmonic side. We see upper and lower sideband for each harmonic line.

only some of those modes are excited coherently. We are looking at the coherent modes one at a time, because usually we have interest only in the one that has the fastest growth rate.

7.2 Mode Mixing

Assume a broadband impedance resonating at ω_r . The impedance will be inductive when $\omega < \omega_r$ and capacitive when $\omega > \omega_r$. If the rms length of the bunch $\sigma_\tau > \omega_r^{-1}$, the bunch particles are seeing mostly the inductive part of the impedance. We can assume that the accelerator ring is operated above the transition energy because the electrons, having small masses, are traveling at almost the velocity of light. This inductive force is repulsive opposing the focusing force of the rf voltage, thus lengthening the bunch and lowering the synchrotron frequency. Therefore, all azimuthal modes will be shifted downward, except for the dipole mode $m = 1$ at least when the beam intensity is low. The $m = 1$ does not shift because this is a rigid dipole motion and the inductive force acting on a beam particle is proportional to the gradient of the linear density as is

demonstrated in Sec. 3.2. The centroid of the bunch does not see any linear density gradient and is therefore not affected by the inductive impedance. This is very similar to the space charge self-field force. In fact, the inductive impedance is just the negative of a capacitive impedance. When the bunch intensity is large enough, the $m = 2$ mode will collide with the $m = 1$ mode, and an instability will occur if the frequencies corresponding to these two modes fall inside the resonant peak of $\Re Z_0^{\parallel}$. Mathematically, the frequency shifts of the two modes become complex. Since one solution is the complex conjugate of the other, one mode is damped while the other one grows. This is called *longitudinal mode-mixing* instability. Sometimes it is also known as *mode-coupling* or *mode-colliding* instability. An illustration is shown in Fig. 7.4 for a parabolic bunch of full length τ_L interacting with a broadband impedance resonating with impedance R at frequency $\omega_r/(2\pi)$.

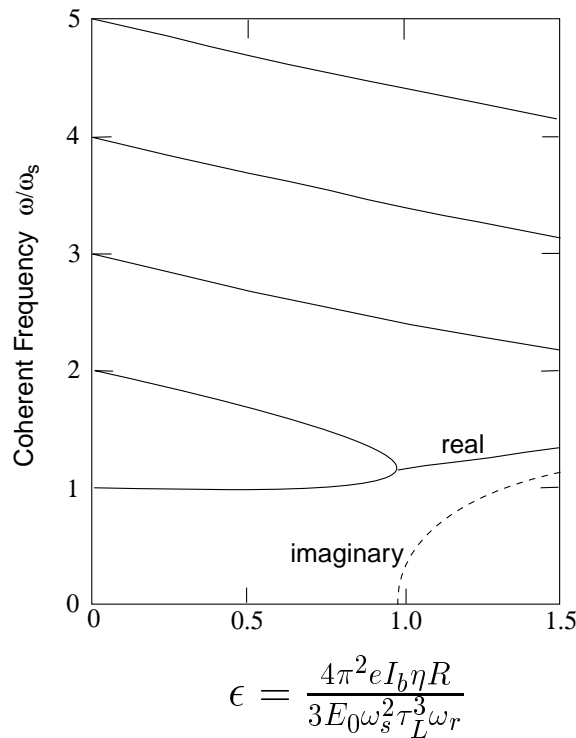


Figure 7.4: Plot showing longitudinal mode-mixing instability of a parabolic bunch of full length τ_L interacting with a broadband impedance resonating with impedance R at frequency $\omega_r/(2\pi)$. The bunch length τ_L is much longer than ω_r^{-1} so that the bunch particles are seeing the inductive part of the impedance. Thus, all modes, except for $m = 1$, shift downward.

A more thorough derivation will be given later after we study Sacherer's integral of instabilities in later chapters. Here, we just give a rough estimate of the threshold and discuss some points of interest. Just as a space charge impedance will counteract the rf focusing force below transition, here an inductive impedance will counteract the rf focusing force above transition. According to Eq. (3.58), the extra voltage seen per turn by an electron at an arrival advance τ from the effect of the inductive impedance is

$$V_{\text{ind}} = \frac{3eN}{2\omega_0\hat{\tau}^2} \left| \frac{Z_0^{\parallel}}{n} \right|_{\text{ind}} \frac{\tau}{\hat{\tau}}, \quad (7.8)$$

where a parabolic linear distribution for the electron bunch of half length $\hat{\tau}$ has been assumed and N is the number of particles in the bunch. Although a parabolic distribution for electron bunches is not realistic, it does provide a linear potential and ease the mathematics. The synchrotron frequency is proportional to the square root of the potential gradient, $dV_{\text{ind}}/d\phi$, where ϕ is the rf phase. This extra voltage will shift the incoherent synchrotron tune downward. If the beam intensity is low, the shift can be obtained by perturbation, giving

$$\frac{\Delta\nu_s}{\nu_{s0}} = \frac{1}{2} \frac{dV_{\text{ind}}/d\phi}{dV_{\text{rf}}/d\phi} = \frac{3e^2 N \eta}{8\pi\omega_{s0}^2 \hat{\tau}^3 \beta^2 E_0} \left| \frac{Z_0^{\parallel}}{n} \right|_{\text{ind}}. \quad (7.9)$$

All the azimuthal modes will have their frequencies shifted downward coherently by roughly by this amount also except for the $m = 1$ mode. The threshold can therefore be estimated roughly by equating the shift to the synchrotron tune. Because this shift is now large, the perturbative result of Eq. (7.9) cannot apply. Instead we equate the gradient of the extra voltage from the inductive impedance directly to the gradient of the rf voltage, to get the threshold

$$\frac{3e^2 N |\eta|}{4\pi\omega_{s0}^2 \hat{\tau}^3 \beta^2 E_0} \left| \frac{Z_0^{\parallel}}{n} \right|_{\text{ind}} \lesssim 1. \quad (7.10)$$

For a broadband impedance of quality factor $Q \approx 1$,

$$\left| \frac{Z_0^{\parallel}}{n} \right|_{\text{ind}} \approx \frac{R_s}{n_r}, \quad (7.11)$$

where R_s is the shunt impedance at the resonance angular frequency $\omega_r = n_r \omega_0$. Written in terms of the dimensionless current parameter ϵ in Fig. 7.4, the threshold of Eq. (7.10) translates to

$$\frac{4\pi^2 e I_b |\eta| R_s}{3 E_0 \omega_s^2 \tau_L^3 \omega_r} \lesssim \frac{\pi^2}{9}, \quad (7.12)$$

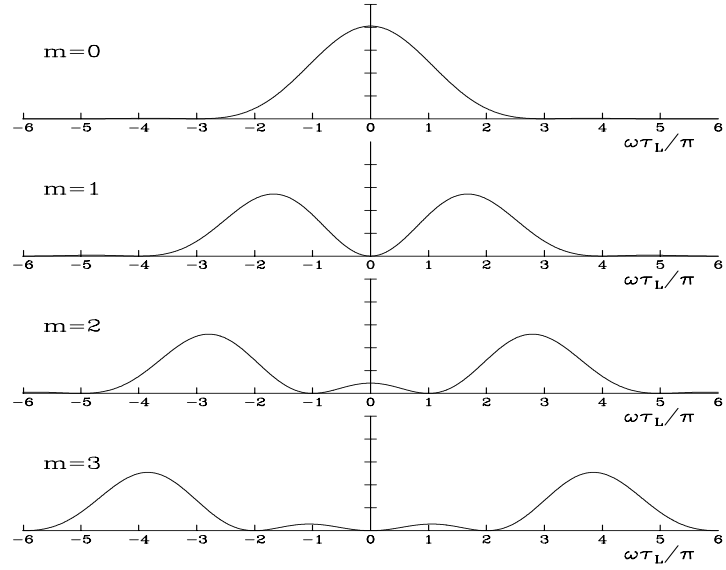


Figure 7.5: Power spectra $h_m(\omega)$ for modes $m = 0$ to 3 with zero chromaticity.

which agrees with the point of mixing in the figure very well, where $\tau_L = 2\hat{\tau}$ is the full bunch length. It can also be written as

$$\frac{R_s}{n_r} \lesssim \frac{8|\eta|E_0}{9eI_{\text{pk}}\beta^2} \left(\frac{\Delta E}{E_0} \right)_{\text{FWHM}}^2. \quad (7.13)$$

This is almost identical to the Keil-Schnell criterion in Eq. (6.22) with the average current replaced by the peak current. For this reason, this longitudinal mode-mixing threshold is often also referred to as the Keil-Schnell threshold. In fact, as will be shown later, unlike the Keil-Schnell criterion, the left-side of Eq. (7.13) is not the usual $|Z_0^{\parallel}/n|$ of a broad resonance. Instead it should be replaced by the *effective impedance*

$$\left| \frac{Z_0^{\parallel}}{n} \right| \rightarrow \left| \frac{Z_0^{\parallel}}{n} \right|_{\text{eff}} = \frac{\int d\omega \frac{Z_0^{\parallel}(\omega)}{\omega} \omega_0 h_m(\omega)}{\int d\omega h_m(\omega)}, \quad (7.14)$$

where $h_m(\omega)$ is the power spectrum of the m th azimuthal mode depicted in Fig. 7.1. In fact, when made dimensionless, h_m is a function of $\omega\hat{\tau}$ only. For Sacherer's approximate sinusoidal modes, the power spectra of some lower azimuthal modes are shown in Fig. 7.5. It is important to point out that it is the reactive part of the impedance that shifts the frequencies of the different azimuthal modes and the resistive part of the impedance that

drive the stability. According to Fig. 7.5, for the azimuth $m = 1$ to mix with azimuth $m = 2$, the peak of the resonance must have frequency between the peak of the power spectra of the two modes, or

$$\omega_r \sim \frac{2\pi}{\tau_L} . \quad (7.15)$$

In fact, this is expected, because with one or two oscillations in the linear density of the bunch, the wavelength of this instability must therefore have wavelength comparable to or shorter than the bunch length. The signal measured should correspond roughly to the rms frequency of the bunch spectrum, which is also in the microwave region because an electron bunch is often shorter than the transverse size of the vacuum chamber. For this reason, this instability is also referred to as microwave instability in the electron communities.

7.3 Bunch Lengthening and Scaling Law

In Fig. (7.4), the dashed curve denotes the growth rate of the instability. It is evident that the growth rate increases very rapidly as soon as the threshold is exceeded. We see that even when the bunch current exceeds the threshold by 20%, the growth rate reaches $\tau^{-1} \sim \omega_s$, or the growth time is $T_s/(2\pi)$, much shorter than a synchrotron period. This means that the radiation damping effect and the use of conventional feedback systems may not effective in damping the instability.

One way to avoid instability is to push the threshold to a higher value. For example, if the bunch is short enough so that $\sigma_\tau < \omega_r^{-1}$, the bunch particles will sample mostly the capacitive part of the broadband impedance. The frequencies of the azimuthal modes will shift upward instead. But the real part of the impedance will eventually bend the mode downward. However, it will become harder for the $m = 2$ and $m = 1$ modes to collide, the threshold will be relatively higher.

In reality, this instability is not devastating. The growth rate shown in Fig. (7.4) only applies when the bunch length and energy spread of the bunch are kept unchanged. As soon as the threshold is past, the bunch will be lengthened and the energy spread increased to such an extent that stability is regained again. Unlike proton bunches no overshoot is observed in electron bunches, probably because of the radiation damping. Typical plots of the bunch length and energy spread are shown in Fig. 7.6. Note that because of the balancing of synchrotron radiation and random quantum excitation, there

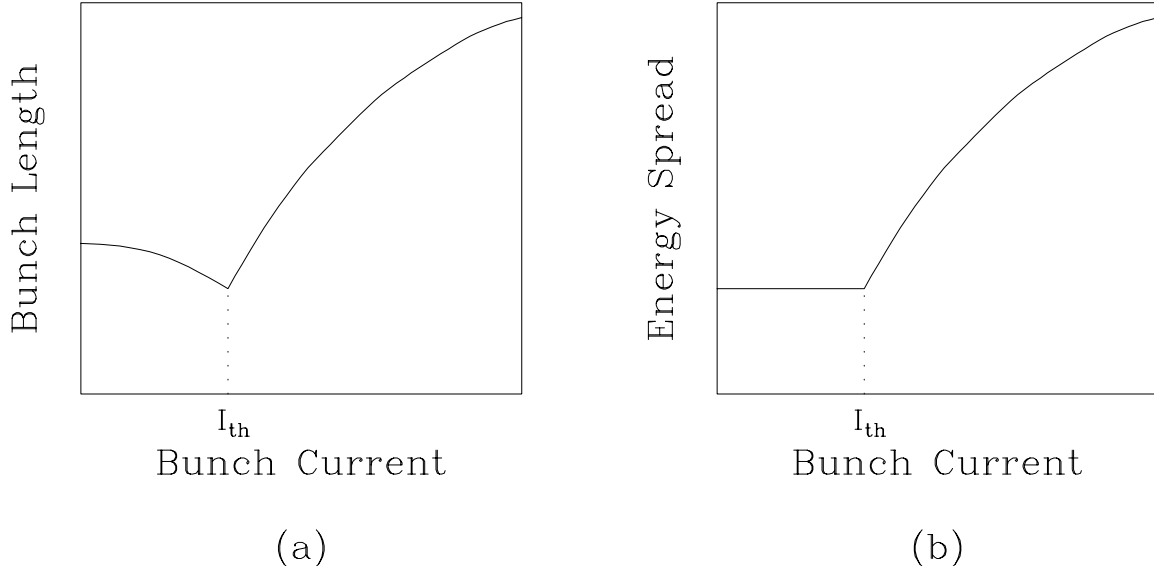


Figure 7.6: Both the bunch length and energy spread begin to grow after the bunch current exceeds its microwave instability threshold I_{th} . (a) The bunch length starts with its natural value at zero current and becomes shortened due to the capacitive potential-well distortion, if the natural bunch length is short enough so that the capacitive part of the impedance is sampled. (b) Below the instability threshold, the energy spread is always at its natural value unaffected by the effect of potential-well distortion.

is a *natural* momentum spread σ_{δ_0} and the corresponding natural bunch length σ_{τ_0} is determined by the rf voltage. This is what we see below the threshold. For a short bunch with $\sigma_{\delta_0} < \omega_r^{-1}$, we will see the bunch length decreases as the bunch intensity increases, because the bunch samples the *attractive* capacitive impedance. This is called *potential-well distortion* which has been discussed in Chapter 3. However, the momentum spread is still determined by its natural value and is not changed. Unlike a proton bunch which can often be lost after the microwave instability threshold, the electron bunch can stabilize itself by self-increasing its length and energy spread, as illustrated in Fig. 7.6.

One way to observe this instability is to measure the increase in bunch length. We can also monitor the synchrotron sidebands and see the $m = 2$ sideband move towards the $m = 1$ sideband. This frequency shift, which is a coherent shift, as a function of beam intensity is a measure of the reactive impedance of the ring. An accurate measurement of the frequency shift of the $m = 2$ mode may sometimes be difficult. An alternate and more accurate determination of the frequency shift can be made by monitoring the

phase shift in the beam transfer function to be discussed in Chapter 14.

Noting that the mode-coupling threshold, Eq. (7.10) or Eq. (7.12), depends on only one parameter

$$\xi = \frac{\eta I_b}{\nu_s^2 E_0} , \quad (7.16)$$

there is a scaling law relating the bunch lengthening and the frequency dependency of the impedance sampled by the bunch. It says that the rms bunch length σ_τ above threshold is given by

$$\sigma_\tau \propto \xi^{1/(2+a)} \quad (7.17)$$

when the part of the impedance sampled by the bunch behaves like

$$Z_0^\parallel \propto \omega^a . \quad (7.18)$$

Here, I_b is the average beam current of the bunch. This scaling law was first derived by Chao and Gareyte [2] and has been verified experimentally in the storage ring SPEAR at SLAC. The results are plotted in Fig. 7.7. The scaling law can be proved easily by dimension argument. To proceed, substitute the effective impedance of Eq. (7.14) into the threshold condition of Eq. (7.12), and note that the power spectrum $h(\omega)$ can be made dimensionless and therefore depends on $\omega\sigma_\tau$ only (Exercise 7.3). A similar proof will be given later in Sec. 13.3 below. Note that if the Keil-Schnell criterion is applied, we always have $\sigma_\tau \propto \xi^{1/3}$ or $a = 1$, implying a long bunch seeing the inductive part of the impedance. However, for SPEAR, measurements point to $\sigma_\tau \propto \xi^{0.76}$ or $a = -0.68$, implying that the SPEAR bunch is short enough to sample the capacitive part of the impedance. This clearly demonstrates that the Keil-Schnell criterion is only suitable for long bunches which sample the inductive part of the broadband impedance, and cannot be used in an electron machine where the bunch length is so short that the capacitive part of the impedance is sampled. There is another big difference between the microwave instability for coasting beam and the mode-mixing instability discussed here. Above transition, which is true for nearly all electron rings, the tear-drop stability curve of the coasting-beam based theory states that the beam will be unstable if it is driven by a capacitive impedance which is large enough. However, it can be shown that pure reactive impedance cannot lead to mode-mixing instability. The modes may cross each other when the frequency shifts are large enough, but no instability will materialize. (See Exercise 13.3 below.)

This instability is not a devastating instability, because it results only in the blowup of the bunch area. In fact, many storage rings, especially collider rings, operate above

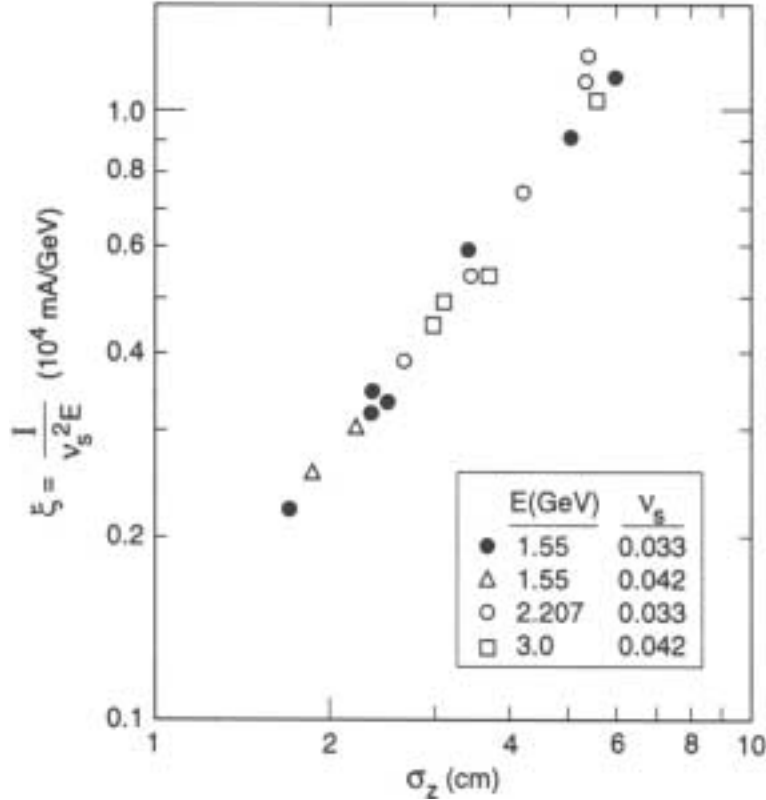


Figure 7.7: RMS bunch length σ_Z versus the scaling parameter ξ for the electron storage ring SPEAR. The momentum compaction factor has been kept constant. The measurement results indicate that $\sigma_\tau \propto \xi^{1/(2+a)}$ with $a = -0.68$.

this threshold, because a much higher beam intensity and therefore luminosity can be attained. However, this may not be the situation for a light source, where we always want to have shorter bunches so as to have smaller spot sizes for the synchrotron light. In order to accomplish this, the electron ring must be carefully designed so that the impedance is as small as possible. On the other hand, it is very difficult to reduce the impedance in a ring already built. For example, some capacitive structures had been placed in the SLAC damping rings, so as to reduce the inductive impedance of the rings. The threshold of the mixing of the $m = 2$ and $m = 1$ mode has been actually pushed higher. However, the beam particles are now seeing mostly the real part of the impedance, which distorts the bunch asymmetrically bringing out the importance of other radial excitation modes. These radial modes actually collide at a threshold much lower than the previous threshold before the modification. Fortunately, this instability due to the mixing of radial modes is much weaker than the instability due to the mixing

of azimuthal modes [4].

7.4 Sawtooth Instability

Before the modification of the vacuum chambers in the SLAC Linear Collider (SLC) damping rings, a new form of longitudinal instability coupling with synchrotron radiation damping was observed. Upon the injection of a bunch, the bunch length decreased rapidly with a longitudinal damping time of the order of 2 ms. When the bunch length passed below a threshold, a sudden blowup in bunch length occurred in a time span comparable to or shorter than the $10 \mu\text{s}$ synchrotron period, as illustrated in Fig. 7.8. This process was self-limiting because of the nonlinear nature of the short-range wake fields responsible for blowing up the bunch. Since the blowup is faster than a synchrotron period, this might have been the type of coasting-beam based microwave instability governed by the Boussard-modified Keil-Schnell criterion. Once the blowup ceased, the bunch damped down until the threshold was reached again in about a synchrotron damping time of ~ 1.3 ms. Thus, a cyclical repetition of the instability was observed and termed according to its shape *sawtooth instability* [5].

The time-dependent nature was seen in the bunch-length signal from the beam-position-monitor (BPM) electrodes and the bunch-phase signal from the synchronous-phase monitor. The bunch phase can be referenced to either the 714 MHz rf of the damping ring or to the 2856 MHz S-band rf of the linac. The synchronous beam phase angle is given by $\phi_s = \sin^{-1}(U_s/V_{\text{rf}})$, where U_s is the energy loss per turn as a result of synchrotron radiation. The higher-order mode losses of a bunch are functions of the line charge density and are inversely proportional to the bunch length. As the bunch blew up, the higher-order losses decreased and the beam phase shifted by about 0.5° at 714 MHz during a sawtooth. This translated into a 2° jump at the S-band in the linac. This magnitude of phase error caused a problem with the rf bunch-length compressor in the ring-to-linac beam line. When this instability took place, the bunch would be incorrectly launched into the linac and might eventually be lost on the downstream collimators, causing the linac to trip the machine protection circuits. For some consequences, see Exercises 7.4 and 7.5.

There is a threshold for this instability, which occurred at around 3×10^{10} particles per bunch for a nominal rf voltage of 1 MV. At higher intensity, the sawteeth appeared

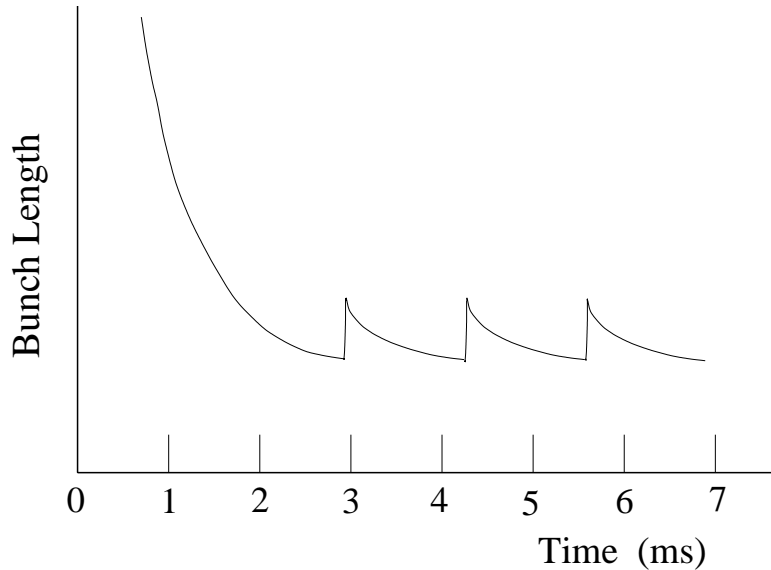


Figure 7.8: Plot of bunch length versus time at the injection of the SLAC Damping ring with an intensity of 3×10^{10} particles per bunch. The bunchlength was damped rapidly in the first 2 ms after injection to a point where it was unstable against microwave instability. Rapid growth took place until the bunch was self-stabilized. After that it was damped by synchrotron radiation to below the instability threshold. This repetition has the shape of sawteeth.

closer together in time. The process could be viewed as a relaxation oscillator where the period is a function of the bunch-length damping time and the trigger threshold. The damping time is constant but the bunch length at which the bunch went unstable increased at higher intensities. When the bunch intensity was increased to 4×10^{10} particles, a transition occurred to a second regime with “continuous sawteeth”.

With the installation of new SLC damping-ring vacuum chambers, the sawtooth instability did not go away as it was expected by simulations. On the contrary, the threshold went down from 3×10^{10} to $1.5-2 \times 10^{10}$ particles per bunch. The new instability has a similar behavior, but it apparently is very much milder and does not affect the phase mismatch of the linac downstream as severely as the old instability. An intense investigation has been going on to study this instability even after the installation of the new vacuum chambers. Podobedov and Siemann [6] tried to measure the longitudinal density bunch profiles from the synchrotron light with a high-resolution Hamamatsu streak camera during the instability. The phase of oscillation of the bunch density was obtained from the high-frequency BPM signals, processed and digitized by an oscillo-

scope. The 295 chosen profiles were binned according to their phases. The $+\frac{\pi}{2} \pm \frac{\pi}{4}$ phase bin implies near maximum deviation, while the $-\frac{\pi}{2} \pm \frac{\pi}{4}$ phase bin implies near minimum deviation. The average shapes for the two phase bins and the overall average profile are shown in Fig. 7.9. The wavelength of oscillation is about 30 ps. The oscillating part of

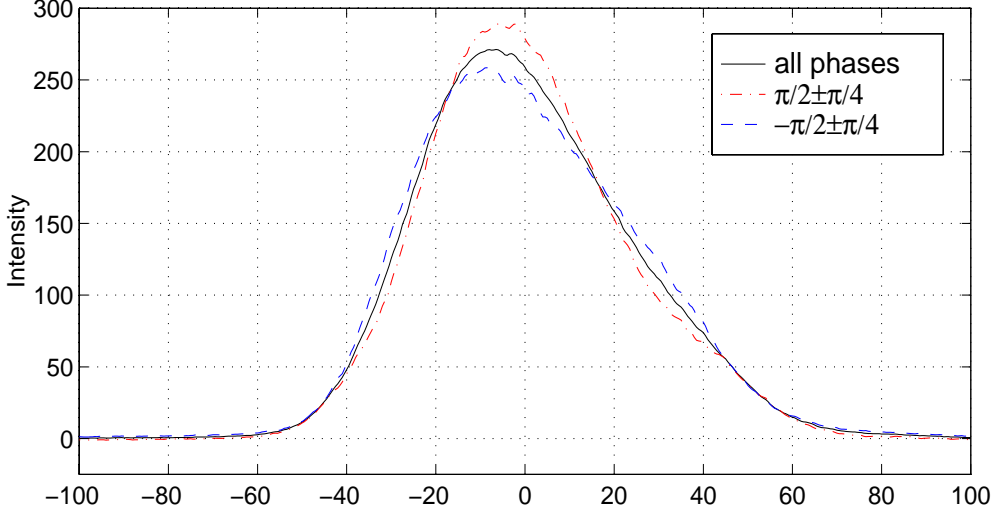


Figure 7.9: (color) Beam density profiles during an instability burst captured by streak camera. The average is in solid. Those with the phase $+\frac{\pi}{2} \pm \frac{\pi}{4}$ are in red dot-dashes and those with phase $-\frac{\pi}{2} \pm \frac{\pi}{4}$ are in blue dashes.

the density was next filtered out using

$$\delta\rho(\tau) = \left\langle \frac{\rho_k(\tau) - \rho_0(\tau)}{\sin \phi_k} \right\rangle, \quad (7.19)$$

where ρ_k are all the profiles with the phases ϕ_k ($k = 1, 2, \dots, 295$), ρ_0 is the phase-averaged profile, and the angle brackets denote the median value. The structure obtained is shown in Fig. 7.10. This linear density resembles the $m = 2$ quadrupole mode in Fig 7.1 with the stationary distribution subtracted. The structure in the longitudinal phase space is shown in the corner of the figure. The ratio of the positive peak area to the one under ρ_0 is about 3%, which measures the amount of redistributed particles creating the quadrupole structure.

The instability was further pursued in the frequency domain by Podobedov and Siemann [7]. A bunch containing 3.5×10^{10} positrons was scanned in the SLC positron damping ring for the whole store of several minutes, during which the bunch intensity

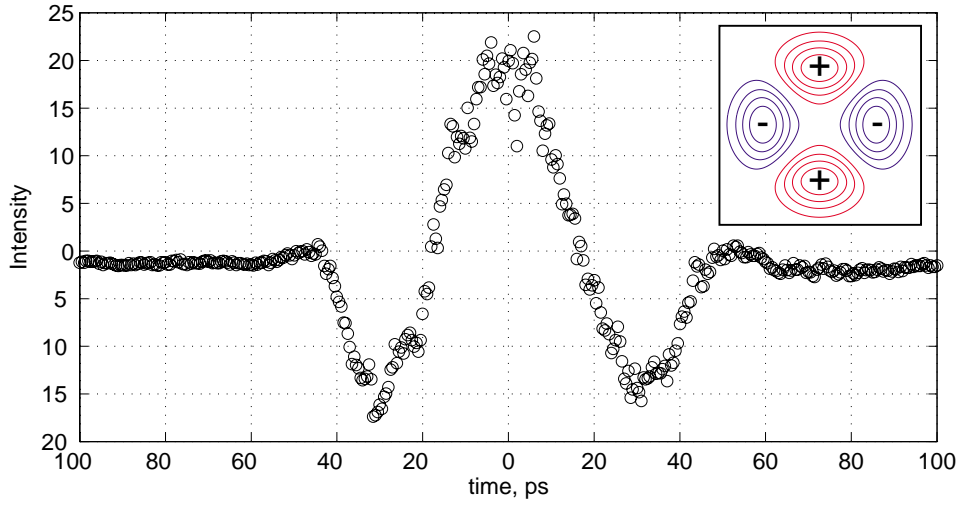


Figure 7.10: (color) Bunch density oscillation with the average distribution subtracted. The structure resembles the projection of the azimuthal $m = 2$ oscillation.

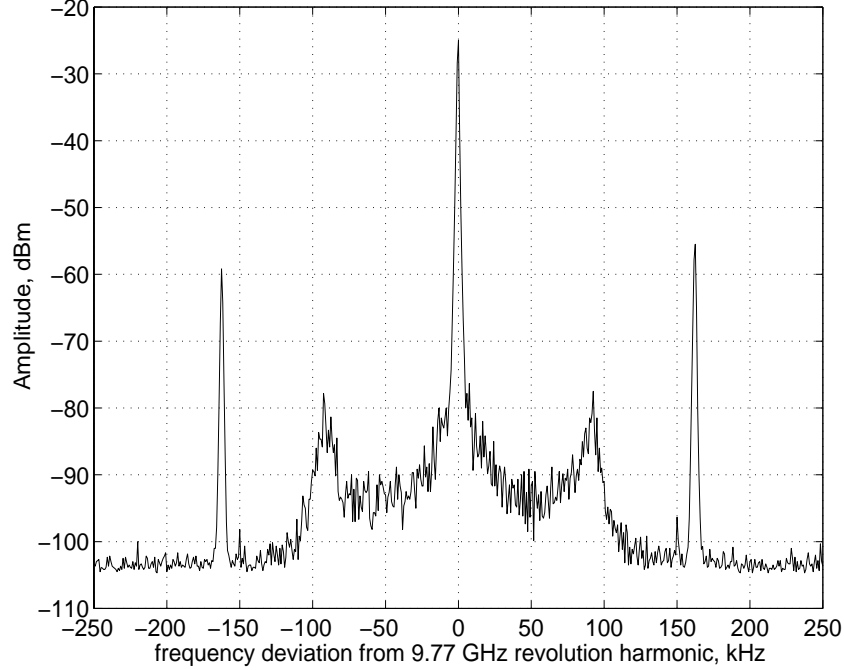


Figure 7.11: Typical spectrum at 3×10^{10} ppb around the 1149th revolution harmonic (9.77 GHz) in the SLC positron damping ring after the installation of the new vacuum chamber. The quadrupole mode sidebands are excited and are displaced ~ 160 kHz from the harmonic, about 10% less than twice the zero-current synchrotron frequency at 690 kV rf.

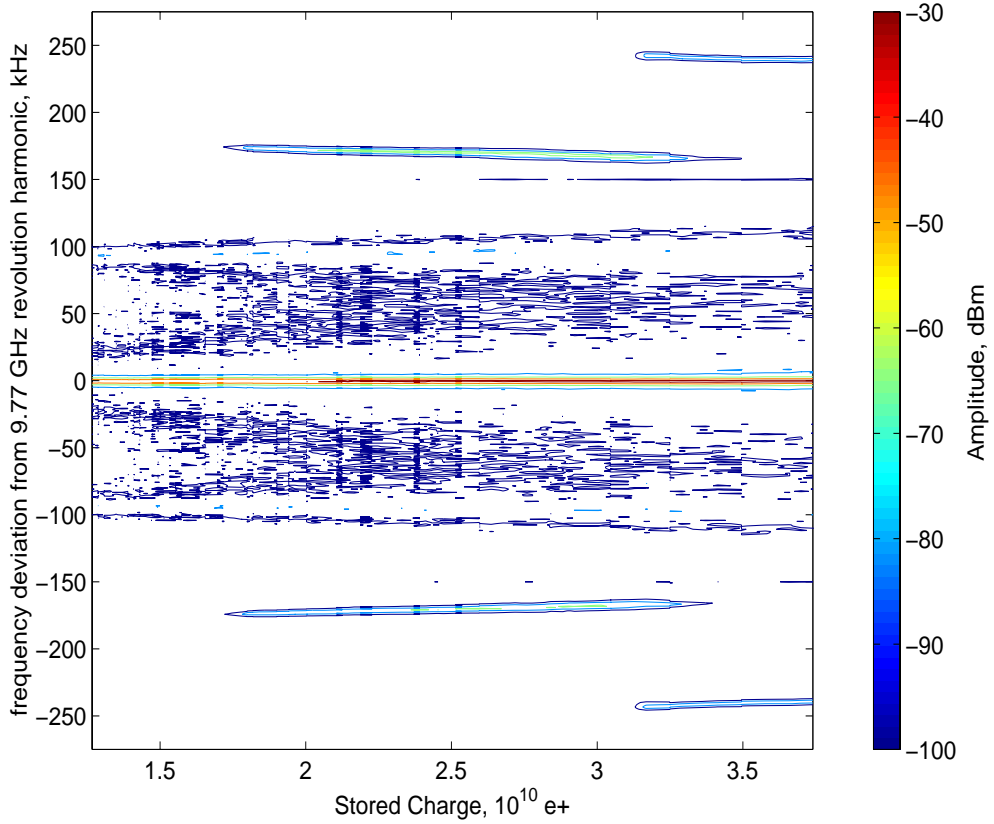


Figure 7.12: (color) Contour plot of all the spectrum analyzer sweeps for a store of a positron bunch in the SLC damping ring. The bunch intensity decays from 3.5×10^{10} to almost half near the end of the store. Sextupole mode instability is first seen and switches to quadrupole mode instability around $3.2-3.4 \times 10^{10}$ ppb. All instabilities stop below the intensity of 1.7×10^{10} ppb.

decayed by roughly a factor of two. The signal processing system consists of a square-law detector which demodulates the instability signal from the sidebands to high-frequency revolution harmonics. This signal is subsequently amplified and the higher-order mixing products are removed by a low-pass filter. Figure 7.11 shows a typical spectrum at bunch intensity 3×10^{10} around the 1149th revolution harmonic (9.77 GHz). We see the quadrupole mode of instability and the quadrupole sidebands to the harmonic displaced by about 160 kHz. This is roughly 10% lower than twice the zero-current synchrotron frequency at the rf voltage of 690 kV. The contour plot in Fig. 7.12 shows all the spectrum analyzer sweeps for the whole store. One can see how the instability jumps from sextupole to a quadrupole mode around the intensity of $3.2-3.4 \times 10^{10}$ ppb. The

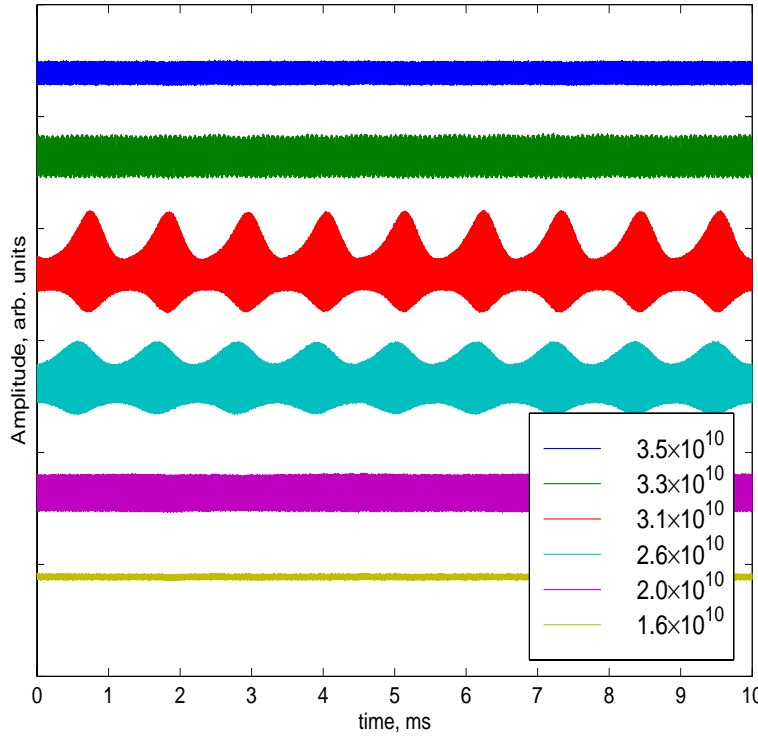


Figure 7.13: (color) Oscilloscope traces of the instability signal from different values of the stored positron bunch. Sawtooth behaviors occur near the intensity of $2.6\text{-}3.1 \times 10^{10}$ ppb when the mode of excitation is purely quadrupole.

quadrupole mode threshold is about 1.7×10^{10} ppb with its frequency linearly decreasing at a rate of ~ 5 kHz/ 10^{10} ppb. Such a behavior is usually attributed to the inductive portion of the ring impedance. However, we do not see the crossing of the quadrupole and sextupole modes or the crossing of the quadrupole and dipole modes. This indicates that the instabilities may arise from the mixing of radial modes belonging to one azimuthal, as postulated by Chao [8]. We believe that before the modification of the vacuum chamber, the instability, which was very much strong, did arise from the mixing of two azimuthal modes. In any case, the physics behind the sawtooth instability is still far from understood.

Along with the spectrum analyzer data, Fig. 7.13 shows some oscilloscope traces taken concurrently. The top trace at 3.5×10^{10} ppb corresponds to a constant amplitude sextupole mode. The next trace corresponds to the case when both sextupole and quadrupole modes coexist. At even smaller current, $2.6\text{-}3.1 \times 10^{10}$ ppb, the two traces

in the middle show the sawtooth bursting behavior of the instability and correspond to pure quadrupole mode. Finally below 2.5×10^{10} ppb, the bursts disappear and the quadrupole mode oscillates with constant amplitude.

Lowering the rf voltage is a means of increasing the equilibrium bunch length and extending the intensity threshold. This is because the Landau damping from the energy spread, which is determined by synchrotron radiation, is unchanged, but lengthening the bunch reduces the local peak current and brings the bunch below the Keil-Schnell threshold according to Eq. (6.22). A low rf voltage, however, is not suitable for efficient injection and extraction for the damping rings. Before the installation of the new vacuum chamber into the damping rings, the rf voltage was ramped down from 1 MV to 0.25 MV approximately 1 ms after injection, as illustrated in Fig. 7.14. It was ramped up back to 1 MV 0.5 ms before extraction. In this way the onset of sawtooth instability had been suppressed up to an intensity of 3.5×10^{10} per bunch.

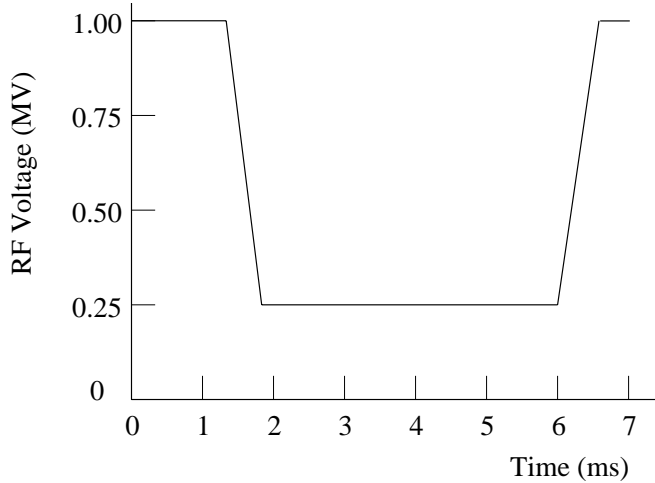


Figure 7.14: The rf voltage was lowered in the SLAC damping ring after injection and before extraction, thus lengthening the bunch and reducing the local charge density. This raised the microwave instability threshold and prevented the sawtooth instability.

Here, we want to mention another difference between electron and proton bunches. Although lowering the rf voltage may stabilize an electron bunch, this certainly will not work for a proton bunch. This is because for an electron bunch, the energy spread is determined by synchrotron radiation and will not change as the rf voltage is lowered. On the other hand, for a proton bunch, the bunch area conserves. Thus, lowering the rf voltage will diminish the energy spread instead, although the local linear density is

decreased. Recall the Boussard-modified Keil-Schnell criterion [3] or the Krinsky-Wang criterion [1] for Gaussian energy spread distribution,

$$\left| \frac{Z_0^{\parallel}}{n} \right| < \frac{2\pi|\eta|E_0}{eI_{\text{pk}}\beta^2} \left(\frac{\sigma_E}{E_0} \right)^2. \quad (7.20)$$

Assuming also a Gaussian linear distribution,

$$I_{\text{pk}} = \frac{eN}{\sqrt{2\pi}\sigma_\tau}, \quad (7.21)$$

where σ_τ is the rms bunch length in time. Constant bunch area of a proton bunch implies constant $\sigma_\tau\sigma_E$. Thus, the threshold is directly proportional to the energy spread σ_E and is inversely proportional to the bunch length σ_τ . Reducing the rf voltage will make the proton bunch more susceptible to microwave instability. Such instability is very often seen when an rf rotation is performed to obtain a narrow proton bunch. The rf voltage is first lowered adiabatically in order to lengthen the bunch to as long as possible. The rf voltage is then raised suddenly to its highest possible value. The long and small-energy-spread bunch will rotate after a quarter of a synchrotron oscillation to a narrow bunch with large energy spread. Because it takes a lot of time to reduce the rf voltage adiabatically, the beam will often suffer from microwave instability when the momentum spread is small. To avoid this instability, one way is to snap the rf voltage down suddenly so that the rf bucket changes from Fig. 7.15(a) to 7.15(b). The bunch will be lengthened after a quarter synchrotron oscillation. The rf voltage is then snapped up again as in Fig. 7.15(c) so that the lengthened bunch rotates into a narrow bunch as required. Since snapping the rf voltage is much faster than lowering it adiabatically, this may prevent the evolution of microwave instability. Such a method is also used in bunch coalescence at Fermilab.

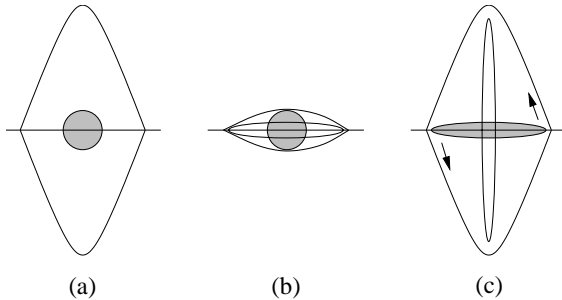


Figure 7.15: Bunch shortening is performed by snapping down the rf voltage V_{rf} , rotating for $\frac{1}{4}$ synchrotron oscillation, snapping up V_{rf} , and rotating for another $\frac{1}{4}$ synchrotron oscillation.

7.5 Exercises

- 7.1. Derive the incoherent synchrotron tune shift in Eq. (7.9) driven by an inductive impedance.
- 7.2. (1) Derive the mode-mixing threshold, Eq. (7.10), by equating the synchrotron tune shift to the synchrotron mode separation.
 (2) Rearrange the result to obtain the Keil-Schnell like criterion of Eq. (7.13).
- 7.3. Prove the scaling law about bunch length dependency using dimension argument as outlined in the text.
- 7.4. There is a difference in energy loss between the head and tail of a bunch in a linac because of the longitudinal wake. Take the SLAC linac as an example. It has a total length of $L = 3$ km and rf cavity cell period $L_0 = 3.5$ cm. The bunch consists of $N = 5 \times 10^{10}$ electrons and is of rms length $\sigma_z = 1.0$ mm. The longitudinal wake per cavity period is $W'_0 = 6.29$ V/pC at $z = 0^+$ mm and 4.04 V/pC at $z = 1$ mm.
 - (1) Consider the bunch as one macro-particle, find the total energy loss by a particle traveling through the whole linac, taking into account the fundamental theorem of beam loading (proved in Sec. 8.4.1 below) that a particle sees exactly one half of its own wake.
 - (2) Consider the bunch as made up of two macro-particles each containing $\frac{1}{2}N$ electrons, separated by the distance σ_z . Find the energy lost by a particle in the head and a particle in the tail as they traverse the whole linac.
- 7.5. A more detailed computation gives 1.2 or 2.1 GeV as the energy lost by a particle $\frac{1}{2}\sigma_z$ ahead or behind the bunch center. This energy spread needs to be corrected to ensure the success of final focusing at the interaction point of the SLAC Linear Collider. The rf voltage is 600 kV per cavity period and the rf frequency is 2.856 GHz.
 - (1) Explain why we cannot compensate for the energy spread by placing the tail of the bunch ($\frac{1}{2}\sigma_z$ behind bunch center) at the crest of the rf wave so that the tail can gain more energy than the head.
 - (2) The correct way to eliminate this energy spread is to place the center of the bunch at an rf phase angle ϕ ahead the crest of the rf wave such that the gradient of the rf voltage is equal to the gradient of the energy loss along the bunch. Show that the suitable phase is $\phi = 17.3^\circ$.

- (3) The accelerating gradient will decrease with this rf phase offset. A compromise phase is $\phi = 12^\circ$. Compute the head-tail energy spread with this phase offset and compare the effective accelerating gradients in the two situations.
- (4) Assume that the sawtooth instability adds a $\pm 2^\circ$ uncertainty in rf phase error, implying that ϕ now becomes 10 to 14° . Compute the head-tail energy spread and the center energy uncertainty under this condition. Repeat the computation if the rf phase jitter is $\pm 5^\circ$ instead.
- 7.6. A particle at time advance τ inside a bunch of linear particle distribution $\lambda(\tau)$ (normalized to total number of particles N when integrated over τ) sees a voltage due to the longitudinal wake,

$$V(z) = -e \int_{\tau}^{\infty} W'_0(z/v) \lambda(\tau - z/v) \frac{dz}{v} \quad (7.22)$$

and suffers an energy loss. The energy loss of the whole bunch, which is often called the *parasitic loss* is

$$\Delta\mathcal{E} = e^2 \int_{-\infty}^{\infty} V(\tau) \lambda(\tau) \frac{ds}{v} . \quad (7.23)$$

- (1) Show that the parasitic loss can also be written as

$$\Delta\mathcal{E} = -2\pi e^2 \int_{-\infty}^{\infty} Z_0^{\parallel}(\omega) \left| \tilde{\lambda}(\omega) \right|^2 d\omega , \quad (7.24)$$

where the Fourier transform of the linear distribution is defined as

$$\lambda(\tau) = \int_{-\infty}^{\infty} \tilde{\lambda}(\omega) e^{-i\omega\tau} d\tau . \quad (7.25)$$

- (2) Show that the space charge-like wake field $W'_0(z) = L\delta'(z/v)$ does not cause parasitic energy losses.
- (3) For a Gaussian bunch with rms length σ_{τ} , show that the parasitic energy loss per unit length due to the resistivity of a circular beam pipe of radius b is

$$\Delta\mathcal{E} = \frac{e^2 N^2 \Gamma(\frac{3}{4})}{4\pi^2 b \sigma_{\tau}^{3/2}} \left(\frac{Z_0 \mu_r}{2\sigma c} \right)^{1/2} , \quad (7.26)$$

where σ is the wall conductivity, μ_r is the wall relative magnetic permeability, and $\Gamma(\frac{3}{4}) = 1.22542$ is the Gamma function. You may use Eq. (1.42) for the wall impedance.

(4) For the SSC the stainless steel beam pipe radius is $b = 1.65$ cm with a conductivity of $\sigma = 2.0 \times 10^6$ ($\Omega\text{-m}$) $^{-1}$ at cryogenic temperature and relative magnetic permeability $\mu_r \approx 1$. There are two proton beams, each of which has $M = 17280$ bunches with $N = 7.3 \times 10^9$ protons each and an rms length $\sigma_z = 7$ cm. Compute the power load on the cryogenic system due to the parasitic power heating of the beam pipe wall. To reduce the cryogenic load, the inner surface of the beam pipe is coated with a layer of copper having $\sigma = 1.8 \times 10^9$ ($\Omega\text{-m}$) $^{-1}$ and $\mu_r = 1$ at cryogenic temperature. Recompute the heat load.

Bibliography

- [1] S. Krinsky and J.M. Wang, Particle Accelerators **17**, 109 (1985).
- [2] A.W. Chao and J. Gareyte, Part. Accel. **25**, 229 (1990).
- [3] E. Keil and W. Schnell, CERN Report TH-RF/69-48 (1969); V.K. Neil and A.M. Sessler, Rev. Sci. Instr. **36**, 429 (1965); D. Boussard, CERN Report Lab II/RF/Int./75-2 (1975).
- [4] K. Bane, et al, *High-Intensity Single Bunch Instability Behavior in the New SLC Damping Ring Vacuum Chamber*, Proc. 1995 Particle Accelerator Conference, May 1-5, 1995, Dallas, Texas, p.3109.
- [5] P. Krejcik, K. Bane, P. Corredoura, F.J. Decker, J. Judkins, T. Limberg, M. Minty, R.H. Siemann, and F. Pedersen, *High Intensity Bunch Length Instabilities in the SLC Damping Ring*, Proc. 1993 Particle Accelerator Conference and International Conference on High-Energy Accelerators, Washington, DC, May 17-20, 1993, p.3240.
- [6] B. Podobedev and R. Siemann, Proc. 1997 Particle Accelerator Conference, Vancouver, B.C., Canada, May 12-16, 1997, Ed. Comyn, M.K. Craddock, M. Reoser, and J. Thomson, p.1629.
- [7] B. Podobedev and R. Siemann, *Signals from Microwave Unstable Beams in the SLC Damping Rings*, Proc. 1999 Particle Accelerator Conference, New York, NY, March 29 - April 2, 1999, p.146.
- [8] A. Chao et al, Proc. 1995 Particle Accelerator Conference, 1995, p.3040.

Chapter 8

BEAM LOADING AND ROBINSON'S STABILITY

Klystron or tetrodes* are employed to drive the rf cavities. When a klystron or tetrode is coupled to an rf cavity, electromagnetic fields are generated inside the cavity. The electric field across the gap of the cavity provides the required power to compensate for the energy loss to synchrotron radiation and coupling impedance, and to supply the necessary acceleration to the particle beam. However, the particle beam, when passing through the gap of the rf cavity, also excites electromagnetic fields inside the cavity in the same way as the klystron or the rf source. This excitation of the cavity by the particle beam is called *beam loading*. Beam loading has two effects on the rf system. First, the electric field from beam loading generates a potential, called the *beam loading voltage*, across the cavity gap and opposes the accelerating voltage delivered by the klystron. Thus more power has to be supplied to the rf cavity in order to overcome the effect of beam loading. Second, to optimize the power of the klystron, the cavity needs to be detuned. The detuning has to be performed correctly. If not, the power delivered by the klystron will not be efficient. Worst of all, an incorrect detuning will excite instability of the phase oscillation. We first study the steady-state beam loading and derive the criterion for phase stability. Later, transient beam loading will be addressed. The general methods to suppress beam loading are also reviewed. Most of the material in this chapter comes from the lecture notes of Wilson [1], Wiedemann [2], and Boussard [3].

*Klystrons are usually used in electron rings where the rf frequencies are high while tetrodes are usually used in proton rings where the rf frequencies are low. In this chapter, there is no intention to distinguish between the two, and we often use the terminology *rf generator* instead.

8.1 Equivalent Circuit

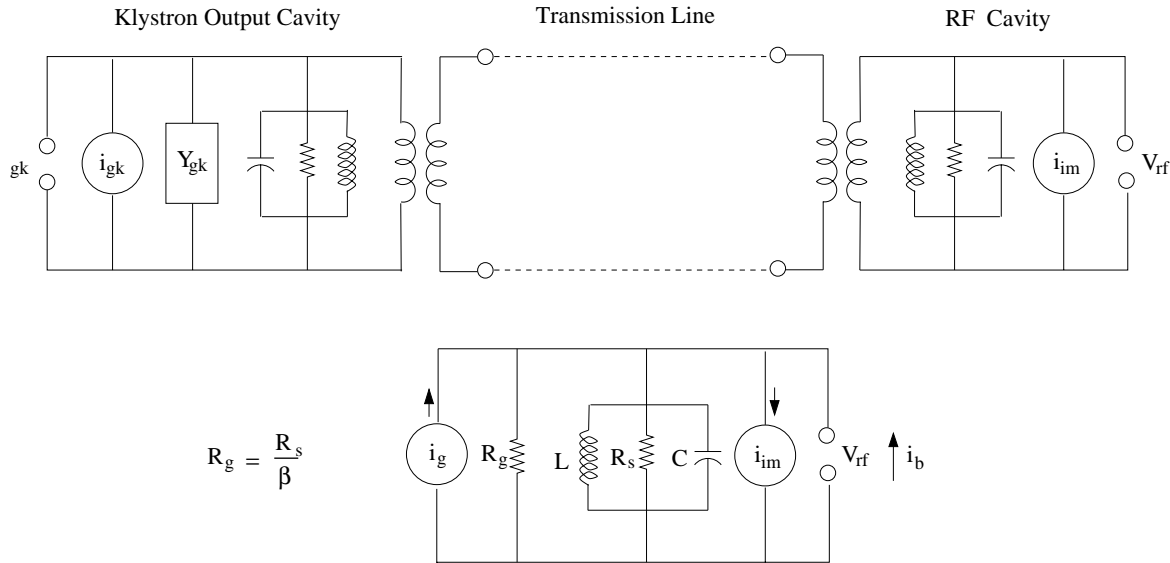


Figure 8.1: Circuit model representing an rf generator current source i_g driving an rf cavity with a beam loading current i_{im} .

The rf system can be represented by an equivalent circuit as shown in the top diagram of Fig. 8.1. The rf cavity is represented by a RLC circuit with angular resonant frequency

$$\omega_r = \frac{1}{\sqrt{LC}} , \quad (8.1)$$

where L and C are the equivalent inductance and capacitance of the rf cavity. The klystron or tetrode is also represented by a RLC circuit with the angular resonant frequency ω_{rf} , which is the actual rf frequency of the accelerator ring. The klystron/tetrode is connected to the rf cavity by waveguides or transmission lines via transformers as illustrated. The problem can be simplified considerably by assuming that there is a circulator or isolator just before the rf cavity, so that any power which is reflected from the cavity and travels back towards the klystron will be absorbed. Such an assumption leads to the equivalent circuit in the lower diagram of Fig. 8.1. The resistor R_s is called the *unloaded shunt impedance* of the rf system, because it is the impedance of the isolated cavity at its resonant frequency. The image current of the particle beam is represented by a current source i_{im} . This is a valid representation from the rigid-bunch approximation, because the velocities and therefore the current of the beam particles are assumed

roughly constant when the beam passes through the cavity gap. We reference image current here instead of the beam current i_b , because it is the image current that flows across the cavity gap and also into the cavity. The image current is in opposite direction to the beam current.

On the other hand, the situation is different for the klystron. The velocities of the electrons as they pass through the the gap of the output cavity of the klystron can change in response to the cavity fields of the klystron. As a consequence, the rf source is represented by a current source i_g in parallel to the loading resistor R_g or admittance $Y_g = 1/R_g$. The latter is written in terms of the shunt admittance Y_s or shunt impedance R_s of the rf cavity as

$$Y_g = \beta Y_s = \frac{\beta}{R_s} , \quad (8.2)$$

where β is the *coupling coefficient* still to be defined. The generator or klystron current i_g and the loading admittance Y_g in the lower equivalent circuit diagram are equivalent values and are different from the actual generator current i_{gk} and actual loading admittance Y_{gk} in the klystron circuit in the top circuit of Fig. 8.1. For example, in the rf system of the Fermilab Main Injector, $i_{gk} = 12i_g$.

The rf generator outputs a generator current I_g in order to produce the rf gap voltage V_{rf} for the beam. The total *required* output power[†] is

$$P_{\text{total}} = \frac{1}{2} \frac{I_g^2}{Y_g + Y_{\text{load}}} , \quad (8.3)$$

where Y_{load} is called the *load cavity admittance*, which includes the admittance of the cavity $Y_s = 1/R_s$ and also all the contribution from the particle beam. An explicit expression will be given in Eq. (8.43) below. In the situation of a very weak beam ($i_b \rightarrow 0$), $Y_{\text{load}} \rightarrow Y_s$. The total power can be rewritten as

$$P_{\text{total}} = \frac{1}{2} \frac{Y_g I_g^2}{(Y_g + Y_{\text{load}})^2} + \frac{1}{2} \frac{Y_{\text{load}} I_g^2}{(Y_g + Y_{\text{load}})^2} . \quad (8.4)$$

The first term on the right is the power dissipated at the generator. The second term is the power required to be transferred to the cavity and the beam, and we denote it

[†]This is the power *required* to transfer a certain energy per unit time to the cavity and the beam, and is different from the power available to the beam and cavity. The latter is given by $\frac{1}{2} \tilde{I}_g \cdot \tilde{V}_{\text{rf}}$ and becomes zero when the load angle $\theta_L = \pi/2$, as indicated in Eq. (8.38). On the other hand, the required power is inversely proportional to $\cos^2 \theta_L$. When $\theta_L \rightarrow \pi/2$, most of the energy energy is being transferred to the cavity as stored energy and very little is given to the beam. Therefore to satisfy the requirement of the beam, an infinite required power by the generator becomes necessary.

by P_g , which is usually referred to loosely as the *generator power*. We wish to obtain the condition for which this power delivered to the cavity and beam is a maximum by equating its derivative with respect to Y_{load} to zero. The condition is

$$Y_{\text{load}} = Y_g = \beta Y_s . \quad (8.5)$$

This is just the usual matching of the input impedance to the output impedance. The maximized generator power is then

$$P_g = \frac{i_g^2}{8\beta Y_s} = \frac{R_s i_g^2}{8\beta} . \quad (8.6)$$

Notice that in the situation of an extremely weak beam, this matched condition is just $Y_g = Y_s$ with the coupling coefficient $\beta = 1$. Equation (8.6) will be used repeatedly below and whenever the generator power P_g is referenced, we always imply the matched condition satisfying Eq. (8.5).

Here, all the currents and voltages referenced are the magnitudes of sinusoidally varying currents and voltages at the rf angular frequency ω_{rf} (not the cavity resonant angular frequency ω_r). Their corresponding phasors always have an overhead tilde. For example, i_{im} is the magnitude of the Fourier component of the image current phasor \tilde{i}_m that flows into the cavity at the rf frequency. Thus, for a *short bunch*, we have (Exercise 8.1),

$$i_{im} = 2I_0 , \quad (8.7)$$

with I_0 being the *dc current* of the beam. As phasors, however, they are in the opposite direction. It will be shown later, the image current phasor \tilde{i}_m may not be equal to the negative beam current phasor \tilde{i}_b because of possible feed-forward. In that case, I_0 in Eq. (8.7) will be the dc image current instead. For this reason, we try to make reference to the image current that actually flows into the cavity instead of the beam current.

In high energy electron linacs, bunches are usually accelerated at the peak or crest of the rf voltage wave in order to achieve maximum possible energy gain. As a result, the klystron is operated at exactly the same frequency as the resonant frequency of the rf cavities, i.e., $\omega_{\text{rf}} = \omega_r$. Without the rf generator, the beam or image current sees the *unloaded shunt impedance* R_s in the cavity and the *unloaded quality factor* Q_0 , which can easily be found to be

$$Q_0 = \omega_r C R_s . \quad (8.8)$$

With the rf generator attached, however, the beam image current source sees an effective shunt impedance R_L in the cavity, which is the parallel combination of the generator

shunt impedance R_g and the cavity shunt impedance R_s . This is called the cavity *loaded shunt impedance* in contrast with the cavity unloaded shunt impedance R_s . We therefore have

$$R_L = (Y_s + Y_g)^{-1} = \frac{R_s}{1 + \beta}. \quad (8.9)$$

Correspondingly, the beam image current sees a *loaded quality factor* in the cavity, which is

$$Q_L = \omega_r C R_L = \frac{Q_0}{1 + \beta}. \quad (8.10)$$

Notice that

$$\frac{R_s}{Q_0} = \frac{R_L}{Q_L}, \quad (8.11)$$

independent of whether it is loaded or unloaded. In fact, R_s/Q_0 is just a geometric factor of the cavity.

The beam loading voltage is the voltage generated by the image current, and is given by

$$V_{br} = \frac{i_{im}}{Y_g + Y_s} = \frac{i_{im}}{Y_s(1 + \beta)}, \quad (8.12)$$

while the voltage produced by the generator is

$$V_{gr} = \frac{i_g}{Y_g + Y_s} = \frac{i_g}{Y_s(1 + \beta)}, \quad (8.13)$$

where the subscript “r” implies that the operation is at the resonant frequency, so that the currents and voltages are in phase, although they may have sign difference. In terms of the generator power P_g in Eq. (8.6), the generator voltage at resonance becomes

$$V_{gr} = \frac{\sqrt{8\beta}}{1 + \beta} \sqrt{R_s P_g}. \quad (8.14)$$

It is clear that the beam loading voltage is in the opposite direction of the generator voltage. Thus, the net accelerating voltage is

$$V_{rf} = V_{gr} - V_{br} = \sqrt{R_s P_g} \left[\frac{\sqrt{8\beta}}{1 + \beta} \left(1 - \frac{K}{2\sqrt{\beta}} \right) \right], \quad (8.15)$$

where

$$K^2 = \frac{i_{im}^2 R_s}{2P_g} \quad (8.16)$$

plays the role of the ratio of the beam loading power to the generator power. Since the shunt impedance R_s of a superconducting cavity is very high, beam loading becomes much more important. The fraction of generator power delivered to the beam is

$$\eta = \frac{i_{im}V_{rf}}{2P_g} = \frac{2\sqrt{\beta}}{1+\beta} K \left(1 - \frac{K}{2\sqrt{\beta}}\right) . \quad (8.17)$$

The power dissipated in the cavity is

$$P_c = \frac{V_{rf}^2}{2R_s} = P_g \left(\frac{2\sqrt{\beta}}{1+\beta}\right)^2 \left(1 - \frac{K}{2\sqrt{\beta}}\right)^2 . \quad (8.18)$$

From the conservation of energy, we must have

$$P_g = \eta P_g + P_c + P_r , \quad (8.19)$$

where P_r is the power reflected back to the generator and is given by

$$\frac{P_r}{P_g} = \left(\frac{\beta - 1 - K\sqrt{\beta}}{1 + \beta}\right)^2 . \quad (8.20)$$

So far we have not said anything about the coupling coefficient β . Now we can choose β so that the generator power is delivered to the cavity and the beam without any reflection, or from Eq. (8.20), the optimum coupling constant is

$$K = \frac{\beta_{op} - 1}{\sqrt{\beta_{op}}} . \quad (8.21)$$

Notice that this optimization is also a maximization of the accelerating voltage V_{rf} , as can be verified by differentiating Eq. (8.15) with respect to β .

8.2 Beam Loading in an Accelerator Ring

In a synchrotron ring or storage ring, it is necessary to operate the rf system off the crest of the accelerating voltage wave form in order to have a sufficient large bucket area to hold the bunched beam and to insure stability of phase oscillation. The klystron or rf generator is operating at the *rf frequency* $\omega_{rf}/(2\pi) = h\omega_0/(2\pi)$, where h is an integer called the *rf harmonic*, and $\omega_0/(2\pi)$ is the revolution frequency of the *synchronized* beam particles. Notice that this rf frequency will be the frequency the beam particles

experience at the cavity gap and is different from the intrinsic resonant frequency of the cavity $\omega_r/(2\pi)$ given by Eq. (8.1). According to the circuit diagram of Fig. 8.1, the impedance of the cavity seen by the particle at rf frequency $\omega_{\text{rf}}/(2\pi)$ can be written as

$$Z_{\text{cav}} = \frac{R_L}{1 - jQ_L \left(\frac{\omega_r}{\omega_{\text{rf}}} - \frac{\omega_{\text{rf}}}{\omega_r} \right)} = R_L \cos \psi e^{j\psi}, \quad (8.22)$$

where ψ is called the *rf detuning angle* or just detuning. As will be shown below, detuning is an essential mechanism to make the beam particle motion stable under the influence of the rf system. It is important to point out that loaded values have been used here, because those are what the image current sees. From Eq. (8.22), the detuning angle is defined as

$$\tan \psi = Q_L \left(\frac{\omega_r}{\omega_{\text{rf}}} - \frac{\omega_{\text{rf}}}{\omega_r} \right). \quad (8.23)$$

When the deviation of ω_{rf} from ω_r is small, an approximation gives

$$\tan \psi = 2Q_L \frac{\omega_r - \omega_{\text{rf}}}{\omega_r}. \quad (8.24)$$

Note that in this section we have used j instead of $-i$, because phasor diagrams are customarily drawn using this convention. Phasors, as illustrated in Fig. 8.2, are represented by overhead tildes rotating counter-clockwise with angular frequency ω_{rf} if there is only one bunch in the ring. If there are N_b equal bunches in the ring separated equally by $h_b = h/N_b$ rf buckets, where h is the rf harmonic, we can also imagine the phasors to be rotating at angular frequency ω_{rf}/h_b . They are therefore the Fourier components at the rf frequency or ω_{rf}/h_b . This implies that we are going to see the same phasor plot for each passage of a bunch through the rf cavity. In order to be so, the beam loading voltage should have negligible decay during the time interval $T_b = 2\pi h_b/\omega_{\text{rf}}$ between two successive bunches. In other words, we require $T_b \ll T_f$ in this discussion, where $T_f = 2Q_L/\omega_r$ is the fill time of the cavity.

Most of the time, the image current phasor \tilde{i}_{im} has the same magnitude as that of the beam current phasor \tilde{i}_b , although in the opposite direction. When the image current \tilde{i}_{im} interacts with the loaded cavity, according to Eq. (8.22), a beam loading voltage phasor \tilde{V}_b will be produced and is given by

$$\tilde{V}_b = \tilde{i}_{\text{im}} R_L \cos \psi e^{j\psi}, \quad (8.25)$$

and

$$V_b = V_{br} \cos \psi. \quad (8.26)$$

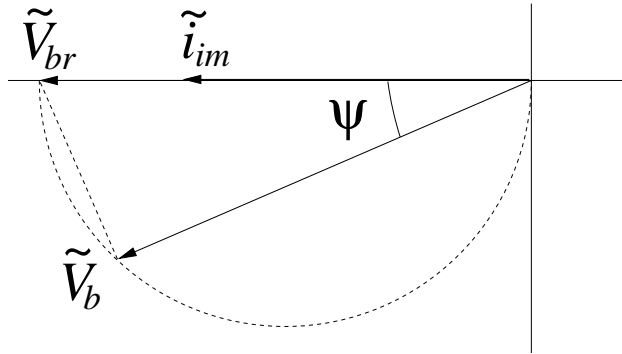


Figure 8.2: Phasor plot showing the beam loading voltage phasor \tilde{V}_b induced in the rf cavity by the image current phasor \tilde{i}_{im} , which lags \tilde{V}_b by the detuning angle ψ . Also plotted is the beam loading voltage phasor \tilde{V}_{br} , with $V_b = V_{br} \cos \psi$ when the beam current is at the crest of the rf wave with no detuning.

Thus the voltage phasor always leads the current phasor by the detuning phase ψ and the magnitude of the phasor \tilde{V}_b is less than its value at the cavity resonant frequency V_{br} by the factor $\cos \psi$. If one likes, one can also introduce the phasor \tilde{V}_{br} which is in phase with the current phasor \tilde{i}_{im} and has the magnitude given by Eq. (8.26). This is illustrated in Fig. 8.2.

Some comments are necessary. Here, we start from only one Fourier component (the one at frequency ω_{rf} or ω_{rf}/h_b) of the image current \tilde{i}_{im} . The beam loading voltage \tilde{V}_b experienced by the beam is also a Fourier component of the same frequency. Since we are investigating the problem in the frequency domain, this is equivalent to a very long interval in the time domain. In other words, the result describes a steady-state problem, implying that the beam has passed by the rf cavities many many times already. The beam loading voltage \tilde{V}_b is therefore a sinusoidal wave in time. However, this is not exactly what we expect from a cavity. The beam loading voltage decays exponentially as soon as the beam leaves the rf cavity. It is charged up again like a step function when the beam passes by again. Thus, the time dependent behavior of the beam loading voltage is more like a sawtooth rather than sinusoidal. Putting it in another way, more than one Fourier component will be necessary to fully describe the beam loading picture. However, if the exponential decay is slow, the beam loading wave will behave more like sinusoidal. Therefore, our description of the beam loading problem here is valid only when the cavity decay time constant (or fill time)

$$T_f = \frac{2Q_L}{\omega_r} \quad (8.27)$$

is very much longer than the interval T_b between successive beam passage. We will address a more accurate description later.

There are good reasons that detuning is necessary. The first one is for the compensation of beam loading, which we describe in the next subsection. One may argue why we do not just employ an extra generator current equal and opposite to the image current for a simple 100% compensation. This requires the generator to deliver unnecessarily large current at a phase angle other than that of the rf voltage. Needless to say, this will result in a degradation of the efficiency of the rf excitation system and an increase in cost. The second reason is phase stability. When the center of the beam deviates from its proper rf phase, proper detuning will damp the deviation and guarantee phase stability. This will be addressed later in the section on Robinson's stability.

8.2.1 Steady-State Compensation

In Fig. 8.3, the total current phasor \tilde{i}_t inside the cavity is the vector sum of the image current phasor \tilde{i}_{im} and the generator current phasor \tilde{i}_g . The rf voltage phasor \tilde{V}_{rf} is at the synchronous angle ϕ_s and leads the total current phasor by the detuning angle ψ . The current phasor \tilde{i}_0 is the projection of \tilde{i}_t along \tilde{V}_{rf} . Thus, \tilde{i}_0 is the generator current required to set up the rf voltage when the cavity is at resonance and when there is no beam current. In other words, $i_0 = V_{\text{rf}}/R_L = (1 + \beta)V_{\text{rf}}/R_s$, where β is the coupling coefficient of the generator to the rf cavity and R_s is the unloaded shunt impedance.

We want to solve for the *load angle* θ_L that the generator current phasor lags the rf voltage phasor. By projecting along and perpendicular to the rf voltage phasor, one obtains

$$\tan \theta_L = \frac{i_0 \tan \psi - i_{\text{im}} \cos \phi_s}{i_0 + i_{\text{im}} \sin \phi_s} , \quad (8.28)$$

and

$$i_g = \frac{i_0 + i_{\text{im}} \sin \phi_s}{\cos \psi} . \quad (8.29)$$

To optimize the efficiency of the generator, the generator current phasor \tilde{i}_g and the rf voltage phasor \tilde{V}_{rf} should be in the same direction, because in this way the load will appear real to the generator and the stored energy will be reduced to a minimum.

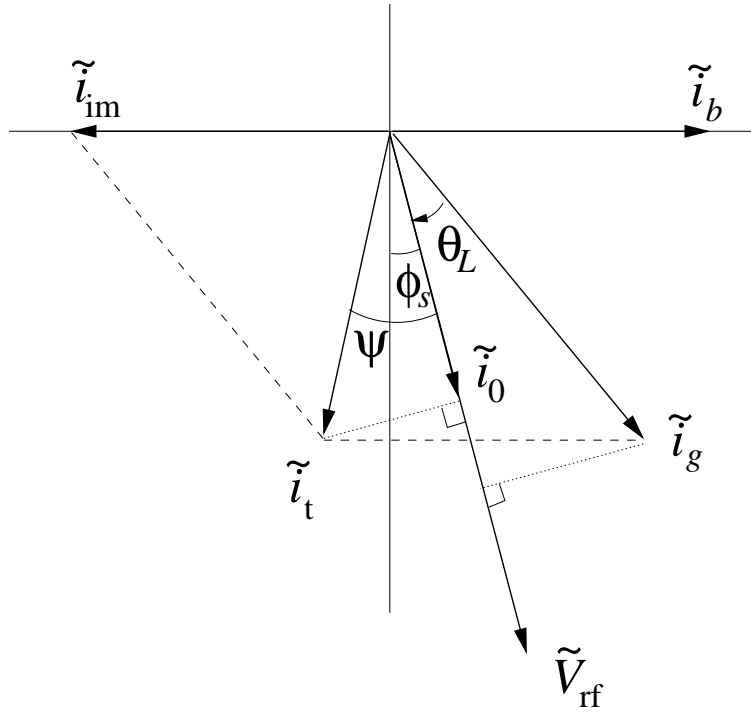


Figure 8.3: Phasor plot showing the vector addition of the image current phasor \tilde{i}_{im} and the generator current phasor \tilde{i}_g to give the total current phasor \tilde{i}_t . The latter lags the rf voltage phasor \tilde{V}_{rf} at synchronous phase ϕ_s by the detuning angle ψ . Note that the generator current phasor is not in phase with the rf voltage phasor. It lags \tilde{V}_{rf} by the load angle θ_L .

Substituting for $\theta_L = 0$, we obtain the in-phase conditions

$$\tan \psi = \frac{i_{im} \cos \phi_s}{i_0} \quad (8.30)$$

and

$$i_g = i_0 + i_{im} \sin \phi_s . \quad (8.31)$$

Figure 8.4 shows the voltage phasors inside the cavity with the rf voltage phasor \tilde{V}_{rf} in phase with the generator current phasor \tilde{i}_g . Here, we see that the beam loading voltage phasor \tilde{V}_b is ahead of the image current phasor \tilde{i}_{im} by the detuning angle ψ . The generator voltage phasor \tilde{V}_g is also ahead of the generator current phasor \tilde{i}_g by the detuning angle ψ . These two voltage phasors add up to give the gap voltage phasor \tilde{V}_{rf} which has a synchronous angle ϕ_s . The in-phase condition can also be obtained from this phasor diagram. Since the voltage components perpendicular to \tilde{i}_g must add up to

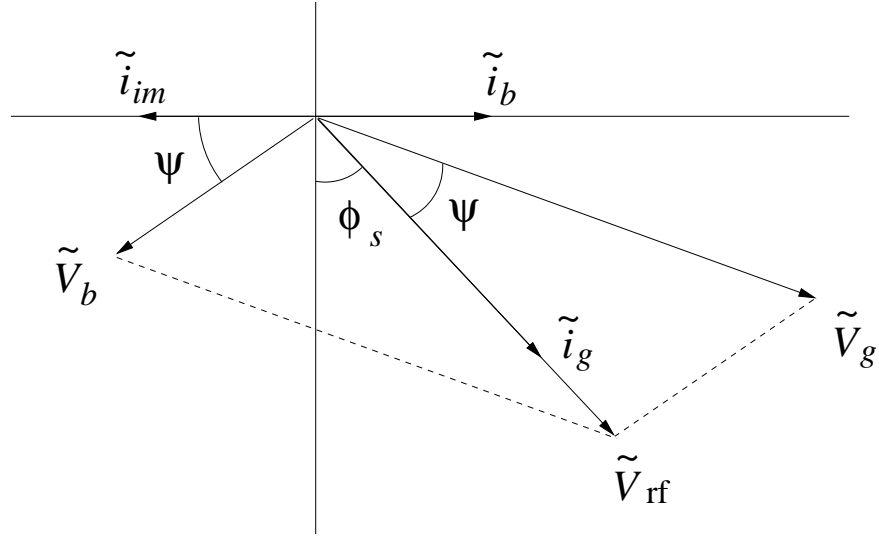


Figure 8.4: Phasor plot showing the vector addition of the generator voltage phasor \tilde{V}_g and the beam loading voltage phasor \tilde{V}_b to give the gap voltage phasor \tilde{V}_{rf} in an rf cavity. Note the detuning angle ψ which puts the gap current phasor \tilde{i}_g in phase with the gap voltage phasor.

zero, after dividing by $R_s \cos \psi$, we get

$$i_g \sin \psi = i_{im} \sin\left(\frac{\pi}{2} + \phi_s - \psi\right). \quad (8.32)$$

Next, resolve the current contributions along \tilde{i}_g and we obtain Eq. (8.31). Finally, eliminate i_g and arrive at the in-phase condition of Eq. (8.30).

Notice that steady-state beam loading has been compensated by the introduction of a suitable generator current. This compensation scheme with detuning is much more efficient than the one without, because part of the beam loading voltage has been utilized in the rf voltage and the generator current is in phase with the rf voltage. In other words, the generator power required will be smaller than when there is no detuning. Actually, it can be readily shown by differentiating Eq. (8.35) below with respect to the detuning angle ψ that the generator power is the smallest when the in-phase condition is met between the generator current phasor and the rf voltage phasor. In the event that the beam intensity is very high, the beam loading voltage V_b can become much larger than the required gap voltage V_{rf} . Needless to say, to balance such a large a very high power amplifier will be necessary to generate the required generator current I_g . When this happens, low-level rf feedback can be installed to reduce the effective cavity impedance as observed by the beam. A low-level rf feed-forward is also possible to cancel partly or

completely the image current. These methods will be discussed later in Sec. 8.4.4.

The generator power P_g can be computed with the aid of Eq. (8.14), namely,

$$P_g = \frac{(1 + \beta)^2 V_{gr}^2}{8\beta R_s}, \quad (8.33)$$

where V_{gr} is the generator voltage at the cavity resonant frequency, and is related to the generator voltage V_g at the rf frequency by $V_g = V_{gr} \cos \psi$. Using the cosine law for the triangle made up from \tilde{V}_g , \tilde{V}_b , and \tilde{V}_{rf} , it is easy to obtain

$$V_g^2 = V_b^2 + V_{rf}^2 - 2V_b V_{rf} \sin(\psi - \phi_s), \quad (8.34)$$

or

$$V_{gr}^2 = V_{br}^2 + V_{rf}^2(1 + \tan^2 \psi) - 2V_{br} V_{rf} (\tan \psi \cos \phi_s - \sin \phi_s), \quad (8.35)$$

where $V_{br} = V_b / \cos \psi$ is the beam loading voltage at the cavity resonant frequency. From Eq. (8.14), the required generator power for the cavity and beam can be expressed as

$$P_g = \frac{R_s}{8\beta} [(i_0 + i_{im} \sin \phi_s)^2 + (i_0 \tan \psi - i_{im} \cos \phi_s)^2], \quad (8.36)$$

where

$$V_{br} = \frac{V_b}{\cos \psi} = \frac{i_{im} R_s}{1 + \beta} \quad (8.37)$$

is the beam loading voltage at the cavity resonant frequency, and the definition of i_0 in Eq. (8.31) has been used. If the correct detuning is made so that \tilde{I}_g and \tilde{V}_{rf} are in phase, the second term on the right-hand side vanishes and the expression is very much simplified. On the other hand, we notice that the two terms on the right-side resemble the denominator and numerator on the right-side of Eq. (8.28). We can therefore rewrite the generator power in terms of the load angle θ_L ,

$$P_g = \frac{R_s}{8\beta} \frac{(i_0 + i_{im} \sin \phi_s)^2}{\cos^2 \theta_L}, \quad (8.38)$$

which recovers the situation of in-phase detuning when $\theta_L = 0$. The factor $\cos^2 \theta_L$ is important. It tells us that when the load angle $\theta_L \rightarrow \pi/2$, an infinite generator power is required. This is because only the fraction $\cos^2 \theta_L$ of the power goes into the beam and the majority, $\sin^2 \theta_L$, goes into charging the cavity.

Again we can optimize the generator power by choosing the best coupling constant β , which turns out to be

$$\beta_{op} = 1 + \frac{i_{im} R_s \sin \phi_s}{V_{rf}} = 1 + \frac{P_b}{P_c}, \quad (8.39)$$

where

$$P_c = \frac{V_{\text{rf}}^2}{2R_s} \quad (8.40)$$

is the power dissipated in the walls of the cavity and

$$P_b = \frac{1}{2} i_{\text{im}} V_{\text{rf}} \sin \phi_s = I_0 V_{\text{rf}} \sin \phi_s \quad (8.41)$$

is the power spent on accelerating the beam, since $V_{\text{rf}} \sin \phi_s$ is the accelerating voltage. Here, we have used Eq. (8.7), the fact that the Fourier component image current at the rf frequency (or at ω_{rf}/h_b) is nearly twice the dc beam current I_0 when the bunch is short. At the optimized coupling constant, the generator power becomes

$$P_{g\text{ op}} = \frac{V_{\text{rf}}^2}{2R_g} = \frac{V_{\text{rf}}^2}{2R_s} \beta_{\text{op}} = P_b + P_c , \quad (8.42)$$

which just states that the power is transmitted to the cavity completely without any reflected. Here, we can identify the *load cavity admittance* Y_{load} defined in earlier in Eq. (8.4) as

$$Y_{\text{load}} = \frac{i_{\text{im}} \sin \phi_s}{V_{\text{rf}}} + \frac{1}{R_s} , \quad (8.43)$$

where the first term on the right is admittance of the beam and the second term is the admittance of the cavity.

Usually there is a servo-tuner which measures the phase difference between the generator current phasor and rf gap voltage phasor, and controls the cavity tune via a mechanical plunger or ferrite bias, so that the phase difference vanishes. At equilibrium of the servo-tuner, Eqs. (8.30) and (8.31) are automatically satisfied, and the cavity detuning corresponds to

$$\Delta\omega = \omega_r - \omega_{\text{rf}} = \frac{\omega_r R_L i_{\text{im}} \cos \phi_s}{2Q_L V_{\text{rf}}} . \quad (8.44)$$

8.3 Robinson's Stability Criteria

8.3.1 Phase Stability at Low Intensity

We are now in the position to discuss the conditions for phase stability. Suppose that center of the bunch has the same energy as the synchronous particle, but is at a small

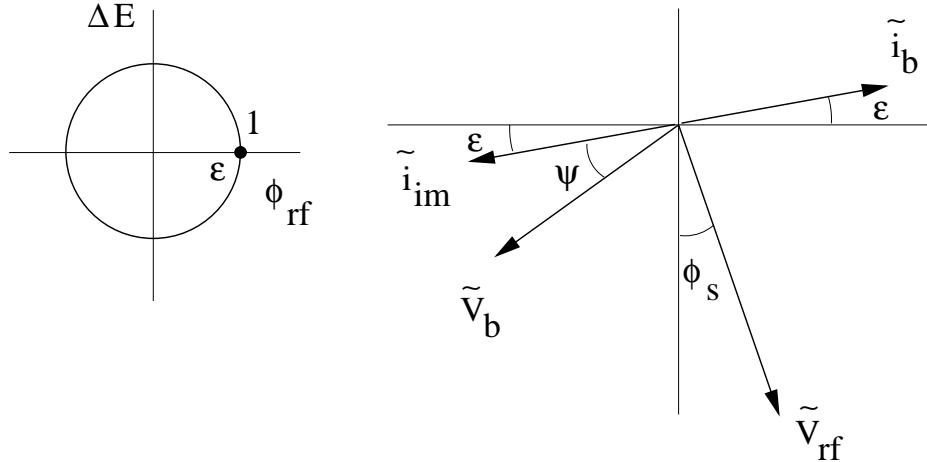


Figure 8.5: With the bunch center at Point 1 in the synchrotron oscillation, the beam current phasor \tilde{i}_b arrives earlier by being ahead of the x -axis at a small angle $\epsilon > 0$ in the phasor plot. The bunch sees a smaller rf voltage $V_{\text{rf}} \sin(\phi_s - \epsilon)$ if the synchronous phase $0 < \phi_s < \frac{1}{2}\pi$. It is decelerated. Below transition, it will arrive not so early in the next turn and phase stability is therefore established.

phase advance $\phi_{\text{rf}} = \epsilon > 0$, as depicted by Point 1 in the synchrotron oscillation and the phasor \tilde{i}_b in the phasor plot in Fig. 8.5. The phasor \tilde{i}_b arrives earlier by being ahead of the x -axis at a small angle $\epsilon > 0$. Then the accelerating voltage it sees will be $V_{\text{rf}} \sin(\phi_s - \epsilon)$ instead of $V_{\text{rf}} \sin \phi_s$, or an extra decelerating voltage of $\epsilon V_{\text{rf}} \cos \phi_s$ if $0 < \phi_s < \frac{1}{2}\pi$. Receiving less energy from the rf voltage than the synchronous particle will slow the bunch. If the beam is below transition, this implies the reduction of its revolution frequency, so that after the next h rf periods its arrival ahead of the synchronous particle will be smaller or ϵ will become smaller. The motion is therefore stable. Therefore to establish stable phase oscillation when beam loading can be neglected, one requires

$$\begin{cases} 0 < \phi_s < \frac{\pi}{2} & \text{below transition,} \\ \frac{\pi}{2} < \phi_s < \pi & \text{above transition.} \end{cases} \quad (8.45)$$

This is exactly the same condition for stable phase oscillation we conclude from the expression for the synchrotron tune in Eq. (2.14). Notice that this is just the condition of phase stability and there is no damping at all. Here, the derivation relies on the fact that the rf voltage phasor \tilde{V}_{rf} is unperturbed and this is approximately correct when the beam intensity and therefore the beam loading voltage is small.

8.3.2 Phase Stability at High Intensity

When the beam current is very intense, we can no longer neglect the contribution of the beam loading voltage. The condition of phase stability in Eq. (8.45) will be modified. Now, go back to Fig. 8.5 when the beam current phasor arrives at an angle $\epsilon > 0$ ahead of the x -axis but is at the same energy as the synchronous particle, the image current phasor \tilde{i}_{im} will also advance by the same angle ϵ after h rf periods. Therefore, there will be an extra beam loading voltage phasor $\epsilon i_{\text{im}} R_L \cos \psi e^{j(\psi+3\pi/2)}$, which constitutes the perturbation of the rf voltage phasor \tilde{V}_{rf} . If $\psi < 0$, this phasor will point into the 3rd quadrant and decelerate the particle in concert with $\epsilon V_{\text{rf}} \cos \phi_s$ in slowing the beam, thus causing no instability below transition. On the other hand, if $\psi > 0$, this phasor will point into the 4th quadrant and accelerate the particle instead. To be stable, the extra accelerating voltage on the beam must be less than the amount of decelerating voltage $\epsilon V_{\text{rf}} \cos \phi_s$, or

$$[V_{\text{rf}} \sin(\phi_s - \epsilon) - V_{\text{rf}} \sin \phi_s] + \epsilon i_{\text{im}} R_L \cos \psi \sin \psi \approx -\epsilon V_{\text{rf}} \cos \phi_s + \epsilon V_{\text{br}} \cos \psi \sin \psi < 0 . \quad (8.46)$$

Thus for phase stability, we require

$$\frac{V_{\text{br}}}{V_{\text{rf}}} < \frac{\cos \phi_s}{\sin \psi \cos \psi} \quad \begin{cases} \psi > 0 & \text{below transition,} \\ \psi < 0 & \text{above transition,} \end{cases} \quad (8.47)$$

which is called Robinson's *high-intensity criterion* of stability. In above, $V_{\text{br}} = i_{\text{im}} R_L$ is the *in-phase* beam loading voltage when the beam is in phase with the loaded cavity impedance.

Notice that this Robinson's high-intensity criterion of stability is only a criterion of phase stability similar to the phase stability condition of Eq. (8.45). Satisfying this criterion just enables stable oscillating like sitting inside a stable potential well. Violating this criterion will place the particle in an unstable potential well so that phase oscillation will not be possible. To include damping or antidamping due to the interaction of the beam with the cavity impedance, another criterion of Robinson stability, Eq. (8.57) below, must be satisfied also.

We can also look at the phase stability problem in another way. In order that the beam can execute stable phase oscillation, it must see a linear restoring force when the beam deviates from its equilibrium position. This force comes from change in the rf voltage \tilde{V}_{rf} seen by the beam when the beam is at an offset. This explains why we have

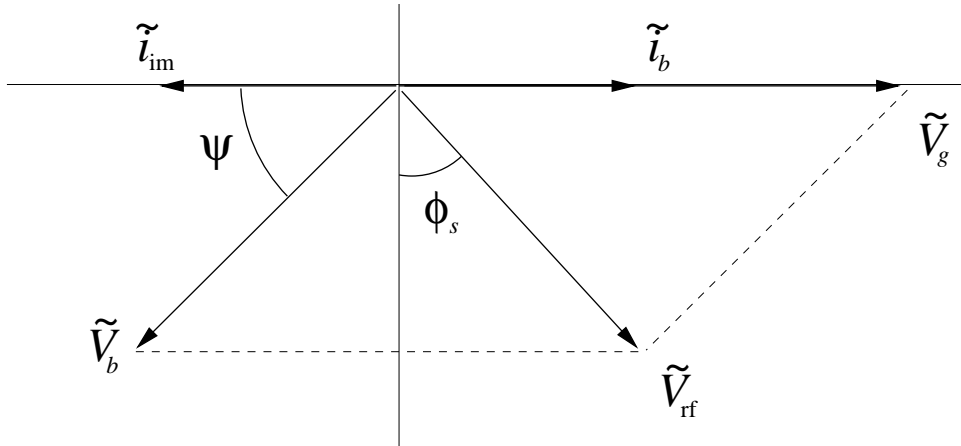


Figure 8.6: When the generator voltage phasor \tilde{V}_g becomes in phase with the beam current phasor, it provides no force gradient to the beam in the direction of the beam. Since the restoring force vanishes for an infinitesimal offset of the beam arrival time, the beam is on the edge of instability in phase oscillation.

the gradient of the rf accelerating voltage or $V_{\text{rf}} \cos \phi_s$ in Eq. (2.14), the expression of the synchrotron tune. Now the rf voltage phasor \tilde{V}_{rf} is the sum of the beam loading voltage phasor \tilde{V}_b and the generator voltage phasor \tilde{V}_g , or

$$\tilde{V}_{\text{rf}} = \tilde{V}_b + \tilde{V}_g . \quad (8.48)$$

Notice that the beam loading voltage phasor \tilde{V}_b moves with the beam and therefore will not provide any force gradient or restoring force to the beam. In other words, $d\tilde{V}_b/d\epsilon = 0$. Thus only the generator voltage phasor \tilde{V}_g can provide such a restoring force. Therefore, we should compute $d\tilde{V}_g/d\epsilon$. If this gradient enhances the displacement of the beam from the synchronous position, the system is unstable; otherwise, it is stable. When the generator voltage phasor is in phase with the beam as illustrated in Fig. 8.6, it is clear that for any small variation of time arrival ϵ of the beam, the beam will not see any variation of the generator voltage phasor \tilde{V}_g in the direction of the beam, or $d\tilde{V}_g/d\epsilon = 0$ in the direction of the beam. In other words, there is no restoring force to alter the energy of the beam so as to push it back to its equilibrium position. Thus the configuration in Fig. 8.6 constitutes the Robinson's limit of phase stability. From the figure, it is evident that the projection of \tilde{V}_{rf} and \tilde{V}_b perpendicular to the beam must be the same or the stability limit is

$$V_{\text{rf}} \cos \phi_s = i_{\text{im}} R_L \cos \psi \sin \psi , \quad (8.49)$$

which is exactly the same as Eq. (8.47).

Now let us impose the condition that the generator current \tilde{i}_g is in phase with the rf voltage \tilde{V}_{rf} . First, we have $i_0 = V_{\text{rf}}/R_L$, so that Robinson's criterion of phase stability in Eq. (8.47) can be rewritten as

$$\frac{i_{\text{im}}}{i_0} < \frac{\cos \phi_s}{\sin \psi \cos \psi} \quad \begin{cases} \psi > 0 & \text{below transition,} \\ \psi < 0 & \text{above transition.} \end{cases} \quad (8.50)$$

Second, the in-phase condition implies Eq. (8.30), which simplifies the above to

$$\frac{i_{\text{im}}}{i_0} < \frac{1}{\sin \phi_s} , \quad (8.51)$$

after eliminating the detuning. If we further optimize the generator power by choosing the coupling constant β_{op} given by Eq. (8.39), it is easy to show that

$$\frac{i_{\text{im}} \sin \phi_s}{i_0} = \frac{\beta_{\text{op}} - 1}{\beta_{\text{op}} + 1} < 1 . \quad (8.52)$$

In other words, the Robinson's phase stability criterion will always be satisfied when the generator current phasor \tilde{i}_g and the rf voltage phasor \tilde{V}_{rf} are in phase and the coupling between the generator and the rf cavities is optimized.

When the generator current phasor and the rf voltage phasor are in phase, Fig. 8.6 immediately gives the phase stability limiting criterion for the detuning as

$$\psi = \frac{\pi}{2} - \phi_s . \quad (8.53)$$

Substituting into the in-phase condition of Eq. (8.30) reproduces the stability criterion of Eq. (8.51). The stability criterion can also be rewritten as

$$\frac{1}{2}V_{\text{rf}}i_{\text{im}}\sin \phi_s < \frac{1}{2}V_{\text{rf}}i_0 , \quad (8.54)$$

where the right side is P_L , the power dissipated in the cavities and the generator, while the left side is P_b , the power supplied to the beam for acceleration and/or compensation of energy lost to radiation and impedance. Thus, Robinson's phase stability criterion can also be reworded as

$$P_b < P_L , \quad (8.55)$$

or the power allocated to dissipation is larger than the power delivered to the beam.

The Robinson's limit of phase stability is correct only if there is no other stabilizing mechanism available. In an accelerator ring, there is usually a loop that monitors the beam loading and feedbacks onto the generator current so as to maintain the required rf gap voltage and synchronous phase. This correction, however, is not instantaneous, because it takes time for the new generator voltage to establish inside the rf cavity. If gain of the feedback is high, the time delay can be much faster than the fill time $T_f = 2Q_L/\omega_r$ of the cavity. If this time delay is short compared with the synchrotron period, phase stability can be established, even if the criterion $P_b < P_L$ is violated. The former Fermilab Main Ring at its peak intensity of $N_p = 3.25 \times 10^{13}$ protons/pulse (about 3.25×10^{10} per bunch for 1000 bunches) serves as an example. The ring had a mean radius of 1 km and therefore a revolution frequency $f_0 = 47.7$ kHz. The dc beam current was $I_0 = eN_p f_0 = 0.245$ A or the image current was $i_{\text{im}} = 2I_0 = 0.490$ A assuming that the bunches are short. With 15 working cavities each supplying 213 kV, the total rf voltage was $V_{\text{rf}} = 3.2$ MV. The acceleration rate was 125 GeV/s or 2.62 MeV/turn. Thus, $\sin \phi_s = 0.819$ and $i_{\text{im}} \sin \phi_0 = 0.407$ A. Each cavity had a loaded shunt impedance of 0.60 MΩ, or the total loaded shunt impedance was $R_L = 9.00$ MΩ. The current required to set up the rf voltage turned out to be $i_0 = V_{\text{rf}}/R_L = 0.355$ A, which less than $i_{\text{im}} \sin \phi_0$. Thus, Robinson's phase stability criterion had been violated. There was a servo-tuner that guaranteed the generator current phasor to be in-phase with with rf voltage phasor. There were also rf voltage magnitude and phase loops to maintain the the proper rf voltage and synchronous phase. The rf cavities were of $\omega_r/(2\pi) = 53.1$ MHz with a loaded quality factor $Q_L \approx 5000$. The cavity fill time was then $T_f = 30.0$ μs or about 1.43 revolution turns, small compared with the synchrotron period of ∼ 100 turns. The modification of the detuning is usually the slowest part of the feedback procedure, but it is definitely faster than the synchrotron frequency. As a result, phase stability was maintained even when Robinson's stability criterion was not fulfilled.

8.3.3 Robinson's Damping

Next, we consider the interaction of the beam with the impedance of the rf system. As we will see, proper detuning damps synchrotron oscillations while improper detuning leads to an oscillation with increasing amplitude. During half of a synchrotron period, the center of the bunch is at a higher energy than the synchronous particle. For the sake of convenience, choose the particular moment when the phase of bunch center is just in phase with the synchronous particle, so that the phasor \tilde{i}_b is exactly along the x -axis.

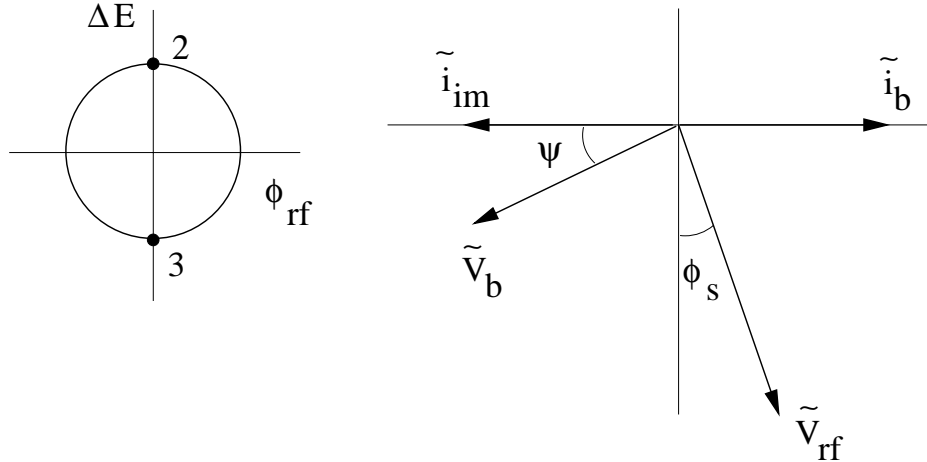


Figure 8.7: With bunch center at Point 2 in the synchrotron oscillation, the beam current phasor \tilde{i}_b is in phase with the x -axis in the phasor plot. Below transition, higher energy implies higher effective rf frequency ω_{rf} . The bunch sees a smaller effective detuning angle and loses more energy per turn than when the bunch is at the synchronous position. The synchrotron oscillation amplitude is therefore damped.

This is illustrated by Point 2 in the synchrotron oscillation and the beam current phasor being in phase with the x -axis in the phasor plot in Fig. 8.7. Below transition, however, higher energy implies higher revolution frequency ω_0 . The detuning ψ which is defined by

$$\tan \psi = 2Q_L \frac{\omega_r - \omega_{rf}}{\omega_r} \quad (8.56)$$

appears effectively smaller from the view of the bunch center, when we consider the effective rf frequency as $\omega_{rf} = h\omega_0$. The energy loss per turn, which is $i_{im}|Z_{cav}| \cos \psi$, will be larger than if the bunch center is synchronous. For the other half of the synchrotron period, the beam particle has an energy smaller than the synchronous particle and revolves with a lower frequency, and therefore sees a larger effective detuning. Again we choose the moment when the phase of the bunch center is just in phase with synchronous particle, or Point 3 in the synchrotron oscillation. The bunch will lose less energy than if it is synchronous. The result is a gradual decrease in the energy offset oscillation after oscillation. This reduction of synchrotron oscillation amplitude is called *Robinson damping*. Notice that if the detuning is in the other direction below transition, $\psi < 0$, the beam particle will lose less energy when its energy is higher than synchronous and lose more energy when its energy is less. The oscillation amplitude will increase turn

after turn and the beam will therefore be Robinson unstable. The opposite is true if the beam is above transition. We therefore have the criterion of Robinson stability:

$$\begin{cases} \psi > 0 \quad \text{or} \quad \omega_r > \omega_{rf} & \text{below transition,} \\ \psi < 0 \quad \text{or} \quad \omega_r < \omega_{rf} & \text{above transition.} \end{cases} \quad (8.57)$$

Notice that so far we have not imposed any optimization condition on the rf system. If the cavity tuning is adjusted so that the generator current \tilde{i}_g is in the same direction as the rf voltage \tilde{V}_{rf} , so that the beam-cavity impedance appears to be real as demonstrated in Fig. 8.4, the beam will always be Robinson stable, because the detuning will always satisfy Eq. (8.57) according to Eq. (8.30).

8.4 Transient Beam Loading

By transient we mean that the fill time of the cavity T_f is not necessarily much longer than the time interval T_b for successive bunches to pass through the cavity. In other words, the beam loading voltage from the first bunch will have significant decay before the successive bunch arrives.

First, let us understand how the transient beam loading occurs. As the bunch of charge $q > 0$ passes through the cavity gap, a negative charge equal to that carried by the bunch will be left by the image current at the upstream end of the cavity gap. Since the negative image current will resume from the downstream end of the cavity gap following the bunch, an equal amount of positive charge will accumulate there. Thus, a voltage will be created at the gap opposing the beam current and this is the transient beam loading voltage as illustrated in Fig. 8.8. For an infinitesimally short bunch, this transient voltage is

$$V_{b0} = \frac{q}{C} = \frac{q\omega_r R_s}{Q_0}, \quad (8.58)$$

where C is the equivalent capacitance across the gap of the cavity. Notice that we will arrive at the same value if the loaded shunt impedance R_L and the loaded quality factor Q_L are used instead. Due to the finite quality factor Q_0 , this induced voltage across the gap starts to decay immediately, hence the name transient beam loading. We will give concrete example about the size of the voltage later. The next question is how much of this beam loading voltage will be seen by the bunch. This question is answered by the fundamental theorem of beam loading first derived by P. Wilson [1].

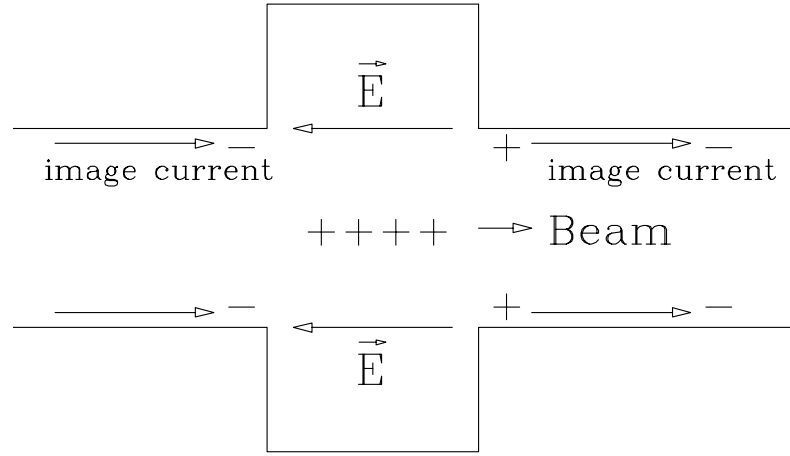


Figure 8.8: As a positively charged bunch passes through a cavity, the image current leaves a negative charge at the upstream end of the cavity gap. As the image current resumes at the downstream side of the cavity, a positive charge is created at the downstream end of the gap because of charge conservation, thus setting up an electric field \vec{E} and therefore the induced beam loading voltage.

8.4.1 Fundamental Theorem of Beam Loading

When a particle of charge q passes through a cavity that is lossless (infinite R_s and infinite Q_0), it induces a voltage V_{b0} which will start to oscillate with the resonant frequency of the cavity. Suppose that the particle sees a fraction f of V_{b0} , which opposes its motion. After half an oscillation of the cavity, a second particle of charge q passes through the cavity. The first induced voltage left by the first is now in the direction of the motion of the second particle and accelerates the particle. At the same time, this second particle will induce another retarding voltage \tilde{V}_{b0} which it will see as a fraction f . This second retarding voltage will cancel exactly the first one inside the cavity, since the cavity is assumed to be lossless. In other words, no field will be left inside the cavity after the passage of the two particles. The net energy gained by the second particle is

$$\Delta E_2 = qV_{b0} - fqV_{b0} , \quad (8.59)$$

while the first particle gains

$$\Delta E_1 = -fqV_{b0} . \quad (8.60)$$

Conservation of energy requires that the total energy gained by the two particles must be zero. This implies $f = \frac{1}{2}$. In other words, the particle sees one half of its transient beam loading voltage, which is the fundamental theorem of beam loading.

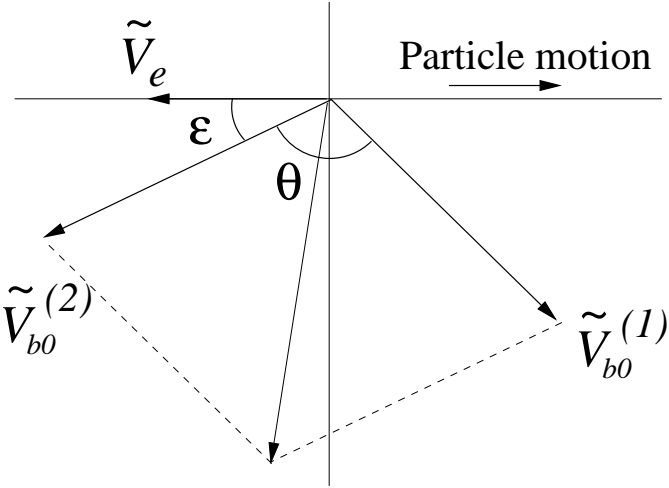


Figure 8.9: Phasor plot showing the instant just after the second passage of the charged particle through the lossless cavity. The induced beam loading voltage phasors for the two passages are labeled as $\tilde{V}_{b0}^{(1)}$ and $\tilde{V}_{b0}^{(2)}$, respectively.

The following is a more general proof by Wilson. The first particle induces a voltage phasor $\tilde{V}_{b0}^{(1)}$ in the lossless cavity which may lie at an angle ϵ with respect to the voltage \tilde{V}_e seen by that particle. As before, we suppose $V_e = fV_{b0}$, where V_e and V_{b0} are the magnitudes of, respectively, \tilde{V}_e and $\tilde{V}_{b0}^{(1)}$. Some time later when the cavity phase changes by θ , the same particle returns via bending magnets or whatever and passes through the cavity again. It induces a second beam loading voltage phasor $\tilde{V}_{b0}^{(2)}$. At this moment, the phasor $\tilde{V}_{b0}^{(1)}$ rotates to a new position as illustrated in Fig. 8.9. The net energy lost by the particle on the two passes is

$$\Delta E = 2fqV_{b0} \cos \epsilon + qV_{b0} \cos(\epsilon + \theta) . \quad (8.61)$$

The cavity, however, gains energy because of the beam loading fields left behind. The energy inside a cavity is proportional to the square of the gap voltage. If the cavity is free of any field to start with, the final energy stored there becomes

$$\Delta E_c = \alpha \left(2V_{b0} \cos \frac{\theta}{2} \right)^2 = 2\alpha V_{b0}^2 (1 + \cos \theta) , \quad (8.62)$$

where α is a proportionality constant. From the conservation of energy, we get

$$2fqV_{b0} \cos \epsilon + qV_{b0} (\cos \epsilon \cos \theta - \sin \epsilon \sin \theta) - 2\alpha V_{b0}^2 (1 + \cos \theta) = 0 . \quad (8.63)$$

Since θ is an arbitrary angle, we obtain

$$\begin{aligned} qV_{b0} \sin \epsilon &= 0 , \\ qV_{b0} \cos \epsilon &= 2\alpha V_{b0}^2 , \\ 2fqV_{b0} \cos \epsilon &= 2\alpha V_{b0}^2 . \end{aligned} \quad (8.64)$$

The first equation gives $\epsilon = 0$ implying that the transient beam loading voltage must have a phase such as to maximally oppose the motion of the inducing charge. Clearly $\epsilon = \pi$ will not be allowed because this leads to the unphysical situation of the particle gaining energy from nowhere. Solving the other two equations, we obtain $f = \frac{1}{2}$.

8.4.2 From Transient to Steady State

Let the bunch spacing be h_b rf buckets or T_b in time. The cavity time constant or filling time is $T_f = 2Q_L/\omega_r$ and the e -folding voltage decay decrement between two successive bunch passages is $\delta_L = T_b/T_f$. During this time period, the phase of the rf fields changes by $\omega_r T_b$ and the rf phase by $\omega_{rf} T_b = 2\pi h_b$. The phasors therefore rotate by the angle $\Psi = \omega_r T_b - 2\pi h_b$, which can also be written in terms of the detuning angle,

$$\Psi = (\omega_r - \omega_{rf})T_b = \delta_L \tan \psi , \quad (8.65)$$

where Eq. (8.24) has been used. The transient beam loading voltage left by the first passage of a short bunch carrying charge q is $V_{b0} = q/C = q\omega_r R_L/Q_L$. The total beam loading voltage V_b seen by a short bunch is obtained by adding up vectorially the beam loading voltage phasors for all previous bunch passages. The result is

$$V_b = \frac{1}{2}V_{b0} + V_{b0} (e^{-\delta_L} e^{j\Psi} + e^{-2\delta_L} e^{j2\Psi} + \dots) , \quad (8.66)$$

where the $\frac{1}{2}$ in the first term on the right side is the result of Wilson's fundamental theorem of beam loading, which states that a particle sees only one-half of its own induced voltage. It is worth pointing out that these voltages are excitations of the cavity and are therefore oscillating at the cavity resonant frequency (all higher order modes of the cavity are neglected). This infinite series of induced voltage phasors is illustrated in Fig. (8.10). The summation can be performed exactly giving the result

$$V_b = V_{b0} [F_1(\delta_L, \psi) + jF_2(\delta_L, \psi)] , \quad (8.67)$$

with

$$F_1 = \frac{1 - e^{-2\delta_L}}{2D} , \quad F_2 = \frac{e^{-\delta_L} \sin(\delta_L \tan \psi)}{D} , \quad (8.68)$$

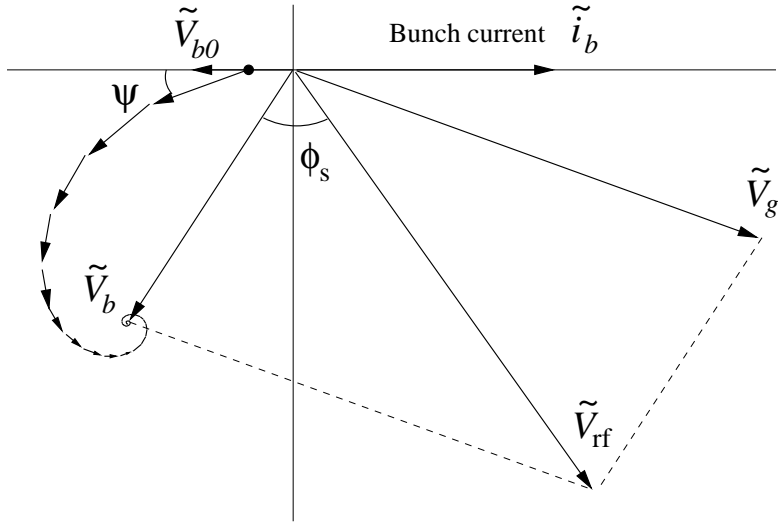


Figure 8.10: Transient beam loading voltages from equally spaced bunches. Each preceding voltage phasor has a phase advance of ψ because of detuning and a decay of $e^{-\delta_L}$. Note that the bunch that is just passing by sees only half of its induced voltage \tilde{V}_{b0} . These voltage phasors add up to the total beam loading voltage phasor \tilde{V}_b . Together with the generator voltage \tilde{V}_g , the cavity gap voltage results at the synchronous angle ϕ_s .

$$D = 1 - 2e^{-\delta_L} \cos(\delta_L \tan \psi) + e^{-2\delta_L} . \quad (8.69)$$

In terms of the coupling constant β and detuning angle ψ , we have

$$\begin{aligned} \tan \psi &= 2Q_L \frac{\omega_r - \omega_{rf}}{\omega_r} , \\ Q_L &= \frac{Q_0}{1 + \beta} , \\ \delta_L &= \delta_0(1 + \beta) , \end{aligned} \quad (8.70)$$

where we have defined $\delta_0 = T_b/T_{f0}$ with T_{f0} being the filling time of the unloaded cavity. Then the single bunch induced beam loading voltage becomes

$$V_{b0} = 2I_0 R_s \delta_0 , \quad (8.71)$$

use has been made of the approximation for short bunches, so that the Fourier component of the current of a bunch at frequency ω_{rf}/h_b is equal to twice its dc value or $i_b = 2I_0$ and $I_0 = q/T_b$. Putting things together, we get

$$V_b = 2I_0 R_s \delta_0 \left[F_1(\delta_0, \beta, \psi) + jF_2(\delta_0, \beta, \psi) \right] , \quad (8.72)$$

with

$$F_1(\delta_0, \beta, \psi) = \frac{1 - e^{-\delta_0(1+\beta)}}{2D}, \quad (8.73)$$

$$F_2(\delta_0, \beta, \psi) = \frac{e^{-\delta_0(1+\beta)} \sin[\delta_0(1+\beta) \tan \psi]}{D}, \quad (8.74)$$

$$D = 1 - 2e^{-\delta_0(1+\beta)} \cos[\delta_0(1+\beta) \tan \psi] + e^{-2\delta_0(1+\beta)}. \quad (8.75)$$

Some comments are in order. Figure 8.10 shows the transient nature of beam loading if the beam loading voltage phasors, that rotate by the angle Ψ and have their magnitudes diminished by the factor $e^{-\delta_L}$ for each successive time period, are excitations of *one* short bunch. However, what we consider is in fact the diminishing beam loading voltage phasors coming from successive bunches that pass through the cavity at successive time periods nT_b earlier with $n = 1, 2, \dots$. For this reason, what Fig. 8.10 shows is actually the steady-state situation of the beam loading voltages, because for each time interval T_b later, we will see exactly the same spiraling beam loading phasor plot and the same total beam loading voltage phasor \tilde{V}_b . Therefore, we can add into the plot the generator voltage phasor \tilde{V}_g in the same way as the plot in Fig. 8.4. In fact, the plot in Fig. 8.4 provides only an approximate steady-state plot, because the beam loading voltage phasor there does attenuate a little bit after a 2π rotation of the phasors, although a high Q_L has been assumed. However, such attenuation has already been taken care of in Fig. 8.10, resulting in the plotting of an exact steady state. When the bunch arrives, the beam loading voltage phasor is \tilde{V}_b as indicated in Fig. 8.10. It rotates counterclockwise and its magnitude decreases because of finite quality factor of the cavity. Just before the arrival of the next bunch, the beam loading voltage phasor becomes $\tilde{V}_b - \frac{1}{2}\tilde{V}_{b0}$. Notice that the beam loading voltage phasor rotates for more than 2π , since $\omega_r > \omega_{rf}$ or the detuning angle ψ is positive in Fig. 8.10. As soon as the next bunch arrives, it jumps by $\frac{1}{2}\tilde{V}_{b0}$ and goes back to \tilde{V}_b . Therefore, the beam loading voltage phasor is not sinusoidal and does not rotate at the speed of ω_{rf} or ω_{rf}/h_b . It approaches sinusoidal only when the jump of the transient beam loading voltage $\frac{1}{2}\tilde{V}_{b0}$ is small and that happens when the loaded quality factor Q_L is large, or when the cavity filling time $T_f = 2Q_L/\omega_r$ is much larger than the time interval T_b between successive bunch passages. On the other hand, the beam loading voltage phasor \tilde{V}_b seen by the bunch in Fig. 8.4 is sinusoidal because it is induced by a sinusoidal component of the beam. In fact, over there, we allow for only one Fourier component.

Using Eq. (8.14), the generator power P_g can now be computed:

$$P_g = \frac{(1 + \beta)^2 V_{\text{rf}}^2}{8\beta R_s \cos^2 \psi} \left\{ \left[\sin \phi_s - \frac{i_b R_s \delta_0}{V_{\text{rf}}} F_1(\delta_0, \beta, \psi) \right]^2 + \left[\cos \phi_s + \frac{i_b R_s \delta_0}{V_{\text{rf}}} F_2(\delta_0, \beta, \psi) \right]^2 \right\}. \quad (8.76)$$

In the situation when the generator current \tilde{i}_g is in phase with the rf voltage \tilde{V}_{rf} , the generator power can be minimized so that there will not be any reflection. Similarly, the generator power can also be optimized by choosing a suitable coupling coefficient β . Unfortunately, these optimized powers cannot be written as simple analytic expressions.

8.4.2.1 Limiting Case with $\delta_0 \rightarrow 0$

When the bunch spacing T_b is short compared to the unloaded cavity filling time T_{f0} , simplified expressions can be written for the total beam loading voltage V_b . One gets

$$F_1(\delta_0, \beta, \psi) = \frac{1}{\delta_0(1 + \beta)(1 + \tan^2 \psi)}, \quad (8.77)$$

$$F_2(\delta_0, \beta, \psi) = \frac{\tan \psi}{\delta_0(1 + \beta)(1 + \tan^2 \psi)}, \quad (8.78)$$

so that

$$V_b = \frac{i_b R_s}{1 + \beta} \frac{1}{1 - j \tan \psi}. \quad (8.79)$$

Notice that this is exactly the same expression in Eq. (8.25). In fact, this is to be expected, because we are in the situation of $T_b \ll T_f$, or the case of a high Q_L resonating cavity.

In the absence of detuning, the beam loading voltages left by previous bunches just added up to give

$$V_b = \frac{V_{b0}}{2} \frac{1 + e^{-\delta_L}}{1 - e^{-\delta_L}}. \quad (8.80)$$

For a high- Q_L cavity, this becomes

$$V_b = \frac{V_{b0}}{\delta_L} = i_b R_L, \quad (8.81)$$

which is the maximum beam loading voltage seen by the beam.

When $\delta_0 \rightarrow 0$, the phase angle $\Psi = \delta_0(1 + \beta) \tan \psi \rightarrow 0$, although the detuning ψ may be finite. Thus, the transient beam loading voltage \tilde{V}_{b0} will not decay and will

also line up for successive former bunch passages, leading to an infinite total beam loading voltage V_b seen by the bunch. However, $\delta_0 \rightarrow 0$ implies letting $Q_0 \rightarrow \infty$ while keeping the shunt impedance fixed. Thus, the instantaneous beam loading voltage $V_{b0} = q/C = q\omega_r R_s/Q_0 = 2i_b R_s \delta_0$ also goes to zero, implying that the summation has to be done with care. For successive V_{b0} 's to wrap around in a circle, one needs approximately $2\pi/\Psi$ V_{b0} 's. The radius of this circle will be V_{b0}/Ψ . As $\delta_0 \rightarrow 0$, this radius becomes

$$\lim_{\delta_0 \rightarrow 0} \frac{V_{b0}}{\Psi} = \frac{2i_b R_s}{\tan \psi}, \quad (8.82)$$

which is finite. In fact, this is roughly the same as the total beam loading voltage V_b as $\delta_0 \rightarrow 0$.

During bunch-to-bunch injection, the transient beam loading voltage in the cavity will add up gradually as is indicated in the spiral in Fig. 8.10. Thus, if the decay decrement is small, the total beam loading voltage will reach a maximum roughly equal to twice the voltage given by Eq. (8.72) before spiraling to its limiting value. The maximum beam loading voltage will be twice the value given by Eq. (8.79) as if the shunt impedance has been doubled.

8.4.2.2 Limiting Case with $T_b \gg T_f$

This is the situation when the instantaneous beam loading voltage decays to zero before a second bunch comes by. It is easy to see that $F_1(\delta_0, \beta, \psi) \rightarrow \frac{1}{2}$ and $F_2(\delta_0, \beta, \psi) \rightarrow 0$. From Eq. (8.76), it is clear that the generator power increases rapidly as the square of δ_0 . This is easy to understand, because the rf power that is supplied to the cavity gets dissipated rapidly. A pulse rf system will then be desirable. In such a system, the power is applied to the cavity for about a filling time preceding the arrival of the bunch. For most of the time interval between bunches, there is no stored energy in the cavity at all and hence no power dissipation.

8.4.3 Transient Beam Loading of a Bunch

When a bunch of linear density $\rho(\tau)$ passes through a cavity gap, electromagnetic fields are excited. The beam loading retarding voltage seen by a particle at time τ ahead of

the bunch center is given by

$$V(\tau) = \int_{\tau}^{\infty} q\rho(\tau') W'_0(\tau' - \tau) d\tau' , \quad (8.83)$$

where q is the total charge in the bunch, $\rho(\tau)$ is normalized to unity when integrated over τ , and $W'_0(\tau)$ is the wake potential left by a point charge at a time τ ago. If we approximate the cavity as a RLC parallel circuit with angular resonant frequency ω_r , loaded quality factor Q_L , and loaded shunt impedance R_L , the wake potential can be written as, for $\tau > 0$,

$$W'_0(\tau) = \frac{\omega_r R_L}{Q_L} e^{-\alpha\tau} \left[\cos \bar{\omega}\tau - \frac{\alpha}{\bar{\omega}} \sin \bar{\omega}\tau \right] . \quad (8.84)$$

For $\tau < 0$, $W'_0(\tau) = 0$ because of causality. For $\tau = 0$, $W'_0(\tau) = \omega_r R_L / (2Q_L)$ because of the fundamental theorem of beam loading. In above, the decay rate α and the shifted resonant angular frequency $\bar{\omega}$ are given by

$$\alpha = \frac{\omega_r}{2Q_L} \quad \text{and} \quad \bar{\omega} = \sqrt{\omega_r^2 - \alpha^2} . \quad (8.85)$$

Notice that this is exactly the same wake potential we studied in Eq. (1.48) of Exercise 1.3. For the convenience of derivation, we introduce the loss angle θ which is defined as[‡]

$$\cos \theta = \frac{\bar{\omega}}{\omega_r} \quad \text{and} \quad \sin \theta = \frac{\alpha}{\omega_r} . \quad (8.86)$$

With this introduction, the wake potential can be conveniently rewritten as

$$W'_0(\tau) = \frac{\omega_r R_L}{Q_L \cos \theta} \operatorname{Re} e^{i(e^{i\theta} \omega_r \tau + \theta)} . \quad (8.87)$$

The first application is for a point bunch with distribution $\rho(\tau) = \delta(\tau)$. Substitution into Eq. (8.83) gives $V(\tau) = qW'_0(-\tau)$, or

$$V(\tau) = \begin{cases} 0 & \tau > 0 , \\ \frac{q\omega_r R_L}{2Q_L} & \tau = 0 , \\ \frac{q\omega_r R_L}{Q_L \cos \theta} \operatorname{Re} e^{i(e^{i\theta} \omega_r \tau + \theta)} & \tau < 0 . \end{cases} \quad (8.88)$$

Thus, the head of the bunch ($\tau = 0+$) sees no beam loading voltage. The tail of the bunch ($\tau = 0-$) sees the transient beam loading voltage $V_{b0} = q/C$ as given by Eq. (8.58). The center of the bunch sees one half of V_{b0} .

[‡]If one prefers, this angle can also be defined as $\cos \theta = \alpha/\omega_r$ and $\sin \theta = \bar{\omega}/\omega_r$.

8.4.3.1 Gaussian Distribution

Consider a Gaussian distributed bunch of rms length σ_τ . The linear density is

$$\rho(\tau) = \frac{1}{\sqrt{2\pi}\sigma_\tau} e^{-\tau^2/(2\sigma_\tau^2)}. \quad (8.89)$$

The beam loading voltage experienced by a beam particle at distance τ ahead the bunch center is (Exercise 8.5)

$$V(\tau) = \frac{q\omega_r R_L}{2Q_L \cos \theta} \mathcal{R}e e^{i\theta - \tau^2/(2\sigma_\tau^2)} w\left(\frac{\sigma_\tau \omega_r e^{i\theta}}{\sqrt{2}} + \frac{i\tau}{\sqrt{2}\sigma_\tau}\right), \quad (8.90)$$

where q is the total charge in the bunch and w is the complex error function defined as

$$w(z) = e^{-z^2} \left[1 + \frac{2i}{\sqrt{\pi}} \int_0^z e^{t^2} dt \right]. \quad (8.91)$$

It can be readily shown that as the bunch length shortens to zero, the head, center, and tail of the bunch are seeing the transient beam loading voltage (Exercise 8.5)

$$V(\tau) = \begin{cases} 0 & \tau = 0 + \text{ (head) ,} \\ \frac{q\omega_r R_L}{2Q_L} & \tau = 0 \quad \text{ (center) ,} \\ \frac{q\omega_r R_L}{Q_L} & \tau = 0 - \text{ (tail) ,} \end{cases} \quad (8.92)$$

exactly the same result for a point bunch. In fact, Eq. (8.92) just serves as another proof of the fundamental theorem of beam loading that the test charge sees one half of its own beam loading voltage. This proof is more general than those presented in the previous subsection, because it involves a lossy cavity or a cavity with a finite quality factor Q_L .

The beam loading voltages of a Gaussian bunch are plotted in Fig. 8.11. They are all normalized to $q\omega_r R_L / Q_L$, which is the beam loading voltage when the bunch is contracted to a point. Each curve is identified by two parameters: (Q_L, F) , where $F = \sqrt{6}\omega_r\sigma_\tau/\pi$ is roughly the fraction of the rf wavelength occupied by the bunch, since we usually equate the half 95% Gaussian bunch length to $\sqrt{6}\sigma_\tau$. The horizontal coordinate is the distance of the test particle ahead the bunch center in units of σ_τ , the rms bunch length. We notice that as the bunch becomes shorter, the beam loading voltage becomes larger. When it becomes very short, the curve with $(1, 0.01)$, we recover the

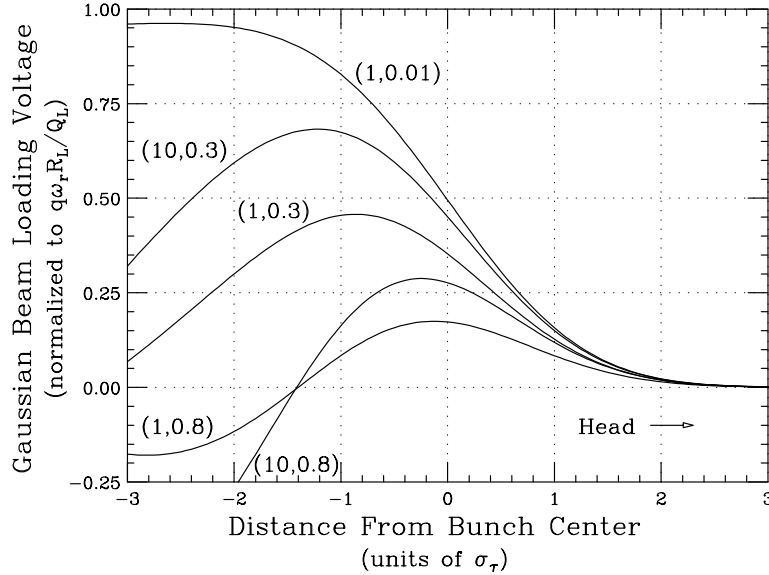


Figure 8.11: The beam loading voltage, normalized to $q\omega_r R_L / Q_L$, of a bunch with Gaussian distribution seen by a particle at distance τ/σ_τ ahead the bunch center, where σ_τ is the bunch rms length and q the total charge in the bunch. Each curve is labeled by (Q_L, F) , where $F = \sqrt{6}\omega_r\sigma_\tau/\pi$ is roughly the fraction of the rf wavelength occupied by the bunch, and Q_L , R_L , and $\omega_r/(2\pi)$ are, respectively, the loaded quality factor, loaded shunt impedance, and resonant frequency of the cavity.

results in Eq. (8.92) that a particle at the center of the bunch sees one half of the bunch beam loading voltage. When the quality factor of the cavity becomes larger, the beam loading voltage does not decay as fast and its reduced amplitude is therefore closer to unity. We also notice that the beam loading voltage seen by each particle in the bunch varies along the bunch. This result is important, because it is difficult to compensate for the beam loading voltage to every point along the bunch.

8.4.3.2 Parabolic Distribution

Consider a bunch with parabolic distribution,

$$\rho(\tau) = \frac{3}{4\hat{\tau}} \left(1 - \frac{\tau^2}{\hat{\tau}^2} \right) \quad |\tau| \leq \hat{\tau}, \quad (8.93)$$

where $\hat{\tau}$ is the half bunch length. As the bunch of total charge q passes through a cavity, the transient beam loading voltage seen by a particle at a distance T behind the head

of the bunch is (Exercise 8.6), for $T \leq 2\hat{\tau}$,

$$V(T) = \frac{q\omega_r R_L}{Q_L} \frac{3p^2}{2\pi^2 \cos \theta} \left\{ \frac{p}{\pi} [\omega_r(\hat{\tau} - T) \cos \theta + \sin 2\theta] + e^{-\alpha T} \left[\sin(\bar{\omega}T - 2\theta) - \frac{p}{\pi} \cos(\bar{\omega}T - \theta) \right] \right\}, \quad (8.94)$$

and for $T > 2\hat{\tau}$,

$$V(T) = \frac{q\omega_r R_L}{Q_L} \frac{3p^2}{2\pi^2 \cos \theta} \left\{ e^{-\alpha(T-2\hat{\tau})} \left[\frac{p}{\pi} \sin(\bar{\omega}(T-2\hat{\tau}) - 2\theta) - \cos(\bar{\omega}(T-2\hat{\tau}) - \theta) \right] + e^{-\alpha T} \left[\sin(\bar{\omega}T - 2\theta) - \frac{p}{\pi} \cos(\bar{\omega}T - \theta) \right] \right\}, \quad (8.95)$$

where

$$p = \frac{\pi}{\omega_r \hat{\tau}}. \quad (8.96)$$

Beside the normalization factor $q\omega_r R_L / Q_L$, the beam loading voltage depends on two parameters: $\omega_r \hat{\tau}$ and the loaded quality factor Q_L .

Figure 8.12 shows the beam loading voltage seen by a bunch with parabolic distribution. The normalization is also to $q\omega_r R_L / Q_L$. The horizontal coordinate is the fractional distance $T/(2\hat{\tau})$ of the test particle behind the head of the bunch. Each voltage curve is labeled by the two parameters (Q_L, F) , where $F = \omega_r \hat{\tau} / \pi = 1/p$ is the ratio of the total bunch length to the rf wavelength. All the comments of the beam loading voltage of the Gaussian bunch apply here also.

8.4.3.3 Cosine-Square Distribution

Consider a bunch with cosine-square linear distribution,

$$\rho(\tau) = \frac{1}{\hat{\tau}} \cos^2 \frac{\pi \tau}{2\hat{\tau}} \quad |\tau| \leq \hat{\tau}, \quad (8.97)$$

where $\hat{\tau}$ is the half bunch length. As the bunch of total charge q passes through a cavity, the transient beam loading voltage seen by a particle at a distance T behind the head

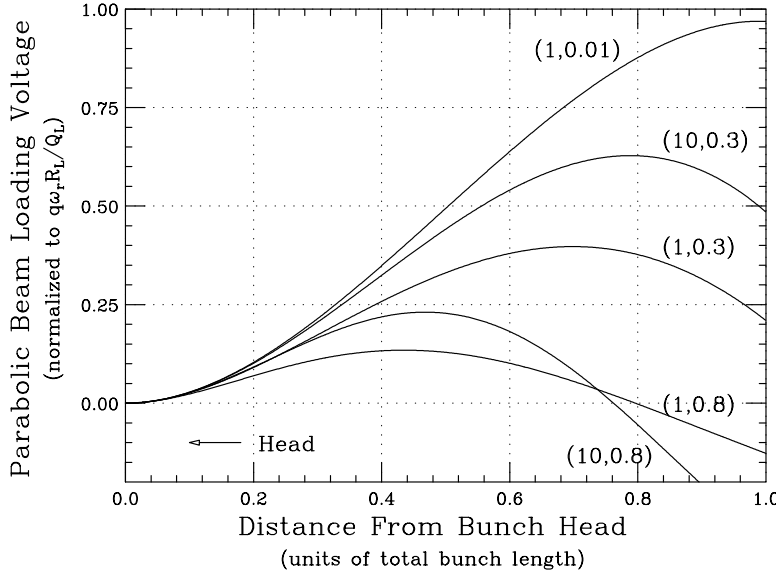


Figure 8.12: The beam loading voltage, normalized to $q\omega_r R_L / Q_L$, of a bunch with parabolic distribution seen by a particle at distance $T/(2\hat{\tau})$ behind of the head of the bunch, where $2\hat{\tau}$ is the total bunch length and q the total charge in the bunch. Each curve is labeled by (Q_L, F) , where $F = \omega_r \hat{\tau} / \pi$ is the fraction of the rf wavelength occupied by the bunch, and Q_L , R_L , and $\omega_r/(2\pi)$ are, respectively, the loaded quality factor, loaded shunt impedance, and resonant frequency of the cavity.

of the bunch is (Exercise 8.6), for $T \leq 2\hat{\tau}$,

$$V(T) = \frac{q\omega_r R_L}{Q_L} \frac{p^2}{2\pi D \cos \theta} \left\{ (1 - p^2) \sin \frac{\pi(\hat{\tau} - T)}{\hat{\tau}} \cos \theta + p \cos \frac{\pi(\hat{\tau} - T)}{\hat{\tau}} \sin 2\theta + p^3 e^{-\alpha T} \sin \bar{\omega} T - p e^{-\alpha T} \sin(\bar{\omega} T - 2\theta) \right\}, \quad (8.98)$$

and for $T > 2\hat{\tau}$,

$$V(T) = \frac{q\omega_r R_L}{Q_L} \frac{p^2}{2\pi D \cos \theta} \left\{ p e^{-\alpha(T - 2\hat{\tau})} \sin [\bar{\omega}(T - 2\hat{\tau}) - 2\theta] - p^3 e^{-\alpha(T - 2\hat{\tau})} \sin \bar{\omega}(T - 2\hat{\tau}) + p^3 e^{-\alpha T} \sin \bar{\omega} T - p e^{-\alpha T} \sin(\bar{\omega} T - 2\theta) \right\}, \quad (8.99)$$

where p is given by Eq. (8.96) and

$$D = 1 - 2p^2 \cos 2\theta + p^4. \quad (8.100)$$

Besides the factor outside the curly brackets, the beam loading voltage depends on two parameters: $\omega_r \hat{\tau}$ and the loaded quality factor Q_L .

Figure 8.13 shows the beam loading voltage seen by a bunch with cosine-square distribution. The normalization is also to $q\omega_r R_L / Q_L$. The test particle is at the fractional distance $T/(2\hat{\tau})$ behind the head of the bunch. We labeled each reduced beam loading voltage curve by (Q_L, F) , where $F = \omega_r \hat{\tau} / \pi = 1/p$ is the ratio of the total bunch length to the rf wavelength. All the comments concerning the beam loading voltage of the Gaussian bunch apply to here as well.

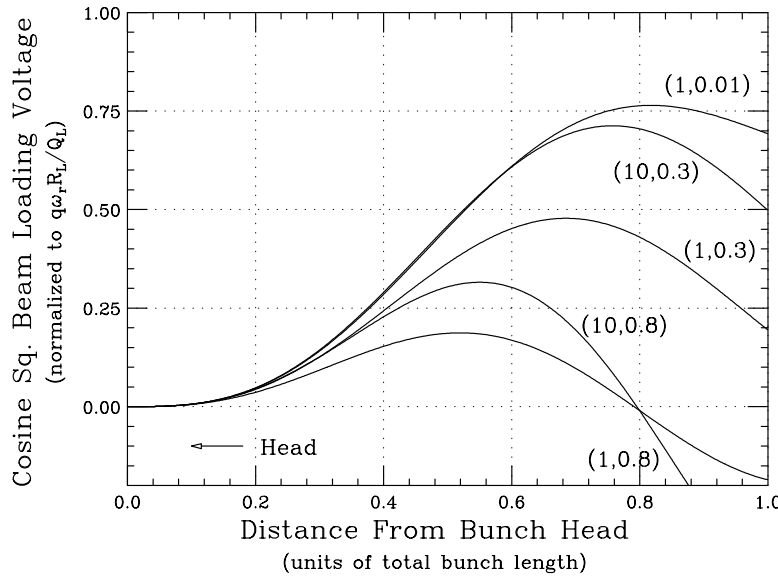


Figure 8.13: The beam loading voltage, normalized to $q\omega_r R_L / Q_L$, of a bunch with cosine-square distribution seen by a particle at distance $T/(2\hat{\tau})$ behind the head of the bunch, where $2\hat{\tau}$ is the total bunch length. Each curve is labeled by (Q_L, F) , where $F = \omega_r \hat{\tau} / \pi$ is the fraction of the rf wavelength occupied by the bunch, and Q_L , R_L , and $\omega_r / (2\pi)$ are, respectively, the loaded quality factor, loaded shunt impedance, and resonant frequency of the cavity.

8.4.3.4 Cosine Distribution

Consider a bunch with cosine linear distribution,

$$\rho(\tau) = \frac{\pi}{4\hat{\tau}} \cos \frac{\pi\tau}{2\hat{\tau}} \quad |\tau| \leq \hat{\tau}, \quad (8.101)$$

where $\hat{\tau}$ is the half bunch length. As the bunch of total charge q passes through a cavity, the transient beam loading voltage seen by a particle at a distance T behind the head

of the bunch is (Exercise 8.6), for $T \leq 2\hat{\tau}$,

$$V(T) = \frac{q\omega_r R_L}{Q_L \cos \theta} \frac{p^2}{8D} \left\{ \left(1 - \frac{p^2}{4} \right) \cos \frac{\pi T}{2\hat{\tau}} \cos \theta + \frac{p}{2} \sin \frac{\pi T}{2\hat{\tau}} \sin 2\theta + e^{-\alpha T} \left[\frac{p^2}{4} \cos(\bar{\omega}T + \theta) - \cos(\bar{\omega}T + \theta) \right] \right\}, \quad (8.102)$$

and for $T > 2\hat{\tau}$,

$$V(T) = \frac{q\omega_r R_L}{Q_L \cos \theta} \frac{p^2}{8D} \left\{ e^{-\alpha(T-2\hat{\tau})} \left[\frac{p^2}{4} \cos(\bar{\omega}(T-2\hat{\tau}) + \theta) - \cos(\bar{\omega}(T-2\hat{\tau}) - \theta) \right] + e^{-\alpha T} \left[\frac{p^2}{4} \cos(\bar{\omega}T + \theta) - \cos(\bar{\omega}T + \theta) \right] \right\}. \quad (8.103)$$

where p and D are given by Eqs. (8.96) and (8.100). Besides the factor outside the curly brackets, the beam loading voltage depends on two parameters: $\omega_r \hat{\tau}$ and the loaded quality factor Q_L .

Figure 8.14 shows the beam loading voltage seen by a bunch with cosine-square distribution. The normalization is also to $q\omega_r R_L / Q_L$. The test particle is at the fractional distance $T\omega_r/(2\pi)$ behind the head of the bunch, or the time is normalized to an rf wavelength. The reduced beam loading voltage depends on two parameters: $\omega_r \hat{\tau}$ and the loaded quality factor Q_L . We labeled each reduced beam loading voltage curve by (Q_L, F) , where $F = \omega_r \hat{\tau} / \pi = 1/p$ is the ratio of the total bunch length to the rf wavelength. All the comments concerning the beam loading voltage of the Gaussian bunch apply to here as well. Both curves are for the high quality factor $Q_L = 5000$. For the example of $F = 0.3$, the reduced transient beam loading voltage has a maximum of 0.681 within the bunch length and later rings for a long time at the frequency $\omega_r/(2\pi)$ of the cavity with an amplitude 0.918 decaying very slowly. This amplitude is roughly equal to $I_1/(2I_0)$, where I_1 is the rf component of the bunch current and I_0 is the average bunch current. Because the e -folding decaying time is Q_L/π rf buckets, the bunch is seeing these ringing amplitudes left by its predecessors. For a ring with all buckets occupied, the beam loading voltage seen by a bunch is

$$V_b = \frac{q\omega_r R_L}{Q_L} [A + B(1 + e^{-\delta_L} + e^{-2\delta_L} + \dots)], \quad (8.104)$$

where δ_L is the decay decrement. Here, A denotes the portion of the beam loading voltage excited instantaneously by the bunch crossing the cavity gap while B denotes

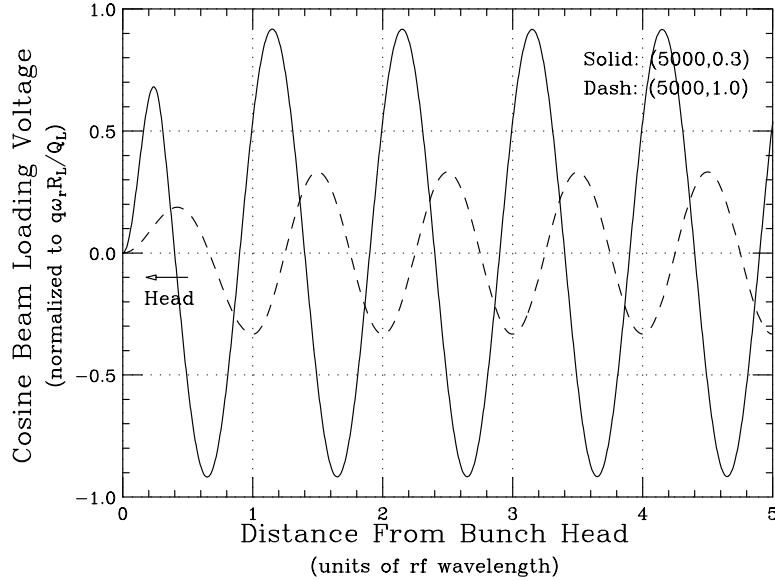


Figure 8.14: The beam loading voltage, normalized to $q\omega_r R_L / Q_L$, of a bunch with cosine distribution seen by a particle at distance T (normalized to the rf wavelength) behind the head of the bunch. Each curve is labeled by (Q_L, F) , where $F = \omega_r \hat{\tau} / \pi$ is the fraction of the rf wavelength occupied by the bunch, and Q_L , R_L and $\omega_r / (2\pi)$ are, respectively, the loaded quality factor, loaded shunt impedance, and resonant frequency of the cavity.

whatever left by the previous crossings. Comparing with Eq. (8.66) for a point bunch ($F = 1$), we have $A = \frac{1}{2}$ and $B = 1$. For a bunch of finite extent, for example $F = 0.3$ in the cosine distribution, we have $A = 0.681$ and $B = I_1/(2I_0) = 0.918$. For a high Q_L , it is the second term that dominates. We can conclude that compared with a point bunch, a distributed bunch of finite length will have its beam loading voltage lowered only by a small amount, i.e., by the fraction $I_1/(2I_0)$.

The situation of $F = 1$ is very special and is represented by the dashed curve. Here, the bunch is as long as the rf wavelength. In fact, the situation corresponds to a bunch filling the rf bucket uniformly. Although the first maximum is $A \sim 0.2$, the actual ringing amplitude is roughly $B \approx 0.33$. It is easy to show that $I_1/(2I_0) = 1/3$. In other words, even when the bunch fills up the bucket, the beam loading voltage is decreased by a factor of only 3.

We plot in Fig. 8.15 $I_1/(2I_0)$ as functions of F , the total bunch length in units of rf wavelength, for various bunch distribution. We see that when the bunch is short, $I_1/(2I_0)$

drops very slowly with F and is distribution weakly-dependent only when the bunch is long. When the total bunch length equal the bucket length or $F = 1$, $I_1/(2I_0) = 1/2$, $\exp(-\pi^2/16)$, $1/3$, and $3/\pi^2$, respectively, for the cosine-square, Gaussian, cosine, and parabolic distribution.

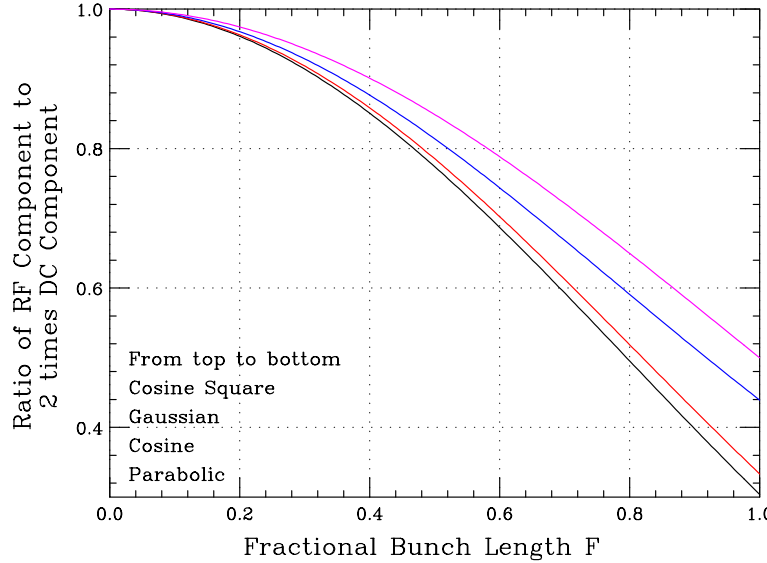


Figure 8.15: Ratio of the rf component of the bunch to two times the dc component, $I_1/(2I_0)$, as functions of F , total bunch length in units of bucket length, for, from top to bottom, cosine-square, Gaussian, cosine, and parabolic distributions.

8.4.4 Transient Compensation

We are going to give a short overview of some methods to cope with transient beam loading. The serious readers are referred to the references for further reading.

For a ring in the storage mode with all rf buckets filled with bunches of equal charges, each bunch is seeing exactly the same beam loading voltage, except for the influence of its small amount of synchrotron motion. We say that the beam loading is in the steady state and compensation can be made by detuning the cavity if the beam intensity is not too high.

However, the beam loading in many circumstances is in the transient state when there is a sudden change in beam intensity. One example is injection when bunches are

injected one by one. The beam loading voltage inside the rf cavity will increase linear with time, and the beam loading voltage seen by a bunch depends on time as well as its location along the ring. Obviously, slow extraction of an intense beam will also lead to sudden changes in the beam loading voltage. Another example is a gap left in an accelerator ring to allow for the firing of the injection and extraction kickers. Such a gap is also beneficial in clearing particles of opposite charge trapped inside the beam in order to eliminate collective two-stream instability. In the presence of a gap, the total beam loading voltage experienced in a cavity will be different during different bunch passages. For example, the bunch just after the gap will see the smallest beam loading voltage and the bunch just preceding the gap will see the most. As a result, the last bunch in the bunch train or batch will always see a lower rf voltage than the first bunch. At best, there will be a synchronous phase difference between the bunches leading to increase in longitudinal bunch area. At worst, the final bunches of the batch will not have enough voltage for stability. Strictly speaking, the word *transient* has been used wrongly for the problem of a gap, because such an effect occurs even when the stored beam is in the steady state. The uneven beam loading voltage experienced by the different bunches in the batch is a result of having many frequency components in the beam loading voltage besides the ones at the rf frequency and its multiples. Because of this, we should define the term *transient beam loading* as effects at frequencies other than the fundamental rf, its multiples, and their synchrotron sidebands.

One way to reduce beam loading, either steady-state or transient, is to reduce the loaded shunt impedance R_L of the cavity seen by the beam [9]. An obvious method is to add a resistance in parallel. Although this reduces the voltage created by both the beam and the power amplifier, however, the power requirements of the amplifier are increased. If the power amplifiers are already operating at their capacity, this is not an applicable solution.

Another possibility for reducing the beam loading voltage generated by the beam is to have another power amplifier to supply an additional generator current I_g equal and opposite to the beam image current. These two currents cancel each other at the cavity gap, making the cavity look like a short circuit to the beam. This method is very fast because there is no need to fight against the filling time of the cavity since there is no net current flowing across the cavity gap at all and therefore no additional fields created inside the cavity. This is a powerful but expensive solution due to the extra amplifier required. It is called high-level feed-forward compensation and is applicable for fixed rf frequency only. It was added to the CERN Intersecting Storage Ring (ISR)

rf system not so much to improve stability but due to a power limitation in the rf power amplifier. It can be shown [3] that the extra power required can become halved if the cavity is halfly pretuned before the injection so that the peak powers before and after injection are the same. In other words, the power is unmodulated even when the beam is fully modulated. The required power can be lowered by a factor of two again if there is optimum matching between the rf generator and the cavity. This can be accomplished by having a circulator inserted between the rf power and the cavity so that the additional current for the beam loading compensation means also real power.

To avoid high power consumption, there are also methods for low-level compensation. One technique is referred to as *feed-forward* [10]. The bunch current at a location preceding the cavity in the accelerator ring is measured and the signal is added to the low-level rf drive of the power amplifier so that an additional generator current I_g equal and opposite beam current is generated at the time the bunch crosses the cavity gap, as illustrated in Fig. 8.16. Experience and analysis show a dramatic increase in the

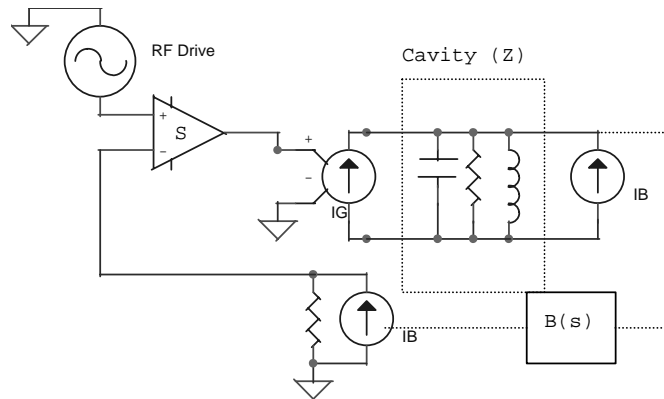


Figure 8.16: Block diagram of direct rf feed-forward, where $B(s)$ is the beam response and S is the transconductance of the amplifier.

instability threshold. This scheme has been successfully applied in the CERN Proton Synchrotron (PS) and the CERN Proton Synchrotron Booster (PSB). The instability threshold can probably be raised an order of magnitude. This is because the cavity voltage is completely decoupled from the beam signal, which nullifies the Robinson's instability. However, it is difficult to apply when the rf frequency is varying. The feed-back path through the beam response is fairly weak, so the risk of creating an unstable system response is low. However, with a weak feedback, any errors in the system will not be compensated, so it is very important that the delay and phase advance of the

systems are properly tuned for beam cancellation. In practice, maintaining an error free system is very difficult when large amounts of impedance reduction is required.

A second technique of reducing the cavity impedance is amplifier feedback. The voltage in the cavity is measured, amplified and added to the low-level rf drive, as is illustrated in Fig. 8.17. To compute the impedance seen by the beam, the input at the

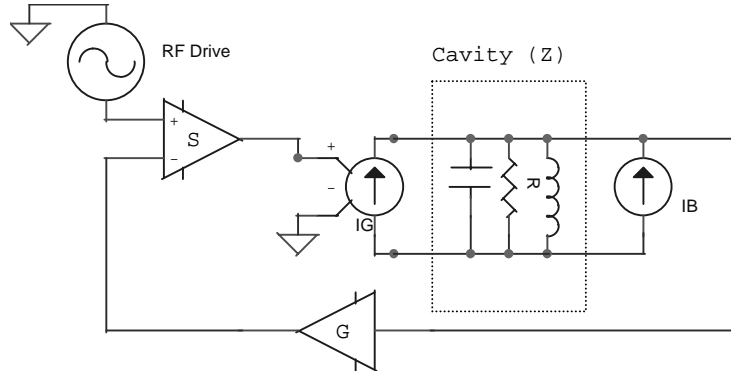


Figure 8.17: Block diagram of direct rf feedback, where the amplifier gain is G and the transconductance is S . The effective impedance seen by the beam is reduced from R_L to $R_L/(1 + SGR_L)$.

generator is turned off. The cavity voltage is amplified to GV_{rf} where G is the gain. It is then transformed into a current $-SGV_{\text{rf}}$ through the transconductance S . This current is next fed through the generator and produces the additional gap voltage $-SGV_{\text{rf}}Z$, giving a total gap voltage of $V_{\text{rf}} = V_b - SGV_{\text{rf}}Z$, where $V_b = R_L i_b$ is the beam loading voltage produced by the beam current i_b in the absence of the feedback loop. The effective impedance experienced by the beam becomes

$$R_{\text{eff}} = \frac{R_L}{1 + SGR_L} , \quad (8.105)$$

where $H = SGR_L$ is called the open loop gain. Thus, by increasing the gain, the shunt impedance can be largely reduced. The main feedback path for this system no longer includes the beam response, and it is much stronger. The low-level feedback is very fast and the delay just depends on the length of the cables of the feedback loop. This is the most powerful method known and can be applied even for varying rf frequency. It has been applied to the CERN ISR at 9.5 MHz with $H = 60$, the CERN Antiproton Accumulator at 1.85 MHz with $H = 120$, and the CERN PSB at 6 to 16 MHz with $H = 5$ to 12.

In addition, there are a number of feedback loops in an rf accelerating system to assure that the particle beam will be accelerated according to the prescribed ramp design and to guarantee stability even when the Robinson's stability limit is exceeded. In the rf system of the former Fermilab Main Ring, for example, there are five feedback loops: [11]

- (1) Rf frequency control loop, which compares the beam bunch phase versus rf phase comparitor and output an error signal. It is dc coupled with very low bandwidth. rf frequency.

- (2) Beam radial position control loop, which controls the radial position of the beam by making small adjustment to the synchronous phase angle. It is dc coupled with bandwidth about 10 kHz.

- (3) Correction loop for cavity gap voltage phase versus generator voltage phase. It is ac coupled with 5 MHz bandwidth and is capable of fast adjustment of cavity excitation phase to compensate for transient beam loading effects.

- (4) Cavity voltage amplitude control loop, which adjusts the generator current such that the rf voltage amplitude developed at the cavity gap equals to its prescribed value. It has a very high dc gain (~ 60 db) and corner frequency 5 Hz.

- (5) Detuning loop, which monitors the load angle between the generator current and the cavity gap voltage and adjusts the cavity tuning through ferrite biasing so that the load impedance presented to the generator appears to be real. It has a high dc gain (~ 60 db) with low bandwidth and corner frequency 1 Hz.

Among these, the second and third loops are the fastest, while the detuning loop is the slowest. These loops are not only limited by their gains, because they are only independent when the beam intensity is low. As the beam intensity increases, they become coupled and gradually lose their function.

For large rf systems, long delays may be unavoidable and the conventional rf feedback would have a too restricted bandwidth, may be much smaller than the cavity bandwidth itself. However, in the spectrum of transient beam loading, it is only those revolution harmonic lines that require nullification, and there is nothing in between the harmonics. With a return path transfer function having a comb-filter shape with maxima at every revolution harmonic, this condition can be satisfied. The overall delay of the system must be extended to exactly one machine turn to ensure the correct phase at the harmonics. Nullifying the beam signals at the revolution harmonics other than the fundamental rf frequency cures the transient beam loading.

8.4.4.1 Coupled-Bunch Instabilities

As will be discussed in Chapter 9, narrow resonances located at the synchrotron sidebands may excite longitudinal coupled-bunch instabilities. Although these narrow resonances originate mostly from the higher-order modes of the cavities, some may also come from the revolution harmonics of the beam loading voltage excited because of having asymmetric fill in the stored beam. These harmonic lines have finite widths due to energy spread of the bunches and the synchrotron oscillations that develop because of the rf phase offsets. Thus, these harmonic components of the beam loading voltage can drive coupled-bunch instabilities and their nullification through comb-filter shape feedback is very essential.

Even for a ring of bunches with asymmetric gaps, the detuning of the cavities may also drive coupled bunch instabilities. This happens for a large machine where the revolution frequency f_0 is low. Detuning can very often shift the peak of the intrinsic resonant frequency of the cavities by more than one or more revolution harmonic. Here, we use a design of the former Superconducting Super Collider (SSC) as an example [5]. The average beam current is $I_0 = 0.073$ A. and a 374.7-MHz rf system is chosen. There are 8 cavities each having a shunt impedance $R_L = 2.01$ MΩ and $R_L/Q_L = 125$ Ω, or $Q_L = 1.608 \times 10^4$. At storage, the rf gap voltage per cavity is $V_{\text{rf}} = 0.5$ MV. Thus the required detuning is given by

$$2Q_L \frac{\omega_r - \omega_{\text{rf}}}{\omega_r} = \tan \psi = \frac{i_i m \cos \phi_s}{i_0} . \quad (8.106)$$

At $\phi_s \approx \pi$ and using short-bunch approximation, we obtain

$$\frac{\omega_r - \omega_{\text{rf}}}{\omega_r} = -\frac{i_{\text{im}} R_L}{2V_{\text{rf}} Q_L} = -0.183 \times 10^{-4} , \quad (8.107)$$

or a detuning of $\Delta f_r = -6.84$ kHz. The half bandwidth of the loaded cavity is $\Delta f = f_r/(2Q_L) = 11.68$ kHz. However the revolution frequency of the collider ring is only $f_0 = 3.614$ kHz. In other words, the resonant impedance of the cavities would occur at a frequency slightly greater than $f_{\text{rf}} - 2f_0$ and have a spread covering about 10 revolution harmonics. Such impedance could drive longitudinal coupled-bunch instabilities with considerable strength. If we compute this with the Fermilab Main Ring at a total of 3.25×10^{13} protons in the ring, we find that $|\Delta f_r/f_f| = 1.33 \times 10^{-4}$ or $|\Delta f_r| = 7.1$ kHz during acceleration, while the half bandwidth of the cavities is ~ 4.4 kHz. These numbers are very much less than the revolution frequency $f_0 = 47.7$ kHz. On the other hand, the

200-MHz traveling-wave accelerating structures in the CERN Super Proton Synchrotron (SPS) have a considerable bandwidth so that the impedance at $f_{\text{rf}} \pm nf_0$ for small n is appreciable. Coupled-bunch instabilities arising from this impedance have been reported [6]. This also happens in the Low Energy Ring (LER) of the SLAC B-factory. Matching the klystron to the rf cavities requires the cavity be detuned to a frequency near $f_{\text{rf}} - 1.5f_0$, thus driving longitudinal coupled-bunch instabilities [7] in modes -1 and -2 . Longitudinal coupled-bunch instabilities are usually alleviated by damping passively the driving resonances in the cavity or employing a mode damper. Here, the problem is quite different. First, we cannot damp this fundamental mode passively because we require it to supply energy to the beam. Second, usually the higher-order resonances that drive the coupled-bunch instabilities are much weaker than the fundamental. However, it is the fundamental that drives the coupled-bunch instabilities here. In other words, a very much powerful damper will be necessary to remove the instabilities. Because of this complication, a solution to this problem proposed in the SSC Conceptual Design Report is not to detune the cavity at the expense of increasing the required rf power.

8.5 Examples

8.5.1 Fermilab Main Ring

Once the former Fermilab Main Ring operated above transition in $M = 567$ consecutive bunches with total intensity 5×10^{13} protons. The ring consisted of $h = 1113$ rf buckets and the rf frequency was $\omega_r/(2\pi) = 53.09$ MHz. There were 15 rf cavities, each of which had a loaded shunt impedance of $R_L = 500$ k Ω and the loaded quality factor was $Q_L = 5000$.

At steady state, the k th bunch in a bunch train of M bunches sees a beam loading voltage of (Exercise 8.7)

$$V_{bk} = V_0 e^{-(k-1)\delta_L} + V_{b0} \left(\frac{1}{2} + e^{-\delta_L} + \dots + e^{-(k-1)\delta_L} \right), \quad (8.108)$$

where $\delta_L = \pi/Q_L$ is the decay decrement,

$$V_{b0} = \frac{qB\omega_r R_L}{Q_L} \quad (8.109)$$

is the transient beam loading voltage left by a bunch carrying charge q , B is a parameter defined in Eq. (8.104) to take care of the fact that the bunch has a finite length, and is

equal to the current component at the rf frequency divided by twice the dc current, and

$$V_0 = V_{b0} \frac{e^{-(h-M+1)\delta_L} - e^{-h\delta_L}}{(1 - e^{-\delta_L})(1 - e^{-h\delta_L})} \quad (8.110)$$

is the beam loading voltage seen by the first bunch due to the excitation by earlier passages of the beam. The difference in beam loading voltage experienced by the last and the first bunch is therefore

$$\Delta V_b = V_{b0} \frac{e^{-\delta_L} [1 - e^{-(M-1)\delta_L}] [1 - e^{-(h-M)\delta_L}]}{(1 - e^{-\delta_L})(1 - e^{-h\delta_L})}. \quad (8.111)$$

For the Fermilab Main Ring with $B = 0.872$, we obtain $V_{b0} = 0.411$ kV and $\Delta V_b = 113$ kV for one cavity. In the storage mode the gap voltage per cavity was $V_{rf} = 66$ kV. Thus, if the generator current I_g is in phase with the gap voltage and the synchronous angle was exactly $\phi_s = \pi$ at the passage of the first bunch through the cavity, the last bunch will see a synchronous angle $\phi_s = \tan^{-1}(\delta V_b/V_{rf}) \approx \frac{1}{3}\pi$. Such a large shift is intolerable because this will lead to a synchrotron oscillation of the center of the last bunch with an amplitude of $\frac{1}{6}\pi$ and finally result in a large growth of longitudinal emittance. There was a correction loop in the rf system that was capable of adding plus or minus quadrature currents up to $\sqrt{3}$ times the existing generator current to the input of the power amplifier [11]. With such an addition the synchronous angle goes back to π . The response time was ~ 300 ns, about 16 bunch periods, and was limited by the length of the cable loop. During such time, a maximum synchrotron phase shift of only 2.8° could develop and was tolerable.

Equation (8.111) shows that ΔV_b is small when there are only a small number of consecutive bunches in the ring ($M \rightarrow 1$). This is expected because it just gives the sum of the beam loading voltages of these few bunches while $V_0 \rightarrow 0$. On the other hand, if the ring is almost filled ($M \rightarrow h$), ΔV_b is also small, because of this is close to a symmetric filling of the ring. It is easy to show that the maximum ΔV_b occurs when the ring is half filled, or when the length of the gap is equal to the length of the bunch train.

8.5.2 Fermilab Booster

The injection into the Fermilab Booster from the Fermilab Linac is continuous for up to 10 Booster turns. After that the beam is bunched by adiabatic capture, which takes

place in about $150 \mu\text{s}$ while the rf voltage increases to 100 kV. During the injection, the beam is coasting and does not contain any component of the rf frequency. However, during adiabatic capture, both the rf voltage and the rf component of the current increase. If the former does not increase fast enough, Robinson's stability criterion will be violated. In general, the most dangerous moment is when the bucket area is equal to the bunch area. After that, the ratio of rf component beam signal to rf voltage decreases. However, the rf voltage during adiabatic capture in the Booster is maintained through counter-phasing. This is accomplished by dividing the 18 cavities into two groups. The required voltage amplitude and synchronous angle are obtained by varying the relative phase between the two groups. Thus the gap voltage in each cavity is not small and individually Robinson's stability is satisfied in each cavity. Counter-phasing is essential during adiabatic capture: First, maintaining too low a gap voltage inside a cavity will cause multi-pactoring. Second, the response of raising rf voltage during the capture through varying the generator current is slow because one has to fight the quality factor of the cavities, whereas controlling the rf voltage through varying the relative phase is fast. Since the beam loading voltage always points in the same direction aside from a detuning angle, to achieve counter-phasing, the generator current must be different in the two sets of cavities. The implication is that it will not be possible to have the generator current in phase with the gap voltage. Thus extra rf power will be required [12].

In the present booster cycle, the maximum power delivered to the beam is $P_b = 265 \text{ kW}$ at $V_{\text{rf}} = 864 \text{ kV}$, while the maximum power lost to the ferrites is $P_L = 830 \text{ kW}$. Since $P_b < P_L$ all the time, phase stability is guaranteed. To ensure that the beam accelerates according to the designed ramp curve, there is a slow low-level feedback loop which keeps the beam at the correct radial position in the aperture of the vacuum chamber by adjusting the synchronous phase angle. There is also a fast low-level feedback loop which damps phase oscillations. At extraction, since all bunches are kicked out at the same location in one revolution turn, the bunches will not see any transient beam loading voltage at all.

Actually, there are usually only $M = 80$ bunches in the ring of rf harmonic $h = 84$, and 4 bunch spaces are reserved for the extraction kicker. At the intensity of 6×10^{10} proton per bunch, the transient beam loading voltage excited in each of the 18 cavities by one bunch at passage is $V_{b0} = q\omega_r R_L / Q_L = 37.9 \text{ V}$ where $R_L / Q_L \sim 13 \Omega$ per cavity. According to Eq. (8.111), the difference in beam loading voltage experienced between the last and first bunch is $\Delta V_b = 3.76 V_{b0} = 142 \text{ V}$. The beam gap is created near the end of the ramp, where the rf voltage has the lowest value of 305 kV at extraction, or

16.9 kV per cavity. This amounts to an rf phase error of 0.48° . Typically, a bunch at extraction has a half width of 2.8 ns or 54° . Thus the phase error is comparatively small and so is the increase in bunch area due to dilution. For this reason, no action is necessary to compensate for this gap-induced beam loading.

8.5.3 Fermilab Main Injector

A batch of 84 bunches is extracted from the Fermilab Booster and injected into the Fermilab Main Injector. The rf frequency is $\omega_r/(2\pi) = 52.8$ MHz and the rf harmonic is $h = 588$. Each bunch contains 6×10^{10} particles. At injection, at the rf voltage of 1.2 MV and a bunch area of 0.15 eV-s, the half length is 28.3 ns. There are 18 rf cavities with a total $R_L/Q_L = 1.872$ k Ω and $Q_L = 5000$. At the passage of the first bunch across the cavities, the transient beam loading voltage excited in all the cavities is $V_b = qB\omega_r R_L/Q_L = 5.46$ kV, where we have taken $B = 0.915$ by assuming a parabolic distribution. At the passage of the last bunch of the batch, the total beam loading voltage excited becomes $V_b = 444$ kV, where we have taken into account the decay decrement but the detuning has been set to zero. If there is a second batch transferred from the Booster, this will take place after one Booster cycle or 66.7 ms. During this time interval, steady-state has already reached, since the fill time of the cavities is $2Q_L/\omega_r = 30$ μ s (about 2.7 turns). Figure 8.18 shows the beam loading voltages experienced by the 84 bunches in the batch in their first, second, and third passages through the cavities. The top trace represents the voltages seen when steady-state is reached. The difference in beam loading voltages seen by last and first bunch can be read out from the figure. It can also be computed analytically from Eq. (8.111) to be $\Delta V_b = 388$ kV. Actually, this difference is not much different from that experienced even in the first revolution turn because of the large quality factor of the cavities. The designed rf voltage at injection is $V_{rf} = 1.2$ MV. If the designed synchronous phase $\phi_s = 0$ is synchronized to the middle bunch of the batch, the phase error introduced becomes $\Delta\phi_s = \pm 9.18^\circ$ for the first and last bunches. This large difference in beam loading voltage, however, will not lead to energy difference along the bunches. The off-phase bunches will be driven into synchrotron motion instead. The first and last bunch will have amplitudes of oscillation $\Delta\phi_s = \pm 9.18^\circ$. Eventually, the bunch area will increase. Measured in rf phase, the half width of the bunch at injection is 53.8° . Thus, the bunch length will increase linearly from the middle bunch towards the front and the rear of the batch, with a maximum fractional increase of $9.18/53.8=17\%$. Such an increase is tolerable at this moment. There is a fast feedback loop with a delay of only 16 bunch spacings (300 ns), implying

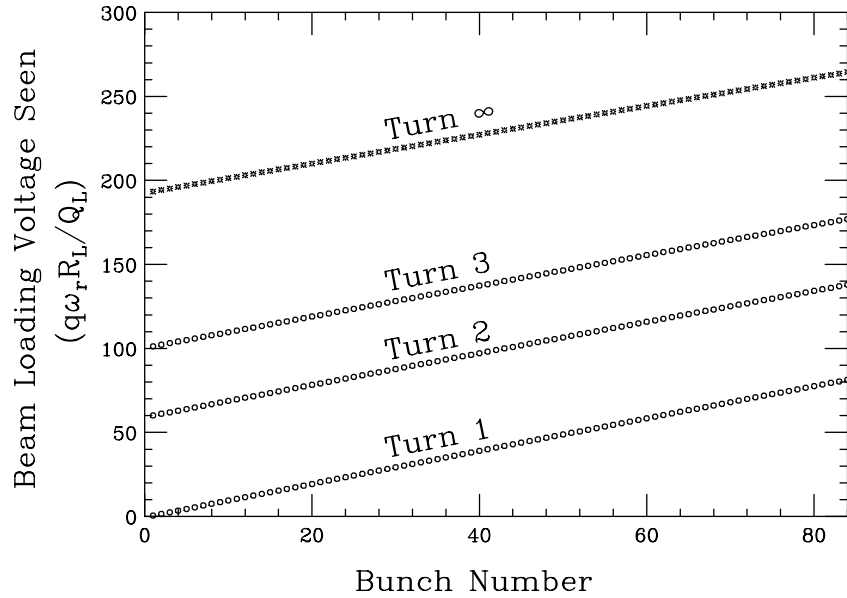


Figure 8.18: Beam loading voltages experienced by the 84 bunches in the batch at their first, second, and third passages of the Main Injector rf cavities. The top trace shows the beam loading voltages when steady state is reached. In the computation, cavity detuning has been set to zero.

that the maximum difference in beam loading voltage will only be ~ 88 kV and the phase error introduced will only be $\sim \pm 2.1^\circ$. Unfortunately, this feedback loop is not working most of the time.

Notice that proper detuning does not help here if we want to keep the generator current in phase with the rf voltage for the middle bunch. For half of the batch (42 bunches), the accumulated phase shift due to detuning is of the order of 1° so that the transient beam loading voltages of individual bunches still add up almost in a straight line (Exercise 8.8).

There is an upgrade plan that increases the bunch intensity by a factor of 5. The transient beam loading will then become intolerable, because the phase error can be as large as $\Delta\phi_s = \pm 58^\circ$. One proposal of compensation is feedforward. One proposal is to replace all the cavities with ones that have the same Q_L , but with R_L/Q_L reduced by a factor of 5. The beam loading effects will be the same as before. However, reducing the shunt impedance R_L 5 times implies the requirement of a larger generator current

$(\sqrt{5} = 2.2$ times) in order to supply the same rf power.

There is a plan to slip-stack two Booster batches and capture them into 84 bunches of double intensity [8]. In order that two series of rf buckets can fit into the momentum aperture of the Main Injector, the rf voltage employed to sustain the bunches will have to decrease to less than 100 kV. Relatively, the transient beam loading problem becomes very severe. To control beam loading, the followings are planned:

1. Using only 2 or 4 of the 18 cavities to produce the required rf voltage and de-Qing the remaining cavities. One simple technique that may de-Q the cavities by a factor of 3 is to turn off the screen voltage to reduce the tube plate resistance.
2. Feed-forward the signal of the wall current monitored at a resistive-wall gap to the cavity drivers. Experience at the Main Ring expects to achieve a 10-fold reduction in the effective wall current flowing into the cavities.
3. Feedback on all the cavities. A signal proportional to the gap voltage is amplified, inverted, and applied to the driver amplifier. Based on experience in the Main Ring and results achieved elsewhere, a 100-fold reduction can be achieved.

8.5.4 Proposed Prebooster

Let us look into the design of a proposed Fermilab prebooster which has a circumference of 158.07 m. It accelerates 4 bunches each containing 0.25×10^{14} protons from the kinetic energy 1 to 3 GeV. Because of the high intensity of the beam, the problems of space charge and beam loading must be addressed. We wish to examine the issues of beam loading and Robinson instabilities based on a preliminary rf system proposed by Griffin [13].

8.5.4.1 The Ramp Curve

Because of the high beam intensity, the longitudinal space-charge impedance per harmonic is $Z_{||}/n|_{\text{spch}} \sim -j100 \Omega$. But the beam pipe discontinuity will contribute only about $Z_{||}/n|_{\text{ind}} \sim j20 \Omega$ of inductive impedance. The space-charge force will be a large fraction of the rf-cavity gap voltage that intends to focus the bunch. A proposal is to insert ferrite rings into the vacuum chamber to counteract this space-charge force [14]. An experiment of ferrite insertion was performed at the Los Alamos Proton Storage Ring and the result has been promising [15]. Here we assume such an insertion will

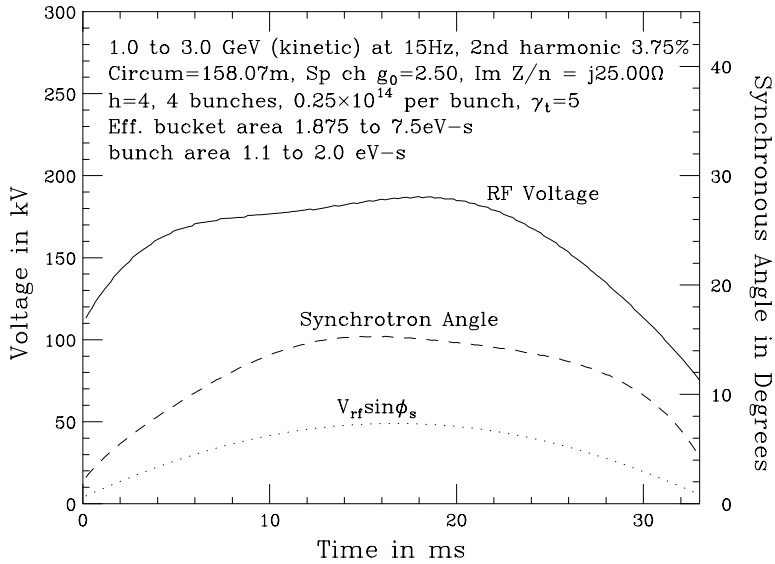


Figure 8.19: A typical ramp curve for a design of the future Fermilab prebooster.

over-compensate all the space-charge force leaving behind about $Z_{||}/n|_{\text{ind}} \approx j25 \Omega$ of inductive impedance. An over-compensation of the space charge will help bunching so that the required rf voltage needed will be smaller.

The acceleration from kinetic energy 1 to 3 GeV in 4 buckets at a repetition rate of 15 Hz is to be performed by resonant ramping. In order to reduce the maximum rf voltage required, about 3.75% of second harmonic is added. A typical ramp curve, with bucket area increasing quadratically with momentum, is shown in Fig. 8.19, which will be used as a reference for the analysis below. If the present choice of initial and final bucket areas and bunch areas is relaxed, the fraction of second harmonic can be increased. However, when the second harmonic is beyond $\sim 12.5\%$, it will only flatten the rf gap voltage in the ramp but will not decrease the maximum significantly.

8.5.4.2 The RF System

According to the ramp curve in Fig. 8.19, the peak voltage of the rf system is $V_{rf} \approx 185$ kV. Griffin proposed 10 cavities [13], each delivering a maximum of 19.0 kV. Each cavity contains 26.8 cm of ferrite rings with inner and outer radii 20 and 35 cm, respectively. The ferrite has a relative magnetic permeability of $\mu_r = 21$. The inductance and capacitance of the cavity are $L \sim 0.630 \mu\text{H}$ and $C \sim 820 \text{ pF}$. Assuming an average

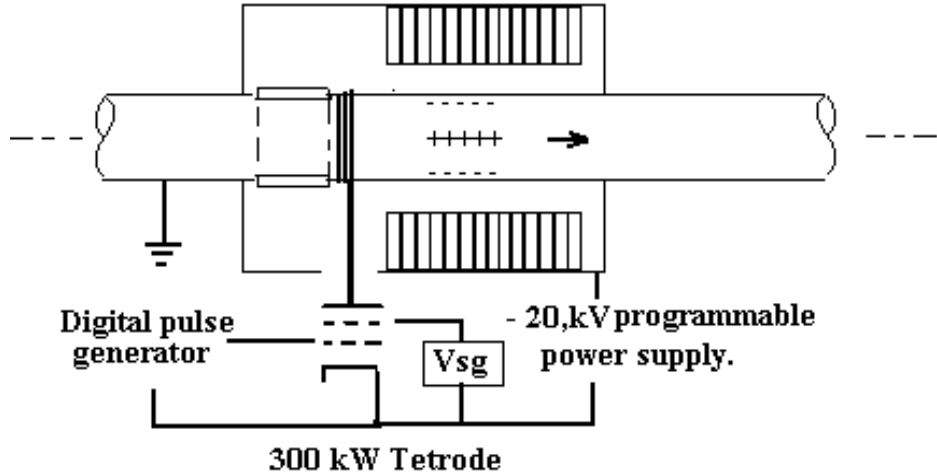


Figure 8.20: Transient beam loading power tetrode connected directly to an rf cavity gap to feed-forward the same amount of negative charge to the downstream end of the cavity gap so as to cancel the positive charge created there as the beam passes by.

ferrite loss of 134 kW/m^3 , the dissipation in the ferrite and wall of the cavity will be $P \sim 14.2 \text{ kW}$. The mean energy stored is $W \sim 0.15 \text{ J}$. Therefore each cavity has a quality factor $Q \sim 459$ and a shunt impedance $R_s \sim 12.7 \text{ k}\Omega$.

Because each bunch contains $q = 4.005 \mu\text{C}$, the transient beam loading is large. For the passage of one bunch, $4.005 \mu\text{C}$ of positive charge will be left at downstream end of the cavity gap creating a transient beam loading voltage of $V_{b0} \sim q/C = 5.0 \text{ kV}$, where $C = 820 \text{ pF}$ is the gap capacitance. We note from Fig. 8.19 that the accelerating gap voltages at both ends of the ramp are only about or less than 10 kV in each cavity. If the wakes due to the bunches ahead do not die out, we need to add up the contribution due to all previous bunch passages. Assuming a loaded quality factor of $Q_L = 45$, we find from Eq. (8.72) that the accumulated beam loading voltage can reach a magnitude of $V_b = 73 \text{ kV}$ when the detuning angle is zero (see Fig. 8.26).

A feed-forward system is suggested which will deliver via a tetrode the same amount of negative charge to the downstream end of the gap so as to cancel the positive charge created there as the beam passes by. Without the excess positive charge, there will not be any more transient beam loading. This is illustrated in Fig. 8.20.

Here, we are in a situation where the image current i_{im} passing through the cavity

gap is not equal to the beam current i_b . However, either at zero detuning or nonzero detuning, Eqs. (8.17) and (8.41) indicate that the portion of generator power transmitted to the acceleration of the beam is directly proportional to the magnitude of the image current. If the image current goes to zero in this feed-forward scheme, this implies that the rf generator is not delivering any power to the particle beam at all, although the beam is seeing an accelerating gap voltage. Then, how can the particle beam be accelerated? The answer is simple, the power comes from the tetrode that is doing the feed-forward. This explains why the tetrode has to be of high power.

Actually, the feed-forward system is not perfect and we assume that the cancellation is 85 %. For a δ -function beam, the component at the fundamental rf frequency is 56.0 A. Therefore, the remaining image current across the gap is $i_{\text{im}} = 8.4$ A. To counter this remaining 15% of beam loading in the steady state, the cavity must be detuned according to Eq. (8.30) by the angle

$$\psi = \tan^{-1} \left(\frac{i_{\text{im}} \cos \phi_s}{i_0} \right), \quad (8.112)$$

where ϕ_s is the synchronous angle and $i_0 = V_{\text{rf}}/R_s$ is the cavity current *in phase* with the cavity gap voltage V_{rf} . For high quality factor of $Q = 459$ which is accompanied by a large shunt impedance, the detuning angle will be large. Corresponding to the ramp curve of Fig. 8.19, the detuning angle is plotted as dashes in Fig. 8.21 along with the synchronous angle and maximum cavity gap voltage. We see that the detuning angle is between 80° and 86° , which is too large. If a large driving tube is installed with anode (or cathode follower) dissipation at ~ 131 kW, the quality factor will be reduced to the loaded value of $Q_L \sim 45$ and the shunt impedance to the loaded value of $R_L \sim 1.38$ k Ω . The detuning angle then reduces to $\psi \sim 29^\circ$ at the center of the ramp and to $\sim 40^\circ$ or $\sim 56^\circ$ at either end. This angle is also plotted in Fig. 8.21 as a dot-dashed curve for comparison. Then, this rf system becomes workable.

8.5.4.3 Fixed-Frequency RF Cavities

Now we want to raise the question whether it is possible to have a fixed resonant frequency for the cavity. A fixed-frequency cavity can be a very much simpler device because it may not need any biasing current at all. Thus the amount of cooling can be very much reduced and even unnecessary. It appears that the resonant frequency of the cavity should be chosen as the rf frequency at the *end* of the ramp, or $f_R = 7.37$ MHz so that the whole ramp will be immune to Robinson's phase-oscillation instability [4].

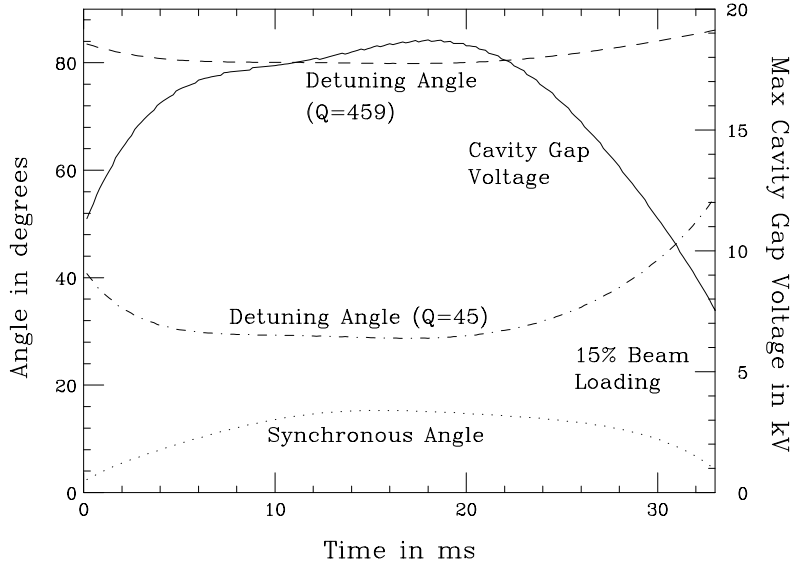


Figure 8.21: Detuning angle for the high $Q = 459$ and low $Q_L = 45$ situations.

However, the detuning will be large. For example, at the beginning of the ramp where $f_{\text{rf}} = 6.64$ MHz, the detuning angle becomes $\psi = 85.2^\circ$. Since the beam loading voltage V_{im} is small, the generator voltage phasor \tilde{V}_g will be very close to the gap voltage phasor \tilde{V}_{rf} . As a result, the angle θ between the gap voltage \tilde{V}_{rf} and the generator current phasor \tilde{i}_g will be close to the detuning angle, as demonstrated in Fig. 8.22. For example, Fig. 8.23 shows that, at the beginning of the ramp, the detuning angle is $\psi = 85.2^\circ$. Although the average total power delivered by the generator

$$\frac{1}{2} \tilde{i}_g \cdot \tilde{V}_{\text{rf}} = \frac{V_{\text{rf}}^2}{2R_L} + \frac{1}{2} i_{\text{im}} V_{\text{rf}} \cos \phi_s \quad (8.113)$$

is independent of θ , the energy capacity of the driving tube has to be very large.

Another alternative is to choose the resonant frequency of the cavity to be the rf frequency near the *middle* of the ramp. Then the detuning angle ψ and therefore the angle θ between \tilde{V}_{rf} and \tilde{i}_g will be much smaller at the middle of the ramp when the gap voltage is large. Although θ will remain large at both ends of the ramp, however, this is not so important because the gap voltages are relatively smaller there. Figure 8.25 shows the scenario of setting the cavity resonating frequency f_R equal to f_{rf} at the ramp time of 13.33 ms.

There is a price to pay for this choice of f_R ; namely, there will be Robinson phase instability for the second half of the ramp when the rf frequency is larger than f_R . The

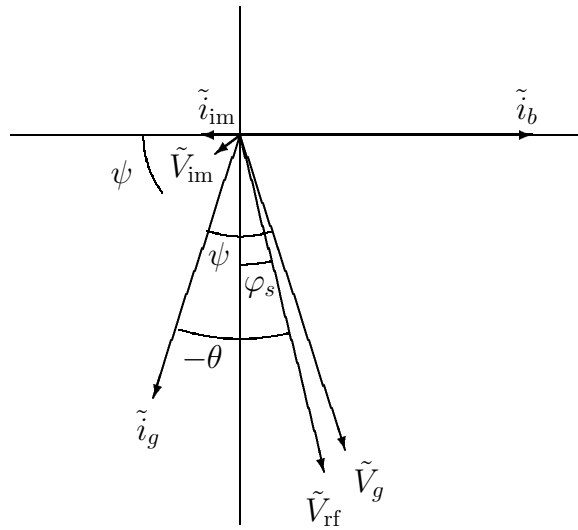


Figure 8.22: For a fixed cavity resonant frequency, the detuning angle ψ is fixed at each ramp time. When beam loading is small, the angle θ between the gap voltage \tilde{V}_{rf} and the generator current \tilde{i}_g will be close to ψ and will be large.

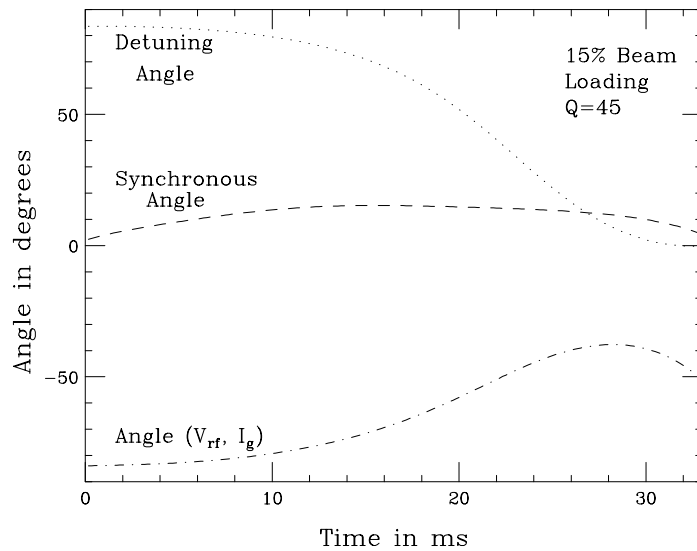


Figure 8.23: When the cavity resonant frequency is chosen as the rf frequency at the end of the ramp, both the detuning angle as well as the angle between the cavity gap voltage \tilde{V}_{rf} and the generator current \tilde{I}_g are large.

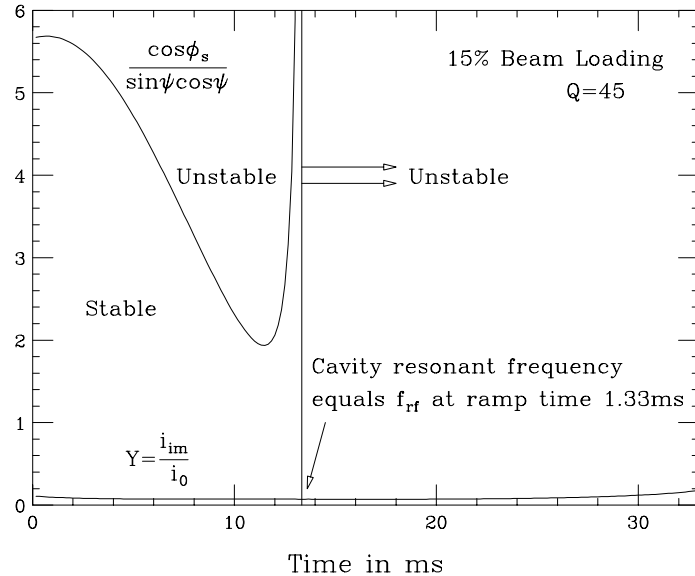


Figure 8.24: Plot showing the high-intensity Robinson's phase-stability criterion is satisfied in the first half of the ramp but not the second. Regions above the curve and to the left of the vertical straight line are unstable.

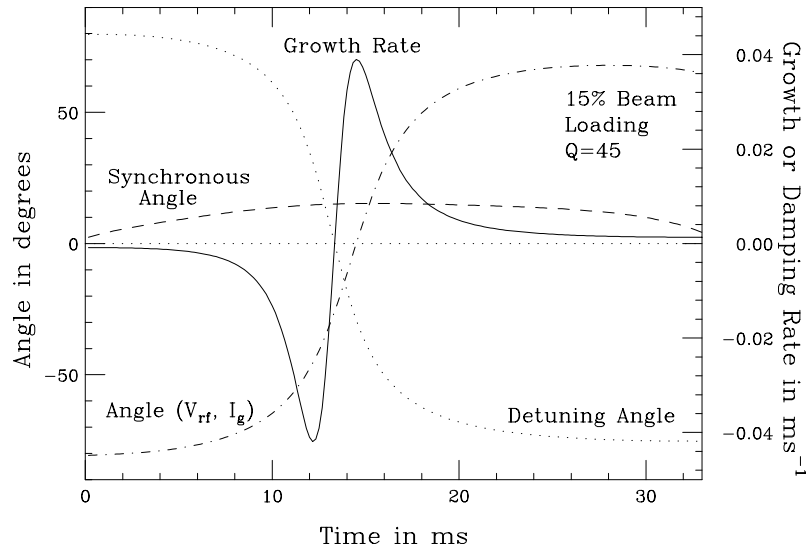


Figure 8.25: When the cavity resonant frequency is chosen as the rf frequency at the middle of the ramp at 13.33 ms, although the detuning angle as well as the angle between the cavity gap voltage \tilde{V}_{rf} and the generator current \tilde{I}_g are large at both ends of the ramp, they are relatively smaller at the middle of the ramp where the gap voltage is large.

sufficient condition for having a potential well for stable oscillation is, from Eq. (8.47), the high-intensity Robinson's criterion:

$$\frac{V_{\text{br}}}{V_{\text{rf}}} < \frac{\cos \phi_s}{\sin \psi \cos \psi} , \quad (8.114)$$

where $V_{\text{br}} = i_{\text{im}} R_L$ is the in-phase beam loading voltage. Below transition, the synchronous angle ϕ_s is between 0 and $\frac{1}{2}\pi$. For the second half of the ramp, the rf frequency becomes higher than the resonant frequency of the cavity, we have $\psi < 0$. Figure 8.24 plots the criterion for the whole ramp. It shows that the criterion is well satisfied for the first half of the ramp but not satisfied for the second half. Therefore, we must rely on control loops in the rf system to maintain phase stability. Of course a low-level feedback loop to reduce the cavity impedance helps tremendously.

Even when the beam is in an potential well for oscillatory motion, we still need to worry whether the oscillation amplitude will grow or be damped. The instability comes from the fact that, below transition, the particles with larger energy have higher revolution frequency and see a smaller real impedance of the cavity, thus losing less energy than particles with smaller energy. Therefore, the synchrotron amplitude will grow. In other words, the upper synchrotron sideband of the image current interacts with a smaller real impedance of the cavity resonant peak than the lower synchrotron sideband. However, since the loaded quality factor Q_L is not small, the difference in real impedance at the two sidebands is only significant when the rf frequency is very close to the cavity resonant frequency. Thus, we expect the instability will last for only a very short time during the second half of the ramp. The growth rate of the synchrotron oscillation amplitude has been computed and is equal to [2]

$$\frac{1}{\tau} = -\frac{i_{\text{im}} \beta \omega_s (R_+ - R_-)}{2V_{\text{rf}} \cos \phi_s} , \quad (8.115)$$

where

$$R_+ - R_- = \mathcal{R}e \left[Z_{\text{cav}}(\omega_{\text{rf}} + \omega_s) - Z_{\text{cav}}(\omega_{\text{rf}} - \omega_s) \right] , \quad (8.116)$$

i_{im} is the image current, β is the velocity with respect to light velocity, $\omega_s/(2\pi)$ is the synchrotron frequency, and Z_{cav} is the longitudinal impedance of the cavity. We see from Fig. 8.25 that the growth occurs for only a few ms and the growth time is at least ~ 25 ms. The total integrated growth increment from ramp time 13.33 ms is $\Delta G = \int \tau^{-1} dt = 0.131$ and the total growth is $e^{\Delta G} - 1 = 14.0\%$ which is acceptable.

Finally let us compute the beam loading voltage seen by a bunch including all the effects of the previous bunch passage. In this example, $\delta_L \approx \pi h_b / Q_L = 0.0698$ for $h_b = 1$

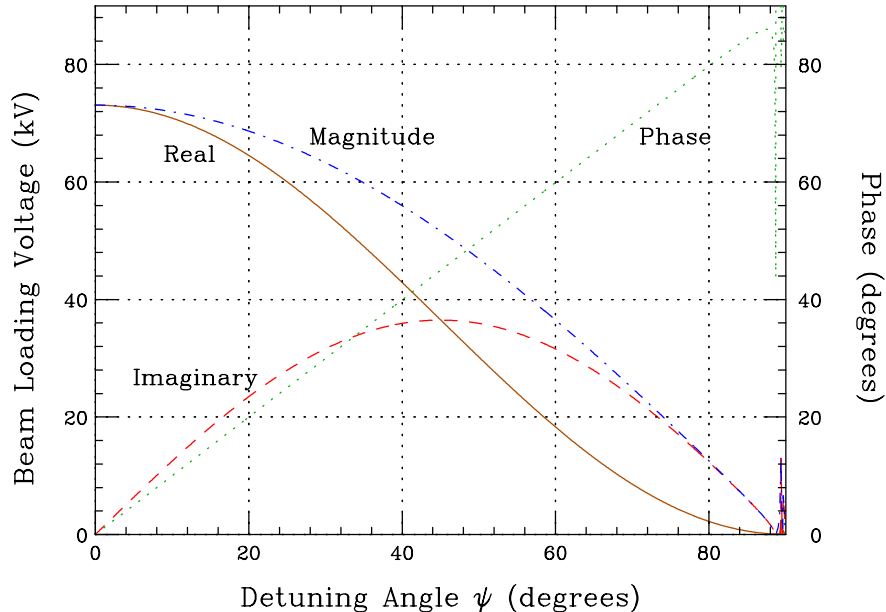


Figure 8.26: (color) Plot of transient beam loading voltage including all previous bunch passages, $\frac{q}{C}(F_1 + jF_2)$, versus detuning angle ψ .

Table 8.1: F_1 and F_2 for some values of the detuning angle ψ .

ψ	$\Psi = \delta_L \tan \psi$	F_1	F_2
0°	0°	$\sim \frac{1}{\delta_L}$	0
84.9°	45°	0.12	1.2
87.5°	90°	$\sim \frac{\delta_L}{2}$	$\sim \frac{1}{2}$
88.7°	180°	$\sim \frac{\delta_L}{4}$	0

and $Q_L = 45$. When the detuning angle $\psi = 0$, $V_b \approx V_{b0}/(2\delta_L)$. The functions F_1 and F_2 are computed at some other values of ψ , which are listed in Table 8.1 and plotted in Fig. 8.26. We see that the total transient beam loading voltage V_t falls rapidly as the detuning angle ψ increases. It vanishes approximately $\sim 88.7^\circ$ and oscillates rapidly after that. However, the choice of a large ψ is not a good method to eliminate beam loading, because in general the angle between the generator current phasor \tilde{i}_g and the rf voltage phasor \tilde{V}_{rf} will be large making the rf system inefficient.

8.6 Exercises

- 8.1. For a Gaussian bunch with rms length σ_τ in a storage ring, find the Fourier component of the current at the rf frequency. Give the condition under which this component is equal to twice the dc current.
- 8.2. Prove the fundamental theorem of beam loading when there are electromagnetic fields inside before the passage of any charged particle.
- 8.3. In Section 8.2, rf-detuning and Robinson's stability condition have been worked out below transition. Show that above transition the detuning according the Fig. 8.4 leads to instability. Draw a new phasor diagram for the situation above transition with stable rf-detuning. Rederive Robinson's high-intensity stability criterion above transition.
- 8.4. Derive Eq. (8.76), the generator power delivered to the rf system with multi-passage of equally spaced bunches.
- 8.5. (a) Derive Eq. (8.90), the beam loading voltage seen a charge particle inside a Gaussian bunch of rms length σ_τ at a distance τ ahead of the bunch center.
 (b) Using the property of the complex error function,

$$\lim_{\sigma_\tau \rightarrow 0} w\left(\frac{i\tau}{\sqrt{2}\sigma_\tau}\right) = \lim_{\sigma_\tau \rightarrow 0} \frac{2}{\sqrt{\pi}} e^{\tau^2/(2\sigma_\tau^2)} \int_{\frac{\tau}{\sqrt{2}\sigma_\tau}}^{\infty} e^{-t^2} dt = \begin{cases} 0 & \tau > 0, \\ 1 & \tau = 0, \\ 2 & \tau < 0, \end{cases} \quad (8.117)$$

derive Eq. (8.92), the transient beam loading voltage seen by the head, center, and tail of the bunch as the bunch length shortens to zero.

- 8.6. (1) Derive Eqs. (8.94) and (8.95), the transient beam loading voltage seen by a charge particle in a bunch with parabolic distribution at a distance T from the head of the bunch.
 (2) Derive Eqs. (8.99) and (8.99), the transient beam loading voltage seen by a charge particle in a bunch with cosine-square distribution at a distance T from the head of the bunch.
 (3) Derive Eqs. (8.102) and (8.103), the transient beam loading voltage seen by a charge particle in a bunch with cosine distribution at a distance T from the head of the bunch.

8.7. For a batch with M consecutive bunches inside a ring of rf harmonic h , the steady-state beam loading voltage experienced by the k th bunch when it crosses the cavity gap is given by Eq. (8.5.1).

- (1) Continuing bucket by bucket, write down the beam loading voltage experienced by the first bunch of the train when it crosses the cavity again. Since this beam loading voltage must equal to the one given by Eq. (8.5.1) with $k = 1$, determine the residual beam loading voltage V_0 in the cavity at that time and show that it is given by Eq. (8.110).
- (2) Show that the difference in beam loading voltage ΔV_b experienced by the last and first bunch is given by Eq. (8.111).
- (3) Show that ΔV_b assumes a maximum

$$\Delta V_b = V_{b0} \frac{e^{-\delta_L} \left[1 - e^{-\frac{1}{2}(h-1)\delta_L} \right]^2}{(1 - e^{-\delta_L})(1 - e^{-h\delta_L})}. \quad (8.118)$$

when $M = \frac{1}{2}(h + 1)$.

8.8. For a batch of 84 bunches inside the Fermilab Main Injector as described in Sec. 8.5.3,

- (1) compute the detuning angle with the requirement that the generator current is in phase with the rf voltage with respect to the middle bunch of the batch,
- (2) compute the rf phase slip between the transient beam loading voltages of successive bunches and show that because of the high quality factor the accumulation for half of the batch (42 bunches) is only around 1° .

8.9. Exercise 8.7 can also be pursued in the frequency domain. Fill in the missing steps of the following derivation.

- (1) Consider $M = 2m$ point bunches each with charge q inside $M = 2m$ consecutive buckets in a ring with rf harmonic h . The current is

$$I(t) = q \sum_{n=1}^m \delta[t - (n - \frac{1}{2})T_b] + q \sum_{n=1}^m \delta[t + (n - \frac{1}{2})T_b], \quad (8.119)$$

where T_b is the bucket width. In the frequency domain, the current at each revolution harmonic is given by

$$I_p = \frac{1}{T_0} \int_{-T_0/2}^{T_0/2} I(t) e^{-j2\pi p t/T_0} dt = \frac{2q}{T_0} \sum_{n=1}^m \cos \frac{2\pi p(n - \frac{1}{2})}{h}, \quad (8.120)$$

where $T_0 = hT_b$ is the revolution period and p is an integer ranging from $-\infty$ to $+\infty$.

(2) The beam loading voltage excited at each harmonic is $V_{bp} = I_p Z_p$ where the loaded impedance of the cavity is

$$Z_p = R_L \cos \psi_p e^{j\psi_p} \quad \text{with} \quad \tan \psi_p = 2Q_L \left(\frac{h}{p} - \frac{p}{h} \right), \quad (8.121)$$

and R_L and Q_L are the loaded shunt impedance and quality factor.

(3) Considering the symmetry of the impedance, the beam loading voltage in the time domain becomes

$$V_b(t) = \sum_p I_p \left(\cos^2 \phi_p \cos \frac{2\pi p t}{T_0} - \cos \phi_p \sin \psi_p \sin \frac{2\pi p t}{T_0} \right). \quad (8.122)$$

(4) Using the information of the Main Injector in Sec. 8.5.3, evaluate numerically and plot I_p , V_{bp} , and $V_b(t)$.

Bibliography

- [1] P.B. Wilson, Fermilab Summer School, 1981, AIP Conference Proceedings, No. 87, 1982, AIP, p.450.
- [2] See for example, H. Wiedemann, *Particle Accelerator Physics II*, Springer, 1995, p.203.
- [3] D. Boussard, *Beam Loading*, Fifth Advanced CERN Accelerator Physics Course, Rhodes, Greece, Sep. 20-Oct. 1, 1993, CERN 95-06, p.415.
- [4] P.B. Robinson, *Stability of Beam in Radiofrequency System*, Cambridge Electron Accel. Report CEAL-1010, 1964.
- [5] E. Raka, *RF System Considerations for a Large Hadron Collider*, AIP Conference Proc. 184, Physics of Particle Accelerators, ed. M. Month and M. Dienes, AIP, New York, 1989, Vol. 1, p.289.
- [6] D. Boussard et al., *Longitudinal Phenomena in the CERN SPS*, IEEE Trans. Nucl. Sc. **NS-24 No. 3**, 1399 (1977).
- [7] *Conceptual Design Report of PEP-II, An Asymmetric B Factory*, June 1993, LBL-PUB-5379, SLAC-418, CALT-68-1869, UCRL-ID-114055, or UC-IIRPA-93-01.
- [8] J. Dey, J. Steimel, J. Reid, *Narrowband Beam Loading Compensation in the Fermilab Main Injector Accelerating Cavities*, Proceedings of the 2001 Particle Accelerator Conference, Chicago, June 18-22, 2001, Ed. P. Lucas and S. Webber, p.876; Shekhar Shukla, John Marriner, and James Griffin, *Slip Stacking in the Fermilab Main Injector*, Proceedings of the Summer Study on the Future of High Energy Physics, Snowmass, July 1-20, 2001.

- [9] J. Steimel, *Summary of RF Cavity Beam Loading Problems and Cures in the CERN PS Complex*, unpublished; D. Boussard and G. Lambert, *Reduction of the Apparent Impedance of Wide Band Accelerating Cavities by RF Feedback*, IEEE Trans. Nucl. Sc. **NS-30 No. 4**, 2239 (1983); D. Boussard, *Control of Cavities with High Beam Loading*, IEEE Trans. Nucl. Sc. **NS-32 No. 5**, 1852 (1985); D. Boussard, *RF Power Requirements for a High Intensity Proton Collider (Parts 1 and 2)*, CERN SL/91-16 (RFS), April 1991.
- [10] F. Pedersen, *Beam Loading Effects in the CERN PS Booster*, IEEE Trans. Nucl. Sc. **NS-22 No. 3**, 1906 (1975); F. Pedersen, *A Novel RF Cavity Tuning Feedback Scheme for Heavy Beam Loading*, IEEE Trans. Nucl. Sc. **NS-32 No. 5**, 2138 (1985).
- [11] J.E. Griffin, *Compensation for Beam Loading in the 400-GeV Fermilab Main Accelerator*, IEEE Trans. Nucl. Sc. **NS-22 No. 3**, 1910 (1975); D. Wildman, *Transient Beam Loading Compensation in the Fermilab Main Ring*, IEEE Trans. Nucl. Sc. **NS-32 No. 5**, 1910 (1985).
- [12] Y. Goren and T.F. Wang, *Voltage Counter-Phasing in the SSC Low Energy Booster*, Proceedings of the 1993 Particle Accelerator Conference, May 17-20, 1993, Washington, DC, p. 883.
- [13] J.E. Griffin, *RF System Considerations for a Muon Collider Proton Driver Synchrotrons*, Fermilab report FN-669, 1998.
- [14] K.Y. Ng and Z.B. Qian, Proc. Phys. at the First Muon Collider and at Front End of a Muon Collider, Fermilab, Batavia, Nov. 6-9, 1997.
- [15] J.E. Griffin, K.Y. Ng, Z.B. Qian, and D. Wildman, *Experimental Study of Passive Compensation of Space Charge Potential Well Distortion at the Los Alamos National Laboratory Proton Storage Ring*, Fermilab Report FN-661, 1997.

Chapter 9

LONGITUDINAL COUPLED-BUNCH INSTABILITIES

When the wake does not decay within the bunch spacing, bunches talk to each other. Assuming M bunches of equal intensity equally spaced in the accelerator ring, there are $\mu = 0, 1, \dots, M-1$ modes of oscillations in which the center-of-mass of a bunch *leads** its predecessor by the phase $2\pi\mu/M$. In addition, an individual bunch in the μ th coupled-bunch mode can oscillate in the synchrotron phase space about its center-of-mass in the m th azimuthal mode with $2m = 2, 4, \dots$ azimuthal nodes† in the perturbed longitudinal phase-space distribution. Of course, there will be in addition radial modes of oscillation in the perturbed distribution. The long-range wake can drive the coupled bunches to instability.

9.1 Sacherer's Integral Equation

Because the beam particles execute synchrotron oscillations, it is more convenient to use circular coordinates r, ϕ in the longitudinal phase space instead of the former time

*We can also formulate the problem by having the bunch *lag* its predecessor by the phase $2\pi\mu'/M$ in the μ' th coupling mode. Then mode μ' will be exactly the same as mode $M-\mu$ discussed in the text.

†For example, the dipole mode $m = 1$ can be written as $\sim \cos \phi$, which has two nodes $\phi = \pm\pi/2$.

advance τ and energy offset ΔE . We define

$$\begin{cases} x = r \cos \phi = \tau , \\ p_x = r \sin \phi = \frac{\eta}{\omega_s \beta^2} \frac{\Delta E}{E_0} , \end{cases} \quad (9.1)$$

so that the equations of motion

$$\begin{cases} \frac{dx}{ds} = -\frac{\omega_s}{v} p_x , \\ \frac{dp_x}{ds} = \frac{\omega_s}{v} x + \frac{\eta}{E_0 \omega_s \beta^2} \langle F_0^{\parallel}(\tau; s) \rangle , \end{cases} \quad (9.2)$$

become more symmetric. In the absence of the wake force $\langle F_0^{\parallel}(\tau; s) \rangle$, the trajectory of a beam particle is just a circle in the longitudinal phase space. In above, ω_s is the angular small-amplitude synchrotron frequency, η the slip factor, and $v = \beta c$ is the velocity and E_0 the energy of the synchronous particle. The phase-space distribution ψ of a bunch can be separated into the unperturbed or stationary part ψ_0 and the perturbed part ψ_1 :

$$\psi(\tau, \Delta E; s) = \psi_0(\tau, \Delta E) + \psi_1(\tau, \Delta E; s) . \quad (9.3)$$

The linearized Vlasov equation becomes

$$\frac{\partial \psi_1}{\partial s} - \frac{\omega_s}{v} p_x \frac{\partial \psi_1}{\partial x} + \frac{\omega_s}{v} x \frac{\partial \psi_1}{\partial p_x} + \frac{\partial \psi_0}{\partial p_x} \frac{\eta}{E_0 \omega_s \beta^2} \langle F_0^{\parallel}(\tau; s) \rangle = 0 . \quad (9.4)$$

Changing to the circular coordinates, the equation simplifies to

$$\frac{\partial \psi_1}{\partial s} + \frac{\omega_s}{v} \frac{\partial \psi_1}{\partial \phi} + \frac{\eta}{E_0 \omega_s \beta^2} \frac{d\psi_0}{dr} \sin \phi \langle F_0^{\parallel}(\tau; s) \rangle = 0 . \quad (9.5)$$

The perturbed distribution can be expanded azimuthally,

$$\psi_1(r, \phi; s) = \sum_m \alpha_m R_m(r) e^{im\phi - i\Omega s/v} , \quad (9.6)$$

where $R_m(r)$ are functions corresponding to the m th azimuthal, α_m are the expansion coefficients, and $\Omega/(2\pi)$ is the collective frequency to be determined. The Vlasov equation becomes

$$(\Omega - m\omega_s) \alpha_m R_m(r) e^{-i\Omega s/v} = -\frac{iv\eta}{E_0 \omega_s \beta^2} \frac{d\psi_0}{dr} \int_{-\pi}^{\pi} \frac{d\phi}{2\pi} e^{-im\phi} \sin \phi \langle F_0^{\parallel}(\tau; s) \rangle . \quad (9.7)$$

Now consider the wake force acting on a beam particle at location s , where a cavity gap is located for example, with time advance τ relative to the synchronous particle due to all preceding particles passing through s at an earlier time. This force can be expressed as

$$\langle F_0^{\parallel}(\tau; s) \rangle = -\frac{e^2}{C} \sum_{k=-\infty}^{\infty} \int_{-\infty}^{\infty} d\tau' \rho_1[\tau', s - kC - v(\tau' - \tau)] W'_0[kC + v(\tau' - \tau)] , \quad (9.8)$$

where only the perturbed density ρ_1 , which is the projection of ψ_1 onto the τ axis, is included, because the unperturbed part should have been considered in the zeroth order of the Vlasov equation during the discussion of potential-well distortion. The summation over k takes care of the contribution of the wake left by the charge distribution in previous turns. The lower limit of the summation and the lower limit of the integral have been extended to $-\infty$ because of the causality property of the wake function. The expression in Eq. (9.8) is more accurate than the one in Eq. (2.7). In the latter, we assume the particle density does not change from the time the source particles pass the reference point to the time when the test particle observes the wake at the same reference point. Such an assumption is no longer valid here because the wake is left by particles in other bunches which may be many revolution turns ahead and these bunches are oscillating azimuthally in the longitudinal phase space. When the source particle, with time advance τ' with reference to the synchronous particle and k turns ahead of the test particle, is at location s to excite the cavity, the test particle is at location $s - kC - v(\tau' - \tau)$. Hence, we have the second argument in the perturbation linear density ρ_1 .

There are M bunches and the synchronous particle in the ℓ th bunch is at location s_ℓ . If the witness particle is in the n th bunch,

$$\begin{aligned} \langle F_{0n}^{\parallel}(\tau; s) \rangle &= -\frac{e^2}{C} \sum_{k=-\infty}^{\infty} \sum_{\ell=0}^{M-1} \int_{-\infty}^{\infty} d\tau' \times \\ &\quad \times \rho_\ell[\tau'; s - kC - (s_\ell - s_n) - v(\tau' - \tau)] W'_0[kC + (s_\ell - s_n) + v(\tau' - \tau)] . \end{aligned} \quad (9.9)$$

We assume the bunches are identical and equally spaced. For the μ th coupled mode, we substitute in the above expression the perturbed density of the n th bunch $\rho_{1n}(\tau) e^{-i\Omega s/v}$ including the phase lead,

$$\rho_\ell(\tau; s) = \rho_{1n}(\tau) e^{i2\pi\mu(\ell-n)/M} e^{-i\Omega s/v} . \quad (9.10)$$

Next, let us go to the frequency domain using the Fourier transforms

$$W'_0(v\tau) = \frac{1}{2\pi} \int_{-\infty}^{\infty} d\omega Z_0^{\parallel}(\omega) e^{-i\omega\tau} , \quad (9.11)$$

$$\rho_{1n}(\tau) = \int_{-\infty}^{\infty} d\omega \tilde{\rho}_{1n}(\omega) e^{i\omega\tau} . \quad (9.12)$$

In Eq. (9.9) above, we shall neglect[‡] the time delay $\tau' - \tau$ in ρ_ℓ because this will only amount to a phase delay $\Omega(\tau' - \tau)$ where $\Omega \approx m\omega_s$, which is very much less than the phase change $\omega_r(\tau' - \tau)$ during the bunch passage, where $\omega_r/(2\pi)$ is the frequency of the driving resonant impedance. Substituting Eqs. (9.11) and (9.12) into Eq. (9.9) and integrating over τ' and one of the ω 's, the wake force for the μ th coupled-bunch mode becomes

$$\begin{aligned} \langle F_{0n\mu}^{\parallel}(\tau; s) \rangle &= -\frac{e^2}{C} \sum_{k=-\infty}^{\infty} \sum_{\ell=0}^{M-1} e^{i2\pi\mu(\ell-n)/M} e^{i\Omega(-s+kC+s_\ell-s_n)/v} \times \\ &\quad \times \int_{-\infty}^{\infty} d\omega \tilde{\rho}_{1n}(\omega) Z_0^{\parallel}(\omega) e^{-i\omega(kC+s_\ell-s_n)/v} e^{i\omega\tau} . \end{aligned} \quad (9.13)$$

The summation over k can now be performed using Poisson formula

$$\sum_k e^{-ik\omega C/v} = \sum_p 2\pi \delta\left(\frac{\omega C}{v} - 2\pi p\right) = \sum_p \omega_0 \delta(\omega - p\omega_0) . \quad (9.14)$$

This leads to

$$\langle F_{0n\mu}^{\parallel}(\tau; s) \rangle = -\frac{e^2}{C} \sum_{p=-\infty}^{\infty} \sum_{\ell=0}^{M-1} e^{i2\pi\mu(\ell-n)/M} e^{-i\Omega s/v + i\omega_p \tau} \omega_0 \tilde{\rho}_{1n}(\omega_p) Z_0^{\parallel}(\omega_p) e^{-ip\omega_0(s_\ell-s_n)/v} , \quad (9.15)$$

where we have used the short-hand notation

$$\omega_p = p\omega_0 + \Omega . \quad (9.16)$$

We next make use of the fact that the unperturbed bunches are equally spaced, or

$$s_\ell - s_n = \frac{\ell - n}{M} C . \quad (9.17)$$

The summation over ℓ can be performed. The sum vanishes unless $(p-\mu)/M = q$, where q is an integer:

$$\sum_{\ell=0}^{M-1} e^{i2\pi(\ell-n)(\mu-p)/M} = \begin{cases} M & \text{if } \frac{p-\mu}{M} = q , \\ 0 & \text{otherwise} . \end{cases} \quad (9.18)$$

[‡]Without this approximation, only Z_0^{\parallel} will have the argument ω_p in Eq. (9.15). The argument of $\tilde{\rho}$ and the factor in front of τ in the exponent will be replaced by $\omega_p - \Omega$. In Eq. (9.19) below, The argument of $\tilde{\rho}$ and the factor in front of τ in the exponent will be replaced by $\omega_q - \Omega$.

The final result is

$$\langle F_{0n\mu}^{\parallel}(\tau; s) \rangle = -\frac{e^2 M \omega_0}{C} e^{-i\Omega s/v} \sum_{q=-\infty}^{\infty} \tilde{\rho}_{1n}(\omega_q) Z_0^{\parallel}(\omega_q) e^{i\omega_q \tau}, \quad (9.19)$$

where

$$\omega_q = (qM + \mu)\omega_0 + \Omega. \quad (9.20)$$

Since the left side of the Vlasov equation is expressed in terms of the radial function $R_m(r)$, we want to do the same for the wake force. First, rewrite the perturbed density in the time domain,

$$\langle F_{0n\mu}^{\parallel}(\tau; s) \rangle = -\frac{e^2 M \omega_0}{C} e^{-i\Omega s/v} \sum_{q=-\infty}^{\infty} Z_0^{\parallel}(\omega_q) \int \frac{d\tau'}{2\pi} \rho_{1n}(\tau') e^{i\omega_q(\tau-\tau')}. \quad (9.21)$$

Since $\rho_{1n}(\tau')$ is the projection of the perturbed distribution onto the τ' axis, we must have

$$\rho_{1n}(\tau') d\tau' = \int \psi_{1n}(\tau', \Delta E') d\tau' d\Delta E' \quad (9.22)$$

$$= \frac{E_0 \omega_s \beta^2}{\eta} \int \psi_{1n}(r', \phi') r' dr' d\phi' \quad (9.23)$$

$$= \frac{E_0 \omega_s \beta^2}{\eta} \sum_{m'} \alpha_{m'} \int R_{m'}(r') e^{im' \phi'} r' dr' d\phi'. \quad (9.24)$$

The wake force then takes the form

$$\langle F_{0n}^{\parallel}(\tau; s) \rangle = -\frac{e^2 \omega_0 M}{2\pi C} \frac{E_0 \omega_s \beta^2}{\eta} e^{-i\Omega s/v} \sum_{q=-\infty}^{\infty} \sum_{m'} Z_0^{\parallel}(\omega_q) \int r' dr' d\phi' \alpha_{m'} R_{m'}(r') e^{im' \phi'} e^{i\omega_q(\tau-\tau')}, \quad (9.25)$$

This wake force is next substituted into the Vlasov equation (9.7). The integrations over ϕ and ϕ' are performed in terms of Bessel function of order m using its integral definition

$$i^m J_m(z) = \frac{1}{2\pi} \int_{-\pi}^{\pi} d\phi e^{\pm im\phi + iz \cos \phi}, \quad (9.26)$$

the recurrence relation

$$J_{m-1}(z) + J_{m+1}(z) = \frac{2m}{z} J_m(z), \quad (9.27)$$

and the fact that

$$J_m(-z) = (-1)^m J_m(z). \quad (9.28)$$

The result is the Sacherer's integral equation for longitudinal instability for the m th azimuthal μ th coupled-bunch mode,

$$(\Omega - m\omega_s)\alpha_m R_m(r) = -\frac{i2\pi e^2 MN\eta}{\beta^2 E_0 T_0^2 \omega_s} \frac{m}{r} \frac{dg_0}{dr} \sum_{m'} i^{m-m'} \alpha_{m'} \int r' dr' R_{m'}(r') \sum_q \frac{Z_0^{\parallel}(\omega_q)}{\omega_q} J_{m'}(\omega_q r') J_m(\omega_q r), \quad (9.29)$$

where transformation of the unperturbed longitudinal distribution

$$\psi_0(r)d\tau d\Delta E = \frac{\omega_s \beta^2 E_0}{\eta} \psi_0 dx dp_x = N g_0(r) r dr d\phi \quad (9.30)$$

has been made so that g_0 is normalized to unity when integrated over $r dr d\phi$.

This is an eigenfunction-eigenvalue problem, the α_m 's being the eigenfunctions and Ω the corresponding eigenvalue. The solution is nontrivial. However, with some approximations, interesting results can be deduced. When the perturbation is not too strong so that the shift in frequency is much less than the synchrotron frequency, there will not be coupling between different azimuthals. The integral equation simplifies to

$$(\Omega - m\omega_s)R_m(r) = -\frac{i2\pi e^2 MN\eta}{\beta^2 E_0 T_0^2 \omega_s} \frac{m}{r} \frac{dg_0}{dr} \int r' dr' R_m(r') \sum_q \frac{Z_0^{\parallel}(\omega_q)}{\omega_q} J_m(\omega_q r') J_m(\omega_q r). \quad (9.31)$$

The spread in synchrotron frequency can be introduced by letting ω_s be a function of r . Moving the factor $\Omega - m\omega_s(r)$ to the right side, the radial distribution R_m can be eliminated by multiplying both sides by $r J_m(r)$ and integrating over dr . We then arrive at the dispersion relation,

$$1 = -\frac{i2\pi e^2 MNm\eta}{\beta^2 E_0 T_0^2 \omega_s} \sum_q \frac{Z_0^{\parallel}(\omega_q)}{\omega_q} \int dr \frac{dg_0}{dr} \frac{J_m^2(\omega_q r)}{\Omega - m\omega_s(r)}. \quad (9.32)$$

Stability and growth contours can be derived from the dispersion relation of Eq. (9.32) in just the same way as in the discussion of microwave instability for a single bunch in Chapter 6.

9.1.1 Synchrotron Tune Shift

When the spread in synchrotron frequency is small, Eq. (9.32) gives the frequency shift

$$\Omega - m\omega_s = \frac{i2\pi e^2 MNm\eta}{\beta^2 E_0 T_0^2 \omega_s} \sum_q \frac{Z_0^{\parallel}(\omega_q)}{\omega_q} \left[- \int dr \frac{dg_0}{dr} J_m^2(\omega_q r) \right], \quad (9.33)$$

where the expression inside the square brackets, denote by F , can be viewed as a distribution dependent form factor, which is positive definite because dg_0/dr is negative. The real part $\mathcal{Re}(\Omega - \omega_s)$ gives the coherent tune shift of the bunch while the imaginary part $\mathcal{Im}\Omega$ gives the growth rate of the instability.

When the bunch length $2\hat{\tau}$ is much shorter than the wavelength of the perturbing impedance, or $\omega_q\hat{\tau} \ll 1$, the Bessel function can be substituted by its small-argument expression:

$$J_m(x) \approx \frac{1}{m!} \left(\frac{x}{2}\right)^m . \quad (9.34)$$

We are interested in particular the synchrotron tune shift of one bunch ($M = 1$) in dipole mode ($m = 1$), and obtain

$$\Delta\Omega = -\frac{e^2 N \eta}{2\beta^2 E_0 T_0^2 \omega_s} \sum_q \omega_q \mathcal{Im} Z_0^{\parallel}(\omega_q) , \quad (9.35)$$

where $\omega_q = q\omega_0 + \omega_s$ and the bunch density normalization

$$\int g_0(r) r dr d\phi = 1 \quad (9.36)$$

has been used. In the situation that the perturbing impedance is a broadband resonance, we can make the approximation $\omega_q = q\omega_0$.

It is important to point out that Eq. (9.35) is only the dynamic part of the synchrotron tune shift contributed by the impedance. There is another contribution coming from the static potential-well distortion. This term is not present in Eq. (9.35), because during the derivation of the Sacherer's growth formula, we have substituted only the perturbed distribution into the wake force in Eq. (9.8) but not the unperturbed distribution. As a result, the static potential-well distortion piece has been left out. This static contribution has been addressed in Eq. (3.50). When the short bunch approximation is made, it can be shown that the static contribution just cancels the dynamic contribution, resulting in no coherent shift for the dipole mode (Exercise 9.2). This is evident physically because the dipole motion is rigid. The whole bunch moves as a whole, and therefore the bunch center does not experience any change in wake field from itself at all. On the other hand, an individual particle moving inside a bunch will experience the time variation of the wake left by the bunch and therefore the incoherent tune shift is nonzero.

9.1.2 Water Bag Model

Take the simple case of a single bunch of length $2\hat{\tau}$ and uniform distribution in the longitudinal phase space, which is usually called the *water bag model*. Then

$$g_0(r) = \frac{1}{\pi\hat{\tau}^2} H(\hat{\tau} - r) , \quad (9.37)$$

where the Heaviside function is defined as $H(x) = 1$ when $x > 0$ and zero otherwise. The form factor, the expression inside the square brackets of Eq. (9.33), becomes

$$F = \frac{1}{\pi\hat{\tau}^2} J_m^2(\omega_q\hat{\tau}) \approx \frac{\omega_q^2}{4\pi} \frac{1}{(m!)^2} \left(\frac{\omega_q\hat{\tau}}{2}\right)^{2m-2} , \quad (9.38)$$

where the assumption of a short bunch has been made in the last step. The growth rate driven by the impedance can now be written as

$$\frac{1}{\tau_m} = \frac{e^2 N \eta}{2\beta^2 E_0 T_0^2 \omega_s} \frac{m}{(m!)^2} \sum_q \left(\frac{\omega_q\hat{\tau}}{2}\right)^{2m-2} \omega_q \operatorname{Re} Z_0^\parallel(\omega_q) , \quad (9.39)$$

where, for one bunch, $\omega_q = q\omega_0 + \Omega$.

9.1.3 Robinson's Instability

The $m = 0$ mode is a trivial mode which gives $\Omega_0 = 0$. It describes the potential-well distortion mode addressed in Chapter 3 and is of not much interest here where the emphasis is on instabilities. The next azimuthal mode is $m = 1$ which describes dipole oscillations and we expect $\Omega_1 \approx \omega_s$. Consider the situation of having the driving impedance as a resonance so narrow that there is only one $q > 0$ that satisfies

$$\omega_r \approx q\omega_0 \pm \omega_s , \quad (9.40)$$

where $\omega_r/(2\pi)$ is the resonant frequency. The growth rate for a short bunch can therefore be obtained from Eq. (9.39),

$$\frac{1}{\tau_1} = \operatorname{Im} \Delta\omega_s = \frac{\eta e^2 N \omega_r}{2\beta^2 E_0 T_0^2 \omega_s} [\operatorname{Re} Z_0^\parallel(q\omega_0 + \omega_s) - \operatorname{Re} Z_0^\parallel(q\omega_0 - \omega_s)] , \quad (9.41)$$

where the first term corresponds to positive frequency and the second negative frequency. If the resonant frequency is slightly above $q\omega_0$ as illustrated in Fig. 9.1(a), we have

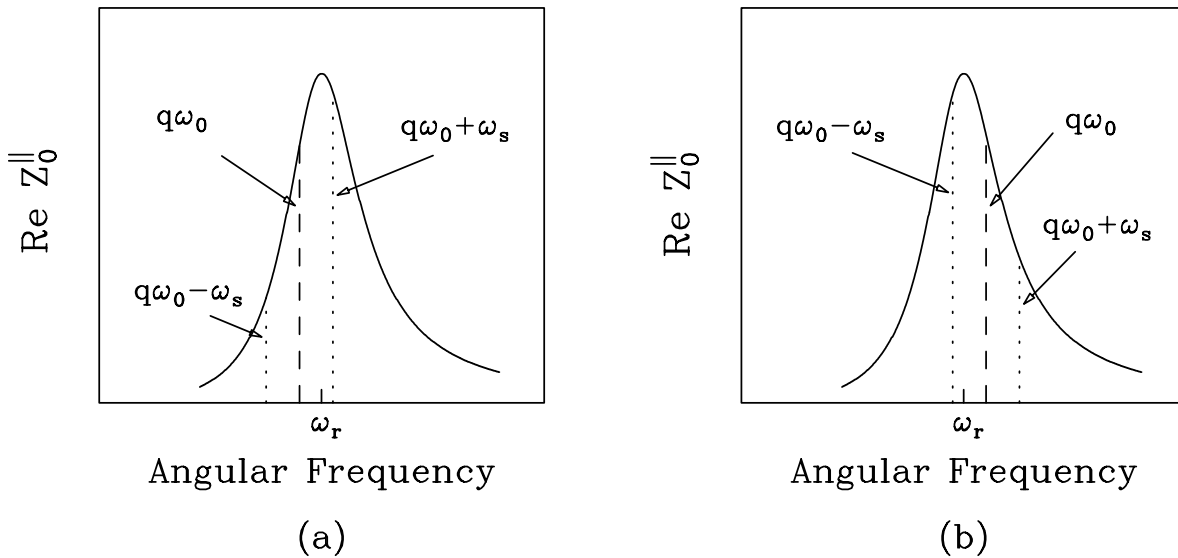


Figure 9.1: (a) Above transition, if the resonant frequency ω_r is slightly above a revolution harmonic $q\omega_0$, $\text{Re } Z_0^{\parallel}$ at the upper synchrotron sideband is larger than at the lower synchrotron sideband. The system is unstable. (b) Above transition, if ω_r is slightly below a harmonic line, $\text{Re } Z_0^{\parallel}$ at the upper sideband is smaller than at the lower sideband. The system is stable.

$\Re Z_0^{\parallel}(q\omega_0 + \omega_s) > \Re Z_0^{\parallel}(q\omega_0 - \omega_s)$. Above transition, the growth rate will be positive or there is instability. On the other hand, if $\omega_r < q\omega_0$ as illustrated in Fig. 9.1(b), the growth rate is negative and the system is damped. This instability criterion was first analyzed by Robinson [1], and we have obtained exactly the same result in Sec. 8.3.3 using phasor diagram analysis. Below transition, the inverse is true; one should tune the resonant frequency of the cavity below a revolution harmonic for stability. Note that the growth rate of Eq. (9.41) is independent of the bunch length when the bunch is short, implying that for the dipole mode, this is a point-bunch theory.[§] Thus, this special case should be obtainable much more easily than the complicated derivation that we have gone through, and it is worthwhile to make a digression into this easier derivation.

9.1.3.1 Point-Bunch Theory

Let us start from the equations of motion of a super particle with arrival time advance $\tau(s)$, carrying charge eN , and seeing its own wake left behind k revolutions before. We

[§]More about Robinson's stability criterion was discussed in Chapter 7.5.

have

$$\frac{d^2\tau}{ds^2} + \frac{\omega_s^2}{v^2} \tau = \frac{e^2 N \eta}{v \beta^2 E_0 C} \sum_{k=-\infty}^{\infty} W'_0 [kT_0 + \tau(s - kC) - \tau(s)] , \quad (9.42)$$

where the summation has been extended to $-\infty$ (the future) because the wake function obeys causality. The arrival time advance of each passage through the cavity gap is of the order of the synchrotron oscillation amplitude, which should be small. We can therefore expand the wake potential about kT_0 . The right side becomes

$$\begin{aligned} \text{R.S.} &= \frac{e^2 N \eta}{v \beta^2 E_0 C} \sum_{k=-\infty}^{\infty} [\tau(s - kC) - \tau(s)] W''_0(kT_0) \\ &= \frac{e^2 N \eta}{v \beta^2 E_0 C} \tau(s) \sum_{k=-\infty}^{\infty} [e^{-i\Omega(s/v - kT_0)} - 1] W''_0(kT_0) , \end{aligned} \quad (9.43)$$

where we have substituted the collective time behavior

$$\tau(s) \propto e^{-i\Omega s/v} , \quad (9.44)$$

with Ω being the collective angular frequency to be determined. Next go to the frequency domain by introducing the longitudinal impedance Z_0^{\parallel} , or

$$W'_0(t) = \frac{1}{2\pi} \int d\omega Z_0^{\parallel}(\omega) e^{-i\omega t} . \quad (9.45)$$

We obtain

$$\text{R.S.} = -\frac{ie^2 N \eta}{v \beta^2 E_0 C} \sum_{k=-\infty}^{\infty} [e^{-i\Omega(s/v - kT_0)} - 1] \int \frac{d\omega}{2\pi} \omega Z_0^{\parallel}(\omega) e^{-i\omega kT_0} . \quad (9.46)$$

The summation over k can now be performed. Substituting the time behavior of τ into the left side, the equation of motion becomes

$$\Omega^2 - \omega_s^2 = \frac{ie^2 N \eta v^2}{\beta^2 E_0 C^2} \sum_{p=-\infty}^{\infty} [(p\omega_0 + \Omega) Z_0^{\parallel}(p\omega_0 + \Omega) - p\omega_0 Z_0^{\parallel}(p\omega_0)] . \quad (9.47)$$

Finally, assuming that the perturbation is small, the result simplifies to

$$\Delta\Omega = \frac{ie^2 N \eta}{2\beta^2 E_0 T_0^2 \omega_s} \sum_{p=-\infty}^{\infty} [(p\omega_0 + \omega_s) Z_0^{\parallel}(p\omega_0 + \omega_s) - p\omega_0 Z_0^{\parallel}(p\omega_0)] . \quad (9.48)$$

The above shift in synchrotron frequency gives exactly the same growth rate as Eq. (9.41) when the driving impedance is a narrow resonance. The only difference is the second

term in Eq. (9.48). This term receives contribution from the imaginary part of the impedance only and describes the tune shift due to potential-well distortion. The origin of this term is very similar to the derivation of Eqs. (3.50) and (3.51). The only thing additional here is the inclusion of the wake effect from preceding bunch passages. Here, the wake field from preceding bunch passages does not move with the bunch as a whole, and therefore contributes a viewable coherent tune shift. This term should also appear in the Sacherer's growth formula. It has been left out because, during the derivation, only the perturbed distribution but not the unperturbed distribution have been substituted into the wake force in Eq. (9.8).

Now let us come back to Eq. (9.41). For M equal bunches, the equation becomes, for coupled-bunch mode μ ,

$$\frac{1}{\tau_{1\mu}} = \frac{\eta e^2 N M \omega_r}{2\beta^2 E_0 T_0^2 \omega_s} \left[\Re Z_0^\parallel(q M \omega_0 + \mu \omega_0 + \omega_s) - \Re Z_0^\parallel(q' M \omega_0 - \mu \omega_0 - \omega_s) \right]. \quad (9.49)$$

When $\mu = 0$, both terms will contribute with $q' = q$ and we have exactly the same Robinson's stability or instability as in the single bunch situation. This is illustrated in Fig. 9.2. When $\mu = M/2$ if M is even, both terms will contribute with $q' = q$, and the same Robinson's stability or instability will apply. For the other $M-2$ modes, only one term will be at or close to the resonant frequency and only one term will contribute. If the positive-frequency term contributes, we have instability. If the negative-frequency term contributes, we have damping instead. If one choose to speak in the language of only positive frequencies, there will be an upper and a lower synchrotron sideband surrounding each revolution harmonic. Above transition, the coupled-bunch system will be unstable if the driving resonance leans towards the upper sideband and stable if it leans towards the lower sideband.

For the higher azimuthal modes ($m > 1$) driven by a narrow resonance, we have the same Robinson's instability. The growth rates are

$$\begin{aligned} \frac{1}{\tau_{m\mu}} = & \frac{\eta e^2 N M \omega_r}{2\beta^2 E_0 T_0^2 \omega_s} \frac{m}{(m!)^2} \left(\frac{\omega_r \hat{\tau}}{2} \right)^{2m-2} \times \\ & \times \left[\Re Z_0^\parallel(q M \omega_0 + \mu \omega_0 + m \omega_s) - \Re Z_0^\parallel(q' M \omega_0 - \mu \omega_0 - m \omega_s) \right], \end{aligned} \quad (9.50)$$

which depend on the bunch length as $\hat{\tau}^{2m-2}$. As a result, higher azimuthal instabilities for short bunches will be much more difficult to excite. For long bunches, we need to evaluate the form factor F . An example will be discussed in Sec. 9.2.

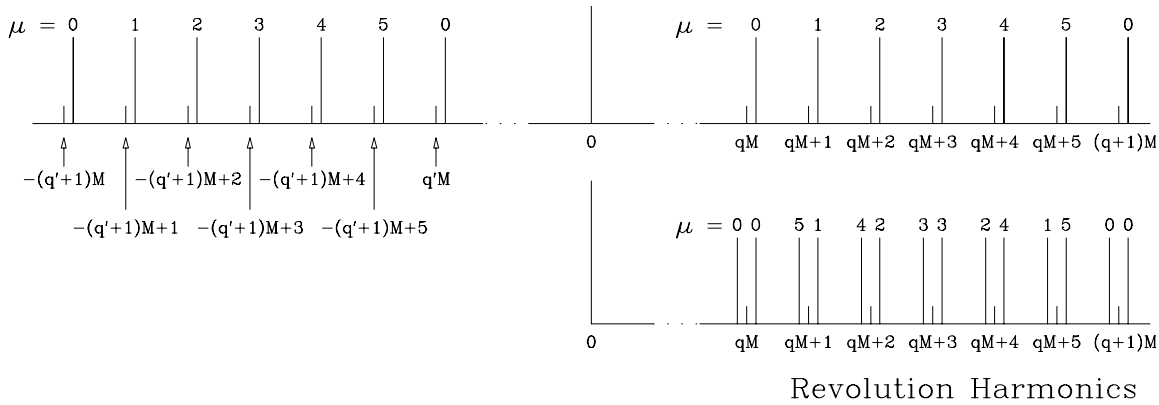


Figure 9.2: Top plot shows the synchrotron lines for both positive and negative revolution harmonics for the situation of $M = 6$ identical equally-spaced bunches. The coupled-bunch modes $\mu = 0, 1, 2, 3, 4, 5$ are listed at the top of the synchrotron lines. Lower plot shows the negative-harmonic side folded onto the positive-harmonic side. We see upper and lower sidebands for each harmonic line.

Landau damping can come from the spread of the synchrotron frequency. The spread due to the nonlinear sinusoidal rf wave form can be written as (Exercise 9.4)

$$\frac{\Delta\omega_s}{\omega_s} = \left(\frac{\pi^2}{16} \right) \left(\frac{1 + \sin^2 \phi_s}{1 - \sin^2 \phi_s} \right) (h\tau_L f_0)^2 , \quad (9.51)$$

where τ_L is the total length of the bunch and ϕ_s is the synchronous angle, and is valid for small amplitudes. The mode will be stable if [2]

$$\frac{1}{\tau} \lesssim \frac{\sqrt{m}}{4} \Delta\omega_s . \quad (9.52)$$

When the synchronous angle $\phi_s \neq 0$, the computation of synchrotron frequency spread is tedious. A numerical calculation is shown in Fig. 9.3 for various $\Gamma = \sin \phi_s$. The expression in Eq. (9.51) comes from a fitting to the numerical calculation at small amplitudes.

9.2 Time Domain

The longitudinal coupled-bunch instabilities can also be studied without going into the frequency domain. We are employing the same Vlasov equation in Eq. (9.7), but using

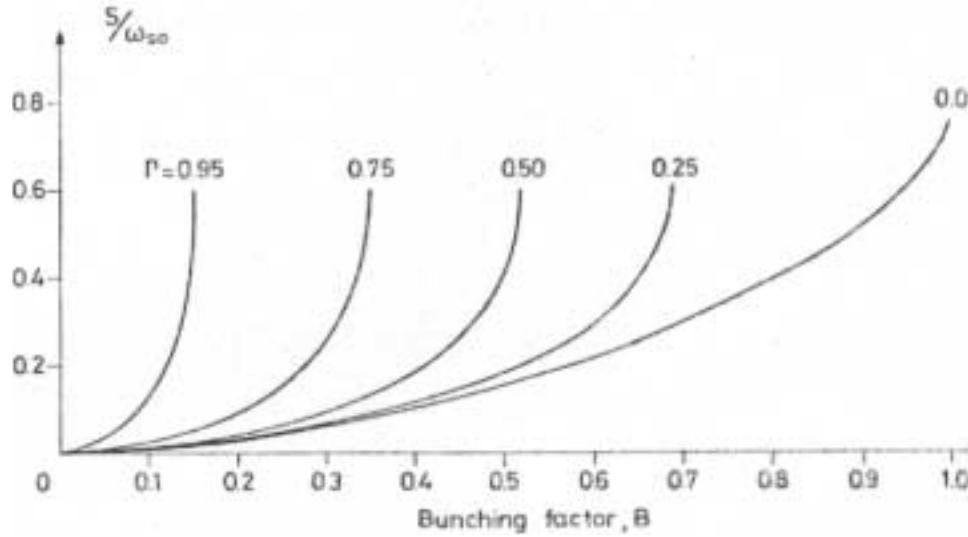


Figure 9.3: Synchrotron frequency spread S as a function of single-bucket bunching factor $B \approx \tau_L f_0$ for various values of $\Gamma = \sin \phi_s$. τ_L is full bunch length, f_0 is revolution frequency, ϕ_s is synchronous angle, and ω_{s0} is unperturbed angular synchrotron frequency.

the wake function of a resonance in the time domain. This derivation was first given by Sacherer [2].

The wake function for a resonance with resonant frequency $\omega_r/(2\pi)$, shunt impedance R_s and quality factor Q was given in Eq. (1.46). For a narrow resonance with $\alpha = \omega_r/(2Q) \ll \omega_r$, we can neglect the sine term[¶] and simplify the wake function to

$$W'_0(z) = \frac{\omega_r R_s}{Q} e^{-\alpha z/v} \cos \frac{\omega_r z}{v} \quad \text{when } z > 0 . \quad (9.53)$$

The wake force is then given by

$$\langle F_0^{\parallel}(\tau; s) \rangle = -\frac{e^2 \omega_r R_s}{QC} \int_{\tau}^{\infty} d\tau' e^{-\alpha(\tau' - \tau)} \cos[\omega_r(\tau' - \tau)] \rho[\tau'; s - v(\tau' - \tau)] , \quad (9.54)$$

where $\rho[\tau'; s - v(\tau' - \tau)]$ is the linear density of the beam particles passing the location s at time $\tau' - \tau$ ago. Now let $\rho(\tau; s)$ represent the line density of the individual bunch, which has a phase lead of $2\pi\mu/M$ for mode μ compared with the preceding bunch $\tau_{\text{sep}} = T_0/M$ ahead, and is influenced by all the preceding bunches. The location argument s

[¶]The sine term can be included at the expense of a slightly more complicated derivation.

of ρ in Eq. (9.54) becomes^{||} $s - k\tau_{\text{sep}} - v(\tau' - \tau)$, with $k = 0, 1, 2, \dots$. For simplicity, we neglect the time delay $\tau' - \tau$. In the time variation $e^{-i\Omega s/v}$ where $\Omega \approx m\omega_s$, this approximation causes a phase delay $\Omega(\tau' - \tau)$ which is negligible in comparison with the phase change due to the resonator. We will also neglect the variation in the attenuation factor over one bunch $e^{-\alpha(\tau' - \tau)}$, but we retain the attenuation factor between bunches $e^{-\alpha k\tau_{\text{sep}}}$. Then the wake force exerted on a particle in the μ th coupled-bunch mode can be written as

$$\langle F_{0\mu}^{\parallel}(\tau; s) \rangle = -\frac{e^2 \omega_r R_s}{QC} \sum_{k=0}^{\infty} e^{2\pi i k \mu / M - k \alpha \tau_{\text{sep}}} \int_{\substack{\text{one} \\ \text{bunch}}} d\tau' \cos[\omega_r(\tau' - \tau + k\tau_{\text{sep}})] \rho_1(\tau') e^{-i\Omega(s/v - k\tau_{\text{sep}})}, \quad (9.55)$$

where Eq. (9.10), the ‘time’ variations of preceding bunches in the μ th coupled mode, have been used. It is worth pointing out that the lower limits of the summation and integration *cannot* be extended to $-\infty$ as before, because the explicit expression of the wake function has been used. Note that only the perturbed line density ρ_1 is included. This is because we are interested in the growth rate here and the unperturbed part ρ_0 will not contribute to the growth rate. Changing the integration variables from $(\tau, \Delta E)$ to (r, ϕ) while keeping only the azimuthal m ,

$$\rho_1(\tau') d\tau' = \int \alpha_m R_m(r') e^{im\phi'} d\tau' d\Delta E' = \int \frac{E_0 \omega_s \beta^2}{\eta} \alpha_m R_m(r') e^{im\phi'} r' dr' d\phi'. \quad (9.56)$$

Substituting the wake force into Eq. (9.7), we arrive at

$$(\Omega - m\omega_s) R_m(r) = \frac{ie^2 N \eta \omega_r R_s}{2\pi \beta^2 E_0 Q T_0 \omega_s} \frac{dg_0}{dr} \sum_{k=0}^{\infty} e^{2\pi i k \mu / M - k(\alpha - i\Omega)\tau_{\text{sep}}} \times \\ \times \int_0^{\infty} r' dr' R_m(r') \int_{-\pi}^{\pi} d\phi e^{-im\phi} \sin \phi \int_{-\pi}^{\pi} d\phi' e^{im\phi'} \cos[\omega_r(r' \cos \phi' - r \cos \phi + k\tau_{\text{sep}})], \quad (9.57)$$

where again we have used the unperturbed distribution $g_0(r)$ given by Eq.(9.30) which is normalized to unity. The integrations over ϕ and ϕ' can now be performed using the formulas for Bessel functions depicted in Eqs. (9.26) to (9.28), giving

$$\int_{-\pi}^{\pi} d\phi e^{-im\phi} \sin \phi \int_{-\pi}^{\pi} d\phi' e^{im\phi'} \cos[\omega_r(r' \cos \phi' - r \cos \phi + k\tau_{\text{sep}})] = \\ i4\pi^2 \sin k\omega_r \tau_{\text{sep}} \frac{m J_m(\omega_r r') J_m(\omega_r r)}{\omega_r r}. \quad (9.58)$$

^{||}Here we include the term $k\tau_{\text{sep}}$ which Sacherer had left out. This term is important to exhibit Robinson’s criterion of phase stability.

Equation (9.57) now becomes

$$(\Omega - m\omega_s)R_m(r) = -\frac{2\pi e^2 N R_s m \eta}{\beta^2 E_0 Q T_0 \omega_s} \frac{dg_0}{dr} \times \sum_{k=0}^{\infty} e^{2\pi i k \mu / M - k(\alpha - i\Omega)\tau_{\text{sep}}} \sin(k\omega_r \tau_{\text{sep}}) \int_0^{\infty} dr' R_m(r') \frac{r' J_m(\omega_r r') J_m(\omega_r r)}{r}. \quad (9.59)$$

Finally, we introduce Landau damping by allowing the synchrotron frequency to be a function of the radial distance from the center of the bunch in the longitudinal phase space. Moving $\Omega - m\omega_s(r)$ to the right side and performing an integration over $r dr$, R_m can be eliminated resulting in the dispersion relation

$$1 = -\frac{i 2\pi e^2 M N m \eta R_s}{\beta^2 E_0 T_0^2 \omega_s \omega_r} D(\alpha \tau_{\text{sep}}) \int_0^{\infty} dr \frac{dg_0}{dr} \frac{J_m^2(\omega_r r)}{\Omega - m\omega_s(r)}, \quad (9.60)$$

where we have defined the function**

$$D(\alpha \tau_{\text{sep}}) = -i 2\alpha \tau_{\text{sep}} \sum_{k=0}^{\infty} e^{2\pi i k \mu / M - k(\alpha - i\Omega)\tau_{\text{sep}}} \sin(k\omega_r \tau_{\text{sep}}), \quad (9.61)$$

which contains all the information about the quality factor of the resonance and its location with respect to the revolution harmonics. It is interesting to note that Eq. (9.60) closely resembles Eq. (9.32). It will be shown below that $D = 1$ for a narrow resonance with the resonant peak located at $(qM + \mu)\omega_0 + m\omega_s$. Thus the two dispersion relations are identical. In fact, they are the same even when the resonant peak is not exactly located at a synchrotron line.

Let us study the function $D(\alpha \tau_{\text{sep}})$. Noting that the bunch separation is $\tau_{\text{sep}} = T_0/M$, this function can be rewritten as

$$D(\alpha \tau_{\text{sep}}) = \alpha \tau_{\text{sep}} \left(\frac{1}{1 - e^{x_+}} - \frac{1}{1 - e^{x_-}} \right), \quad (9.62)$$

where

$$x_{\pm} = \frac{2\pi i}{M} \left(q_{\pm} M + \mu + m \frac{\omega_s}{\omega_0} \mp \frac{\omega_r}{\omega_0} \right) - \alpha \tau_{\text{sep}}. \quad (9.63)$$

The $q_{\pm} M$ term comes about because we can replace μ in Eq. (9.61) by $q_{\pm} M + \mu$, where q_{\pm} are positive/negative integers and $\mu = 0, 1, \dots, M-1$. When the resonance is

**We would like $D = \pm 1$ when the resonance is at the upper/lower sideband. As a result, our definition of D differs from Sacherer's by a phase.

extremely narrow, we have $\alpha\tau_{\text{sep}} = \omega_r\tau_{\text{sep}}/(2Q) \ll 1$. The two terms in Eq. (9.62) almost cancel each other so that $D(\alpha\tau_{\text{sep}}) \approx 0$ unless $\omega_r \approx (|q_{\pm}|M \pm \mu)\omega_0$. For modes $\mu \neq 0$ and $\mu \neq \frac{1}{2}M$ if M is even, only one of the two terms in Eq. (9.62) contributes. If $\omega_r \approx (|q_{\pm}|M \pm \mu)\omega_0 \pm m\omega_s$, we have $|x_+| \ll 1$ or $|x_-| \ll 1$ and

$$D(\alpha\tau_{\text{sep}}) \approx \mp \frac{\alpha\tau_{\text{sep}}}{x_{\pm}} = \frac{-i\omega_r/(2Q)}{\omega_r - [(|q_{\pm}|M \pm \mu)\omega_0 \pm m\omega_s] \mp i\omega_r/(2Q)} \approx \pm 1. \quad (9.64)$$

When $\mu = 0$ or $\mu = M/2$ if M is even, it is possible to choose q_+ and q_- so that both terms will contribute. We have

$$D \approx \frac{-i\omega_r/(2Q)}{\omega_r - [(q_+M + \mu)\omega_0 + m\omega_s] - i\omega_r/(2Q)} + \frac{-i\omega_r/(2Q)}{\omega_r - [(|q_-|M - \mu)\omega_0 - m\omega_s] + i\omega_r/(2Q)}, \quad (9.65)$$

where $q_+ = |q_-|$ for $\mu = 0$ and $|q_-| = q_+ + 1$ for $\mu = M/2$. Note that Eq. (9.65) is just proportional to the difference between $Z_0^{\parallel}(q_+M\omega_0 + \mu\omega_0 + m\omega_s + i\alpha)$ and $Z_0^{\parallel}(|q_-|M\omega_0 - \mu\omega_0 - m\omega_s - i\alpha)$; the Robinson's stability criterion derived in Eq. (9.49) is therefore recovered.

On the other hand, when the resonance is broad, $\alpha\tau_{\text{sep}} \gg 1$. The first few terms in Eq. (9.61) dominate. Since $k = 0$ does not contribute, we include here only the next term,

$$D(\alpha\tau_{\text{sep}}) \approx -i2\alpha\tau_{\text{sep}} \sin(\omega_r\tau_{\text{sep}}) e^{2\pi i\mu/M - \alpha\tau_{\text{sep}}}. \quad (9.66)$$

The magnitude $|D|$ becomes mode independent and exhibits a maximum when $\omega_r\tau_{\text{sep}} = 2\pi (q + \frac{1}{4})$. Thus the coupled-bunch modes near $\mu = \pm\frac{1}{4}M$ are most strongly excited, although $|D|$ will be much less than unity. Figure 9.4 plots $|D|$ versus ω_r/ω_0 for the situation of $M = 10$ bunches. The solid vertical lines show $|D| \approx 1$ for narrow resonance. The dotted curve are for broadband resonance when the bunch-to-bunch attenuation decrement is $\alpha\tau_{\text{sep}} = 4$; the values of $|D|$ are small and appear to be mode-independent. The dashed curves correspond the intermediate case with bunch-to-bunch attenuation decrement $\alpha\tau_{\text{sep}} = 1$. From left to right, they are for modes $\mu = 0, 1$ and $9, 2$ and $8, 3$ and $7, 4$ and $6, 5$. We see that $|D|_{\text{max}}$ is roughly the same for each mode. Note that $\alpha\tau_{\text{sep}} = 1$ translates into $(\Delta\omega_r/\omega_0)_{\text{FWHM}} = M/\pi = 3.2$ or the resonance covers more than 3 revolution harmonics. Apparently, the figure shows that no mode will be excited if the ω_r/ω_0 falls exactly on qM or $q(\frac{1}{2}M)$ if M is even. This incorrect result appears because in drawing the plot, the limit $\omega_s \rightarrow 0$ has been taken. Figure 9.5 plots $|D|_{\text{max}}$ versus the bunch-to-bunch decrement $\alpha\tau_{\text{sep}}$, showing that it is less than 5% from unity when $\alpha\tau_{\text{sep}} < 0.55$.

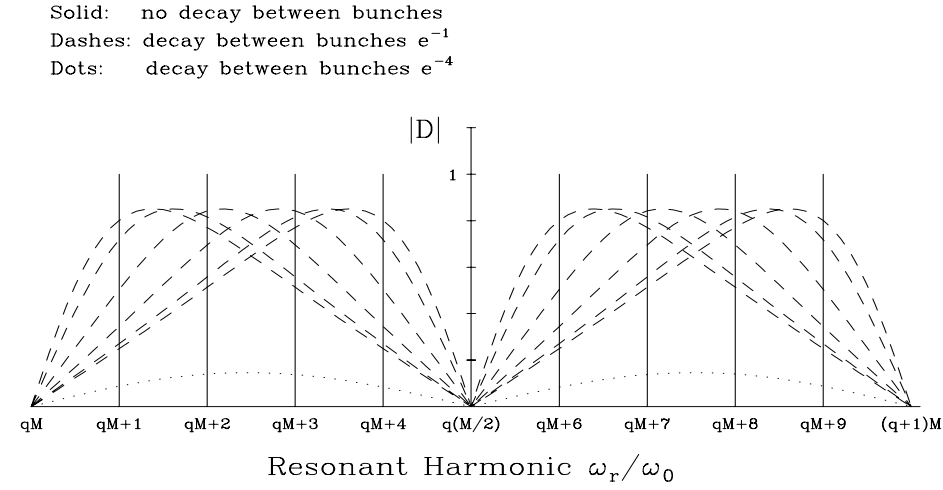


Figure 9.4: $|D|$ as functions of resonant harmonic ω_r/ω_0 for $M = 10$ bunches when bunch-to-bunch decay decrement $\alpha\tau_{\text{sep}} \ll 1$ for narrowband resonance (solid), $\alpha\tau_{\text{sep}} = 4$ for broadband resonance (dots), and $\alpha\tau_{\text{sep}} = 1$ for resonance in between (dashes). The dashed curves from left to right represent coupled-bunch modes $\mu = 0, 1$ and $9, 2$ and $8, 3$ and $7, 4$ and $6, 5$. The excitations at $\omega_r/\omega_0 = 0$, or $M/2$ are zero, because we have set the synchrotron frequency to zero in the plot.

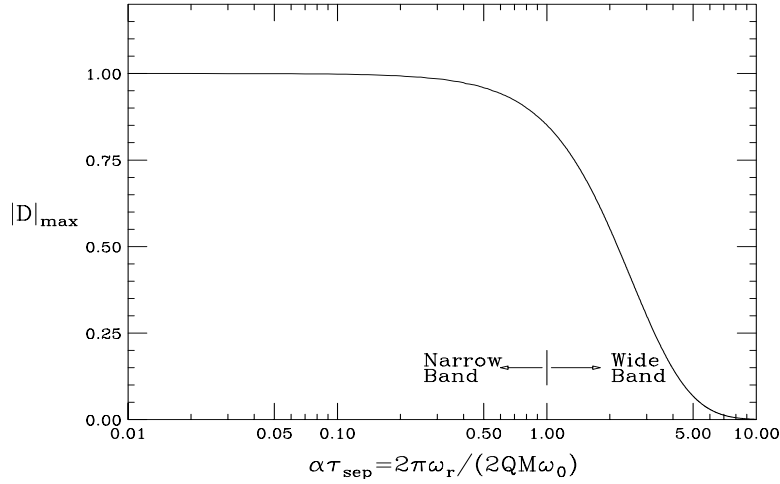


Figure 9.5: $|D|_{\text{max}}$ as a function of bunch-to-bunch decay decrement $\alpha\tau_{\text{sep}}$. Note that $|D|_{\text{max}} \approx 1$ for narrow resonances but drops very rapidly as the resonance becomes broader.

In the event that the spread in synchrotron frequency is small, we can obtain from Eq. (9.60) the synchrotron frequency shift

$$\Omega - m\omega_s = -\frac{i2\pi e^2 NR_s m M \eta}{\beta^2 E_0 \omega_s \omega_r T_0^2} D(\alpha \tau_{\text{sep}}) \int_0^\infty dr \frac{dg_0}{dr} J_m^2(\omega_r r) , \quad (9.67)$$

where the integral can be viewed as a form factor which is distribution dependent. A dimensionless form factor

$$F_m(\Delta\phi) = -\frac{4\pi m \hat{\tau}}{\omega_r} \int_0^\infty dr \frac{dg_0}{dr} J_m^2(\omega_r r) \quad (9.68)$$

can now be defined for each azimuthal, where $\hat{\tau}$ is the half bunch length and $\Delta\phi = 2\omega_r \hat{\tau}$ is the change in phase of the resonator during the passage of the whole bunch. Then the frequency shift can be rewritten as

$$\Omega - m\omega_s = \frac{i\eta e^2 NMR_s}{4\pi \beta^2 E_0 \nu_s T_0 \hat{\tau}} D(\alpha \tau_{\text{sep}}) F_m(\Delta\phi) , \quad (9.69)$$

where $\nu_s = \omega_s / \omega_0$ is the synchrotron tune.

We take as an example the *parabolic* distribution in the longitudinal phase space^{††}, which implies

$$g_0(r) = \frac{2}{\pi \hat{\tau}^4} (\hat{\tau}^2 - r^2) \quad \text{and} \quad \frac{dg_0}{dr} = -\frac{4r}{\pi \hat{\tau}^4} . \quad (9.70)$$

The form factor is

$$\begin{aligned} F_m(\Delta\phi) &= \frac{32m}{\Delta\phi} \int_0^1 J_m^2\left(\frac{1}{2}x\Delta\phi\right) x dx \\ &= \frac{16m}{\Delta\phi} \left[J_m^2\left(\frac{1}{2}\Delta\phi\right) - J_{m+1}\left(\frac{1}{2}\Delta\phi\right) J_{m-1}\left(\frac{1}{2}\Delta\phi\right) \right] , \end{aligned} \quad (9.71)$$

which is plotted in Fig. 9.6 for $m = 1$ to 6. The form factor specifies the efficiency with which the resonator can drive a given mode. We see that the maximum value of F_1 for the dipole mode occurs when $\Delta\phi \approx \pi$. This is to be expected because the head and tail of the bunch will be driven in opposite directions. Similarly, the quadrupole or breathing mode is most efficiently driven when $\Delta\phi \approx 2\pi$, and so on for the higher modes. In general, mode m is most efficiently driven when the resonator frequency is $\Delta\phi \approx m\pi$. Note also that the maximum value of F_m drops faster than $m^{-1/2}$, implying that higher azimuthal modes are harder to excite. For distributions other than the “parabolic” of Eq. (9.70),

^{††}This is different from the so-called parabolic distribution, which is actually parabolic line density.

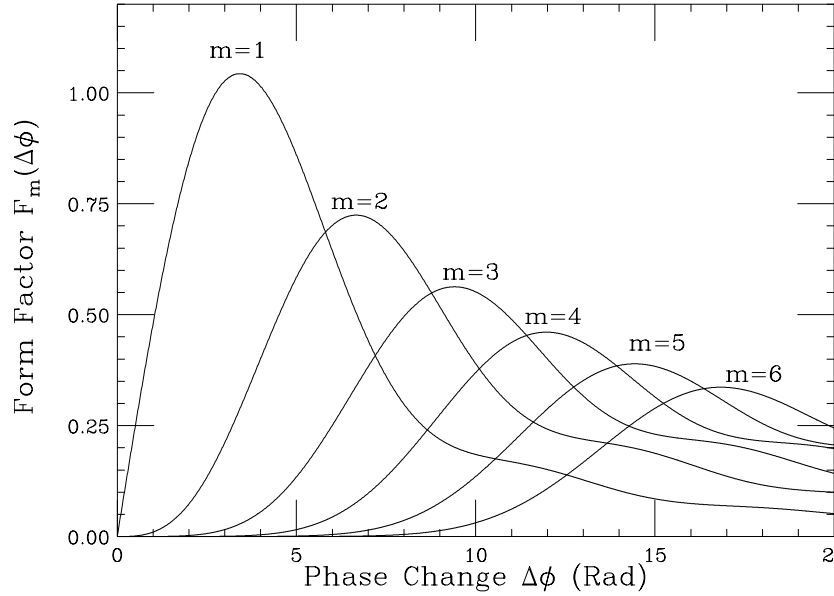


Figure 9.6: Sacherer's form factor for longitudinal oscillation inside a bunch with azimuthal modes $m = 1, 2, 3, 4, 5$ and 6 . The unperturbed parabolic distribution in the longitudinal phase space, Eq. (9.70), is assumed.

we expect the form factors to have similar properties. However, a shorter bunch does not necessarily imply a slower growth especially for the $m = 1$ mode, although the excitation in the form factor $F_m(\Delta\phi)$ is small. According to Eq. (9.69), the growth rate is obtained from multiplying the form factor $F_m(\Delta\phi)$ with $eN/\hat{\tau}$, the local linear charge density or peak current. In fact, with a fixed number of particles in the bunch, as the bunch length is shortened, the local linear charge density increases, thus enhancing the growth rate. As a result, a more practical form factor should be $\bar{F}_m(\Delta\phi) = 2F_m(\Delta\phi)/\Delta\phi$ as plotted in Fig. 9.7 in logarithmic scale. It is clear that for small $\Delta\phi$, $F_1 \approx \frac{1}{2}\Delta\phi$ and $\bar{F}_1 \approx 1$. From Eq. (9.67), the growth rate for the dipole mode above transition can be written as

$$\frac{1}{\tau_1} = \mathcal{I}_m \Omega = \frac{\eta e^2 N M R_s \omega_r}{2\beta^2 E_0 \omega_s T_0^2} D(\alpha \tau_{\text{sep}}) , \quad (9.72)$$

which agrees with the expression in Eq. (9.49) derived for short bunches. It is also evident from Fig. 9.7 that the excitations of higher azimuthal modes will be very much smaller.

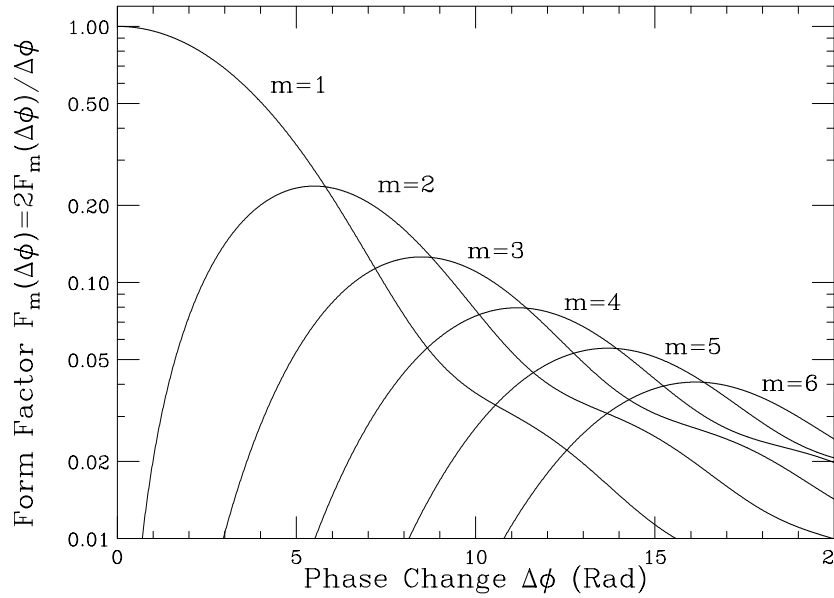


Figure 9.7: A more useful form factor $\bar{F}(\Delta\phi)$ in logarithmic scale for longitudinal oscillation inside a bunch with azimuthal modes $m = 1, 2, 3, 4, 5$ and 6 . The unperturbed parabolic distribution in the longitudinal phase space is assumed. It is related to the Sacherer's form factor of Fig. 9.6 by $\bar{F}(\Delta\phi) = 2F(\Delta\phi)/\Delta\phi$.

9.3 Observation and Cures

The easiest way to observe longitudinal coupled-bunch instability is in a mountain-range plot, where bunches oscillate in a particular pattern as time advances. Examples are shown in Figs. 9.8 and 9.9. Streak camera can also be used to capture the phases of adjacent bunches as a function of time. From the pattern of coupling, the coupled-mode μ can be determined. From the frequency of oscillation, the azimuthal mode m can also be determined. We can then pin down the frequency $\omega_r/(2\pi)$ of the offending resonance driving the instability.

Observation can also be made in the frequency domain by zooming in the region between two rf harmonics in the way illustrated in Fig. 9.2. The coupled-bunch mode excited will be shown as a strong spectral line in between.

Longitudinal coupled-bunch instability will lead to an increase in bunch length and an increase in energy spread. For a light source, this translates into an increase in the spot size of the synchrotron light.

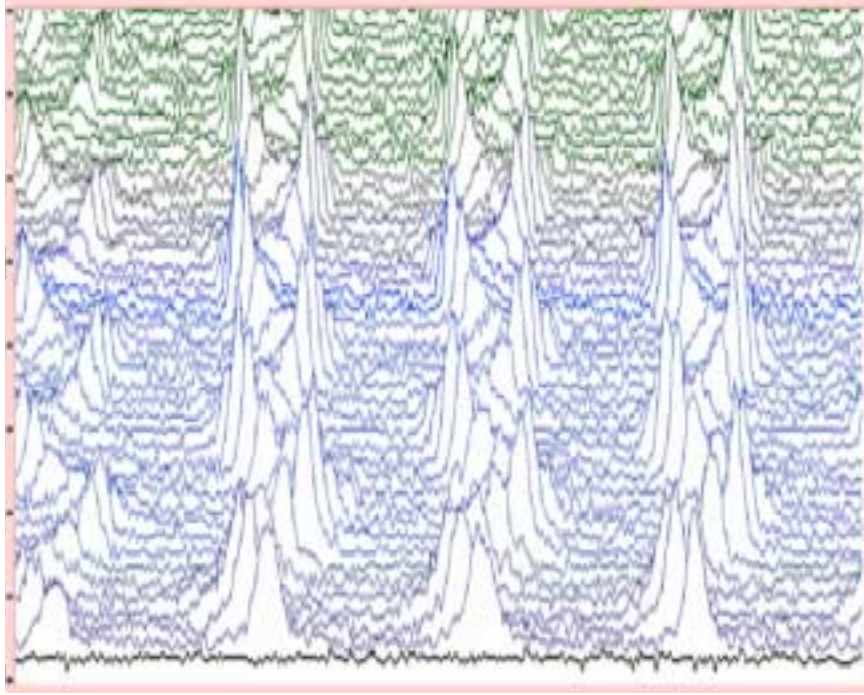


Figure 9.8: (color) Mountain-range plot showing coupled-bunch instability in the Fermilab Main Injector just after injection at 8 GeV.

There are many ways to cure longitudinal coupled bunch instability. The driving resonances are often the higher-order modes inside the rf cavities. When the particular resonance is identified and if it is much narrower than the revolution frequency of the ring, we can try to shift its frequency so that it resides in between two revolution harmonics and becomes invisible to the beam particles. We can also study the electromagnetic field pattern of this resonance mode inside the cavity and install passive resistors and antennae to damp this particular mode. This method has been used widely in the Fermilab Booster, where longitudinal coupled-bunch instability had been very severe after the beam passed the transition energy. At that time, the bunch area increased almost linearly with bunch intensity. Passive damping of several offending modes cured this instability to such a point that the bunch area does not increase with bunch intensity anymore.

Longitudinal coupled-bunch instability had also been observed in the former Fermilab Main Ring. Besides passive damping of the cavity resonant modes, the instability was also reduced by lowering the rf voltage. Lowering the rf voltage will lengthen the bunch and reduce the form factor $F_m(\Delta\phi)$. This is only possible for a proton machine

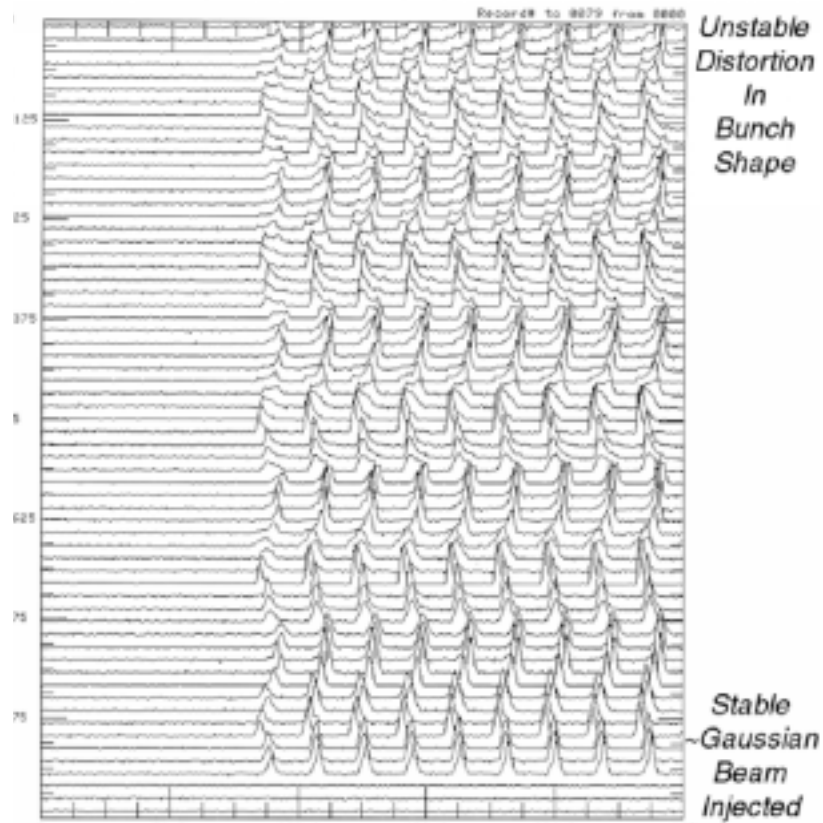


Figure 9.9: Mountain range plot showing bunches in a batch executing coupled-bunch instability in the Fermilab Main Injector just after injection at 8 GeV

where the bunches are long. It will not work for the short electron bunches for the $m = 1$ dipole mode. This is because, as mentioned before, the form factor for the dipole mode is not sensitive to the bunch length for short bunches. Even for a proton machine, the rf voltage cannot be reduced by a large amount because proton bunches are usually rather tight inside the rf bucket, especially during ramping.

If the growth turns out to be harmful, a fast bunch-by-bunch damper may be necessary to damp the dipole mode ($m = 1$). A damper for the quadrupole mode ($m = 2$) may also be necessary. This consists essentially of a wall-gap pickup monitoring the changes in bunch length and the corresponding excitation of a modulation of the rf waveform with roughly twice the synchrotron frequency. A feed-back correction is then made to the rf voltage. Another way to damp the longitudinal coupled-bunch instability is to break the symmetry between the M bunches. For example, a 5% to 10% variation in the intensity of the bunches will help. Another way to break the symmetry

is to have bunches not placed symmetrically in the ring. Some analysis shows that the stability will be improved if some bunches in the symmetric configuration are missing [3]. Prabhakar [4] recently proposed a new way to cure longitudinal coupled-bunch instability using uneven fill in a storage ring. We are going to discuss this method in more detail in Sec. 9.3.4.

There can also be Landau damping, which comes from the spread of the synchrotron frequency. The spread due to the nonlinear sinusoidal rf wave form as given by Eq. (9.51) is usually small unless the synchronous angle is large. Electron bunches are usually much smaller in size than the rf bucket. As a result, the spread in synchrotron frequency is very minimal and does not help much in Landau damping.

9.3.1 Higher-Harmonic Cavity

In order to Landau damp longitudinal coupled-bunch instability, a large spread in synchrotron frequency inside the bunch is required. One way to do this is to install a higher-harmonic cavity, sometime known as *Landau cavity* [5] because it provides Landau damping. For example, the higher-harmonic cavity has resonant angular frequency $m\omega_{\text{rf}}$ and voltage rV_{rf} , where ω_{rf} is the resonant angular frequency and V_{rf} the voltage of the fundamental rf cavity. The total rf voltage seen by the beam particles becomes

$$V(\tau) = V_{\text{rf}} [\sin(\phi_s - \omega_{\text{rf}}\tau) - r \sin(\phi_m - m\omega_{\text{rf}}\tau)] - \frac{U_s}{e} , \quad (9.73)$$

where the phase angles ϕ_s and ϕ_m are chosen to compensate for U_s , the radiation energy loss, or to provide any required acceleration. We would like the bottom of the potential well, which is the integral of $V(\tau)$, to be as flat as possible. The rf voltage seen by the synchronous particle is compensated to zero by the energy lost to synchrotron radiation. In addition, we further require

$$\left. \frac{\partial V}{\partial \tau} \right|_{\tau=0} = 0 \quad \text{and} \quad \left. \frac{\partial^2 V}{\partial \tau^2} \right|_{\tau=0} = 0 , \quad (9.74)$$

so that the potential will become quartic instead. We therefore have 3 equations in 3 unknowns:

$$\sin \phi_s = r \sin \phi_m + \frac{U_s}{eV_{\text{rf}}} , \quad (9.75)$$

$$\cos \phi_s = rm \cos \phi_m , \quad (9.76)$$

$$\sin \phi_s = rm^2 \sin \phi_m , \quad (9.77)$$

from which ϕ_m and r can be solved easily (Exercise 9.5). For small-amplitude oscillation, the potential becomes

$$-\int V(\tau) d(\omega_{\text{rf}} \tau) \longrightarrow \frac{m^2 - 1}{24} (\omega_{\text{rf}} \tau)^4 V_{\text{rf}} \cos \phi_s , \quad (9.78)$$

which is quartic and the synchrotron frequency is (Exercise 9.6)

$$\frac{\omega_s(\tau)}{\omega_{s0}} = \frac{\pi}{2} \left(\frac{m^2 - 1}{6} \right)^{1/2} \frac{\omega_{\text{rf}} \tau}{K(1/\sqrt{2})} \left[\frac{1 - \left(\frac{m^2}{m^2 - 1} \frac{U_s}{eV_{\text{rf}}} \right)^2}{1 - \left(\frac{U_s}{eV_{\text{rf}}} \right)^2} \right]^{1/4} , \quad (9.79)$$

where the last factor can usually be neglected; its deviates from unity by only $\sim [(m^2 - 1)U_s/(2eV_{\text{rf}})]^2$ if the synchronous angle is small. In above, ω_{s0} is the synchrotron angular frequency at zero amplitude when the higher-harmonic cavity voltage is turned off, and $K(1/\sqrt{2}) = 1.854$ is the complete elliptic integral of the first kind which is defined as

$$K(t) = \int_0^{\pi/2} \frac{d\theta}{\sqrt{1 - t^2 \sin^2 \theta}} . \quad (9.80)$$

We see that the synchrotron frequency is zero at zero amplitude and increases linearly with amplitude. This large spread in synchrotron frequency may be able to supply ample Landau damping to the longitudinal coupled-bunch instability.

In the situation where there is no radiation loss and no acceleration, $U_s = 0$, the solution of Eqs. (9.75) to (9.77) simplifies, giving $\phi_s = \phi_m = 0$ and the ratio of the voltages of higher-harmonic cavity to the fundamental $r = 1/m$. Of course, it is also possible to have $r \neq 1/m$. Then the synchrotron frequency at the zero amplitude will not be zero and the spread in synchrotron frequency can still be appreciable. When $m = 2$, i.e., having a second-harmonic cavity, the mathematics simplifies. The synchrotron frequencies for various values of r are plotted in Fig. 9.10. Here, $r = 0$ implies having only the fundamental rf while $r = \frac{1}{2}$ the situation of having the synchrotron frequency linear in amplitude for small amplitudes. In between, the synchrotron frequency spread decreases as r decreases. Notice that for $0.3 \lesssim r < 0.5$, the synchrotron frequency has a maximum near the rf phase of $\sim 100^\circ$. Particles near there will have no Landau damping at all and experience instability. Thus the size of the bunch is limited when a double cavity is used. Also the size of the bunch cannot be too small because of two reasons: first, the average synchrotron frequency may have been too low, and second, the central region of the phase space is a sea of chaos [7].

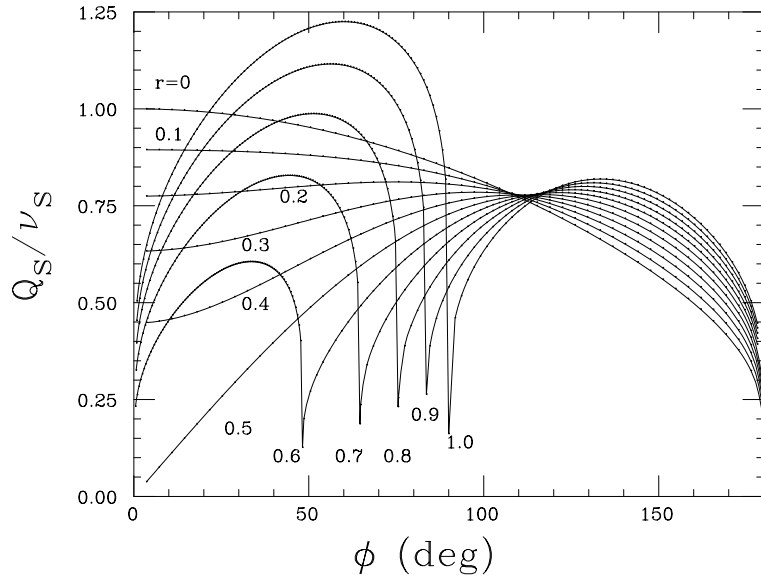


Figure 9.10: The normalized synchrotron tune of a double rf system as a function of the peak rf phase ϕ for various voltage ratio r . Here, the higher-harmonic cavity has frequency twice that of the fundamental. When $r > \frac{1}{2}$, the center of the bucket becomes an unstable fixed point and two stable fixed points emerge [7].

A Landau cavity increases the spread in synchrotron frequency, therefore it is ideal in damping mode-coupling instability and coupled-bunch instability. However, it may be not helpful for the Keil-Schnell type longitudinal microwave instability, which is valid for coasting beams. This method was first applied successfully with a third-harmonic cavity to increase Landau damping at the Cambridge Electron Accelerator (CEA) [8]. It was later applied to the Intersecting Storage Ring (ISR) at CERN SR a 6th harmonic cavity to cure mode-coupling instability [9]. Recently, a third-harmonic cavity has been reported in the SOLEIL ring in France to give a relative frequency spread of about 200%. However, since the center frequency has been dramatically decreased (not exactly to zero), the net result is a poor improvement in the stabilization. The gain in the stability threshold has been only 30% [6].

Actually, with a higher-harmonic cavity, the bunch becomes more rectangular-like in the longitudinal phase space, or particles are not so concentrated at the center of the bunch. Assuming the bunch area to be the same, the Boussard-modified Keil-Schnell threshold is proportional to the energy spread. Since the bunch becomes more flattened, the maximum energy spread which is at the center of the bunch is actually reduced, and

so will be the instability threshold. However, spreading out the particles longitudinally does help to increase the bunching factor and decrease the incoherent self-field or space-charge tune shift. At the CERN Proton Synchrotron Booster, an rf system with higher harmonics 5 to 10 has raised the beam intensity by about 25 to 30% [10]. For the Cooler Ring at the Indiana University Cyclotron Facility, a double cavity has been able to quadruple the beam intensity [7].

9.3.2 Passive Landau Cavity

Higher-harmonic cavities are useful in producing a large spread in synchrotron frequency so that single-bunch mode-mixing instability and coupled-bunch instability can be damped. However, the power source to drive this higher-harmonic rf system can be rather costly. One way to overcome this is to do away with the power source and let the higher-harmonic cavity or cavities be driven by the beam loading voltage of the circulating beam.

Let the ratio of the resonant frequencies of the higher-harmonic cavity to the fundamental rf cavity be m and the rf harmonic of the fundamental rf cavity be h . If the higher-harmonic cavity has a high quality factor, the beam loading voltage is just i_b , the current component at the cavity resonant frequency, multiplied by the impedance of the cavity. Here, for a Gaussian bunch

$$i_b = 2I_0 e^{-\frac{1}{2}(mh\omega_0\sigma_\tau)^2} , \quad (9.81)$$

where σ_τ is the rms bunch length and ω_0 is the angular revolution frequency. Thus for a short bunch, $i_b \approx 2I_0$ with I_0 being the average current of the bunch.

The higher-harmonic cavity must have suitable shunt impedance R_s and quality factor Q , and this can be accomplished by installing necessary resistor across the cavity gap. Thus, R_s and Q can be referred to as the loaded quantities of the cavity. For a particle arriving at time τ ahead of the synchronous particle, it sees the total voltage

$$V(\tau) = V_{\text{rf}} \sin(\phi_s - \omega_{\text{rf}}\tau) - i_b R_s \Re \left[\frac{1}{1 + i2Q\delta} e^{im\omega_{\text{rf}}\tau} \right] - \frac{U_s}{e} , \quad (9.82)$$

where $\omega_{\text{rf}} = h\omega_0$ is the angular rf frequency determined by the resonator in the rf klystron that drives the fundamental rf cavity and the negative sign in front of i_b indicates that

this beam loading voltage is induced by the image current and opposes the beam current. In above,

$$\delta = \frac{1}{2} \left(\frac{\omega_r}{m\omega_{\text{rf}}} - \frac{m\omega_{\text{rf}}}{\omega_r} \right) \approx \frac{\omega_r - m\omega_{\text{rf}}}{\omega_r} \quad (9.83)$$

represents the deviation of the resonant angular frequency ω_r of the higher-harmonic cavity from the m th multiple of the rf angular frequency. Of course, this is related to the detuning angle ψ of the higher-harmonic cavity, which we introduce in the usual way as

$$\tan \psi = 2Q\delta . \quad (9.84)$$

Now, Eq. (9.82) can be rewritten as

$$V(\tau) = V_{\text{rf}} \sin(\phi_s - \omega_{\text{rf}}\tau) - i_b R_s \cos \psi \cos(\psi - m\omega_{\text{rf}}\tau) - \frac{U_s}{e} . \quad (9.85)$$

Again to acquire the largest spread in synchrotron frequency, we require

$$V(0) = 0 , \quad V'(0) = 0 , \quad V''(0) = 0 , \quad (9.86)$$

so that the potential for small amplitudes becomes quartic,

$$U(\tau) = - \int V(\tau) d\tau = - \frac{\tau^4}{4!} V'''(0) . \quad (9.87)$$

Since we are having exactly the same quartic potential as in an rf system with an active Landau cavity, we expect the synchrotron frequency to be exactly the same as the expression given by Eq. (9.79) when the oscillation amplitude is small.

The set of requirements, however, are different from that of the active Landau cavity system. Here, the requirements are

$$V_{\text{rf}} \sin \phi_s = i_b R_s \cos^2 \psi + U_s/e , \quad (9.88)$$

$$V_{\text{rf}} \cos \phi_s = -m i_b R_s \cos \psi \sin \psi , \quad (9.89)$$

$$V_{\text{rf}} \sin \phi_s = m^2 i_b R_s \cos^2 \psi . \quad (9.90)$$

For an electron machine which is mostly above transition, the synchronous angle ϕ_s is between $\frac{1}{2}\pi$ and π . Thus, from Eq. (9.89), we immediately obtain

$$\sin 2\psi > 0 \implies 0 < \psi < \frac{\pi}{2} , \quad (9.91)$$

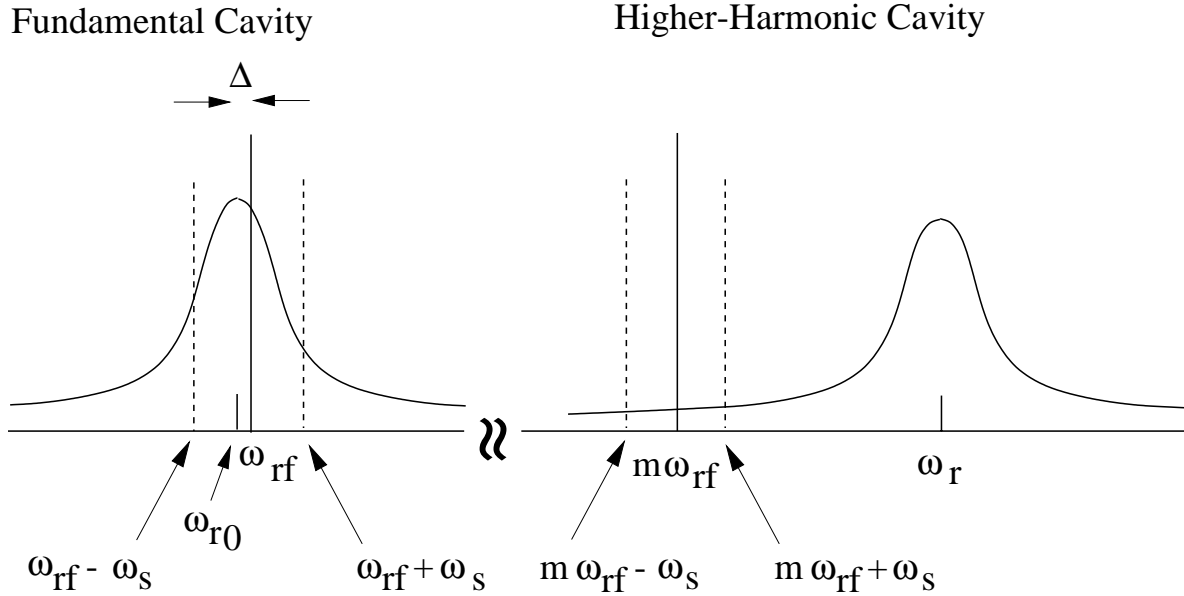


Figure 9.11: For the higher-harmonic cavity, the resonant frequency ω_r is above the m th multiple of the rf frequency. The beam will be Robinson unstable above transition. For the fundamental cavity, the resonant frequency ω_{r0} is below the rf frequency $\omega_{rf} = h\omega_0$, and the beam will be Robinson stable. The detuning of the fundamental rf should be so chosen that the beam will be stable after traversing both cavities.

and from Eqs. (9.83) and (9.84), $\omega_r > m\omega_{rf}$. This means that the beam in the higher-harmonic cavity is Robinson unstable [4], as is illustrated in Fig. 9.11. Of course, the fundamental rf cavity should be Robinson stable, and it will be nice if the detuning is so chosen that the beam remains stable after traversing both cavities.

The synchrotron light source electron ring at LNLS, Brazil would like to install a passive Landau cavity with $m = 3$ in order to alleviate the longitudinal coupled-bunch instabilities. The fundamental rf system has harmonic $h = 148$ or rf frequency $f_{rf} = \omega_{rf}/(2\pi) = 476.0$ MHz with a tuning range of ± 10 kHz, and rf voltage $V_{rf} = 350$ kV. To overcome the radiation loss, the synchronous phase is set at $\phi_{s0} = 180^\circ - 19.0^\circ$. This gives a synchrotron tune at small amplitudes $\nu_s = 6.87 \times 10^{-3}$ or a synchronous frequency $f_s = 22.1$ kHz.

With the installation of the passive Landau cavity, the synchronous phase must be modified to a new ϕ_s , which is obtained by solving Eqs. (9.88) and (9.90):

$$\sin \phi_s = \left(\frac{m^2}{m^2 - 1} \right) \left(\frac{U_s}{eV_{\text{rf}}} \right) = \frac{m^2}{m^2 - 1} \sin \phi_{s0} . \quad (9.92)$$

Thus,

$$\phi_{s0} = 180^\circ - 19.0^\circ \implies \phi_s = 180^\circ - 21.49^\circ , \quad (9.93)$$

where $m = 3$ has been used. The detuning ψ of the higher-harmonic cavity can be obtained from Eqs. (9.89) and (9.90), or

$$\tan \psi = -m \cot \phi_s \implies \psi = 82.53^\circ . \quad (9.94)$$

Finally from Eq. (9.90),

$$i_b R_s = \frac{V_{\text{rf}} \sin \phi_s}{m^2 \cos^2 \psi} . \quad (9.95)$$

With $i_b = 2I_0 = 0.300$ A and $V_{\text{rf}} = 350$ kV, we obtain the shunt impedance of the higher-harmonic cavity to be $R_s = 2.81$ MΩ. The power taken out from the beam is

$$P = \frac{1}{2} \frac{i_b^2 R_s}{1 + \tan^2 \psi} = 2.14 \text{ kW} , \quad (9.96)$$

which is not large when compared with the power loss due to radiation

$$P_{\text{rad}} = N U_s f_0 = I_0 V_{\text{rf}} \sin \phi_{s0} = 17.09 \text{ kW} , \quad (9.97)$$

where N is the number of electrons in the bunch. The higher-harmonic cavity has a quality factor of $Q = 45000$ and a resonant frequency $f_r \sim 3f_{r0} = 1428$ MHz. From the detuning, it can easily found that the frequency offset is $f_r - 3f_{\text{rf}} = 121$ kHz.

Now let us compute the growth rate for one bunch at the coherent frequency Ω . For one particle of time advance τ , we have from Sacherer's integral equation for a short bunch [2],

$$\Omega^2 - \omega_s(\tau)^2 = \frac{i\eta e I_0}{E_0 T_0} \sum_q (q\omega_0 + \Omega) Z_0^{\parallel}(q\omega_0 + \Omega) . \quad (9.98)$$

where η is the slip factor and we have retained the dependency of the synchrotron frequency ω_s on τ because of its large spread in the presence of the higher-harmonic cavity. From Eq. (9.79), this dependency is

$$\frac{\omega_s(\tau)}{\omega_{s0}} = \frac{\pi}{2} \left(\frac{m^2 - 1}{6} \right)^{1/2} \frac{\omega_{\text{rf}} \tau}{K(1/\sqrt{2})} \sqrt{\frac{\cos \phi_s}{\cos \phi_{s0}}} , \quad (9.99)$$

where the last factor amounts to 0.9920 and can therefore be safely abandoned. Thus, the average ω_s^2 over the whole bunch just gives the square of the rms frequency spread,

$$\langle \omega_s^2 \rangle = \sigma_{\omega_s}^2 = \left[\frac{\pi \omega_{s0}}{2} \sqrt{\frac{m^2 - 1}{6}} \frac{\omega_{rf} \sigma_\tau}{K(1/\sqrt{2})} \right]^2. \quad (9.100)$$

The FWHM natural bunch length at $V_{rf} = 350$ kV is $\tau_{FWHM} = 70.6$ ps; thus $\sigma_\tau = 30.0$ ps. This gives $\sigma_{\omega_s} = \tau_{FWHM}/(2\sqrt{2 \ln 2}) = 12.2$ kHz.

Since the synchrotron frequency is now a function of the offset from the stable fixed point of the rf bucket, a dispersion relation can be obtained from Eq. (9.98) by integrating over the synchrotron frequency distribution of the bunch. Here, we are interested in the growth rate without Landau damping, which is given approximately by

$$\frac{1}{\tau} = \text{Im } \Omega \approx \frac{\eta e I_0 \omega_{rf}}{2E_0 T_0 (2\sigma_{\omega_s})} \left\{ \left[\Re Z_0^\parallel(\omega_{rf} + 2\sigma_{\omega_s}) - \Re Z_0^\parallel(\omega_{rf} - 2\sigma_{\omega_s}) \right] + m \left[\Re Z_0^\parallel(m\omega_{rf} + 2\sigma_{\omega_s}) - \Re Z_0^\parallel(m\omega_{rf} - 2\sigma_{\omega_s}) \right] \right\}, \quad (9.101)$$

where the mean angular synchrotron frequency has been assumed to be

$$\bar{\omega}_s = 2\sigma_{\omega_s}. \quad (9.102)$$

The growth rate can be computed easily by substituting into Eq. (9.101) the expression for $\Re Z_0^\parallel$. However, the differences in Eq. (9.101) can also be approximated by derivatives. For the higher-harmonic cavity, both the upper and lower synchrotron sidebands lie on the same side of the higher-harmonic resonance as indicated in Fig. 9.11. Their difference, $\sim 4\sigma_{\omega_s}/(2\pi) = 7.76$ kHz, is also very much less than the cavity detuning $(\omega_r - m\omega_{rf})/(2\pi) = 121$ kHz. Recalling that

$$\Re Z_0^\parallel(\omega) = R_s \cos^2 \psi, \quad (9.103)$$

where the detuning ψ is given by Eq. (9.84), the second term can be written as a differential,

$$\Re Z_0^\parallel(m\omega_{rf} + 2\sigma_{\omega_s}) - \Re Z_0^\parallel(m\omega_{rf} - 2\sigma_{\omega_s}) \approx \left[R_s \cos^2 \psi \sin 2\psi \frac{2Q}{\omega_r} \right] 4\sigma_{\omega_s}. \quad (9.104)$$

For the fundamental cavity, the resonant frequency is $\omega_{r0}/(2\pi) = 476.00$ MHz. The detuning is usually $\Delta = -10$ kHz at injection and is reduced to $\Delta = -2$ kHz in

storage mode when the highest electron energy is reached. Thus, the upper and lower synchrotron sidebands lie on either side of the resonance as illustrated in Fig. 9.11. Since $\Delta \ll \sigma_{\omega_s}$, we can also write the first term of Eq. (9.101) as a differential about $\omega_{r0} + \bar{\omega}_s$, with the assumption that the resonance is symmetric about the resonant frequency ω_{r0} . Thus,

$$\begin{aligned} & \operatorname{Re} Z_0^{\parallel}(\omega_{\text{rf}} + \bar{\omega}_s) - \operatorname{Re} Z_0^{\parallel}(\omega_{\text{rf}} - \bar{\omega}_s) \\ &= \operatorname{Re} Z_0^{\parallel}(\omega_{r0} + \Delta + \bar{\omega}_s) - \operatorname{Re} Z_0^{\parallel}(\omega_{r0} - \Delta + \bar{\omega}_s) \approx \left[R_s \cos^2 \psi_{\omega_s} \sin 2\psi_{\omega_s} \frac{2Q}{\omega_{r0}} \right] 2\Delta , \end{aligned} \quad (9.105)$$

where ψ_{ω_s} , which is similar to a detuning angle by the amount $\bar{\omega}_s$, is defined as

$$\tan \psi_{\omega_s} = 2Q \frac{\bar{\omega}_s}{\omega_{r0}} . \quad (9.106)$$

We arrive at

$$\frac{1}{\tau} = \frac{2\eta e I_0 Q}{E_0 T_0} \left[\frac{\Delta}{\bar{\omega}_s} R_s \cos^2 \psi_{\omega_s} \sin 2\psi_{\omega_s} \Big|_{\text{fund}} + R_s \cos^2 \psi \sin 2\psi \Big|_{\text{higher}} \right] , \quad (9.107)$$

where the contributions from the fundamental and higher-harmonic cavities are indicated by the subscripts ‘fund’ and ‘higher’, respectively. The square bracketed factor in Eq. (9.107) becomes

$$\left[\frac{\Delta}{\bar{\omega}_s} R_s \cos^2 \psi_{\omega_s} \sin 2\psi_{\omega_s} \Big|_{\text{fund}} + R_s \cos^2 \psi \sin 2\psi \Big|_{\text{higher}} \right] = (-0.1953 + 0.0122) \text{ M}\Omega , \quad (9.108)$$

where we have used for the fundamental cavity, the shunt impedance $R_s = 3.84 \text{ M}\Omega$, and quality factor $Q = 45000$ exactly the same as the higher harmonic cavity. The two-rf system turns out to be Robinson stable; the damping rate is 54600 s^{-1} or a damping time of 0.018 ms. However, it is important to point out that the growth rate formula given by Eq. (9.101) is valid only if the shift and spread of the synchrotron frequency are much less than some unperturbed synchrotron frequency. Here, the synchrotron frequency is linear with the offset from the stable fixed point of the longitudinal phase space and the spread is therefore very large. Thus, Eq. (9.101) can only be viewed as an estimate. The employment of a mean synchrotron angular frequency $\bar{\omega}_s$ can also be questionable. Although the assumption of the mean synchrotron angular frequency in Eq. (9.102) is not sensitive to the higher-harmonic-cavity term in Eq. (9.101), however, it is rather sensitive to the fundamental-cavity term. The dependence is complicated since the equivalent detuning ψ_{ω_s} depends on $\bar{\omega}_s$ also. For example, if we use $\bar{\omega}_s = 1.5\sigma_{\omega_s}$ instead,

the damping time decreases to 0.013 ms, while $\bar{\omega}_s = 3.0\sigma_{\omega_s}$ increases the damping time to 0.036 ms. With this uncertainty, a suggestion may be to increase the detuning Δ of the fundamental to $\Delta \sim -4$ kHz so that it becomes more certain that the two-rf system will be Robinson stable, otherwise, the purpose of the higher-harmonic cavity can be defeated, because some of the spread of the synchrotron frequency obtained will be used to fight the Robinson's instability created instead of other longitudinal collective instabilities of concern.

Now let us estimate how large a Landau damping we obtain from the passive Landau cavity coming from the spread of the synchrotron frequency. Following Eq. (9.52), the stability criterion is roughly

$$\frac{1}{\tau} \lesssim \frac{\omega_s(\sqrt{6}\sigma_\tau)}{4}, \quad (9.109)$$

where the synchrotron angular frequency spread is given by Eq. (9.79). The spread in synchrotron angular frequency has been found to be $\omega_s(\sqrt{6}\sigma_\tau) = 39.6$ kHz. In other words, the higher-harmonic cavity is able to damp an instability that has a growth time longer than 0.101 ms, an improvement of 57 folds better than when the higher-harmonic cavity is absent. Thus, theoretically, this Landau damping is large enough to alleviate the Robinson's antidamping of higher-harmonic cavity as well.

We notice that the required shunt impedance of the passive Landau cavity $R_s = 2.81$ MΩ is large, although it is still smaller than the shunt impedance of 3.84 MΩ of the fundamental cavity. It is easy to understand why such large impedance is required. The synchronous angle for a storage ring without the Landau cavity is usually just not too much from 180°, here $\phi_{s0} = 180^\circ - 19.0^\circ$, because of the compensation of a small amount of radiation loss. The rf gap voltage phasor is therefore almost perpendicular to the beam current phasor. In order that the beam loading voltage contributes significantly to the rf voltage, the detuning angle of the passive higher-harmonic cavity must therefore be large also, here $\psi = 82.53^\circ$. In fact, without radiation loss to compensate, the beam loading voltage phasor would have been exactly perpendicular to the beam current phasor. Since $\cos \psi = 0.130$ is small, the shunt impedance of the higher-harmonic cavity must therefore be large. In some sense, the employment of the higher-harmonic cavity is not efficient at all, because we are using only the tail of a large resonance impedance, as is depicted in Fig. 9.11. This is not a waste at all, however, because we can do away with the generator power source for this cavity. Also, the large detuning angle implies not much power will be taken out from the beam as it loads the cavity, only 2.14 kW here. On the other hand, the detuning of the fundamental cavity need not be too large. This is because

the rf gap voltage is supplied mostly by the generator voltage and only partially by the beam loading in the cavity.

The most important question here is how do we generate a large shunt impedance for the higher-harmonic cavity. Usually it is easy to lower the shunt impedance by adding a resistor across the cavity gap. Some other means will be required to raise the shunt impedance, in case it is not large enough. One way is to coat the interior of the higher-harmonic cavity with a layer of medium that has a higher conductivity. However, it is hard to think of any medium that has a conductivity very much higher than that of the copper surface of the cavity. For example, the conductivity of silver is only slightly higher. Another way to increase the conductivity significantly is the reduction of temperature to the cryogenic region. Notice that R_s/Q is a geometric property of the cavity. Raising R_s will raise Q also. However, a higher quality factor is of no concern here, because the requirements in Eqs. (9.88), (9.89), and (9.90) depend on the detuning ψ only and are independent of Q . With the same detuning ψ , a higher Q just implies a smaller frequency offset between the resonant angular frequency ω_r of the higher-harmonic cavity and the m th multiple of the rf angular frequency.

The shunt impedance of the higher-harmonic cavity determines the rf voltage to be used in the fundamental cavity. We can rewrite Eq. (9.95) as

$$\frac{i_b R_s}{U_s/e} = \left(\frac{m^2 - 1}{m^2} \right) \left(\frac{V_{\text{rf}}}{U_s/e} \right)^2 - 1 , \quad (9.110)$$

after eliminating ϕ_s and ψ with the aid of Eqs. (9.92) and (9.94). Thus, for a given beam current, a small shunt impedance of the higher-harmonic cavity translates into small rf voltage. Notice that the right side is quadratic in V_{rf} . For example, with the same radiation loss, when the shunt impedance of the higher-order cavity decreases from 6.12 to 2.81 MΩ, the rf voltage V_{rf} has to decrease from 500 kV to 350 kV. A low rf voltage is usually not favored because the electron bunches will become too long.

In order to maximize Landau damping, criteria must be met so that the rf potential becomes quartic. As is shown in Fig. 9.10 for a $m = 2$ double rf system, when the rf voltage ratio deviates from $r = 1/m = 0.5$ by 20% to 0.4, the spread in synchrotron frequency for a small bunch decreases tremendously to almost the same tiny value as in the single rf system. There is a big difference between an active Landau cavity and a passive Landau cavity. In an active Landau cavity, the criteria in Eqs. (9.77) to (9.77) are independent of the beam intensity. On the other hand, the criteria for the operation of a passive cavity, Eqs. (9.88), (9.89), and (9.90), depend on the bunch intensity. What

will happen when the bunch intensity changes significantly? Let us recall how we arrive at the solution of the three equations of the passive two-rf system. The new synchronous phase ϕ_s , as given by Eq. (9.92), is determined solely by the ratio of the radiation loss U_s to the rf voltage V_{rf} . While the detuning ψ is just given by $-m \cot \phi_s$. The only parameter that depends on the beam current is the shunt impedance R_s . Thus, the easiest solution is to install a variable resistor across the gap of the higher-harmonic cavity and adjust the proper shunt impedance by monitoring the intensity of the electron bunches.

In the event that the shunt impedance is not adjustable, one can adjust instead the rf voltage so that Eq. (9.110) remains satisfied with the new current but with the preset R_s . With the new rf voltage, the synchronous phase ϕ_s has to be adjusted so that Eq. (9.92) remains satisfied. This will alter the detuning ψ according to Eq. (9.94). The only way to achieve the new detuning is to vary the rf frequency. This will push the beam radially inward or outward. As the beam current changes by $\Delta I_0/I_0$, to maintain the criteria of the quartic rf potential, the required changes in rf voltage, synchronous angle, and detuning of the higher-harmonic cavity are, respectively,

$$\frac{\Delta V_{\text{rf}}}{V_s} = \frac{1}{2} \left[\frac{m^2 - 1}{m^2 + 1} \frac{V_s}{V_{\text{rf}}} \right] \left[\frac{m^2 - 1}{m^2} \frac{V_{\text{rf}}^2}{V_s^2} - 1 \right] \frac{\Delta I_0}{I_0}, \quad (9.111)$$

$$\Delta(\pi - \phi_s) = - \left[\left(\frac{m^2 - 1}{m^2} \frac{V_{\text{rf}}}{V_s} \right)^2 - 1 \right]^{-1/2} \frac{\Delta V_{\text{rf}}}{V_s}, \quad (9.112)$$

$$\Delta\psi = \frac{1}{2m} \left[\left(\frac{m^2 - 1}{m^2} \frac{V_{\text{rf}}}{V_s} \right)^2 - 1 \right]^{-1/2} \frac{\Delta I_0}{I_0}, \quad (9.113)$$

where $U_s = eV_s$ is the energy loss per turn due to synchrotron radiation. The change of the detuning angle ψ leads to a fractional change in the rf frequency and therefore a fractional change in orbit radius

$$\frac{\Delta R}{R} = - \frac{m^2 - 1}{4mQ} \left[\frac{m^2 - 1}{m^2} \frac{V_{\text{rf}}^2}{V_s^2} - 1 \right] \left[\left(\frac{m^2 - 1}{m^2} \frac{V_{\text{rf}}}{V_s} \right)^2 - 1 \right]^{-1/2} \frac{\Delta I_0}{I_0}, \quad (9.114)$$

where R is the radius of the storage ring. These changes are plotted in Fig. 9.12 for the LNLS double rf system when the beam current varies by $\pm 20\%$. Because of the high quality factors Q of the cavities, the radial offset of the beam turns out to be very small, less than ± 0.14 mm for a $\pm 20\%$ variation of beam current.

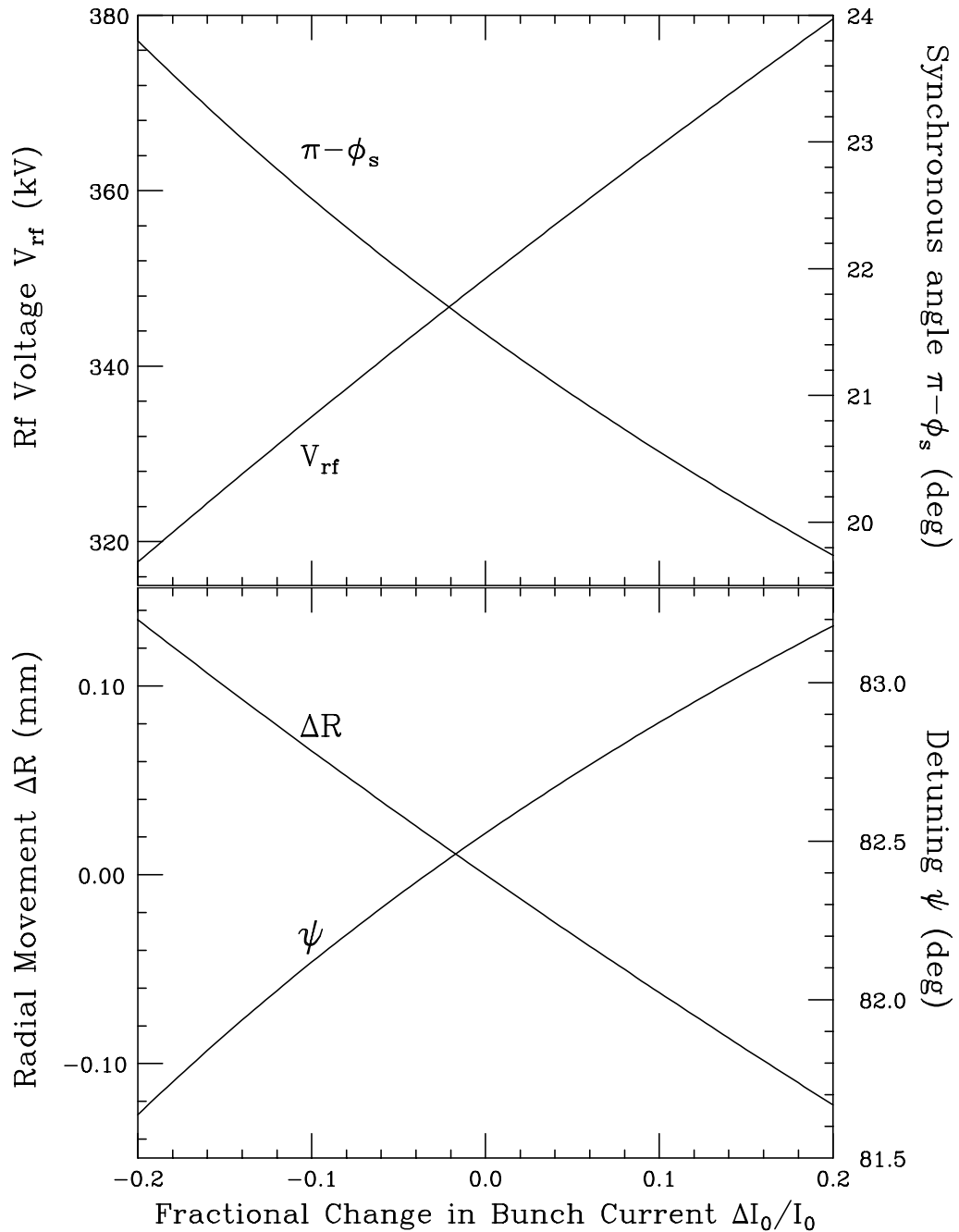


Figure 9.12: Plots showing the required variations of rf voltage V_{rf} , synchronous angle ϕ_s , higher-harmonic-cavity detuning ψ , and beam radial offset Δr to maintain the criteria of the quartic rf potential, when the beam current varies by $\pm 20\%$.

9.3.3 Rf Voltage Modulation

The modulation of the rf system will create nonlinear parametric resonances, which redistribute particles in the longitudinal phase plane. The formation of islands within an rf bucket reduces the density in the bunch core and decouples the coupling between bunches. As a result, beam dynamics properties related to the bunch density, such as beam lifetime, beam collective instabilities, etc, can be improved.

Here we try to modulate the rf voltage with a frequency $\nu_m \omega_0 / (2\pi)$ and amplitude ϵ , so that the energy equation becomes [11]

$$\frac{d\Delta E}{dn} = eV_{rf}[1 + \epsilon \sin(2\pi\nu_m n + \xi)][\sin(\phi_s - h\omega_0\tau) - \sin\phi_s] - [U(\delta) - U_s] , \quad (9.115)$$

where ξ is a randomly chosen phase, ν_m is the modulating tune, ϵ is the fractional voltage modulation amplitude, U_s and $U(\delta)$ denote the energy loss due to synchrotron radiation for the synchronous particle and a particle with momentum offset δ . This modulation will introduce resonant-island structure in the longitudinal phase plane. There are two critical tunes:

$$\begin{cases} \nu_1 = 2\nu_s + \frac{1}{2}\epsilon\nu_s , \\ \nu_2 = 2\nu_s - \frac{1}{2}\epsilon\nu_s . \end{cases} \quad (9.116)$$

If we start the modulation by gradually increasing the modulating tune ν_m towards ν_2 from below, two islands appear inside the bucket from both sides, as shown in the second plot of Fig. 9.13. The phase space showing the islands is depicted in Fig. 9.14. As ν_m is increased, these two islands come closer and closer to the center of the bucket and the particles in the bunch core gradually spill into these two islands, forming 3 beamlets. When ν_m reaches ν_2 , the central core disappears and all the particles are shared by the two beamlets in the two islands. Further increase of ν_m above ν_2 moves the two beamlets closer together. When ν_m equals ν_1 , the two beamlets merge into one. Under all these situations, the two outer islands rotate around the center of the rf bucket with frequency equal to one half the modulation frequency. Every rf bucket has the same phase space structure of having two or three islands rotating at the same angular velocity and with the roughly same phase. The only possible small phase lag is due to time-of-flight. Therefore, only coupled mode $\mu = 0$ will be allowed, unless the driving force is large enough to overcome the voltage modulation.

Rf voltage modulation has been introduced into the light source at the Synchrotron Radiation Research Center (SRRC) of Taiwan to cope with longitudinal coupled-bunch

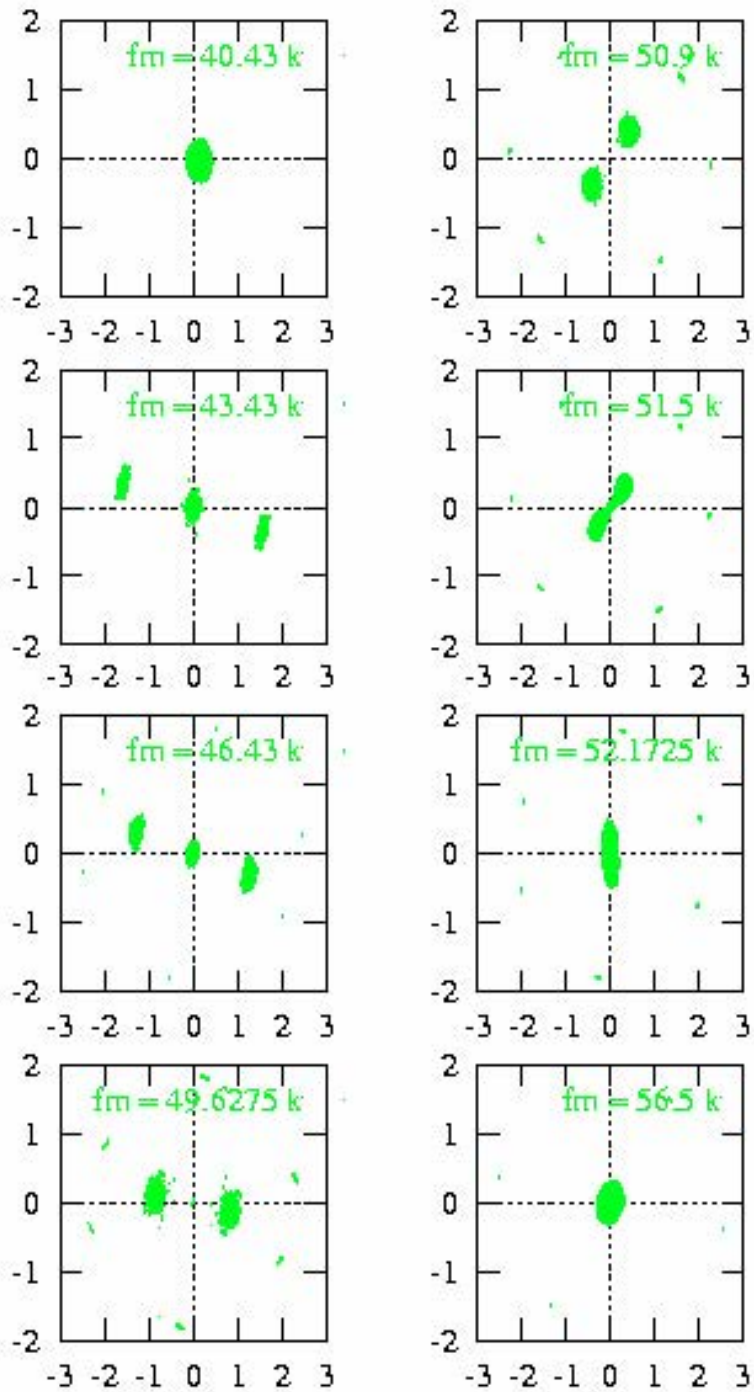


Figure 9.13: (Color) Simulation results of rf voltage modulation. The modulation frequency is increased from top to bottom and left to right. The modulation amplitude is 10% of the cavity voltage. The 4th plot is right at critical frequency $\nu_2 f_0 = 49.6275$ kHz and the 7th plot right at critical frequency $\nu_1 f_0 = 52.1725$ kHz.

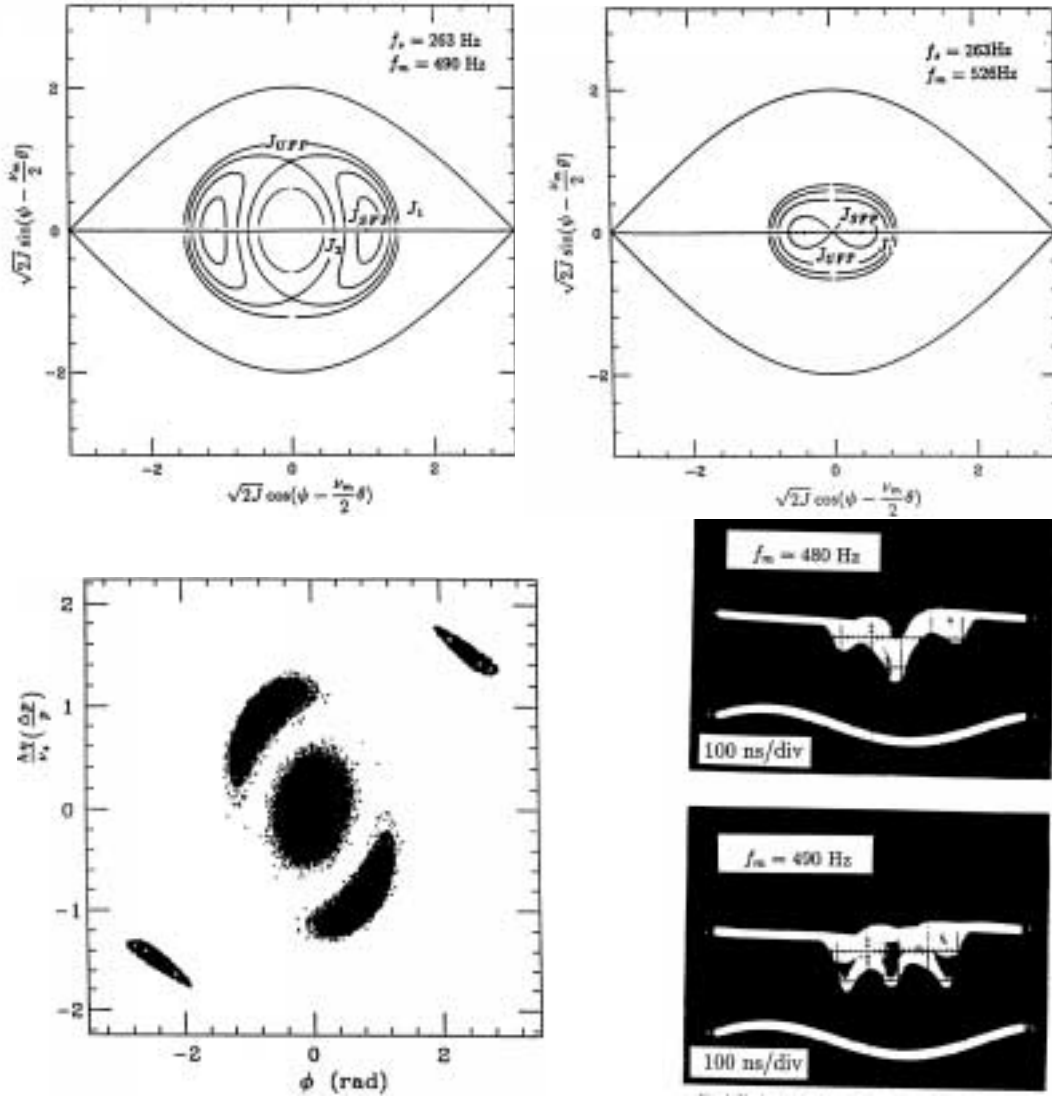


Figure 9.14: Top figures show separatrices and tori of the time-independent Hamiltonian with voltage modulation in multi-particle simulation for an experiment at Indiana University Cyclotron Facility. The modulation tune is below ν_2 with the formation of 3 islands on the left, while the modulation tune is above ν_2 with the formation of 2 islands on the right. The lower-left plot shows the final beam distribution when there are 3 islands, a damping rate of 2.5 s^{-1} has been assumed. The lower-right plot shows the longitudinal beam distribution from a BPM sum signal accumulated over many synchrotron periods. Note that the outer two beamlets rotate around the center beamlet at frequency equal to one-half the modulation frequency.

instability [12]. The synchrotron frequency was $\nu_s f_0 = 25.450$ kHz. A modulation frequency slightly below twice the synchrotron frequency with $\epsilon = 10\%$ voltage modulation was applied to the rf system. The beam spectrum measured from the beam-position monitor (BPM) sum from a HP4396A network analyzer before and after the modulation is shown in Fig. 9.15. It is evident that the intensities of the beam spectrum at the annoying frequencies have been largely reduced after the application of the modulation. The sidebands around the harmonics of 587.106 Hz and 911.888 MHz are magnified in Fig. 9.16. We see that the synchrotron sidebands have been suppressed by very much. The multi-bunch beam motion under rf voltage modulation was also recorded by streak camera, which did not reveal any coupled motion of the bunches. Because of the successful damping of the longitudinal coupled-bunch instabilities, this modulation process has been incorporated into the routine operation of the light source at SRRC.

9.3.4 Uneven Fill

In a storage ring with M identical bunches evenly spaced, there will be M modes of coupled-bunch oscillation, of which about half are stable and half unstable in the presence of an impedance, if all other means of damping are neglected. Take the example of having the rf harmonic $h = M = 6$ as illustrated in Fig. 9.2. If there is a narrow resonant impedance in the rf cavity located at $\omega_r \approx (qM + \mu)\omega_0$ with $\mu = 4$, coupled-bunch mode $\mu = 4$ becomes highly unstable. At the same time, this resonant impedance also damps coupled-bunch mode $M - \mu = 2$ heavily. Usually, we only care for the mode that is unstable and pay no attention to the mode that is damped. In some sense, the damping provided by the impedance is rendered useless or has been wasted. However, if there is another narrow resonant impedance located at the angular frequency $(qM + \mu')\omega_0$ with $\mu' = 2$. This impedance excites coupled-bunch mode 2, but damps coupled-bunch mode 4. If this impedance is of the same magnitude as the first one, both coupled-bunch modes 2 and 4 can become stable. Thus, having more narrow resonances in the impedance does not necessarily imply more instabilities. If they are located at the desired frequencies, they can be helping each other so that the excitation of one can be canceled by the other. This method of curing coupled-bunch instability was proposed in Ref. [13] by creating extra resonances in the impedance in the accelerator ring. However, extra resonances in the impedance are not necessary. The same purpose can also be served if we can couple the two coupled-bunch modes together, for example modes 2 and 4 in the above example, the damped mode will be helping the growth mode. If the resulting growth

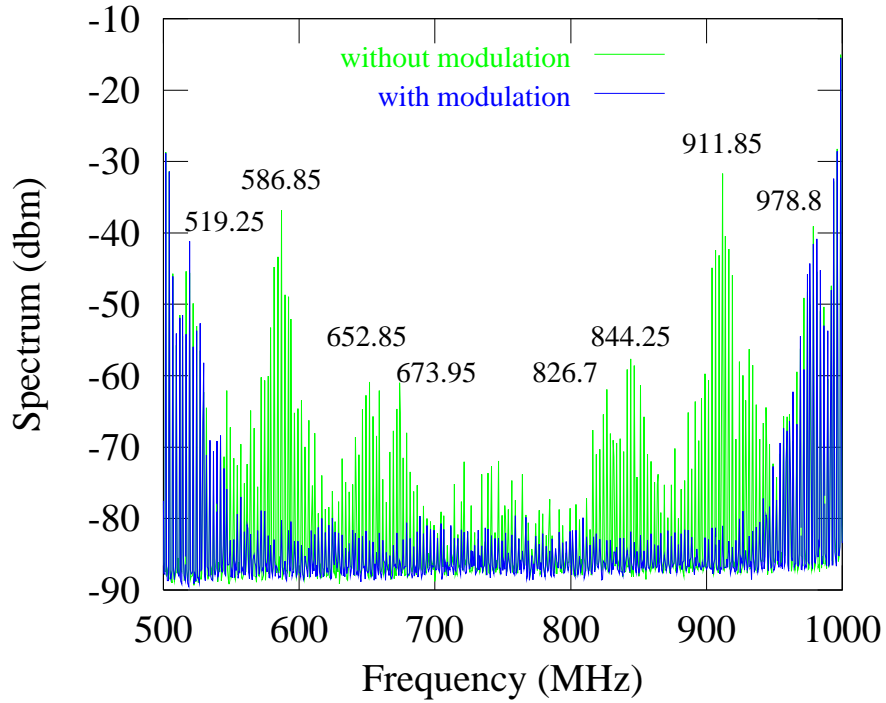


Figure 9.15: (Color) Beam spectrum from BPM sum signal before and after applying rf voltage modulation. The synchrotron frequency was 25.450 kHz. The voltage was modulated by 10% at 50.155 kHz. The frequency span of the spectrum is 500 MHz, which is the rf frequency.

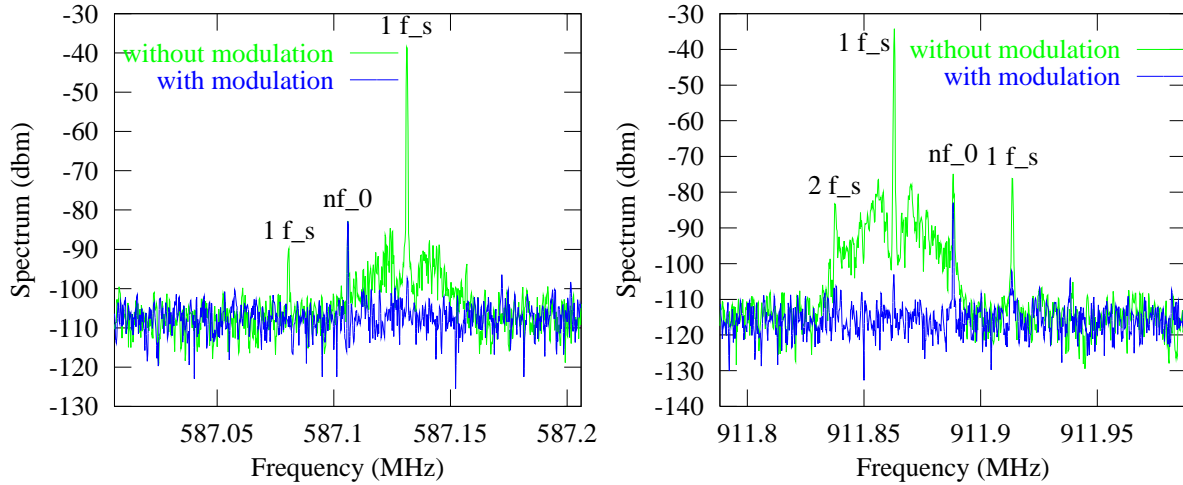


Figure 9.16: (Color) Beam spectrum zoom in from Fig. 9.15. The revolution harmonic frequency of the left is 587.106 MHz and the right is 911.888 MHz. The frequency span of the spectrum is 200 kHz.

rates of the two coupled modes fall lower than the synchrotron radiation damping rate and the Landau damping rate in the ring, the coupled-bunch instability will be cured. This method of cure is called *modulating coupling* proposed by Prabhakar [4, 14], and the coupling is accomplished with an uneven fill in the ring. We saw in Eq. (9.48) that wake field left by previous bunch passages contributes to a coherent synchrotron tune shift in the bunch. For an unevenly filled ring, the tune shifts for different bunches will be different. This provides a spread in synchrotron tune and therefore extra Landau damping, which is another idea proposed by Prabhakar.

Let us go over the uneven-fill theory briefly. Consider M point bunches evenly placed in the ring, but they may carry different charges. The arrival time advance τ_n of the n th bunch at time s obeys the equation of motion,

$$\ddot{\tau}_n + 2d_r \dot{\tau}_n + \omega_s^2 \tau_n = \frac{e\eta}{\beta^2 E_0 T_0} V_n , \quad (9.117)$$

where d_r is the synchrotron radiation damping rate and the overdot represents derivative with respect to s/v . Here $V_n(s)$ is the total wake voltage seen by bunch n , and is given by

$$V_n(s) = \sum_{p=-\infty}^{\infty} \sum_{k=0}^{M-1} q_k W'_0 [t_{n,k}^p + \tau_k(s - vt_{n,k}^p) - \tau_n(s)] , \quad (9.118)$$

where q_k is the charge of bunch k , $t_{n,k}^p = (pM + n - k)T_b$ is the time bunch k is ahead of bunch n p turns ago, and $T_b = T_0/M$ is the bunch spacing[†]. Since the deviation due to synchrotron motion is small compared with the bunch spacing, Eq. (9.118) can be expanded, resulting

$$V_n(s) = \sum_{p=-\infty}^{\infty} \sum_{k=0}^{M-1} q_k [\tau_k(s - vt_{n,k}^p) - \tau_n(s)] W''_0(t_{n,k}^p) . \quad (9.119)$$

[†]In Eq. (9.9), we have $kC + (s_\ell - s_n)$ in the argument of the wake function W'_0 , where we are sampling the wake force on the n th bunch due to the ℓ th bunch. There, s_n represent the distance along the ring measured from some reference point to the n th bunch in the *same* direction of bunch motion. Thus, the ℓ th bunch is ahead of the n th bunch by the distance $s_\ell - s_n$. In Eq. (9.118), we count the number of bunch spacings instead. Thus, the k th bunch is ahead the n th bunch by the time $(n - k)T_b$, since we number the bunches from upstream to downstream or in the *opposite* direction of bunch motion. Note that the term $v(\tau' - \tau)$ in the argument of the linear density in Eq. (9.8) has been neglected because this will only amount to a phase delay $\Omega(\tau' - \tau)$ where $\Omega \approx \omega_s$ and is very much less than the phase change $\omega_r(\tau' - \tau)$.

If all bunches carry the same charge, we have the situation of even fill and the M symmetric eigenmodes are[‡]

$$\mathbf{v}_\ell = \frac{1}{\sqrt{M}} \begin{pmatrix} 1 \\ e^{-i\ell\theta} \\ e^{-2i\ell\theta} \\ \vdots \\ e^{-i(M-1)\ell\theta} \end{pmatrix}, \quad \ell = 0, 1, \dots, M-1, \quad \theta = \frac{2\pi}{M}. \quad (9.120)$$

They form an orthonormal basis which we called the *even-fill-eigenmode* (EFEM) basis. For an uneven fill, it is natural to expand the new eigenmodes using as a basis the EFEMs. The arrival time advances $\tau_n(s)$ for the M bunches in Eq. (9.117) can now be written as

$$\begin{pmatrix} \tau_0 \\ \vdots \\ \tau_{M-1} \end{pmatrix} = \varsigma^0 \mathbf{v}_0 + \dots + \varsigma^{M-1} \mathbf{v}_{M-1} \quad \text{or} \quad \tau_n(s) = \frac{1}{\sqrt{M}} \sum_{m=0}^{M-1} \varsigma^m(s) e^{-i2\pi nm/M}, \quad (9.121)$$

where the expansion coefficients can be written inversely as

$$\varsigma^m(s) = \frac{1}{\sqrt{M}} \sum_{n=0}^{M-1} \tau_n(s) e^{i2\pi nm/M}. \quad (9.122)$$

Assuming the ansatz

$$\tau_k(s) \propto e^{-i\Omega s/v}, \quad (9.123)$$

where the collective frequency Ω is to be determined, the voltage from the wake can now be written as

$$V_n(s) = \frac{1}{\sqrt{M}} \sum_{p=-\infty}^{\infty} \sum_{k,m=0}^{M-1} q_k \varsigma^m(s) e^{-i2\pi nm/M} \left[e^{i(m\omega_0 + \Omega)t_{n,k}^p} - 1 \right] W''_0(t_{n,k}^p), \quad (9.124)$$

where

$$\varsigma^m(s) \propto e^{-i\Omega s/v}. \quad (9.125)$$

[‡]Here, coupled-bunch mode ℓ implies the center-of-mass of a bunch *lags* its predecessor by the phase $2\pi\ell/M$. Thus, coupled-bunch mode ℓ here is the same as coupled-bunch mode $M - \ell$ discussed in the earlier part of this Chapter. There, the center-of-mass of a bunch *leads* its predecessor by the phase $2\pi\ell/M$.

Next project the whole Eq. (9.117) onto the ℓ th EFEM, giving

$$\ddot{\zeta}^\ell + 2d_r\dot{\zeta}^\ell + \omega_s^2\zeta^\ell = \frac{e\eta}{\beta^2 E_0 M} \sum_{p=-\infty}^{\infty} \sum_{n,m,k=0}^{M-1} \frac{q_k}{T_0} \zeta^m(s) e^{i2\pi n(\ell-m)/M} [e^{i(m\omega_0+\Omega)t_{n,k}^p} - 1] W_0''(t_{n,k}^p). \quad (9.126)$$

There are too many summations over bunch number. We can eliminate one by defining the integer variable $u = pM + n - k = t_{n,k}^p/T_b$. After that, $\sum_p \rightarrow \frac{1}{M} \sum_u$. The summand becomes independent of n and we have $\sum_n = M$. The right side of Eq. (9.126) becomes

$$\text{R.S.} = \frac{e\eta}{\beta^2 E_0 M} \sum_{u=-\infty}^{\infty} \sum_{m=0}^{M-1} I_{l-m} \zeta^m(s) e^{i2\pi u(\ell-m)/M} [e^{i(m\omega_0+\Omega)uT_b} - 1] W_0''(uT_b), \quad (9.127)$$

where we have introduced the complex amplitude of the p th revolution harmonic in the beam spectrum,

$$I_p = \sum_{k=0}^{M-1} i_k e^{i2\pi kp/M}, \quad (9.128)$$

with $i_k = q_k/T_0$ denoting the average current of bunch k . For an evenly filled ring, the average beam current of each bunch is the same. Let us go to the frequency space by introducing the longitudinal impedance,

$$W'_0(t) = \int \frac{d\omega}{2\pi} Z_0^{\parallel}(\omega) e^{-i\omega t}. \quad (9.129)$$

The summation over u can now be performed using Poisson formula resulting in the difference of two δ -functions, which facilitate the integration over ω resulting in

$$\text{R.S.} = -\frac{ie\eta}{\beta^2 E_0 T_0} \sum_{p=-\infty}^{\infty} \sum_{m=0}^{M-1} I_{l-m} \zeta^m(s) \left\{ [(pM+\ell)\omega_0+\Omega] Z_0^{\parallel}[(pM+\ell)\omega_0+\Omega] - [(pM+\ell-m)\omega_0] Z_0^{\parallel}[(pM+\ell-m)\omega_0] \right\}. \quad (9.130)$$

With the introduction of the coupling impedance,

$$\begin{aligned} Z_{\ell m}(\omega) &= Z_{\text{eff}}[\ell\omega_0 + \omega] - Z_{\text{eff}}[(\ell-m)\omega_0] \\ Z_{\text{eff}}(\omega) &= \frac{1}{\omega_{\text{rf}}} \sum_{p=-\infty}^{\infty} [pM\omega_0 + \omega] Z_0^{\parallel}[pM\omega_0 + \omega], \end{aligned} \quad (9.131)$$

the equation of motion for the bunches can be written in the simplified form,

$$\ddot{\zeta}^\ell + 2d_r\dot{\zeta}^\ell + \omega_s^2\zeta^\ell = -\frac{ie\eta\omega_{\text{rf}}}{\beta^2 E_0 T_0} \sum_{m=0}^{M-1} I_{l-m} Z_{\ell m}(\Omega) \zeta^m . \quad (9.132)$$

The next simplification is to exclude all solutions when $\Omega \approx -\omega_s$ and include only those near $+\omega_s$. From the ansatz (9.123) or (9.125), one has

$$\ddot{\zeta}^\ell + 2d_r\dot{\zeta}^\ell + \omega_s^2\zeta^\ell \approx -2i\omega_s [\dot{\zeta}^\ell - (d_r - i\omega_s)\zeta^\ell] , \quad (9.133)$$

provided that $d_r \ll \omega_s$ and $|\Omega - \omega_s| \ll \omega_s$. We finally obtain

$$\dot{\zeta}^\ell - (d_r - i\omega_s)\zeta^\ell = \sum_{m=0}^{M-1} A_{\ell m} \zeta^m , \quad (9.134)$$

with

$$A_{\ell m} = \frac{e\eta\omega_{\text{rf}}}{2\beta^2 E_0 T_0 \omega_s} I_{\ell-m} Z_{\ell m}(\omega_s) . \quad (9.135)$$

This is just a M -dimensional eigenvalue problem. In the situation of an evenly filled ring, all bunch current i_k are the same and the harmonic spectrum amplitude

$$I_p = \begin{cases} I_0 = \sum_k i_k & p = 0 \\ 0 & p \neq 0 \end{cases} , \quad (9.136)$$

where I_0 is the total average current in the ring. This implies no coupling between the EFEMs, as expected, and the eigenvalues are

$$\lambda_\ell = A_{\ell\ell} = \frac{e\eta\omega_{\text{rf}}}{2\beta^2 E_0 T_0 \omega_s} I_0 [Z_{\text{eff}}(\ell\omega_0 + \omega_s) - Z_{\text{eff}}(0)] , \quad \ell = 1, \dots, M-1 . \quad (9.137)$$

Some results are apparent:

- The sum of eigenvalues, $\sum A_{\ell\ell}$, is independent of fill shapes.
- Uneven-fill eigenvalues vary linearly as I_0 .
- Radiation damping merely shifts all eigenvalues by d_r , regardless of fill shape.
- If all filled buckets have the same charge q_k , then broadband bunch-by-bunch feedback also damps all uneven-fill modes equally, since it behaves like radiation damping.
- The EFEM basis yields a sparse A -matrix because usually coupled-bunch instabilities are driven by only a few parasitic higher-order resonances in the rf cavities.

9.3.4.1 Modulation Coupling

Let us study some special case[§] when $I_k Z_{\text{eff}}(k\omega_0) = 0$ except for $k = 0$. This implies that the modulation coupling terms are the only manifestation of fill unevenness. The problem simplifies considerably. In addition, if there is only one sharp resonance exciting instability for mode ℓ in the EFEM basis, this resonance will initiate damping for mode m . We try to couple these two modes by filling the ring unevenly so that $I_{\ell-m}$ is maximized. The A -matrix is now diagonal except for the coupling between these two modes. The coupling A -matrix reduces to a two-by-two matrix. The new eigenvalues for these two modes are

$$\lambda = \frac{1}{2}(\lambda_\ell + \lambda_m) \pm \frac{1}{2}\sqrt{(\lambda_\ell - \lambda_m)^2 + 4C_{\ell-m}^2\lambda_\ell\lambda_m}, \quad (9.138)$$

where $C_p = |I_p|/I_0$ is called the *modulation parameter* and its value cannot exceed unity. If $C_{\ell-m} = 0$, the even-fill eigenvalues λ_ℓ and λ_m are not perturbed. As $C_{\ell-m}$ approaches unity, one eigenvalue approaches zero and so is its growth rate. The other eigenvalue approaches $\lambda_\ell + \lambda_m$ so that the damping rate of mode m is helping the growth rate of mode ℓ .

To optimize the modulation parameter C_p , we resort to the definition of the harmonic amplitude I_p in Eq. (9.128). As an example, take a ring of $M = 900$ even-fill bunches and we wish to optimize C_p with $p = 3$. According to the definition of the harmonic amplitude I_p in Eq. (9.128), the easiest way to accomplish this is to fill the ring every $M/p = 900/3 = 300$ -th bucket (assuming that the total number of bucket is also $M = 900$). Since we wish to keep the same current I_0 in the ring, each of these $p = 3$ chosen buckets will be filled with bunch current $I_0/p = I_0/3$ and the modulation parameter becomes $C_3 = 1$. However, with so much charge concentrated at these 3 buckets, each bunch can become unstable by itself. To cope with this single-bunch instability, we can fill several adjacent buckets around each of these 3 chosen locations. If the maximum allowable bunch current is i_{\max} , we need to fill up $I_0/(pi_{\max})$ adjacent buckets. If $I_0 = 450$ mA and $i_{\max} = 2$ mA, we need to fill up 75 adjacent buckets at

[§]Consider a ring with $M = 84$ buckets. If there is a sharp resonance at $\omega_r = (pM + \ell)\omega_0$ with $\ell = 79$, coupled-bunch mode $\ell = 79$ in the EFEM basis will be excited, but mode $m = M - \ell = 5$ will be damped. To couple these two modes, we need to maximize I_k or I_{-k} with $k = \ell - m = 74$. Under this situation, $I_k Z_{\text{eff}}(k\omega_0) = 0$ except for $k = 0$, because (1) although $I_{74} \neq 0$, there is no impedance at $(pM \pm 74)\omega_0$, and (2) although $Z_{\text{eff}}(k\omega_0) \neq 0$ for $k = \ell$ and $k = m$, I_ℓ and I_m are zero because we maximize $I_{\ell-m}$ only. The same is true if there are a few sharp resonances. This condition, however, excludes the extra Landau damping to be studied in the Sec. 9.3.4.2.

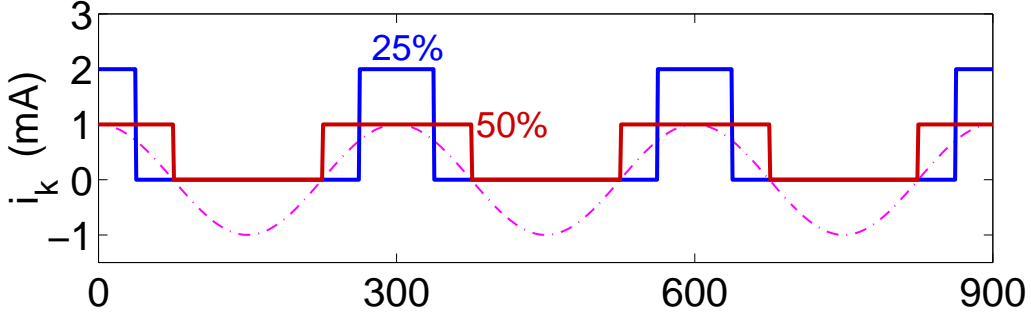


Figure 9.17: (color) Illustration of fill optimization for a ring with $M = 900$ bunches when evenly filled and total beam current $I_0 = 450$ mA. Solid: 50% fill and 25% fill maximize C_3 for $i_{\max} = 1$ mA and 2 mA. Dash-dot: Reference sinusoid at 3 times revolution frequency.

each of the 3 locations. So all in total $x = I_0/(Mi_{\max})$ or 25% of the buckets are filled. If $i_{\max} = 1$ mA instead, 150 adjacent buckets have to be filled in each of the 3 chosen locations, which makes 50% of the ring filled. These patterns are illustrated in Fig. 9.17. When a fraction x of the ring filled in this way, the modulation parameter C_p will be reduced. In general, we can calculate a corresponding “weight” $\cos(2\pi pn/M)$ for each bucket n and fill each of the “heaviest” I_0/i_{\max} buckets to the same current i_{\max} . The modulation parameter will be

$$C_p \approx \frac{\sin(\pi x)}{\pi x}. \quad (9.139)$$

9.3.4.2 Landau Damping

We need to be a little careful to derive the tune shift for the bunches because, for example, Eq. (9.132) is the equation of motion for a coupled-bunch mode ℓ and not for a particular bunch. We need to use Eq. (9.121) to transform back to the equation of motion of τ_k for bunch k . The frequency shift for bunch k relative to the mean tune is found to be

$$\Delta\omega_s^k = -\frac{ie\eta\omega_{\text{rf}}}{\beta^2 E_0 T_0 \omega_s} \sum_{\ell=0}^{M-1} [Z_{\text{eff}}(\ell\omega_0) I_\ell e^{-i2\pi k\ell/M}], \quad (9.140)$$

which is purely real because the real part of the summand is an odd function of ℓ with period M . For an evenly fill pattern, $I_\ell = 0$ unless $\ell = 0$. the tune shift for each bunch will be the same. For $I_\ell \neq 0$ when $\ell \neq 0$, however, different bunches receive different tune shifts, creating a tune spread for Landau damping.

Consider a sharp impedance resonance at $n\omega_0$ which is not a multiple of the bunch frequency $M\omega_0$. If we design a fill optimized for C_n , we excite a sinusoidal ringing in the wake voltage at $n\omega_0$, which contributes to an uneven frequency shift to Eq. (9.140). The larger the modulation parameter the larger will be the tune spread. Figure 9.18 shows the increase in Landau damping as the fill fraction x is decreased. In the figure, $\Re \lambda$ is proportional to the growth rate while $\Im \lambda$ is proportional to the tune shift. Interestingly, eigenvalues with large imaginary parts are completely damped even by 80% fills.

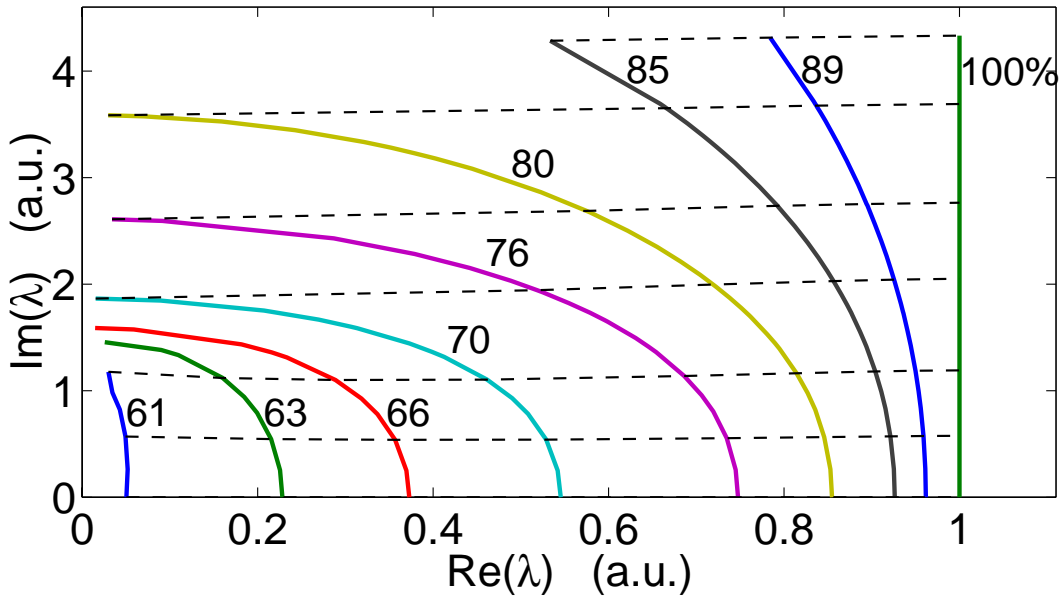


Figure 9.18: (color) Graphic look-up table for fill-induced damping of eigenvalue of unstable longitudinal EFEM n as C_n is increased from 0 (100% of ring filled) to 0.5 (61% filled). Dashes: Evolution of λ_n from a few even-fill starting points.

9.3.4.3 APPLICATION

There are longitudinal coupled-bunch instabilities in the PEP-II Low Energy Ring (LER) at $I_0 = 1$ A and $M = 873$ [14]. The two largest cavity resonances are expected to drive bands of modes centered at 93.1 MHz (EFEM 683) and 105 MHz (EFEM 770) unstable. They also stabilize the corresponding bands at 25.9 MHz (EFEM 190) and 14 MHz (EFEM 103). The growth and damping rate spectrum are shown in Fig. 9.19(a). The best modulation-coupling cure is to couple the modes around 105 MHz to those near 25.9 MHz by maximizing C_{580} or C_{293} ($C_p = C_{M-p}$). This will automatically couples

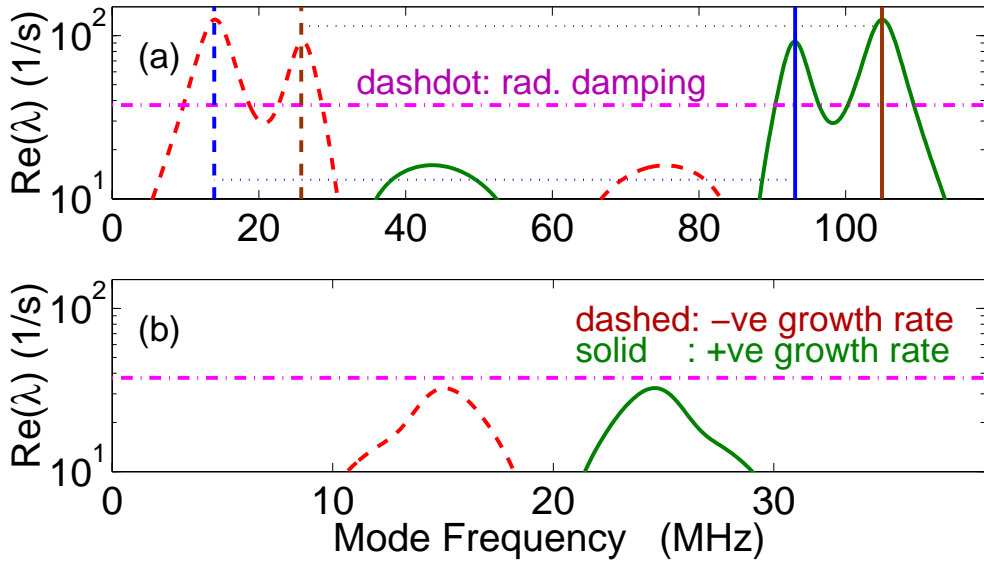


Figure 9.19: (color) Illustration of fill optimization for a ring with $M = 1000$ bunches when evenly filled and total beam current $I_0 = 500$ mA. Solid: 50% fill and 25% fill maximize C_4 for $i_{\max} = 1$ mA and 2 mA. Dash-dot: Reference sinusoid at 4 times revolution frequency.

93.1 MHz to 14 MHz. The optimization can be easily accomplished by filling every third nominally-spaced bucket, since $873/3 = 291$ is close to 293. This is equivalent to slicing the frequency range from zero to $M\omega_0$ and placing the three parts of the growth or damping spectrum on each other. Thus the damping parts will help the growing parts. The calculation illustrated in Fig. 9.19(b) shows that such a fill should be stable at 1 A.

Modulation coupling was expected to raise the instability threshold from 305 mA (nominal spacing) to 1.16 A (3 times nominal spacing). The measured thresholds are 350 mA and 660 mA, respectively.

Theoretical predictions of fill-induced Landau damping were first tested at the Advanced Light Source (ALS). Only two of the 328 ALS modes were unstable: mode 204 and 233. The effective impedance at $233\omega_0$ was used to create a tune spread by maximizing C_{233} .

A baseline even-fill instability measurement was first made at $I_0 = 172$ mA. This gave the two eigenvalues $\lambda_{204} = (0.47 \pm 0.02) + i(0.05 \pm 0.03)$ ms $^{-1}$ and $\lambda_{233} = (0.61 \pm 0.02) + i(1.16 \pm 0.03)$ ms $^{-1}$, assuming that the radiation damping rate $d_r = 0.074$ ms $^{-1}$. It is evident from Fig. 9.18 that fill fraction less than 60% will damp the target mode almost completely. Thus, any residual instability in the Landau fill must correspond to

the Landau-damped mode 204. Numerical calculation gives us only one unstable mode with eigenvalue $(0.1 \pm 0.04) - i(1.62 \pm 0.06) \text{ ms}^{-1}$, whose real part is about 6 times less than in the even-fill case. The measured eigenvalue for a 175-mA beam with $C_{233} = 0.67$ is $(0.09 \pm 0.003) - i(1.63 \pm 0.005) \text{ ms}^{-1}$, in agreement with the theoretical prediction.

Prediction of uneven fill has also been made on the light source at SRRC of Taiwan [15]. The main source of longitudinal impedance is from the Doris type rf cavities, which have a resonance at 744.1948 MHz, loaded $Q_L = 2219$ and $R_L/Q_L = 31.95 \Omega$. But from the observation on the real machine, the unstable mode number is 97 or resonance frequency is 742 MHz. There are $M = 200$ rf bucket in the SRRC ring. Thus, the most stable mode is 103. To couple the two modes, one must maximize C_6 , or the filling pattern is in 6 groups of buckets. The simulations consist of using three uneven fill patterns as illustrated on the left side of Fig. 9.20 with a total beam current of 200 mA.

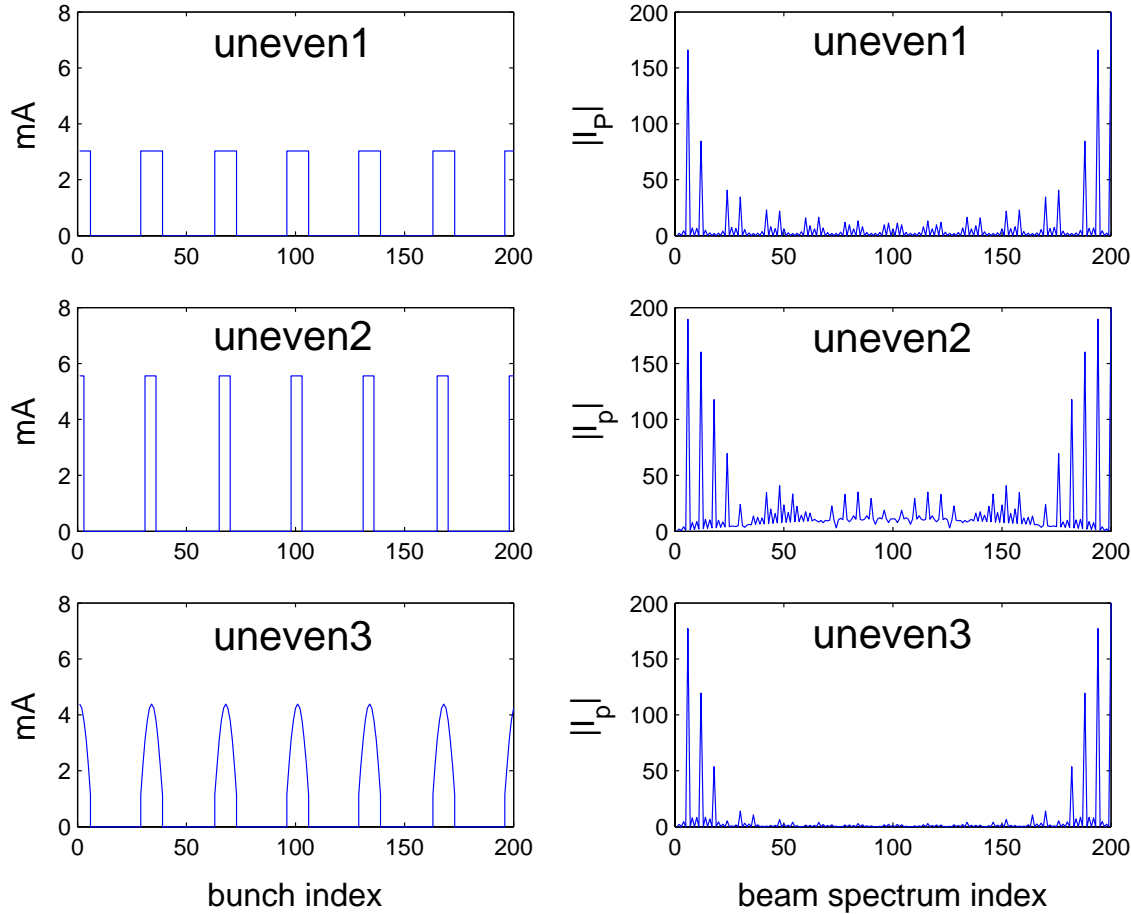


Figure 9.20: Fill patterns used in the simulation of the Taiwan Light Source.

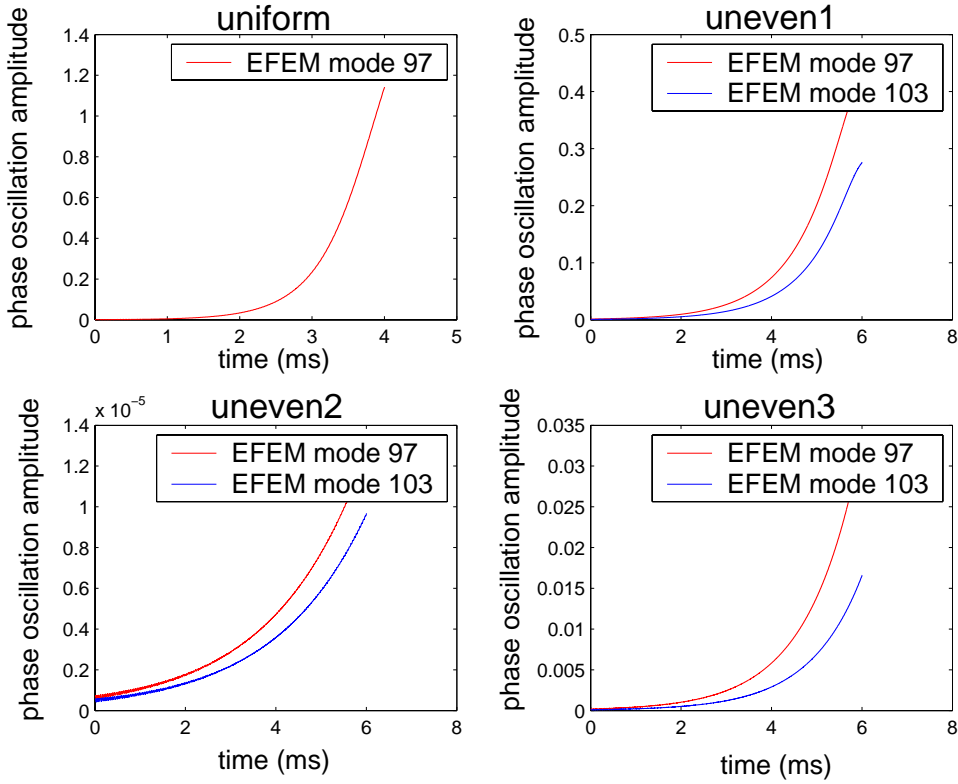


Figure 9.21: (color) The evolution of EFEM 97 and EFEM 103 of four fill patterns from simulation.

Table 9.1: Simulation results of growth rates of EFEM 97 and 103 of four fill patterns. 5 ms radiation damping time has been included.

Fill pattern	C_6	Growth rate ms^{-1}	
		EFEM 97	EFEM 103
uniform	0	1.9399	—
uneven1	0.8302	1.0004	1.0182
uneven2	0.9476	0.4947	0.4947
uneven3	0.8855	0.8659	0.8703

The spectra are shown on the right side. The growth rates for the two modes are displayed in Fig. 9.21 and listed in Table 9.1. Note that the derived growth rates include 5 ms radiation damping time. We see that the uneven fills do help to damp the beam instability, although the result has not been completely satisfactory because the instability still grows.

9.4 Exercises

- 9.1. Above/below transition, with the angular resonant frequency ω_r offset by $\Delta\omega = \pm(\omega_r - h\omega_0)$ where $\omega_{\text{rf}} = h\omega_0$ is the angular rf frequency, h is the rf harmonic, and ω_0 is the revolution angular velocity, the bunch suffers Robinson's instability.
- (1) Assuming that $\omega_s \ll |\Delta\omega| \ll \omega_{\text{rf}}$ and using the expression for resonant impedance in Eq. (1.40), show that the Robinson's growth rate in Eq. (9.41) can be written as

$$\frac{1}{\tau} = -\frac{2e^2 N \eta R_s Q}{\beta^2 E_0 T_0^2} \cos^2 \psi \sin 2\psi , \quad (9.141)$$

where N is the number of particles in the bunch, E_0 is the synchronous energy, βc is the velocity of the synchronous particle with c being the velocity of light, $T_0 = 2\pi/\omega_0$ is the revolution period, η is the slip factor, and the detuning angle ψ is defined as

$$\tan \psi = 2Q \frac{\omega_r - \omega_{\text{rf}}}{\omega_r}$$

for the resonant impedance with shunt impedance R_s , resonant frequency $\omega_r/(2\pi)$, and quality factor Q .

- (2) Assuming further that $|\Delta\omega|$ is much less than the resonator width $\omega_r/(2Q)$ which, in turn, is much less than ω_0 , show that the Robinson's growth rate can be written as

$$\frac{1}{\tau} = -\frac{4e^2 N R_s Q^2 \eta \Delta\omega}{\pi \beta^2 E_0 h T_0} . \quad (9.142)$$

(3) Robinson instability is usually more pronounced in electron than proton machines because high shunt impedance and quality factor are often required in the rf system. Take for example a ring of circumference 180 m with slip factor $|\eta| = 0.03$. To store a typical bunch with 1×10^{11} electrons at $E_0 = 1$ GeV, one may need an rf system with $h = 240$, $R_s = 1.0$ MΩ, and $Q = 2000$. On the other hand, to store a bunch of 1×10^{11} protons at kinetic energy $E_0 = 1$ GeV in the same ring, one may need an rf system with $h = 4$, $R_s = 0.12$ MΩ, and $Q = 45$. Compare the Robinson's growth rates for the two situations when the resonant frequencies are offset in the wrong directions by $|\Delta\omega| = \omega_s$. Assume the synchrotron tune to be 0.01 in both cases.

- 9.2. From Eq. (3.50), derive the potential-well contribution to the coherent synchrotron tune shift of a short bunch in the dipole mode. Show that this static contribution just cancels the dynamical contribution in Eq. (9.35) when the driving impedance is broadband.

9.3. Using the definition of the form factor in Eq. (9.68), compute numerically the form factor when the unperturbed distribution is bi-Gaussian. The half bunch length can be taken as $\hat{\tau} = \sqrt{6}\sigma_\tau$, where σ_τ is the rms bunch length.

9.4. Consider a single sinusoidal rf system operating at synchronous angle $\phi_s = 0$.

(1) Show that the synchrotron frequency of a particle at rf phase ϕ is given by

$$\frac{f_s(\phi)}{f_{s0}} = \frac{\pi}{2K(t)}, \quad (9.143)$$

where $t = \sin \phi/2$, f_{s0} is the synchrotron frequency at zero amplitude, and $K(t)$ is the complete elliptic integral of the first kind defined in Eq. (9.80).

(2) Show that Eq. (9.143) is consistent with Eq. (9.51) at small amplitudes.

9.5. Solve the set of equations in Eqs. (9.75) to (9.77) to obtain the fundamental rf phase ϕ_s , the higher-harmonic rf phase ϕ_m and the voltage ratio r in terms of the harmonic ratio m and U_s/eV_{rf} .

Answer:

$$\sin \phi_s = \frac{m^2}{m^2 - 1} \frac{U_s}{eV_{\text{rf}}}, \quad \tan \phi_m = \frac{\frac{m}{m^2 - 1} \frac{U_s}{eV_{\text{rf}}}}{\sqrt{1 - \left(\frac{m^2}{m^2 - 1} \frac{U_s}{eV_{\text{rf}}} \right)^2}}, \quad r = \sqrt{\frac{1}{m^2} - \frac{1}{m^2 - 1} \frac{U_s^2}{(eV_{\text{rf}})^2}}.$$

9.6. Derive the small-amplitude synchrotron frequency as given by Eq. (9.79).

Bibliography

- [1] P.B. Robinson, *Stability of Beam in Radiofrequency System*, Cambridge Electron Accel. Report CEAL-1010, 1964.
- [2] F.J. Sacherer, *A Longitudinal Stability Criterion for Bunched Beams*, CERN report CERN/MPS/BR 73-1, 1973; IEEE Trans. Nuclear Sci. **NS** **20**, 3, 825 (1973).
- [3] R.D. Kohaupt, DESY Report No. DESY 85-139, 1985.
- [4] S. Prabhakar, *New Diagnostic and Cures for Coupled-Bunch Instabilities*, Ph.D. thesis, Stanford University, 2000, 1999, SLAC Preprint SLAC-R-554.
- [5] A. Hofmann and S. Myers, *Beam Dynamics in a Double RF System*, Proc. 11th Int. Conf. High Energy Accel., Geneva, 1980.
- [6] A. Mosnier, *Cures of Coupled Bunch Instabilities*, PAC'99, Paper FRBR2.
- [7] S.Y. Lee *et al.*, Phys. Rev. **E49**, 5717 (1994); J.Y. Liu *et al.*, Phys. Rev. **E50**, R3349 (1994); J.Y. Liu *et al.*, Part. Accel. **49**, 221-251 (1995).
- [8] R. Averill *et al.*, Proceedings of 8th International Conference on High Energy Accelerators, CERN (1971) p. 301.
- [9] P. Bramham *et al.*, Proceedings of 9th International Conference on High Energy Accelerators, CERN (1974); P. Bramham *et al.*, IEEE Trans. Nucl. Sci. **NS-24**, 1490 (1977).
- [10] J.M. Baillod *et al.*, IEEE Trans. Nucl. Sci. **NS-30**, 3499 (1983); G. Galato *et al.*, Proceedings of the IEEE Particle Accel. Conference, 1987, p. 1298.

- [11] D. Li, M. Ball, B. Brabson, J. Budnick, D.D. Caussyn, A.W. Chao, V. Derenchuk, S. Dutt, G. East, M. Ellison, D. Friesel, B. Hamilton, H. Huang, W.P. Jones, S.Y. Lee, J.Y. Liu, M.G. Minty, K.Y. Ng, X. Pei, A. Riabko, T. Sloan, M. Syphers, Y. Wang, Y. Yan, and P.L. Zhang, ‘*Effects of Rf Voltage Modulation on Particle Motion*, Nucl. Inst. Meth. **A364**, 205 (1995).
- [12] M.H. Wang, Peace Chang, P.J. Chou, K.T. Hsu, C.C. Kuo, J.C. Lee, and W.K. Lau, *Experiment of RF Voltage Modulation at at SRRCC*, PAC'99, Paper THA106.
- [13] K.Y. Ng, *Damping of Coupled-Bunch Growth by Self-Excited Cavity*, Fermilab Internal Report FERMILAB-FN-456, 1987; K.Y. Ng, *Longitudinal Coupled-Bunch Instability in the Fermilab Booster*, Fermilab Internal Report FERMILAB-FN-464, 1987 (KEK Report 87-17).
- [14] S. Prabhakar, *New Diagnostic and Cures for Coupled-Bunch Instabilities*, Proceedings of the IEEE Particle Accel. Conference, Chicago, 2001.
- [15] M.H. Wang, P.J. Chou, and A.W. Chao, *Study of Uneven Fills to Cure the Coupled-Bunch Instability in SRRCC*, Proceedings of the IEEE Particle Accel. Conference, Chicago, 2001.

Chapter 10

TRANSVERSE INSTABILITIES

10.1 Transverse Focusing and Transverse Wake

Transverse focusing of the particle beam is necessary. If not the beam will diverge hitting the vacuum chamber and get lost. The alternating gradient focusing scheme suggested by Courant and Synder [1] employs F-quadrupoles and D-quadrupoles to provide for strong focusing of the beam in both the horizontal and vertical planes. For this reason, the transverse beam size can be made very small and so is the size of the vacuum chamber and the aperture of the magnets. In light sources, usually the Chasman-Green lattices are used. They consist of double achromats or triple achromats, which are strong focusing and give zero dispersion at both ends. Another merit of the achromats is that they can provide much smaller transverse emittances for the electron beam than the alternating gradient scheme of Courant and Synder.

Because quadrupoles can focus in only one transverse plane and defocus in the other, transverse oscillations develop in both transverse planes. These are called *betatron oscillations*, and the oscillation frequencies, $\omega_\beta/(2\pi)$, are called *betatron frequencies*, which are usually different in the two transverse planes. The number of betatron oscillations made in a revolution turn of the beam, $\nu_\beta = \omega_\beta/\omega_0$, is called the *betatron tune*. The equation of motion of a beam particle in, for example, the vertical plane, is given by

$$\frac{d^2y}{dn^2} + (2\pi\nu_\beta)^2 y = \frac{C^2 \langle F_1^\perp \rangle}{\beta^2 E_0}, \quad (10.1)$$

where n denotes turn number and the right side is the contribution due to the transverse

electromagnetic wake $W_1(\tau)$. Consider a coasting beam with current I_0 . The transverse force averaged over the circumference of the ring, $\langle F_1^\perp \rangle$ acting on the test particle is related to the transverse impedance through Eqs. (1.26) to (1.28):

$$Z_1^\perp = -\frac{iC\langle F_1^\perp \rangle}{e\beta I_0 \bar{y}} \quad (10.2)$$

where \bar{y} is the transverse displacement of the beam center. After averaging over all the beam particles, we obtain the equation of motion for the transverse motion of the beam center:

$$\frac{d^2\bar{y}}{dn^2} + (2\pi\nu_\beta)^2 \bar{y} = \frac{ie\beta I_0 Z_1^\perp C}{\beta^2 E_0} \bar{y} . \quad (10.3)$$

Thus, the transverse wake amounts to a betatron frequency shift

$$\Delta\omega_\beta = -\frac{i\beta c^2}{2\omega_\beta E_0} \frac{I_0}{C} Z_1^\perp , \quad (10.4)$$

where c is the velocity of light. For a coasting beam, transverse excitation comes from the transverse impedance that samples one or more of the betatron sidebands $n\omega_0 + \omega_\beta$ flanking the revolution harmonic n . The reactive part of $Z_1^\perp(\omega)$ produces a real frequency shift. The resistive part of the impedance produces an imaginary frequency shift, which if positive implies instability. Since $\Re Z_1^\perp(\omega) \gtrless 0$ when $\omega \gtrless 0$, the resistive part causes instability for negative frequency. Therefore only coasting-beam modes with $n < -\nu_\beta$ can be unstable.

There is a direct parallel between the transverse dynamics and the longitudinal dynamics, as is illustrated in the equations of motion in the longitudinal phase plane and the transverse phase plane. However, there is a big difference that the betatron tune $\nu_\beta \gg 1$ while the synchrotron tune $\nu_s \ll 1$.

10.2 Separation of Transverse and Longitudinal Motions

Just as for synchrotron oscillations, it is more convenient to change from (y, p_y) to the circular coordinates (r_β, θ) in the transverse betatron phase space. Following Eq. (7.1), we have

$$\begin{cases} y = r_\beta \cos \theta \\ p_y = r_\beta \sin \theta \end{cases} , \quad (10.5)$$

and Eq. (10.1) is transformed into

$$\begin{cases} \frac{dy}{ds} = -\frac{\omega_\beta}{v} p_y \\ \frac{dp_y}{ds} = \frac{\omega_\beta}{v} y - \frac{c}{E_0 \omega_\beta \beta} \langle F_1^\perp(\tau; s) \rangle , \end{cases} \quad (10.6)$$

where instead of turn number, the continuous variable s , denoting the distance along the designed orbit, has been used as the independent variable.

For a bunched beam, longitudinal motion has to be included. For time period much less than the synchrotron damping time, Hamiltonian theory can be used. The Hamiltonian for motions in both the longitudinal phase space and transverse phase space can be written as

$$H = H_{\parallel} + H_{\perp} , \quad (10.7)$$

where H_{\parallel} is the same Hamiltonian describing the longitudinal motion:

$$H_{\parallel} = -\frac{\eta(\Delta E)^2}{2v_0\beta_0^2E_0} - \frac{eV_{\text{rf}}}{C_0h\omega_0} \left[\cos(\phi_s - h\omega_0\tau) - \cos \phi_s - h\omega_0\tau \sin \phi_s \right] + V(\tau) \Big|_{\text{wake}} , \quad (10.8)$$

while H_{\perp} is the additional term coming from the equations of motion in the transverse phase space as given by Eq. (10.6). Note that the transverse force $\langle F_1^\perp(\tau; s) \rangle$ in Eq. (10.6) depends on the longitudinal variable τ ; therefore

$$[H_{\parallel}, H_{\perp}] \neq 0 . \quad (10.9)$$

We assume that the perturbation is small and synchro-betatron coupling is avoided. Then

$$[H_{\parallel}, H_{\perp}] \approx 0 . \quad (10.10)$$

This implies that in the transverse phase space, the azimuthal modes $m_{\perp} = 1, 2, \dots$, and the radial modes $k_{\perp} = 1, 2, \dots$ are good eigenmodes. In fact, this is very reasonable because at small perturbation, the transverse azimuthal modes m_{\perp} correspond to frequencies $m_{\perp}\omega_{\beta}$ with separation ω_{β} . Since

$$\omega_{\beta} \gg \omega_0 \gg \omega_s , \quad (10.11)$$

the possibility for different transverse azimuthals to couple is remote. A direct result of Eq. (10.10) is the factorization of the bunch distribution Ψ in the combined longitudinal-transverse phase space; i.e.,

$$\Psi(r, \phi; r_{\beta}, \theta) = \psi(r, \phi)f(r_{\beta}, \theta) , \quad (10.12)$$

where $\psi(r, \phi)$ is the distribution in the longitudinal phase space and $f(r_\beta, \theta)$ the distribution in the transverse phase space. Now decompose ψ and f into the unperturbed parts and the perturbed parts:

$$\begin{aligned}\psi(r, \phi) &= \psi_0(r) + \psi_1(r, \phi) , \\ f(r_\beta, \theta) &= f_0(r_\beta) + f_1(r_\beta, \theta) .\end{aligned}\quad (10.13)$$

When substituted into Eq. (10.12), there are four terms. The term $\psi_1 f_0$ implies only the longitudinal-mode excitations driven by the longitudinal impedance without any transverse excitations. This is what we have discussed in the previous sections and we do not want to include it again in the present discussion. The term $\psi_0 f_1$ describes the transverse excitations driven by the transverse impedance only. This term will be included in the $\psi_1 f_1$ term if we retain the azimuthal $m = 0$ longitudinal mode. For this reason, the bunch distribution Ψ in the combined longitudinal-transverse phase space contains only two terms

$$\Psi(r, \phi; r_\beta, \theta) = \psi_0(r) f_0(r_\beta) + \psi_1(r, \phi) f_1(r_\beta, \theta) e^{-i\Omega s/v} , \quad (10.14)$$

where we have separated out the collective angular frequency Ω from $\psi_1 f_1$.

10.3 Sacherer's Integral Equation

The linearized Vlasov equation is studied in the circular coordinates in both the longitudinal phase space and transverse phase space. However, only the transverse wake force will be included in the discussion here. After substituting the distribution in Eq. (10.14), the first order terms of the equation become

$$\left[-i \frac{\Omega}{v} f_1 \psi_1 + \frac{\omega_s}{v} f_1 \frac{\partial \psi_1}{\partial \phi} + \frac{\omega_\beta}{v} \psi_1 \frac{\partial f_1}{\partial \theta} \right] e^{-i\Omega s/v} - \psi_0 \frac{df_0}{dr_\beta} \sin \theta \frac{c}{E_0 \omega_\beta \beta} \langle F_1^\perp(\tau; s) \rangle = 0 . \quad (10.15)$$

It is worth pointing out that since the transverse wake force $\langle F_1^\perp(\tau; s) \rangle$ is a function of the longitudinal coordinate τ , it should also contribute to the second equation of Eq. (9.2) although the longitudinal wake force has been neglected here. It is, however, legitimate to drop this contribution if synchro-betatron resonance is avoided and the transverse beam size has not grown too large (see Exercise 10.4).

The next approximation is to consider only the rigid dipole mode in the transverse phase space; i.e., the bunch is displaced by an infinitesimal amount D from the center

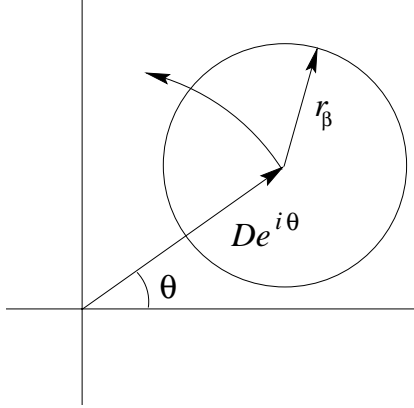


Figure 10.1: A bunch executing betatron motion with an amplitude D in the rigid dipole mode. In the transverse phase space, it is rotating counterclockwise rigidly with the radial offset D .

of the transverse phase space and executes betatron oscillations as a rigid object by revolving at frequency $\omega_\beta/(2\pi)$ counterclockwise. Then according to the convention of Eq. (10.5) and Fig 10.1, we must have,

$$f_0(r_\beta) + f_1(\vec{r}_\beta) = f_0(\vec{r} - De^{i\theta}) , \quad (10.16)$$

where \vec{r}_β and \vec{r} are treated as complex number in the transverse phase plane. When $D \rightarrow 0$, this becomes

$$f_1(r_\beta, \theta) = -D f'_0(r_\beta) e^{i\theta} . \quad (10.17)$$

Since we are retaining only one mode of transverse motion, all the modes that we are going to study are again synchrotron motion on top of this transverse mode. For this reasons, these synchrotron modes are no longer sidebands of the revolution harmonics; they are now sidebands of the betatron sidebands. Some of the transverse modes are shown in Fig. 10.2.

Equation. (10.15) then becomes

$$\left[i(\Omega - \omega_\beta)\psi_1 - \omega_s \frac{\partial \psi_1}{\partial \phi} \right] De^{-i\Omega s/v} + \frac{ic^2}{2E_0 \omega_\beta} \psi_0 \langle F_1^\perp(\tau; s) \rangle = 0 , \quad (10.18)$$

where we have dropped the $e^{-i\theta}$ component of $\sin \theta$ because that corresponds to rotation in the transverse phase space with frequency $-\omega_\beta/(2\pi)$ which is very far from $\omega_\beta/(2\pi)$ provided that the frequency shift due to the wake force is small. Notice that the transverse distribution $f_1(r_\beta, \theta)$ has been removed and the Vlasov equation involves only the

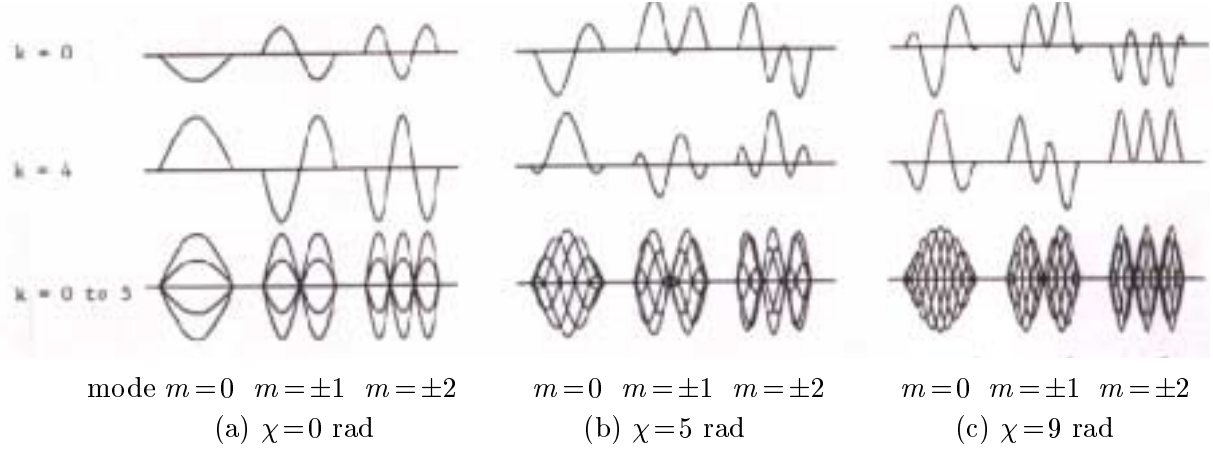


Figure 10.2: Head-tail modes of transverse oscillation. The plots show the contortions of a single bunch on separate revolutions, and with six revolutions superimposed (denoted by k). Vertical axis is difference signal from position monitor, horizontal axis is time, and $\nu_\beta = 4.833$. The chromaticity phases are (a) $\chi = 0$ rad, (b) $\chi = 5$ rad, and (c) $\chi = 9$ rad. Chromaticity will be introduced in Sec. 10.6.

longitudinal perturbed distribution function $\psi_1(r, \phi)$. This ψ_1 is the same perturbed distribution that we studied before with the exception that the azimuthal mode $m = 0$ is included.

The transverse wake force on a beam particle in the n th bunch at a time advance τ is, similar to the longitudinal counterpart in Eq. (9.9),

$$\begin{aligned} \langle F_{1n}^\perp(\tau; s) \rangle &= -\frac{e^2 D}{C} \sum_{k=-\infty}^{\infty} \sum_{\ell=0}^{M-1} \int_{-\infty}^{\infty} d\tau' \times \\ &\quad \times \rho_\ell[\tau'; s - kC - (s_\ell - s_n) - v(\tau' - \tau)] W_1[kC + (s_\ell - s_n) + v(\tau' - \tau)]. \end{aligned} \quad (10.19)$$

We assume M identical bunches equally spaced. For the μ th coupled mode, we substitute in the above expression the perturbed density of the n th bunch $\rho_{1n}(\tau)e^{-i\Omega s/v}$ including the phase lead as given by Eq. (9.10). Now the derivation follows exactly the longitudinal counterpart in Chapter 9 and we obtain

$$\langle F_{1n\mu}^\perp(\tau; s) \rangle = \frac{ie^2 M D \omega_0 \beta}{C} e^{-i\Omega s/v} \sum_{q=-\infty}^{\infty} \tilde{\rho}_{1n}(\omega_q) Z_1^\perp(\omega_q) e^{i\omega_q \tau}, \quad (10.20)$$

where $\omega_q = (qM + \mu)\omega_0 + \omega_\beta + \Omega$. We next substitute the result into the linearized Vlasov equation and expand ψ_1 into azimuthals according to $\psi_1(r, \phi) = \sum_m \alpha_m R_m(r) e^{im\phi}$. We

finally obtain Sacherer's integral equation for transverse instability

$$(\Omega - \omega_\beta - m\omega_s)\alpha_m R_m(r) = -\frac{i\pi e^2 MNc}{E_0 \omega_\beta T_0^2} g_0 \sum_{m'} i^{m-m'} \alpha_{m'} \int r' dr' R_{m'}(r') \sum_q Z_1^\perp(\omega_q) J_{m'}(\omega_q r') J_m(\omega_q r), \quad (10.21)$$

where the unperturbed distribution $g_0(r)$ defined in Eq. (9.30) has been used instead of $\psi_0(r)$. Notice that all transverse distributions are not present in the equation and what we have are longitudinal distributions. This is not unexpected because we have retained only one transverse mode of motion, namely the rigid dipole mode, in the transverse phase space. Therefore, the Sacherer's integral equation for transverse instability is almost the same as the one for longitudinal instability. There are only two differences. First, the unperturbed longitudinal distribution $g_0(r)$ appears in the former but $r^{-1}dg_0(r)/dr$ appears in the latter. Second, although the $m=0$ mode does not occur in the longitudinal equation because of violation of energy conservation, however, it is a valid azimuthal mode in the transverse equation because it describes rigid betatron oscillation.

10.4 Solution of Sacherer's Integral Equations

Consider first the transverse integral equation, where $W(r) = g_0(r)$ is considered to be a weight function. For each azimuthal m , find a complete set of orthonormal functions $g_{mk}(r)$ ($k = 1, 2, \dots$) such that

$$\int W(r) g_{mk}(r) g_{mk'}(r) r dr = \delta_{kk'} . \quad (10.22)$$

On both sides of the integral equation, perform the expansion

$$\alpha_m R_m(r) e^{im\phi} = \sum_k a_{mk} W(r) g_{mk}(r) e^{im\phi} . \quad (10.23)$$

Some comments are necessary. From Eq. (10.22), it appears that the orthonormal functions $g_{mk}(r)$ depend on the weight function $W(r)$ only and are independent of the azimuthal m . As a result, $g_{mk}(r)$ will not be uniquely defined, because the weight function $W(r) = g_0(r)$ is independent of m . In fact, this is not true. If we look into either

the Sacherer's longitudinal integral equation (9.31) or the transverse integral equation (10.21) for one single azimuthal, it is easy to see that

$$R_m(r) \propto W(r) J_m(\omega_q r) . \quad (10.24)$$

Therefore, for small r , we must have the behavior

$$R_m(r) \sim r^m \lim_{r \rightarrow 0} W(r) . \quad (10.25)$$

Taking the parabolic distribution in the longitudinal case as an example, $\lim_{r \rightarrow 0} W(r)$ is a constant implying that $R_m(r) \sim r^m$. From Eq. (10.23), since $g_{mk}(r)$ is the expansion of $R_m(r)$, the small- r behavior of $g_{mk}(r)$ will be constrained. This makes the set of orthonormal functions $g_{mk}(r)$ dependent on the azimuthal m and become, in fact, unique.

After substituting the expansion of $\alpha_m R_m$ into both sides of Eq. (10.21), multiply on both sides by $g_{mk}(r)$ and integrate over $r dr$. Sacherer's integral equation becomes

$$(\Omega - \omega_\beta - m\omega_s) a_{mk} = -\frac{i\pi e^2 MNc}{E_0 \omega_\beta T_0^2} \sum_{m'k'} a_{m'k'} \sum_q Z_1^\perp(\omega_q) \tilde{\lambda}_{mk}^*(\omega_q) \tilde{\lambda}_{m'k'}(\omega_q) , \quad (10.26)$$

where we have defined

$$\tilde{\lambda}_{mk}(\omega) = \int i^{-m} W(r) J_m(\omega r) g_{mk}(r) r dr . \quad (10.27)$$

The $\tilde{\lambda}_{mk}(\omega)$ is the Fourier transform of the eigenmode $\lambda_{mk}(\tau)$, which can be shown to be in fact the (mk) component of the perturbed linear density $\rho_1(\tau)$. Let us start from the Fourier transform of the linear density of the (mk) th mode

$$\tilde{\rho}_1^{(mk)}(\omega) = \frac{1}{2\pi} \int d\tau \rho_1^{(mk)}(\tau) e^{-i\omega\tau} = \frac{1}{2\pi} \int d\tau d\Delta E \psi_1^{(mk)}(\tau, \Delta E) e^{-i\omega\tau} . \quad (10.28)$$

Now substitute the (mk) th mode of Eq. (10.23) for $\psi_1^{(mk)}$ to obtain

$$\tilde{\rho}_1^{(mk)}(\omega) = \frac{\omega_s \beta^2 E_0}{2\pi\eta} \int r dr d\phi W(r) g_{mk}(r) e^{im\phi - i\omega\tau} . \quad (10.29)$$

The integration over ϕ can be performed to yield a Bessel function. Finally using the definition of $\tilde{\lambda}_{mk}(\omega)$ given in Eq. (10.27), we arrive at

$$\tilde{\rho}_1^{(mk)}(\omega) = \frac{\omega_s \beta^2 E_0}{\eta} \int r dr W(r) g_{mk}(r) i^{-m} J_m(\omega r) = \frac{\omega_s \beta^2 E_0}{\eta} \tilde{\lambda}_{mk}(\omega) . \quad (10.30)$$

Taking the Fourier transform, we therefore obtain

$$\rho_1^{(mk)}(\tau) = \frac{\omega_s \beta^2 E_0}{\eta} \lambda_{mk}(\tau) . \quad (10.31)$$

Notice that $\tilde{\lambda}_{mk}(\omega)$ is dimensionless; therefore it must be a function of $\omega \tau_L$ where τ_L is the total bunch length. The sum over the power spectrum should give us

$$\sum_q |\tilde{\lambda}_{mk}(\omega_q)|^2 \approx \int \frac{d\omega}{M\omega_0} |\tilde{\lambda}_{mk}(\omega)|^2 \sim \frac{1}{M\omega_0 \tau_L} , \quad (10.32)$$

where $\omega_q = (qM + \mu)\omega_0 + \omega_\beta + m\omega_s$. For this reason, Eq. (10.26) can roughly be transformed into

$$(\Omega - \omega_\beta - m\omega_s) a_{mk} = -\frac{i}{1+m} \frac{e\beta c^2}{2\omega_\beta E_0} \frac{I_b}{L} \sum_{m'k'} a_{m'k'} \frac{\sum_q Z_1^\perp(\omega_q) \tilde{\lambda}_{mk}^*(\omega_q) \lambda_{m'k'}(\omega_q)}{\sum_q \tilde{\lambda}_{mk}^*(\omega_q) \lambda_{mk}(\omega_q)} , \quad (10.33)$$

where I_b is the current of one bunch and $L = \beta c \tau_L$ is the total bunch length. Equation (10.33) is especially useful if we include only one mode of excitation. For example, the lowest radial mode $k = 1$ is usually the most prominent one to be excited and the different azimuthal modes do not mix when the perturbation is small.

This expression is very similar to the coasting-beam formula of Eq. (10.4). Besides the averaging over the power spectra, the coasting beam current per unit length I_0/C is replaced by the average single bunch current I_b divided by the total bunch length L in meters. The factor $(1+m)^{-1}$ in front says that higher-order modes are harder to excite, and is introduced under some assumption of the unperturbed distribution in phase space [2]. It is easy to understand why the power spectrum $h_{mk}(\omega) = |\tilde{\lambda}_{mk}(\omega)|^2$ enters because $Z_1^\perp(\omega) \tilde{\lambda}_{mk}(\omega)$ gives the deflecting field, which must be integrated over the bunch spectrum to get the total force. Written in the form of Eq. (10.33), there is no need for $\tilde{\lambda}_{mk}(\omega)$ or $\lambda_{mk}(\tau)$ to have any special normalization.

The Sacherer's longitudinal integral equation (9.29) can be solved in exactly the same way by identifying the weight function as

$$W(r) = -\frac{1}{r} \frac{dg_0(r)}{dr} , \quad (10.34)$$

where the negative sign is included because $dg_0(r)/dr < 0$. The result is

$$(\Omega - m\omega_s) a_{mk} = \frac{i 2\pi e^2 M N m \eta}{\beta^2 E_0 T_0^2 \omega_s} \sum_{m'k'} a_{m'k'} \sum_q \frac{Z_0^\parallel(\omega_q)}{\omega_q} \tilde{\lambda}_{mk}^*(\omega_q) \tilde{\lambda}_{m'k'}(\omega_q) , \quad (10.35)$$

where $\tilde{\lambda}_{mk}(\omega_q)$ is again given by Eq. (10.27), but with the weight function replaced by Eq. (10.34). However, $\tilde{\lambda}_{mk}(\omega_q)$ now has the dimension of of $(\text{time})^{-1}$ because the weight function is different. Dimensional analysis gives

$$\sum_q |\tilde{\lambda}_{mk}(\omega_q)|^2 \approx \int \frac{d\omega}{M\omega_0} |\tilde{\lambda}_{mk}(\omega)|^2 \sim \frac{1}{M\omega_0\tau_L^3}. \quad (10.36)$$

Equation (10.35) becomes approximately

$$(\Omega - m\omega_s)a_{mk} = \frac{im}{1+m} \frac{4\pi^2 e I_b \eta}{3\beta^2 E_0 \omega_s \tau_L^3} \sum_{m'k'} a_{m'k'} \frac{\sum_q \frac{Z_0^{\parallel}(\omega_q)}{\omega_q} \tilde{\lambda}_{m'k'}(\omega_q) \tilde{\lambda}_{mk}^*(\omega_q)}{\sum_q \tilde{\lambda}_{mk}^*(\omega_q) \tilde{\lambda}_{mk}(\omega_q)}, \quad (10.37)$$

where the extra factor in front is a result of the assumption of some particular unperturbed phase-space distribution. A more detailed derivation of Eq. (10.37) can be found in Ref. [2].

10.5 Sacherer's Sinusoidal Modes

Assuming the perturbation is small so that only a single azimuthal mode will contribute, we learn from the Sacherer's integral equation (10.21) that the perturbed excitation is

$$R_m(r)e^{im\phi} \propto W(r)J_m(\omega_q r)e^{im\phi}. \quad (10.38)$$

For a bunch of half length $\hat{\tau} = \frac{1}{2}\tau_L$, $R_m(\hat{\tau}) = 0$. So it is reasonable to write the k th radial mode corresponding to azimuthal m as

$$R_{mk}(r)e^{im\phi} \propto W(r)J_m\left(x_{mk}\frac{r}{\hat{\tau}}\right)e^{im\phi}, \quad (10.39)$$

where x_{mk} is the k th zero of the Bessel function J_m . Sacherer [3] discovered that, assuming a uniform or water-bag unperturbed distribution; i.e., $W(r)$ is constant for $r < \hat{\tau}$, the projection of $R_{mk}(r)e^{im\phi}$ onto the τ axis

$$\rho_{(mk)}(\tau) \propto \int W(r)J_m\left(x_{mk}\frac{r}{\hat{\tau}}\right)e^{im\phi} d\Delta E \quad (10.40)$$

is approximately sinusoidal. In fact, head-tail excitations that are sinusoidal-like had been observed in the CERN Proton Synchrotron (PS) booster. For this reason, instead

of solving the integral equation, Sacherer approximated $\rho_{(mk)}(\tau)$ by a linear combination of sinusoidal functions, and these modes are called sinusoidal modes. He introduced a set of orthonormal functions

$$\lambda_m(\tau) \propto \begin{cases} \cos(m+1)\pi\frac{\tau}{\tau_L} & m = 0, 2, \dots, \\ \sin(m+1)\pi\frac{\tau}{\tau_L} & m = 1, 3, \dots. \end{cases} \quad (10.41)$$

Note that $\lambda_m(\tau)$ has exactly m nodes along the bunch not including the two ends. If we restrict ourselves to the most prominent lowest radial mode ($k = 1$), these $\lambda_m(\tau)$'s are just the approximates to $\rho_{(m1)}(\tau)$. From now on, the radial mode index k will be dropped.

The power spectrum of the modes in Eq. (10.41) is proportional to

$$h_m(\omega) = \frac{4(m+1)^2}{\pi^2} \frac{1 + (-1)^m \cos \pi y}{[y^2 - (m+1)^2]^2} \quad (10.42)$$

where $y = \omega\tau_L/\pi$ and $\tau_L = L/v$ is the total length of the bunch in time. They are plotted in Fig. 7.5. The normalization of $h_m(\omega)$ in Eq. (10.42) has been chosen in such a way that, when the smooth approximation is applied to the summation over k , we have

$$B \sum_{q=-\infty}^{+\infty} h_m(\omega_q) \approx \frac{B}{M\omega_0} \int_{-\infty}^{+\infty} h_m(\omega) d\omega = 1. \quad (10.43)$$

Here $B = M\omega_0\tau_L/(2\pi)$ is the bunching factor in the presence of M identical equally-spaced bunches, or the ratio of full bunch length to bunch separation.

For the elliptical distribution in the longitudinal phase space, $g_0(r) \propto (\hat{\tau}^2 - r^2)^{-1/2}$, so that the linear density becomes constant, the spectral excitations of the lowest radial mode $\lambda_m(\tau)$ are the Legendre polynomials, the Fourier transform $\tilde{\lambda}_m(\omega)$ are the spherical Bessel functions j_m , and the power spectra $h_m \propto |j_m|^2$. We called these the Legendre modes. For the bi-Gaussian distribution in the longitudinal phase space, $\lambda_m(\tau)$ are the Hermite polynomials and $\tilde{\lambda}_m(\omega)$ are ω^m multiplied by a Gaussian. We call these the Hermite modes.

For the longitudinal integral equation, we have the same modes if we have the same weight function. For the longitudinal case, the weight function is $W(r) = g'_0(r)/r$ instead. Therefore the sinusoidal modes correspond to $g_0(r) \propto (\hat{\tau}^2 - r^2)$ or linear density

$\rho(\tau) \propto (\hat{\tau}^2 - \tau^2)^{3/2}$. The Legendre modes correspond to $g_0(r) \propto (\hat{\tau}^2 - r^2)^{1/2}$ or parabolic linear density $\rho(\tau) \propto (\hat{\tau}^2 - \tau^2)$. The Hermite modes correspond to the same bi-Gaussian distribution as in the transverse situation. These solutions are summarized in Table 10.1.

Sometimes the growth rates computed are rather sensitive to the longitudinal bunch distribution assumed. Therefore, results using the sinusoidal modes are estimates only.

After so much mathematics, it is possible to present some simple expressions for the growth rates. From Eq. (10.37) for the longitudinal and Eq. (10.33) for the transverse, let us assume that there is no mixing between azimuthal modes as well as radial modes. Then the longitudinal growth rate simplifies to

$$\frac{1}{\tau_{mk\mu}} = \text{Im} \Omega \approx \frac{m}{1+m} \frac{4\pi^2 e I_b \eta}{3\beta^2 E_0 \omega_s \tau_L^3} \sum_q \frac{\Re Z_0^{\parallel}(\omega_q)}{\omega_q} h_{mk}(\omega_q), \quad (10.44)$$

where $\omega_q = (qM + \mu)\omega_0 + m\omega_s$ and the power spectrum has been normalized to unity according to Eq. (10.43). The transverse growth rate simplifies to

$$\frac{1}{\tau_{mk\mu}} = \text{Im} \Omega \approx -\frac{1}{1+m} \frac{e I_b c}{4\pi \nu_\beta E_0} \sum_q \Re Z_1^{\perp}(\omega_q) h_{mk}(\omega_q), \quad (10.45)$$

where $\omega_q = (qM + \mu)\omega_0 + \omega_\beta + m\omega_s$.

10.6 Chromaticity Frequency Shift

The betatron tune ν_β of a beam particle depends on its momentum offset δ . The chromatic betatron tune shift is defined as

$$\Delta\nu_\beta = \xi\delta, \quad (10.46)$$

where ξ is called the *chromaticity**. Because the beam particle makes synchrotron oscillations, its betatron tune will be changing from turn to turn depending on its momentum offset. There will be a betatron phase offset which will accumulate. Consider a beam particle which is currently at the head of the bunch. It will be executing betatron oscillations with the same betatron tune as the synchronous particle, because it is at the synchronous momentum. Below transition, the synchrotron oscillation is clockwise in

*Sometimes, especially in Europe, the chromaticity ξ is also defined by $\Delta\nu_\beta = \xi\nu_\beta\delta$.

Table 10.1: Some solutions of the Sacherer's integral equations for longitudinal and transverse excitations with only one radial mode included in each case.

Longitudinal Integral Equation		Transverse Integral Equation		Weight Function	Azimuthal Excitation Modes	
Phase-space Distribution	Linear Distribution	Phase-space Distribution	Linear Distribution	$W(r)$	Linear Distribution	Spectral Distribution
$f_0(r)$	$\lambda(\tau)$	$g_0(r)$	$\lambda(\tau)$	$\sim g_0(r) \sim \frac{f'_0(r)}{r}$	$\lambda_{m1}(\tau)$	$\tilde{\lambda}_{m1}(\omega)$
Water-bag		Air-bag				
$H(\hat{\tau} - r)$	$\sqrt{\hat{\tau}^2 - \tau^2}$	$\delta(\hat{\tau} - r)$	$\frac{1}{\sqrt{\hat{\tau}^2 - \tau^2}}$	$\delta(\hat{\tau} - r)$	$\frac{T_m(\tau/\hat{\tau})}{\sqrt{1 - (\tau/\hat{\tau})^2}}$	$J_m(\omega\hat{\tau})$
$\hat{\tau}^2 - r^2$	$(\hat{\tau}^2 - \tau^2)^{\frac{3}{2}}$	constant	$\sqrt{\hat{\tau}^2 - \tau^2}$	constant	sinusoidal	$\sqrt{h_m(\omega)}$
$\sqrt{\hat{\tau}^2 - r^2}$	$\hat{\tau}^2 - \tau^2$	$\frac{1}{\sqrt{\hat{\tau}^2 - \tau^2}}$	constant	$\frac{1}{\sqrt{\hat{\tau}^2 - \tau^2}}$	$P_m(\tau/\hat{\tau})$	of Eq. (10.42)
$e^{-\frac{r^2}{2\sigma^2}}$	$e^{-\frac{\tau^2}{2\sigma^2}}$	$e^{-\frac{r^2}{2\sigma^2}}$	$e^{-\frac{\tau^2}{2\sigma^2}}$	$e^{-\frac{r^2}{2\sigma^2}}$	$H_m\left(\frac{\tau}{\sqrt{2\sigma}}\right)$	$(\omega\sigma)^m e^{-\frac{\omega^2}{2\sigma^2}}$

the longitudinal phase space as indicated in Fig. 10.3, because, for example, at a positive momentum offset, the particle comes back earlier or its arrival time advance increases. Thus leaving the head of the bunch, the particle loses energy and starts to oscillate

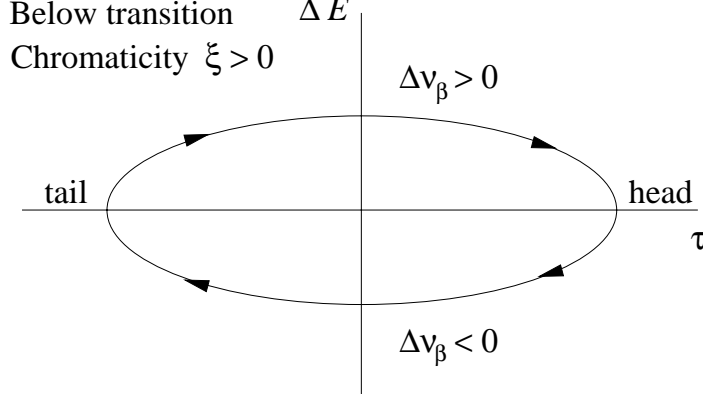


Figure 10.3: Synchrotron motion in the longitudinal phase space below transition. If chromaticity ξ is positive, the betatron tune will be larger/smaller than that of the synchrotron particle, when the particle energy offset is positive/negative.

with smaller betatron tune if the chromaticity ξ is positive. Turn by turn, the slip in betatron phase accumulates and reaches a maximum when the particle arrives at the tail of the bunch. After that the momentum offset of the second half of the synchrotron oscillation becomes positive. The betatron tune is larger than the nominal value and the accumulated betatron phase slip gradually reduces. When the particle arrives at the head all the betatron phase slip vanishes. This phase slip is illustrated schematically in Fig. 10.4.

We would like to compute the phase slip for a particle that has a time advance τ relative to the synchronous particle. The momentum offset in Eq. (10.46) can be eliminated using the equation of motion of the phase

$$\Delta\tau = -\eta T_0 \delta , \quad (10.47)$$

where η is the slip factor and $\Delta\tau$ is the change in time advance of the particle in a turn. The phase lag in a turn is then

$$\int 2\pi \Delta\nu_\beta = -2\pi \frac{\xi}{\eta} \int \frac{\Delta\tau}{T_0} = -\frac{\xi\omega_0}{\eta}\tau . \quad (10.48)$$

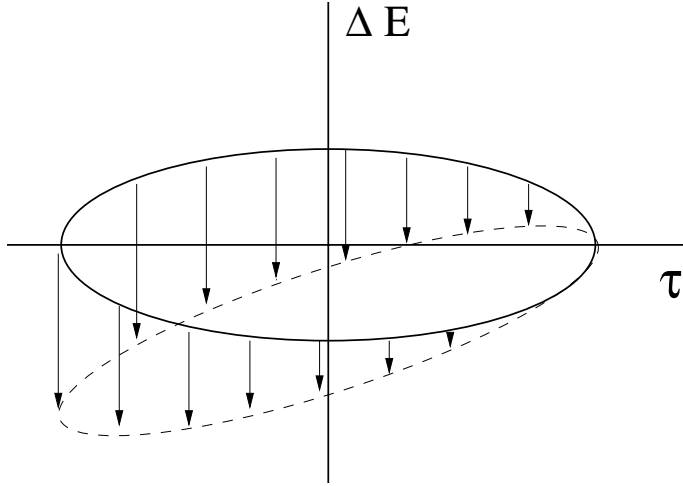


Figure 10.4: Schematic drawing showing the lagging of the betatron phase, depicted by the arrows, from the head (right) to the tail (left) of the bunch when the chromaticity ξ and slip factor η have the same signs.

Thus, below transition ($\eta < 0$), a particle at the bunch head ($\tau = \hat{\tau}$) has an accumulated betatron phase advance of $-\xi\omega_0\hat{\tau}/\eta$ relative to the synchronous particle, while a particle at the tail ($\tau = -\hat{\tau}$) has an accumulated betatron phase slip of $-\xi\omega_0\hat{\tau}/\eta$. Equation (10.48) indicates that the phase lag increases linearly along the bunch and is independent of the momentum offset. Relative to the synchronous particle, we write this accumulated betatron phase for a particle at arrival time advance τ as

$$-\frac{\xi\omega_0}{\eta}\tau = -\omega_\xi\tau , \quad (10.49)$$

where

$$\omega_\xi = \frac{\xi\omega_0}{\eta} \quad (10.50)$$

is called the *betatron angular frequency shift due to chromaticity*. Below transition and for positive chromaticity, ω_ξ is negative, but the accumulated betatron phase at the bunch head is positive. Thus, in previous derivation we should make the substitution

$$e^{i\omega_q\tau} \rightarrow e^{i(\omega_q - \omega_\xi)\tau} . \quad (10.51)$$

where $\omega_q = (qM + \mu)\omega_0 + m\omega_s$. For this reason, ω_ξ should be subtracted from ω_q in the argument of the power spectrum h_m but not in the argument of $\text{Re } Z_1^\perp$ of the growth rate formula like Eq. (10.45) and also not in the argument of $\text{Im } Z_1^\perp$ of the tune shift formula. The total betatron phase shift from head to tail is represented by $\chi = \omega_\xi\tau_L$,

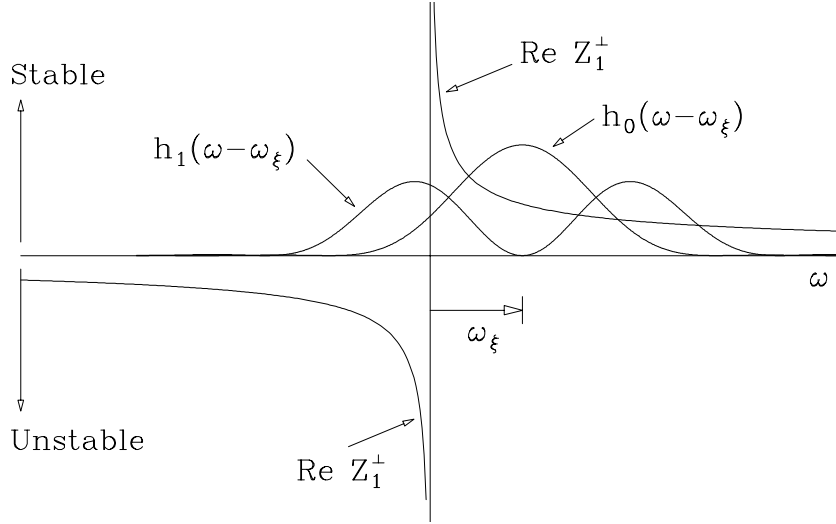


Figure 10.5: Positive chromaticity above transition shifts the all modes of excitation towards the positive frequency side by ω_ξ . Mode $m = 0$ becomes stable, but mode $m = 1$ may be unstable because it samples more negative $\Re Z_1^\perp$ than positive $\Re Z_1^\perp$.

where τ_L is the total length of the bunch from head to tail. The head-tail modes for various values of χ are shown in Fig. 10.2.

For positive chromaticity above transition, $\omega_\xi > 0$, the modes of excitation in Fig. 7.5 are therefore shifted to the right by the angular frequency ω_ξ . As shown in Fig. 10.5, mode $m = 0$ sees more impedance in positive frequency than negative frequency and is therefore stable. However, it is possible that mode $m = 1$, as in the illustration of Fig. 10.5, samples more the highly negative $\Re Z_1^\perp$ at negative frequencies than positive $\Re Z_1^\perp$ at positive frequencies and becomes unstable.

If the transverse impedance is sufficiently smooth, it can be removed from the summation in Eq. (10.45). The growth rate for the $m = 0$ mode becomes

$$\frac{1}{\tau_0} = -\frac{eI_{bc}}{2\omega_\beta E_0 \tau_L} \Re Z_1^\perp(\omega_\xi) . \quad (10.52)$$

The transverse impedance of the CERN Proton Synchrotron (PS) had been measured in this way by recording the growth rates of a bunch at different chromaticities.

10.7 Exercises

- 10.1. Fill in all the steps in the derivation of Sacherer's integral equation for transverse instabilities.
- 10.2. Derive the power spectra of the sinusoidal modes of excitation in Eq. (10.41), and show that they are given by Eq. (10.42) when properly normalized according to Eq. (10.43).
- 10.3. If the transverse impedance is sufficiently smooth, it can be removed from the summation in Eq. (10.33). Show that the growth rate for the $m = 0$ mode becomes

$$\frac{1}{\tau_0} = -\frac{eI_b c}{2\omega_\beta E_0 \tau_L} \operatorname{Re} Z_1^\perp(\omega_\xi) . \quad (10.53)$$

The transverse impedance of the CERN PS has been measured in this way by recording the growth rates of a bunch at different chromaticities. The CERN PS has a mean radius of 100 m and it can store proton bunches from 1 to 26 GeV with a transition gamma of $\gamma_t = 6$. The bunch has a spectral spread of $\sim \pm 100$ MHz, implying that each measurement of the impedance is averaged over an interval of ~ 200 MHz. If the impedance has to be measured up to ~ 2 GHz and the sextupoles in the PS can attain chromaticities in the range of ± 10 , at what proton energy should this experiment be carried out?

- 10.4. Redefine the longitudinal coordinates in Eq. (9.1) by $X = xv$ and $P_x = p_x v$, where v is the particle velocity, so that X carries the dimension of length.
 - (a) Show that, for the equations of motion (9.2) in the longitudinal phase space and (10.6) in the transverse phase space, the Hamiltonian is

$$H = -\frac{\omega_s}{2v}(X^2 + P_x^2) - \frac{\omega_\beta}{2v}(y^2 + p_y^2) - \frac{v\eta}{E_0\omega_s\beta^2} \int_0^X dX' \langle F_0^{\parallel}(X'/v; s) \rangle + \frac{cy}{E_0\omega_\beta\beta^2} \langle F_1^{\perp}(X/v; s) \rangle . \quad (10.54)$$

- (b) Show that the second equation of motion in Eq. (9.2) needs to be modified to

$$\frac{dp_x}{ds} = \frac{\omega_s}{v}x + \frac{\eta}{E_0\omega_s\beta^2} \langle F_0^{\parallel}(x; s) \rangle - \frac{y}{E_0\omega_\beta\beta^3 v} \frac{\partial}{\partial x} \langle F_1^{\perp}(x; s) \rangle , \quad (10.55)$$

where the last term is the synchro-betatron coupling term which we dropped in our discussion.

Bibliography

- [1] E.D. Courant and H.S. Synder, *Theory of the Alternating-Gradient Synchrotron*, Annals of Physics **3**, 1 (1958).
- [2] See for example, J.L. Laclare, *Bunch-Beam Instabilities, —Memorial Talk for F.J. Sacherer*, Proc. 11th Int. Conf. High-Energy Accelerators, Geneva, July 7-11, 1980, p. 526.
- [3] F.J. Sacherer, *Methods for Computing Bunched-Beam Instabilities*, CERN Report CERN/SI-BR/72-5, 1972.

Chapter 11

TRANSVERSE COUPLED BUNCH INSTABILITIES

11.1 Resistive Wall

If there are M identical equally spaced bunches in the ring, there are $\mu = 0, \dots, M-1$ transverse coupled modes when the center-of-mass of one bunch leads its predecessor by the betatron phase of $2\pi\mu/M$. The transverse growth rate for the μ -th coupled-bunch mode is given by Eq. (10.45). Including chromaticity, it becomes

$$\frac{1}{\tau_{m\mu}} = -\frac{1}{1+m} \frac{eMI_b c}{4\pi\nu_\beta E_0} \frac{\sum_q \Re Z_1^\perp(\omega_q) h_m(\omega_q - \chi/\tau_L)}{B \sum_q h_m(\omega_q - \chi/\tau_L)}, \quad (11.1)$$

where $\omega_q = (qM + \mu)\omega_0 + \omega_\beta + m\omega_s$, the bunching factor $B = M\tau_L/T_0$ has been used, $\chi = \omega_\xi\tau_L$ is the chromaticity phase shift across the bunch of full length τ_L and T_0 is the revolution period. Here, we assume that all the bunches are executing synchrotron oscillations in the same longitudinal azimuthal mode m .

The most serious transverse coupled-bunch instability that occurs in nearly all storage rings is the one driven by the resistive wall [1]. Since* $\Re Z_1^\perp \propto \omega^{-1/2}$ and is positive (negative) when the angular frequency ω is positive (negative), the betatron line at the

*Here, we assume that the wall is thicker than one skin depth at revolution frequency. Otherwise, $\Re Z_1^\perp \propto \omega^{-1}$.

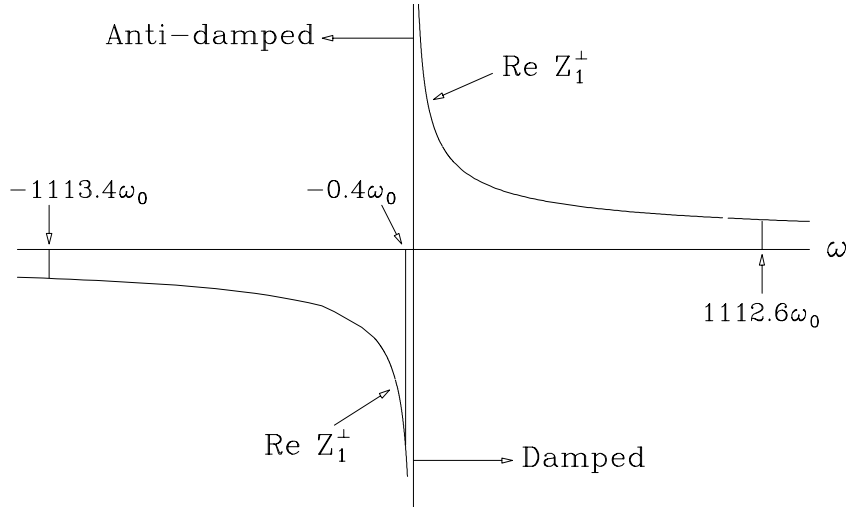


Figure 11.1: The $-0.4\omega_0$ betatron line in the Tevatron dominates over all other betatron lines for the $\mu = 1093$ mode coupled-bunch instability driven by the resistive wall impedance.

lowest negative frequency acts like a narrow resonance and drives transverse coupled-bunch instabilities. Take, for example, the Fermilab Tevatron in the fixed-target mode, where there are $M = 1113$ equally spaced bunches. The betatron tune is $\nu_\beta = 19.6$. The lowest-negative-betatron-frequency line is at $(qM+\mu)\omega_0 + \omega_\beta = -0.4\omega_0$, for mode $\mu = 1093$ and $q = -1$. The closest damped betatron line ($q = 0$) is at $(1113 - 0.4)\omega_0$, but $\mathcal{R}e Z_1^\perp$ is only $-\sqrt{0.4/1112.6}$ the value at $-0.4\omega_0$. The next anti-damped betatron line ($q = -2$) is at $-1113.4\omega_0$, with $\mathcal{R}e Z_1^\perp$ equal to $\sqrt{0.4/1113.4}$ the value at $-0.4\omega_0$. This is illustrated in Fig. 11.1. Thus, it is the $-0.4\omega_0$ betatron line that dominates. From Eq. (11.1), the growth rate for this mode can therefore be simplified to

$$\frac{1}{\tau_{m\mu}} \approx -\frac{1}{1+m} \frac{eMI_b c}{4\pi\nu_\beta E_0} \mathcal{R}e Z_1^\perp(\omega_q) F'_m(\omega_q\tau_L - \chi), \quad (11.2)$$

where $\chi = \omega_\xi\tau_L$ and the form factor is

$$F'_m(\omega\tau_L) = \frac{2\pi h_m(\omega)}{\tau_L \int_{-\infty}^{\infty} h_m(\omega)d\omega}, \quad (11.3)$$

which is plotted in Fig. 11.2 for the sinusoidal modes. For zero chromaticity, only the $m = 0$ mode can be unstable because the power spectra for all the $m \neq 0$ modes are nearly zero near zero frequency. Since the perturbing betatron line is at extremely low

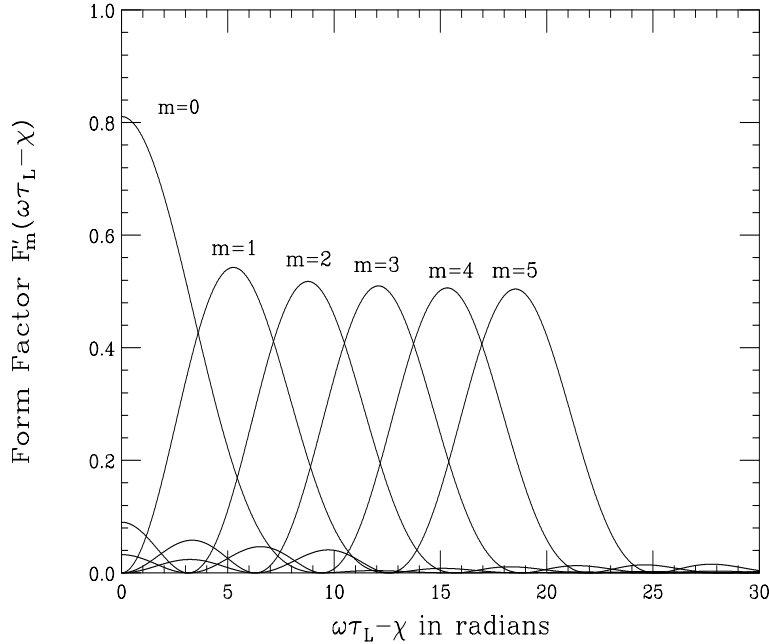


Figure 11.2: Plot of form factor $F'_m(\omega\tau_L - \chi)$ for modes $m = 0$ to 5 . With the normalization in Eq. (10.43), these are exactly the power spectra h_m .

frequency, we can evaluate the form factor at zero frequency. For the sinusoidal modes, we get $F'_0(0) = 8/\pi^2 = 0.811$.

One method to make this coupled-bunch mode less unstable or even stable is by introducing positive chromaticity when the machine is above transition. For the Tevatron with slip factor $\eta = 0.0028$, total bunch length $\tau_L = 5$ ns, and revolution frequency $f_0 = 47.7$ kHz, a chromaticity of $\xi = +10$ will shift the spectra by the amount $\chi = \omega_\xi\tau_L = 2\pi f_0 \xi \tau_L / \eta = 5.4$. The form factor and thus the growth rate is reduced by more than 4 times. However, from Figs. 7.5 and 10.5, we see that the spectra are shifted by $\omega_\xi\tau_L/\pi = 1.7$ and the $m = 1$ mode becomes unstable. Another method for damping the instability is to introduce a betatron angular frequency spread using octupoles, with the spread larger than the growth rate.

A third method is to employ a damper. Let us derive the displacements of consecutive bunches at a beam-position monitor (BPM). Suppose the first bunch is at the BPM with betatron phase $\phi_{\beta 0} = 0$; its displacement registered at the BPM is proportional to $\cos \phi_{\beta 0} = 1$. At that moment, the next bunch has phase $2\pi\bar{\mu}/M$ in advance, where $\bar{\mu} = qM + \mu = -20$. When this bunch arrives at the BPM, the time elapsed is T_0/M and

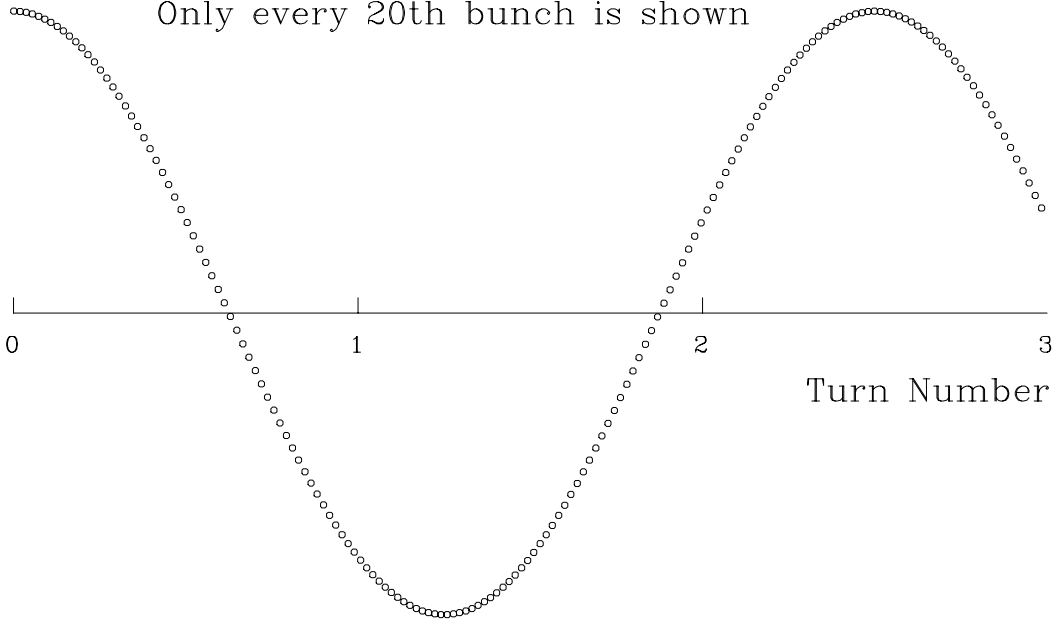


Figure 11.3: Difference signal at a BPM displaying the displacement of every 20th bunch, when the $\mu = 1093$ mode of transverse coupled-bunch is excited by the resistive wall impedance.

the change in betatron phase is $\omega_\beta T_0/M = 2\pi\nu_\beta/M$. The total betatron phase on arrival at the BPM is therefore $\phi_{\beta 1} = 2\pi\bar{\mu}/M + 2\pi\nu_\beta/M = 2\pi(\bar{\mu} + \nu_\beta)/M = (-0.4)2\pi/M$, and the displacement registered is $\cos \phi_{\beta 1}$. When the n th consecutive bunch arrives at the BPM, its phase will be $\phi_{\beta n} = n(-0.4)2\pi/M$. This is illustrated in Fig. 11.3 when the BPM is registering every 20th bunch [2]. What we see at the BPM is a wave of frequency -0.4 harmonic or about 19.1 kHz. Because we know that the bunches follow the pattern of such a slow wave, we only require a very narrow-band feedback system to damp the instability. Usually the adjacent modes $\mu = 1092, 1091, \dots$ will also be unstable at the $-1.4\omega_0, -2.4\omega_0, \dots$ betatron lines; but the growth rates will be smaller.

When all the $h = 1113$ rf buckets are filled with 6×10^{10} protons each in one scenario of the Tevatron in the fixed-target mode, the average total current is $MI_b = 0.511$ A. The vertical resistive-wall impedance has a real part $\Re Z_1^\perp = 43.74$ M Ω /m at the revolution harmonic. Thus, at $-0.4\omega_0$, it becomes $\Re Z_1^\perp = -69.16$ M Ω /m. At the injection energy of $E_0 = 150$ GeV and zero chromaticity, the transverse coupled-bunch growth rate driven by the resistive-wall impedance is $\tau_\mu^{-1} = 232$ s $^{-1}$ and the growth time is 4.30 ms or 204

revolution turns. The mean radius of the Tevatron ring is $R = 1$ km. In fact, this growth time is more or less the same for all accelerator rings [3]. For example, preceding the Tevatron, there are the Main Injector and the Booster. All of them have the same 53-MHz rf. The Main Injector has 588 rf buckets and the Booster has 84 rf buckets. First, if all the buckets of each ring are filled, the average total current MI_b should be the same for all the 3 rings. Second, the beam energy E_0 scales as the size of the ring or the mean radius R and betatron tune ν_β scales as \sqrt{R} . Third, the resistive-wall impedance, as given by

$$Z_1^\perp(\omega) = [1 - i \operatorname{sgn}(\omega)] \frac{2Rc\rho}{\omega b^3 \delta_{\text{skin}}} \quad (11.4)$$

in Eq. (1.44), where b is the beam pipe radius, δ_{skin} is the skin depth, and ρ is the resistivity, scales as $R^{3/2}$ because the revolution frequency scales as R^{-1} . Substituting into Eq. (11.2), we find that the growth rate turns out to be independent of the size of the ring. Of course, usually there are differences in the vacuum chamber, and number of particles per bunch, and also the residual betatron tune. However, it is safe to say that the growth time of transverse couple-bunch instability for every completely filled accelerator ring should be of the order of a few to a few tens of milliseconds. Although the growth time is independent of the size of the ring, the growth time in turn number is inversely proportional to the size of the ring. Thus, for the Very Large Hadron Collider (VLHC) under consideration with a circumference of 233 km, the growth time will be only 5.5 revolution turns according to this scaling and assuming the residual tune to be $\frac{1}{2}$. For this reason, large machines will require powerful feedback systems, for example, criss-crossing feedback and/or one-turn correction scheme.

11.2 Narrow Resonances

The narrow higher-order transverse resonant modes of the rf cavities will also drive transverse coupled-bunch instabilities. The growth rates are described by the general growth formula of Eq. (11.1). When the resonance is narrow enough, only the betatron lines closest to the resonant frequency $\omega_r/(2\pi)$ contribute in the summation. The growth rate is therefore given by Eq. (11.2), where two betatron lines are included.

$$\frac{1}{\tau_{m\mu}} \approx -\frac{1}{1+m} \frac{eMI_b c}{4\pi\nu_\beta E_0} [\Re Z_1^\perp(\omega_q) F'_m(\omega_q \tau_L - \chi) - \Re Z_1^\perp(\omega_{q'}) F'_m(\omega_{q'} \tau_L - \chi)] , \quad (11.5)$$

where q and q' satisfy

$$\begin{cases} -\omega_r \approx \omega_q = (qM + \mu + \nu_\beta + m\nu_s)\omega_0 \\ \omega_r \approx \omega_{q'} = (q'M + \mu + \nu_\beta + m\nu_s)\omega_0 \end{cases} . \quad (11.6)$$

Similar to the situation of longitudinal coupled-bunch instabilities, mode $\mu = 0$ and mode $\mu = \frac{1}{2}M$ if M is even receive contributions from both the positive-frequency side and negative-frequency side. In the language of only positive frequencies, there are the upper and lower betatron sidebands flanking each revolution harmonic line. The lower sideband originates from negative frequency and is therefore antidamped. For these two modes, both the upper and lower sidebands correspond to the same coupled-bunch mode. If the resonant frequency of the resonance leans more towards the lower sideband, there will be a growth. If the resonant frequency leans more towards the upper side band, there will be damping. This is the Robinson's stability analog in the transverse phase plane. However, sometimes it is not so easy to identify which is the lower sideband and which is the upper sideband. This is because the residual betatron tune $[\nu_\beta]$ or the noninteger part of the betatron tune can assume any value between 0 and 1. If $[\nu_\beta] > 0.5$, the upper betatron sideband of a harmonic will have a higher frequency than the lower betatron sideband of the next harmonic.

There is one important difference between transverse coupled-bunch instabilities driven by the resistive-wall impedance and by the higher-order resonant modes. The former is at very low frequency and therefore the form factor F'_0 is close to 1 when the chromaticity is zero. The latter, however, is at the high frequencies of the resonances. The form factor usually assumes a much smaller value unless the bunch is very short and we sometimes refer this to "damping" from the spread of the bunch.

This instability can be observed easily in the frequency domain at the lower betatron sidebands flanking the harmonic lines. If a particular lower betatron sideband grows strongly, we subtract the betatron tune ν_β (not $[\nu_\beta]$) to find out which harmonic line it is associated with. Then from Eq. (11.6), we can determine which coupled-bunch mode μ it is. To damp this transverse coupled-bunch instability, one can identify the offending resonant modes in the cavities and damp them passively using an antenna. A tune spread due to the slip factor η or from an octupole can also contribute to the damping. When the above are not efficient enough, a transverse bunch-to-bunch damper will be required. If we can identify the annoying mode, a mode damper of narrow band will do the job. To damp couple-bunch instabilities without knowing the annoying mode, a wideband bunch-by-bunch damper is necessary.

Similar to longitudinal coupled-bunch instabilities, transverse coupled-bunch instabilities can also be damped by modulation coupling from an uneven fill in the ring discussed in Sec. 9.3.4.

11.3 Exercises

- 11.1. For the example of resistive-wall driven coupled-bunch instability of the Tevatron at the fixed target mode, try to sum up the contribution for all frequencies for the $\mu = 1093$ mode and compare the result of taking only the lowest frequency line.
- 11.2. For the same example in Exercise 11.1, compare the growth rates of mode $\mu = 1092, 1091, \dots$, with mode 1093. How many modes do we need to include so that the growth rate drops to below $\frac{1}{4}$ of that of mode 1093?
- 11.3. For a narrow resonance that has a total width larger than $2[\nu_\beta]\omega_0$ where $[\nu_\beta]$ is the residual betatron tune and the bunch power spectrum is much wider than the revolution frequency, show that the growth rate is given by

$$\begin{aligned} \frac{1}{\tau_{m\mu}} \approx & \frac{eMI_b c}{4\pi\nu_\beta E_0} \frac{h_m(\omega_r - \chi/\tau_L)}{B \sum_{q'} h_m(\omega_{q'} - \chi/\tau_L)} \times \\ & \times \left\{ \Re Z_1^\perp[(q_1 M - \mu - \nu_\beta)\omega_0 - m\omega_s] - \Re Z_1^\perp[(q_2 M + \mu + \nu_\beta)\omega_0 + m\omega_s] \right\}, \end{aligned} \quad (11.7)$$

where q_1 and q_2 are some positive integer so that

$$\begin{aligned} (q_1 M - \mu - \nu_\beta)\omega_0 &\approx \omega_r, \\ (q_2 M + \mu + \nu_\beta)\omega_0 &\approx \omega_r. \end{aligned} \quad (11.8)$$

Such q_1 and q_2 are possible only when $\mu = 0$ or $\mu = M/2$ if M is even. Therefore whether the coupled-bunch mode is stable or unstable depends on whether the resonance is leaning more towards the upper betatron sideband or the lower betatron sideband.

Bibliography

- [1] F.J. Sacherer, *Theoretical Aspects of the Behaviour of Beams in Accelerators and Storage Rings*, Proc. First Course of Int. School of Part. Accel., Erice, Nov. 10-22, 1976, p.198.
- [2] K.Y. Ng, *Impedances and Collective Instabilities of the Tevatron at Run II*, Fermilab Report TM-2055, 1998.
- [3] W. Chou and J. Griffin, *Impedance Scaling and Impedance Control*, Proceedings of the 1997 Particle Accelerator Conference, Vancouver, Canada, May 12-16, 1997, p. 1724.es

Chapter 12

HEAD-TAIL INSTABILITIES

12.1 Transverse Head-Tail

Let us now consider the short-range field of the transverse impedance; i.e., $Z_1^\perp(\omega)$ when ω is large. This is equivalent to replacing the discrete line spectrum by a continuous spectrum. The summation in Eq. (10.33) or Eq. (11.1) can be transformed into an integration. The coherent angular frequency for the m th azimuthal mode is therefore

$$\Omega_m - m\omega_s = -\frac{i}{1+m} \frac{ecI_b}{4\pi E_0 \omega_\beta} \int_{-\infty}^{\infty} d\omega Z_1^\perp(\omega) h_m(\omega - \omega_\xi) , \quad (12.1)$$

where $\omega_\xi = \xi\omega_0/\eta$ is the betatron frequency shift due to chromaticity ξ , η is the slip factor, ω_0 is the revolution angular frequency, and E_0 is the particle energy. Note that the factor of M , the number of bunches, in the numerator and denominator cancel. This is to be expected because the perturbation mechanism is driven by the short-range wake field and the instability is therefore a single-bunch effect. This explains why we do not include the subscript μ describing phase relationship of consecutive bunches. The growth rate, which is the imaginary part of Eq. (12.1) is given by

$$\frac{1}{\tau_m} = -\frac{1}{1+m} \frac{ecI_b}{4\pi E_0 \omega_\beta} \int_0^{\infty} d\omega \operatorname{Re} Z_1^\perp(\omega) [h_m(\omega - \omega_\xi) - h_m(\omega + \omega_\xi)] , \quad (12.2)$$

where use has been made of the antisymmetry of $\operatorname{Re} Z_1^\perp(\omega)$. It is clear that there can be no instability when the chromaticity is zero. When there is finite chromaticity, however,

the growth does not have a threshold. On the other hand, the tune shift, given by

$$\Delta\Omega_m = \frac{1}{1+m} \frac{ecI_b}{4\pi E_0 \omega_\beta} \int_0^\infty d\omega \operatorname{Im} Z_1^\perp(\omega) [h_m(\omega - \omega_\xi) + h_m(\omega + \omega_\xi)] , \quad (12.3)$$

does not vanish when the chromaticity is zero.

Let us demonstrate this by using the resistive wall impedance. We substitute the expression of the resistive wall impedance of Eq. (1.44) into Eq. (12.1). The result of the integration over ω is [1]

$$\frac{1}{\tau_m} = -\frac{1}{1+m} \frac{eI_b c}{4\nu_\beta E_0} \left(\frac{2}{\omega_0 \tau_L} \right)^{1/2} |Z_1^\perp(\omega_0)| \operatorname{Re} F_m(\chi) , \quad (12.4)$$

where $|Z_1^\perp(\omega_0)|$ is the magnitude of the resistive wall impedance at the revolution frequency. The tune shift is given by

$$\Delta\Omega_m = \frac{1}{1+m} \frac{eI_b c}{4\nu_\beta E_0} \left(\frac{2}{\omega_0 \tau_L} \right)^{1/2} |Z_1^\perp(\omega_0)| \operatorname{Im} F_m(\chi) , \quad (12.5)$$

The form factor is given by

$$\begin{Bmatrix} \operatorname{Re} F_m(\chi) \\ \operatorname{Im} F_m(\chi) \end{Bmatrix} = \frac{1}{2\sqrt{\pi}} \int_0^\infty \frac{dy}{\sqrt{y}} [h_m(y - y_\xi) \mp (y + y_\xi)] , \quad (12.6)$$

where h_m are power spectra of the m th excitation mode in Eq. (10.41) written as functions of $y = \omega \tau_L / \pi$ and $y_\xi = \chi / \pi = \xi \omega_0 \tau_L / (\pi \eta)$. The first term in the integrand comes from contributions by positive frequencies while the second term by negative frequencies. The form factors for $m = 0$ to 5 are plotted in Fig. 12.1.

This single-bunch instability will occur in nearly all machines. The $m = 0$ mode is the rigid-bunch mode when the whole bunch oscillates transversely as a rigid unit. For the $m = 1$ mode, the head of the bunch moves transversely in one direction while the tail moves transversely in the opposite direction with the center-of-mass stationary, and is called the dipole head-tail mode. This is the head-tail instability first analyzed by Pellegrini and Sands [2, 3].

For small chromaticity phase $\chi \lesssim 2.3$, the integrand in Eq. (12.6) can be expanded and the growth rate becomes proportional to chromaticity. The form factor has been computed and listed in Table 12.1, where positive sign implies damping. We see from Table 12.1 that mode $m=0$ is stable for positive chromaticity (above transition or $\eta > 0$).

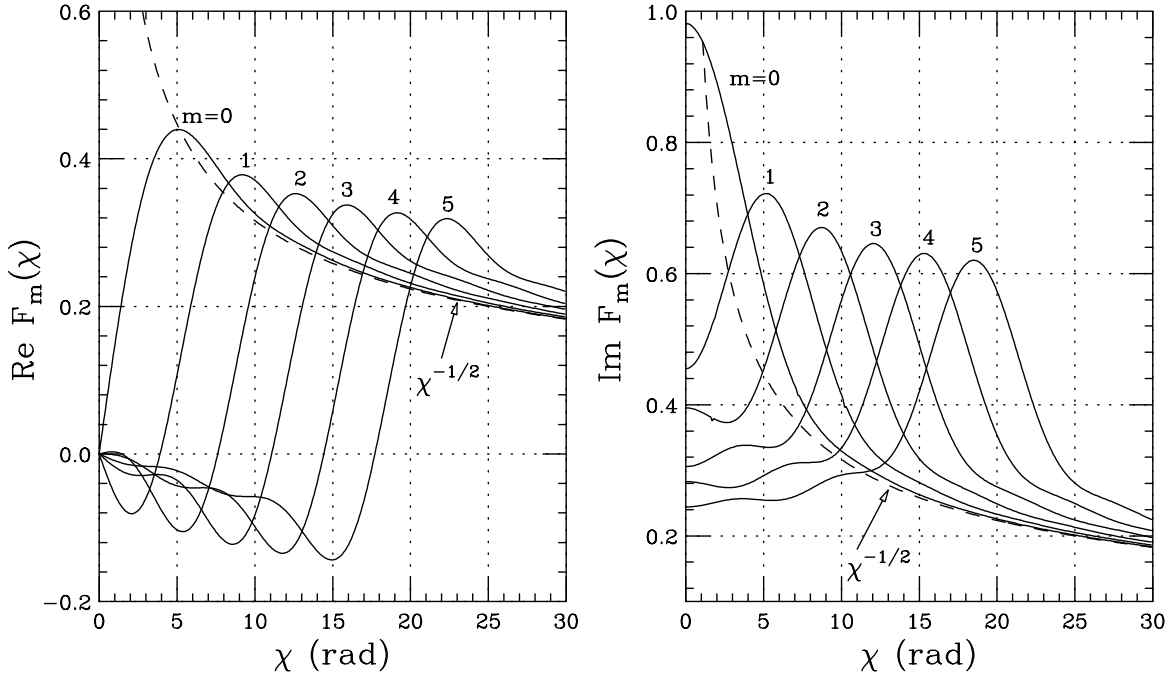


Figure 12.1: Real and imaginary parts of the form factor $F_m(\chi)$ for head-tail instability resulting from the resistive-wall impedance, for modes $m = 0$ to 5.

This is expected because the excitation spectrum for this mode has been pushed towards the positive-frequency side. All other modes ($m > 0$) should be unstable because their spectra see relatively more negative $\mathcal{R}e Z_1^\perp$. Looking into the form factors in Fig. 12.1, however, the growth rate for $m = 4$ is tiny and mode $m = 2$ is even stable. This can be clarified by looking closely into the excitation spectra in Fig. 7.5. We find that while mode $m = 0$ has a large maximum at zero frequency, all the other higher even m modes also have small maxima at zero frequency. As these even m spectra are pushed to the right, these small central maxima see more impedance from positive frequency than negative frequency. Since these small central maxima are near zero frequency where $|\mathcal{R}e Z_1^\perp|$ is large, their effect may cancel out the opposite effect from the larger maxima which interact with the impedance at much higher frequency where $|\mathcal{R}e Z_1^\perp|$ is smaller. This anomalous effect does not exist in the Legendre modes or the Hermite modes, because the corresponding power spectra vanish at zero frequency when $m > 0$.

A broadband resonance can also drive the head-tail instability. However, the power spectrum must be so frequency shifted by chromaticity that it overlaps with the resonance peak. For example, the $m = 0$ mode must be shifted by negative chromaticity

Table 12.1: Linearized form factor of transverse head-tail modes driven by the resistive wall impedance when $\chi \lesssim 2.3$.

Mode	Form Factor
m	F_m
0	$+0.1495 \chi$
1	-0.0600χ
2	$+0.0053 \chi$
3	-0.0191χ
4	-0.0003χ
5	-0.0098χ

(above transition) so that $\omega_\xi \approx -\omega_r$, where ω_r is the resonant frequency of the impedance. Mode m peaks roughly at

$$\frac{\omega\tau_L}{\pi} \approx m + 1 , \quad (12.7)$$

where τ_L is the full bunch length. Therefore to be excited by the resonance impedance, the betatron frequency shift due to chromaticity, ω_ξ , required is roughly given by

$$\omega_\xi = - \left[\omega_r - \frac{\pi(m+1)}{\tau_L} \right] . \quad (12.8)$$

Although the head-tail instabilities can be damped by the incoherent spread in betatron frequency, it is advisable to run the machine at a negative chromaticity above transition. In this case, all the higher modes with $m \neq 0$ will be stable, and the unstable $m = 0$ mode can be damped with a damper.

Head-tail modes of oscillations can be excited by shifting the chromaticity to the unstable direction and observed using a wideband pickup. These modes were first observed in the CERN PS Booster [4] and depicted in Fig. 12.2. They have also been measured in the Fermilab rings.

12.2 Longitudinal Head-Tail

The transverse head-tail instability comes about because of nonzero chromaticity or the betatron tune is a function of energy spread. Most important of all, the introduction of

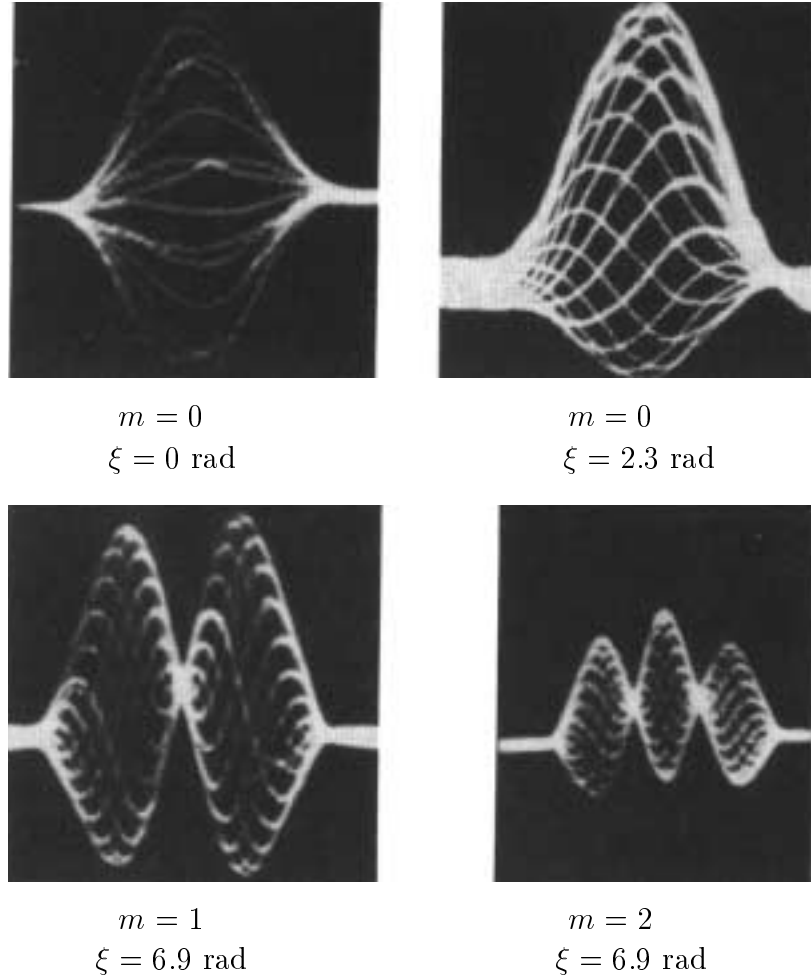


Figure 12.2: A single bunch in the CERN PS Booster monitored in about 20 consecutive revolutions with a wideband pickup (bandwidth ~ 150 MHz). Vertical axis: difference pickup signal. Horizontal axis: time (50 ns per division). The azimuthal mode number and chromaticity in each plot are as labeled.

a nonzero chromaticity breaks the symmetry of the transverse impedance times beam power spectrum between positive and negative frequencies. There is also such an analog in the longitudinal phase space when the synchrotron tune depends on the momentum offset. This comes about because the slip factor η is momentum-offset dependent. In a lattice we can write in general at a certain momentum-offset δ ,

$$\eta = \eta_0 + \eta_1\delta + \eta_2\delta^2 + \cdots . \quad (12.9)$$

Usually, because of the small momentum spread δ , the contribution of the higher-order terms is small. However, when the operation of the ring is near transition or $\eta_0 \approx 0$, most of the contribution of the slippage factor will come from the η_1 term. When η_0 and η_1 are of the same sign, the phase drift of a particle will be larger in one half of the synchrotron oscillation where the momentum spread is positive and smaller in the second half where the momentum spread is negative. The inverse will be true when η_0 and η_1 have opposite signs. Similar to the transverse situation, this loss of symmetry can excite an instability, which we call longitudinal head-tail instability. In fact, this instability has been observed at the CERN SPS [5] and later at the Fermilab Tevatron. Figure 12.3 shows the output of the rf-bunch phase detector at the CERN SPS, where the bunch length, which was 7 ns at the beginning, is seen increasing for every synchrotron oscillation. This is an instability in the dipole mode with $\sim 10^{11}$ protons in the bunch. The horizontal scale is 2 s per division or 20 s in total. Thus the growth rate is very slow. To higher order in momentum spread, the off-momentum orbit length can be written as*

$$C(\delta) = C_0 [1 + \alpha_0\delta(1 + \alpha_1\delta + \alpha_2\delta^2 + \cdots)] , \quad (12.10)$$

with $C_0 = C(0)$ being the length of the on-momentum orbit. It will be proved in Sec. 18.1 that with the expansion of η in Eq. (12.9), the expressions for the higher-order components of the slip factor are

$$\eta_0 = \alpha_0 - \frac{1}{\gamma^2} , \quad (12.11)$$

$$\eta_1 = \alpha_0\alpha_1 + \frac{3\beta^2}{2\gamma^2} - \frac{\eta_0}{\gamma^2} , \quad (12.12)$$

$$\eta_2 = \alpha_0\alpha_2 + \frac{\alpha_0\alpha_1}{\gamma^2} - \frac{2\beta^4}{\gamma^2} + \frac{3\alpha_0\beta^2}{2\gamma^2} + \frac{\eta_0}{\gamma^4} , \quad (12.13)$$

*In Europe, α_0 , α_1 , α_2 , etc. are usually referred to as α_1 , α_2 , α_3 , etc. There is also another common definition, where $C(\delta) = C_0 [1 + \alpha_0\delta + \alpha_1\delta^2 + \alpha_2\delta^3 + \cdots]$.

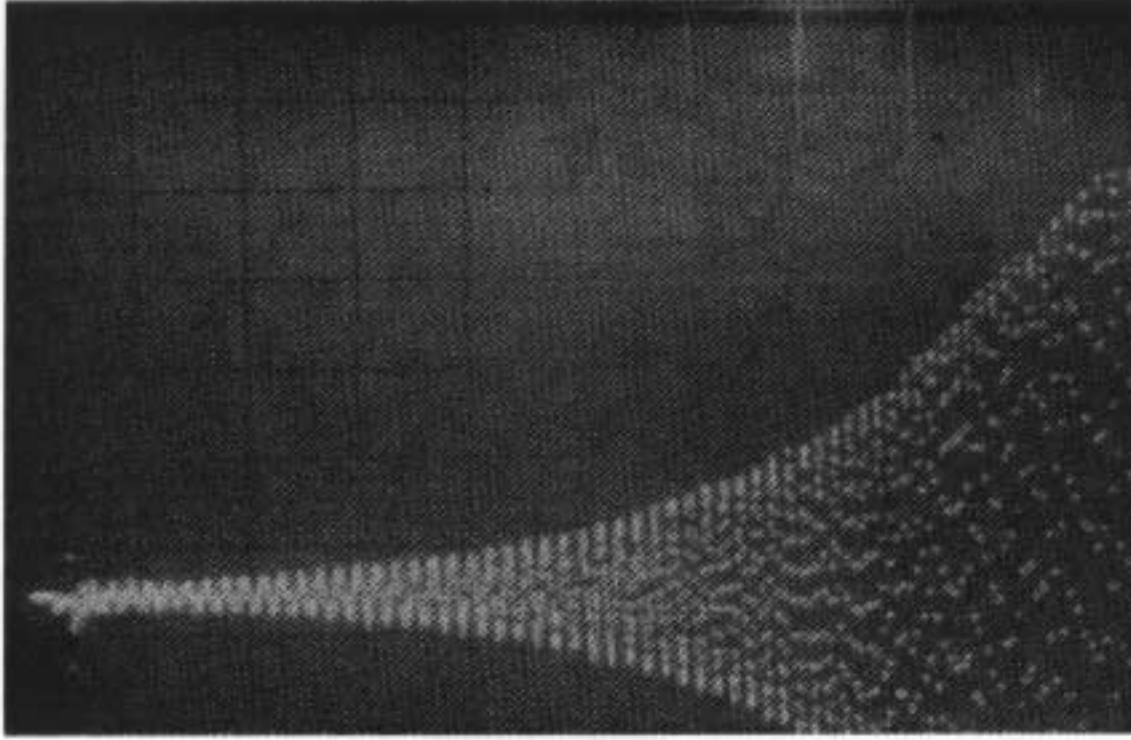


Figure 12.3: Longitudinal head-tail growth of the dipole synchrotron oscillation amplitude recorded from the output of the rf phase detector at the CERN SPS for a bunch with $\sim 10^{11}$ protons. Horizontal scale is 2 s/div or 20 s total.

where β and α are the relativistic factors of the synchronous particle. For a high-energy ring like the Fermilab Tevatron, we have almost $\eta_1 = \alpha_0 \alpha_1$. For a FODO lattice without special correction, α_1 is positive. Thus, the particle spends more time at positive momentum offset than at negative momentum offset. Then, the bunch becomes relatively longer at positive momentum offset than at negative momentum offset, as is illustrated in Fig. 12.4. The bunch will therefore lose more energy in the lower trajectory than in the upper trajectory. The amplitude of synchrotron oscillation will therefore grow. The energy loss by a beam particle per turn is

$$U(\sigma_\tau) = 2\pi e^2 N_b \int d\omega |\tilde{\rho}(\omega, \sigma_\tau)|^2 \operatorname{Re} Z_0^\parallel(\omega) , \quad (12.14)$$

where N_b is the number of particles in the bunch, and

$$\tilde{\rho}(\omega, \sigma_\tau) = \frac{1}{2\pi} \int d\tau \rho(\tau, \sigma_\tau) e^{i\omega\tau} \quad (12.15)$$

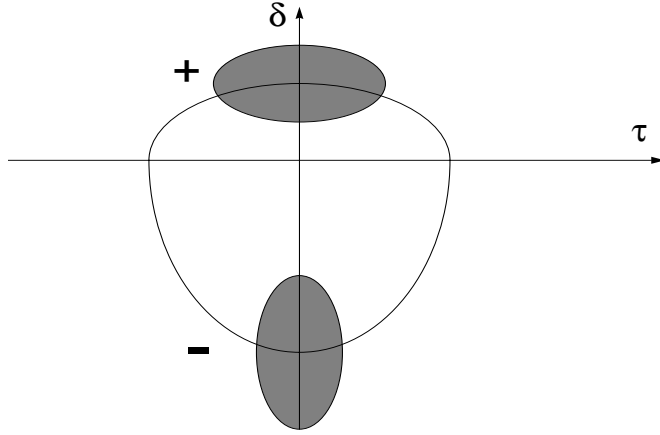


Figure 12.4: A particle trajectory is asymmetric about the on-momentum axis when the slippage factor is not an even function of momentum offset. The bunch will be longer at positive than negative momentum offset when the first-order momentum compaction $\alpha_0\alpha_1 > 0$ and above transition.

is the spectrum of the bunch of rms length σ_τ with a distribution $\rho(\tau, \sigma_\tau)$ normalized to unity. The rms bunch length σ_τ and the rms energy spread σ_E are related by

$$\omega_s \sigma_\tau = \frac{|\eta| \sigma_E}{\beta^2 E_0}, \quad (12.16)$$

where E_0 is the synchronous energy of the beam and ω_s is the small-amplitude synchrotron angular frequency. At the onset of the growth, bunch area is still approximately constant for a proton bunch. Thus, we have

$$\sigma_\tau \propto \sqrt{\frac{|\eta|}{\omega_s}} \propto |\eta|^{1/4} \approx |\eta_0|^{1/4} \left(1 + \frac{\eta_1 \delta}{4\eta_0}\right), \quad (12.17)$$

and

$$\sigma_\tau = \sigma_{\tau 0} \left(1 + \frac{\eta_1 \delta}{4\eta_0}\right), \quad (12.18)$$

where $\sigma_{\tau 0}$ is the rms bunch length in the absence of the η_1 term. The bunch particle gains energy for half a synchrotron period when $\delta > 0$ and loses energy for the other half synchrotron period when $\delta < 0$. Averaging over a synchrotron period, the increase in energy spread per turn is

$$\Delta E = \frac{dU}{d\sigma_\tau} \sigma_\tau \Big|_{\delta>0} - \frac{dU}{d\sigma_\tau} \sigma_\tau \Big|_{\delta<0} = \frac{dU}{d\sigma_\tau} \sigma_{\tau 0} \frac{\delta}{2} \chi, \quad (12.19)$$

where the asymmetry factor χ is just the fractional difference in bunch length for $\delta \gtrless 0$, and is given, from Eq. (12.18), by

$$\chi = \frac{\eta_1}{\eta_0} = \frac{\alpha_0 \alpha_1 + (\frac{3}{2}\beta^2 - \eta_0)\gamma^{-2}}{\eta_0} \approx \alpha_1 + \frac{3}{2\alpha_0 \gamma^2} \approx \alpha_1 , \quad (12.20)$$

for a proton beam at high energies so that $\eta_0 \approx \alpha_0$. In above, Eq. (12.12) has been used and γ and β are the relativistic factors of the synchronous particle. Near transition when $\alpha_0 \approx \gamma^{-2}$, however, the asymmetry factor becomes

$$\chi \approx \frac{\alpha_0 \left(\alpha_1 + \frac{3}{2} \right)}{\eta_0} . \quad (12.21)$$

Therefore, this phenomenon is best observed near transition when η_0 is small. The time development of the energy spread is given by $\Delta E \propto e^{t/\tau}$. The growth rate of the fractional energy spread is therefore [6]

$$\frac{1}{\tau} = -\frac{f_0}{2} \frac{dU}{d\sigma_\tau} \frac{\sigma_{\tau 0}}{\beta^2 E_0} \chi , \quad (12.22)$$

where f_0 is the revolution frequency and $dU/d\sigma_\tau$ is usually negative. In parallel to the transverse head-tail instability, this instability does not have a threshold although the growth rate is intensity dependent. This instability is essentially a growth of the amplitude of the synchrotron oscillation in the dipole mode. The frequency involved will be the synchrotron frequency. The growth rate is usually very slow. For example, the photo recorded at the CERN SPS, Fig. 12.3 has a horizontal time span of 20 s.

If the driving impedance $\Re Z_0^\parallel$ comes from a narrow resonance with shunt impedance R_s at resonant frequency $\omega_r/(2\pi)$ and quality factor Q , we have for the energy loss per turn

$$U(\sigma_\tau) = \frac{\pi R_s \omega_r e^2 N_b}{Q} |\tilde{\rho}(\omega_r)|^2 , \quad (12.23)$$

for a bunch containing N_b particles. For a broadband impedance, $U(\sigma_\tau)$ drops much faster with bunch length. For a general resonance, we have computed the asymmetric energy loss for a parabolic bunch distribution [7],

$$\begin{aligned} \frac{dU(\sigma_\tau)}{d\sigma_\tau} \sigma_\tau &= \frac{9e^2 N_b \omega_r R_s}{4sQ} \left\{ \frac{2}{z^3} [e^{-2cz} \sin(2sz+2\theta) - \sin 2\theta] \right. \\ &\quad \left. + \frac{4}{z^4} [2e^{-2cz} \sin(2sz+3\theta) + \sin 3\theta] + \frac{12}{z^5} e^{-2cz} \sin(2sz+4\theta) \right\} \end{aligned}$$

$$+ \frac{6}{z^6} [e^{-2cz} \sin(2sz + 5\theta) - \sin 5\theta] \Big\} , \quad (12.24)$$

where $z = \sqrt{5}\omega_r\sigma_\tau$, $c = \cos\theta = 1/(2Q)$, and $s = \sin\theta$. This is plotted in Fig. 12.5 for the case of a sharp resonance and in Fig. 12.6 for the case of a broadband with $Q = 1$.

As is shown in Fig. 12.5, the asymmetric energy loss vanishes when the bunch length goes to zero, because the change in bunch length from positive momentum offset to negative momentum offset also goes to zero. On the other hand, when the bunch length is very long, the asymmetric energy loss will also be small, because the energy loss for a long bunch is small.

Let us apply the theory to the Fermilab Tevatron in the collider mode [7]. The asymmetric factor in Eq. (12.20) has been measured to be $\chi \sim +1.17$. The fundamental resonance of the 8 rf cavities serves as a good driving force for this instability. Each cavity has resonant frequency $f_r = 53.1$ MHz, $R_s = 1.2$ MΩ, and $Q = 7000$. For Run I, where the rms bunch length was $\sigma_\tau \approx 2.684$ ns or $f_r\sigma_\tau \approx 0.1425$, $(dU/d\sigma_\tau)\sigma_\tau \sim -0.3890 e^2 N_b \omega_r R_s / Q$ is large and leads to a growth rate of $\tau^{-1} = 1.433 \times 10^{-3}$ s⁻¹ at the injection energy of $E_0 = 150$ GeV for a bunch containing $N_b = 2.70 \times 10^{11}$ particles. However, for Run II, the bunch will be much shorter. With $\sigma_\tau = 1.234$ ns or $f_r\sigma_\tau \approx 0.0655$, the asymmetric energy loss $(dU/d\sigma_\tau)\sigma_\tau \sim -0.1464 e^2 N_b \omega_r R_s / Q$ is much smaller and the head-tail growth rate becomes $\tau^{-1} = 0.539 \times 10^{-3}$ s⁻¹. As is shown in Fig. 12.5, we are on the left side of the $(dU/d\sigma_\tau)\sigma_\tau$ peak; therefore a shorter bunch length leads to slower growth.

The broadband impedance can also have similar contributions since the resonance frequency is usually a few GHz and $\Re Z_0^\parallel$ is large although Z_0^\parallel/n is just a couple of ohms. Now $\omega_r\sigma_\tau$ falls on the right side of the $(dU/d\sigma_\tau)\sigma_\tau$ peak instead. We expect shorter bunch lengths to have faster growth rates, as is indicated in Fig. 12.6. Table 12.2 shows the longitudinal head-tail growth rates for different resonant frequencies and quality factors; $Z_0^\parallel/n = 2 \Omega$ has been assumed. The growth rates driven by the fundamental rf resonance are also listed in the last row for comparison. It is obvious that the longitudinal head-tail instability for Run I is dominated by the rf narrow resonance and that for Run II by the broadband impedance instead. We observed a growth time of ~ 250 s in Run I. From Table VI, it is very plausible that the growth of this head-tail instability will be at least as fast as that in Run I.

Let us go back to the observation at the CERN SPS. The bunch has a synchronous momentum of 26 GeV/c. The transition gamma is $\gamma_t = 23.4$, giving $\eta = 5.26 \times 10^{-4}$. For

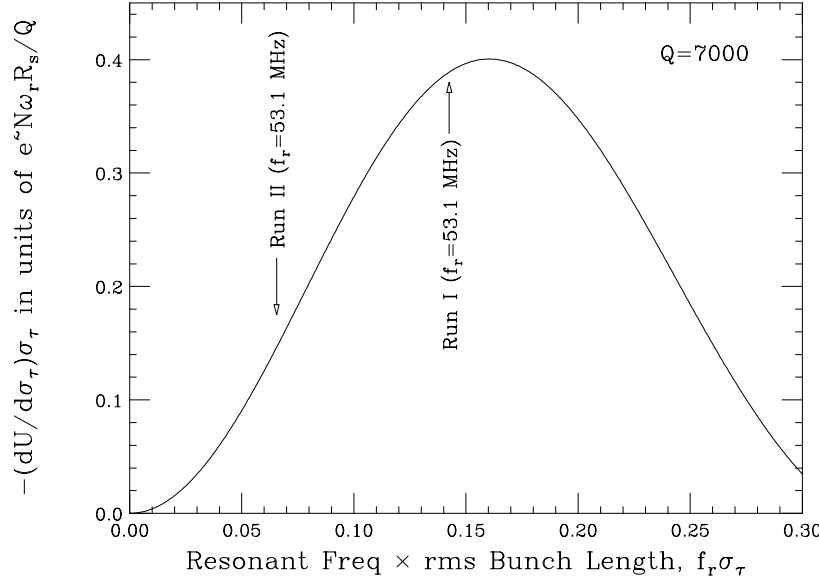


Figure 12.5: Plot of differential bunch energy loss $(dU/d\sigma_\tau)\sigma_\tau$ versus $f_r\sigma_\tau$ due to a sharp resonance. Note that the effect on the Run II bunch is much less than that on the Run I bunch because of the shorter Run II bunch length.

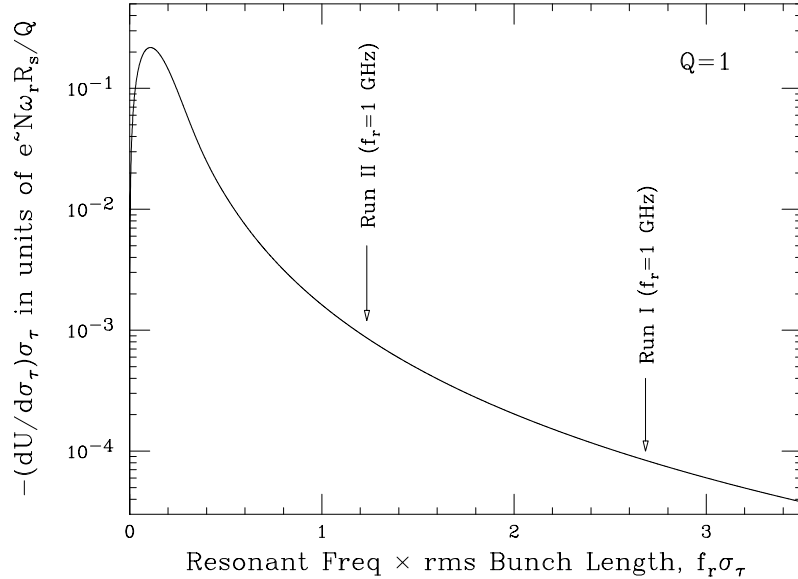


Figure 12.6: Plot of differential bunch energy loss $(dU/d\sigma_\tau)\sigma_\tau$ versus $f_r\sigma_\tau$ due to a broadband resonance with $Q = 1$. Note that the effect on the Run II bunch is much more than that on the Run I bunch because of the shorter Run II bunch length.

Table 12.2: Growth rates for a broadband resonance of $Z_0^{\parallel}/n = 2 \Omega$ at various frequencies and quality factors.

f_r (GHz)	Q	Growth Rate (s^{-1})	
		Run I	Run II
1	1	0.178×10^{-3}	1.829×10^{-3}
1	3	0.022×10^{-3}	0.267×10^{-3}
2	1	0.089×10^{-3}	0.915×10^{-3}
2	2	0.023×10^{-3}	0.249×10^{-3}
1	5	0.009×10^{-3}	0.114×10^{-3}
2	3	0.011×10^{-3}	0.117×10^{-3}
2	4	0.006×10^{-3}	0.070×10^{-3}
Fundamental Rf Resonance		1.433×10^{-3}	0.539×10^{-3}

the horizontal chromaticity setting used during the observation of the longitudinal head-tail growth in Fig. 12.3, a lattice-code simulation program gives the next higher-order component of the momentum compaction to be $\alpha_1 = -0.7$. The asymmetry parameter turns out to be $\chi = 1.28$. We therefore expect an instability if $dU/d\sigma_{\tau} < 0$ which is normally the case. In other words, to observe such an instability, one should perform the experiment above transition, but not too much above transition so as to enhance the asymmetry parameter χ .

The longitudinal head-tail instability can also be driven by the resistive wall impedance. The differential energy loss in Eq (12.20) integrates to

$$\frac{dU}{d\sigma_{\tau}} \sigma_{\tau} = -\frac{3\Gamma(\frac{3}{4})}{8\pi^2} \frac{e^2 N_b [\Re Z_{\parallel}]_1}{\omega_0^{1/2} \sigma_{\tau}^{3/2}}, \quad (12.25)$$

where

$$[\Re Z_{\parallel}]_1 = \frac{R\rho}{b\delta_1} \quad (12.26)$$

is the resistive part of the wall impedance at revolution frequency. The skin depth at revolution frequency is

$$\delta_1 = \sqrt{\frac{2\rho}{\mu_0 \mu_r \omega_0}}, \quad (12.27)$$

where μ_r is the relative magnetic permeability and ρ is the electric resistivity of the beam pipe. $\Gamma(\frac{3}{4}) = 1.2254167$ is the Gamma function at $\frac{3}{4}$. Because of the $\sigma_{\tau}^{3/2}$ in the denominator, the contribution can be important for very short bunches.

The longitudinal head-tail instability can be important in quasi-isochronous storage rings, because the the asymmetric factor as defined in Eq. (12.21) can become very large when the ring operation is close to transition. Such rings have been designed for the muon colliders. An isochronous ring is preferred because the muon bunches will be short, roughly 3 mm, which requires an rf voltage in the 50 MV range [8]. Such an rf system will be very expensive. In most of these designs, the muons only have a lifetime of about 1000 turns. If the ring is quasi-isochronous, even without rf, the debunching will be rather insignificant. In order not to degrade the luminosity of the collider, however, one must make sure that the growth time of the longitudinal head-tail instability will be much longer than 1000 turns.

12.3 Exercises

- 12.1. The degrees of freedom of a system are coupled internally. Some degrees of freedom continue to gain energy and grow while some lose energy and are damped. When the system is not getting energy from outside, the sum of the damping or antidamping rates of all degrees of freedom must add up to zero. If the head-tail stability or instability for all azimuthal modes do not draw energy from outside, energy must be conserved, or

$$\sum_{m=0}^{\infty} \frac{1}{\tau_m} = 0 , \quad (12.28)$$

where τ_m^{-1} is given by Eq. (12.1), independent of chromaticity and the detail of the transverse impedance. Show that Eq. (12.28) is only satisfied if the factor $(1+m)^{-1}$ in Eq. (12.1) is removed. We may conclude that either the factor $(1+m)^{-1}$ should not be present in Sacherer's formula or this is not an internal system.

Hint: Show that $\sum_m |h_m(\omega)|^2$ is a constant independent of ω by performing the summation numerically. This follows from the fact that the modes of excitation $\lambda_m(\tau)$ form a complete set. Then the integration over $\mathcal{R}e Z_1^\perp(\omega_0)$ gives zero.

- 12.2. In an isochronous ring or an ultra-relativistic linac[†], the particle at the head of the bunch will not exchange position with the particle at the tail. Thus the particle at the tail suffers from the wake of the head all the time. We can consider a macro-particle model with only two macro-particles, each carrying charge $eN/2$ and separated by a distance \hat{z} longitudinally. The head particle executes a free betatron oscillation

$$y_1(s) = \hat{y} \cos k_\beta s , \quad (12.29)$$

while the tail sees a deflecting wake force $\langle F_1^\perp \rangle = e^2 N W_1(\hat{z}) y_1(s)/(2\ell)$ and its transverse motion is determined by

$$y_2'' + k_\beta^2 y_2 = -\frac{e^2 N W_1(\hat{z})}{2E_0 \ell} , \quad (12.30)$$

where $k_\beta = \omega_\beta/v$ is the betatron wave number, ℓ is the length of the vacuum chamber that supplies the wake. If one prefers, one can define W_1 as the wake

[†]For all the proton linacs in existence, the highest energy is less than 1 GeV, or proton velocity less than 0.875 of the velocity of light. Thus, normal synchrotron motion takes place, implying that head and tail of a bunch do exchange position. Therefore, Exercise 12.2 applies mostly to electron linacs.

force integrated over one rf-cavity period; then ℓ will be the length of the cavity period. Show that the solution of Eq. (12.30) is

$$y_2(s) = \hat{y} \left[\cos k_\beta s - \frac{e^2 N W_1(\hat{z})}{4k_\beta E_0 \ell} s \sin k_\beta s \right]. \quad (12.31)$$

The second term is the resonant response to the wake force and grows linearly. Show that the total growth in transverse amplitude along a length ℓ_0 of the linac relative to the head particle is

$$\Upsilon = -\frac{e^2 N W_1(\hat{z}) \ell_0}{4k_\beta E_0 \ell}. \quad (12.32)$$

The above mechanism is called beam breakup.

- 12.3. Derive the asymmetric energy loss, $[dU(\sigma_\tau)/d\sigma_\tau]\sigma_\tau$ as given by Eq. (12.24) of a particle in a bunch with linear parabolic distribution driven by a resonance.

Bibliography

- [1] F.J. Sacherer, *Theoretical Aspects of the Behaviour of Beams in Accelerators and Storage Rings*, Proc. First Course of Int. School of Part. Accel., Erice, Nov. 10-22, 1976, p.198.
- [2] C. Pellegrini, Nuovo Cimento **64**, 447 (1969).
- [3] M. Sands, SLAC-TM-69-8 (1969).
- [4] K. Hübner, P. Strolin, V. Vaccaro, and B. Zotter, *Concerning the Stability of the ISR Beam Against Coherent Dipole Oscillations*, CERN/ISR-RF-TH/70-2 (1970).
- [5] D. Boussard and T. Linnecar, Proc. 2nd EPAC, Nice, 1990, ed. Marin and Mandrillon, p.1560.
- [6] B. Chen, *The Longitudinal Collective Instabilities of Nonlinear Hamiltonian Systems in a Circular Accelerator*, Thesis, U. of Texas at Austin, May, 1995.
- [7] K.Y. Ng, *Impedances and Collective Instabilities of the Tevatron at Run II*, Fermilab report TM-2055, 1998.
- [8] King-Yuen Ng *Quasi-Isochronous Buckets in Storage Rings*, Nucl. Inst. Meth. **A404**, 199 (1988).

Chapter 13

MODE COUPLING

As the beam intensity increases, the shift of each longitudinal azimuthal mode becomes so big that two adjacent modes overlap each other. When this happens, the longitudinal azimuthal mode number m is no longer a good eigennumber, and we can no longer represent the perturbation distribution ψ_1 as a single azimuthal mode. Instead, ψ_1 should be represented by a linear combination of all azimuthal modes. This phenomenon has been referred to as “mode mixing,” “mode coupling,” “strong head-tail,” and “transverse or longitudinal turbulence.”

13.1 Transverse

Let us first consider transverse instability driven by a broadband impedance. This implies a single-bunch mechanism. We also set the chromaticity to zero. For the m th azimuthal mode and k th radial mode, Eq. (10.33) or (11.1) becomes

$$(\Omega - \omega_\beta - m\omega_s)\delta_{mm'}\delta_{kk'} = M_{mm'kk'} \quad (13.1)$$

where, with the aid of Eq. (10.33), the matrix M is defined as

$$M_{mm'kk'} = -\frac{ieI_b c}{2\omega_\beta E_0 \tau_L} \frac{\int d\omega Z_1^\perp(\omega) \tilde{\lambda}_{m'k'}(\omega) \tilde{\lambda}_{mk}^*(\omega)}{\int d\omega \tilde{\lambda}_{mk}(\omega) \tilde{\lambda}_{mk}^*(\omega)}. \quad (13.2)$$

The summations have been converted to integrations because the impedance is so broadband that there is no need to distinguish the individual betatron lines. A further sim-

plification is to keep only the first most easily excited radial modes. Then, the problem becomes coupling in the azimuthal modes.

Since $\Re Z_1^\perp(\omega)$ is odd in ω and $\Im Z_1^\perp(\omega)$ is even in ω , only $\Im Z_1^\perp(\omega)$ will contribute to the diagonal terms of the matrix M giving only real frequency shifts which will not lead to instability. As the beam current becomes larger, two modes will collide and merge together, resulting in two complex eigenfrequencies, one is the complex conjugate of the other, thus introducing instability. Therefore, coupling should originate from the off-diagonal elements closest to the diagonal. We learn from Eq. (10.41) that the m th mode of excitation $\tilde{\lambda}_m(\omega)$ is even in ω when m is even, and odd in ω when m is odd. Thus, it is $\Re Z_1^\perp(\omega)$ that gives the coupling.

The eigenfrequencies are solved by

$$\det[(\Omega - \omega_\beta - m\omega_s)I - M] = 0 . \quad (13.3)$$

We recall Eq. (10.21), Sacherer integral equation for transverse instability in Chapter 10,

$$(\Omega - \omega_\beta - m\omega_s)\alpha_m R_m(r) = -\frac{i\pi e^2 MNc}{E_0 \omega_\beta T_0^2} g_0(r) \sum_{m'} i^{m-m'} \alpha_{m'} \int r' dr' R_{m'}(r') \sum_q Z_1^\perp(\omega_q) J_{m'}(\omega_q r') J_m(\omega_q r) , \quad (13.4)$$

where $g_0(r)$ is the unperturbed normalized distribution in the longitudinal phase space in circular coordinate. Clearly the equation is solvable if $g_0(r)$ is a δ -function. This is the air-bag model with beam particles residing only at the outer edge or $g_0(r) \propto \delta(r - \hat{r})$ with \hat{r} representing the half length of the bunch.

Let us choose a simple transverse wake which is a constant W_1 . The corresponding transverse impedance is

$$Z_1^\perp(\omega) = \frac{W_1}{\omega + i\epsilon} = \wp\left(\frac{W_1}{\omega}\right) - i\pi W_1 \delta(\omega) . \quad (13.5)$$

The infinite matrix is truncated and the eigenvalues solved numerically. The solution is shown in Fig. 13.1 [2]. This impedance corresponds to a real part that falls off as frequency increases. The imaginary part is a δ -function at zero frequency, and therefore interacts with the $m = 0$ mode only, since all $m \neq 0$ modes have spectral distribution $\tilde{\lambda}_m(0) = 0$. This explains why all other modes remain almost unshifted with the exception of $m = 0$. The downward frequency shift of the $m = 0$ mode as the beam intensity increases from zero is a general behavior for short bunches. The transverse wake force

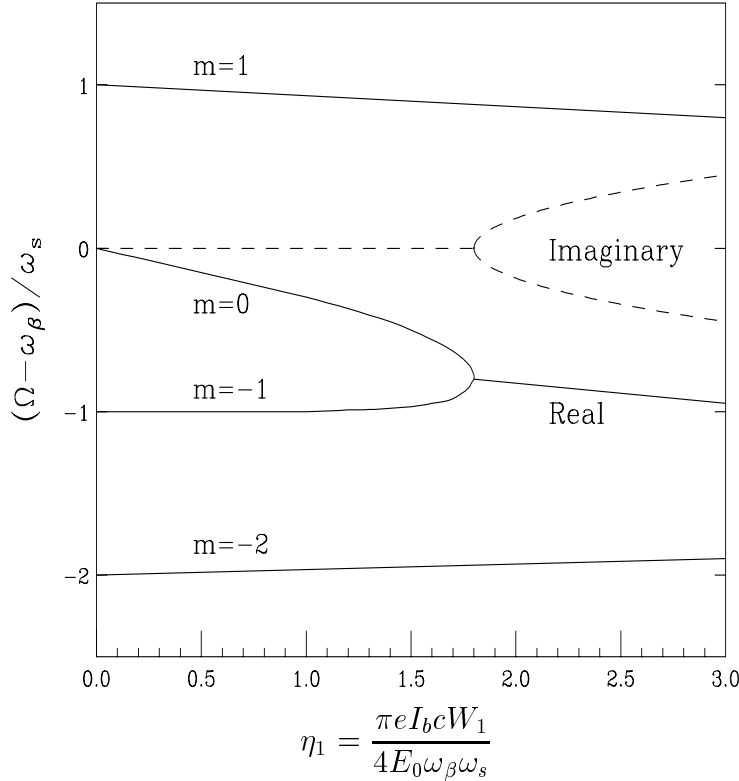


Figure 13.1: Transverse mode frequencies $(\Omega - \omega_\beta)/\omega_s$ versus the current intensity parameter η_1 for an air-bag bunch distribution perturbed by a constant wake potential W_1 . The instability occurs at $\eta_1 \approx 1.8$, when the $m = 0$ and $m = -1$ modes collide. The dashed curves are the imaginary part of the mode frequencies or growth/damping rate for the two colliding modes.

produced by an off-axis beam has the polarity that deflects the beam further away from the pipe axis. This force acts as a defocusing force for the rigid beam mode, and therefore the frequency shifts downward. Such a downshift of the betatron frequency is routinely observed in electron accelerators and serves as an important tool of probing the impedance. Notice that unlike the situation of the longitudinal mode coupling described in Chapter 7 and later in this chapter, there is no symmetry of the azimuthal modes about the $m = 0$ mode. This is because these are now sidebands of the betatron lines, and the betatron lines do not have any symmetry about the zero frequency. The implication is that we need to include both positive and negative azimuthals in the discussion.

Eventually the $m = 0$ shifts downwards and meets with the $m = -1$ mode, thus

exciting an instability. The threshold is at

$$\eta_1 = \frac{\pi e I_b c W_1}{4 E_0 \omega_\beta \omega_s} \approx 1.8 , \quad (13.6)$$

and is bunch-length independent. We can also obtain an approximate threshold from Eqs. (13.1) and (13.2) by equating the frequency shift to ω_s , and get

$$\frac{e I_b c |Z_1^\perp|_{\text{eff}}}{2 E_0 \omega_\beta \omega_s \tau_L} \approx 1 , \quad (13.7)$$

where

$$|Z_1^\perp|_{\text{eff}} = \frac{\int d\omega Z_1^\perp(\omega) h_m(\omega)}{\int d\omega h_m(\omega)} \quad (13.8)$$

is called the *effective transverse impedance* for mode m . Comparing Eqs. (13.6) and (13.7), we find the two thresholds are almost the same except for the bunch-length dependency, which we think should be understood as follows. The imaginary part of the impedance in Eq. (13.5) is a δ -function at zero frequency which interacts only with the $m = 0$ mode. As the bunch length becomes shorter, the spectrum spreads out wider, so that the spectrum at zero frequency becomes smaller, and $|Z_1^\perp|_{\text{eff}}$ is also smaller accordingly. In fact, from Eq. (10.43), the normalization of the power spectrum in the denominator of Eq. (13.8) is just τ_L^{-1} and from Eq. (10.42), $h(0)$ is τ_L independent. It is clear that $|Z_1^\perp|_{\text{eff}} \propto \tau_L$, thus explaining why η_1 in Eq. (13.6) is bunch-length independent.

Now consider the situation when the impedance is a broadband resonance. For a very short bunch, the $m = 0$ mode extends to very high frequencies and will cover part of the high-frequency capacitive part of the resonance. Thus, the effective impedance $|Z_1^\perp|_{\text{eff}}$ can become small due to the cancellation of the inductive and capacitive parts. At the same time, the peak of $\Re Z_1^\perp$ is far from the peak of the $m = -1$ mode, thus making the coupling between the $m = 0$ and $m = -1$ mode very weak. Since the frequency shift is small and the coupling is weak, it will take a much higher beam current for the $m = 0$ mode to meet with the $m = -1$ mode, thus pushing up the threshold current. For a long bunch, the $m = 0$ mode has a small frequency spread. If it stays inside the inductive region where $\Im Z_1^\perp$ is almost constant, $\Im Z_1^\perp$ can be taken out of the integral and $|Z_1^\perp|_{\text{eff}}$ will be almost constant. Therefore, the threshold current, given by Eq. (13.7), increases linearly with the bunch length. When the bunch is very long, the $m = \pm 1$ and even $m = \pm 2$ and $m = \pm 3$ modes may stay inside the constant inductive region of the

impedance. This implies that the higher azimuthal modes also interact strongly with the impedance and these modes will have large shifts so that the threshold can become much smaller. Several collisions may occur around a small beam-current interval and the bunch can become very unstable suddenly.

The transverse mode-coupling instability was first observed at the DESY PETRA and later also at the SLAC PEP and the CERN LEP. The strong head-tail instability is one of the cleanest instabilities to observe in electron storage rings [1]. In particular, one may measure the threshold beam intensity when the beam becomes unstable transversely. Another approach is to measure the betatron frequency as the beam intensity is varied. From the shift of the betatron frequency per unit intensity increase, the transverse wake can be inferred. The transverse motion of the bunch across its length can also be observed easily using a streak camera.

In the longitudinal mode-mixing instability, the bunch lengthens as the beam becomes unstable essentially without losing beam particles. This does not happen in the transverse case. The instability is devastating; as soon as the threshold is reached, the bunch disappears. However, so far no strong head-tail instabilities have ever been observed in hadron machines.

Radiation damping is too slow to damp the strong head-tail instability. A damper significantly faster than the angular synchrotron frequency ω_s is required. As shown in Fig. 13.1, it is mode $m = 0$ that is shifted downward to collide with mode $m = -1$ so as to start the instability. But mode $m = 0$ is the pure rigid dipole betatron oscillation without longitudinal excitation. Therefore, if we can introduce a positive coherent betatron tune shift, it will slow this mode from coming down and therefore push the threshold to a higher value. A conventional feedback system is resistive; i.e., the kicker is located at an odd multiple of 90° from the pickup. Here, a reactive feedback system is preferred [2]. The kicker is located at an even multiple of 90° from the pickup. In a two-particle model, where the bunch is represented by two macro-particles, the equations of motion are, in the first half of the synchrotron period,

$$\begin{aligned} \frac{d^2y_1}{dn^2} + (2\pi\nu_\beta)^2 y_1 &= \sigma(y_1 + y_2) , \\ \frac{d^2y_2}{dn^2} + (2\pi\nu_\beta)^2 y_2 &= \sigma(y_1 + y_2) + \alpha y_1 , \end{aligned} \quad (13.9)$$

where y_1 and y_2 are, respectively, the transverse displacements of the head and tail macro-particles, σ is the gain of the reactive feed back, and α represents the effect of the

transverse wake from head to tail. Notice that the reactive feedback acts on the center of the bunch and is in phase with the particle displacements. It therefore modifies ν_β by introducing a tune shift. The instability threshold can then be raised by properly choosing the feedback strength σ . In low-energy hadron machines, the space charge tune shift constitutes a natural reactive feedback system which tends to shift the $m = 0$ mode upwards. We shall study this in more detail in the next section.

This instability can also be damped by Balakin-Novokhatsky-Smirnov (BNS) damping [3], which delivers a betatron tune spread from the head of the bunch to the tail. This can be achieved by tilting the longitudinal phase space distribution of the bunch so that the tail has a lower energy relative to the head through chromaticity. Another method to implement BNS damping is to introduce a radio-frequency quadrupole magnet system, so that particles along the bunch will see a gradual shift in betatron tune.

13.2 Space Charge and Mode Coupling

It was reported in a recent paper of Blaskiewicz [4] that the space charge tune shift can strongly damp the transverse mode-coupling instability (TMCI), which is also known as strong head-tail instability. The investigation was made on the basis of particle tracking and the analytically solvable *square-well air-bag model* [5]. This is different from the air-bag model we used in the last section, although all the beam particles reside at the edge of the bunch. The formation of this model is sketched in Fig. 13.2. From a ring of particles in the longitudinal phase space on the left, the top semi-circle is stretched out and so is the lower semi-circle as illustrated in the right plot. The stretching continues until the top and lower semi-circles become two horizontal lines at energy offset $\pm\widehat{\Delta E}$. The lower one is described by the synchrotron phase ϕ from $-\pi$ to 0, while the upper one by ϕ from 0 to π for one synchrotron oscillation. Such a synchrotron oscillation requires, of course, a special rf potential. The bunch will be very long. The head is represented by $\phi = 0$ while the tail is represented by $\phi = \pm\pi$. We use the synchrotron phase ϕ and the energy offset ΔE as a set of variables for the description of the particle position in the longitudinal phase space. Although z remains the coordinate orthogonal to ΔE , the linear position of the particle can also be referenced by ϕ . The bunch particle distribution is given by

$$\psi(\phi, \Delta E) = \frac{1}{2}\rho(\phi)\left[\delta(\Delta E - \widehat{\Delta E}) + \delta(\Delta E + \widehat{\Delta E})\right], \quad (13.10)$$

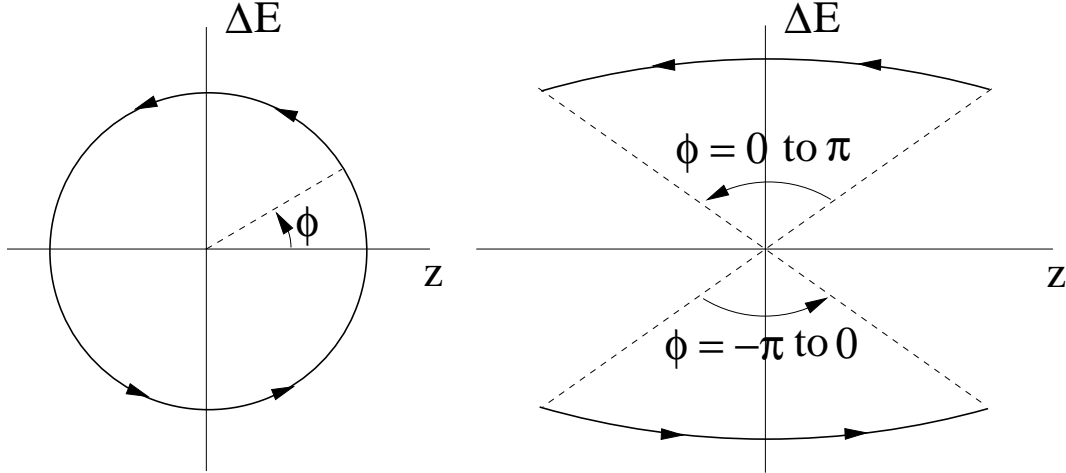


Figure 13.2: The ordinary air-bag model in the longitudinal phase space (left) is transformed into the square-well air-bag model (right) by stretching out the upper and lower semi circles until they become two infinite parallel lines at the energy spread $\pm\widehat{\Delta E}$. The longitudinal position of the particle remains specified by ϕ from $-\pi$ to 0 and from 0 to π .

where $\rho(\phi) = 1/(2\pi)$ is the projection onto the synchrotron phase.

What is going to be presented here is a qualitative explanation why the space charge helps TMCI. Without space charge, the bunch starts to be unstable when two neighboring synchro-betatron modes merge under the influence of the wake forces. Typically, the pure betatron mode (the azimuthal or synchrotron harmonic $m = 0$ mode, also known as the rigid-bunch mode) is affected by the wake force and shifts downward, while the other azimuthal modes are not much affected, at least at low intensity. The transverse wake force produced by an off-axis beam has the polarity that deflects the beam further away from the pipe axis. This force acts as a defocusing force for the rigid beam mode, and therefore the frequency shifts downward. As a result, the instability threshold is determined by the coupling of the 0 and -1 modes, as illustrated in the left plot of Fig. 13.3, (see below for definition of parameters).

The space charge by itself also shifts all the frequencies downward, as illustrated in the right plot of Fig. 13.3. The only exception is the azimuthal $m = 0$ mode, which describes the motion of the bunch as a whole, and, therefore, is not influenced by the space charge at all. Thus, in the presence of space charge, the $m = 0$ mode will couple with the $m = -1$ mode at a higher current intensity and therefore the threshold is raised

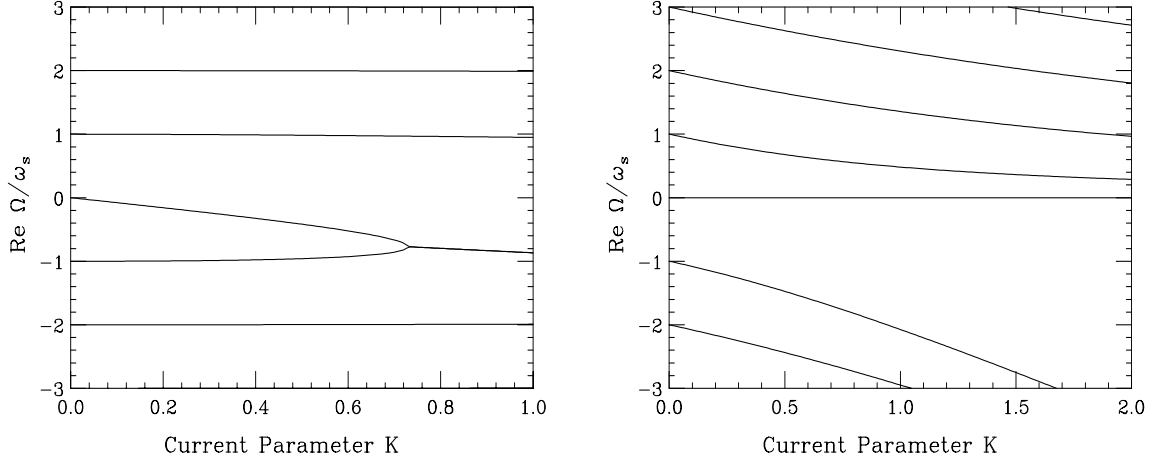


Figure 13.3: Left: The transverse wake force shifts mostly the azimuthal $m = 0$ mode downward but not the other modes. Instability occurs when the $m = 0$ and -1 modes meet with each other. Right: The space charge force in the absence of the wake forces shifts all modes downward with the exception of the $m = 0$ mode.

in the presence of space charge. This is illustrated in the left plot of Fig. 13.4.

Let us go in more details with mathematics. The transverse displacement $x(\phi)$ of a particle at the synchrotron phase ϕ satisfies the equation of motion:

$$\frac{d^2x(\phi)}{dt^2} + \omega_\beta^2 x(\phi) = F(\phi) + S\rho(\phi)[x(\phi) - \bar{x}(\phi)] , \quad (13.11)$$

where $\omega_\beta/(2\pi)$ is the unperturbed betatron frequency and the smooth approximation for the betatron oscillations has been applied. To incorporate synchrotron oscillation, the total time derivative takes the form

$$\frac{d}{dt} = \frac{\partial}{\partial t} + \omega_s \frac{\partial}{\partial \phi} , \quad (13.12)$$

with $\omega_s/(2\pi)$ being the synchrotron frequency. The right-hand side of Eq. (13.11) contains the transverse driving forces. The first term is the transverse wake force

$$F(\phi) = -\frac{N_b e^2 c^2}{E_0 C} \int_0^{|\phi|} W_1[z(\phi') - z(\phi)]\rho(\phi')\bar{x}(\phi')d\phi' , \quad (13.13)$$

where N_b is the number of particles in the bunch, W_1 the transverse wake function, $z(\phi)$ the longitudinal position of the beam particle. The second term is the space charge contribution. It is proportional to the linear density $\rho(\phi)$ and the displacement relative

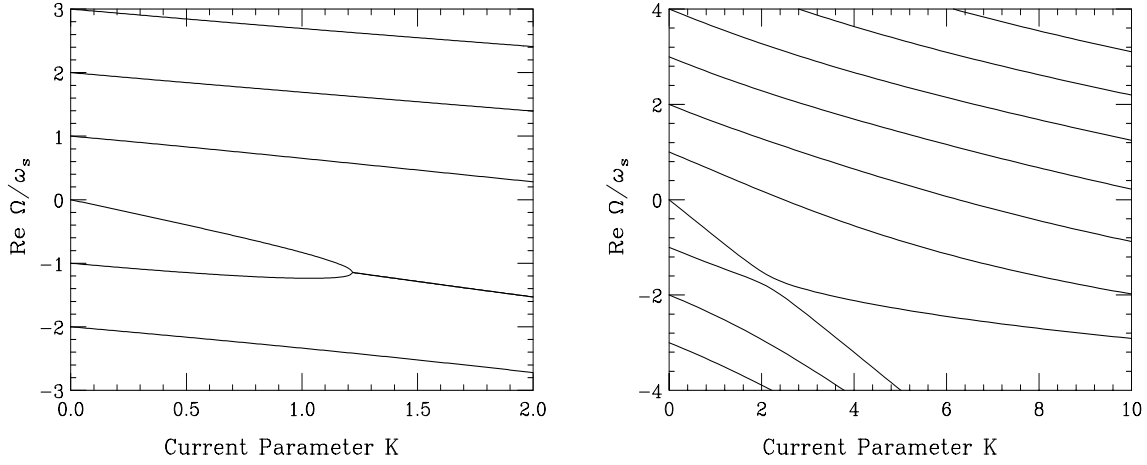


Figure 13.4: Left: With the transverse space charge force added to the wake forces, all modes except the $m = 0$ mode are shifted downward, thus requiring the $m = 0$ and -1 modes to couple at a much higher current threshold. Right: When space charge reaches the critical value of $\xi = 5$, the $m = -1$ mode is shifted away from the $m = 0$ mode by so much that they do not couple anymore.

to the local beam center, $x(\phi) - \bar{x}(\phi)$, with the constant S representing the space charge strength.

To solve the problem quantitatively, we expand the offset into the synchrotron harmonics (or azimuthals):

$$x(\phi, t) = e^{-i\omega_\beta t - i\Omega t} \sum_{n=-\infty}^{\infty} x_n e^{in\phi}, \quad (13.14)$$

where $\Omega/(2\pi)$ is the collective frequency shift. In this air-bag model, all particles reside at the edge of the bunch distribution in the longitudinal phase space. Note that because of the square-well air-bag model, these synchrotron azimuthals are slightly different from the conventional ones. The average offset at the synchrotron phase ϕ is therefore given by

$$\bar{x}(\phi, t) = \frac{1}{2} [x(\phi, t) + x(-\phi, t)] = e^{-i\omega_\beta t - i\Omega t} \sum_{n=-\infty}^{\infty} x_n \cos n\phi. \quad (13.15)$$

Following basically Ref. [6], Eq. (13.11) transforms into an eigenvalue equation,

$$\left(\frac{\Omega}{\omega_s} - n \right) x_n = -K \sum_{m=-\infty}^{\infty} x_m (\mathcal{W}_{nm} + \xi \mathcal{Q}_{nm}). \quad (13.16)$$

Here, the current parameter is written as

$$K = \frac{N_b e^2 c^2 W_0}{2\pi^2 \omega_\beta \omega_s C E_0} . \quad (13.17)$$

The wake matrix elements are then given by

$$\mathcal{W}_{nm} = \int_0^\pi d\phi \int_0^\phi d\phi' w[z(\phi') - z(\phi)] \cos(n\phi) \cos(m\phi') , \quad (13.18)$$

where the wake function is presented as $W(z) = -W_0 w(z)$ with W_0 serving as a normalizing constant. The space charge parameter

$$\xi = \frac{\Delta\omega_\beta}{2K\omega_s} \quad (13.19)$$

is a current-dependent ratio of the incoherent tune shift

$$\Delta\omega_\beta = \frac{S\rho}{2\omega_\beta} \quad (13.20)$$

to the current parameter K . The space charge matrix elements are

$$\mathcal{Q}_{nm} = \delta_{nm} - \delta_{n,-m} \quad (13.21)$$

in the assumed air-bag distribution.

Without wake forces, the eigenvalue equation leads to the mode behavior presented in the right plot of Fig. 13.3. For the simplest step-like wake function $w(z) = H(z)$, $H(z)$ being the Heaviside step function, and without space charge ($\xi = 0$), the mode coupling is shown in the left plot of Fig. 13.3, where the threshold is $K = 0.73$. Now space charge is introduced with the space charge parameter $\xi = 4$. We do see in the left plot of Fig. 13.4 that, because the $m = -1$ mode is shifted downward by the space charge, the instability threshold has been pushed up to $K = 1.25$ as compared with the left plot of Fig. 13.3.

Further increasing the space charge parameter to $\xi = 5$, we see in the right plot of Fig. 13.4 that modes $m = 0$ and -1 do not merge any more. What is not shown in the plot is a much higher new threshold where the 0 mode couples with the $m = 1$ mode instead. This new threshold is very much model dependent. In the present model, it depends strongly on the number of modes included in the truncated matrix. For truncation at modes $|n| = 32$, this new threshold is at least a factor of 30 higher than

when space charge is absent. A dependence of the calculated threshold K_{th} on the mode truncation number $|n|$ was found as $K_{th} \propto |n|^{1/2}$ for $|n| \leq 10$ and even weaker,

$$K_{th} \propto |n|^{1/3}, \quad (13.22)$$

for $10 \leq |n| \leq 32$. The divergence is caused by the fact that the Fourier components of the space charge in Eq. (13.21) do not roll off at high frequencies. Taking into account the finite value of the ratio of transverse bunch size σ_\perp to longitudinal bunch size σ_\parallel , we estimate this roll-off limit as $|n| \simeq \sigma_\perp/\sigma_\parallel \simeq 200$ to 1000 for typical hadron bunches. Extrapolation of the dependence Eq. (13.22) into this area brings to a conclusion that the actual threshold can be 2 to 3 times higher than the result reported for $|n| = 32$. So for this simplified wake-beam model, the space charge is found to be able to increase the TMCI threshold by one or two orders of magnitude.

As discussed in the previous section, a reactive feedback shifts mode $m = 0$ upwards resulting in pushing the threshold to a higher current. Here, the space charge force shifts all the modes downwards except $m = 0$, and the result is also to have the threshold pushed towards a higher current. Therefore, the space charge tune shift in a proton machine, as discussed above, constitutes a natural inverse reactive feedback.

13.3 Longitudinal

The azimuthal modes are not a good description of the collective motion of the bunch when the beam current is high enough. Therefore there is also mode coupling in the longitudinal motion. Similar to the transverse coupled problem in Eqs. (13.1) and (13.2), we have here

$$(\Omega - m\omega_s)\delta_{mm'}\delta_{kk'} = M_{mm'kk'} \quad (13.23)$$

where, with the aid of Eq. (10.37), the matrix M is defined as

$$M_{mm'kk'} = \frac{im}{1+m} \frac{4\pi^2 e I_b \eta}{3\beta^2 E_0 \omega_s \tau_L^3} \frac{\int d\omega \frac{Z_0^\parallel(\omega)}{\omega} \tilde{\lambda}_{m'k'}(\omega) \tilde{\lambda}_{mk}^*(\omega)}{\int d\omega \tilde{\lambda}_{mk}(\omega) \tilde{\lambda}_{mk}^*(\omega)}, \quad (13.24)$$

where the unperturbed distribution has been assumed to be parabolic. Again here the impedance is broadband so that the discrete summations over the synchrotron sidebands

have been replaced by integrals. We have also thrown away all the higher-order radial modes keeping the most easily excited $k = 1$. Exactly the same as in the transverse situation, only $\text{Im } Z_0^{\parallel}(\omega)/\omega$ contributes to the diagonal elements of the coupling matrix and thus to the real frequency shifts of the modes. The coupling of two modes, mostly adjacent, will give instability, which is determined by $\text{Re } Z_0^{\parallel}(\omega)/\omega$ in the off-diagonal elements next to the diagonal ones. All the discussions about bunch-length dependency on threshold in the transverse case apply here also. A rough estimate of the threshold can be obtained from Eq. (13.24) by equating the frequency shift to ω_s . The threshold is therefore

$$\eta_2 = \frac{4\pi^2 e I_b \eta}{3\beta^2 E_0 \omega_s^2 \tau_L^3} \left. \frac{Z_0^{\parallel}}{\omega} \right|_{\text{eff}} \approx 1 , \quad (13.25)$$

where the effective longitudinal impedance for mode m is defined as

$$\left. \frac{Z_0^{\parallel}}{\omega} \right|_{\text{eff}} = \frac{\int d\omega \frac{Z_0^{\parallel}(\omega)}{\omega} h_m(\omega)}{\int d\omega h_m(\omega)} , \quad (13.26)$$

For convenience, let us introduce a parameter $x = \omega \tau_L / \pi$, so that, with the exception of $m = 0$ which is not an allowed mode in the longitudinal motion, the m th mode of excitation peaks at $x \approx m+1$ and has a half width of $\Delta x \approx 1$. Now consider the Fermilab Main Ring with a revolution frequency 47.7 kHz and total bunch length $\tau_L \approx 2$ ns. Assume the impedance to be broadband centered at $x_r = 7.5$ or $f_r \sim 1.88$ GHz and quality factor $Q = 1$. Numerical diagonalization of the coupling matrix gives frequency shifts as shown in Fig. 13.5 [8]. We see the first instability occurs when mode $m = 6$ couples with mode $m = 7$, and in the vicinity of the threshold, there are also couplings between modes $m = 4$ and 5 and modes $m = 8$ and 9 . This happens because the resonance centered at $x_r = 7.5$ has a half width $\Delta x_r = x_r/(2Q) = 3.75$. Thus the $\text{Re } Z_0^{\parallel}/\omega$ resonant peak encompasses modes $m = 4$ to 9 , which peak at $x = 5$ to 10 . This is a typical picture of mode-coupling instability for long bunches. From the figure, the first instability occurs at

$$\epsilon = \frac{4\pi^2 e I_b \eta}{3\beta^2 E_0 \omega_s^2 \tau_L^3} \frac{R_s}{\omega_r} \approx 0.93 . \quad (13.27)$$

On the other hand, the Keil-Schnell criterion of Eq. (6.22) gives a threshold of

$$\frac{e I_b \eta}{\beta^2 E_0 \omega_s^2 \tau_L^3} \frac{R_s}{\omega_r} = \frac{1}{6\pi} \frac{1}{F} , \quad (13.28)$$

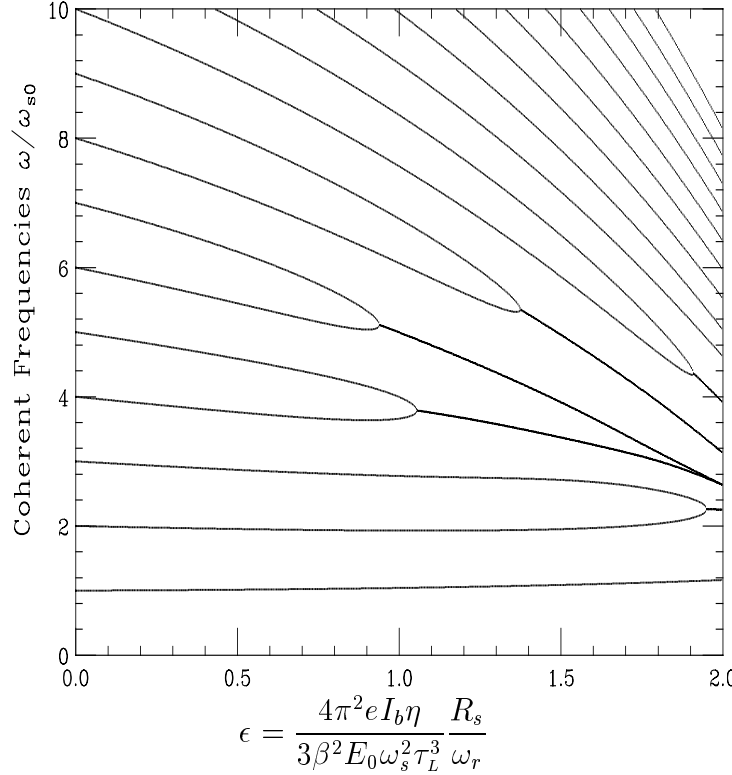


Figure 13.5: Coupling of modes $m = 6$ and 7 in the presence of a resonance at $x_r = 7.5$ and $Q = 1$ above transition.

where F is the form factor. This is equivalent to

$$\epsilon = \frac{2\pi}{9} \frac{1}{F} . \quad (13.29)$$

Thus, the mode-coupling threshold is very close to the Keil-Schnell threshold. However, mode-coupling instability is quite different from microwave instability. In the latter, pure reactive impedance can drive an instability; for example, the negative-mass instability just above transition is driven by the space charge force. It can be demonstrated that pure capacitive impedance will only lead to real frequency shifts of the modes. Although two modes may cross each other, they will not be degenerate to form complex modes. Thus, there is no instability (Exercise 13.2).

When the bunch is short, for example, electron bunches, the modes of excitation spread out to higher frequencies. Therefore when the bunch is short enough, the resonant peak of $\Re Z_0^\parallel/\omega$ will encompass only modes $m = 1$ and 2 . Thus, we expect these two

modes will collide first to give instability. The $m = 1$ is the dipole mode and is not shifted at low beam current because the bunch center does not see any reactive impedance. The $m = 2$ is the quadrupole mode, which is shifted downward above transition. This downshift is a way to measure the reactive impedance of the ring.

When the beam current is above threshold and instability starts, the energy spread increases and so does the bunch length. In an electron ring where there is radiation damping, there is no overshooting and the increase stops when the stability criterion is fulfilled again. The bunch lengthening is therefore determined by the stability criterion. If the bunch samples the impedance at a frequency range where $Z_0^{\parallel}(\omega) \propto \omega^a$, the effective impedance is

$$\left. \frac{Z_0^{\parallel}}{\omega} \right|_{\text{eff}} \propto \frac{\int d\omega \omega^{a-1} h_m(\omega)}{\int d\omega h_m(\omega)} \propto \tau_L^{1-a}, \quad (13.30)$$

where use has been made of the fact that the power spectrum h_m is a function of the dimensionless quantity $\omega \tau_L$ according to Eq. (10.42) and the result is independent of the functional form of h_m . From the threshold condition in Eq. (13.25), we have

$$\frac{4\pi^2 e I_b \eta}{3\beta^2 E_0 \omega_s^2 \tau_L^{2+a}} = \text{constant independent of } I_b, \eta, E_0, \omega_s, \tau_L. \quad (13.31)$$

Thus the bunch length obeys the scaling criterion of

$$\tau_L \propto \xi^{1/(2+a)}, \quad (13.32)$$

where

$$\xi = \frac{\eta I_b}{\nu_s^2 E_0} \quad (13.33)$$

is the scaling parameter introduced by Chao and Gareyte [2].

Longitudinal mode coupling is different from transverse mode coupling. In the latter, the betatron frequency ($m = 0$) is shifted downward to meet with the $m = -1$ mode. The amount of shift is small, since $\nu_s/[\nu_\beta] \ll 1$, where $[\nu_\beta]$ is the residual betatron tune. Transverse mode coupling has been measured in many electron rings and the results agree with theory. In the longitudinal case, the synchrotron quadrupole frequency ($m = 2$) has to be shifted downward to meet with the synchrotron dipole frequency ($m = 1$) and this shift is 100% of the synchrotron tune. At the CERN LEP which is above transition, we expect the synchrotron quadrupole mode to shift downward

when the beam current increases from zero. However, it was observed that this mode shifts slightly upward instead. Since the dipole frequency is not shifted, it is hard to visualize how the two modes will be coupled. Some argue that the coupling may not be between two azimuthal modes, but instead between two radial modes that we have discarded in our discussion. But the coupling between two radial modes is generally much weaker. Some say that the actual coupling of the two modes has never been observed experimentally, and the scaling law for bunch lengthening may have been the result of some other theories. Anyway, the theory of longitudinal mode coupling is far from satisfactory.

13.4 High Energy Accelerators

So far transverse mode-coupling instability has never been observed in hadron machines. In this section, we would like to analyze how this instability would affect the higher energy accelerators under design.

For protons, particle energy E_0 is directly proportional to the size of the accelerator. So we have

$$E_0 \propto R \quad \text{and} \quad \omega_0 \propto \frac{1}{R}. \quad (13.34)$$

The resistive-wall impedance is

$$\frac{Z_0^{\parallel}}{n} = [1 - i \operatorname{sgn}(\omega)] \frac{R\rho}{nb} \sqrt{\frac{\mu\omega}{2\rho}}, \quad (13.35)$$

where ρ is the resistivity and μ the magnetic permeability of the beam pipe of radius b . At a fixed frequency ω , we have

$$\frac{Z_0^{\parallel}}{n} \sim \frac{1}{b\sqrt{\omega}}, \quad (13.36)$$

$$Z_1^{\perp} \sim \frac{R}{b^3\sqrt{\omega}}. \quad (13.37)$$

For M pairs of strip-line BPM's at low frequencies $\omega \lesssim c/\ell$, where ℓ is the length of the

strip lines,

$$\frac{\text{Im } Z_0^{\parallel}}{n} = -i2M Z_c \left(\frac{\phi_0}{2\pi}\right)^2 \frac{\ell}{R}, \quad (13.38)$$

$$\text{Im } Z_1^{\perp} = \frac{c}{2b^2} \left(\frac{4}{\phi_0}\right)^2 \sin^2 \frac{\phi_0}{2} \frac{\text{Im } Z_0^{\parallel}}{\omega}. \quad (13.39)$$

where Z_c is the characteristic impedance and ϕ_0/π is the fraction of the beam pipe covered by the strip lines. The betatron functions $\beta_{x,y}$ scale as \sqrt{R} . Thus, the betatron tunes and the number of BPM's required also scale as \sqrt{R} . At a fixed frequency we have

$$\frac{\text{Im } Z_0^{\parallel}}{n} \sim \frac{\ell}{\sqrt{R}}, \quad (13.40)$$

$$\text{Im } Z_1^{\perp} \sim \frac{\ell}{b^2} \sqrt{R}. \quad (13.41)$$

We see that when the size of an accelerator is increased, the resistive-wall impedance will dominate over all other contributions. We also see that Z_0^{\parallel}/n at a fixed frequency remains roughly independent of the size of the accelerator. From now on, we will consider resistive-wall impedance only.

The Keil-Schnell criterion for longitudinal microwave instability is

$$\left| \frac{Z_0^{\parallel}}{n} \right| < \frac{2\pi|\eta|E_0\sigma_{\delta}^2}{eI_{\text{peak}}}. \quad (13.42)$$

For a large accelerator, the energy is usually very much larger than the transition energy. The slip factor $\eta \sim \gamma_t^{-2} \sim \nu_{\beta}^{-2}$ for a FODO lattice. We therefore have $\eta \sim R^{-1}$. The peak current is $I_{\text{peak}} \sim N_b/\sigma_{\tau}$. Putting in the wall resistivity at $\omega \sim \sigma_{\tau}^{-1}$, the stability criterion takes the form

$$\frac{\sqrt{\sigma_{\tau}}}{b} \lesssim \frac{A\sigma_{\delta}}{N_b R}, \quad (13.43)$$

where the bunch area in eV-s is

$$A = E_0\sigma_{\delta}\sigma_{\tau}. \quad (13.44)$$

For an accelerator of higher energy, if we want to have roughly the same fractional energy spread and bunch length, the bunch area will scale as R . The above stability criterion becomes

$$\frac{\sqrt{\sigma_{\tau}}}{b} \lesssim \frac{\sigma_{\tau}\sigma_{\delta}^2}{N_b}. \quad (13.45)$$

This leads to the conclusion that longitudinal microwave instability will not be worsen for higher energy accelerators.

Now let us turn to transverse mode-coupling instability and consider Eq. (13.7), which we rewrite as a stability criterion

$$Z_1^\perp|_{\text{eff}} \lesssim \frac{4\pi E_0 \omega_0 \nu_\beta \nu_s \tau_L}{e^2 N_b c} . \quad (13.46)$$

The effective impedance on the left side will be taken as the resistive-wall impedance of Eq. (13.37) multiplied by a constant. When we substitute $E_0 \sim R$, $\omega_0 \sim 1/R$, and $\nu_\beta \sim \sqrt{R}$, we obtain

$$\frac{R\sqrt{\sigma_\tau}}{b^3} \lesssim \frac{\sqrt{R}\nu_s\sigma_\tau}{N_b} . \quad (13.47)$$

Thus, transverse mode-coupling instability will occur when the size of the accelerator becomes bigger and bigger.

According to all the accelerator rings ever built, for electron machines, particle energy scales as $E_0 \sim \sqrt{R}$ instead. This implies that there will be no \sqrt{R} on the right side of Eq. (13.47), or

$$\frac{R\sqrt{\sigma_\tau}}{b^3} \lesssim \frac{\nu_s\sigma_\tau}{N_b} , \quad (13.48)$$

and the instability will come at a smaller accelerator size. This may explain why electron machines are more susceptible for transverse mode-coupling instabilities. For the longitudinal microwave instability, Eq. (13.45) becomes

$$\frac{\sqrt{\sigma_\tau}}{b} \lesssim \frac{\sigma_\tau\sigma_\delta^2}{N_b\sqrt{R}} , \quad (13.49)$$

showing that this instability will be worsen as the size of the ring increases. For electron rings, because of the short bunch length, the longitudinal mode-coupling instability is more of interest. The stability condition for azimuthal modes $m = 2$ and 1 colliding is given by Eq. (7.10), or

$$\left| \frac{Z_0^\parallel}{n} \right|_{\text{ind}} \lesssim \frac{4\pi\nu_s^2\omega_0^2\hat{\tau}^3\beta^2E_0}{3e^2N|\eta|} . \quad (13.50)$$

Assuming again that the resistive-wall impedance dominates, we obtain

$$\frac{\sigma_\tau}{b} \lesssim \frac{\nu_s^2\sigma_\tau^3}{N_b R^{1/2}} , \quad (13.51)$$

again showing that this threshold becomes more severe for a larger ring.

In Chapter 10, we show that for a proton ring, the growth rate for transverse coupled-bunch instability driven by the resistive-wall impedance should be more or less independent of the size of the accelerator ring. However, for electron rings we have $E_0 \propto \sqrt{R}$ instead. The growth rate for this instability now increases according to \sqrt{R} for large electron rings. The growth time in revolution turns therefore decreases according to $R^{-3/2}$, making it much harder for the feedback damper to damp the instability in Very Large Lepton Colliders (VLLC) than in Very Large Hadron Colliders (VLHC).

13.5 Exercises

- 13.1. There is a simple two-particle model which gives a clear picture of transverse mode coupling [2]. Assume the head and tail particles are always separated by \hat{z} for one half of a synchrotron period T_s and exchange position for the other half. Similar to Exercise 12.2, we have during $0 < s/v < T_s/2$,

$$\begin{aligned} y_1'' + k_\beta^2 y_1 &= 0 , \\ y_2'' + k_\beta^2 y_2 &= -\frac{e^2 N W_1(\hat{z})}{2E_0 C} y_1 . \end{aligned} \quad (13.52)$$

(1) Show that the solution is

$$\begin{aligned} \tilde{y}_1(s) &= \tilde{y}_1(0)e^{-ik_\beta s} , \\ \tilde{y}_2(s) &= \tilde{y}_2(0)e^{-ik_\beta s} - i\frac{e^2 N W_1(\hat{z})}{4E_0 C k_\beta} \left[\frac{\tilde{y}_1^*(0)}{k_\beta} \sin(k_\beta s) + \tilde{y}_1(0) s e^{-ik_\beta s} \right] , \end{aligned} \quad (13.53)$$

where

$$\tilde{y}_\ell = y_\ell + i\frac{y'_\ell}{k_\beta} , \quad \ell = 1, 2 . \quad (13.54)$$

The term with $\sin(k_\beta s)$ in Eq. (13.53) can be dropped because $\omega_\beta T_s/2 \ll 1$. We can therefore write

$$\begin{pmatrix} \tilde{y}_1 \\ \tilde{y}_2 \end{pmatrix}_{s=vT_s/2} = e^{-i\omega_\beta T_s/2} \begin{pmatrix} 1 & 0 \\ i\Upsilon & 1 \end{pmatrix} \begin{pmatrix} \tilde{y}_1 \\ \tilde{y}_2 \end{pmatrix}_{s=0} , \quad (13.55)$$

where

$$\Upsilon = -\frac{\pi e^2 N W_1 v^2}{4E_0 C \omega_\beta \omega_s} . \quad (13.56)$$

(2) During $T_s/2 < s/v < T_s$, show that we have instead

$$\begin{aligned} y_1'' + k_\beta^2 y_1 &= \frac{e^2 N W_1(\hat{z})}{2E_0 C} y_2 , \\ y_2'' + k_\beta^2 y_2 &= 0 , \end{aligned} \quad (13.57)$$

so that for one synchrotron period,

$$\begin{pmatrix} \tilde{y}_1 \\ \tilde{y}_2 \end{pmatrix}_{s=vT_s} = e^{-i\omega_\beta T_s} \begin{pmatrix} 1 & i\Upsilon \\ 0 & 1 \end{pmatrix} \begin{pmatrix} 1 & 0 \\ i\Upsilon & 1 \end{pmatrix} \begin{pmatrix} \tilde{y}_1 \\ \tilde{y}_2 \end{pmatrix}_{s=0} . \quad (13.58)$$

(3) Show that the two eigenvalues are

$$\lambda_{\pm} = e^{\pm i\phi}, \quad \sin \frac{\phi}{2} = \frac{\Upsilon}{2}, \quad (13.59)$$

and stability requires $\Upsilon \leq 2$. Compare the result with Eq. (13.6). Note that for a short bunch $W_1(\hat{z}) < 0$; thus Υ is positive.

13.2. In the two-particle model in Exercise 13.1, if the beam current is slightly above threshold; i.e.,

$$\Upsilon = 2 + \epsilon, \quad (13.60)$$

where $\epsilon \ll 1$, compute the complex phase ϕ of the eigenvalues λ_{\pm} . The growth rate is then

$$\frac{1}{\tau} = \frac{\mathcal{I}m \phi}{T_s} = \frac{2\sqrt{\epsilon}}{T_s}. \quad (13.61)$$

Show that for an intensity 10% above threshold, the growth time is of the order of the synchrotron period.

13.3. For longitudinal mode coupling, the coupling matrix of Eq. (13.24) can be written as, after keeping only the lowest radial modes,

$$M_{mm'} = \epsilon \omega_s A_{mm'} \quad (13.62)$$

where ϵ is given by Eq. (13.27),

$$A_{mm'} = \frac{im}{1+m} \frac{\int d\omega \frac{\omega_r \hat{Z}_0^{||}(\omega)}{\omega} \tilde{\lambda}_{m'}(\omega) \tilde{\lambda}_m^*(\omega)}{\int d\omega \tilde{\lambda}_m(\omega) \tilde{\lambda}_m^*(\omega)}, \quad (13.63)$$

and $\hat{Z}_0^{||}(\omega)$ has been normalized to the shunt impedance R_s .

If the coupling is not too strong, we can truncate the matrix to 2×2 for the coupling between two modes:

$$\begin{vmatrix} \frac{\Omega}{\omega_{s0}} - m - \epsilon A_{mm} & \epsilon A_{mm'} \\ \epsilon A_{m'm} & \frac{\Omega}{\omega_s} - m' - \epsilon A_{m'm'} \end{vmatrix} = 0. \quad (13.64)$$

(1) Show that the collective frequency is given by

$$\Omega = \frac{1}{2}\omega_s \left[(\nu_m + \nu_{m'}) \pm \sqrt{(\nu_{m'} - \nu_m)^2 + 4\epsilon^2 A_{mm'} A_{m'm'}} \right], \quad (13.65)$$

where $\nu_k = k + \epsilon A_{kk}$, $k = m$ or m' .

(2) For simplicity, let us neglect the factor $m/(1+m)$ on the right side of Eq. (13.63). For two adjacent modes ($m' = m + 1$) that are coupled by a resonant peak, the higher-frequency mode samples mostly the capacitive part of the resonance while the lower-frequency mode samples the inductive part. Therefore $A_{mm} - A_{m'm'} > 0$. Show that $A_{mm'} A_{m'm} = -|A_{mm'}|^2$ and the threshold of instability ϵ_{th} is given by

$$|\epsilon_{\text{th}} A_{mm'}| = \frac{1}{2} |\epsilon_{\text{th}} (A_{mm} - A_{m'm'}) - 1|. \quad (13.66)$$

The solution is different depending on whether the bunch energy is above or below transition:

$$\epsilon_{\text{th}} = \frac{1}{2|A_{mm'}| + |A_{m'm'} - A_{mm}|} \quad \text{above transition,} \quad (13.67)$$

$$|\epsilon_{\text{th}}| = \frac{1}{2|A_{mm'}| - |A_{m'm'} - A_{mm}|} \quad \text{below transition.} \quad (13.68)$$

The above shows that the threshold will be higher when the ring is below transition. In fact, the system becomes completely stable below transition if the coupling provided by the real part of the impedance is not strong enough (or $2|A_{mm'}| < |A_{m'm'} - A_{mm}|$). For this reason, it is advantageous for the ring to be of imaginary γ_t [9].

(3) When the impedance is purely reactive, the next-to-diagonal elements are zero. So we talk about coupling of two modes m and $m' = m + 2$ instead. Show that $A_{mm'} A_{m'm} = |A_{mm'}|^2$ and instability cannot occur.

(4) Show that the same conclusions in Parts (2) and (3) can be drawn when the factor $m/(1+m)$ is not neglected in Eq. (13.63), although Eqs. (13.66) and (13.68) will be slightly modified.

Bibliography

- [1] R. Kohaupt, IEEE Trans. Nucl. Sci. **NS-26**, 3480 (1979); D. Rice, et al., IEEE Trans. Nucl. Sci. **NS-28**, 2446 (1981); PEP Group, Proc. 12th Int. Conf. High Energy Accel. Fermilab, 1983, p.209.
- [2] R. Ruth, CERN Report LEP-TH/83-22 (1983); S. Myers, Proc. IEEE Part. Accel. Conf., Washington, 1987, p.503; B. Zotter, IEEE Trans. Nucl. Sci. **NS-32**, 2191 (1985); S. Myers, CERN Report LEP -523 (1984).
- [3] V. Balakin, A. Novokhatsky, and V. Smirnov, Proc. 12th Int. Conf. High Energy Accel., Fermilab, 1983, p.11.
- [4] M. Blaskiewicz, *Fast Head-tail Instability with Space Charge*, Phys. Rev. ST Accel. Beams, **1**, 044201 (1998).
- [5] V. Danilov and E. Perevedentsev, *Strong Head-Tail Effect and Decoupled Modes in the Space-Time Domain*, Proceedings of XVth International Conference on High Energy Accelerators, p.1163 (Hamburg, 1992).
- [6] V. Danilov and E. Perevedentsev, *Feedback system for elimination of the TMCI*, Nucl. Instr. and Methods, **A391**, 77 (1997).
- [7] B. Chen, *The Longitudinal Collective Instabilities of Nonlinear Hamiltonian Systems in a Circular Accelerator*, Thesis, U. of Texas at Austin, May, 1995.
- [8] K.Y. Ng, *Potential-Well Distortion and Mode-Mixing Instability in Proton Machines*, Fermilab Report FN-630, 1995; K.Y. Ng, *Mode-Coupling Instability and Bunch Lengthening in Proton Machines*, Proc. 1995 Particle Accelerator Conference and International Conference on High-Energy Accelerators, Dallas, Texas, May 1-7, 1995, p.2977.

- [9] S.Y. Lee, K.Y. Ng, and D. Trbojevic, Phys. Rev. **E48**, 3040 (1993).

Chapter 14

LANDAU DAMPING

As we have seen in previous chapters, collective instabilities occur in bunched and unbunched beam as a result of the interaction of the beam particles with their own wake fields. There are various way to damp these instabilities. Aside from mechanical dampers, there is a natural stabilization mechanism against collective instabilities when the beam particles have a small spread in their frequencies, such as betatron frequency, synchrotron frequency, or revolution frequency as the situation requires. This damping mechanism is called *Landau damping*, which was first formulated by Landau [1]. Unfortunately, Landau's original paper is rather difficult to understand. Later, Jackson [2] wrote an article on longitudinal plasma oscillations and had the concept well explained.

Neil and Sessler [3] first formulated the theory of Landau damping on longitudinal instabilities, while Laslett, Neil and Sessler [4] first applied the theory to transverse instabilities. There have been quite a number of good papers written on this subject by Hereward [5], Hofmann [6], and Chao [7].

We encountered Landau damping in Chapter 6 when we formulated the dispersion relation for longitudinal microwave instability using the Vlasov equation. There, we came across the ambiguity of a singularity in the denominator which is critical in determining whether the system will be stable or unstable. That ambiguity can only be avoided when the problem is treated as an initial-value problem. This will be covered in this chapter. We first study the beam response of an harmonic driving force, the beam response of shock or δ -pulse excitation. After that, we try to understand the physics of Landau damping and derive dispersion relations for bunched and unbunched beam in transverse and longitudinal instabilities.

14.1 Harmonic Beam Response

Consider a particle having a natural angular frequency ω and is driven by a force of angular frequency Ω . The equation describing its displacement $x(t)$ is

$$\ddot{x} + \omega^2 x = A \cos \Omega t , \quad (14.1)$$

where the overdot represents derivative with respect to time and A denotes the amplitude of the force. The most general solution is

$$x(t) = x_0 \cos \omega t + \dot{x}_0 \frac{\sin \omega t}{\omega} + \frac{A}{\omega^2 - \Omega^2} [\cos \Omega t - \cos \omega t] , \quad (14.2)$$

where x_0 and \dot{x}_0 are, respectively the initial value of x and \dot{x} at $t = 0$. The first two terms are due to a shock or δ -pulse excitation. Although they are important, we shall postpone the discussion to the next section.

Let us pay attention to the excitation by the harmonic force. Notice that the response is well-behaved even at $\omega = \Omega$. For a large number of particles having a distribution $\rho(\omega)$ in frequency and normalized to unity, the displacement of the center of mass is

$$\langle x(t) \rangle = A \int_{-\infty}^{\infty} d\omega \frac{\rho(\omega)}{\omega^2 - \Omega^2} [\cos \Omega t - \cos \omega t] . \quad (14.3)$$

As is the case in particle beams, the distribution is mostly a narrow one centered at angular frequency $\bar{\omega}$. For simplicity, let us assume that this distribution does not peak at any other frequency, not even the negative frequencies. In order to drive this system of particles, the driving frequency must also be close to this center frequency, or $\Omega \approx \bar{\omega}$. We can therefore do the expansion $\omega = \Omega + (\omega - \Omega)$, and the Eq. (14.3) can be approximated by

$$\langle x(t) \rangle = \frac{A}{2\bar{\omega}} \left[\cos \Omega t \int_{-\infty}^{\infty} d\omega \rho(\omega) \frac{1 - \cos(\omega - \Omega)t}{\omega - \Omega} + \sin \Omega t \int_{-\infty}^{\infty} d\omega \rho(\omega) \frac{\sin(\omega - \Omega)t}{\omega - \Omega} \right] . \quad (14.4)$$

Notice that we have separated the fast-oscillating term of angular frequency Ω and the slow-oscillating envelope-like terms with angular frequency $\omega - \Omega$. We also see a part, the $\cos \Omega t$ term, that is not driven *in phase** by the force, and the other part, the $\sin \Omega t$ term, that is driven in phase by the force. More discussion will follow later. The functions

$$p(\omega) = \frac{1 - \cos \omega t}{\omega} \quad \text{and} \quad d(\omega) = \frac{\sin \omega t}{\omega} \quad (14.5)$$

*Actually, “in phase” here implies the driving phase is in phase with the velocity \dot{x} .

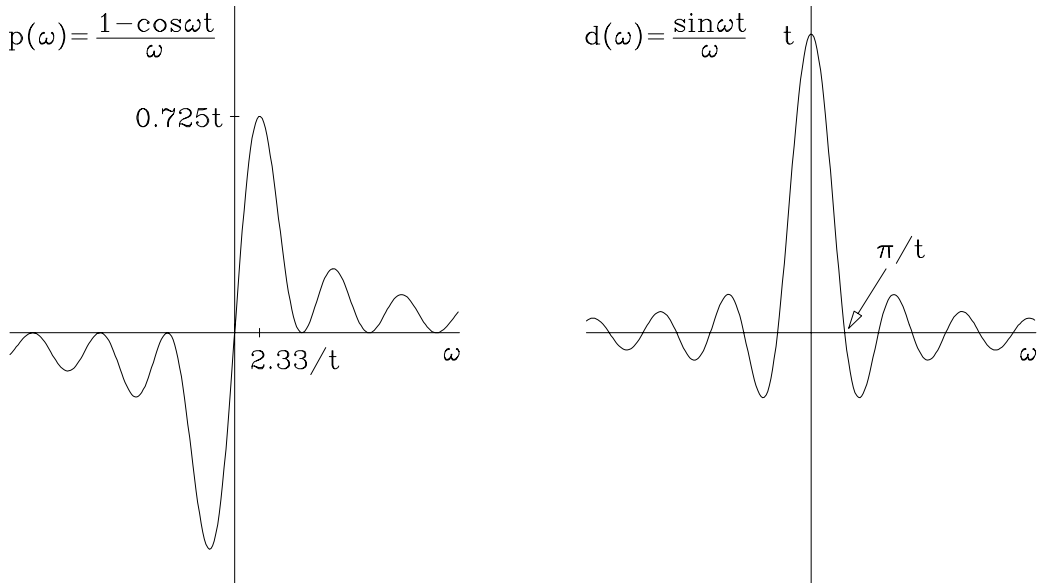


Figure 14.1: Plots of the functions $p(\omega)$ and $d(\omega)$ with t being a parameter. As $t \rightarrow \infty$, $p(\omega) \rightarrow \wp \omega^{-1}$ and $d(\omega) \rightarrow \pi \delta(\omega)$, where \wp denotes principal value.

are illustrated in Fig. 14.1. The function $p(\omega)$ always vanishes at $\omega = 0$ and decays as ω^{-1} when $\omega \rightarrow \pm\infty$. It has peaks of value $\pm at$ at $\pm b/t$, where $b = 2.3311$ is the root of $b = \tan(b/2)$ and $a = 2b/(1 + b^2) = 0.7246$. These peaks grow linearly with t and move closer to $\omega = 0$ as t increases. We therefore have

$$\lim_{t \rightarrow \infty} p(\omega) = \wp \frac{1}{\omega}, \quad (14.6)$$

where \wp stands for the principal value. On the other hand, $d(\omega)$ has a peak of value t at $\omega = 0$ and rolls off as ω^{-1} for large ω , having the first zeroes at $\omega = \pm\pi/t$. As $t \rightarrow \infty$, the peak at $\omega = 0$ grows linearly while its width also shrinks inversely with t ; the area enclosed is always π . Outside the peak, the function oscillates very fast as $t \rightarrow 0$. We therefore have

$$\lim_{t \rightarrow \infty} d(\omega) = \pi \delta(\omega). \quad (14.7)$$

Coming back to Eq. (14.4), as $t \gg 1/\Delta\omega$, where $\Delta\omega$ is a measure of the width of the frequency distribution $\rho(\omega)$, all the transients die, leaving us with

$$\langle x(t) \rangle = \frac{A}{2\bar{\omega}} \left[\cos \Omega t \wp \int_{-\infty}^{\infty} d\omega \frac{\rho(\omega)}{\omega - \Omega} + \pi \rho(\Omega) \sin \Omega t \right]. \quad (14.8)$$

Let now us repeat the derivation with the force $A \sin \Omega t$ and combine the solution

with the former to get the long-term response to the force $Ae^{-i\Omega t}$:

$$\langle x(t) \rangle = \frac{Ae^{-i\Omega t}}{2\bar{\omega}} \left[\wp \int_{-\infty}^{\infty} d\omega \frac{\rho(\omega)}{\omega - \Omega} + i\pi\rho(\Omega) \right] = \frac{Ae^{-i\Omega t}}{2\bar{\omega}\Delta\omega} R(u) , \quad (14.9)$$

where the beam transfer function (BTF) is defined as

$$R(u) = f(u) + ig(u) , \quad (14.10)$$

with

$$u = \frac{\bar{\omega} - \Omega}{\Delta\omega} , \quad (14.11)$$

and

$$f(u) = \Delta\omega \wp \int_{-\infty}^{\infty} d\omega \frac{\rho(\omega)}{\omega - \Omega} \quad \text{and} \quad g(u) = \pi\Delta\omega\rho(\bar{\omega} - u\Delta\omega) , \quad (14.12)$$

where again $\Delta\omega$ is a measure of the width of the frequency distribution. The BTF is an important function, because it can be measured and it gives valuable information to the distribution function $\rho(\omega)$ and also the impedance of the vacuum chamber, as will be demonstrated below. We can also combine the two expressions in Eq. (14.12) into one and obtain

$$R(u) = f(u) + ig(u) = \Delta\omega \int_{-\infty}^{\infty} d\omega \frac{\rho(\omega)}{\omega - \Omega - i\epsilon} \quad \text{with} \quad u = \frac{\bar{\omega} - \Omega}{\Delta\omega} . \quad (14.13)$$

There is a singularity in $R(u)$ when $\Omega = \omega - i\epsilon$ or $u\Delta\omega = \bar{\omega} - \omega + i\epsilon$. This implies that $R(u)$ is an analytic function with singularities only in the upper u -plane. Notice that instead of the derivation starting from the initial condition, the displacement of the center of the bunch, Eq. (14.9), can also be obtained directly by writing the force as

$$Ae^{-i(\Omega+i\epsilon)t} = Ae^{-i\Omega t}e^{i\epsilon t} , \quad (14.14)$$

where ϵ is an infinitesimal positive number, so that the solution becomes

$$\langle x(t) \rangle = \frac{Ae^{-i\Omega t}}{2\bar{\omega}} \int_{-\infty}^{\infty} d\omega \frac{\rho(\omega)}{\omega - \Omega - i\epsilon} = \frac{Ae^{-i\Omega t}}{2\bar{\omega}} \left[\wp \int_{-\infty}^{\infty} d\omega \frac{\rho(\omega)}{\omega - \Omega} + i\pi\rho(\Omega) \right] , \quad (14.15)$$

which is exactly the same as Eq. (14.9). The addition of the small ϵ implies that the force in Eq. (14.14) is zero at $t = -\infty$ and increases adiabatically.

14.2 Shock Response

The beam is suddenly excited by a shock or a δ -pulse, imparting to the beam particles either a displacement x_0 or a velocity displacement \dot{x}_0 , but not both. From Eq. (14.2), we have the shock response defined by either

$$G(t) = \frac{\langle x(t) \rangle}{x_0} = H(t) \int_{-\infty}^{\infty} d\omega \rho(\omega) \cos \omega t , \quad (14.16)$$

or

$$G(t) = \frac{\langle \dot{x}(t) \rangle}{\dot{x}_0} = H(t) \int_{-\infty}^{\infty} d\omega \rho(\omega) \cos \omega t , \quad (14.17)$$

where $H(t)$ is the Heaviside step function. Thus the shock response function (SRF) is always real and vanishes when $t < 0$. The SRF is important because it is an easily measured function and it can give information about the distribution function of the frequency as well as the BTF.

It is interesting to show that there is a relation between the the SRF and the BTF. The Fourier transform of the SRF is

$$\tilde{G}(\omega) = \frac{1}{2\pi} \int_0^{\infty} dt G(t) e^{i\omega t} . \quad (14.18)$$

where attention has to be paid that the integral starts from zero. The real part is

$$\begin{aligned} \mathcal{R}e \tilde{G}(\omega) &= \frac{1}{2\pi} \int_0^{\infty} dt G(t) \cos \omega t \\ &= \frac{1}{2\pi} \int_0^{\infty} dt \cos \omega t \int_{-\infty}^{\infty} d\omega' \rho(\omega') \cos \omega' t \\ &= \frac{1}{4\pi} \int_{-\infty}^{\infty} d\omega' \rho(\omega') \int_{-\infty}^{\infty} dt \cos \omega t \cos \omega' t \\ &= \frac{1}{4} \int_{-\infty}^{\infty} d\omega' \rho(\omega') [\delta(\omega' - \omega) + \delta(\omega' + \omega)] \\ &= \frac{1}{4} \rho(\omega) , \end{aligned} \quad (14.19)$$

where $\delta(\omega' + \omega)$ has no contribution because the distribution is narrow and is centered

at only one positive frequency. The imaginary part is

$$\begin{aligned}
\text{Im } \tilde{G}(\omega) &= \frac{1}{2\pi} \int_0^\infty dt G(t) \sin \omega t \\
&= \frac{1}{2\pi} \int_0^\infty dt \sin \omega t \int_{-\infty}^\infty d\omega' \rho(\omega') \cos \omega' t \\
&= \frac{1}{4\pi} \int_{-\infty}^\infty d\omega' \rho(\omega') \int_0^\infty dt \left[\sin(\omega - \omega')t + \sin(\omega + \omega')t \right] \\
&= \frac{1}{4\pi} \left[\wp \int_{-\infty}^\infty d\omega' \frac{\rho(\omega')}{\omega - \omega'} + \wp \int_{-\infty}^\infty d\omega' \frac{\rho(\omega')}{\omega + \omega'} \right]
\end{aligned} \tag{14.20}$$

where again the last principal-value integral involving $\omega + \omega'$ can be neglected because of the narrow spread of the distribution ρ . We write these integrals as principal-value integrals because during the derivation, one integrand vanishes when $\omega' - \omega = 0$ and the other vanishes when $\omega + \omega' = 0$. Combining the result,

$$\begin{aligned}
\tilde{G}(\omega) &= \frac{-i}{4\pi} \left[\wp \int_{-\infty}^\infty d\omega' \frac{\rho(\omega')}{\omega' - \omega} + i\pi\rho(\omega) \right] \\
&= \frac{-i}{4\pi\Delta\omega} \left[f(u) + ig(u) \right] = \frac{-i}{4\pi\Delta\omega} R(u)
\end{aligned} \tag{14.21}$$

In other words, the Fourier transform of the SRF is equal to the BTF multiplied by $-i/(4\pi\Delta\omega)$. This also provides us with a way to compute the BTF. The procedure is: compute the SRF $G(t)$, find its Fourier transform $\tilde{G}(\omega)$, and then infer the BTF $R(u)$.

As an example, take the Lorentz distribution

$$\rho(\omega) = \frac{\Delta\omega}{\pi} \frac{1}{(\omega - \bar{\omega})^2 + (\Delta\omega)^2}. \tag{14.22}$$

The SRF is

$$\begin{aligned}
G(t) &= H(t) \mathcal{R}e \int_{-\infty}^\infty d\omega \frac{\Delta\omega}{\pi} \frac{e^{i\omega t}}{(\omega - \bar{\omega})^2 + (\Delta\omega)^2} \\
&= H(t) \mathcal{R}e e^{i(\bar{\omega} + i\Delta\omega)t} = H(t) e^{-\Delta\omega t} \cos \bar{\omega} t
\end{aligned} \tag{14.23}$$

Next the Fourier transform,

$$\begin{aligned}
\tilde{G}(\omega) &= \frac{1}{2\pi} \int_0^\infty dt \cos \bar{\omega} t e^{(-\Delta\omega+i\omega)t} \\
&= \frac{1}{4\pi} \int_0^\infty dt [e^{i(\bar{\omega}+i\Delta\omega+\omega)t} + e^{i(-\bar{\omega}+i\Delta\omega+\omega)t}] \\
&= \frac{1}{4\pi} \left[\frac{1}{-i(\bar{\omega}+\omega+i\Delta\omega)} + \frac{1}{i(\bar{\omega}-\omega-i\Delta\omega)} \right] \\
&= \frac{-i}{4\pi\Delta\omega} \frac{1}{u-i} = \frac{-i}{4\pi\Delta\omega} \frac{u+i}{u^2+1}, \tag{14.24}
\end{aligned}$$

where again the smaller term involving $\omega_r + \omega$ has been removed. Thus the BTF is

$$R(u) = f(u) + ig(u) = \frac{u+i}{u^2+1}, \tag{14.25}$$

which is equal to the Fourier transform of the SRF $G(t)$ multiplied by $-i/(4\pi\Delta\omega)$. These results are depicted in Fig. 14.2. As expected the shock excitation is the decay of the center displacement $\langle x \rangle$ or the center velocity displacement $\langle \dot{x} \rangle$. The decay comes from the distribution $\rho(\omega)$ so that each particle oscillates with a slightly different frequency. The particles will spread out and therefore the decay of the center displacement or the center velocity displacement. This is usually known as *decoherence* or *filamentation*. For the Lorentz distribution, the decay turns out to be exponential. However, it is important to point out that the center $\langle \dot{x} \rangle$ decays because initially we have a nonzero x_0 but $\dot{x}_0 = 0$. In case $\dot{x}_0 \neq 0$, the Lorentz distribution *does not* give a decay of the center displacement, (Exercise 14.1).

Table 14.1 lists the BTF and SRF for some commonly used frequency distributions (Exercise 14.2): the Lorentz distribution, the rectangular distribution, the parabolic distribution, the elliptical distribution, the bi-Lorentz distribution, and the Gaussian distribution.

Because the BTF is the Fourier transform of SRF, $G(t)$ is also the inverse Fourier transform of $R(u)$:

$$G(t) = \mathcal{Re} \frac{-i}{4\pi\Delta\omega} \int_{-\infty}^{\infty} d\omega R \left(\frac{\bar{\omega}-\omega}{\Delta\omega} \right) e^{-i\omega t}. \tag{14.26}$$

The \mathcal{Re} should not be there. It is there because we have consistently neglected the frequencies around $-\bar{\omega}$.

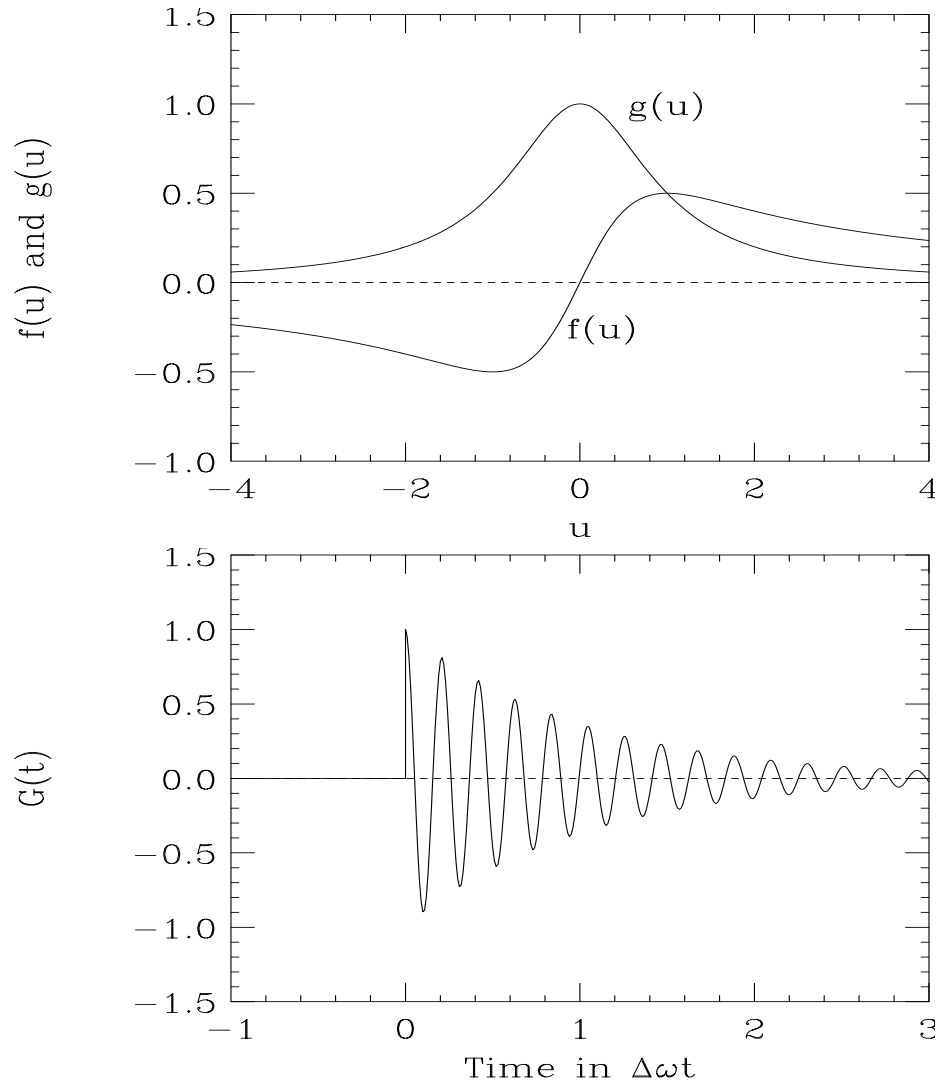


Figure 14.2: For Lorentz frequency distribution, plots showing beam transfer function $R(u) = f(u) + ig(u)$ (top) and shock response function $G(t)$ (bottom).

Table 14.1: Shock excitation function $G(t)$ and beam transfer function $R(u) = f(u) + ig(u)$ for various frequency distributions $\rho(\omega)$ with $v = (\omega_x - \omega)/\Delta\omega$.

Type	Frequency Distribution	Shock Response		Beam response function	
		Distribution	$G(t)$	$f(u)$	$g(u)$
Lorentz	$\frac{1}{\pi\Delta\omega}\frac{1}{v^2+1}$	$e^{-\Delta\omega t} \cos \omega_x t$	$\frac{u}{u^2+1}$	$\frac{1}{u^2+1}$	
rectangular	$\frac{1}{2\Delta\omega}H(1- v)$		$\frac{1}{2}\ln\left \frac{u+1}{u-1}\right $		$\frac{\pi}{2}H(1- u)$
parabolic	$\frac{3}{4\Delta\omega}(1-v^2)H(1- v)$		$\frac{3}{4}\left[(1-u^2)\ln\left \frac{u+1}{u-1}\right +2u\right]$		$\frac{3\pi}{4}(1-u^2)H(1- u)$
elliptical	$\frac{2}{\pi\Delta\omega}\sqrt{1-v^2}H(1- v)$		$2[u-\text{sgn}(u)\sqrt{1-u^2}H(1- u)]$		$2\sqrt{1-u^2}H(1- u)$
bi-Lorentz	$\frac{2}{\pi\Delta\omega}\frac{1}{(v^2+1)^2}$		$\frac{u(u^2+3)}{(u^2+1)^2}$		$\frac{2}{(u^2+1)^2}$
Gaussian	$\frac{1}{\sqrt{2\pi}\Delta\omega}e^{-v^2/2}$	$e^{-(\Delta\omega t)^2/2} \cos \omega_x t$	$\sqrt{\frac{2}{\pi}}e^{-u^2/2} \int_0^\infty \frac{dy}{y} e^{-y^2/2} \sinh uy$		$\sqrt{\frac{\pi}{2}}e^{-u^2/2}$

14.3 Landau Damping

After understanding the BTF and the SRF, let us come back to the transient response of a harmonic excitation; i.e., Eq. (14.4). The term proportional to $\sin \Omega t$ is driven in phase by the harmonic force, and the particle should be absorbing energy. Let us rewrite Eq. (14.3) in the approximation that the frequency distribution $\rho(\omega)$ is narrow around $\bar{\omega}$:

$$\langle x(t) \rangle = \frac{A \sin \bar{\omega} t}{\bar{\omega}} \int_{-\infty}^{\infty} d\omega \rho(\omega) \frac{\sin \frac{1}{2}(\omega - \Omega)t}{\omega - \Omega}. \quad (14.27)$$

Consider a component corresponding to the frequency ω , its envelope is

$$\text{Amplitude}(\omega) = \frac{A}{\bar{\omega}} \frac{\sin \frac{1}{2}(\omega - \Omega)t}{\omega - \Omega}. \quad (14.28)$$

This means that all particles having frequency ω are excited at $t = 0$, increase to a maximum of $A/[\bar{\omega}(\omega - \Omega)]$ at $t \approx \pi/(\omega - \Omega)$, and die down to zero again at $t = 2\pi/(\omega - \Omega)$. Thus, energy is gained but is given back to the system. For ω closer to Ω , the response amplitude rises to a larger amplitude and the energy is given back to the system at a later time. For those particles that have exactly frequency Ω , the amplitude grows linearly with time and the energy keeps on growing. This is called *Landau damping*. An illustration is shown in Fig. 14.3, where the solid curve shows a particle having exactly the same frequency as Ω and growing linearly, while the dashed curve shows a particle with frequency 95% of Ω decaying after about 10 oscillations. In other words, particles with ω far away from Ω get excited, but the energy is returned to those particles having ω close to Ω , which are still absorbing energy. As time increases, particles with frequencies closer to Ω give up their energies to particles with frequencies much closer to Ω . Thus, as time progresses, less and less particles are still absorbing energy. As $t \rightarrow \infty$, only particles with frequency exactly equal to Ω will be absorbing energy, and there are only very few particles doing this. So particles with frequencies very close to Ω will have their amplitudes keep on increasing. In practice, when these growing amplitudes hit the vacuum chamber, the process will stop. This sets the time limit for Landau damping to stop. The damping process starts when the amplitude of the first particle is damped and this time is $t \approx 2\pi/\Delta\omega$.

Let us study the energy in the system. The energy is proportional to the square of the amplitude. Therefore the energy of all the particles is

$$\mathcal{E} = \frac{NA^2}{\bar{\omega}^2} \int_{-\infty}^{\infty} d\omega \rho(\omega) \frac{\sin^2(\omega - \Omega)t/2}{(\omega - \Omega)^2}, \quad (14.29)$$

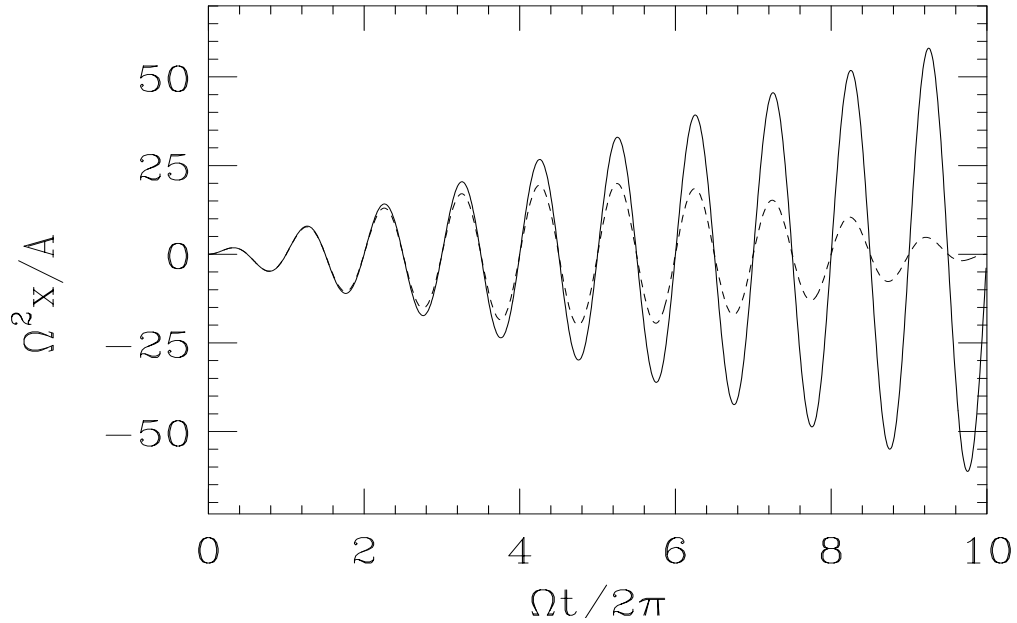


Figure 14.3: Solid: the response of a particle having exactly the same frequency Ω as the driving force grows linearly in time. Dashes: the response of a particle having frequency 95% of Ω gives up its energy after about 10 oscillations.

where N is the total number of beam particles in the system. We see that as time progresses the amplitude square,

$$\text{Amplitude}(\omega)^2 = \frac{\sin^2(\omega - \Omega)t/2}{(\omega - \Omega)^2}, \quad (14.30)$$

becomes sharper and sharper while its width shrinks. This verifies that energy is being transferred by the particles having frequencies far away from Ω to particles having frequencies closer to Ω . Since the square of the amplitude always has an area of $\pi t/2$, we have

$$\lim_{t \rightarrow \infty} \text{Amplitude}(\omega)^2 = \lim_{t \rightarrow \infty} \frac{\sin^2(\omega - \Omega)t/2}{(\omega - \Omega)^2} = \frac{\pi t}{2} \delta(\omega - \Omega). \quad (14.31)$$

Thus, at $t \rightarrow \infty$, the steady-state energy of the system is

$$\mathcal{E} = \frac{\pi}{2} \frac{NA^2}{\bar{\omega}^2} \rho(\Omega) t, \quad (14.32)$$

which increases linearly with time, and all this energy goes into those few particles having exactly the same frequency as Ω . However, we do see in the asymptotic solution of Eq. (14.8) that $\langle x(t) \rangle$ does not go to infinity. This is not a contradiction, because

even when a few particles have very large and still growing amplitudes, the centroid will not be affected.

In our study so far, the amplitude A of the driving force is independent of the system of particles. For an instability in a particle beam, the situation is slightly different. The driving force comes from the wake fields of the beam particles interacting with the discontinuities of the vacuum chamber, and usually has an amplitude proportional to the center displacement of the beam. When there is a kick to the beam that creates a center displacement $\langle x(0) \rangle$ or a center displacement velocity $\langle \dot{x}(0) \rangle$, a force with amplitude $A \propto \langle x(0) \rangle$ or $\langle \dot{x}(0) \rangle$ is generated and drives the whole system of particles with the coherent frequency Ω . Each frequency component of the beam will receive the amount of response according to Eq. (14.28). Now two things happen. First, the particles give up their excited energy gradually to those particles having frequencies extremely close to Ω , the frequency of the driving force, and the center of displacement approaches the BTF $R(u)$. Second, the center of displacement of the beam starts to decay according to the SRF $G(t)$. As $\langle x(t) \rangle$ decreases, the driving force decreases also. Finally, the disturbance goes away. This is how Landau damping takes place in a beam. In fact, this process starts whenever the disturbance is of infinitesimal magnitude. This implies that any disturbance will be damped as soon as it occurs. We say that there will be enough Landau damping to keep the beam stable. Notice that no frictional force has ever been introduced in the discussion. Thus, there is still conservation of energy in the presence of Landau damping, which merely redistributes energy from waves of one frequency to another.

In case the frequency spread $\Delta\omega$ is very very narrow, it will take $t \approx \pi/\Delta\omega$ for the first wave to surrender its energy to another that has frequency closer to Ω . This time will be very long. Before this time arrives, all frequency components continue to receive energy and $\langle x(t) \rangle$ increases and so will be the driving force. This is the picture of how an instability develops when the spread of frequency is not large enough to invoke Landau damping. However, the conservation of energy still holds. The energy that feeds the instability may be extracted from the longitudinal kinetic energy of the beam resulting in a slower speed, or from the rf system that replenish the beam energy.

14.4 Transverse Bunched Beam Instabilities

Consider a bunch with infinitesimal longitudinal length but with finite transverse extent. We call this a slice bunch. We want to study its transverse motion. The frequency of interest here is the betatron frequency ω_β which has the incoherent tune shift included. The equation of motion of a particle with transverse displacement y is

$$\frac{d^2y}{ds^2} + \frac{\omega_\beta^2}{v^2}y = \frac{\langle F(\bar{y}) \rangle}{\gamma m \beta^2 c^2}, \quad (14.33)$$

where $v = \beta c$ is the particle longitudinal velocity and \bar{y} is the average displacement of the bunch (sometimes we use the notation $\langle y \rangle$). This is the same as Eq. (4.4) in Chapter 4, but with the average wake force linear in y absorbed into ω_β^2 . The force on the right side of Eq. (14.33) is related to the transverse wake function,

$$\langle F(\bar{y}) \rangle = -\frac{e^2 N}{C} \sum_{k=1}^{\infty} \bar{y}(s - kC) W_1(kC) \quad (14.34)$$

where the summation is over previous turns. The negative sign shows that the force is opposing the displacement. Because this is a slice bunch, the wake force can only come from the passage of the same bunch in previous turns. Let us denote a collective excitation of the dipole moment D of the bunch center $\bar{y}(s)$ at the collective frequency Ω by the ansatz

$$\bar{y}(s) = D e^{-i\Omega s / (\beta c)}, \quad (14.35)$$

where $\Omega \rightarrow \Omega + i\epsilon$ is assumed. Expressing in terms of the transverse impedance Z_1^\perp , Eq. (14.33) becomes

$$\frac{d^2y}{ds^2} + \frac{\omega_\beta^2}{v^2}y = \frac{ie^2 ND}{\gamma m c C^2} \sum_{p=-\infty}^{\infty} Z_1^\perp(\Omega + p\omega_0) e^{-i\Omega s / (\beta c)}. \quad (14.36)$$

If we average the equation over all the particles in the bunch, we get the equation of motion of the center of the bunch, \bar{y} , and therefore the *coherent* betatron tune shift

$$(\Delta\omega_\beta)_{coh} = -\frac{ie^2 N \beta^2 c \mathcal{Z}_\perp}{2\omega_\beta \gamma m C^2}, \quad (14.37)$$

where we have introduced a short-hand form for the impedance

$$\mathcal{Z}_\perp = \sum_{p=-\infty}^{\infty} Z_1^\perp(\Omega + p\omega_0). \quad (14.38)$$

The imaginary part of the impedance contributes a real coherent tune shift. However, when $\Re \mathcal{Z}_\perp < 0$, the coherent tune shift has a positive imaginary part and the bunch will be unstable. If the driving impedance is narrow and covers less than one revolution harmonic centering roughly at $q\omega_0$, only two terms, $p = \pm q$, survive and Eq. (14.38) becomes

$$\Re \mathcal{Z}_\perp \approx \Re Z_1^\perp [(q + [\nu_\beta])\omega_0] - \Re Z_1^\perp [(q - [\nu_\beta])\omega_0], \quad (14.39)$$

where $[\nu_\beta]$ denotes the residual or decimal part of the betatron tune. The bunch will be stable/unstable if the impedance peaks above/below $q\omega_0$ giving an example of Robinson Instability in the transverse plane. The above summarizes what we have learned before without Landau damping.

Now let us introduce a distribution $\rho(\omega_\beta)$ for the betatron frequency among the beam particles. This distribution is centered at $\bar{\omega}_\beta$ with a spread $\Delta\omega$. The solution of Eq. (14.36) becomes

$$\begin{aligned} \bar{y}(s) &= \frac{ie^2 ND\beta^2 c \mathcal{Z}_\perp}{2\bar{\omega}_\beta \gamma m C^2} e^{-i\Omega s / (\beta c)} \int_{-\infty}^{\infty} d\omega_\beta \frac{\rho(\omega_\beta)}{\omega_\beta - \Omega - i\epsilon} \\ &= \frac{ie^2 ND\beta^2 c \mathcal{Z}_\perp}{2\bar{\omega}_\beta \Delta\omega \gamma m C^2} e^{-i\Omega s / (\beta c)} R(u), \end{aligned} \quad (14.40)$$

where the relation has been made to the BTF $R(u)$ with $u = (\bar{\omega}_\beta - \Omega) / \Delta\omega$. If the ansatz of Eq. (14.35) is employed for $\bar{y}(s)$, we obtain

$$\frac{ie^2 N \beta^2 c \mathcal{Z}_\perp}{2\bar{\omega}_\beta \Delta\omega \gamma m C^2} = \frac{1}{R(u)}, \quad (14.41)$$

or

$$-\frac{(\Delta\omega_\beta)_{\text{coh}}}{\Delta\omega} = \frac{1}{R(u)}. \quad (14.42)$$

This is an equation of the coherent frequency Ω . Given the impedance \mathcal{Z}_\perp , the left side is a constant and Ω can be solved. More practically, we start with a fixed $\Im \Omega$, and solve for the impedance \mathcal{Z} while varying $\Re \Omega$. The result plotted in the complex impedance plane will be a contour for a fixed growth rate. In particular, we are interested in the contour for the threshold when $\Im \Omega = 0+$. This will be exactly the same as the loci of $\Re u$ in the complex $1/R(u)$ plane with $\Im u = 0$. Such threshold contours are plotted in Fig. 14.4 for various distributions. Remember that instability is generated by $\Omega \rightarrow \Omega + i\epsilon$ with ϵ real and positive. This translates to $u \rightarrow u - i\epsilon$. For the Lorentz distribution,

$$\frac{1}{R(u)} = u - i, \quad (14.43)$$

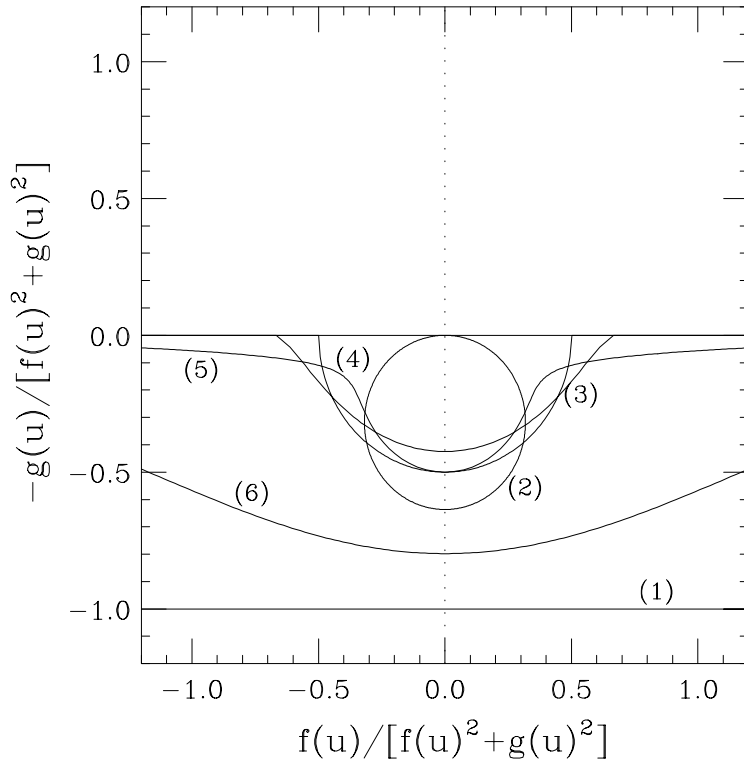


Figure 14.4: Threshold curves in the $1/R(u)$ plane, where in every case the stability region is to the top of the curve and the instability region to the bottom. (1) Lorentz distribution, (2) rectangular distribution (a circle touching the V -axis), (3) parabolic distribution, (4) elliptical distribution (part of the dashed circle centered at origin), (5) bi-Lorentz distribution, (6) Gaussian distribution.

and it will be unstable if

$$\frac{1}{R(\mathcal{R}e u - i\epsilon)} = \mathcal{R}e u - i(1 + \epsilon). \quad (14.44)$$

Therefore the unstable region is below $\mathcal{I}m R(u)^{-1} = -i$, while the stable region is above $\mathcal{I}m R(u)^{-1} = -1$. Since the various distributions have been introduced with all different definitions of frequency spread $\Delta\omega$, Fig. 14.4 is not a good plot for the comparison of various distributions. Instead, we would like to reference everything with respect to the HWHM frequency spread $\Delta\omega_{\text{HWHM}}$. Thus, we define a new variable x to replace u :

$$u = xS \quad \text{with} \quad S = \frac{\Delta\omega_{\text{HWHM}}}{\Delta\omega}. \quad (14.45)$$

Equation (14.42) is rewritten as

$$-\frac{(\Delta\omega_\beta)_{\text{coh}}}{\Delta\omega_{\text{HWHM}}} = \frac{1}{\hat{R}(x)} . \quad (14.46)$$

where

$$\hat{R}(x) = \hat{f}(x) + i\hat{g}(x) = [f(u) + ig(u)]S . \quad (14.47)$$

It is customary to call the left side of Eq. (14.46) $-i(U + iV)$, following the counterpart in longitudinal microwave threshold, or

$$U + iV = \frac{i}{\hat{R}(x)} = \frac{i\hat{f}(x) + \hat{g}(x)}{\hat{f}^2(x) + \hat{g}^2(x)} . \quad (14.48)$$

so that $U \propto -\mathcal{R}\mathcal{E}\mathcal{Z}_\perp$ and $V \propto -\mathcal{I}\mathcal{M}\mathcal{Z}_\perp$. The threshold curves for various frequency distributions are plotted in Fig. 14.5. Thus, whatever values of (U, V) lie to the left of the locus will be stable and whatever is on the right will be unstable. Without Landau damping, any $U > 0$, which implies betatron frequency shift with a positive imaginary part, will be unstable. Now, with Landau damping, the threshold has shifted to, for example, $U = 1$ for the Lorentz distribution. There is one point on the stability curve that is simple to obtain. It is the point at $x = 0$. There $\hat{f}(x) = 0$, so that $V = 0$ and $U = 1/\hat{g}(0)$. This point is important because it gives a rough idea of the threshold of instability. Similar to the Keil-Schnell stability circle for longitudinal microwave stability, we try to enclose the stability region in the U - V plane by a circle of radius $\frac{1}{\sqrt{3}}$, which is shown in Fig. 14.5 as a dashed circle. This threshold circle coincides with the semi-circle of the elliptical distribution. Thus, the stability limit can be written as

$$|(\Delta\omega_\beta)_{\text{coh}}| \lesssim \frac{1}{\sqrt{3}} (\Delta\omega_\beta)_{\text{HWHM}} F , \quad (14.49)$$

where F is a form factor depending on the distribution and is equal to unity for the elliptical distribution. Form factors for various distributions are tabulated in Table 14.2 (Exercise 14.3). Figure 14.5 shows how far a frequency distribution has its instability threshold deviated from the Keil-Schnell type circle of Eq. (14.49). We see that the deviation of F from unity or the threshold curve from the Keil-Schnell circle increases as the distribution goes from elliptical, parabolic, rectangular, Gaussian, bi-Lorentz, to Lorentz.

Thus, a betatron tune spread can provide Landau damping for instabilities driven by the discontinuities of the vacuum chamber, provided that the driving impedance is not

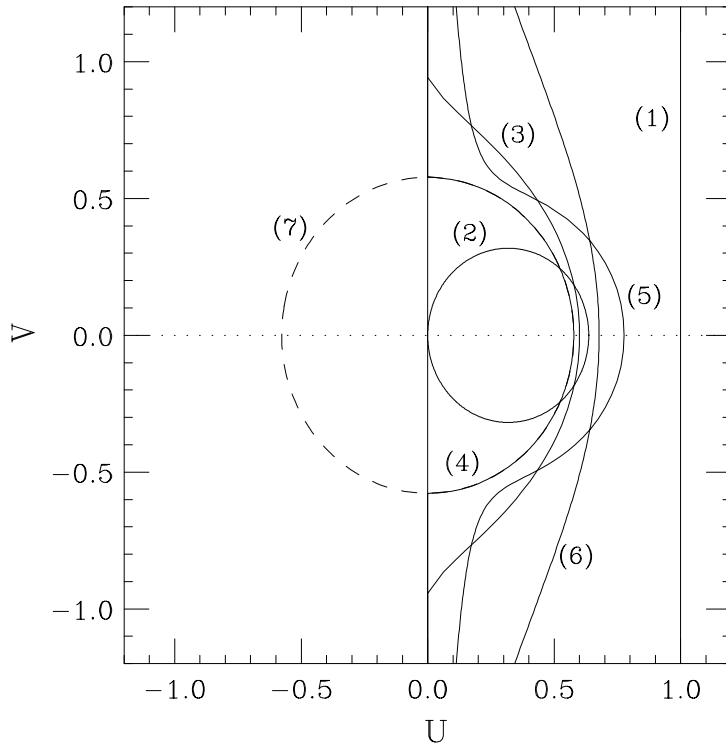


Figure 14.5: Threshold curves in the U - V plane plotted with reference to the HWHM frequency spread. In every case the stability region is to the left of the curve and the instability region to the right. (1) Lorentz distribution, (2) rectangular distribution (a circle touching the V -axis), (3) parabolic distribution, (4) elliptical distribution (part of the dashed circle centered at origin), (5) bi-Lorentz distribution, (6) Gaussian distribution. The Keil-Schnell type stability circle is depicted in dashes by (7).

too large. The transverse mode-mixing or mode-coupling instabilities that we studied in Chapter 13 have not had Landau damping included. However, mode-coupling instability involves the coherent shifting of a betatron spectral line by as much as the synchrotron frequency. In order for Landau damping to work, a betatron tune spread of the order of the synchrotron frequency will be necessary. This amount of tune spread is quite simple for proton machines where the synchrotron tune is of the order $\nu_s \sim 0.001$. This provides for another explanation why transverse mode-mixing instabilities are usually not seen in proton machines. On the other hand, the synchrotron tunes for electron machines are usually $\nu_s \sim 0.01$. A betatron tune spread of this size is considered too large. For this reason, transverse mode-mixing instabilities in electron machines are usually alleviated by reactive dampers instead.

Table 14.2: U -intercept and form factor F defined in Eq. (14.49) for various distributions.

Distribution	$g(0)^{-1}$	$S = \frac{(\Delta\omega_\beta)_{\text{HWHM}}}{\Delta\omega}$	U -intercept $\hat{g}(0)^{-1} = g(0)^{-1}S^{-1}$	Form factor $F = \sqrt{3}\hat{g}(0)^{-1}$
Lorentz	1	1	1	$\sqrt{3}$
rectangular	$\frac{2}{\pi}$	1	$\frac{2}{\pi}$	$\frac{2\sqrt{3}}{\pi}$
parabolic	$\frac{4}{3\pi}$	$\frac{1}{\sqrt{2}}$	$\frac{4\sqrt{2}}{3\pi}$	$\frac{4}{\pi}\sqrt{\frac{2}{3}}$
elliptical	$\frac{1}{2}$	$\frac{\sqrt{3}}{2}$	$\frac{1}{\sqrt{3}}$	1
bi-Lorentz	$\frac{1}{2}$	$\sqrt{\sqrt{2}-1}$	$\frac{1}{2\sqrt{\sqrt{2}-1}}$	$\frac{1}{2}\sqrt{\frac{3}{\sqrt{2}-1}}$
Gaussian	$\sqrt{\frac{2}{\pi}}$	$\sqrt{2\ln 2}$	$\frac{1}{\sqrt{\pi\ln 2}}$	$\sqrt{\frac{3}{\pi\ln 2}}$

14.5 Longitudinal Bunched Beam Instabilities

In a bunch, Landau damping proceeds through the spread in synchrotron frequency. Consider a short bunch consisting of N particles. The arrival time τ ahead of the synchronous particle is governed by the equation of motion

$$\begin{aligned} \frac{d^2\tau}{ds^2} + \frac{\omega_s^2}{v^2}\tau &= \frac{e^2N\eta}{v\beta^2E_0C} \sum_{k=-\infty}^{\infty} W'_0[kT_0 + \bar{\tau}(s - kC) - \bar{\tau}(s)] \\ &= \frac{e^2N\eta}{v\beta^2E_0C} \sum_{k=-\infty}^{\infty} [\bar{\tau}(s - kC) - \bar{\tau}(s)] W''_0(kT_0), \end{aligned} \quad (14.50)$$

where $v = \beta c$ is the particle velocity, and a Taylor's expansion has been made because the amplitude of synchrotron oscillation is much smaller than the circumference of the ring. Comparing with Eq. (9.42), we have ignored the wake field within the bunch because the bunch is very short, and only included the effects from the bunch passage

through a fixed location of the accelerator ring in previous turns. Introduce the ansatz

$$\bar{\tau}(s) = Be^{-i\Omega s/v} , \quad (14.51)$$

with Ω being the collective angular frequency to be determined. We next go to the frequency domain by introducing the longitudinal impedance Z_0^{\parallel} . Equation (14.50) can be written as

$$\frac{d^2\tau}{ds^2} + \frac{\omega_s^2}{v^2}\tau = -\frac{ie^2N\eta B\omega_0 Z_{\parallel}}{\beta^2 E_0 C^2} e^{-i\Omega s/v} , \quad (14.52)$$

where we have used and the short-hand notation

$$Z_{\parallel} = \sum_{p=-\infty}^{\infty} \left[\left(p + \frac{\Omega}{\omega_0} \right) Z_0^{\parallel}(p\omega_0 + \Omega) - p Z_0^{\parallel}(p\omega_0) \right] . \quad (14.53)$$

Averaging Eq. (14.52) over all the particles in the bunch, we obtain the equation of motion for the center of the bunch, and therefore the *coherent* synchrotron frequency shift

$$(\Delta\omega_s)_{\text{coh}} = \Omega - \omega_s = \frac{ie^2 N \omega_0 c^2 \eta Z_{\parallel}}{2\omega_s E_0 C^2} . \quad (14.54)$$

If the impedance is a narrow resonance of centered at ω_r near $q\omega$, only two terms contributes to $\Re Z_{\parallel}$:

$$\Re Z_{\parallel} \approx \frac{\omega_r}{\omega_0} [\Re Z_0^{\parallel}(\Omega + p\omega_0) - \Re Z_0^{\parallel}(p\omega_0 - \Omega)] , \quad (14.55)$$

where the coherent frequency Ω is close to the synchrotron frequency ω_s . Above transition ($\eta > 0$), this leads to stability/instability if the resonance peak leans towards the lower/upper synchrotron sideband, in agreement with Robinson stability criterion. So far no Landau damping has been included.

Suppose that the particles in the bunch has a distribution $\rho(\omega_s)$ in synchrotron frequency, centering at $\bar{\omega}_s$ with spread $\Delta\omega_s$. We solve for $\tau(s)$ in Eq. (14.52). Then integrate with the distribution to get

$$\bar{\tau}(s) = -\frac{ie^2 N \eta B \omega_0 c^2 Z_{\parallel}}{2\bar{\omega}_s E_0 C^2} e^{-i\Omega s/v} \int d\omega_s \frac{\rho(\omega_s)}{\omega_s - \Omega - i\epsilon} . \quad (14.56)$$

Substituting the ansatz of Eq. (14.51), self-consistency leads to the relation

$$-\frac{ie^2 N \omega_0 v^2 \eta Z_{\parallel}}{2\bar{\omega}_s \beta^2 E_0 C^2 \Delta\omega_s} = \frac{1}{R(u)} , \quad (14.57)$$

with $u = (\bar{\omega}_s - \Omega)/\Delta\omega_s$. Thus, from Eq. (14.54), we can again write

$$-\frac{(\Delta\omega_s)_{\text{coh}}}{\Delta\omega_s} = \frac{1}{R(u)} . \quad (14.58)$$

Therefore, we can define

$$U + iV = -i \frac{(\Delta\omega_s)_{\text{coh}}}{\Delta\omega_{s\text{HWHM}}} = \frac{i}{\hat{R}(x)} = \frac{\hat{g}(u) + i\hat{f}(x)}{\hat{f}^2(x) + \hat{g}^2(x)} \quad \text{with} \quad u = x \frac{\Delta\omega_{s\text{HWHM}}}{\Delta\omega_s} . \quad (14.59)$$

The stability threshold curve in the U - V plane is exactly the same as in the transverse bunch instability analyzed in the previous section. The Keil-Schnell like stability circle is

$$|(\Delta\omega_s)_{\text{coh}}| \lesssim \frac{1}{\sqrt{3}} (\Delta\omega_s)_{\text{HWHM}} F , \quad (14.60)$$

where $(\Delta\omega_s)_{\text{HWHM}}$ is the half-width-at-half-maximum of the synchrotron frequency spread, and the form factors F for various distribution are exactly the same as given in Table 14.2.

The above example is a demonstration of Landau damping in the presence of Robinson stability or instability. Therefore, even if the rf resonant peak is shifted in the wrong way so that the beam is Robinson unstable, there is still Landau damping from the spread in synchrotron frequency that may be able to stabilize the beam. However, this will not help much because the synchrotron frequency spread is usually not large enough unless there is a higher-harmonic rf system.

14.6 Transverse Unbunched Beam Instabilities

Consider an unbunched beam containing N particles oscillating in the transverse plane. The beam has a transverse dipole $D(s, t)$ density (per unit longitudinal length) which depends on the location s along the ring and also time t . This is in fact the perturbed part of the beam: i.e., with the stationary distribution subtracted. Assume the ansatz

$$D(s, t) = \frac{eN}{C} \langle y(s, t) \rangle = \frac{eN\Delta}{C} \exp \left(i \frac{n}{R} s - i\Omega t \right) . \quad (14.61)$$

where Δ is the maximum transverse deviation, n is a revolution harmonic, $R = C/(2\pi)$ is the ring mean radius, and Ω is the coherent frequency to be determined. This is a

snapshot view of the deviation of the perturbed beam and therefore must be a periodic function of the ring circumference. The ansatz in Eq. (14.61) assumes that the revolution harmonics are not related and each one can be studied independently.

A test particle at a fixed location s along the ring experiences a transverse force left by the dipole wave. At time t , this force is

$$\langle F_{\perp}(s, t) \rangle = -\frac{e}{C} \int_t^{\infty} v dt' W_1(vt' - vt) D(s, t') = \frac{iev\beta D(s, t) Z_1^{\perp}(\Omega)}{C}, \quad (14.62)$$

where $v = \beta c$ is the velocity of the beam particles. Since the impedance is at a fixed location, observing the dipole density of Eq. (14.61), the impedance at s will see the time variation only and sample only the frequency Ω of the dipole wave. The impedance will have no knowledge about the harmonic variation of the wave around the ring. However, as will be shown below, the solution of Ω does depend on the revolution harmonic.

For a particle inside the beam, the situation is different because it moves with the beam at velocity v . Consider the specific particle which passes the location S at time $t = 0$. Its location at a later time changes according to $s = S + vt$. Its transverse displacement $y(s, t)$ is governed by the equation of motion,

$$\frac{d^2y}{dt^2} + \omega_{\beta}^2 y = \frac{\langle F(S + vt, t) \rangle}{\gamma m} = \frac{ie^2 N c Z_1^{\perp}(\Omega) \Delta}{E_0 T_0^2} e^{inS/R - i(\Omega - n\omega_0)t}, \quad (14.63)$$

where $E_0 = \gamma mc^2$ is the energy of the beam particle, m is its mass and T_0 is revolution period. Although the impedance is still sampling the frequency Ω , the transverse motion of the particle is driven by a force at the frequency $\Omega - n\omega_0$, with $\omega_0 = v/R$ denoting the revolution angular frequency of the particle around the ring. It is important to point out that the time derivative in this equation is the *total* time derivative, because we are studying the particle displacement while traveling with the particle longitudinally. That explains why we have substituted $s = S + vt$ in the exponent on the right hand side. In order to have a clearer picture, let us travel with the particle longitudinally and at the same time count the number of transverse oscillations the particle makes in a revolution turn. The result is the incoherent tune of the particle ν_{β} , which equals $(\Omega - n\omega_0)/\omega_0$. On the other hand, from a beam-position monitor (BPM) at a fixed location monitoring the transverse motion of the particle, what it measures is the frequency Ω or the residual betatron tune (the fractional part of the betatron tune) of the particle.

This force-driven differential equation (14.63) can be solved easily, giving the solu-

tion

$$[\omega_\beta^2 - (\Omega - n\omega_0)^2] y(s, t) = \frac{ie^2 N c Z_1^\perp(\Omega) \Delta}{E_0 T_0^2} e^{inS/R - i(\Omega - n\omega_0)t}. \quad (14.64)$$

Self-consistency requires $y(s, t) = \Delta e^{i(ns/R - \Omega t)}$, which cancels the exponential on both sides. For small perturbation, there are two solutions for the coherent frequency, $\Omega \approx n\omega_0 \pm \omega_\beta$. For a coasting beam, when we are talking about positive and negative revolution harmonics, we will arrive at the same physical conclusion when we choose either $n\omega_0 + \omega_\beta$ or $n\omega_0 - \omega_\beta$. This is because (1) the beam spectra of the two choices are related by symmetry and (2) $Z_1^\perp(\omega)$ has definite symmetry about $\omega = 0$. This reminds us of the similar situation when we studied synchrotron sidebands in Chapter 7. However, one must be aware that for a bunch beam, there will be synchrotron sidebands around the betatron line and the beam spectrum will no longer possess this property. With the convention in Fig. 10.1 or Eq. (10.17), we need to choose the positive sign, or there is only upper betatron sidebands. This leads us to the coherence betatron tune shift of the beam

$$(\Delta\omega_\beta)_{coh} = \Omega - (n\omega_0 + \omega_\beta) \approx -\frac{ie^2 N c}{2\omega_\beta E_0 T_0^2} Z_1^\perp(n\omega_0 + \omega_\beta). \quad (14.65)$$

The imaginary part of the transverse impedance provides a true betatron tune shift. The real part, $\Re Z_1^\perp$, however, will lead to damping/instability if the frequency sampled by the impedance is positive/negative. Actually when $n\omega_0 + \omega_\beta = (n + \nu_\beta)\omega_0 < 0$, we write $n + \nu_\beta = -(|n| - \nu_\beta)$ so that the betatron line appears to be the lower sideband of the positive harmonic $|n|$. Thus, we have the conclusion that the beam is stable when a sharp resonance is driving at the upper sideband and unstable when it is driving at the lower sideband. Here, one must be careful that not all *upper* sidebands of a negative revolution harmonics will become *lower* sidebands in the language of positive frequency and hence can be unstable. This is because the betatron tune $\nu_\beta = \nu_\beta^I + [\nu_\beta]$ has an integer part ν_β^I and a residual (or decimal) part $[\nu_\beta]$. The *upper* sideband of the harmonic n can be unstable[†] only if $(n + \nu_\beta^I) < 0$.

To introduce Landau damping, let us allow a distribution $\rho(\omega_\beta)$ in betatron frequency among the beam particles. The distribution is centered at $\bar{\omega}_\beta$ with a narrow spread $\delta\omega_\beta$. From Eq. (14.65) we obtain the dispersion relation

$$1 = \frac{ie^2 N c Z_1^\perp(\Omega)}{2\bar{\omega}_\beta E_0 T_0^2} \int d\omega_\beta \frac{\rho(\omega_\beta)}{\omega_\beta - (\Omega - n\omega_0)}. \quad (14.66)$$

[†]There is no such complexity with the synchrotron sidebands, because the synchrotron tune does not have an integer part.

This is a dispersion relation because it gives the relation between the wave number n/R and frequency Ω . Or

$$-\frac{(\Delta\omega_\beta)_{\text{coh}}}{\Delta\omega_\beta} = \frac{1}{R(u)} , \quad (14.67)$$

where $u = (\bar{\omega}_\beta - \Omega - n\omega_0)/\Delta\omega_\beta$. This relation is exactly the same as Eq. (14.42). The only difference is the dependence of the coherent betatron tune shift on impedance is different. Thus, we have also the Keil-Schnell like stability threshold

$$(\Delta\omega_\beta)_{\text{coh}} \lesssim \frac{1}{\sqrt{3}} (\Delta\omega_\beta)_{\text{HWHM}} F . \quad (14.68)$$

Some comments are in order.

1. In the dispersion relation of Eq. (14.66), the solution gives, for small driving impedance, $\Omega \approx (n + \nu_\beta)\omega_0$. Depending on whether $n + \nu_\beta^I$ is positive or negative, this corresponds to two different dipole waves, one with a higher velocity is called the *fast wave*, while the one with a lower velocity is called the *slow wave*. As per discussion above, only the slow wave will lead to beam instability.
2. We have introduced a spread of the betatron frequency in order to arrive at Landau damping. In fact, the revolution frequency ω_0 in the denominator of the integrand of Eq. (14.66) also has a spread and can therefore contribute to Landau damping. Instead of the betatron frequency distribution $\rho(\omega_\beta)$, it will be more general to introduce the particle momentum distribution $\rho(\delta)$. We can develop the local betatron frequency up to the terms linear in the fractional momentum spread δ :

$$(n + \nu_\beta)\omega_0 = (n + \bar{\nu}_\beta)\bar{\omega}_0 + [\xi - (n + \bar{\nu}_\beta)\eta]\bar{\omega}_0\delta , \quad (14.69)$$

where ξ is the chromaticity and η the slip factor in the longitudinal phase space, while $\bar{\nu}_\beta$ and $\bar{\omega}_0$ represent the nominal betatron tune and revolution frequency. For the dangerous slow wave, let us denote $\hat{n} = -(n + \nu_\beta^I)$ where $\hat{n} > 0$. The above leads to

$$\Delta(n + \nu_\beta)\omega_0 = [\xi + (\hat{n} - [\bar{\nu}_\beta])\eta]\bar{\omega}_0\delta . \quad (14.70)$$

The integral in the dispersion relation becomes

$$\int d\omega_\beta \frac{\rho(\omega_\beta)}{\omega_\beta - (\Omega - n\omega_0)} \rightarrow \int d\delta \frac{\rho(\delta)}{[\xi + (\hat{n} - [\bar{\nu}_\beta])\eta]\bar{\omega}_0\delta - \hat{\Omega}} , \quad (14.71)$$

with $\hat{\Omega} = \Omega - (n + \bar{\nu}_\beta)\bar{\omega}_0$. One immediate conclusion is that when the chromaticity is negative and the ring is operating above transition ($\eta > 0$), it may happen for some \hat{n} that $\xi + (\hat{n} - [\bar{\nu}_\beta])\eta \approx 0$. When this happens there will not be any Landau damping at all. The same is true for a positive chromaticity below transition. The dispersion relation can be rewritten as

$$-\frac{(\Delta\omega_\beta)_{\text{coh}}}{[\xi + (\hat{n} - [\bar{\nu}_\beta])\eta]\bar{\omega}_0\Delta\delta} = \frac{1}{R(u)} , \quad (14.72)$$

where

$$u = \frac{1}{\Delta\delta} \left[\bar{\delta} - \frac{\hat{\Omega}}{[\xi + (\hat{n} - [\bar{\nu}_\beta])\eta]\bar{\omega}_0} \right] , \quad (14.73)$$

$\Delta\delta$ is the spread in momentum spread, and $\bar{\delta}$ (usually zero) is the momentum spread where the distribution $\rho(\delta)$ peaks at. The Keil-Schnell like stability threshold becomes

$$(\Delta\omega_\beta)_{\text{coh}} \lesssim \frac{1}{\sqrt{3}} |\xi + (\hat{n} - [\bar{\nu}_\beta])\eta| \bar{\omega}_0 (\Delta\delta)_{\text{HWHM}} F , \quad (14.74)$$

which, with the help of the coherent betatron tune shift in Eq. (14.65), can be rewritten as

$$|Z_1^\perp| \lesssim \frac{4\pi\omega_\beta E_0}{\sqrt{3}eI_0c} |\xi + (\hat{n} - [\bar{\nu}_\beta])\eta| (\Delta\delta)_{\text{HWHM}} F . \quad (14.75)$$

Zotter [8] was the first to derive this Keil-Schnell like transverse stability criterion for a coasting beam. His numerical coefficient on the right side is 8 which is very close to our value of $4\pi/\sqrt{3}$. Of course, the spread in betatron tune can also come from the betatron oscillation amplitude, and this spread should also be included in Eq. (14.69) for a more complete description.

14.7 Longitudinal Unbunched Beam Instabilities

For the last three categories, the transverse bunched beam instabilities, the transverse unbunched beam instabilities, and the longitudinal bunched beam instabilities, the treatment had been very similar. In each case, we first derived the tune shifts. Landau damping was next introduced by including the distribution of the tune. The dispersion relation derived was related to the BTF $R(u)$, from which the stable and unstable regions in the impedance phase space could be identified. The longitudinal instabilities of an unbunched beam is very much different, because there is no stabilizing oscillation

like the betatron motion or synchrotron motion. Thus, there is no betatron frequency or synchrotron frequency, from which a coherent frequency spread can be obtained to provide Landau damping. As a result, the derivation of the stability criterion will be very different from the last three categories. Here, the collective beam instability is the longitudinal microwave instability, and Landau damping is supplied by the spread in revolution frequency of the beam particles. The dispersion relation, Eq. (6.13), has been derived in Chapter 6 and the stability curves are shown in Fig. 6.4. Over there, the dispersion relation was derived employing the Vlasov equation which deals with the evolution of the particle distribution. We will show another derivation in this section making use of only the equations of motion without resorting to the Vlasov equation.

Let us start from the linear distribution $\lambda(s, t)$ which has a stationary part λ_0 and a perturbation $\Delta\hat{\lambda}$. The stationary part is just a uniform distribution

$$\lambda_0 = \frac{N}{C} , \quad (14.76)$$

where N is the total number of particles in the unbunched beam. For the perturbation, we postulate the ansatz

$$\Delta\lambda(s, t) = \Delta\hat{\lambda}e^{ins/R - i\Omega t} , \quad (14.77)$$

where $\Delta\hat{\lambda}$ represents the maximum modulation of the longitudinal density and is assumed to be small, and the harmonic $n = 0$ is excluded because of charge conservation. A snapshot view at a specific time will show the n -fold modulation of the linear density.

For a test particle at the fixed location s , the average longitudinal force experienced from the longitudinal wave is

$$\langle F(s, t) \rangle = -\frac{e^2}{C} \int v dt' W'_0(vt - vt') \Delta\lambda(s, t') = -\frac{e^2 v Z_0^{\parallel}(\Omega)}{C} \Delta\lambda(s, t) , \quad (14.78)$$

where the impedance only samples the collective frequency Ω .

Next consider a particle moving with the beam. It passes the location S at time $t = 0$ and is at location $s = S + vt$ at later time t . The motion of a beam particle consists of its phase drift and energy drift in the longitudinal phase space. The particle's off-momentum spread $\delta(s, t)$ increases per unit time as a result of the wake force and is governed by

$$\frac{d\delta(s, t)}{dt} = -\frac{e^2 c^2}{CE} Z_0^{\parallel}(\Omega) \Delta\hat{\lambda} e^{ins/R - i\Omega t} . \quad (14.79)$$

while the rate of the phase drift is governed by

$$\frac{dz(s, t)}{dt} = -\eta v \delta(s, t) , \quad (14.80)$$

where η is the slip parameter and we have actually employed a distance drift $z(s, t)$ rather than a phase. Here,

$$\frac{d}{dt} = \frac{\partial}{\partial t} + \frac{ds}{dt} \frac{\partial}{\partial s} \quad (14.81)$$

is the *total* time derivative. Thus, in solving Eqs. (14.79) and (14.80), we must first make the substitution $s = S + vt$. The momentum-offset equation can be integrated readily to give

$$\delta(s, t) = \frac{e^2 c^2}{CE} Z_0^{\parallel}(\Omega) \Delta \hat{\lambda} \frac{e^{ins/R-i\Omega t}}{i(\Omega - n\omega_0)} . \quad (14.82)$$

Substituting the result into the phase-drift equation, we obtain by another integration

$$z(s, t) = -\frac{e^2 \eta c^2 v}{CE_0} Z_0^{\parallel}(\Omega) \Delta \hat{\lambda} \frac{e^{ins/R-i\Omega t}}{(\Omega - n\omega_0)^2} . \quad (14.83)$$

Notice that in the above solution we have kept only the contribution due to the wake field.

If we can relate the particle longitudinal displacement $z(s, t)$ to the longitudinal density perturbation $\Delta\lambda$, the loop will be closed in Eq. (14.83) and a dispersion relation will result. There is in fact such a relation from the equation of continuity. The particles in the original unperturbed volume from s to $s + \Delta s$ at time t are displaced into the new perturbed volume between $s + z(s, t)$ and $s + \Delta s + z(s + \Delta s, t)$ at time t in the presence of the wake force. The number of particles in each of the volumes is

$$\lambda_0 ds = [\lambda_0 + \Delta\lambda(s, t)] \left\{ [s + \Delta s + z(s + \Delta s, t)] - [s + z(s, t)] \right\} , \quad (14.84)$$

from which we obtain, for small Δs ,

$$\Delta\lambda(s, t) = -\lambda_0 \frac{\partial z}{\partial s} = \frac{ine I_0 \eta \omega_0^2 Z_0^{\parallel}(\Omega)}{2\pi \beta^2 E_0} \Delta \hat{\lambda} \frac{e^{ins/R-\Omega t}}{(\Omega - n\omega_0)^2} , \quad (14.85)$$

where we have introduced the average beam current $I_0 = eN\omega_0/(2\pi)$ with $\omega_0 = v/R$ being the angular revolution frequency. Self-consistency allow us to cancel $\Delta\lambda(s, t)$ on both sides. The growth rate of the longitudinal wave ω_G is given by the imaginary part of Ω , which can be readily obtained from Eq. (14.85),

$$\omega_G^2 = -\frac{ie I_0 Z_0^{\parallel}(\Omega) n \eta}{2\pi \beta^2 E_0} \omega_0^2 , \quad (14.86)$$

which is very similar to the definition of the synchrotron frequency, if we identify the rf voltage as $I_0 Z_0^{\parallel}$ and the rf harmonic as n . For this reason, the growth rate can be visualized as the synchrotron angular frequency inside a bucket created by the voltage the beam experiences from the impedance. We can draw the immediate condition that the longitudinal wave perturbation is stable above/below transition (\lessgtr) only if the impedance is purely inductive/capacitive.

Landau damping can now be introduced by allowing a spread in the revolution frequency inside the beam. Let $\rho(\omega_0)$ be the distribution in revolution frequency centering at $\bar{\omega}_0$ with a spread $\Delta\omega_0$. Multiplying both sides of Eq. (14.85) by $\rho(\omega_0)$ and integrating over $d\omega_0$, we obtain the dispersion relation

$$1 = \frac{ieI_0 Z_0^{\parallel}(\Omega)n\eta}{2\pi\beta^2 E_0} \int d\omega_0 \frac{\rho(\omega_0)}{(\Omega - n\omega_0 + i\epsilon)^2} . \quad (14.87)$$

The dispersion relation can be rewritten as

$$1 = \left[\frac{\omega_g^2}{n^2(\Delta\omega_0)^2} \right] \left[n(\Delta\omega_0)^2 \int d\omega_0 \frac{\rho'(\omega_0)}{n\omega_0 - \Omega - i\epsilon} \right] = \left[\frac{\omega_g^2}{n^2(\Delta\omega_0)^2} \right] R_{\parallel}(u) , \quad (14.88)$$

where an integration by part has been performed. The function R_{\parallel} on the right is defined as

$$R_{\parallel}(u) = f_{\parallel}(u) + ig_{\parallel}(u) = (\Delta\omega_0)^2 \left[\wp \int d\omega_0 \frac{\rho'(\omega_0)}{\omega_0 - \Omega/n} + i\pi\rho' \left(\frac{\Omega}{n} \right) \right] , \quad (14.89)$$

and

$$u = \frac{\bar{\omega}_0 - \Omega/n}{\Delta\omega_0} . \quad (14.90)$$

Usually one writes

$$V - iU = \frac{\omega_g^2}{n^2(\Delta\omega_0)^2} = \frac{f_{\parallel}(u) - ig_{\parallel}(u)}{f_{\parallel}^2(u) + g_{\parallel}^2(u)} , \quad (14.91)$$

so that $U \propto -\mathcal{Re} Z_0^{\parallel}$ and $V \propto -\mathcal{Im} Z_0^{\parallel}$. This will give the threshold and growth curves for longitudinal microwave instability in Chapter 6.

14.8 Beam Transfer Function and Impedance Measurements

Consider a coasting beam. In addition to the transverse wake, if we give an extra sinusoidal kick with harmonic n and frequency Ω , the equation of motion is

$$\ddot{y} + \omega_\beta^2 y = -2(\Delta\omega_\beta)_{\text{coh}}\omega_\beta \langle y \rangle + A e^{ins/R-i\Omega t}, \quad (14.92)$$

where the coherent betatron tune shift $(\Delta\omega_\beta)_{\text{coh}}$ is given by Eq. (14.37). For the particular solution, try the ansatz

$$\langle y(s, t) \rangle = B e^{ins/R-i\Omega t}. \quad (14.93)$$

As before, $s = S + vt$, and we obtain

$$y(s, t) = \frac{[-2(\Delta\omega_\beta)_{\text{coh}}\omega_\beta B + A] e^{ins/R-i\Omega t}}{\omega_\beta^2 - (n\omega_0 - \Omega)^2}. \quad (14.94)$$

Consistency requires

$$B \approx \frac{-2(\Delta\omega_\beta)_{\text{coh}}\omega_\beta B + A}{2\omega_\beta} \int d\omega \frac{\rho(\omega)}{\omega - (\Omega - n\omega_0)} = \frac{-2(\Delta\omega_\beta)_{\text{coh}}\omega_\beta B + A}{2\omega_\beta \Delta\omega} R(u), \quad (14.95)$$

and after rearranging,

$$\frac{A}{2\omega_\beta \Delta\omega B} = \frac{1}{R(u)} + \frac{(\Delta\omega_\beta)_{\text{coh}}}{\Delta\omega}. \quad (14.96)$$

In a measurement, the beam is kicked at a certain harmonic but with various frequencies ω and the response is measured in its amplitude and phase. If the beam is of very weak intensity, the coherent tune shift term can be neglected and one can therefore obtain the BTF $R(u)$. Next, the beam intensity is increased to such a large value that the beam is still stable. The measurement of the beam response will give a stability curve shifted by $(\Delta\omega_\beta)_{\text{coh}}/\Delta\omega$. From the shift one can infer the impedance Z_1^\perp of the vacuum chamber as illustrated in the left plot of Fig. 14.6

For the longitudinal BTF, we add a longitudinal kicking voltage per unit length, A with revolution harmonic n and frequency Ω . Then the longitudinal force seen by a particle changes from Eq. (14.78) to

$$\langle F(s, t) \rangle = -\frac{e^2}{C} \int v dt' W'_0(vt - vt') \Delta\lambda(s, t) \rho(\omega_0) + A e^{ins/R-i\Omega t}. \quad (14.97)$$

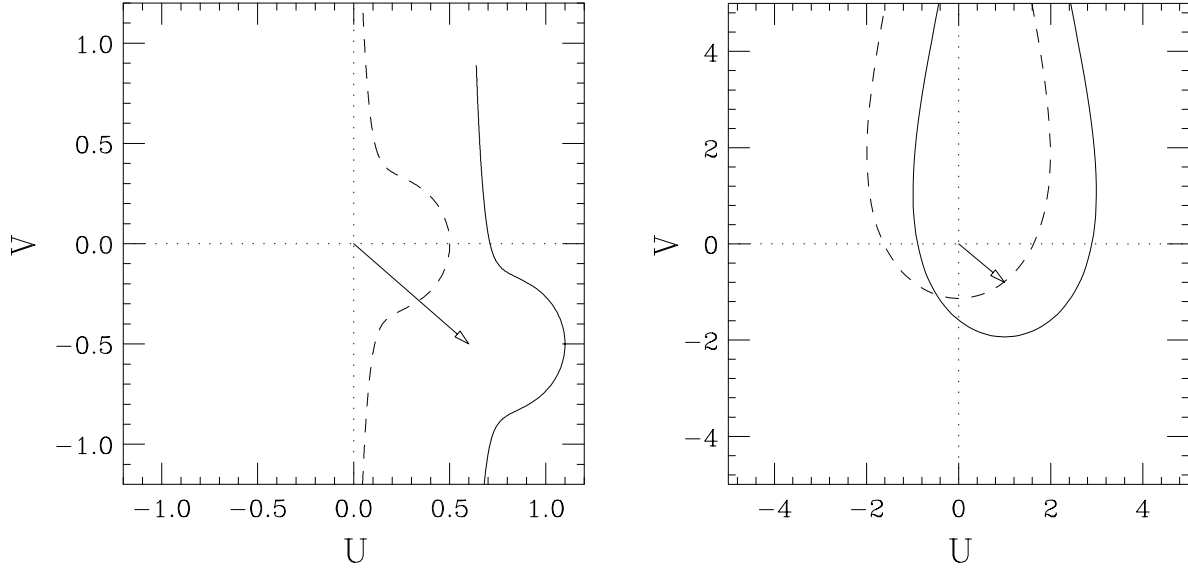


Figure 14.6: Left: Transverse beam response function of a coasting beam. Dash curve is for a very low-intensity beam, thus showing the threshold curve. But it is shifted to the solid curve at high intensity. The transverse impedance can be inferred from the shift indicated by the arrow. Right: Longitudinal beam response function of a coasting beam. The dashed curve is for low intensity and is shifted to the solid curve at high intensity. The arrow is proportional to the longitudinal impedance.

Assume the ansatz

$$\Delta\lambda(s, t) = Be^{ins/R - i\Omega t} . \quad (14.98)$$

Then the solution of the momentum spread and longitudinal drift become

$$\delta(s, t) = \frac{-e^2 c^2}{CE} Z_0^{\parallel}(\Omega) B + A \frac{e^{ins/R - i\Omega t}}{-i(\Omega - n\omega_0)} . \quad (14.99)$$

$$z(s, t) = \eta v \frac{-e^2 c^2}{CE} Z_0^{\parallel}(\Omega) B + A \frac{e^{ins/R - i\Omega t}}{(\Omega - n\omega_0)^2} . \quad (14.100)$$

Doing the same as Eqs. (14.85) and (14.87), we obtain

$$B = \left[\frac{\omega_g^2}{n^2(\Delta\omega)^2} B + \frac{i2\pi\eta v N}{n^2(\Delta\omega)^2 C^2} A \right] R_{\parallel}(u) . \quad (14.101)$$

Or,

$$\frac{i2\pi\eta v N}{n^2(\Delta\omega)^2 C^2} \frac{A}{B} = \frac{1}{R_{||}(u)} - \frac{\omega_g^2}{n^2(\Delta\omega)^2}. \quad (14.102)$$

Exactly in the same way as the transverse counterpart, for a very low-intensity beam, the response of the kick gives the threshold curve. For an intense beam, this threshold curve will be shifted. The amount and direction of shift will be proportional to the magnitude and phase of the longitudinal impedance. This is shown in the right plot of Fig. 14.6.

BTF and impedance measurements have been attempted by Spentzouris [9] at the Fermilab Accumulator Antiproton Storage Ring. The Accumulator stores antiprotons at $E_0 = 8.696$ GeV with an rms spread of $1-4 \times 10^{-4}$. The ring has a revolution frequency $f_0 = 628.955$ kHz and a slip parameter $\eta = 0.023$. There are 3 rf cavities in the ring, ARF2 and ARF3 are at rf harmonic $h = 2$. The third one ARF1 at rf harmonic 84 has been used as a kicker. The impedance of cavity ARF3 was the target for measurement. The hardware setup for the BTF measurement is shown in Fig. 14.7. The network

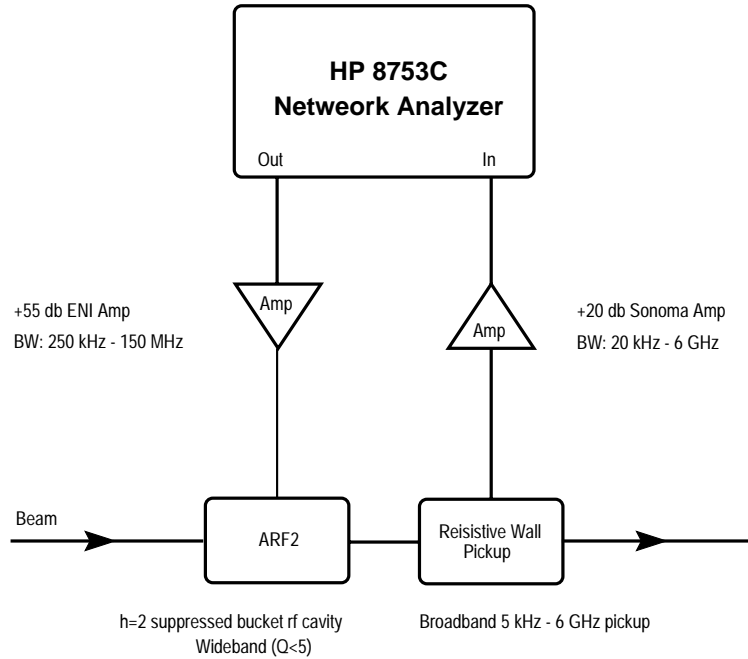


Figure 14.7: Block diagram of Accumulator transfer function measurement setup.

analyzer excited the beam longitudinally by applying a swept frequency of sinusoidal wave to the broadband cavity ARF2 (quality factor $Q < 5$). The resulting frequency

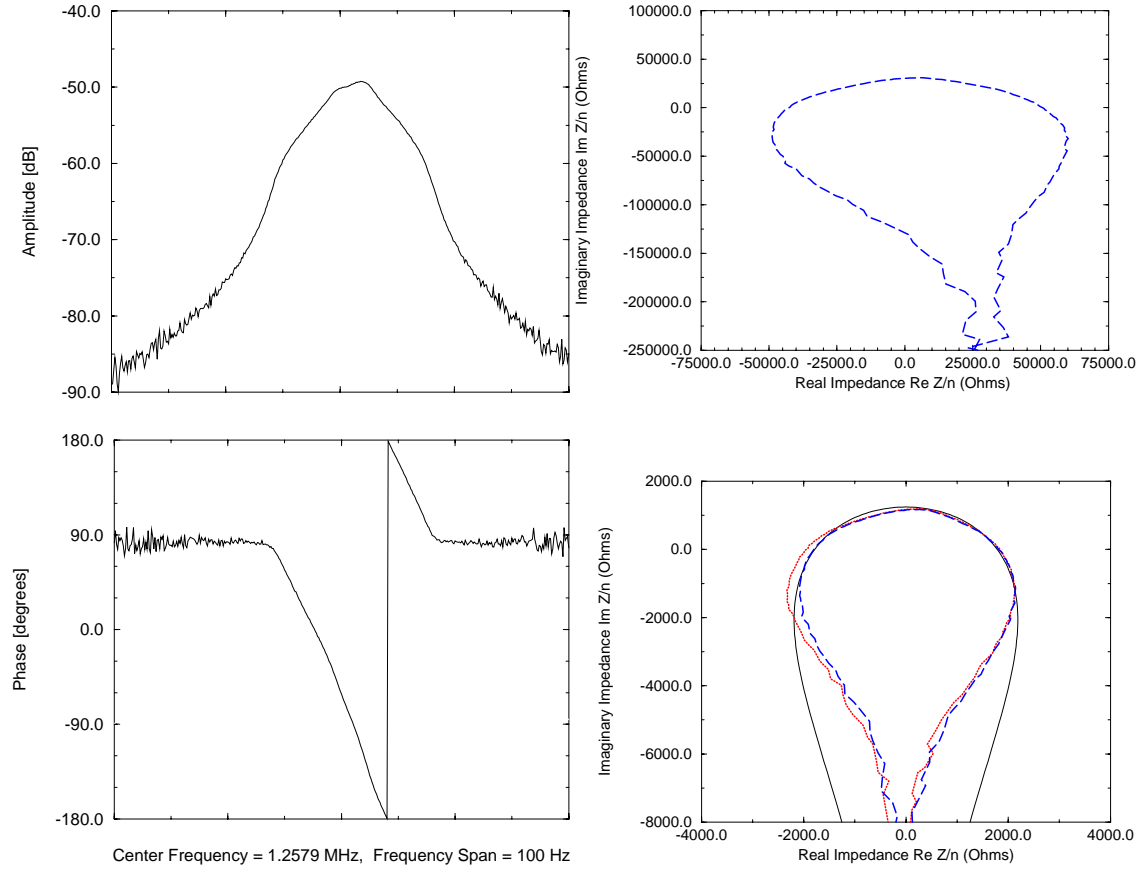


Figure 14.8: (color) Top left and bottom left: Amplitude and phase response of S_{21} measurement at $h = 2$ in the Accumulator with cavity ARF3 shorted mechanically. Frequency sweeps were injected at cavity ARF2. Beam parameters: intensity 68 mA and energy 8.696 GeV with rms spread 2.6 MeV. Network analyzer setup: 401 data points, sweep time 41 s, and resolution bandwidth 10 Hz. Top right: Un-calibrated stability threshold curve from data displayed at the left. Bottom right: Same stability threshold curve (blue dashes) as in above, but fitted to the theoretical threshold curve (solid) after scaling and rotational corrections. Dotted red curve shows another set of measurement.

response of the beam picked up by a resistive wall monitor was directed to the return port of the analyzer.

Cavity ARF3 was first shorted mechanically and the signals of the beam response of the frequency sweep was monitored. A typical BTF measurement is shown in two left plots of Fig. 14.8, where the sweep was centered at $2f_0 = 1.25791$ MHz with a span of 100 Hz which was wide enough to encompass the frequency content of the beam.

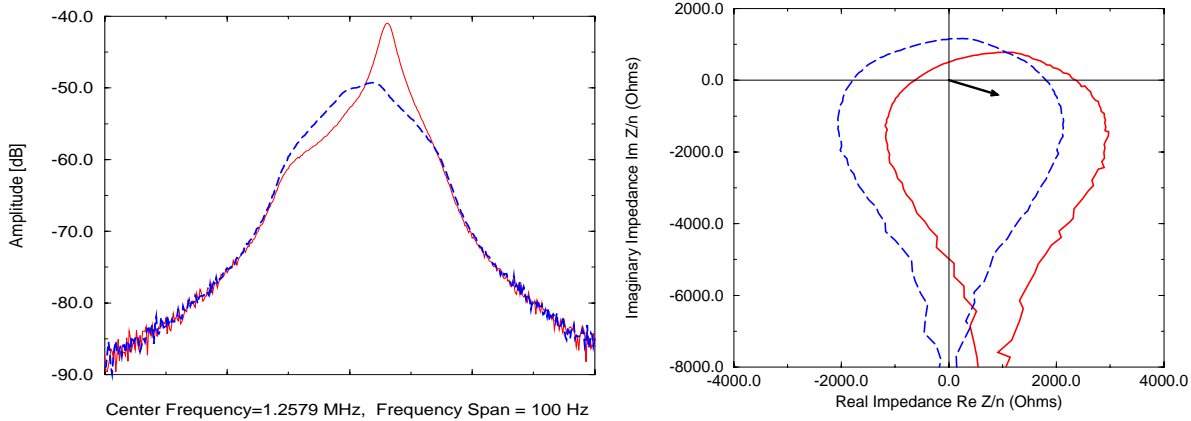


Figure 14.9: (color) Left: BTF measurements of the Accumulator with the ARF3 cavity shorted mechanically (blue-dashes) and with the mechanical short removed (solid red). Right: Stability threshold curves in the impedance complex plane with the ARF3 cavity shorted mechanically (blue-dashes) and with the mechanical shorts removed (solid red). The shift, indicated by the arrow, is the impedance per harmonic of the ARF3 cavity. The origin of the threshold curve with shorts out is shifted by approximately $(x, y) = (900, -390)$ Ω , which gives an ARF3 cavity impedance of $Z_0^{\parallel}/n = 490 \pm 110 \Omega$ with a phase angle of -23° .

Notice that the response monitored shows more uncertainty at both ends of the sweep because of the decreasing particle population at those outlying frequencies. The setup of the network analyzer were 401 data points, sweep time 41 s, and resolution bandwidth 10 Hz. Inverting the BTF gives the stability threshold curve of the Accumulator as depicted in top right plot of Fig. 14.8. A series of corrections were made to convert this uncalibrated threshold curve to the one in blue dashes in the bottom right plot. This includes scaling, rotation, and fitting to the central part of the theoretical threshold curve which is shown as solid in the same plot. The red dotted curve is the result of another set of sweep measurement.

The mechanical shorts in cavity ARF3 were removed and the BTF measurement repeated. The frequency response or the BTF is shown in solid red in the left plot of Fig 14.9. The original BTF with the ARF3 shorted (top left plot of Fig 14.8) is also shown in blue dashes for comparison. The BTF's are inverted and are displaced in the impedance complex plane in the right plot of Fig 14.9. The calibrated threshold curve is shifted from the one with the mechanical shorts (blue dashes) to the one without the mechanical shorts (red solid). The shift represented by the arrow is the impedance per unit harmonic of the ARF3 cavity: $Z_0^{\parallel}/n = 490 \pm 110 \Omega$ with a phase angle of -23° .

14.9 Exercises

- 14.1. A shock excitation is given to a bunch with a Lorentz frequency distribution $\rho(\omega)$ so that at $t = 0$ each particle has $\dot{x}(t) = \dot{x}_0$. Compute the response of the displacement of the center of the bunch $\langle x(t) \rangle$ and show that it does not decay to zero. Show that this is because $\rho(0) \neq 0$.
- 14.2. Derive the shock response function $G(t)$ and beam transfer function $R(u)$ for the various frequency distributions as listed in Table 14.1. Fill in those items that have been left blank.
- 14.3. Derive the U -intercept and the form factor F defined in Eq. (14.49) for various distributions as listed in Table 14.2.

Bibliography

- [1] L.D. Landau, J. Phys. USSR **10**, 25 (1946).
- [2] J.D. Jackson, Nuclear Energy Part C: Plasma physics **1**, 171 (1960).
- [3] V.K. Neil and A.M. Sessler, Rev. Sci. Instr. **6**, 429 (1965).
- [4] L.J.Laslett, V.K. Neil, and A.M. Sessler, Rev. Sci. Instr. **6**, 46 (1965).
- [5] H.G. Hereward, CERN Report 65-20 (1965).
- [6] A. Hofmann, *Frontiers of Part. Beams: Intensity Limitations*, Hilton Head Island, Lecture in Phys. **400**, Springer-Verlag, 1990, p.110.
- [7] A.W. Chao, *Physics of Collective Beam Instabilities in High Energy Accelerators*, Wiley Interscience, 1993, Chapter 5.
- [8] B. Zotter and F. Sacherer, *Transverse instabilities of Relativistic Particle Beams in Accelerator and Storage Rings*, Proceedings of the First Course of the International School of Particle Accelerators of the ‘Ettore Majorana’ Centre for Scientific Culture, Erice, 10-22 November 1976, p.176.
- [9] L.K. Spentzouris, *Coherent Nonlinear Longitudinal Phenomena in Unbunched Synchrotron Beams*, Phd Thesis, Northwestern University, 1996.

Chapter 15

BEAM BREAKUP

In a high-energy electron linac*, the relative longitudinal positions of the beam particles inside a bunch do not change. Thus, the tail particles are always affected by the head particles. We have shown that the longitudinal wake will cause the tail particles to lose energy. This loss, accumulated throughout the whole length of the linac, can be appreciable, leading to an undesirable spread in energy within the bunch. If the linac is the upstream part of a linear collider, this energy spread will have chromatic effect on the final focusing and eventually enlarging the spot size of the beam at the interaction point. We have also discussed how this energy spread can be corrected by placing the center of the bunch at an rf phase angle where the rf voltage gradient is equal and opposite to the energy gradient along the bunch.

Here, we would like to address the effect of the transverse wake potential. A small offset of the head particles will translate into a transverse force on the particles following. The deflections of the tail particles will accumulate along the linac. When the particles hit the vacuum chamber, they will be lost. Even if the aperture is large enough, the transverse emittance will be increased to an undesirable size. This phenomenon is called *beam breakup*. This is not a collective instability, however.

Recently, there is a lot of interest in isochronous or quasi-isochronous rings, where the spread in the slippage factor for all the particles in the bunch is very tiny, for example, $\Delta\eta \lesssim 10^{-6}$. In some of these rings, like the muon colliders where the beam is stored

*All proton linacs in existence are not ultra-relativistic. The highest energy is less than 1 GeV. Therefore synchrotron oscillations occur.

to about 1000 turns, the head and tail particles hardly exchange longitudinal position, and we are having a situation very similar to linacs. Problems of beam breakup will also show up in these rings. The beam breakup discussed in this chapter does not allow particles to exchange longitudinal positions or change their longitudinal positions. We therefore assume that their velocities are equal to the velocity of light.

15.1 Two-Particle Model

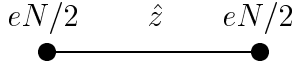


Figure 15.1: The two-particle model, where the bunch is represented by two macro-particles each carrying half the charge of the bunch separated by a distance \hat{z} .

Take the simple two-particle model in Fig. 15.1, by which the bunch is represented by two macro-particles of charge $\frac{1}{2}eN$ separated by a distance \hat{z} . The transverse displacements of the head, y_1 , and the tail, y_2 , satisfy

$$\frac{d^2y_1}{ds^2} + k_{\beta_1}^2 y_1 = 0 , \quad (15.1)$$

$$\frac{d^2y_2}{ds^2} + k_{\beta_2}^2 y_2 = -\frac{e^2 N W_1(\hat{z})}{2 L E_0} y_1 , \quad (15.2)$$

where E_0 is the energy of the beam particles and s is the longitudinal distance measured along the designed particle path, W_1 is the transverse wake function for one linac cavity of length L , and k_β is the betatron wave number. For an isochronous ring, L will be taken as the ring circumference $C = 2\pi R$ and

$$k_\beta = \frac{\nu_\beta}{R} = \frac{1}{\langle \beta \rangle} , \quad (15.3)$$

where ν_β is the betatron tune and $\langle \beta \rangle$ is the average betatron function. We can also define a betatron tune $\nu_\beta = L k_\beta / (2\pi)$ for a linac as the number of betatron oscillations a particle makes along the whole length L of the linac. This model has been giving a reasonably accurate description to the beam breakup mechanism for short electron bunches when \hat{z} is taken as the rms bunch length. The head makes simple harmonic motion $y_1(s) = y_{10} \cos k_\beta s$ according to Eq. (15.1), where y_{10} is its initial displacement.

If the tail is initially at $y_2 = y_{10}$ with $y'_2 = dy_2/ds = 0$, its displacement can be readily solved and the result is

$$y_2(s) = y_{10} \cos \bar{k}_\beta s \cos \frac{\Delta k_\beta s}{2} - y_{10} \sin \bar{k}_\beta s \left[\frac{\Delta k_\beta}{2} + \frac{e^2 N W_1(\hat{z})}{4 E_0 L k_\beta} \right] \left[\frac{\sin \Delta k_\beta s / 2}{\Delta k_\beta / 2} \right], \quad (15.4)$$

where $\bar{k}_\beta = \frac{1}{2}(k_{\beta_1} + k_{\beta_2})$ is the mean of the two betatron wave numbers of the head and tail. When the tune difference $\Delta k_\beta = k_{\beta_2} - k_{\beta_1}$ approaches zero, the tail is driven resonantly by the head and its displacement grows linearly with s :

$$y_2(s) = y_{10} \left[1 - \frac{e^2 N W_1(\hat{z})}{4 E_0 L k_\beta} \right] \sin k_{\beta_1} s + y_{10} \sin k_{\beta_1} s \cdot \frac{e^2 N W_1(\hat{z})}{4 E_0 L k_\beta} s. \quad (15.5)$$

In the length ℓ , the displacement of the tail will grow by Υ folds, where [2]

$$\Upsilon = -\frac{e^2 N W_1(\hat{z}) \ell}{4 E_0 L k_\beta} = -\frac{e^2 N W_1(\hat{z}) \langle \beta \rangle \ell}{4 E_0 L}, \quad (15.6)$$

and $W_1(\hat{z})$ is negative for small \hat{z} . In the above, we have written the growth in term of the average betatron function $\langle \beta \rangle$. This is because the transverse impedance initiates a kick y' of the beam and the size of the kicked displacement depends on the betatron function at the location of the impedance. This can be easily visualized from the transfer matrix.

For a broadband impedance, the transverse wake function at a distance z behind the source particle is, for $z > 0$,

$$W_1(z) = -\frac{\omega_r^2 Z_1^\perp}{Q \bar{\omega}} e^{-\alpha z/c} \sin \frac{\bar{\omega} z}{c}, \quad (15.7)$$

where Z_1^\perp is the transverse impedance at the angular resonant frequency ω_r , which is shifted to $\bar{\omega} = \sqrt{\omega_r^2 - \alpha^2}$ by the decay rate $\alpha = \omega_r/(2Q)$ of the wake with Q being the quality factor. Let us introduce the dimensionless variables

$$v = \frac{\omega_r \sigma_\ell}{c}, \quad t = \frac{z}{\sigma_\ell}, \quad \text{and} \quad \phi = vt \cos \phi_0 = \frac{\bar{\omega} z}{c}, \quad (15.8)$$

where the angle ϕ_0 is defined as

$$\cos \phi_0 = \sqrt{1 - \frac{1}{4Q^2}} \quad \text{or} \quad \sin \phi_0 = \frac{1}{2Q}, \quad (15.9)$$

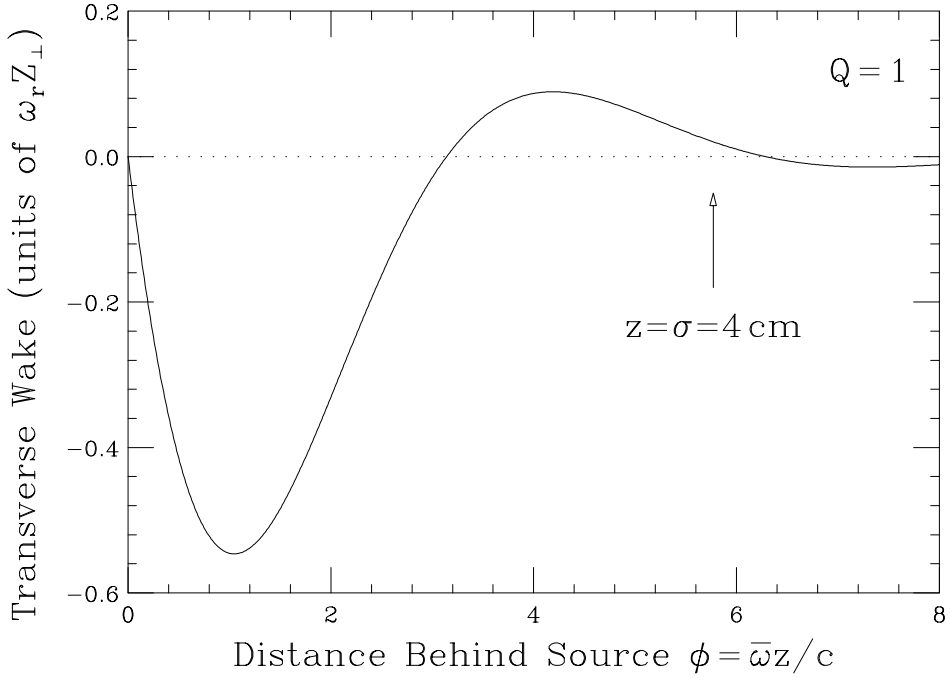


Figure 15.2: Transverse wake function for a broadband impedance with $Q = 1$ in units of $\omega_r Z_1^\perp$ as a function of $\phi = \bar{\omega}z/c$ behind the source. With resonant angular frequency $\omega_r = 50$ GHz, the position for $z = \sigma_\ell$ for the 4-cm bunch is marked, which is certainly outside the linear region and the 2-particle model will not apply.

assuming that $Q > \frac{1}{2}$. Then, the transverse wake in Eq. (15.7) can be rewritten as, for $\phi > 0$,

$$W_1(\phi) = -2\omega_r Z_1^\perp \tan \phi_0 \sin \phi e^{-\phi \tan \phi_0}, \quad (15.10)$$

The wake function decreases linearly from zero when $\phi = \bar{\omega}z/c \ll 1$ and reaches a minimum

$$W_1|_{\min} = -2\omega_r Z_1^\perp \tan \phi_0 \cos \phi_0 e^{-(\frac{\pi}{2} - \phi_0) \tan \phi_0} \quad (15.11)$$

at

$$\phi = \frac{\pi}{2} - \phi_0 \quad \text{or} \quad \frac{\alpha z}{c} = \left(\frac{\pi}{2} - \phi_0\right) \tan \phi_0. \quad (15.12)$$

After that it oscillates with amplitude decaying at the rate of $\alpha = \omega_r/(2Q)$, crossing zero at steps of $\Delta\phi = \bar{\omega}z/c = \pi$. This is illustrated in Fig. 15.2.

Obviously, the growth expression of Eq. (15.6) does not apply to all bunch lengths. For example, if \hat{z} just happens to fall on the first zero of $W_1(\hat{z})$, Eq. (15.6) says there is

no growth at all. However, particles in between will be deflected and they will certainly affect the tail particle. Thus, the criterion for Eq. (15.6) to hold is the variation of the wake function along the bunch must be smooth. In other words, we must be in the linear region of the wake function, or

$$\phi = \frac{\bar{\omega}z}{c} \ll 1 \quad \longrightarrow \quad \sigma_\ell \ll \frac{1}{2} \frac{\lambda}{2\pi}, \quad (15.13)$$

i.e., the rms bunch length must be less than half the reduced wavelength λ of the resonant impedance. As an example, if the broadband impedance with $Q \sim 1$ has resonant frequency 7.96 GHz ($\omega_r = 50$ GHz), the two-particle model works only when the rms bunch length $\sigma_\ell \ll 3$ mm. Therefore, the model cannot be applied to the usual proton bunches. For the 50 GeV on 50 GeV muon collider, the muon bunches have an rms length of 4 cm, and will not be able to fit into this model also.

15.2 Long Bunch

For a bunch with linear density $\rho(z)$, the transverse motion $y(z, s)$ at a distance z behind the bunch center and at position s along the linac is given by

$$\frac{d^2y(z, s)}{ds^2} + k_\beta^2 y(z, s) = -\frac{e^2 N}{LE_0} \int_{-\infty}^z dz' \rho(z') W_1(z - z') y(z', s). \quad (15.14)$$

This equation can be solved first by letting $y(z, s)$ be a free oscillation on the right-hand side and solving for the displacement $y(z, s)$ on the left-hand side. Then, iterations are made until the solution becomes stable. Therefore, when Υ is large, the growth will be proportional to powers of Υ and even exponential in Υ . Thus, $\langle \beta \rangle Z_1^\perp$, ω_r , as well as Q can be very sensitive to the growth.

Simulations have been performed for the 4-cm and 13-cm muon bunches in a quasi-isochronous collider ring, with a betatron tune $\nu_\beta \sim 6.24$, interacting with a broadband impedance with $Q = 1$ and $Z_1^\perp = 0.1$ MΩ/m at the angular resonant frequency $\omega_r = 50$ GHz. Initially, a bunch is populated with a vertical Gaussian spread of $\sigma_y = 3$ mm and $y' = 0$ for all particles. There is no offset for the center of the bunch. Ten thousand macro-particles are used to represent the bunch containing 4×10^{12} beam particles. The half-triangular bin size is 15 ps (or 0.45 cm). In Fig. 15.3 we show the total growth of the *normalized* beam size $\sigma_y \equiv \langle y^2 + (\langle \beta \rangle y')^2 \rangle^{1/2}$ relative to the initial beam size up to

1000 turns for various values of $\langle\beta\rangle$, respectively, for the 13-cm and 4-cm bunches. The turn-by-turn decay of the muons has been taken into account. We see that the beam size grows very much faster for larger betatron function. Also the growths for the 4-cm bunch are much larger than those for the 13-cm bunch because the linear charge density of the former is larger.

15.2.1 Balakin-Novokhatsky-Smirnov Damping

Kim, Wurtele, and Sessler [2] suggested to suppress the growth of the transverse beam breakup by a small tune spread in the beam, coming either through chromaticity, amplitude dependency, or beam-beam interaction. This is because a beam particle will be resonantly driven by only a small number of particles in front that have the same betatron tune. This is a form of Balakin-Novokhatsky-Smirnov (BNS) damping suggested in 1983 [3].

To implement this, we add a detuning term

$$\Delta\nu_{\beta_i} = a[y_i^2 + (\langle\beta\rangle y'_i)^2] \quad (15.15)$$

to the i th particle, as if it is contributed by an octupole or sextupole. In Fig. 15.4, we plot the growths of the normalized beam size relative to the initial beam size with various rms tune spreads $\sigma_{\nu_\beta} = a(\sigma_y^2 + (\langle\beta\rangle\sigma_{y'})^2)$. Here, an average betatron function of $\langle\beta\rangle = 20$ m has been used. This is because BPMs, which contribute significantly to the transverse impedance, are usually installed at locations where the betatron function is large. We see in the top plot that to damp the growth of the 13-cm bunch to less than 1%, we need an rms tune spread of $\sigma_{\nu_\beta} = 0.0008$ or a total tune spread of $\Delta\nu_\beta = 3\sigma_{\nu_\beta} = 0.0024$. On the other hand, to damp the growth of the 4-cm bunch to less than 1%, we need (lower plot) an rms tune spread of $\sigma_{\nu_\beta} = 0.006$ or a total tune spread of $\Delta\nu_\beta = 3\sigma_{\nu_\beta} = 0.018$. We also see a saturation of the emittance growth for the 4-cm bunch. However, if the transverse impedance is larger, the average betatron function is larger, the resonant frequency is larger, or the quality factor is smaller, this required tune spread may become too large to be acceptable. This is because a large amplitude-dependent tune spread can lead to reduction of the dynamical aperture of the collider ring.

For the lattice of the muon collider ring designed by Trbojevic and Ng [1], in order to allow for a large enough momentum aperture, the amplitude-dependent tune shifts

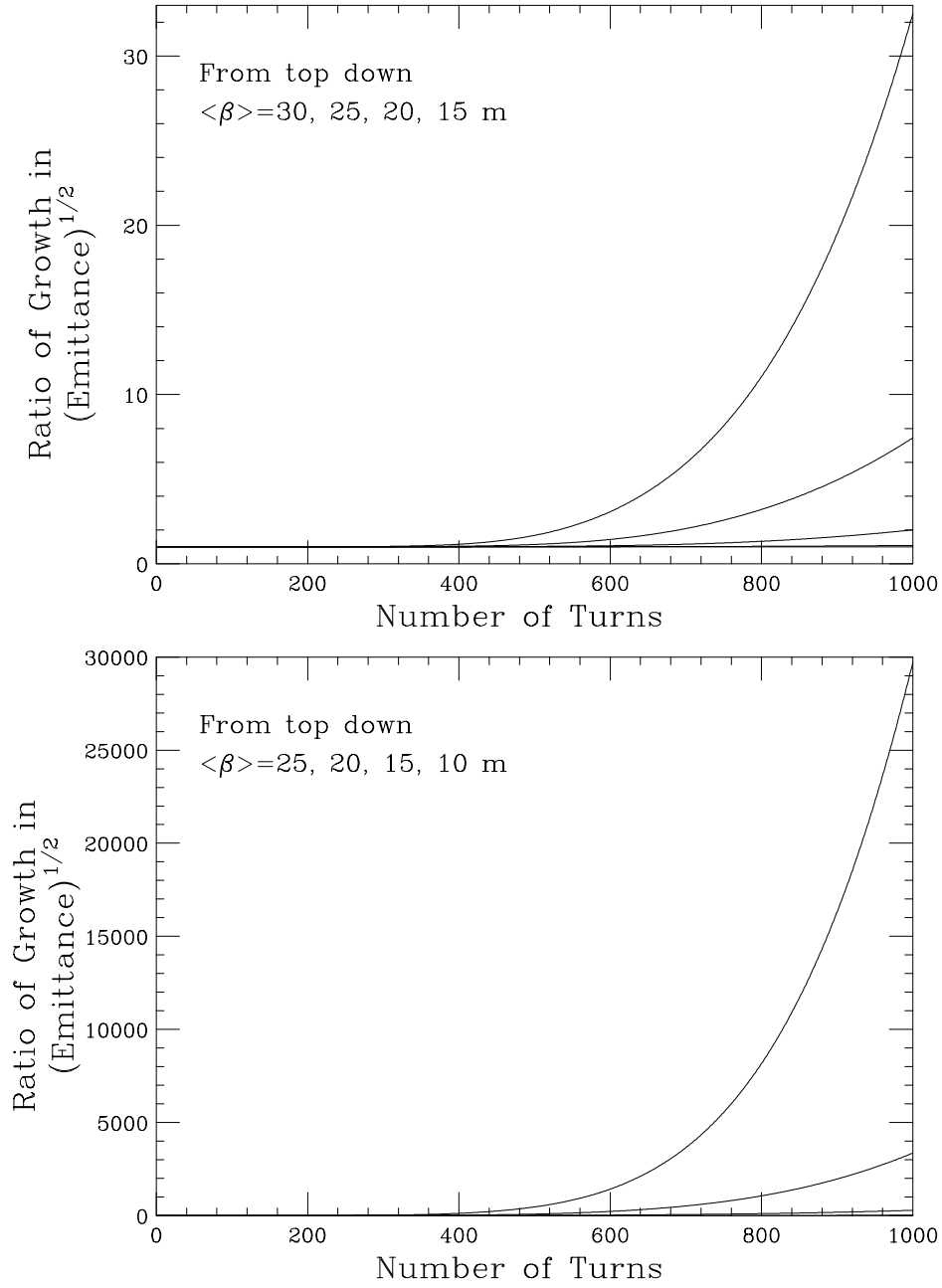


Figure 15.3: Beam-breakup growth for 1000 turns of a muon bunch interacting with a broadband impedance of $Q = 1$, $Z_1^\perp = 0.1 \text{ M}\Omega/\text{m}$ at the angular resonant frequency of $\omega_r = 50 \text{ GHz}$. Top: rms 13 cm bunch has total growths of 32.50, 7.4, 2.0, 1.09, 1.006, respectively for $\langle\beta\rangle = 30, 25, 20, 15, 10$ m. Bottom: rms 4 cm bunch has total growths of 29713, 3361, 287, 16.2, respectively for $\langle\beta\rangle = 25, 20, 15, 10$ m.

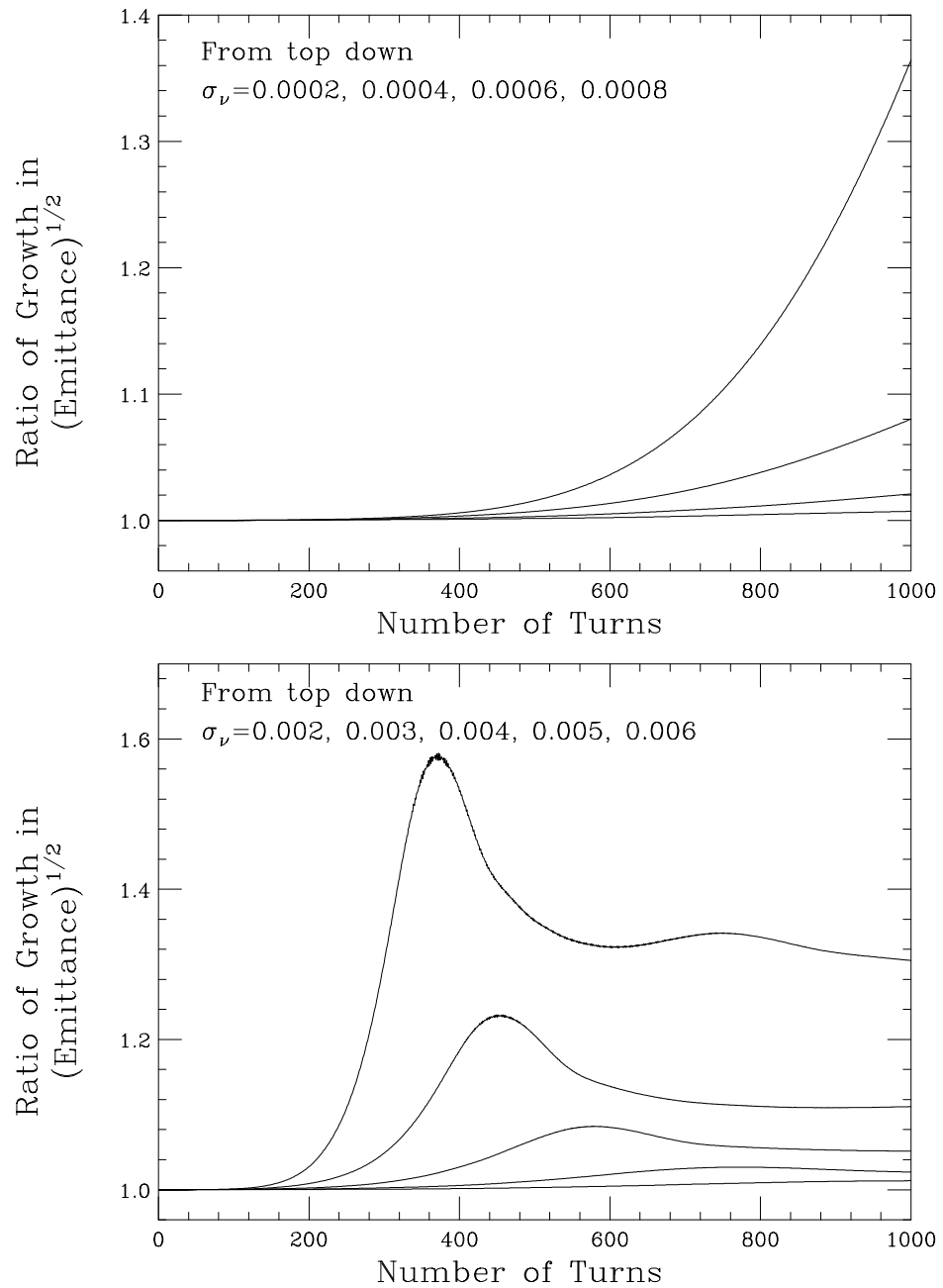


Figure 15.4: Total growth in 1000 turns in the presence of an amplitude dependent tune shift, such as provided by an octupole. An average betatron function of $\langle \beta \rangle = 20$ m has been assumed. Top: growths of the rms 13 cm bunch are 1.36, 1.08, 1.02, 1.007, respectively for rms tune spread of $\sigma_{\nu_\beta} = 0.0002, 0.0004, 0.0006, 0.0008$. Bottom: growths of the rms 4 cm bunch are 1.58, 1.23, 1.08, 1.03, 1.012, respectively for rms tune spread of $\sigma_{\nu_\beta} = 0.002, 0.003, 0.004, 0.005, 0.006$.

are

$$\begin{aligned}\nu_{\beta x} &= 8.126 - 100\epsilon_x - 4140\epsilon_y \\ \nu_{\beta y} &= 6.240 - 4140\epsilon_x - 50.6\epsilon_y\end{aligned}\quad (15.16)$$

for the on-momentum particles, where the unnormalized emittances ϵ_x and ϵ_y are measured in πm . For the 4-cm bunch, the normalized rms emittance is $\epsilon_{\text{Nrms}} = 85 \times 10^{-6} \pi\text{m}$. Since the muon energy is 50 GeV, the unnormalized rms emittance is $\epsilon_{\text{rms}} = 1.80 \times 10^{-7} \pi\text{m}$, and becomes $1.62 \times 10^{-6} \pi\text{m}$ when 3σ are taken. Thus, the allowable tune spread for the on-momentum particles is $\Delta\nu_\beta = 4140\epsilon_y = 0.0067$. Tune spreads larger than this will lead to much larger tune spreads for the off-momentum particles, thus reducing the momentum aperture of the collider ring. For 4-cm bunch, to damp beam breakup to about 1% when $Z_1^\perp = 0.1 \text{ M}\Omega/\text{m}$ and $\langle\beta\rangle = 20 \text{ m}$, one needs $\Delta\nu_\beta = 0.018$. However, we do not know exactly what $\langle\beta\rangle$ and Z_1^\perp are. Simulations show that if $\langle\beta\rangle Z_1^\perp$ becomes doubled, 2.5 times, 5 times, and 10 times, the tune spreads required jump to, respectively, $\sim 0.054, 0.073, 0.18$, and 0.54 . Thus, it appears that pure tune spread may be able to damp beam breakup for the 13-cm bunch but may not work for the 4-cm bunch. Although tune spreads due to chromaticity and beam-beam interaction will also damp beam breakup, it is unclear how much the momentum aperture will be reduced due to these tune spreads.

15.2.2 Autophasing

The transverse beam breakup can be cured by varying the betatron tune of the beam particles along the bunch, so that resonant growth can be avoided. In the two-particle model, if we allow

$$\Delta k_\beta = -\frac{e^2 N W_1(\hat{z})}{2 L E_0 \bar{k}_\beta} \quad (15.17)$$

in Eq. (15.4), it appears that the linear increasing term will be eliminated and the tail particle motion

$$y_2(s) = y_{10} \cos \bar{k}s \cos \frac{\Delta ks}{2} \quad (15.18)$$

will be bounded. However, if we set

$$\Delta k_\beta = -\frac{e^2 N W_1(\hat{z})}{4 L E_0 \bar{k}_\beta} = \frac{\Upsilon(\ell)}{\ell} \quad (15.19)$$

instead, the tail particle motion becomes

$$y_2(s) = y_{10} \left[\cos \bar{k}s \cos \frac{\Delta k_\beta s}{2} - \sin \bar{k}s \sin \frac{\Delta k_\beta s}{2} \right] = y_{10} \cos k_1 s , \quad (15.20)$$

which is exactly the same as the head particle. Being in phase all the time, the tail cannot be driven by the head at all. This is another form of BNS damping known as *autophasing* [4]. Exactly the same result will evolve if we solve Eq. (15.2) directly by enforcing $y_2(s) = y_1(s) = y_{10} \cos k_1 s$. Thus autophasing implies

$$\frac{\Delta k_\beta}{k_\beta} = \frac{\Upsilon}{\bar{k}_\beta \ell} . \quad (15.21)$$

For a particle-distributed bunch, in order that all particles will perform betatron oscillation with the same frequency and same phase after the consideration of the perturbation of the transverse wake, special focusing force is required to compensate for the variation of unperturbed betatron tune along the bunch. With the linear distribution $\rho(z)$, the equations of motion of Eq. (15.2) in the two-particle model generalize to

$$\frac{d^2 y(z, s)}{ds^2} + [k_\beta + \Delta k_\beta(z)]^2 y(z, s) = -\frac{e^2 N}{LE_0} \int_{-\infty}^z dz' \rho(z') W_1(z - z') y(z', s) , \quad (15.22)$$

where $z > 0$ denotes the tail and $z < 0$ the head, or the bunch is traveling towards the left. We need to choose the compensation $\Delta k_\beta(z)$ along the bunch in such a way that the betatron oscillation amplitude

$$y(z, s) \sim \sin(k_\beta s + \varphi_0) \quad (15.23)$$

is independent of z , the position along the bunch, with φ_0 being some phase, because only in this way any particle will not be driven by a resonant force from any particle in front. The solution is then simply

$$2k_\beta \Delta k_\beta + \Delta k_\beta^2(z) = -\frac{e^2 N}{LE_0} \int_{-\infty}^z dz' \rho(z') W_1(z - z') , \quad (15.24)$$

or, for small compensation $\Delta k_\beta(z)$,

$$\frac{\Delta k_\beta(z)}{k_\beta} = -\frac{e^2 N R}{2LE_0 k_\beta^2} \int_{-\infty}^z dz' \rho(z') W_1(z - z') . \quad (15.25)$$

If the linear bunch distribution $\rho(z)$ is a Gaussian interacting with a broadband impedance, the integration can be performed exactly to give

$$\frac{\Delta k_\beta(z)}{k_\beta} = \frac{e^2 N}{2L E_0 k_\beta^2} \frac{\omega_r^2 Z_1^\perp}{2\bar{\omega}Q} e^{-z^2/(2\sigma_\ell^2)} \operatorname{Im} w \left[\frac{ve^{i\phi_0}}{\sqrt{2}} - \frac{iz}{\sqrt{2}\sigma_\ell} \right], \quad (15.26)$$

where

$$w(z) = e^{-z^2} \left[1 + \frac{2i}{\sqrt{\pi}} \int_0^z e^{t^2} dt \right]. \quad (15.27)$$

is the complex error function while $\sin \phi_0 = 1/(2Q)$ and $v = \omega_r \sigma_\ell / c$ as defined in Eqs. (15.8) and (15.9). For long bunches and high resonant frequency, or $v \gg Q$, the complex error function behaves as

$$w(z) = \frac{i}{\sqrt{\pi}z} + \mathcal{O}\left(\frac{1}{|z|^3}\right). \quad (15.28)$$

This is certainly satisfied by both the 4-cm and 13-cm muon bunches, where $v = 6.67$ and 21.7, respectively, but not by the short electron bunches. Let us first discuss the long muon bunches in a storage ring. For convenience, we convert the betatron number to betatron tune by $k_\beta = \nu_\beta/R$ and the length L to the ring circumference $C = 2\pi R$. Thus Δk_β , the shift in betatron wave number in a cavity length L , becomes $\Delta\nu_\beta/R$, where $\Delta\nu_\beta$ is the betatron tune shift in a turn. Then, the relative tune shift compensation in Eq. (15.26) can be simplified to

$$\frac{\Delta\nu_\beta(z)}{\nu_\beta} \approx \frac{e^2 N \omega_r Z_1^\perp R}{2(2\pi)^{3/2} \nu_\beta^2 Q v E_0} \left[1 + \frac{z}{vQ\sigma_\ell} \right] e^{-z^2/(2\sigma_\ell^2)}. \quad (15.29)$$

This is the situation for the autophasing of the longer muon bunches, which is very different from the autophasing for the short electron bunches. The relative tune shift compensations required for the two long bunches are shown in the top plot of Fig. 15.5. Note that in Eq. (15.29), vQ controls the asymmetry of the tune shift compensation curve. When $vQ \rightarrow \infty$, there is no asymmetry and the compensation curve reduces to just a Gaussian, and, at the same time, $\Delta\nu_\beta/\nu_\beta$ decreases to zero. On the other hand, when $v \ll Q$ for short bunches or low broadband resonant frequency, the relative tune shift becomes rather linear as depicted by the 1.8 mm ($v = 0.3$) curve in the lower plot of Fig. 15.5. The curves for the 5.0 mm, 1.0 cm, and 4 cm bunch ($v = 0.83, 1.67$, and 6.67) are also shown for comparison. Note that as the bunch length gets shorter, the frequency components of the tune compensation become much lower. For a very short bunch, the compensation becomes nearly linear in the region of the bunch.

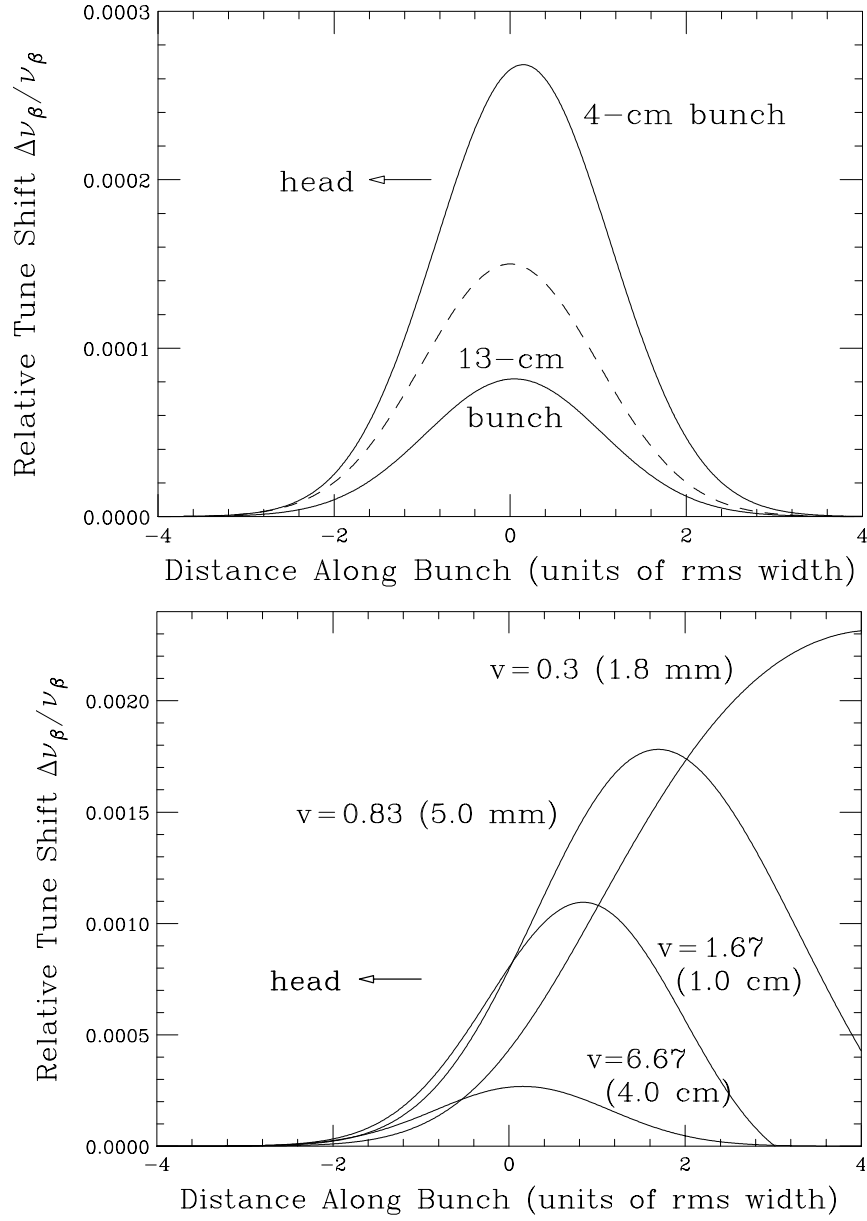


Figure 15.5: Relative tune shift autophasing compensation at distance z/σ_ℓ behind the bunch center (or bunch going to the left) to cure beam breakup. Impedance is broadband resonating at $\omega_r = 50$ GHz. Top: for the rms 4-cm and 13-cm bunches, where $v = \omega_r \sigma_\ell / c = 6.67$ and 21.7 respectively, with bunch profile plotted in dashes as a reference. Bottom: for short bunches, rms 1.8, 5.0, 10.0 mm, with $v = 0.3, 0.83, 1.67$, respectively. The curve for the 4-cm bunch is plotted as comparison. Note that when v is small, the compensation is of much lower frequencies.

To cure beam breakup with autophasing damping in an electron linac, the electron bunch is usually placed off the crest of the rf wave so that the head and tail of the bunch will acquire slightly different energies, and therefore slightly different betatron tunes through chromaticity. For muon bunches in the collider ring, however, this method cannot be used. If one insists on having autophasing, an rf quadrupole must be installed and pulsed according to the compensation curve for each bunch as the bunch is passing through it. The variation of a quadrupole field at such high frequencies is not possible at all. Another method is to install cavities that have dipole oscillations at these frequencies, which is not simple either. For this reason, autophasing for long bunches is not practical at all.

15.3 Linac

15.3.1 Adiabatic Damping

Let us come back to the short electron bunches in a linac. An expression was given in Eq. (15.6) for the deflection of the tail particle in the two-particle model. In a linac, the bunches are accelerated and the energy change of the beam particles cannot be neglected. The equations of motion of the head and tail macro-particles now become

$$\frac{1}{\gamma} \frac{d}{ds} \left(\gamma \frac{dy_1}{ds} \right) + k_\beta^2 y_1 = 0 , \quad (15.30)$$

$$\frac{1}{\gamma} \frac{d}{ds} \left(\gamma \frac{dy_2}{ds} \right) + k_\beta^2 y_2 = -\frac{e^2 N W_1(\hat{z})}{2L\gamma E_{\text{rest}}} y_1 , \quad (15.31)$$

where E_{rest} is the particle rest energy. The betatron wave number, which we have set to be the same for the two macro-particles, can have different dependency on energy. One way is to have k_β energy independent or the particle makes the same number of betatron oscillations per unit length along the linac. This is actually the operation of a synchrotron, where the quadrupole fields are ramped in the same way as the dipole field. If we further assume a constant acceleration

$$\gamma(s) = \gamma_i(1 + \alpha s) , \quad (15.32)$$

where γ_i is the initial gamma and α is a constant, the equation of motion of the head becomes

$$\frac{d}{du} \left(u \frac{dy_1}{du} \right) + \frac{k_\beta^2}{\alpha^2} u y_1 = 0 , \quad (15.33)$$

where $u = 1 + \alpha s$. Usually the acceleration gradient α is much slower than the betatron wave number k_β . For example, in the $L_0 = 3$ km SLAC linac where electrons are accelerated from $E_i = 1$ GeV to $E_f = 50$ GeV, $\alpha = 0.0163 \text{ m}^{-1}$, while the betatron wave number is $k_\beta = 0.06 \text{ m}^{-1}$. In that case, the solution is (Exercise 15.1)

$$y_1(s) = \frac{\hat{y}}{\sqrt{1 + \alpha s}} \cos k_\beta s , \quad (15.34)$$

which is obtained by letting $y_1 = A \cos k_\beta s$ with A a slowly varying function of u . In fact, Eq. (15.33) is the Bessel equation; Eq. (15.34) is just the asymptotic behavior of $y_1(s) = \hat{y} J_0[k_\beta(1 + \alpha s)/\alpha]$.

The equation of motion of the tail becomes

$$\frac{d}{du} \left(u \frac{dy_2}{du} \right) + \frac{k_\beta^2}{\alpha^2} u y_2 = -\frac{e^2 N W_1(\hat{z})}{2 L E_i \alpha^2} \frac{\hat{y}}{\sqrt{u}} \cos k_\beta s . \quad (15.35)$$

To obtain the particular solution, we try $y_2 = D \sin k_\beta s / \sqrt{u}$ with D a slowly varying function of u^\dagger . The final solution is

$$y_2(s) = \frac{\hat{y}}{\sqrt{1 + \alpha s}} \left[\cos k_\beta s - \frac{e^2 N W_1(\hat{z})}{4 L E_i \alpha k_\beta} \ln(1 + \alpha s) \sin k_\beta s \right] . \quad (15.36)$$

Noticing that $E_i \alpha \approx E_f / L_0$, the growth for the whole length L_0 of the linac is

$$\Upsilon = -\frac{e^2 N W_1(\hat{z}) L_0}{4 k_\beta E_f L} \ln \frac{E_f}{E_i} . \quad (15.37)$$

This is to be compared with Eq. (15.6), where we gain here a factor of

$$\mathcal{F} = \frac{E_i}{E_f} \ln \frac{E_f}{E_i} \quad (15.38)$$

For the SLAC linac, this factor is $\mathcal{F} = 1/12.8 = 0.0782$, meaning that the tail will be deflected by 12.8 less with the acceleration. This effect is called *adiabatic damping*.

15.3.2 Detuned Cavity Structure

The dipole wake function of a cavity structure is given by

$$W_1(z) = -2 \sum_n K_n \sin \frac{2\pi\nu_n z}{c} e^{-\pi\nu_v z/(cQ_n)} \quad z > 0 , \quad (15.39)$$

[†]One can also try $y_2 = D \sin k_\beta s$ with D a slowly varying function of u .

where K_n , ν_n , and Q_n are the kick factor, resonant frequency, and quality factor of the n th eigenmode in the structure, and the particle velocity has been set to c . The kick factor is defined as

$$K_n = \frac{\pi R_n \nu_n}{Q_n}, \quad (15.40)$$

with R_n being the dipole shunt impedance of the n th mode. To reduce beam break up, it is important to reduce this dipole wake function.

One way to reduce the dipole wake is to manufacture the cavity structure with cell dimension varying gradually so that each cell has a slightly different resonant frequency. In this case, the effect of the wake due to each individual cell will not add together and the wake of the whole structure will be reduced. Such a structure is called a *detuned cavity structure* [5].

Let us first study the short-range part of the dipole wake. The assumption that all the cells do not couple can be made, and the wake function of Eq. (15.39) can be considered as the summation of the wake due to each individual cell. Thus, K_n , ν_n , and Q_n become the kick factor, resonant frequency, and quality factor of the n th cell. Since the variation from cell to cell is small, the summation can be replaced by an integral

$$W_1(z) \approx -2 \int d\nu K \frac{dn}{d\nu} \sin \frac{2\pi\nu z}{c}. \quad (15.41)$$

Some comments are in order. First, the decays due to the quality factors have been neglected, because these are high- Q cavities and we are interested in the short-range wake only. Second, $K(dn/d\nu)$ is considered a function of ν and the normalization of $dn/d\nu$ is unity because $W_1(z)$ in Eq. (15.41) is referred to as the *dipole wake per cell*. Since $K(dn/d\nu)$ must be a narrow function centered about the average resonant frequency of the cells $\bar{\nu}$, the wake can be rewritten as

$$W_1(z) \approx -2 \operatorname{Im} \left[e^{2i\pi\bar{\nu}z/c} \int dx K(\bar{\nu} + x) \frac{dn}{d\nu}(\bar{\nu} + x) e^{2\pi i x z/c} \right], \quad (15.42)$$

with $\nu = \bar{\nu} + x$. We see that the wake consists of a rapidly varying part, oscillating at frequency $\bar{\nu}$, and a slowly varying part, the envelope, that is given by the Fourier transform of the function $K(dn/d\nu)$ after it has been centered about zero. For uniform frequency distribution with *full* frequency spread $\Delta\nu$, the wake is given by

$$W_1(z) \approx -2\bar{K} \sin \frac{2\pi\bar{\nu}z}{c} \frac{\sin(\pi\Delta\nu z/c)}{\pi\Delta\nu z/c}, \quad (15.43)$$

with \bar{K} the average value of K . If the frequency distribution is Gaussian with rms width σ_ν , then

$$W_1(z) \approx -2\bar{K} \sin \frac{2\pi\bar{\nu}z}{c} e^{-2(\pi\sigma_\nu z/c)^2}. \quad (15.44)$$

In this case, the envelope also rolls off as a Gaussian. It seems reasonable to expect that the proper Gaussian frequency distribution is near ideal in the sense of giving a rapid drop in the wake function for a given total frequency spread, and this is the motivation for choosing the Gaussian detuning.

Take the example of the Next Linear Collider (NLC). Consider a detuned structure with $N = 206$ cells. The central frequency is $\bar{\nu} = 15.25$ GHz. The detuned frequency distribution is Gaussian with $\pm 2.5\sigma_\nu$, where the rms spread σ_ν is chosen as 2.5% of $\bar{\nu}$. It is found that the average kick factor is $\bar{K} = 40$ MV/nC/m². The envelope of such a wake is shown in the top plot of Fig. 15.6. Notice that the wake function in fact does start from zero and has a first peak around 80 MV/nC/m² at $z \approx c/(4\bar{\nu}) = 4.91$ mm. It is important to point out that the dipole wake function defined in this way differs from our usual definition; it is equal to our usual W_1/L with $L = 1$ m. The designed rms bunch length is $\sigma_\ell = 0.150$ mm which is much less than the first peak. Therefore, the detuned structure will not help the single-bunch breakup at all. The bunch spacing is 42 cm in one scenario and 82 cm in another. At the location of the second bunch, the wake has dropped by more than two orders of magnitude. Thus, this lowering of the wake will definitely help the multi-bunch train beam breakup.

There are some comments on the wake depicted in the top plot of Fig. 15.6. First, the wake does not continue to drop as a Gaussian (the dashed curve) after about 0.4 m. Instead, it rises again having another peak around 4.2 m, although this peak is very much less than the first one. The main reason is due to the finite number of cells in the structure and the Gaussian distribution has been truncated at $\pm 2.5\sigma_\nu$. It is easy to understand the situation when we look at the uniform frequency distribution of Eq. (15.43). The envelope is dominated by the $\sin x/x$ term which gives a main peak at $x = 0$ and starts to oscillate after the first zero at $z = c/\Delta\nu$. Second, the coupling of the cells will nevertheless become important at some larger distance. Thus, the long-range part of the wake cannot be trusted at all. Bane and Gluckstern [5] used a circuit model with coupled resonators to give a more realistic computation of the long range wake. Later, Kroll, Jones, *et al.* [6] introduced four damping manifolds with four holes in the cells to carry away the dipole wave generated by the beam. Their final wake is shown in the bottom plot of Fig. 15.6. We see that the short-range part of the wake is almost

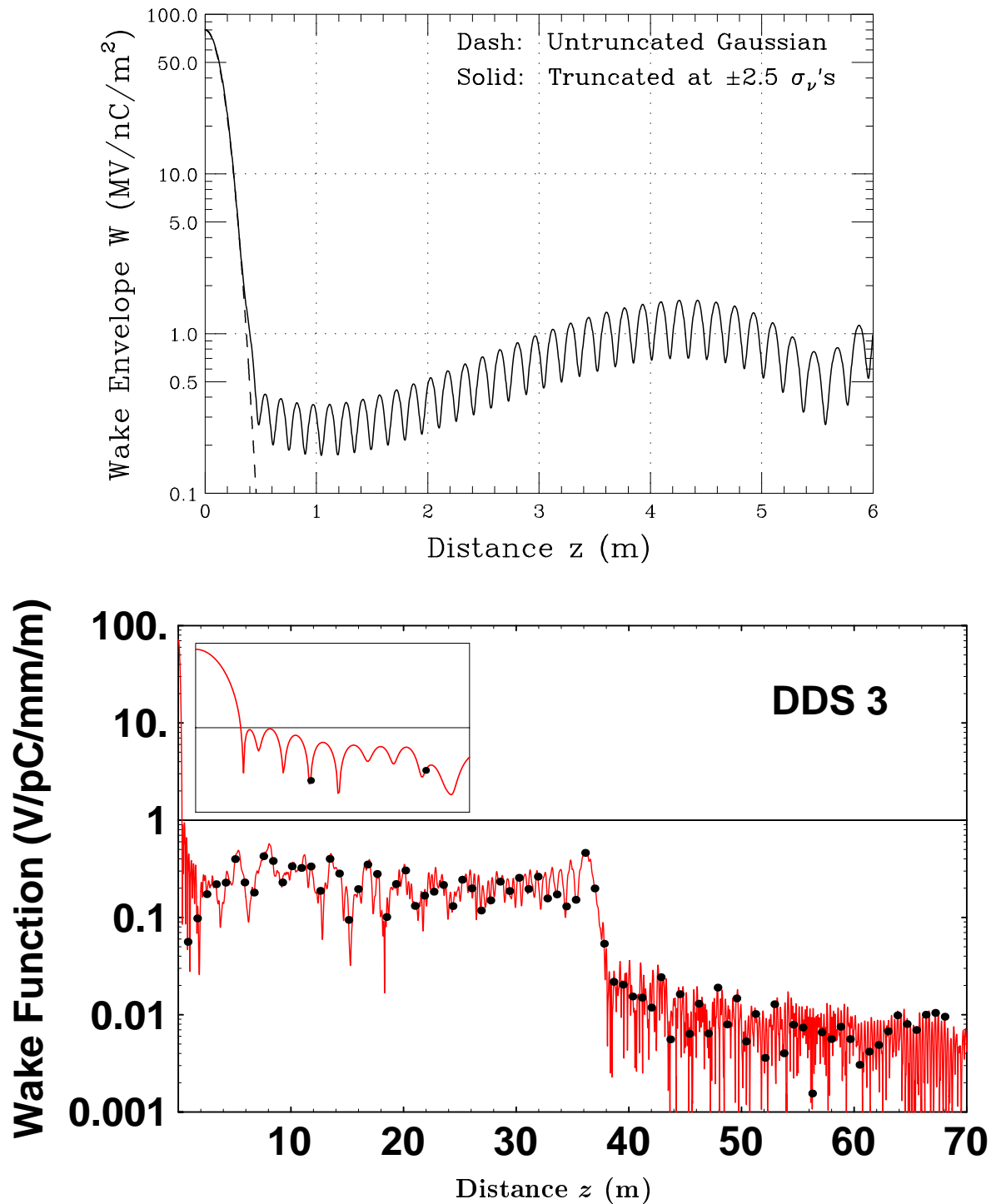


Figure 15.6: Envelope of the dipole wake function of a Gaussian detuned structure. Top: Coupling between cells has been ignored. Bottom: Coupling between cells has been included using a model with 2 circuits coupled to 4 manifolds. The dots represent the 82 bunches with 84-cm bunch spacing in one scenario.

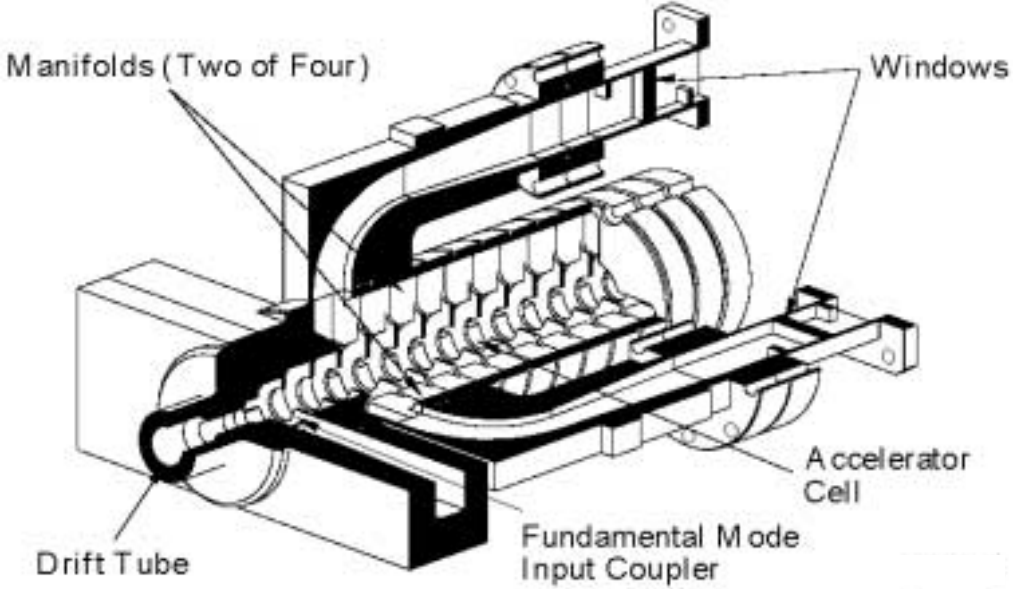


Figure 15.7: A drawing of the detuned structure consisting of 206 cavities coupled to 4 damped manifolds.

the same as is given by the top plot of Fig. 15.6. On the other hand, the long-range wake has been kept much below 1 MV/nC/m^2 . This wake has been computed first in the frequency domain as a spectral function and is then converted to the time or space domain via a Fourier transform. For this reason, we do not expect it to deliver the correct values at very short distances. The interested readers are referred to Refs. [5] and [6]. The dots on the plot represent the scenario of 82 bunches with 84-cm bunch spacing. A picture of the detuned structure consisting of 206 cavities coupled to four damped manifolds is shown in Fig. 15.7.

For the NLC, assuming a uniform energy independent betatron focusing with 100 betatron oscillations in the linac of total length $L = 10 \text{ km}$, the betatron wave number is $k_\beta = 0.06283 \text{ m}^{-1}$. Initially at 10 GeV, the NLC bunch has a vertical rms beam size of $\sigma_{y0} = 4.8 \mu\text{m}$, or the effective normalized rms vertical emittance $\epsilon_y = 0.028 \mu\text{m}$. At the linac exit (500 GeV), the deflection of the tail particle in the two-particle model is multiplied only $\Upsilon \sim 2.1$ fold per unit offset of the head particle (see Exercise 15.3). Assuming 1 μm initial offset of the head particle, and conservation of normalized emittance in the absence of beam breakup, the normalized vertical emittance becomes $\epsilon_y = 0.30 \mu\text{m}$. For

autophasing, assuming a chromaticity $\xi = 1$ defined by

$$\frac{\Delta k_\beta}{k_\beta} = \xi\delta , \quad (15.45)$$

an energy spread of 0.34% will be sufficient to damp the growth of the tail. These values are in close agreement of the simulations performed by Stupakov [10], as illustrated in Fig. 15.8.

15.3.3 Multi-Bunch Breakup

The NLC delivers a train of 95 bunches with bunch spacing 42 cm. Even if there is no beam breakup for a single bunch, the bunches in the train can also suffer beam breakup driven by the bunches preceding them. The first thing to do to ameliorate the situation is to design the linac cavities in such a way that the long-range dipole wake function will be as small as possible. The Gaussian detuned structure has been a way to lower the dipole wake by as much as two orders of magnitudes. According to the lower plot of Fig. 15.6, at 42 cm, the dipole wake is only $\sim 0.21 \text{ MV/nC/m}^2$.

The two-particle model can be extended to accommodate the study of multi-bunch beam breakup. Each bunch is visualized as a macro-particle containing N electrons. Then the equation governing the displacement of the first bunch is

$$\frac{d^2y_1}{ds^2} + k_\beta^2 y_1 = 0 , \quad (15.46)$$

and that of the second bunch is

$$\frac{d^2y_2}{ds^2} + k_\beta^2 y_2 = -\frac{e^2 N W_1(\hat{z})}{L E} y_1 , \quad (15.47)$$

where L is the cavity length and W_1 is the transverse wake per cavity. The first equation is the free betatron oscillation and is the same as Eq. (15.1). The second equation differs slightly from Eq. (15.2) in not having the factor 2 in the denominator. This is because in the two-particle model of a bunch, each macro-particle contains $\frac{1}{2}N$ electrons and here each macro-particle represents one bunch which is composed of N electrons. Also the dipole wake $W_1(\hat{z})$ in Eq. (15.47) is evaluated at the bunch spacing \hat{z} . Recall that the two-particle model will not work when the bunch length is too long and falls out of the linear region of the dipole wake, because some particles in between the head and the tail

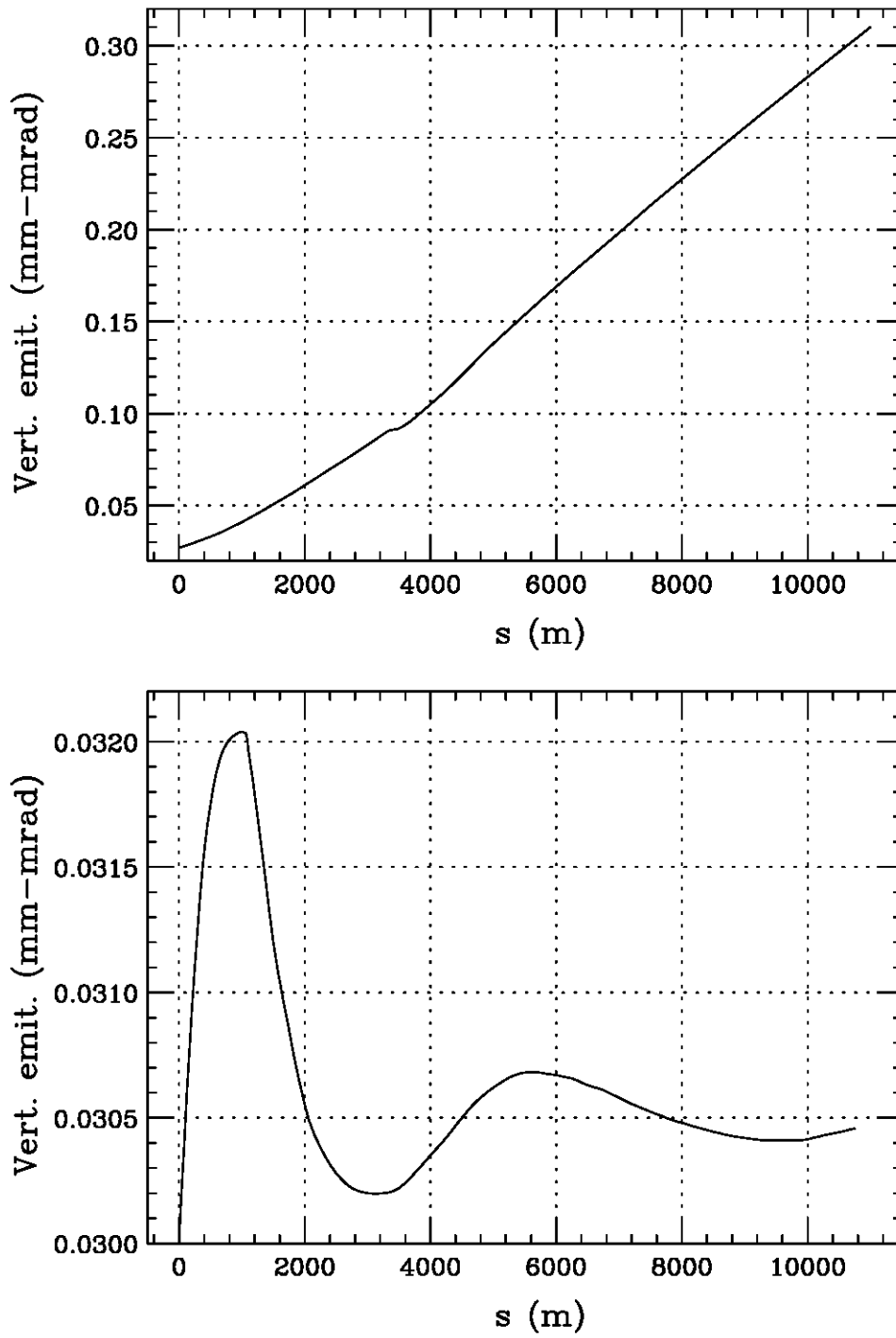


Figure 15.8: The normalized vertical emittance of a NLC bunch from the beginning to the end of the main linac, assuming an initial vertical offset of 1 μm . Top: The emittance increases to $\sim 0.3 \mu\text{m}$ because of beam breakup. Bottom: An energy spread of $\sim 0.8\%$ is added across the bunch by offsetting the rf phase. The emittance increase has been damped.

will suffer more beam-breakup deflections than the tail. However, this model still works for a long train of bunches, because unlike a long bunch, there are no particles between the point bunches.

Now the solution for the first bunch is

$$y_1(s) = \mathcal{R}e \hat{y} e^{ik_\beta s} . \quad (15.48)$$

The solution for the second bunch is

$$y_2(s) = \mathcal{R}e \hat{y} \Gamma s e^{ik_\beta s} , \quad (15.49)$$

where

$$\Gamma = \frac{ie^2 NW_1(\hat{z})}{2k_\beta LE_0} , \quad (15.50)$$

and we have neglected the general solution

$$y_2(s)|_{\text{general}} = \hat{y} e^{\pm ik_\beta s} , \quad (15.51)$$

which is much smaller than the particular solution in Eq. (15.49) which grows linearly as s . The equation for the deflection of the third bunch is

$$\frac{d^2 y_3}{ds^2} + k_\beta^2 y_3 = -\frac{e^2 NW_1(2\hat{z})}{LE_0} y_1 - \frac{e^2 NW_1(\hat{z})}{LE_0} y_2 . \quad (15.52)$$

Here, we are going to retain only the largest driving force on the right-side. This means that the driving force from y_1 can be neglected and so is the force from the general solution of y_2 . Substituting Eq. (15.49) in Eq. (15.52), we solve for the most divergent solution

$$y_3(s) = \mathcal{R}e \hat{y} \frac{1}{2} \Gamma^2 s^2 e^{ik_\beta s} . \quad (15.53)$$

Continuing this way, the deflection for the m th bunch will be (Exercise 15.4)

$$y_m(s) = \mathcal{R}e \hat{y} \frac{1}{(m-1)!} \Gamma^{m-1} s^{m-1} e^{ik_\beta s} . \quad (15.54)$$

Stupakov [11] tries to estimate how much energy spread will be required to BNS damp the multi-bunch beam breakup. In order to damp the deflection of the second bunch, the amount of tune spread is

$$\frac{\Delta k_\beta}{k_\beta} = -\frac{e^2 NW_1(\hat{z})}{2k_\beta^2 E_f} \ln \frac{E_f}{E_i} , \quad (15.55)$$

taking the linac acceleration into account. It is reasonable to assume that n_b times the spread necessary for the second bunch will be required for n_b bunches. Next the natural chromaticity for a FODO lattice of phase advance μ is

$$\xi = -\frac{2}{\pi} \tan \frac{\mu}{2}. \quad (15.56)$$

For 95 bunches, one gets the required energy spread of 2.7% (Exercise 15.5). The simulations by Stupakov are shown in Fig. 15.9. The initial bunch offset is 1 μm and it takes an rms energy spread of 0.8% among the bunches to damp the growth.

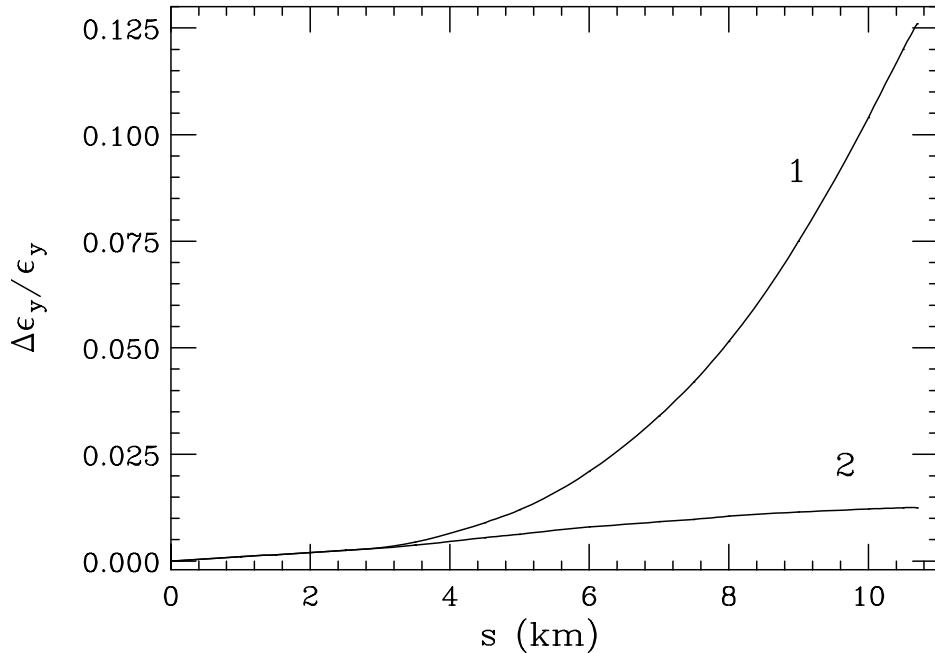


Figure 15.9: The relative change in vertical emittance of the 95th bunch, taking the vertical size as the vertical offset of the bunch center added to the actual rms vertical size in quadrature. The initial vertical offset is 1 μm . Curve 1 shows the growth without any energy variation in the bunches. Curve 2 shows that the beam-breakup growth has been damped with a 0.8% rms energy spread varying linearly from the first to the 95th bunch.

15.3.4 Analytic Treatment

Analytic computation of beam breakup for a bunch train has been attempted by many authors [8, 7]. In all these papers, the dipole wake has been taken as a single dipole

resonance and BNS damping has not been included. Recently, Bohn and Ng [9] have been able to include an energy chirp and derive analytic expressions for the BNS damping of a train of point bunches. Essentially, the energy chirp gives rise to a spread in betatron wave number among the bunches. An outline of the analytic derivation is given below.

Introduce the dimensionless *spatial* parameter $\sigma = s/L_0$ normalized to the total linac length L_0 . The real time t is reduced to the dimensionless *time* parameter $\zeta = \omega_r(t - s/c)$, with ω_r being the dipole resonant angular frequency, to describe the arrival of the a particle of the beam at position s along the linac, with $\zeta = 0$ as the arrival time of the first particle. Thus, ζ measures the longitudinal position of the particle inside the beam. The transverse displacement of a particle in the beam, represented by $y(\sigma, \zeta)$, depends on both σ and ζ and its motion is governed by[‡]

$$\left[\frac{1}{\gamma} \frac{\partial}{\partial \sigma} \left(\gamma \frac{\partial}{\partial \sigma} \right) + \kappa^2(\sigma, \zeta) \right] y(\sigma, \zeta) = -\epsilon(\sigma) \int_0^\zeta d\zeta' w(\zeta - \zeta') F(\zeta') y(\sigma, \zeta') , \quad (15.57)$$

which is just another way of writing Eq. (15.14) with beam particle acceleration included as in Eq. (15.31). This equation is usually referred to as the multi-bunch cumulative beam breakup (MBBU) equation. Here, the normalized betatron wave number is $\kappa = k_\beta L_0$. The beam profile $F(\zeta)$ will be defined in Eq. (15.60) below. The normalized dipole wake is[§]

$$w(\zeta) = -H(\zeta) e^{-\zeta/(2Q)} \sin \zeta , \quad (15.58)$$

where Q is its quality factor and $H(\zeta)$ is the Heaviside step function. All the rest is lumped into the dimensionless beam-breakup coupling strength

$$\epsilon(\sigma) = \frac{e^2 N w_0 L_0^2}{\gamma E_{\text{rest}} \omega_r \tau} , \quad (15.59)$$

where w_0 is the sum-wake amplitude or twice the kick factor of the dipole resonance measured in V/C/m² and $N/(\omega_r \tau)$ is the number of electrons per *longitudinal time* ζ . For a train of bunches with temporal spacing τ , N becomes the number per bunch. When these bunches are further considered as points, the beam profile in above is represented by

$$F(\zeta) = \sum_{n=-\infty}^{\infty} \delta \left(\frac{\zeta}{\omega_r \tau} - n \right) . \quad (15.60)$$

[‡]The arrival time is $\xi = 0$ for the first particle and $\xi > 0$ for later particles, or it represents a arrival time *behind* the first particle.

[§]This is another convention of defining the transverse wake so that it increases with a positive slope at the beginning. This is also called the *sum wake* because it represents the sum of the wake fields left by all preceding particles.

All bunches with arrival time $\zeta < 0$ will be excluded by the causal property of the wake.

A betatron linear chirp is now introduced,

$$\kappa(\sigma, \zeta) = \kappa_0(\sigma) + \kappa_1(\sigma, 0)\zeta , \quad (15.61)$$

where $\kappa_0(\sigma)$ is the normalized betatron wave number without the chirp and $\kappa_1(\sigma, 0)$ represents the strength of a linear chirp across the bunches. With the assumption that the acceleration gradient is much less than the betatron wave number, we can introduce a new transverse offset variable

$$\xi(\sigma, \zeta) = \sqrt{\gamma(\sigma)} y(\sigma, \zeta) e^{-i\zeta\Delta(\sigma)} , \quad (15.62)$$

where $\Delta(\sigma) = \int_0^\sigma d\sigma' \kappa_1(\sigma', 0)$. Now Eq. (15.57) can be rewritten as[¶]

$$\left[\frac{\partial^2}{\partial \sigma^2} + \kappa_0^2(\sigma) \right] \xi(\sigma, \zeta) \simeq -\epsilon(\sigma) \int_0^\zeta d\zeta' w_\Delta(\sigma, \zeta - \zeta') F(\zeta') \xi(\sigma, \zeta') , \quad (15.63)$$

where the assumption of strong focusing, $\partial \xi(\sigma, \zeta) / \partial \sigma \simeq i \kappa_0 \xi(\sigma, \zeta)$, has been used. Strong focusing actually implies that the quadrupole focusing is the most important force, while the wake, the acceleration gradient, and the variation of focusing due to chirping are small. The chirped-modified wake in Eq. (15.63) is defined as

$$w_\Delta(\sigma, \zeta) = w(\zeta) e^{-i\zeta\Delta(\sigma)} , \quad (15.64)$$

where obviously the exponential comes from the definition of $\xi(\sigma, \zeta)$. This exponential, when combined with the exponential of the original wake of Eq. (15.58), gives an *effective quality factor* Q_{eff} , where

$$\frac{1}{2Q_{\text{eff}}} = \frac{1}{2Q} + i\Delta . \quad (15.65)$$

Immediately, a result can be drawn that the chirp will be important if the quality factor Q of the transverse wake is high, but will be masked if Q is sufficiently low.

The transformation into Eq. (15.63) is important, because the operator on the left side no longer depends on ζ , and the chirp has been incorporated into the dipole wake. To proceed, we Fourier transform the whole equation with respect to the variable $\xi = n\omega_r \tau$ to obtain

$$\left[\frac{\partial^2}{\partial \sigma^2} + \kappa_0^2(\sigma) \right] \tilde{\xi}(\sigma, \theta) \simeq -\epsilon(\sigma) \omega_r \tau \tilde{w}_\Delta(\sigma, \theta) \tilde{\xi}(\sigma, \theta) , \quad (15.66)$$

[¶](γ')² and γ'' will be neglected in below, where the prime implies derivative with respect to σ , but $\gamma' \xi'$ will be retained.

where

$$\begin{aligned}\tilde{\xi}(\sigma, \theta) &= \sum_{m=0}^{\infty} e^{-im\theta} \xi(\sigma, m\omega_r \tau) , \\ \tilde{w}_{\Delta}(\sigma, \theta) &= \sum_{m=0}^{\infty} e^{-im[\theta+\omega_r \tau \Delta(\sigma)]} w_m = w(\sigma, m\omega_r \tau) .\end{aligned}\quad (15.67)$$

In this form, the WKB method can be employed to give a formal solution

$$\tilde{\xi}(\sigma, \theta) = \sqrt{\frac{\Lambda(0, \theta)}{\Lambda(\sigma, \theta)}} \exp \left[i \int_0^\sigma d\sigma' \Lambda(\sigma', \theta) \right] , \quad (15.68)$$

where

$$\Lambda^2(\sigma, \theta) = \kappa_0^2(\sigma) + \epsilon(\sigma) \omega_r \tau \tilde{w}_{\Delta}(\sigma, \theta) . \quad (15.69)$$

Here $\Lambda(\sigma, \theta)$ is an auxiliary function reflecting the coupling between the bunch spacing and the deflecting-mode frequency, and when $\tilde{w}_{\Delta}(\sigma, \theta)$ is substituted, it takes the form

$$\Lambda(\sigma, \theta) = \kappa_0(\sigma) \left[1 - \frac{\epsilon(\sigma)}{4\kappa_0^2(\sigma)} \frac{\omega_r \tau \sin \omega_r \tau}{\cos[\theta + \omega_r \tau \Delta(\sigma)] - \cos \omega_r \tau} \right] . \quad (15.70)$$

Denoting the displacement for the $(m+1)$ th bunch as $y_m(\sigma) = y(\sigma, m\omega_r \tau)$, the inverse Fourier transform give [8, 12]

$$y_m(\sigma) = \frac{1}{2\pi} \sum_{n=0}^m e^{-n\omega_r \tau / (2Q)} \int_{-\pi}^{\pi} d\theta e^{-in\theta} \left\{ y_{m-n}(0) \mathcal{C}(\sigma, \theta; m) + y'_{m-n}(0) \frac{\mathcal{S}(\sigma, \theta; m)}{\Lambda(0, \theta)} \right\} , \quad (15.71)$$

in which

$$\left\{ \begin{array}{l} \mathcal{C}(\sigma, \theta; m) \\ \mathcal{S}(\sigma, \theta; m) \end{array} \right\} = \sqrt{\frac{E_i \Lambda(0, \theta)}{E_\sigma \Lambda(\sigma, \theta)}} \left\{ \begin{array}{l} \mathcal{Re} \\ \mathcal{Im} \end{array} \right\} \exp \left[im\omega_r \tau \Delta(\sigma) + \int_0^\sigma d\sigma' \Lambda(\sigma', \theta) \right] \quad (15.72)$$

are cosine-like and sine-like functionals, respectively. In above, we have written, for convenience, the energy of the beam particle at location σ as $E_\sigma = \gamma(\sigma) E_{\text{rest}}$ and the initial energy as $E_i = \gamma(0) E_{\text{rest}}$. Later we will also write the energy at linac exit as $E_f = \gamma(1) E_{\text{rest}}$.

It is evident from Eq. (15.71) that upon taking $\theta \rightarrow -\theta$ and remembering that y_m is real, the algebraic sign of $\Delta(\sigma)$ affects only the phase of $y_m(\sigma)$ but not the envelope. This demonstrates that, as expected intuitively, the effect of a linear increase in focusing from head to tail is the same as a linear decrease.

In order for the derivation to go through analytically further, it is necessary to make the assumption that the betatron wave number decreases as $\gamma^{-1/2}$. This focusing arrangement implies that all the quadrupoles are identical and they can be on one common bus, because the focusing field gradient will be exactly the same along the linac. This implies the focusing becomes weaker as the energy increases. In fact, the NLC quadrupoles are deployed roughly in this way, although the quadrupoles there are all on separate buses for the ease of beam alignment. With this assumption, $\epsilon(\sigma)/[4\kappa_0^2(\sigma)]$ in the defining equation of $\Lambda(\sigma, \theta)$ above will no longer be dependent on σ . This simplifies the integration to be performed later.

For further discussion, let us set the initial conditions $y_m(0) = y_0$ and $y'_m(0) = 0$ for every bunch, and assume a constant acceleration gradient in the linac. The sum in Eq. (15.71) can be decomposed into two parts: $\sum_0^m = \sum_0^\infty - \sum_m^\infty$. The first part pertains to the *steady-state* displacement y_{ss} that would arise were the deflecting wake first seeded with an infinitely long bunch train immediately preceding the actual bunch train. Given strong focusing, the steady-state displacement is

$$y_{ss}(\sigma, m\omega_r\tau) \simeq y_0 \left[\frac{E_i}{E_\sigma} \right]^{1/4} \cos \left[m\omega_r\tau\Delta(\sigma) + \int_0^\sigma d\sigma' \kappa_0(\sigma') \right]. \quad (15.73)$$

The second part pertains to the *transient* displacement $\delta y_m = y_m - y_{ss}$. Saddle-point integration gives a closed-form solution for δy_m , whose bounding envelope takes the form:

$$\frac{|\delta y_m|}{y_0} \simeq \left[\frac{E_i}{E_\sigma} \right]^{\frac{1}{4}} \frac{\sqrt{\mathcal{E}} \exp[q(\eta)\mathcal{E} - m\omega_r\tau/(2Q)]}{4m\sqrt{2\pi} |\sin(\omega_r\tau/2)|} \times \begin{cases} |1 - \eta^2|^{-\frac{1}{4}} & \eta \text{ not near } 1 \\ \left(\frac{4}{3}\right)^{\frac{1}{6}} \mathcal{E}^{\frac{1}{6}} \frac{\Gamma(\frac{1}{3})}{\sqrt{2\pi}} & \eta = 1. \end{cases} \quad (15.74)$$

The auxiliary relations comprising Eq. (15.74) are:

$$\mathcal{E}(\sigma, m) = \left[\frac{4mw_0e^2NL_0^2}{\bar{\kappa}_0 E_i} \right]^{1/2} \frac{\left[(\sqrt{E_f/E_i} - 1) (\sqrt{E_\sigma/E_i} - 1) \right]^{1/2}}{E_f/E_i - 1},$$

$$\eta(\sigma, m) = \frac{\bar{\kappa}_0 |f_\gamma|}{2\mathcal{E}} \frac{m}{M} \frac{\sqrt{E_\sigma/E_i} - 1}{\sqrt{E_f/E_i} - 1},$$

$$q(\eta) = \begin{cases} \frac{\sqrt{1-\eta^2}}{2} + \frac{1}{4\eta} \tan^{-1} \left(\frac{2\eta\sqrt{1-\eta^2}}{1-2\eta^2} \right) & \eta < 1 \\ \frac{\pi}{4\eta} & \eta \geq 1 \end{cases}$$

in which $\bar{\kappa}_0$ is the focusing strength averaged over the linac and is related to the focusing strength at entrance $\kappa_0(0)$ by

$$\bar{\kappa}_0 = \frac{2\kappa_0(0)}{\sqrt{E_f/E_i} + 1}, \quad (15.76)$$

M is the total number of bunches in the train, $|f_\gamma|$ is the magnitude of the total fractional energy spread across the bunch train, or twice the total fractional focusing variation.

The expression for $|\delta y_m|$ in Eq. (15.74) reflects a number of physical processes. The coefficient involving beam energy manifests adiabatic damping. The factor $|\sin(\omega_r \tau/2)|$ is a relic of a resonance function deriving from the coupling between the bunch spacing and the deflecting-mode frequency. Resonances lie near even-order wake zero-crossings [8]; because the solution is valid only away from zero-crossing, resonance is removed. The focusing variation represented by $|f_\gamma|$ regulates exponential growth, and finite Q yields exponential damping. Yet “ $\eta=1$ ” does have special physical significance; it demarks the onset of saturation of exponential growth and, with infinite Q , algebraic decay of the envelope. For $\eta \geq 1$ the “growth factor” $q(\eta)\mathcal{E}$ is independent of bunch number m and of linac coordinate σ ; temporal “damping” then ensues through a negative power of m , and spatial “damping” ensues adiabatically as already mentioned. Therefore $\eta = 1$ corresponds to a global maximum in the envelope $|\delta y_m|$. The effect of the focusing variation is the saturation of the exponential growth, not damping; its action distinctly differs from that of a real effective Q .

We now apply the solution to designs of the SLAC NLC and DESY TESLA. Some parameters are listed in Table 15.1.

15.3.5 Amount of Energy Chirp

The transient displacements of the 90 bunches of the NLC at the linac exit were simulated and shown in Fig. 15.10 for energy spreads $f_\gamma = 1.5$ and 3.0%. The plots are made with the scenario that the linac is $L_0 = 10$ km long, accelerating 90 bunches with bunch spacing $\tau = 2.8$ ns from 10 GeV to 1 TeV. Each bunch contains 1 nC of charges or

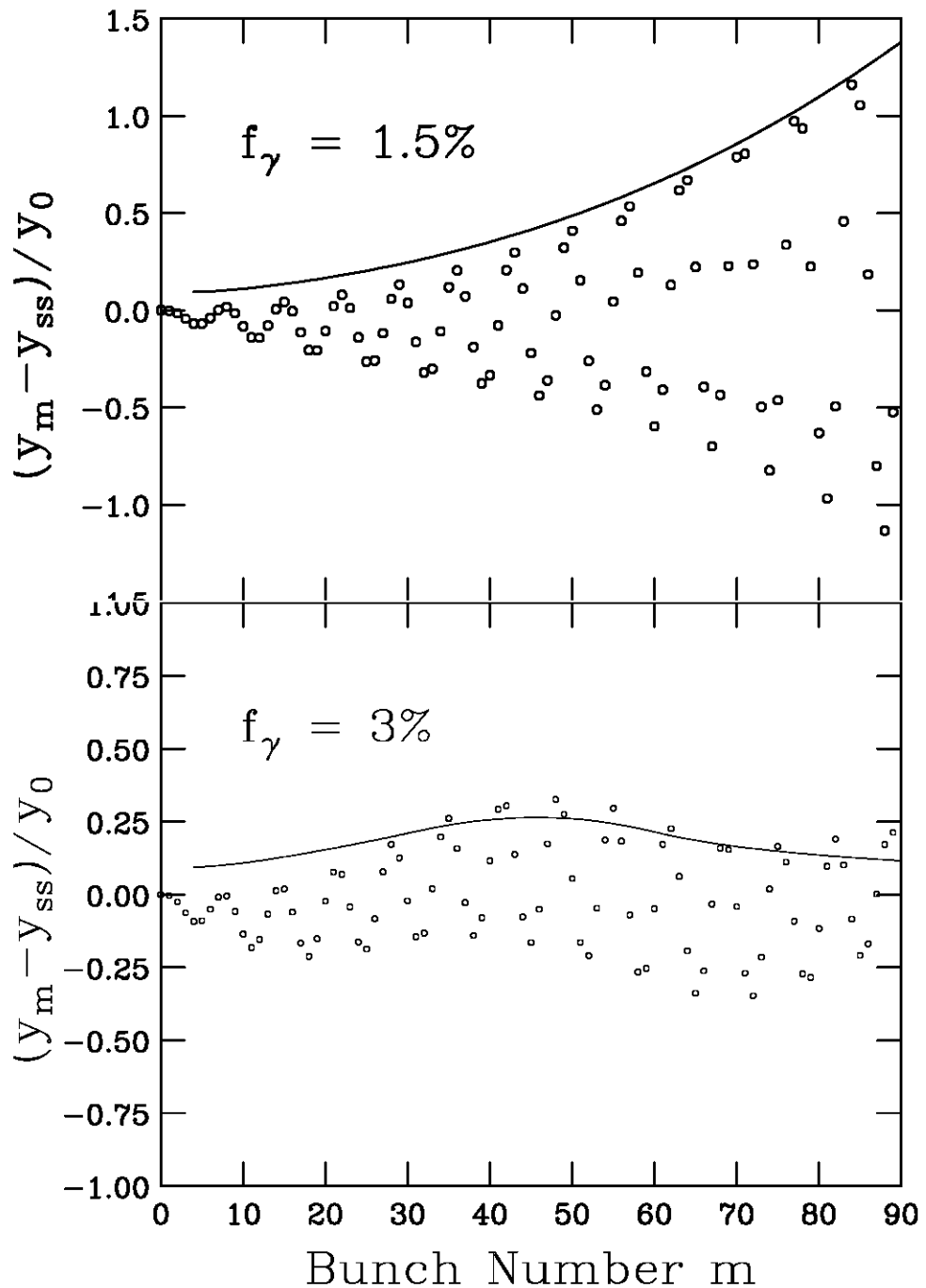


Figure 15.10: Analytic envelope at the linac exit (solid curve) plotted against the transverse displacement of bunches calculated numerically, with total energy spreads of 1.5% (top) and 3% (bottom).

Table 15.1: Some parameters of the SLAC NLC and DESY TESLA.

	NLC [†]	TESLA
Linac length ℓ (km)	10.0	14.4
No of betatron wavelengths ν_β	100	60
Entry/exit energy (GeV)	10/1000	5/250
No of bunches per train M	90	2820
Bunch charge q (nC)	-1.0	-1.6
Bunch spacing τ (ns)	2.8	377
Transverse wake:		
amplitude w_0 (V/pC/m/mm)	1	0.015
frequency $\omega_r/(2\pi)$ (GHz)	14.95	1.70
effective quality factor Q	∞	~ 125000

[†]The above belong to an older model of the SLAC NLC. and are chosen to illustrate MBBU. The parameters w_0 and Q represent a worst-case wake.

$N = 6.24 \times 10^9$ electrons, making 100 betatron oscillations along the linac. The dipole wake of the SLAC NLC cavities is of resonant frequency $\omega_r/(2\pi) = 14.95$ GHz. Its long-range transverse behavior is shown in Fig. 15.6, which is computed using a circuit model. We see that the envelope of the wake is almost constant for the first 30 m or the first 36 bunch spacings. This allows us to assign an effective quality factor of $Q = \infty$ and sum-wake amplitude^{||} $w_0 \sim 1$ MV/nC/m². It is clear that BNS damping is helping to control the emittance growth. The relative displacement of the 90th bunch would be as large as 2.1 when $f_\gamma = 0$. We also see that with $f_\gamma = 3.0\%$ the envelope reaches a maximum at the 48th bunch and decays algebraically afterward approaching steady state slowly. An effective BNS damping requires an energy spread sufficient to have the maximum to reach some bunches before they leave the linac.

The special significance of $\eta = 1$ translates into a criterion for the focusing variation to be effective. Specifically, one should choose a value of f_γ that ensures $\eta(1, M) > 1$, *i.e.*, that $\eta = 1$ is reached somewhere along the bunch train before it leaves the linac.

^{||}The plot in Fig. 15.6 shows $w_0 \sim 0.3$ MV/nC/m². Here, we use $w_0 \sim 1$ MV/nC/m² as a reference model.

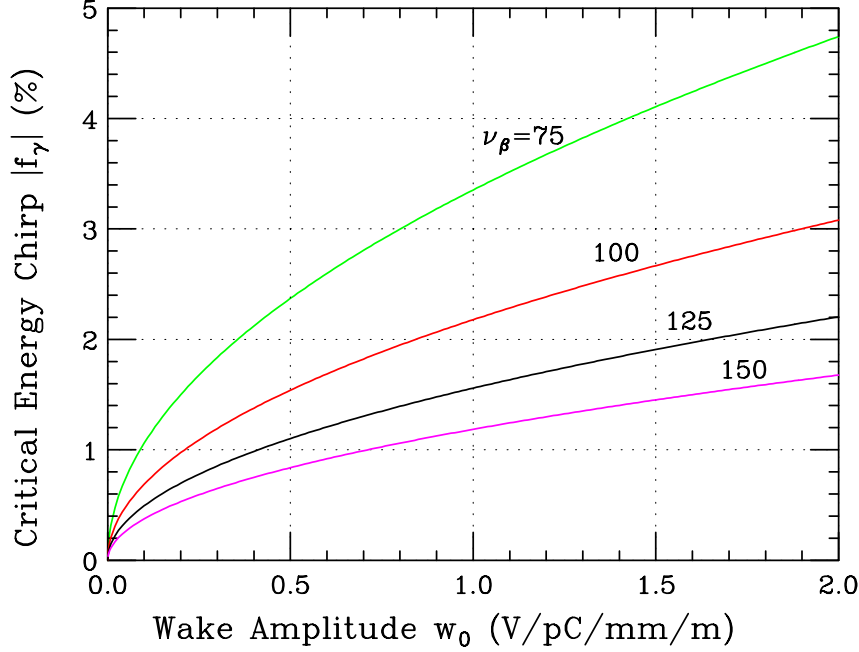


Figure 15.11: (color) Critical energy chirp required for BNS damping in the SLAC NLC versus deflecting wake amplitude, with number of betatron wavelengths $\nu_\beta = 75, 100, 125$, and 150 .

According to the auxiliary relations to Eq. (15.74), the criterion is

$$|f_\gamma| > \frac{2\mathcal{E}(1, M-1)}{\bar{\kappa}_0} = \frac{\mathcal{E}(1, M-1)}{\pi\nu_\beta}, \quad (15.77)$$

which is plotted in Fig. 15.11 versus the wake amplitude for various strength of betatron focusing. For example, for the parameters in Table 15.1, an energy chirp of $|f_\gamma| \gtrsim 2.18\%$ in the NLC will be required. However, as will be seen in the next subsection, this is not the only criterion to control emittance growth.

15.3.5.1 Emittance Growth

The steady-state and transient displacements, being uncorrelated, comprise a measure of the total projected normalized emittance as

$$\varepsilon \equiv (|y_{ss}|^2 + |\delta y_m|_{max}^2) \frac{\gamma\kappa_0}{L_0}, \quad (15.78)$$

wherein $|y_{ss}| = y_0[E_i/E_\sigma]^{1/4}$ per Eq. (15.73), and $|\delta y_m|_{max}$ is the maximum value of the transient envelope reached along the bunch train. If $\eta < 1$ always, then the maximum is

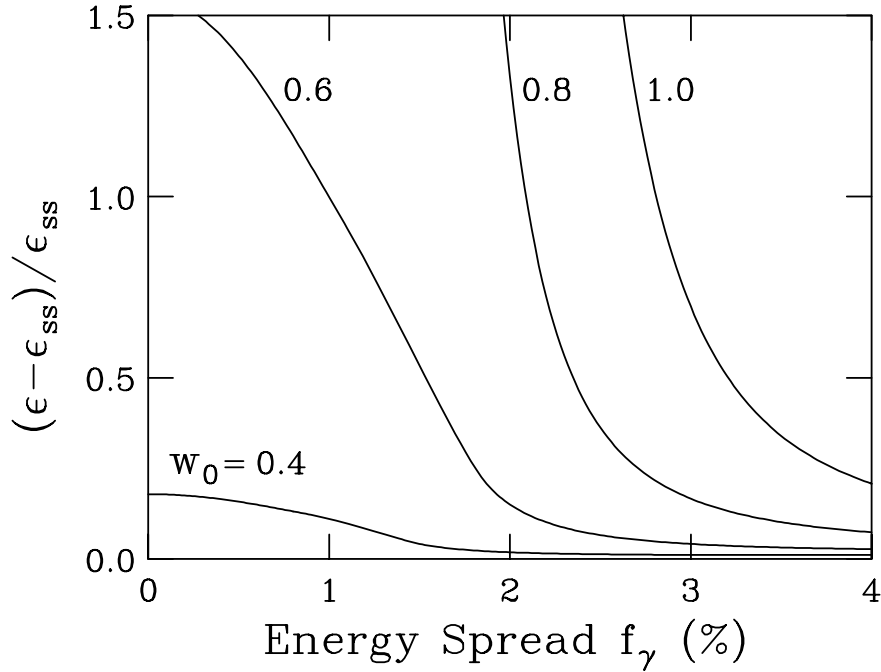


Figure 15.12: Total normalized transverse multi-bunch emittance at the linac exit, referenced to its steady-state value, versus total energy spread across the bunch train, plotted for various sum-wake amplitudes w_0 .

reached at the last bunch $m = M$. Otherwise, the maximum corresponds to the value of $|\delta y_m|$ at which $\eta = 1$. Imposing a focusing variation will reduce the transient envelope, but it also will establish a harmonic variation of y_{ss} with m and thereby introduce a nonzero steady-state emittance ε_{ss} . For this reason the quantity of interest is the ratio

$$(\varepsilon - \varepsilon_{ss})/\varepsilon_{ss} = \left(\frac{|\delta y_m|_{max}}{|y_{ss}|} \right)^2, \quad (15.79)$$

from which one sees the benefit of keeping the ratio of envelopes small. This quantity, calculated from the analytic expressions given in Eqs. (15.73) and (15.74), is plotted against $|f_\gamma|$ in Fig. 15.12 for various values of the sum-wake amplitude w_0 . Fig. 15.12 points to the region of parameter space that, respecting multi-bunch beam breakup, admits viable linear-collider designs. In particular it shows that to achieve low multi-bunch emittance without aid from a focusing variation requires small sum-wake amplitudes, $w_0 \lesssim 0.5$ V/pC/mm/m. Otherwise, as depicted, a few-percent energy spread relieves the constraint on sum-wake amplitude. There are, of course, practical limitations on the energy spread, to include longitudinal beam requirements at the interaction point,

lattice chromaticity, degradation in acceleration, etc. Nonetheless, introducing a modest energy spread constitutes a backup in case sufficiently low wake amplitudes prove generally infeasible.

It is worth mentioning that the plots in Figs. 15.10 and 15.12 have been performed with the data of the upgraded NLC. If we use the present lower energy design of accelerating the bunches up to only 500 GeV and 1.1×10^{10} particles per bunch, the reduction in adiabatic damping will increase the growths of the bunch deflections at the linac exit tremendously. To BNS damp such growths, an energy chirp of 10 to 15% will be necessary. Certainly this is not workable because of the large momentum spread of the bunches which later translates into unacceptable transverse bunch sizes at the interaction point. The acceleration gradient will also be largely reduced. Needless to say, the linac itself will hardly have such large energy aperture for the bunches to pass through. What we actually want to point out is that BNS damping is only feasible when the actual beam breakup is not too large, because only a small amount of energy chirp is acceptable in reality.

15.3.5.2 The Quality Factor

Now let us apply the computed displacement envelope to the DESY TESLA. If the quality factor of the deflecting wake were infinite, Eq. (15.77) would require an energy chirp of $|f_\gamma| = 9.27\%$. This chirp is rather large because of the long bunch train of 2820 bunches. Even with such a large chirp, Eq. (15.74) predicts a normalized transient displacement envelope of $|\Delta y_m/y_0| = 296$ for the last bunch at the linac exit, and such emittance growth is totally unacceptable. Fortunately, the transverse long-range wake of the TESLA linac in Fig. 15.13 shows considerable amount of damping [14]. However, the wake does not correspond to a damped resonance of a single frequency. Assuming a resonant frequency of 1.7 GHz, one obtains a quality factor of $Q = 22400$ by comparing the wake envelope at the first and 10th bunch spacings, $Q = 69000$ by comparing the wake envelope at the first and 100th bunch spacings, and $Q = 124000$ by comparing the wake envelope at the first and 265th bunch spacings (which is the end of the wake displayed in Fig. 15.13). In the discussion below, the quality factor of $Q = 125000$ is assumed. Numerically, we find that $|\Delta y_m/y_0|$ never exceeds 0.012 and damps to less than 0.010 within the first 150 bunches, where no energy chirp has been applied (see top plot Fig. 15.13 below). It is important to mention that the theoretical prediction of Eq. (15.74) may not apply to the TESLA linac, where MBBU is not severe because

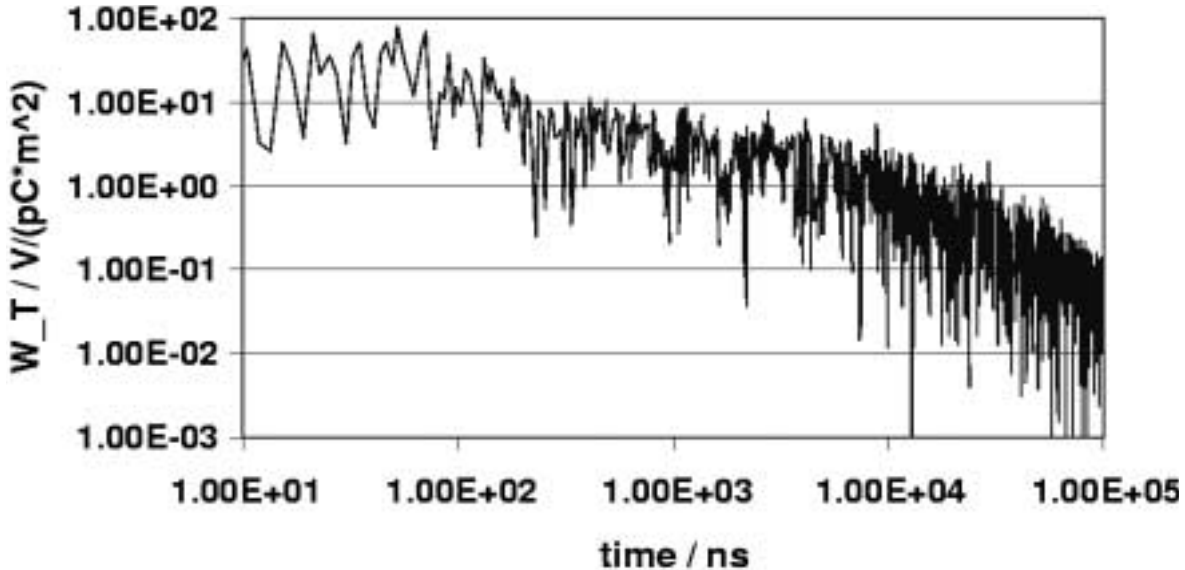


Figure 15.13: Plot of transverse long-range wake of the TESLA linac.

of the rather small effect from the transverse wake. Instead of the method of steepest descent, the MBBU equation should be solved by iteration with the coupling coefficient ϵ considered as a small quantity.

We can also visualize a finite quality factor Q of the deflecting wake as acting like an energy chirp. From the growth exponent of Eq. (15.74), it is evident that a finite quality factor will offset a certain amount of growth [13]. Setting $\eta=1$ in the exponent, we obtain for the last bunch at the linac exit

$$|f_\gamma| = \frac{2M\omega_r\tau}{\pi^2 Q \nu_\beta}, \quad (15.80)$$

which is the equivalent amount of energy-chirp-like damping provided by the quality factor. In Fig. 15.14, we plot the normalized envelope displacement of the last bunch at the exit of the SLAC NLC linac as a function of the energy chirp $|f_\gamma|$ for various values of the quality factor. The large dots are the equivalent energy-chirp-like damping provided by the quality factor. The dashed curve joining all the large dots depicts Eq. (15.80). Notice that the displacement is approximately independent of the energy chirp until the stated threshold is exceeded, after which the displacement drops off relatively fast with increasing $|f_\gamma|$. As an illustration, recall that for a wake with an infinite quality factor, $|f_\gamma| = 2.18\%$ is required for BNS damping. However, when the quality factor is lowered to $Q = 5000$, Fig. 15.14 indicates an equivalent energy chirp of 0.96%. Thus,

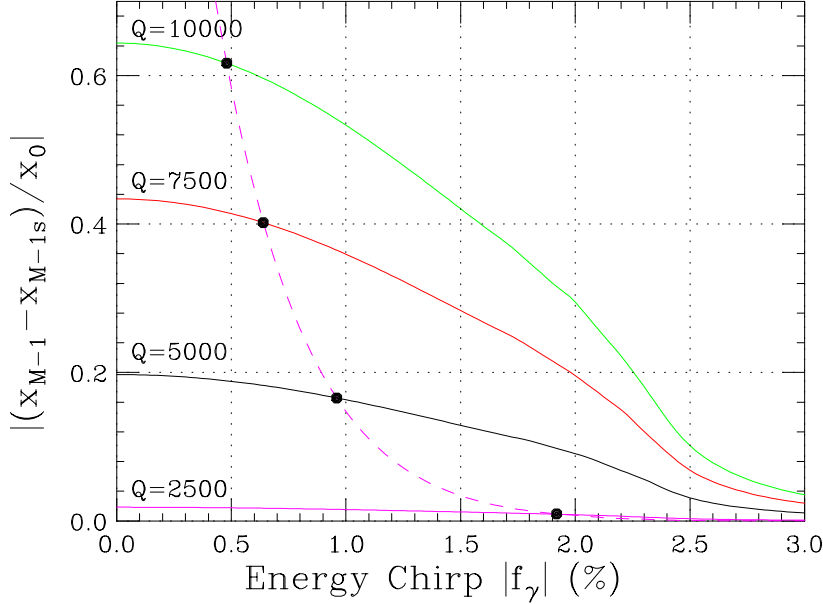


Figure 15.14: (color) Plot of normalized transient displacement envelope of the last bunch at the linac exit of the SLAC NLC versus energy chirp $|f_\gamma|$ for various quality factors Q of the deflecting wake. The amount of equivalent energy-chirp-like damping provided by the finite quality factor is also shown as dashes.

only $|f_\gamma| = 2.18 - 0.96 = 1.22\%$ will now be required. This is demonstrated in Fig. 15.15, where we can see the maxima of the displacement envelopes reside at the last bunch at the linac exit in both situations. A smaller quality factor not only reduces the amount of energy chirp required for BNS damping; it also helps to reduce the transient transverse displacement along the bunch train from $|\Delta y_m/y_0| = 0.76$ to a very much smaller value of 0.15. Thus, for the sake of controlling emittance growth and damping MBBU, it is beneficial to have lower quality factors for the deflecting modes. Returning to the TESLA linac, Eq. (15.80) gives an “effective” energy chirp of $|f_\gamma| = 4600\%$ for the last bunch of the bunch train and 1.6% for the second bunch ($M = 1$). This explains why the transient displacement envelope was so heavily damped.

15.4 Misaligned Linac

So far we have been considering linacs with perfect alignment, which is impossible in reality. Suppose that the quadrupole at location σ has misalignment $y_Q(\sigma)$ and the cavities have misalignment $y_A(\sigma)$ at location σ . The equation of motion governing the

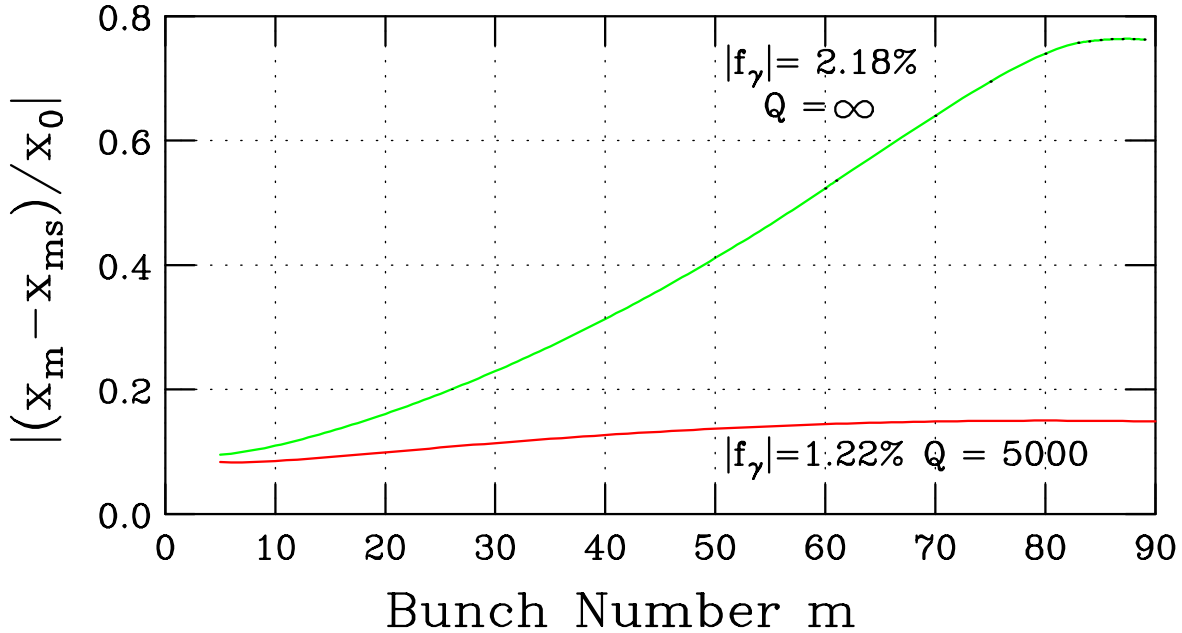


Figure 15.15: (color) Plot of normalized transient displacement envelope at the linac exit of the SLAC NLC when envelope maximum occurs at the last bunch. Notice that the energy chirp $|f_\gamma|$ is reduced from 2.18% to 1.22% when the quality factor is reduced from $Q = \infty$ to 5000.

transverse motion of the beam will be modified from Eq. (15.57) to [15]

$$\begin{aligned} & \left[\frac{1}{\gamma} \frac{\partial}{\partial \sigma} \left(\gamma \frac{\partial}{\partial \sigma} \right) + \kappa^2(\sigma, \zeta) \right] [y(\sigma, \zeta) - y_Q(\sigma)] \\ &= -\epsilon(\sigma) \int_0^\zeta d\zeta' w(\zeta - \zeta') F(\zeta') [y(\sigma, \zeta') - y_A(\sigma)] . \end{aligned} \quad (15.81)$$

To arrive at an analytic solution, some assumptions are necessary. Consider the linac to be comprised of girders. On each girder is an accelerating length there are some number of rf structures and an optical element. Assume that the structures and quadrupoles are sufficiently well-aligned on the girders, leaving the girder misalignments as the dominating offset errors. If there are a large number of girders in each betatron wavelength, the beam will experience the same number of kicks due to the girder misalignments. Since the betatron wavelength is the characteristic *dynamic length*, the kicks act roughly as *white noise* on the beam. With these considerations, the quadrupole misalignment error $y_Q(\sigma)$ and structure misalignment error $y_A(\sigma)$ in Eq. (15.81) are the same random

variable. In other words,

$$\langle y_{Q,A}(\sigma_1) y_{Q,A}(\sigma_2) \rangle = \frac{d_g^2}{N_g} \Sigma(\sigma) \delta(\sigma_1 - \sigma_2) , \quad (15.82)$$

where N_g is the total number of girders in the linac and d_g is the rms girder misalignment. When the betatron focusing is strong, the MBBU equation can be solved in the same way as before when there were no misalignments. The result can be expressed analytically as

$$\frac{\langle \Delta y_m^e(\sigma)^2 \rangle^{\frac{1}{2}}}{\Delta y_m(\sigma)} \approx \frac{d_g}{y_0} \frac{2\pi\nu_\beta}{\sqrt{N_g}} \begin{cases} \frac{1}{\sqrt{\mathcal{E}(\sigma, m)}} & \eta \leq 1 \\ \sqrt{\frac{2}{3}} & \eta > 1 , \end{cases} \quad (15.83)$$

where $\Delta y_m^e(\sigma)$ is the transient displacement of the m th bunch in the bunch train which enters the misaligned linac without any displacement errors, while $\Delta y_m(\sigma)$, given by Eq. (15.74), is the transient displacement of the m th bunch in the bunch train which enters a perfectly aligned linac with initial displacement y_0 for all the bunches. The result is remarkable. First, it is simple. Second, it is independent of the amount of energy chirp f_γ either when $\eta \leq 1$ or $\eta > 1$. For $\eta = 0$, Eq. (15.83) reduces to Eq. (5.6) of Yokoya [16], which was derived without any energy chirp. The other difference from Yokoya is that his derivation is for the square roots of the total emittances rather than the transient displacements.

15.4.0.3 Comparison with Simulations

In order to reduce the fluctuations due to betatron oscillation, we try to compute the transient square-root-emittance $\Delta\epsilon_m^{e \frac{1}{2}}$ instead of the transient displacement Δy_m^e , where the former is defined as**

$$\Delta\epsilon_m^{e \frac{1}{2}} = \left[(y_m^e)^2 + (\beta y_m'^e)^2 \right]^{\frac{1}{2}} - \left[(y_{ms})^2 + (\beta y_{ms}')^2 \right]^{\frac{1}{2}} , \quad (15.84)$$

with β being the betatron function at the location along the linac under consideration and $y_m'^e$ the divergence of the particle bunch. The subscript s denotes steady state. Thus, the left side of Eq. (15.83) is replaced by $|\langle \Delta\epsilon_m^e(\sigma)^{\frac{1}{2}} \rangle| / \Delta\epsilon_m(\sigma)^{\frac{1}{2}}$.

**The emittance defined here when divided by the betatron function is the usual unnormalized emittance.

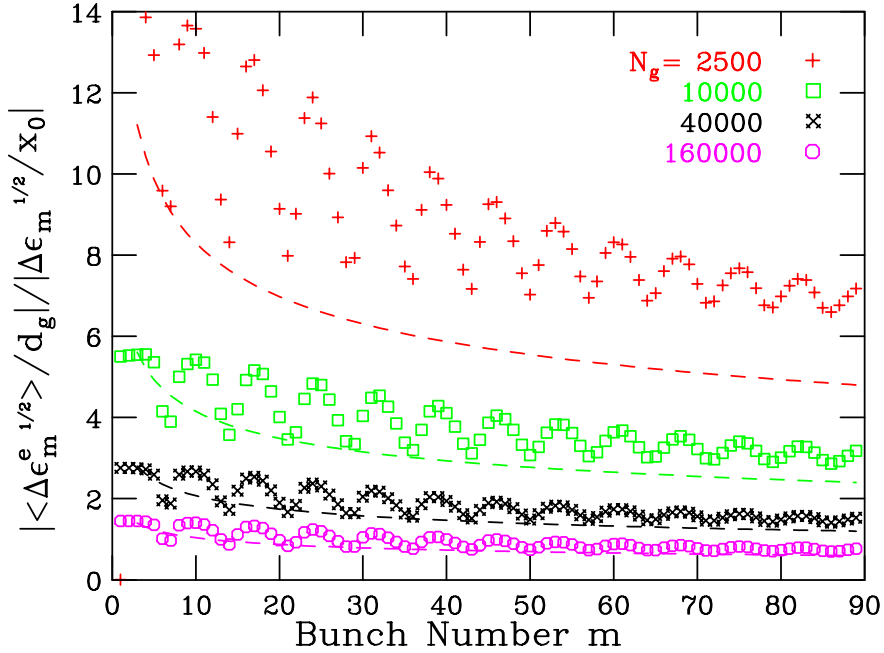


Figure 15.16: (color) Plot of ratio of transient square-root-emittance with girder misalignments but no beam offsets to that with beam offset but no girder misalignments at the linac exit of the SLAC NLC. The results verify the $N_g^{-1/2}$ dependency of the theoretical predictions which are shown here in dashes. The energy chirp is 1.0%.

We performed simulations of the SLAC NLC linac and computed beam quantities at its exit ($\sigma = 1$). In order to reduce the large spreads of the bunch displacements due to the randomness of the girder misalignments, each situation was simulated with 20 seeds and the results averaged. Figure 15.16 shows the simulated results when girder numbers $N_g = 2500, 10000, 40000$, and 160000 were used, while the energy chirp was kept at $f_\gamma = 1.0\%$ all the time. The plot actually verifies the $N_g^{-1/2}$ dependency stated in Eq. (15.83). The theoretical predictions are also shown in dashes with the understanding that η is always less than unity. We see that Eq. (15.83) agrees with the simulated results, although it tends to underestimate the results in general^{††}. Actually, there will not be $N_g = 160000$ girders in the NLC linac. This number is created only for the purpose to check the theoretical prediction. With a linac length of $\ell = 10$ km and $\nu_\beta = 100$

^{††}The agreement of theoretical predictions with simulations would be as good as in Figs. 11 and 12 of Ref. [16] if we had plotted the simulation results of all seeds instead of just the averages and also with the vertical axis in a logarithmic scale.

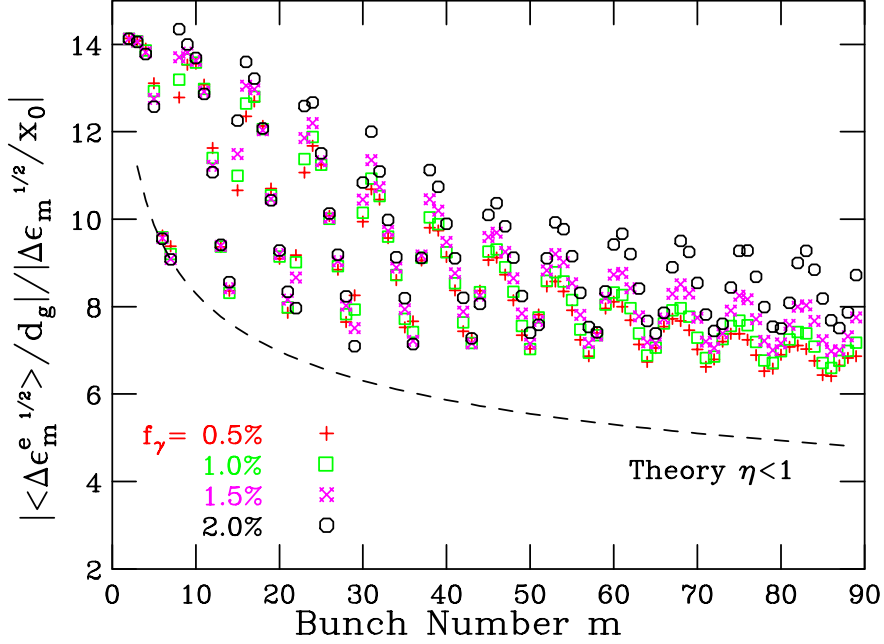


Figure 15.17: (color) Plot of ratio of transient square-root-emittance with girder misalignments but no beam offsets to that with beam offsets but no girder misalignments at the linac exit of the SLAC NLC with energy chirp $f_\gamma = 0.5, 1.0, 1.5$, and 2.0% . The results appears to be f_γ -independent and follow the trend of the theoretical prediction for $\eta < 1$ shown in dashes.

betatron wavelengths, $N_g = 2500$ may be a reasonable number, which will be used in the discussions below.

Next we vary the energy chirp to $f_\gamma = 0.5\%, 1.0\%, 1.5\%$, and 2.0% . In all these cases, $\eta < 1$. We see in Fig. 15.17 that the simulation results fall on each other implying that there is no dependency on f_γ . Careful examination reveals that the ratio of the emittances appears to become larger for larger energy chirp especially when $f_\gamma = 2.0\%$. This is understandable, because the parameter η is closer to unity. The theoretical prediction is also shown; it appears to underestimate the simulation results.

Now let us examine the situation when $\eta > 1$. At the linac exit, η turns unity at the 48th bunch when the energy chirp $|f_\gamma| = 3.0\%$, at the 18th bunch when $|f_\gamma| = 5.0\%$, and at the 10th bunch when $|f_\gamma| = 7.0\%^{††}$. Simulations for these values of energy chirp

^{††} $|f_\gamma| = 5$ and 7% would be unrealistically too high to survive the dispersive regions of the linear

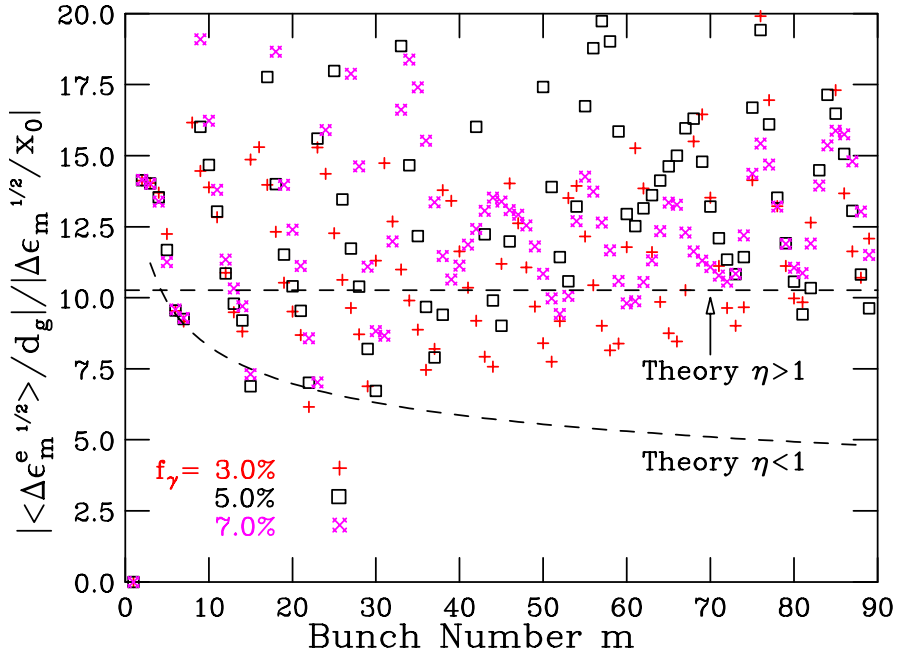


Figure 15.18: (color) Plot of ratio of transient emittance with girder misalignment errors but no initial displacement errors to that with initial displacement errors but no misalignment errors at the linac exit of the SLAC NLC with energy chirp $f_\gamma = 3.0, 5.0$, and 7.0% . The results appear to be f_γ -independent and follow the trend of the theoretical prediction for $\eta > 1$ shown in dashes.

are shown in Fig. 15.18. First, these results appear to be f_γ -independent. Second, the ratios of emittances are definitely larger than those in Fig. 15.17 where $\eta < 1$. Third, these results are mostly bunch-number-independent, unlike those in Fig. 15.17. These observations lead us to conclude that the results follow the theoretical prediction for $\eta > 1$.

15.4.0.4 Application

We learn from Figs. 15.17 and 15.18 that the ratios of the normalized transient square-root-emittances are, respectively, of the order 5 ($\eta < 1$) and 10 ($\eta > 1$) for the SLAC NLC linac, implying that the emittance growth from girder misalignments is much more serious than the growth from beam misalignment at linac entrance. In Fig. 15.19, we

collider; $|f_\gamma| = 3\%$ is marginal.

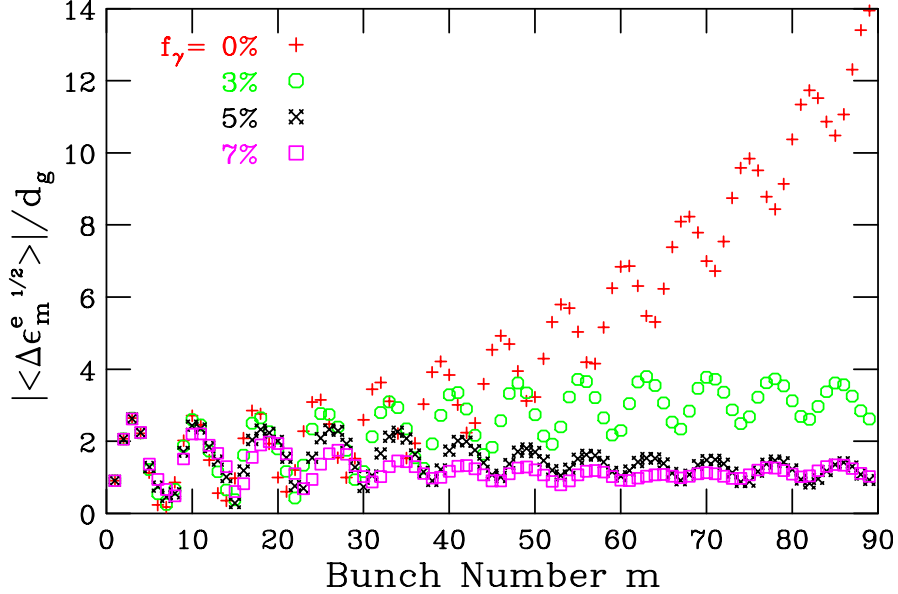


Figure 15.19: (color) Plot of transient square-root-emittance with girder misalignments but no beam offsets at the linac exit of the SLAC NLC with energy chirp $f_\gamma = 0.0, 3.0, 5.0$, and 7.0% . Compared with Fig. 15.10, larger energy chirp will be necessary for BNS damping.

show the simulated normalized growth of transient square-root-emittance at the linac exit due to girder misalignment errors but without initial beam displacement errors. This growth is larger than the same growth of an initially displaced beam but without misalignment errors shown in Fig. 15.10. As a result, a larger energy chirp will be necessary to damp MBBU and control emittance growth. We see that although the growth saturates at an energy chirp of $f_\gamma < 3\%$, the normalized growth has been 4-fold, and one needs an energy chirp of 5 to 7% to lower the growth to within 2-fold. On the other hand, for an initially displaced beam in a perfectly aligned linac, a 3% energy chirp controls the growth to less than 0.5 as indicated by Fig. 15.10.

Let us come back to the TESLA linac. Because of the small influence of the transverse wake, the displacements of the bunches possess rather good memory of their initial offsets when injected into the linac. As a result, in the absence of an energy chirp, the transient displacements, $\Delta y_m(\sigma)$, for all the bunches are more or less in phase during their betatron oscillations along the linac. The envelope of $\Delta y_m(\sigma)$ will become rather sensitive to the location of observation. To avoid ambiguity, the transient square-root-emittance, $\Delta \epsilon_m^{1/2}$, defined in Eq. (15.84) must be used. The top plot of Fig. 15.20 shows

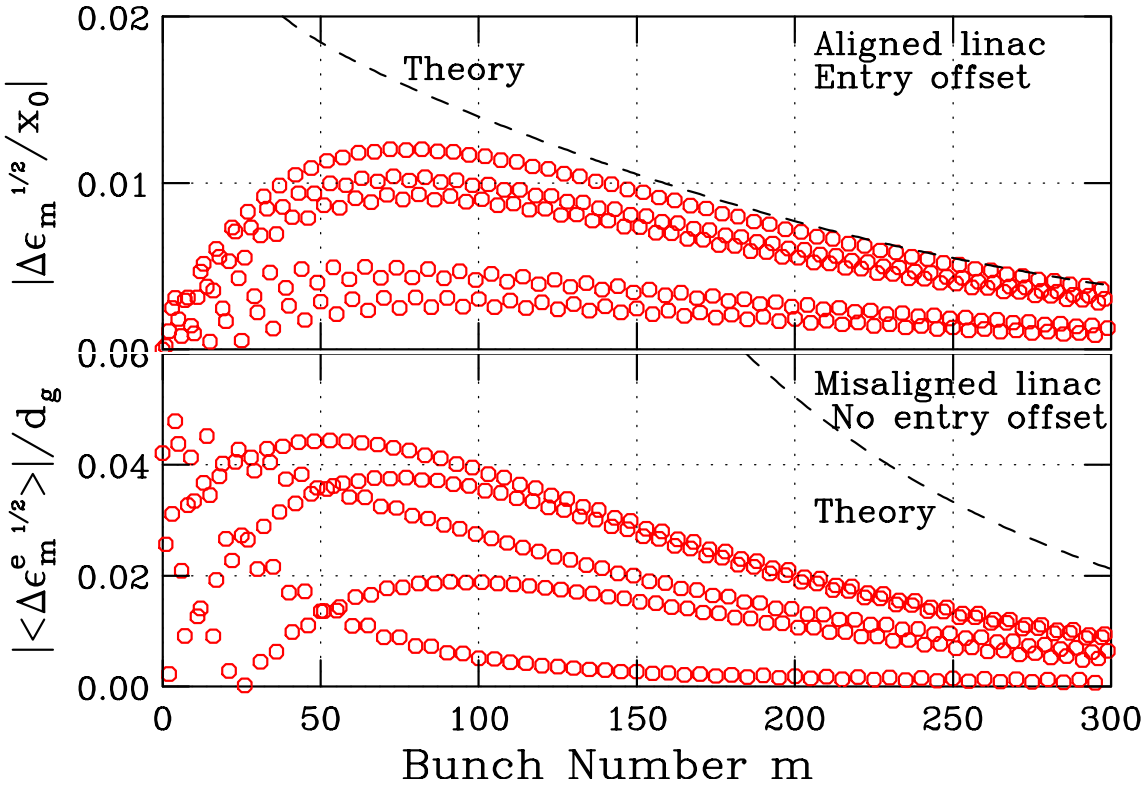


Figure 15.20: (color) Simulated normalized transient square-root-emittances for the first 300 TESLA bunches without energy chirp at the linac exit. Top plot is for bunches injected all with offset y_0 but no divergence in a perfectly aligned linac. Lower plot is for no injection offset, but the 2500 linac girders have rms misalignment d_g . Theoretical predictions are shown as dashes.

the simulated normalized transient square-root-emittance for a TESLA beam without energy chirp at the linac exit, where the linac elements are perfectly aligned while the beam is injected with the same offset y_0 but no divergence for all the bunches. We see that with an effective quality factor of $Q = 125000$, the maximum normalized transient square-root-emittance is small and completely acceptable, around ~ 0.012 near the beginning of the bunch train and rolling off to ~ 0.005 near the 300th bunch. The theoretical prediction [Eq. (15.74)] is shown as dashes, and unexpectedly agrees well with simulations for bunch number $m \gtrsim 150$. The lower plot shows the beam without offset at injection into the linac, but there are random misalignment errors in the 2500 girders. (Actually, each TESLA linac has less number of girders.) Although the normalized transient square-root-emittance becomes almost 4 times larger than the top plot, starting

with the maximum of ~ 0.045 and rolling off to ~ 0.012 near the 300th bunch, it is still acceptable. The theoretical prediction is shown as dashes and highly overestimates the simulation results. The disagreement is not hard to understand. Both Eqs. (15.83) and (15.81) do not apply well to the TESLA situation where the wake effect and MBBU are small. This prediction here is the product of the expressions in Eqs. (15.83) and (15.81) and therefore accumulates more uncertainty.

15.5 Exercises

- 15.1. (1) Assuming that the acceleration gradient is much less than the betatron wave number, derive the beam-breakup solutions, Eqs. (15.34) and Eq. (15.36), for the displacements of the head and tail in the two-particle model.
- (2) The dipole transverse wake function of the SLAC linac per cavity cell at 1 mm is 62.9 V/pC/m. The bunch is of rms length 1 mm containing 5×10^{10} electrons. The cavity accelerating frequency is 2.856 GHz, with each cavity having the length of $\frac{1}{3}$ wavelength. The betatron wave number is $k_\beta = 0.06 \text{ m}^{-1}$. In a two-particle model, compute the ratio of the deflection of the tail particle versus that of the head particle along the whole linac. Compute the same ratio if the linac stays at 1 GeV without acceleration.
- 15.2. A linac has a lattice consisting of N FODO cells. In between two consecutive quadrupoles, there is an acceleration structure of length ℓ , which is half of the FODO cell length. The acceleration is linear with $E_f/E_i = 1 + 2N\alpha\ell$ where E_i and E_f are, respectively, the initial and final energy across the N FODO cells.
- (1) Show that the transverse transfer matrix across the n th acceleration structure is
- $$\begin{pmatrix} 1 & \frac{1+n\alpha\ell}{\alpha} \ln \frac{1+(n+1)\alpha\ell}{1+n\alpha\ell} \\ 0 & \frac{1+n\alpha\ell}{1+(n+1)\alpha\ell} \end{pmatrix}. \quad (15.85)$$
- (2) Is the transfer matrix symplectic? Give a physical answer.
Hint: Solve Eq. (15.33) with $k_\beta = 0$.
- 15.3. The NLC bunch has an rms length of $\sigma_\ell = 150 \mu\text{m}$ containing 1.1×10^{10} electrons. The linac has a length of 10 km, accelerating electrons from 10 GeV to 500 GeV. Assume a uniform betatron focusing with 100 betatron oscillations in the linac. The accelerating structure has a transverse mode at the mean frequency of $\bar{\nu} = 15.25 \text{ GHz}$ with an rms spread $\sigma_\nu = 25\%$ of $\bar{\nu}$.
- (1) Use Eq. (15.44) to compute the transverse wake function at a distance σ_ℓ , assuming that the average kick factor is $\bar{K} = 40 \text{ MV/nC/m}^2$.
- (2) Compute the multiplication factor of the tail particle in the two-particle model at the end of the linac.
- (3) Assuming the natural chromaticity of $\xi = (\Delta k_\beta/k_\beta)/\delta = -1$ for the FODO-cell lattice, compute the energy spread between the head and tail of the bunch in

order to damp the deflection of the tail.

- 15.4. (1) Complete the derivation of the beam-breakup deflection of the m th bunch as given by Eq. (15.54).
(2) For the NLC with 95 bunches with spacing 42 cm, estimate the deflection of the last bunch if the first bunch has an initial offset of 1 μm . You may take the mean energy of the linac in the computation and the dipole wake at one bunch spacing as 0.21 MV/nC/m².
- 15.5. Fill in the steps and give the estimate of the energy spread from the first to the 95th bunch in order to damp the beam breakup instability of the bunch train as outlined in Sec. 15.3.3.

Bibliography

- [1] C.M. Ankenbrandt *et al.* (Muon Collider Collaboration), Phys. Rev. ST Accel. Beams **2**, 081001 (1999).
- [2] E.-S. Kim, A.M. Sessler, and J.S. Wurtele, Part. Accel. Conf., March 29 - April 2, 1999, New York City, Article THP45.
- [3] V. Balakin, A. Novokhatsky, and V. Smirnov, Proc. 12th Int. Conf. High Energy Accel., Fermilab 1983, p.119.
- [4] V.E. Balakin, Proc. Workshop on Linear Colliders, SLAC, 1988, p.55.
- [5] K.L.F. Bane and R.L. Gluckstern, Particle Accelerators **42**, 123 (1993).
- [6] R. Jones, K. Ko, N.M. Kroll, R.H. Miller, and K.A. Thompson, *Equivalent Circuit Analysis of the SLAC Damped Detuned Structure*, EPAC'96, 1996, p.1292; R. Jones, K. Ko, N.M. Kroll, and R.H. Miller, *Spectral Function Calculation of Angle Wakes, Wake Moments, and Misalignment Wakes for the SLAC Damped Detuned Structures (DDS)*, PAC'97, 1997, p.551; R. Jones, N.M. Kroll, and R.H. Miller, R.D. Ruth, and J.W. Wang, *Advanced Damped Detuned Structure Development at SLAC*, PAC'97, 1997, p.548; M. Dehler, R.M. Jones, N.M. Kroll, and R.H. Miller, I. Wilson and J.W. Wuensch, *Design of a 30 GHz Damped Accelerating Structure*, PAC'97, 1997, p.518.
- [7] K. Yokoya, *Cumulative Beam Breakup in Large-Scale Linacs*, DESY 86-084, ISSN 0418-9833, 1986.
- [8] C.L. Bohn and J.R. Delayen, Phys. Rev. **A45**, 5964 (1992). “Multibunch Domain B” introduced in this reference is the limit of zero focusing variation away from wake zero-crossing.

- [9] C.L. Bohn and K.Y. Ng, Phys. Rev. Lett. **85**, 984 (2000); *Preserving High Multibunch Luminosity in Linear Colliders*, Fermilab Report FERMILAB-PUB-00-072-T, 2000.
- [10] G. Stupakov, talk given in SLAC-Fermilab Video Conference, September, 1999.
- [11] G. Stupakov, *Effect of Energy Spread in the Beam Train on Beam Breakup Instability*, SLAC Report, LLC-0027, 1999.
- [12] C.L. Bohn, Proceedings of the 1990 Linear Accelerator Conference, Los Alamos National Laboratory Report No. LA-12004-C, p. 306.
- [13] C.L. Bohn and K.Y. Ng, “Theory and Suppression of Multibunch Beam Breakup in Linear Colliders”, Proc. of XX Int. Linac Conf., Aug. 21-25, 2000, Monterey, CA.
- [14] TESLA Technical Design Report, DESY Report 2001-011.
- [15] K.Y. Ng and C.L. Bohn, *Theory of Cumulative Beam-Breakup with BNS Damping*, Proc. of 2nd Asian Particle Accelerator Conference, Sep. 17-21, 2001, Beijing, China.
- [16] K. Yokoya, “Cumulative Beam Breakup in Large-scale Linacs”, DESY Report 86-084, 1986.

Chapter 16

TRANSITION AND SPACE CHARGE MISMATCH

The slippage factor has been defined as

$$\eta = \frac{1}{\gamma_t^2} - \frac{1}{\gamma^2} \quad (16.1)$$

in earlier chapters, where $E_0 = \gamma E_{\text{rest}}$ is the total energy of the synchronous particle having rest energy E_{rest} , and $\gamma_t E_{\text{rest}}$ is the transition energy of the lattice. As the particle crosses transition through ramping, the slippage factor passes through zero and switches sign from negative to positive. To maintain phase stability, it is also necessary for the synchronous phase ϕ_s to jump from $0 \leq \phi_s < \frac{1}{2}\pi$ to $\frac{1}{2}\pi < \phi_s \leq \pi$. The synchrotron angular frequency is defined as

$$\omega_s = \sqrt{-\frac{eh\eta V_{\text{rf}} \cos \phi_s}{2\pi\beta^2 E_0}} \omega_0 , \quad (16.2)$$

where V_{rf} is the rf voltage, h is the rf harmonic, β is the velocity of the synchronous particle with respect to the velocity of light, and ω_0 is the revolution angular frequency. Because of its dependency on η , the synchrotron frequency also slows down as transition is approached. Thus, the motion of the particle cannot follow the rf bucket in the longitudinal phase space when it is close to transition. Here, we first study the kinematics as the bunch is ramped through transition, and then the space charge mismatch of the bunch length below and above transition.

16.1 Equations of Motion

Physically, η measures the amount of time or phase slippage of a bunch particle with respect to the synchronous particle. Thus, for a particle with energy deviation ΔE , its rf phase $\Delta\phi$ slips at a rate of*

$$\frac{d\Delta\phi}{dt} = \frac{h\eta\omega_0}{\beta^2 E_0} \Delta E . \quad (16.3)$$

At the same time, this off-energy particle receives additional energy from the rf cavities at the rate of

$$\frac{d\Delta E}{dt} = \frac{eV_{rf}\omega_0}{2\pi} [\sin(\phi_s + \Delta\phi) - \sin\phi_s] . \quad (16.4)$$

Formerly, when we characterize the beam particle by τ , its arrival time ahead of the synchronous particle, the right side of $d\tau/ds$ in Eq. (2.9) or (2.11) is preceded by a negative sign, implying that the particle will arrive late ($\tau < 0$) above transition ($\eta > 0$) for a positive momentum offset. Here, $\Delta\phi$ is the slip in rf phase relative to the synchronous particle. When the particle arrives late at the cavity gap, the rf phase will have evolved more than $2\pi h$. Thus, the rf phase slip is positive and so is the sign preceding the right side of Eq. (16.3). Eliminating ΔE , we obtain for small $\Delta\phi$ the equation governing the motion of the phase of the particle:

$$\frac{d}{dt} \left(\frac{\beta^2 E_0}{h\eta\omega_0} \frac{d\Delta\phi}{dt} \right) - \frac{eV_{rf} \cos\phi_s \omega_0}{2\pi} \Delta\phi = 0 . \quad (16.5)$$

Unlike our previous discussion, β , E_0 , η , and ω_0 vary with time and should not be taken out from the first derivative operator. This is especially true for η which appears in the denominator. However, as an approximation, we can neglect the slow time variations of all the parameters except η/E_0 . This leads to

$$\frac{d}{dt} \left(\frac{E_0}{\eta} \frac{d\Delta\phi}{dt} \right) - \left(\frac{heV_{rf} \cos\phi_s \omega_0^2}{2\pi\beta^2} \right) \Delta\phi = 0 . \quad (16.6)$$

Under the approximation that the second bracketed term is considered time independent and also the variation of η/E_0 is linear in time near transition,[†] or

$$\frac{\eta}{E_0} = \frac{2\dot{\gamma}_t t}{\gamma_t^4 E_{rest}} , \quad (16.7)$$

* $d\Delta\phi/dt$ is the rf phase slip in one revolution period of the *synchronous particle*, not the off-energy particle under consideration. Therefore, this is not equal to $-\Delta\omega/h$ where $\Delta\omega$ is the slip in angular frequency of the particle. See Sec. 18.1 for detail

[†]Some authors assume η to be linear in t instead. In that case, one needs also the additional assumption that $\dot{\gamma}_t T_c \ll 1$.

Eq. (16.6) can be solved exactly in terms of Bessel functions of fractional orders [3]. However, all the important features of the solution can be estimated easily without going into the differential equation and Bessel functions [1]. Best of all, through the estimation, one can have a clear picture of what is going on during transition. In Eq. (16.7), the time t is measured from transition. Thus, $t < 0$ is below transition and $t > 0$ is above. On the other hand, the subscript t implies evaluation of the respective quantity at the moment when transition is crossed. Thus,

$$\dot{\gamma}_t = \frac{eV_{\text{rf}}\omega_0}{2\pi E_{\text{rest}}} \sin \phi_s \quad (16.8)$$

is the rate at which γ is ramped right at transition.

We can also rewrite Eq. (16.6) in the form

$$\frac{d}{dt} \left(\frac{1}{\omega_s^2} \frac{d\Delta\phi}{dt} \right) + \Delta\phi = 0 , \quad (16.9)$$

where ω_s is given by Eq. (16.2). However, Eq. (16.2) should be considered as a definition of ω_s only. This is because the beam particle does not follow the invariant trajectory of the Hamiltonian when it is near transition and therefore does not make synchrotron oscillations, so that ω_s , as defined by Eq. (16.2), loses its meaning of frequency.

16.2 Nonadiabatic Time

When η^{-1} is not changing rapidly, a bucket can be defined. The bucket height is given by

$$(\Delta E)_{\text{bucket}} \propto \left(\frac{E_0}{|\eta|} \right)^{1/2} . \quad (16.10)$$

However, as the bunch particle passes through transition, η^{-1} changes rapidly. Here, we follow the assumption of a linear time variation for η/E_0 as given by Eq. (16.7), while all other parameters such as the rf voltage and the synchronous phase, aside from flipping from ϕ_s to $\pi - \phi_s$, are held fixed near transition. This means that when transition is approached, synchrotron frequency slows down to zero and the bucket height increases to infinity. In other words, when it is close enough to transition, the particle will not be able to catch up with the rapid changing of the bucket shape. This time period, from

$t = -T_c$ to $t = T_c$ is called the nonadiabatic region, and T_c the *nonadiabatic time*. Here, we define this region by

$$\omega_s \leq \frac{2}{(\Delta E)_{\text{bucket}}} \frac{d(\Delta E)_{\text{bucket}}}{dt} . \quad (16.11)$$

This just implies that inside this region, the rate at which the bucket height is changing is faster than the rate of executing synchrotron oscillations. The right side is

$$\left. \frac{2}{(\Delta E)_{\text{bucket}}} \frac{d(\Delta E)_{\text{bucket}}}{dt} \right|_{t=-T_c} = 2 \left. \frac{d}{dt} \sqrt{\frac{T_c}{-t}} \right|_{t=-T_c} = \left. \sqrt{\frac{T_c}{(-t)^3}} \right|_{t=-T_c} = \frac{1}{T_c} . \quad (16.12)$$

Evaluating at $t = -T_c$, the left side of Eq. (16.11) is

$$\omega_s|_{t=-T_c} = \sqrt{\frac{h\dot{\gamma}_t T_c e V_{\text{rf}} \cos \phi_s}{\pi \gamma_t^4 E_{\text{rest}}}} \omega_\infty , \quad (16.13)$$

where $\omega_\infty = \omega_0/\beta$ and is time independent. We then obtain the nonadiabatic time from Eq. (16.11):

$$T_c = \left[\left(\frac{\beta_t \gamma_t^4}{2\omega_\infty h} \right) \left(\frac{|\tan \phi_s|}{\dot{\gamma}_t^2} \right) \right]^{1/3} , \quad (16.14)$$

where the expression of $\dot{\gamma}_t$ in Eq. (16.8) has been used. Note that the nonadiabatic time is just an approximate time. The factor 2 on the right side of Eq. (16.11) was inserted for the purpose that T_c given by Eq. (16.14) is exactly the same as the adiabatic time quoted in the literature. We have written Eq. (16.14) in such a way that the factor in the first brackets contains parameters of the lattice, while $\dot{\gamma}_t$ in the second brackets is determined by the ramp curve and ϕ_s , the synchronous phase at transition, is determined by the rf-voltage table.

16.3 Bunch Shape at Transition

For the sake of simplicity, we adopt a model which states that,

- (1) when $|t| > T_c$, the beam particles follow the bucket with synchrotron oscillations, and
- (2) when $|t| < T_c$, the beam particles make no synchrotron oscillations at all.

At $t = -T_c$, the beam particle still follows the bucket. Therefore, From Eq. (16.3), the bunch length σ_ϕ is related to the rms energy spread σ_E by

$$\nu_s \sigma_\phi = \frac{h|\eta|}{\beta_t^2 \gamma_t E_{\text{rest}}} \sigma_E , \quad (16.15)$$

where η is to be evaluated at $t = -T_c$, and the energy E_0 is evaluated approximately right at transition since the change is slow. The 95% bunch area is defined as

$$S = 6\pi\sigma_\tau\sigma_E , \quad (16.16)$$

where this expression should hold in the adiabatic region. From Eqs. (16.15) and (16.16), we obtain the rms bunch length in time $\sigma_\phi = h\omega_0\sigma_\tau$ as

$$\sigma_\tau = \left(\frac{S|\eta|}{6\pi\nu_s\omega_0\beta_t^2\gamma_t E_{\text{rest}}} \right)^{1/2} . \quad (16.17)$$

Substituting $\eta(-T_c)$ from Eq. (16.7) and $\omega_s(-T_c)$ from Eqs. (16.11) and (16.12), we arrive at

$$\sigma_\tau = \frac{1}{\sqrt{3\pi}} \left(\frac{ST_c^2\dot{\gamma}_t}{\beta_t^2\gamma_t^4 E_{\text{rest}}} \right)^{1/2} . \quad (16.18)$$

Our simple model requires no synchrotron oscillation inside the nonadiabatic region. This is equivalent to having $\eta = 0$ in Eq. (16.3); or the phase of each particle will not change at all. Therefore, Eq. (16.18) is also the bunch length right at transition, where the exact expression from solving the differential equation is

$$\sigma_\tau = \frac{2}{3^{5/6}\Gamma(\frac{1}{3})} \left(\frac{ST_c^2\dot{\gamma}_t}{\beta_t^2\gamma_t^4 E_{\text{rest}}} \right)^{1/2} . \quad (16.19)$$

This just amounts to the replacement of $1/\sqrt{3\pi} = 0.326$ by $2/[3^{5/6}\Gamma(\frac{1}{3})] = 0.300$, where $\Gamma(\frac{1}{3}) = 2.678939$ is the Gamma function. Our estimate is about 8.8% too large because our simple model does not allow the bunch to continue to shrink in the nonadiabatic region.

On the other hand, without synchrotron oscillations, the energy of each beam particle is accelerated by the focusing rf force according to Eq. (16.4). From $t = -T_c$ to $t = 0$, a particle at a phase offset $\Delta\phi$ from the synchronous particle will acquire an energy

$$\Delta E = T_c E_{\text{rest}} \frac{d\dot{\gamma}}{d\Delta\phi} \Delta\phi , \quad (16.20)$$

where, according to Eq. (16.4),

$$\frac{d\dot{\gamma}}{d\Delta\phi} \approx \frac{\dot{\gamma}_t}{\tan\phi_s}, \quad (16.21)$$

and the small phase-offset approximation has been made. At $t = -T_c$, when there are still synchrotron oscillations in our simple model, if we write the phase offset as

$$\Delta\phi = \widehat{\Delta\phi} \cos\omega_s t, \quad (16.22)$$

according to the phase-drift equation, the energy spread of the particle is

$$\Delta E = -\frac{\nu_s \beta_t^2 \gamma_t E_{\text{rest}}}{h\eta} \widehat{\Delta\phi} \sin\omega_s t = -\frac{\nu_s \beta_t^2 \gamma_t E_{\text{rest}}}{h\eta} \sqrt{\widehat{\Delta\phi}^2 - (\Delta\phi)^2}, \quad (16.23)$$

where $\widehat{\Delta\phi} = \sqrt{6}\sigma_\tau h\omega_0$ is the half width of the bunch at $t = -T_c$ as given by Eq. (16.18). When evaluated at $t = -T_c$, it is found that the coefficient of Eq. (16.23) is equal to that of Eq. (16.20), and we denote it by

$$a = -\frac{\nu_s \beta_t^2 \gamma_t E_{\text{rest}}}{h\eta} = T_c E_{\text{rest}} \frac{d\dot{\gamma}}{d\Delta\phi}. \quad (16.24)$$

Therefore, the total energy spread at transition is given by

$$(\Delta E)_{\text{total}} = a \left[\sqrt{\widehat{\Delta\phi}^2 - (\Delta\phi)^2} + \Delta\phi \right]. \quad (16.25)$$

The maximum total energy spread comes out to be

$$(\Delta E)_{\text{total, max}} = \frac{1}{\sqrt{\pi}} \left(\frac{S \beta_t^2 \gamma_t^4 E_{\text{rest}}}{T_c^2 \dot{\gamma}_t} \right)^{1/2} \quad (16.26)$$

at $\Delta\phi = 2^{-1/2} \widehat{\Delta\phi}$. The exact value from the solution of a differential equation is

$$(\Delta E)_{\text{max}} = \frac{\Gamma(\frac{1}{3})}{3^{1/6} 2^{1/2} \pi} \left(\frac{S \beta_t^2 \gamma_t^4 E_{\text{rest}}}{T_c^2 \dot{\gamma}_t} \right)^{1/2}, \quad (16.27)$$

or just a replacement of $1/\sqrt{\pi} = 0.564$ by $\Gamma(\frac{1}{3})/(3^{1/6} 2^{1/2} \pi) = 0.502$. By the same token, the particle at the tail of the bunch will be decelerated by the same energy. Particles in between will be accelerated accordingly. The bunch shape at transition is therefore given by Fig. 1, which is slanted at an angle from the ΔE -axis. Our estimate of $(\Delta E)_{\text{total}}$ is about 11% too large. This is to be expected because we allow pure increment in energy

by the focusing rf potential in the nonadiabatic region without any motion in the phase direction.

As we recall, the maximum energy spread at transition is *not* derived via Eq. (16.16) and one should not expect Eq. (16.16) to hold in the nonadiabatic region. Here, we derive another expression for the bunch area right at transition. Using Eqs. (16.18) and (16.26) and the fact that the maximum half bunch length is $\hat{\tau} = \sqrt{6}\sigma_\tau$, we obtain the bunch area

$$S = \frac{1}{\sqrt{2}} \pi \hat{\tau} \widehat{\Delta E} \quad (16.28)$$

If the exact solutions in Eqs. (16.19) and (16.30) are used, one gets instead

$$S = \frac{\sqrt{3}}{2} \pi \hat{\tau} \widehat{\Delta E}, \quad (16.29)$$

or the replacement of $1/\sqrt{2} = 0.707$ by $\sqrt{3}/2 = 0.866$. Notice that so far we are still within a Hamiltonian system, the bunch area should be conserved. The fact that the bunch area is now less than $\pi \hat{\tau} \widehat{\Delta E}$ indicates that the bunch ellipse has been tilted, as illustrated in Fig. 16.1. This is because phase motion in the nonadiabatic region has almost (totally in our simplified model) been frozen and the energy change has been uneven along the bunch. This problem will be studied again in the next section.

To conclude this section, let us write the rms time spread and rms energy spread at transition as well as the nonadiabatic time in terms of the parameters that we can control, namely, the synchronous phase ϕ_s and ramping rate $\dot{\gamma}_t$ (Exercise 16.1):

$$\sigma_\tau \propto \frac{\tan^{\frac{1}{3}} \phi_s}{\dot{\gamma}_t^{\frac{1}{6}}}, \quad \sigma_E \propto \frac{\dot{\gamma}_t^{\frac{1}{6}}}{\tan^{\frac{1}{3}} \phi_s}, \quad T_c \propto \frac{\tan^{\frac{1}{3}} \phi_s}{\dot{\gamma}_t^{\frac{2}{3}}}. \quad (16.30)$$

16.4 More Sophisticated Approximation

16.4.1 Adiabatic Region

We now discard the simple model in the previous section and come back to Eq. (16.9), the equation governing motion of small phase offset. Instead of solving the differential

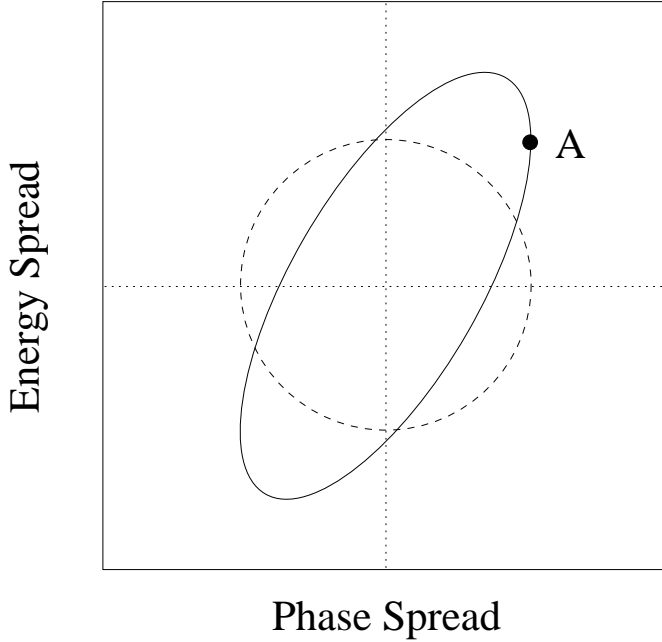


Figure 16.1: The evolution of the bunch, according to the simple model, from $t = -T_c$ (dashes) to the time when transition is crossed (solid). In the exact solution of the differential equation, there is an additional shrinkage in the phase spread of the ellipse. Point A indicates that when the phase offset is at a maximum, the energy offset is not at a maximum.

equation exactly, we are looking into approximates instead. In the adiabatic region that is not too far away from transition, the particle is performing synchrotron oscillations with a slowly changing frequency $\omega_s/2\pi$ given by Eq. (16.2). The solution of Eq. (16.9) is therefore of the form

$$\Delta\phi = Ae^{i \int \omega_s dt}, \quad (16.31)$$

where the amplitude A is also slowly changing with time. We then have

$$\frac{d}{dt} \left(\frac{1}{\omega_s^2} \frac{d\Delta\phi}{dt} \right) = -\Delta\phi + \left[\left(\frac{2i\dot{A}}{\omega_s} - \frac{iA\dot{\omega}_s}{\omega_s^2} \right) + \left(\frac{\ddot{A}}{\omega_s^2} - \frac{2\dot{A}\dot{\omega}_s}{\omega_s^3} \right) \right] e^{i \int \omega_s dt}. \quad (16.32)$$

Since $\Delta\phi$ varies much faster than A and ω_s , we can neglect \ddot{A} , $\ddot{\omega}_s$, and $\dot{A}\dot{\omega}_s$, and set

$$\frac{2\dot{A}}{\omega_s} = \frac{A\dot{\omega}_s}{\omega_s^2}, \quad (16.33)$$

so that Eq. (16.9) is satisfied. The relation in Eq. (16.33) leads to

$$\frac{A^2}{\omega_s} = \text{constant} , \quad (16.34)$$

implying that the solution of Eq. (16.9) or the rf phase of a beam particle in the adiabatic region can be written as

$$\Delta\phi = B\sqrt{\omega_s} e^{i\int \omega_s dt} , \quad (16.35)$$

with B being constant.

The dropping of the slowly varying terms from Eq. (16.32) is equivalent to assuming

$$\frac{\ddot{A}}{\omega_s^2} \ll \frac{A\dot{\omega}_s}{\omega_s^2} , \quad (16.36)$$

$$\frac{2\dot{A}\dot{\omega}_s}{\omega_s^3} \ll \frac{A\dot{\omega}_s}{\omega_s^2} . \quad (16.37)$$

Again, with the assumption of constant rf voltage V_{rf} , constant synchronous phase ϕ_s , and linear time variation of η/E_0 , we can write, using Eqs. (16.2), (16.7), and (16.8),

$$\omega_s^2(t) = b|t| \quad \text{with} \quad b = \frac{\dot{\gamma}_t h e V_{\text{rf}} |\cos \phi_s| \omega_\infty^2}{\pi \gamma_t^4 E_{\text{rest}}} . \quad (16.38)$$

Then, together with Eq. (16.34), it is easy to show that (Exercise 16.2),

$$\text{Eq. (4.6)} \implies |t| \gg \left(\frac{3}{8}\right)^{2/3} \left(\frac{1}{b}\right)^{1/3} , \quad (16.39)$$

$$\text{Eq. (4.7)} \implies |t| \gg \left(\frac{1}{2}\right)^{2/3} \left(\frac{1}{b}\right)^{1/3} . \quad (16.40)$$

In other words, the adiabatic solution is only valid if Eqs. (16.39) and (16.40) hold. A nonadiabatic time T_c can therefore be defined by letting

$$T_c = \left(\frac{1}{b}\right)^{1/3} , \quad (16.41)$$

which turns out to be exactly the same expression as our former definition in Eq. (16.12). Here, we arrive at a neat way to remember the nonadiabatic time:

$$\omega_s^2 = \frac{|t|}{T_c^3} \quad \text{or} \quad \omega_s|_{t=-T_c} = \frac{1}{T_c} . \quad (16.42)$$

Now, let us continue the study of the bunch shape in the adiabatic region. Differentiating Eq. (16.35) and using Eq. (16.34), we get

$$\frac{d\Delta\phi}{dt} = iB\omega_s^{3/2} \left[1 - \frac{i}{4} \left(\frac{T_c}{|t|} \right)^{3/2} \right] e^{i \int \omega_s dt}, \quad (16.43)$$

or

$$\frac{d\Delta\phi}{dt} = i\omega_s \Delta\phi \left[1 + \frac{1}{16} \left(\frac{T_c}{|t|} \right)^3 \right]^{1/2} e^{-i\varphi}, \quad (16.44)$$

with

$$\varphi = \tan^{-1} \frac{1}{4} \left(\frac{T_c}{|t|} \right)^{3/2}. \quad (16.45)$$

Then, using Eq. (16.3), we arrive at the energy offset of the particle

$$\Delta E = i\omega_s \Delta\phi \frac{\beta^2 \gamma E_{\text{rest}}}{|\eta| h\omega_0} \left[1 + \frac{1}{16} \left(\frac{T_c}{|t|} \right)^3 \right]^{1/2} e^{-i\varphi}. \quad (16.46)$$

We see from Eq. (16.35) that, as the bunch is approaching the nonadiabatic region, its width shrinks in the same way as the decrease of $\sqrt{\omega_s}$. On the other hand, from Eq. (16.46), the height of the bunch increases because of the square root term and the $t^{-1/4}$ dependency in the front factor. We also see that there is a phase advance φ of the energy offset, or a tilt in the bunch shape in the longitudinal phase space. This tells us that there is already slowing down in the phase motion in the adiabatic region when transition is approached. This reminds us again that there is no clearcut boundary between the adiabatic and nonadiabatic regions.

The next task is to relate the constant B to the bunch area. The motion of the particle described by Eqs. (16.35) and (16.46) is of the form

$$\Delta\phi = \widehat{\Delta\phi} \cos\theta, \quad \Delta E = \widehat{\Delta E} \sin(\varphi - \theta), \quad (16.47)$$

which map out a tilted ellipse of area

$$S = \pi \frac{\widehat{\Delta\phi}}{h\omega_0} \widehat{\Delta E} \cos\varphi, \quad (16.48)$$

inscribed inside the rectangle of half-width $\widehat{\Delta\phi}/(h\omega_0)$ and half-height $\widehat{\Delta E}$, and this is the bunch area in eV-s.

The half bunch length in the adiabatic region can be read off from Eq. (16.35):

$$\widehat{\Delta\phi} = B\omega_s^{1/2} . \quad (16.49)$$

Substituting into Eq. (16.46), we obtain the half energy spread

$$\widehat{\Delta E} = \frac{\beta^2 \gamma E_{\text{rest}}}{|\eta| h \omega_0} \omega_s^{3/2} \left[1 + \frac{1}{16} \left(\frac{T_c}{|t|} \right)^3 \right]^{1/2} . \quad (16.50)$$

where the last square bracket term is just $\sec \varphi$, as given by Eq. (16.45). When they are substituted in the bunch area in Eq. (16.48), the constant B will be determined,

$$S = \frac{B^2 e V_{\text{rf}} |\cos \phi_s|}{2h} , \quad (16.51)$$

which is time independent as anticipated.

Using the linear time dependency of ω_s^2 from Eq. (16.42) and replacing the constant B with Eq. (16.51), we obtain the time dependency of the half bunch length,

$$\widehat{\Delta\phi} = \left(\frac{2hS}{eV_{\text{rf}} |\cos \phi_s| T_c} \right)^{1/2} \left(\frac{|t|}{T_c} \right)^{1/4} , \quad (16.52)$$

and also

$$\widehat{\Delta E} = \frac{\omega_0}{\pi} \left(\frac{hSeV_{\text{rf}} |\cos \phi_s| T_c}{2} \right)^{1/2} \left(\frac{T_c}{|t|} \right)^{1/4} \left[1 + \frac{1}{16} \left(\frac{T_c}{|t|} \right)^3 \right]^{1/2} . \quad (16.53)$$

Through the definition of the nonadiabatic time, the half bunch length and half energy spread can be written in the form that resembles the expressions in Eqs. (16.19) and (16.27):

$$\widehat{\Delta\phi} = h\omega_0 \left(\frac{2ST_c^2 \dot{\gamma}_t}{\pi \beta_t^2 \gamma_t^4 E_{\text{rest}}} \right)^{1/2} \left(\frac{|t|}{T_c} \right)^{1/4} , \quad (16.54)$$

and also the

$$\widehat{\Delta E} = \left(\frac{S\beta_t^2 \gamma_t^4 E_{\text{rest}}}{2\pi T_c^2 \dot{\gamma}_t} \right)^{1/2} \left(\frac{T_c}{|t|} \right)^{1/4} \left[1 + \frac{1}{16} \left(\frac{T_c}{|t|} \right)^3 \right]^{1/2} . \quad (16.55)$$

16.4.2 Nonadiabatic Region

We can also study the nonadiabatic region of the Eq. (16.14), which can be transformed to

$$\frac{d}{dx} \left(\frac{1}{|x|} \frac{d\Delta\phi}{dx} \right) + \Delta\phi = 0 , \quad (16.56)$$

where $x = t/T_c$ and use has been made of Eq. (16.38). However, we find it easier to solve instead the differential equation governing energy offset, which reads

$$\frac{d^2\Delta E}{dx^2} + |x|\Delta E = 0 . \quad (16.57)$$

We would like to introduce a *normalized* energy-offset

$$\Delta p(x) = \frac{2\pi}{\omega_0 e V_{\text{rf}} \cos \phi_s T_c} \Delta E(x) = \frac{\tan \phi_s}{\dot{\gamma}_t E_{\text{rest}} T_c} \Delta E(x) , \quad (16.58)$$

so that $\Delta p(x)$ will have the same dimension as $\Delta\phi$, the energy equation of motion becomes the simple relation

$$\Delta\phi = - \operatorname{sgn}(x) \frac{d\Delta p}{dx} . \quad (16.59)$$

For the sake of convenience, we concentrate on the situation above transition only when $x \geq 0$ so that the absolute-value sign can be dropped and $\operatorname{sgn}(x)$ can be ignored. At the end, we can replace x by $|x|$ everywhere in the solution so that it applies to both above and below transition. Note that both $\cos \phi_s$ and $\tan \phi_s$ are now negative.

To seek a solution within the nonadiabatic region where $|x| < 1$, it is natural to resort to power series:

$$\Delta p = \sum_{n=0}^{\infty} a_n x^{n+k} , \quad (16.60)$$

where k is to be determined. Substitution into of Eq. (16.57) leads to

$$\sum_{n=-3}^{\infty} a_{n+3} (n+k+3)(n+k+2)x^{n+k+1} + \sum_{n=0}^{\infty} a_n x^{n+k+1} = 0 . \quad (16.61)$$

The indicial equations determine that $k = 0$ and $a_2 = 0$. The solution can be written as

$$\Delta p = \left(a_0 + a_3 x^3 + a_6 x^6 + \dots \right) + \left(a_1 x + a_4 x^4 + a_7 x^7 + \dots \right) , \quad (16.62)$$

where the coefficients are related by the recurrence relation

$$a_{n+3} = -\frac{a_n}{(n+3)(n+2)} . \quad (16.63)$$

Thus, there are two free constants a_0 and a_1 , which are to be expected from a second-order differential equation. It is more convenient to rewrite Eq. (16.62) as

$$\Delta p = a_0 \left(1 + a'_3 x^3 + a'_6 x^6 + \dots \right) + a_1 \left(x + a'_4 x^4 + a'_7 x^7 + \dots \right) , \quad (16.64)$$

where we have redefined the coefficients as $a'_n = a_n/a_0$ for $n = 3, 6, 9, \dots$, and $a'_n = a_n/a_1$ for $n = 4, 7, 8, \dots$. They can be readily computed from the recurrence relation:

$$\begin{cases} a'_3 = -\frac{1}{(3.2)}, \quad a'_6 = +\frac{1}{(6.5)(3.2)}, \quad a'_9 = -\frac{1}{(9.8)(6.5)(3.2)}, \quad \dots, \\ a'_4 = -\frac{1}{(4.3)}, \quad a'_7 = +\frac{1}{(7.6)(4.3)}, \quad a'_{10} = -\frac{1}{(10.9)(7.6)(4.3)}, \quad \dots, \end{cases} \quad (16.65)$$

where the periods or dots in above denote multiplication. The phase offset can now be obtained using Eq. (16.59):

$$\Delta\phi = -a_0 \left(3a'_3 x^2 + 6a'_6 x^5 + \dots \right) - a_1 \left(1 + 4a'_4 x^3 + 7a'_7 x^6 + \dots \right) . \quad (16.66)$$

Now we are going to derive the trajectory of a particle which is at its maximum phase offset right at transition. Thus we obtain

$$-a_1 = \widehat{\Delta\phi}_0 = \frac{2^{3/2} h\omega_0}{3^{1/3} \Gamma(\frac{1}{3})} \left(\frac{ST_c^2 \dot{\gamma}_t}{\beta_t^2 \gamma_t^4 E_{\text{rest}}} \right)^{1/2} , \quad (16.67)$$

with the aid of Eq. (16.19), where an extra subscript “0” has been added to denote “right at transition” or $x = 0$ for the sake of clarity. This position of the beam particle corresponds to Point A in Fig. 16.1, where the energy offset is *not* at its maximum, but is related to it by

$$\Delta E = \widehat{\Delta E}_0 \sin \varphi , \quad (16.68)$$

where φ is the tilde angle referenced in Eq. (16.47), and it modifies the expression of bunch area to $S = \pi \widehat{\tau}_0 \widehat{\Delta E}_0 \cos \varphi$. However, from Eq. (16.29), the angle is found to be $\cos \varphi = \sqrt{3}/2$. We therefore have

$$a_0 = \frac{1}{2} \widehat{\Delta p}_0 = \frac{1}{2} \frac{|\tan \phi_s|}{\dot{\gamma}_t E_{\text{rest}} T_c} \widehat{\Delta E}_0 = \frac{1}{2} \frac{3^{1/6} \Gamma^2(\frac{1}{3})}{2\pi} \widehat{\Delta\phi}_0 , \quad (16.69)$$

where Eqs. (16.19) and (16.27) have been used, and obtain the relation

$$\frac{a_1}{a_0} = -\frac{2\widehat{\Delta\phi}_0}{\widehat{\Delta p}_0} = \frac{4\pi}{3^{1/6}\Gamma^2(\frac{1}{3})}. \quad (16.70)$$

The trajectory of the beam particle is governed by

$$\Delta p(x) = \widehat{\Delta\phi}_0 \left[-x(1 + a'_4 x^3 + a'_7 x^6 + \dots) - \frac{a_0}{a_1} (1 + a'_3 x^3 + a'_6 x^6 + \dots) \right], \quad (16.71)$$

$$\Delta\phi(x) = \widehat{\Delta\phi}_0 \left[(1 + 4a'_4 x^3 + 7a'_7 x^6 + \dots) + \frac{a_0}{a_1} (3a'_3 x^2 + 6a'_6 x^5 + 9a'_9 x^8 + \dots) \right]. \quad (16.72)$$

However, we are not so interested in the motion of a single particle. What we wish to derive are the half width and half energy spread of a bunch at different times. For this, we have to solve an envelope equation given by Eq. (16.89) below with the space charge coefficient n_{spch} set to zero. However, that is a nonlinear equation which is difficult to tackle. Instead, we try to extract the bunch length energy from the solution we obtained in Eqs. (16.71) and (16.72). To accomplish this, we introduce an ensemble of beam particles at the phase ellipse. This can be easily done by writing out the general solution of the differential equation [Eq. (16.57)] by a taking a linear combination of the Eq. (16.71) or (16.72) and another solution of the differential equation. Thus, we have

$$\begin{aligned} \Delta p(x) = & \widehat{\Delta\phi}_0 \left\{ \cos \psi \left[-x(1 + a'_4 x^3 + a'_7 x^6 + \dots) - \frac{a_0}{a_1} (1 + a'_3 x^3 + a'_6 x^6 + \dots) \right] \right. \\ & \left. - \sin \psi \left[\frac{\sqrt{3}a_0}{a_1} (1 + a'_3 x^3 + a'_6 x^6 + \dots) \right] \right\}, \end{aligned} \quad (16.73)$$

$$\begin{aligned} \Delta\phi(x) = & \widehat{\Delta\phi}_0 \left\{ \cos \psi \left[(1 + 4a'_4 x^3 + 7a'_7 x^6 + \dots) + \frac{a_0}{a_1} (3a'_3 x^2 + 6a'_6 x^5 + 9a'_9 x^8 + \dots) \right] \right. \\ & \left. + \sin \psi \left[\frac{\sqrt{3}a_0}{a_1} (3a'_3 x^2 + 6a'_6 x^5 + 9a'_9 x^8 + \dots) \right] \right\}, \end{aligned} \quad (16.74)$$

where $-\sqrt{3}a_0/a_1$ is included purely for convenience and the relation $\Delta\phi = -d\Delta p/dx$ still holds. One constant in these equation is $\widehat{\Delta\phi}_0$, the maximum phase offset of the phase ellipse at $x = 0$. In fact, it solely determines bunch area or the area of the ellipse (Exercise 16.4). The other constant is the phase angle ψ , which represents different particles on the ellipse in the longitudinal phase space.

As a first application, at $x = 0$, Eq. (16.73) becomes

$$\Delta p(x) = -\widehat{\Delta\phi}_0 \frac{a_0}{a_1} \left(\cos \psi + \sqrt{3} \sin \psi \right), \quad (16.75)$$

whose maximum occurs when $\psi = \pi/3$. This gives the normalized energy spread at transition

$$\widehat{\Delta p}_0 = -\frac{2a_0}{a_1} \widehat{\Delta\phi}_0, \quad (16.76)$$

agreeing with what we have in Eq. (16.70). The phase spread at transition is trivial because only the cosine term in Eq. (16.74) contributes.

Now let us proceed up to the order x . The energy spread in Eq. (16.73) gives

$$\Delta p(x) = -\widehat{\Delta\phi}_0 \frac{a_0}{a_1} \left[\cos \psi \left(1 + \frac{a_1}{a_0} x \right) + \sqrt{3} \sin \psi \right]. \quad (16.77)$$

For the maximum,

$$\cos \psi = \frac{1}{2} \left(1 + \frac{3a_1}{4a_0} x \right) \quad \text{and} \quad \sin \psi = \frac{\sqrt{3}}{2} \left(1 - \frac{a_1}{4a_0} x \right). \quad (16.78)$$

Thus, the half energy spread is

$$\widehat{\Delta p}(x) = \widehat{\Delta p}_0 \left[1 + \frac{a_1}{4a_0} x \right] = \widehat{\Delta p}_0 \left[1 - \frac{\pi}{3^{1/6} \Gamma^2(\frac{1}{3})} x \right]. \quad (16.79)$$

There is no $\mathcal{O}(x)$ in the correction to the half bunch length. The next order is $\mathcal{O}(x^2)$:

$$\Delta\phi(x) = \widehat{\Delta\phi}_0 \left[\cos \psi \left(1 - \frac{a_0}{2a_1} x^2 \right) - \sin \psi \frac{\sqrt{3}a_0}{2a_1} x^2 \right], \quad (16.80)$$

whose maximum occurs when $\psi = \mathcal{O}(x^2)$. Thus the half bunch length becomes

$$\widehat{\Delta\phi}(x) = \widehat{\Delta\phi}_0 \left[1 - \frac{a_0}{2a_1} x^2 \right] = \widehat{\Delta p}_0 \left[1 + \frac{3^{1/6} \Gamma^2(\frac{1}{3})}{8\pi} x^2 \right]. \quad (16.81)$$

Higher orders in x of the half energy spread and half bunch length of the bunch can therefore be computed.

It is evident that from time $|t|$ in the nonadiabatic region to the time when transition is crossed, the shrinkage of the bunch length is of order $(|t|/T_c)^2$ and is therefore small,

while the increase in energy spread is of order $(|t|/T_c)$ which is much larger. This explains why in the simple model of Sec. 16.3, we can just approximate the bunch length at transition to be the bunch length at the nonadiabatic time. On the other hand, we have to compute the increase in energy spread within the nonadiabatic region more accurately.

There is an important comment on why that particular combination of independent solutions are used for the phase ellipse in Eq. (16.73) or (16.74). We choose the trajectory in Eqs. (16.71) and (16.72) as one of the independent solution so as to ensure that at the time when transition is crossed the bunch ellipse will be tilted to the correct amount, so that the half bunch length and half energy spread will be correct. Any other combination is also a valid solution of the differential equation, but it will lead to the bunch ellipse to be tilted differently at transition, which in turn implies the possible unphysical situation that the bunch does not fit the rf bucket when it is well below transition.

In passing, we list the exact solution for the phase offset and energy offset:

$$\begin{aligned}\Delta p(x) &= A y^{1/3} [\cos \psi_1 J_{-1/3}(y) + \sin \psi_1 N_{-1/3}(y)] , \\ \left(\frac{2}{3}\right)^{1/3} \Delta\phi(x) &= A y^{2/3} [\cos \psi_1 J_{2/3}(y) + \sin \psi_1 N_{2/3}(y)] ,\end{aligned}\quad (16.82)$$

where $y = \frac{2}{3}|x|^{3/2}$, and J and N are the Bessel and Neumann functions of order $\frac{2}{3}$ or $-\frac{1}{3}$. Here, A and ψ_1 are the two constants. Unlike our solution, this solution is valid for all x . When we are very far from transition, or $|x| \gg 1$, the Bessel functions have the asymptotic expansions:

$$\begin{aligned}J_\nu(y) &\approx \sqrt{\frac{2}{\pi y}} \cos \left[y - \frac{\pi}{2} \left(\nu + \frac{1}{2} \right) \right] , \\ N_\nu(y) &\approx \sqrt{\frac{2}{\pi y}} \sin \left[y - \frac{\pi}{2} \left(\nu + \frac{1}{2} \right) \right] .\end{aligned}\quad (16.83)$$

Thus, Δp and $\Delta\phi$ are 90° out of phase, or the bunch fits the bucket far from transition. Therefore, at the moment when transition is crossed, the bunch ellipse will be tilted to the right amount so that one can read off the correct half bunch length and the half energy spread. This explains why we have chosen the combination of $J_{-1/3}$ and $N_{-1/3}$ for Δp in Eq. (16.82) instead of, for example, $J_{-1/3}$ and $J_{1/3}$. This method of asymptotic behavior cannot be applied to the power-series solution we pursuit in this section, because the power-series solution is only valid when $|x| < 1$.

16.5 Space Charge Mismatch

In the previous section, the equations of motion are symmetric about the transition time. This means that the bunch becomes shorter and taller while approaching transition, but restores its shape after crossing transition. Most important of all, the equilibrium bunch length is continuous across transition and the bunch area remains constant. However, the introduction of space charge breaks this symmetry. Below transition, the space charge force is repulsive. The rf potential well is distorted, resulting in the lengthening of the bunch. But the situation is different above transition. With the switching of sign of the slippage factor, the space charge force changes sign also. Now it becomes attractive. It adds constructively to the rf focusing force and the equilibrium bunch length becomes shorter instead. This is illustrated in the top plot of Fig. 16.2.

A space charge parameter can easily be defined. We have derived in Eq. (3.19) the reactive force on a beam particle due to a reactive impedance, which is proportional to the gradient of the longitudinal beam profile. If we assume a parabolic beam profile, this reactive force is linear. Thus, for a linearized rf voltage, the space charge force implies the replacement,

$$[eV_{\text{rf}} \cos \phi_s] \Delta\phi \rightarrow [eV_{\text{rf}} \cos \phi_s] \Delta\phi - \frac{3\pi N_b r_0 E_{\text{rest}} g_0 h^2}{R \gamma_t^2 \widehat{\Delta\phi}^3} \Delta\phi, \quad (16.84)$$

where N_b is the number of particles per bunch with half width $\widehat{\Delta\phi}$ in rf radian, r_0 the classical particle radius, and R the accelerator radius. Use has been made of the fact that the reactive impedance is the space charge impedance $Z_0^{\parallel}/n = iZ_0 g_0/(2\beta_t \gamma_t^2)$ at transition energy as given by Eq. (3.15). Notice that $\cos \phi_s$ changes sign from positive to negative on crossing transition. Thus, the space charge force counteracts the rf force below transition and enhances the rf force above. The ratio of the space charge force to the rf force is

$$\eta_{\text{spch}} = \frac{3\pi N_b r_0 E_{\text{rest}} g_0 h^2}{R \gamma_t^2 e V_{\text{rf}} |\cos \phi_s| \widehat{\Delta\phi}^3}. \quad (16.85)$$

This ratio is, however, time dependent, because the bunch length changes with time. One can evaluate this ratio right at transition and called it the *space charge parameter*. Thus

$$\eta_{\text{spch}}(0) = \frac{9\Gamma^3(\frac{1}{3})}{16\sqrt{2}} \frac{N_b r_0 g_0 h}{R} \left[\frac{\beta_t E_{\text{rest}}}{S h \omega_0} \right]^{3/2} \left[\frac{h \omega_0}{\beta_t \dot{\gamma}_t} \right]^{1/2}, \quad (16.86)$$

where use has been made of Eq. (16.19). Figure 16.2 is computed according to the space charge parameter $\eta_{\text{spch}}(0) = 2$.

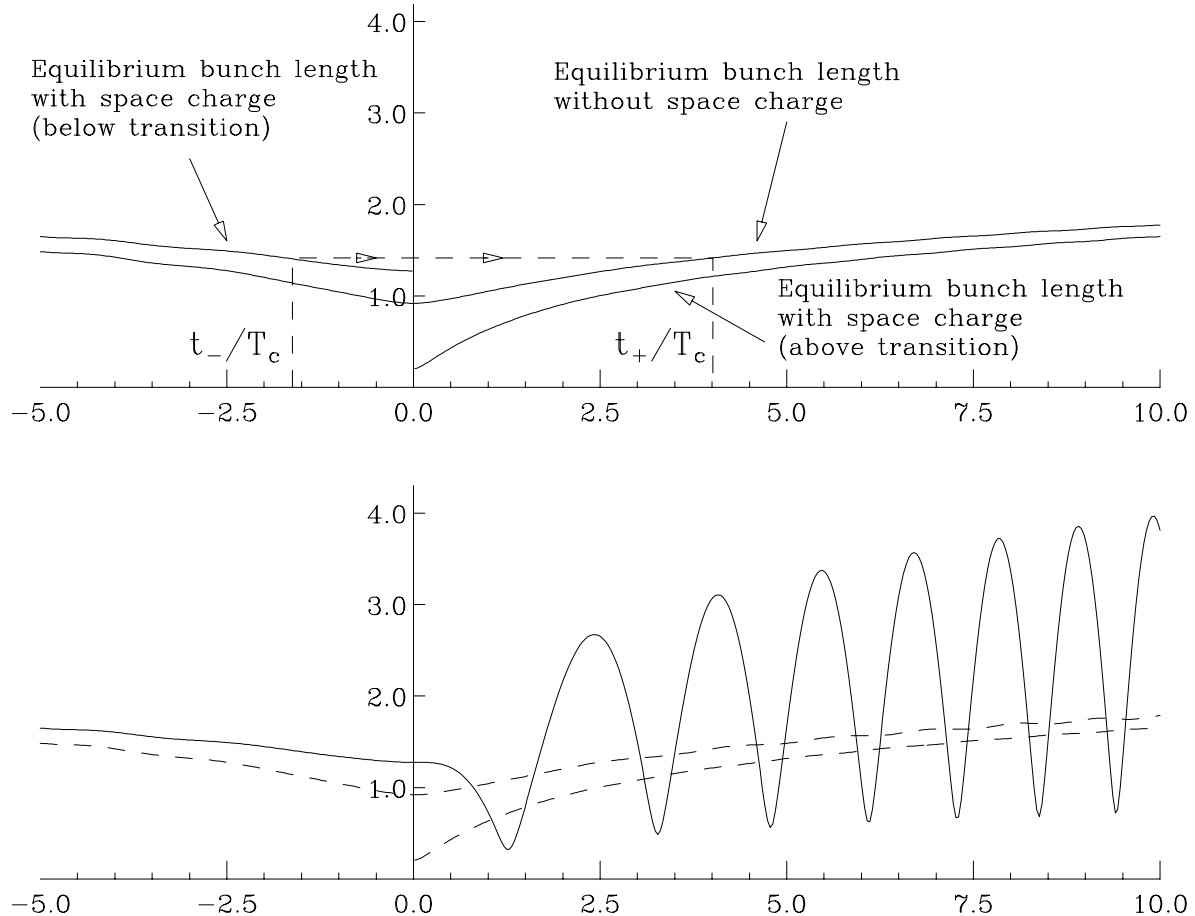


Figure 16.2: Bunch length is plotted versus x , time normalized to the nonadiabatic time T_c , across transition. Below transition (negative time), the space charge force is repulsive, thus giving a longer equilibrium bunch length. Above transition (positive time), the space charge force becomes attractive and therefore shortens the equilibrium bunch length. Top plot shows the mismatch of equilibrium bunch length across transition. A possible transition jump from $x = t_-/T_c$ to $x = t_+/T_c$ should have bunch length matched from the beginning to the end of jump, and is therefore asymmetric with respect to $x = 0$. Lower plot shows the bunch that matches to the space charge distorted bucket below transition overshoots after crossing transition and oscillates about the shorter equilibrium length.

Thus, as soon as transition is crossed, the bunch will find itself not able to fit the rf bucket. The bunch tumbles inside the bucket performing synchrotron oscillations in the quadrupole mode. In the worst situation, there will be beam loss. Even if the bucket is large enough to hold the bunch, the bunch area will increase due to filamentation. Such phenomenon has been observed in the Fermilab Booster, Main Ring, and the present Main Injector. A longitudinal quadrupole damping has been installed in each of the rings to cope with the oscillations. Such a damper consists mainly of a pickup which sends signals of the bunch length to modify the rf voltage, which in turn damp the oscillations. Figure 16.3 shows such a mismatched oscillation at the Fermilab Main Ring. In the top plot, the quadrupole damper is turned off. The lowest trace, which is green in color, measures the bunch length by comparing the spectral signal of the third rf harmonic to the fundamental. The bunch length goes through a minimum around 0.78 s when transition is crossed. After that it oscillates at twice the synchrotron frequency in the quadrupole mode with increasing amplitude, as a result of the space charge mismatch of the equilibrium bunch lengths before and after transition. Note that the quadrupole synchrotron period is diminishing away from transition due to the fact the slippage factor η is increasing. In the lower plot, the quadrupole damper is turned on. The lowest trace, which is green in color, measures the bunch length. It is evident that although there are some quadrupole oscillations after transition, they are of much smaller amplitudes and are completely damped later.

16.5.1 Mathematical Formulation

Mathematically, this phenomenon can be formulated as follows. As a result of Eqs. (16.84) and (16.86), the equation of motion governing $\Delta\phi$ is modified from Eq. (16.9) to

$$\frac{d}{dt} \left[\frac{1}{\omega_s^2} \frac{d\Delta\phi}{dt} \right] + \Delta\phi + \text{sgn}(t) \frac{n_{\text{spch}}}{\widehat{\Delta\phi}^3} \Delta\phi = 0 , \quad (16.87)$$

where $n_{\text{spch}} = \eta_{\text{spch}} \widehat{\Delta\phi}^3$ and is no more time dependent. In terms of the normalized time coordinate $x = t/T_c$, the differential equation becomes

$$\frac{d}{dx} \left[\frac{1}{x} \frac{d\Delta\phi}{dx} \right] + \text{sgn}(x) \Delta\phi + \frac{n_{\text{spch}}}{\widehat{\Delta\phi}^3} \Delta\phi = 0 . \quad (16.88)$$

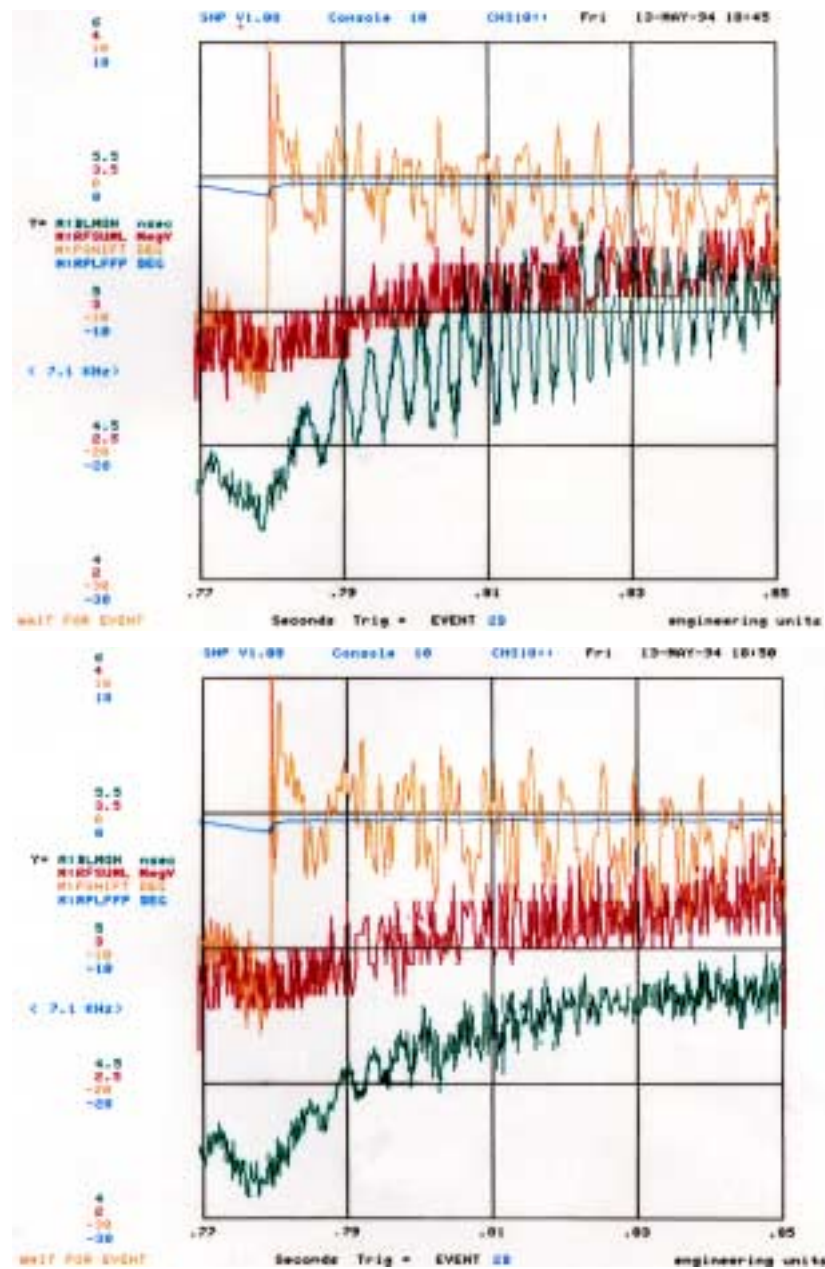


Figure 16.3: (color) A bunch is crossing transition at the Fermilab Main Ring. The lowest (green) trace of the top plot measures the bunch length. It dips to a minimum at ~ 0.78 s when transition is crossed. It then oscillates at twice the synchrotron frequency with large amplitudes due to space charge mismatch. In the lower plot, the quadrupole damper is turned on. Quadrupole oscillations of small amplitudes are seen in the lowest (green) trace after transition and are completely damped later.

The half bunch length $\widehat{\Delta\phi}$, however, satisfies a slightly different differential equation,

$$\frac{d}{dx} \left[\frac{1}{x} \frac{d\widehat{\Delta\phi}}{dx} \right] + \text{sgn}(x)\widehat{\Delta\phi} + \frac{n_{\text{spch}}}{\widehat{\Delta\phi}^2} - x \frac{(S_N/\pi)^2}{\widehat{\Delta\phi}^3} = 0 , \quad (16.89)$$

where S_N is a *normalized dimensionless* bunch area when the bunch ellipse is transformed to a circle. It is related to our usual bunch area S in eV-s (true area of the tilted ellipse not just π multiplied by the width and height) by

$$S_N = \frac{2h^2\omega_0^2\dot{\gamma}_t T_c^2}{\beta_t^2\gamma_t^4 E_{\text{rest}}} S . \quad (16.90)$$

The derivation was first given by Sørensen [3]. This is just an envelope equation in the longitudinal phase space and can be derived easily (Exercise 16.6). Comparing with the single-particle equation, Eq. (16.88), there is one extra term proportional to the square of the emittance and inversely to the third power of the the bunch length $\widehat{\Delta\phi}$. Such an extra last term also arises in the Kapchinskij-Vladimirskij beam envelope equation for transverse oscillation [4]. In fact, it occurs also in the equation satisfied by the betatron function, where the betatron function takes the place of $\widehat{\Delta\phi}$ while the transverse emittance takes the place of $(S_N/\pi)^2$. This equation cannot be solved analytically. However, when it is far away from transition, $|x| \gg 1$, the variation of $\widehat{\Delta\phi}$ with respect to x should be small, and we obtain the algebraic equation

$$\widehat{\Delta\phi}^4 + \text{sgn}(x)n_{\text{spch}}\widehat{\Delta\phi} = \frac{S_N^2}{\pi^2} |x| . \quad (16.91)$$

In the absence of space charge, $n_{\text{spch}} = 0$, we recover the solution in Eq. (16.54), namely,

$$\widehat{\Delta\phi} = \left[\frac{S_N}{\pi} \right]^{1/2} |x|^{1/4} = h\omega_0 \left[\frac{2ST_c^2\dot{\gamma}_t}{\pi\beta_t^2\gamma_t^4 E_{\text{rest}}} \right]^{1/2} |x|^{1/4} . \quad (16.92)$$

If we wish, we may also consider this as a derivation of the half-bunch-length differential equation [Eq. (16.89)], since we have already derived this expression for half bunch length and we know that such a term proportional to $(\widehat{\Delta\phi})^{-3}$ must exist in an envelope equation.

Equation (16.91), the quartic in bunch length, can be further simplified to

$$\theta^4 + \text{sgn}(x)\eta_{N0}\theta = |x| , \quad (16.93)$$

where the *normalized* bunch length θ is defined as

$$\widehat{\Delta\phi} = \sqrt{\frac{S_N}{\pi}} \theta = h\omega_0 \sqrt{\frac{2\dot{\gamma}_t T_c^2 S}{\pi \beta_t^2 \gamma_t^4 E_{\text{rest}}}} \theta = \sqrt{\frac{2h\omega_0 \dot{\gamma}_t T_c^2 S_c}{\pi \beta_t \gamma_t^4}} \theta , \quad (16.94)$$

and the normalized space charge parameter is

$$\eta_{N0} = n_{\text{spch}} \left[\frac{\pi}{S_N} \right]^{3/2} = \frac{3\pi^2 N_b r_0 g_0 h}{2R} \left[\frac{\beta_t E_{\text{rest}}}{Sh\omega_0} \right]^{3/2} \left[\frac{h\omega_0}{2\pi\beta_t \dot{\gamma}_t} \right]^{1/2} = \frac{3\pi^2 N_b r_0 g_0 h}{2RS_c^{3/2}} \left[\frac{h\omega_0}{2\pi\beta_t \dot{\gamma}_t} \right]^{1/2} , \quad (16.95)$$

where the explicit expression of T_c has been used. In above, S_c is another commonly used dimensionless bunch area, which is defined as

$$S_c = \pi \widehat{\Delta(\beta\gamma)} \widehat{\Delta\phi} = \frac{h\omega_0}{\beta E_{\text{rest}}} S . \quad (16.96)$$

Written in terms of these normalized quantities, the differential equation satisfied by the bunch length is also simplified and becomes

$$\frac{d}{dx} \left[\frac{1}{x} \frac{d\theta}{dx} \right] + \text{sgn}(x)\theta + \frac{\eta_{N0}}{\theta^2} - \frac{x}{\theta^3} = 0 . \quad (16.97)$$

Notice that $\widehat{\Delta\phi}/\theta$ is proportional to the bunch length at transition,

$$\widehat{\Delta\phi}_0 = \frac{2^{3/2} h\omega_0}{3^{1/3} \Gamma(\frac{1}{3})} \left[\frac{ST_c^2 \dot{\gamma}_t}{\beta_t^2 \gamma_t^4 E_{\text{rest}}} \right]^{1/2} . \quad (16.98)$$

Thus, aside from a constant, θ can also be considered as normalized to the bunch length at transition. In fact, evaluated at transition without space charge, $\theta = 2\pi^{1/2} 3^{-1/3} / \Gamma(\frac{1}{3}) = 0.91748$ radian, as indicated in Fig. 16.2. Comparing the original space charge parameter $\eta_{\text{spch}}(0)$ in Eq. (16.86) with the normalized space charge parameter η_{N0} , we find

$$\eta_{N0} = \frac{8\pi^{3/2}}{3 [\Gamma(\frac{1}{3})]^3} \eta_{\text{spch}}(0) = 0.77233 \eta_{\text{spch}}(0) . \quad (16.99)$$

The lower plot in Fig. 16.2 is derived from solving Eq. (16.97) numerically starting with a bunch that is matched to the equilibrium bunch length far below transition.

We conclude this section by listing in Table 16.1 some transition crossing properties as well as the space charger parameters of the Fermilab Booster, Fermilab Main Ring, and Fermilab Main Injector. We have used in the table the designed intensity of 6×10^{10}

for the Main Injector. At its former commissioned intensity of 4×10^{10} , the space charge parameter was $\eta_{\text{spch}}(0) = 0.303$ only. Notice that the space charge parameter for the Fermilab Booster is about ten times those for the Main Ring and Main Injector. Thus, bunch-length oscillations due to space charge mismatch can be very serious at the Booster before the installation of the quadrupole damper. In fact, this has been one of the reasons of bunch area increases due to filamentation after crossing transition.

Table 16.1: Some transition crossing properties and the space charge parameters of the Fermilab Booster, Main Ring, and Main Injector.

	Booster	Main Ring	Main Injector	
Circumference	474.203	6283.185	3319.419	m
Transition γ_t	5.373	18.85	21.80	
Revolution frequency f_0	621.157	47.646	90.220	kHz
Rf harmonic h	84	1113	588	
Rf voltage V_{rf}	0.763	2.5	2.78	MV
Synchronous angle ϕ_s	53.6	60.0	37.6	degrees
Ramp rate $\dot{\gamma}_t$	406.7	109.94	163.10	s^{-1}
nonadiabatic time T_c	0.216	3.00	2.14	ms
Number per bunch N_b	3×10^{10}	3×10^{10}	6×10^{10}	
95% bunch area S	0.025	0.15	0.15	eV-s
Rms bunch length at γ_t	0.237	0.335	0.217	ns
Space charge g_0	4.5	4.89	4.34	
$ Z_0^{\parallel} /n _{\text{spch}}$	29.9	2.63	1.72	Ohms
space charge parameter $\eta_{\text{spch}}(0)$	2.117	0.277	0.455	

16.6 Transition Jump

A transition jump is a way to go around transition crossing so that all the demise can be avoided [5, 6, 7]. It consists of the following steps. At some time $t = t_- < 0$, the currents of some quadrupoles are triggered so that γ_t of the ring is suddenly raised and the beam becomes far below transition (usually $\Delta\gamma_t \approx -1$). Next, at some time $t = t_+ > 0$, these quadrupoles are triggered back to their original currents and the γ_t of the ring returns to

its original value. However, at this moment the beam is far above (usually $\Delta\gamma_t \approx 1$) the original γ_t already. Because we need to avoid the bunch-length mismatch due to space charge, we need to make sure that the equilibrium bunch lengths at t_- and t_+ are equal. This means that $|t_-| < t_+$, or the transition jump will be asymmetric about $t = 0$. This is illustrated in the top plot of Fig. 16.2 (see also Exercise 16.7).

It is important to understand that a transition jump scheme does not really eliminate the crossing of transition. This is because when the transition gamma is returned to its original value by triggering the quadrupoles the second time, the beam particles that were below transition suddenly find themselves above transition. In other words, transition is crossed by changing suddenly the value of γ_t of the lattice instead of ramping the particles. However, crossing transition this way is much faster than ramping, usually faster by a factor of more than 10. The effective $\dot{\gamma}_t$ is therefore very large and the effective nonadiabatic time becomes very small. The manipulation of the quadrupoles at $t = t_-$ can be much slower because there is no transition crossing during that manipulation. We win here because the demise of crossing transition will not have enough time to develop. On the other hand, changing the lattice of the accelerator ring so fast can bring about other problems also. One possibility is a sudden increase in dispersion resulting in a sudden increase in the horizontal beam size which may lead to beam loss. Recently, Visnijic has been able to limit the propagation of this dispersion wave by the installation of a three-quadrupole cell [8].

In the nonadiabatic region, the particles near the head/tail of the bunch will be gaining/losing excess energy than the synchronous particle. The momentum spread of the bunch may be increased by such an extent that the momentum acceptance will be passed and beam loss occurs. There is a suggestion to add a third or second harmonic to the rf wave so that the latter becomes flat within the length of the bunch. In this way all particles in the bunch will accelerate equally and the excess increase in momentum spread will be suppressed reducing most of the particle loss. This method had been applied to the former Fermilab Main Ring [9].

16.7 Exercises

- 16.1. Derive the variation of the nonadiabatic time T_c and the rms time and energy spreads of a bunch right at transition with respect to the synchronous phase ϕ_s and the ramping rate $\dot{\gamma}_t$, as given in Eq. (16.30).

- 16.2. Show that the time evaluation of the phase offset,

$$\Delta\phi(t) = B\sqrt{\omega_s}e^{i\int \omega_s dt}, \quad (16.100)$$

where B is a constant, is valid only in the adiabatic region.

Hint: Show that the approximations made in Eqs. (16.36) and (16.37) are in accordance with $t \gg T_c$, where T_c is the nonadiabatic time.

- 16.3. Show that the half bunch length and half energy spread given by Eqs. (16.52) and (16.53) can also be obtained by relation from the phase equation:

$$\widehat{\Delta\phi} = \frac{h|\eta|\omega_0}{\beta^2 E_0 \omega_s} \widehat{\Delta E}, \quad (16.101)$$

together with the assumption of linear time variation of η/E_0 .

- 16.4. (1) If $f(x)$ and $g(x)$ are two independent solutions of the differential equation (16.57), show that the Wronskian $W(f, g) \equiv f(x)g'(x) - f'(x)g(x)$ is independent of x and can therefore be evaluated at any x , especially at $x = 0$.

(2) The solution can be written as

$$\begin{aligned} \Delta p &= B [f(x) \cos \psi + g(x) \sin \psi] , \\ \Delta\phi &= -B [f'(x) \cos \psi + g'(x) \sin \psi] , \end{aligned} \quad (16.102)$$

where B is a constant. Show that these two equations trace out an ellipse by varying ψ , with the ellipse area \mathcal{A} given by

$$\mathcal{A}^2 \propto (f^2 + g^2)(f'^2 + g'^2) - (ff' + gg')^2 . \quad (16.103)$$

- (3) Show that the right side of Eq. (16.103) is equal to the Wronskian $W(f, g)$ and the bunch area is therefore conserved and is determined only by the constant B .

- 16.5. Show that the power-series expansion of the Eqs. (16.82) gives exactly the same solution as Eqs. (16.73) and (16.74). Note that ψ in the two solutions can be different.

16.6. (1) Using as canonical coordinates

$$\Delta\phi \quad \text{and} \quad p = \frac{\hbar\omega_0}{\beta^2\gamma E_{\text{rest}}} \Delta E , \quad (16.104)$$

derive the envelope equation for $\tilde{\phi} = \sqrt{\langle \Delta\phi^2 \rangle}$ far away from transition:

$$\ddot{\tilde{\phi}} + \omega_s^2 \tilde{\phi} + \frac{\omega_s^2 n_{\text{spch}}}{\widehat{\Delta\phi}^3} \tilde{\phi} - \frac{E_0^3}{\tilde{\phi}^3} = 0 , \quad (16.105)$$

where the half length of the bunch is $\widehat{\Delta\phi} = \sqrt{5}\tilde{\phi}$ for the parabolic distribution. The symbol $n_{\text{spch}}/\widehat{\Delta\phi}^3$ is the ratio of the space charge force to the rf force defined in Eqs. (16.85) and (16.87),

$$E_0 = \sqrt{\langle \Delta\phi^2 \rangle \langle p^2 \rangle - \langle p\Delta\phi \rangle^2} \quad (16.106)$$

is proportional to the longitudinal emittance, and ω_s is the angular synchrotron frequency. Then convert the envelope equation to one for the half bunch length $\widehat{\Delta\phi}$.

(2) Near transition, $\omega_s^2 = t/T_c^3 = x/T_c^2$, where T_c is the nonadiabatic time. Because of the rapidly varying ω_s^2 , show that in the former derivation we need to make the substitution

$$\frac{1}{\omega_s^2} \frac{d^2 \widehat{\Delta\phi}}{dx^2} \rightarrow \frac{d}{dx} \left(\frac{1}{\omega_s^2} \frac{d \widehat{\Delta\phi}}{dx} \right) . \quad (16.107)$$

Then derive the envelope equation of Eq. (16.89).

16.7. A transition jump is to be designed for the Fermilab Main Injector with a total jump of $\Delta\gamma_t = 2.0$. Because of space charge mismatch of the bunch length near transition, the jump will be asymmetric; i.e., $|t_-| < t_+$, where t_- is the start-jump time before transition and t_+ the end-jump time after transition. Using Eq. (16.93), compute t_- , t_+ , $\Delta\gamma_{t-}$, and $\Delta\gamma_{t+}$, where the latter are, respectively, the amounts of jump from $t = t_-$ to $t = 0$ and from $t = 0$ to $t = t_+$. For the Main Injector, the ramp rate across transition is $\dot{\gamma}_t = 163.1 \text{ s}^{-1}$ and the nonadiabatic time is $T_c = 2.14 \text{ ms}$.

Bibliography

- [1] K.Y. Ng *Bunch Shape Evolution Near Transition, — an Intuitive Approach*, Fermilab report FN-644, 1996.
- [2] I. Kourbanis, private communication; E.C. Raka, *Damping Bunch shape Oscillations in the Brookhaven AGS*, IEEE, **NS16**, 3, 182 (1969).
- [3] A. Sørenssen, *The Effect of Strong Longitudinal Space-Charge Forces at Transition*, CERN Report MPS/Int. MU/EP 67-2, 1967.
- [4] I.M. Kapchinskij and V.V. Vladimirkij, *Limitations of Proton Beam Current in a strong Focusing Linear Accelerator Associated with the Beam Charge*, International Conference on High Energy Accelerators and Instrumentation, CERN 1959, p.274.
- [5] S. Holmes, *Main Injector Transition Jump*, Fermilab Report MI-0008, 1989.
- [6] T. Risselada, CERN 4th General Accel. School, Jükuch, Germany, 1990, p.161.
- [7] K.Y. Ng and A. Bogacz, *Dispersion γ_t Jump for the Main Injector*, Proceedings of the 1995 Particle Accelerator Conference and International Conference on High Energy Accelerators, Dallas, May 1-5, 1995, p.3340.
- [8] V. Visnjic, *Local Dispersion Insert: the γ_t Knob for Accelerators*, Fermilab Report TM-1888, 1994.
- [9] C.M. Bhat, J. Griffin, J. MacLachlan, M. Martens, K. Meisner, K.Y. Ng, *Transition Crossing in Proton Synchrotrons using a Flattened rf Wave*, Phys. Rev. **E55**, 1028 (1997).

Chapter 17

NEGATIVE-MASS INSTABILITY

Near transition, the slippage factor η decreases rapidly, thus decreasing the revolution frequency spread coming from the energy spread. Landau damping therefore diminishes and the beam is subject to instability. Below transition, most proton machines are dominated by space charge impedance. If the resistive part of the total impedance is small, the proton bunches should be stable against microwave instability. However, as soon as transition is crossed, the space charge force switches sign which together with the vanishingly small value of the slippage factor will drive the beam to instability. This is called *negative-mass instability*, the name coming from the fact that particle behaviors above transition, for example, attractive space charge force and repulsive inductive force, are the same as if they are having negative mass. All low-energy proton machines will suffer from negative-mass instability while crossing transition. However, this instability grows for a limited time only until the slippage factor η becomes large enough to damp the instability. If the ring is well-designed so that the time interval of growth and the growth rate are both small, negative-mass instability just results in a small increase in bunch area. If the ring is not well-designed, the increase in bunch area will be so large that the bunch may exceed the bucket height and even the momentum aperture of the vacuum chamber resulting in beam loss. In a machine like the Fermilab Main Ring where bunch coalescence is required to feed the Tevatron which is a colliding storage ring, the growth in bunch area is especially important. This is because too large a bunch area after transition will lead to undesirable large bunch area after coalescence, which will in turn lower the luminosity of the Tevatron.

As was discussed in Sec. 6.1.3, while the Landau damping rate decreases as η , the

microwave instability growth rate decreases as $\sqrt{|\eta|}$ as well. The growth rate is therefore time dependent, thus complicating the calculation of the total amount of growth in bunch area.

17.1 Growth at Cutoff

In the absence of space charge or other coupling impedances, the motion of a particle in the longitudinal phase space can be derived analytically [3] at any time near transition in terms of Bessel function $J_{\frac{2}{3}}$ and Neumann function $N_{\frac{2}{3}}$. With the introduction of space charge, the growth rate of a small excitation amplitude can be evaluated by integrating the Vlasov equation when the bunch has either an elliptical or bi-Gaussian distribution in the longitudinal phase space. The total growth can then be tallied up by small time steps across transition. Lee and Wang [1] made such a calculation for the Relativistic Heavy Ion Collider (RHIC) at Brookhaven before the machine was built. The emittance growth was taken as two times the growth of the excitation amplitude at the cutoff frequency of the beam pipe, and the result was considered satisfactory. The choice of the cutoff frequency comes from the assumption that electromagnetic waves emitted by the bunch at higher frequencies will not bounce back from the beam pipe to interact with the bunch. Wei [2] later studied the emittance growth of the Alternating Gradient Synchrotron (AGS) at Brookhaven using similar approach. His simulation showed that the emittance blowup had been very much overestimated. Wei pointed out that the bunch emittance had been kept constant by Lee and Wang in the computation of the growth for each time step. The bunch emittance was in fact growing and would provide more Landau damping to counteract the instability. With the emittance updated at each time step, he found the numerical calculations agree with the simulations.

17.1.1 Simple Model

With some suitable assumptions, the model of Lee-Wang-Wei can be made analytic, resulting in some simple formulas for easy estimation [3]. First, let us begin with the dispersion relation of Eq. (6.19) derived in Chapter 6 for the revolution harmonic n :

$$1 = - \left(\frac{\Delta\Omega_0}{n} \right)^2 \int \frac{F'(\omega)}{\Delta\Omega/n - \omega} d\omega , \quad (17.1)$$

where $\Delta\Omega = \Omega - n\omega_0$ is the coherent angular frequency shift, Ω the coherent angular frequency of the instability, and ω_0 the revolution angular frequency. In above, $\Delta\Omega_0$ is the coherent frequency shift driven by the longitudinal impedance Z_0^{\parallel}/n without Landau damping, which can be expressed as

$$\left(\frac{\Delta\Omega_0}{n}\right)^2 = \frac{ie\eta\omega_0^2 I_{\text{pk}}}{2\pi\beta^2 E_0} \frac{Z_0^{\parallel}}{n}, \quad (17.2)$$

and $F(\omega)$ is the distribution in angular revolution frequency ω ,

$$F(\omega) = \frac{1}{\sqrt{2\pi\sigma_\omega}} e^{-\omega^2/(2\sigma_\omega^2)}, \quad (17.3)$$

with

$$\sigma_\omega = \frac{|\eta|\omega_0}{\beta^2 E_0} \sigma_E \quad (17.4)$$

the rms angular frequency spread in the bunch, σ_E the rms energy spread, E_0 the energy and ω_0 the angular revolution frequency of the synchronous particle, and $I_{\text{pk}} = eN_b/(\sqrt{2\pi}\sigma_\tau)$ the peak current of the bunch of N_b particles and rms length $\sigma_\tau = 1/\sigma_\omega$. Dimensionless variables are now introduced,

$$u = \frac{\omega}{\sigma_\omega}, \quad z = \frac{\Delta\Omega}{n\sigma_\omega}, \quad (17.5)$$

and the dispersion relation takes the form

$$1 = - \left(\frac{\Delta\Omega_0}{n\sigma_\omega} \right)^2 \int \frac{G'(u)}{z-u} du, \quad (17.6)$$

with

$$G(u) = \frac{1}{\sqrt{2\pi}} e^{-u^2/2}. \quad (17.7)$$

Again, we assume the slip factor η to be linear in time near transition as given by

$$\frac{\eta}{E_0} = \frac{2\dot{\gamma}_t}{\gamma_t^4 E_{\text{rest}}} t = \frac{eV_{\text{rf}}\omega_0 \sin\phi_s}{\pi\gamma_t^4 E_{\text{rest}}} t, \quad (17.8)$$

where t is the time measured from the moment transition is crossed, E_{rest} the rest energy of the beam particles and V_{rf} the rf voltage. We get, from Eqs. (17.2), (17.6), and (17.8),

$$1 = -i\frac{a}{t} \int \frac{G'(u)}{z-u} du, \quad (17.9)$$

where

$$a = \frac{eN_b(Z_0^{\parallel}/n)\beta^2\gamma_t^4 E_{\text{rest}}^2}{2\sqrt{2\pi}\omega_0\sigma_{\tau}\sigma_E^2 V_{\text{rf}} \sin \phi_s} , \quad (17.10)$$

is a slowly varying function of t . Written in this form, all accelerator and bunch parameters have been embedded in the variable a and integral in Eq. (17.9) becomes machine and beam independent.

Next, we want to compute the time t_0 when η increases to such a value that stability is regained. There are two simple situations. The first one is when the longitudinal impedance is purely space charge or capacitive. Therefore, the parameter a is positive imaginary number or $-ia$ is real and positive. The integral must therefore be real. At the edge of instability $\Delta\Omega/n$ is replaced by $\Delta\Omega/n + i\epsilon$, where ϵ is a positive infinitesimal real number. The imaginary part of the integral is just $-i\pi G'(z) = 0$ or $z = 0$. This corresponds to Point A on the threshold curve shown in Fig. 17.1. The principal value part of the integral can now be performed easily and it integrates to unity exactly. We obtain the solution

$$t_0 = -ia(t_0) , \quad (17.11)$$

where we write $a(t_0)$ because a is a function of σ_{τ} , σ_E , ω_0 , etc, which depend on time. The quantities of largest variation with time in $a(t)$ are σ_{τ} and σ_E . It turns out that t_0 in most cases is of the order of the nonadiabatic time T_c or larger, so that the bunch area, which is conserved, is close to $S = 6\pi\sigma_{\tau}\sigma_E$. Thus $a(t) \propto \sigma_{\tau}$. We notice from Eqs. (16.19) and (16.54) that the variation of σ_{τ} from $t = 0$ to $t = T_c$ is at most $\sim 10\%$. Therefore, we can make the approximation that $a(t) \approx a(t_0)$ for all the later time at which the bunch is unstable. With this approximation, we can compute from Eq (17.9) the growth rate at other time $t = t't_0$, where $0 \leq t' \leq 1$. The equation to solve is

$$t' = \int \frac{G'(u)}{z-u} du . \quad (17.12)$$

The solution is simple because the imaginary part of the right side has to vanish, leading to $z = iy$, where y is real. We obtain*

$$t' = 1 - \sqrt{\frac{\pi}{2}} y e^{y^2/2} \operatorname{erfc} \left(\frac{y}{\sqrt{2}} \right) , \quad (17.13)$$

*First express the right side of Eq. (17.12) in terms of the complex error function $w(iy/\sqrt{2})$ and then use another representation of the complex error function to cast the result in the form of Eq. (17.13).

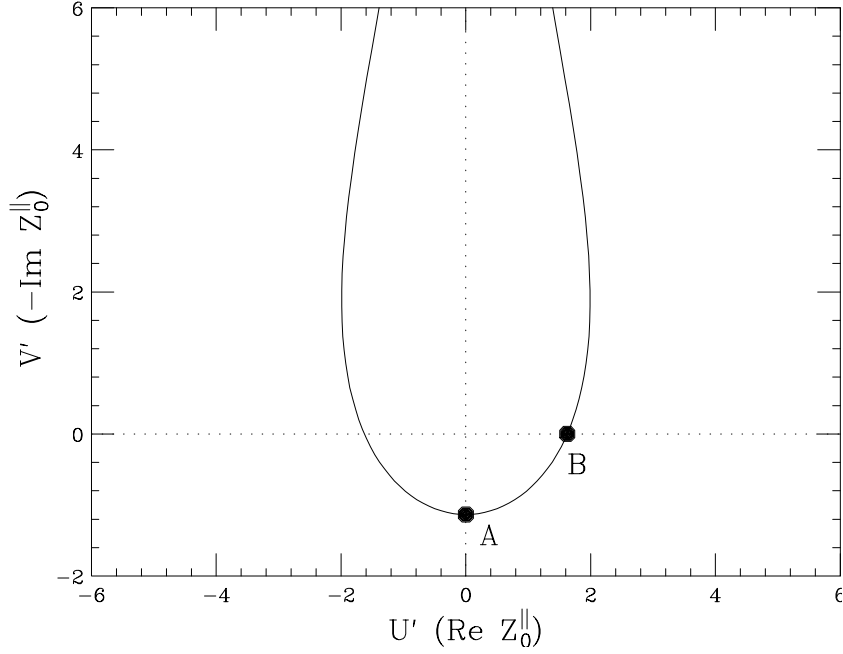


Figure 17.1: The threshold dispersion curve for Gaussian distribution. Point A corresponds to the situation where the longitudinal impedance is purely capacitive such as space charge. Point B corresponds to the situation where the longitudinal impedance is purely real such as the peak of a broad resonance.

where $\text{erfc}(x) = 1 - \text{erf}(x)$ is the complimentary error function. The integrated growth per harmonic is given by

$$\frac{S_+}{n} = \int_0^{t_0} \mathcal{I}m \frac{\Delta\Omega}{n} dt = t_0 \int_0^1 \sigma_\omega \mathcal{I}m z dt' = \frac{\sigma_E e V_{\text{rf}} \sin \phi_s \omega_0^2 t_0^2}{\pi \beta_t^2 \gamma_t^4 E_{\text{rest}}^2} \int_0^1 t' \mathcal{I}m z dt' , \quad (17.14)$$

where Eqs. (17.4) and (17.8) have been used. In Fig. 17.2(a), we plot $t' \mathcal{I}m z$ as a function of t' with the aid of Eq. (17.13). The last integral in Eq. (17.14) is 0.10346. With the aid of Eqs. (17.10) and (17.11), the integrated growth per harmonic becomes

$$\frac{S_+}{n} = F_1^{\text{spch}} \sigma_\tau \frac{\left(e^2 N_b |Z_0^|| / n | \beta_t \gamma_t^2 E_{\text{rest}} \right)^2}{S^3 e V_{\text{rf}} \sin \phi_s} , \quad (17.15)$$

where the constant is machine independent and is given by

$$F_1^{\text{spch}} = 27\pi \int_0^1 t' \mathcal{I}m z dt' = 8.776 . \quad (17.16)$$

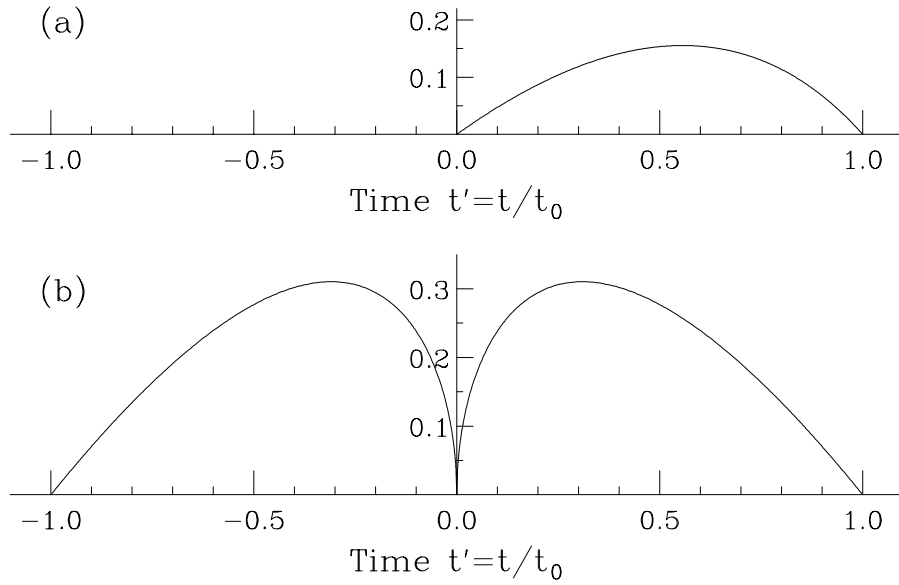


Figure 17.2: Plot of $t' \operatorname{Im} z$, which is proportional to the growth rate as a function of normalized time $t' = t/t_0$, where t is measured from the moment when transition is crossed ($t < 0$ below transition and $t > 0$ above transition), and t_0 is the time when the slip factor η becomes large enough so that stability is achieved. Plot (a) is the situation when the longitudinal impedance is purely capacitance like space charge. Plot (b) is the situation when the longitudinal impedance is purely real like the peak of a broad resonance. Note that there is no growth below transition when the impedance is purely capacitive.

In above, we have used the fact that the 95% bunch area is $S \approx 6\pi\sigma_\tau\sigma_E$, since $t_0 \gtrsim T_c$. The rms bunch length σ_τ will be evaluated using Eq. (16.52).

Another possibility to have a simple solution to Eq. (17.9) is to assume Z_0^{\parallel}/n to be purely real, for example at the peak of a broad resonance. Now the variable a in Eq. (17.9) is real and positive. Therefore, we require the real part of the dispersion integral to vanish. To derive the time t_0 where the beam regains stability, we seek the solution $z = x + i\epsilon$, where ϵ is a positive infinitesimal number. We find that x satisfies

$$1 - \sqrt{2}x e^{-x^2/2} \int_0^{x/\sqrt{2}} e^{t^2} dt = 0 . \quad (17.17)$$

This gives $x/\sqrt{2} = 0.924139$ or

$$t_0 = \sqrt{\frac{\pi}{2}} x e^{-x^2/2} = 0.6972853 a(t_0) . \quad (17.18)$$

This solution corresponds to Point B in Fig.17.1. Again, we approximate the problem by evaluating $a(t)$ at t_0 . Substituting back into the dispersion relation, the Eq. (17.9) becomes

$$0.697285 t' = -i \int \frac{G'(u)}{z-u} du = -i \left[1 + i \sqrt{\frac{\pi}{2}} z w \left(\frac{z}{\sqrt{2}} \right) \right] , \quad (17.19)$$

where $t' = t/t_0$ and $w(z)$ is the complex error function. Next we need to relate the growth rate, which is proportional to $\mathcal{Im} z$, to the time t' before stability is regained. For each value of $y = \mathcal{Im} z$, we require

$$1 - \mathcal{Im} \left[\sqrt{\frac{\pi}{2}} z w \left(\frac{z}{\sqrt{2}} \right) \right] = 0 , \quad (17.20)$$

by solving for x , where $z = x + iy$. This has to be solved numerically. The relation of $t' \mathcal{Im} z$ as a function of t' is plotted in Fig. 17.2(b). The area under the growth-rate curve is 0.211765 for $0 \leq t' \leq 1$. Unlike the situation of a purely capacitive impedance, there is microwave growth both after and before transition. In this particular model of a purely real impedance, the growth is symmetric about the time when transition is crossed. The integrated growth above transition per harmonic S_+/n is exactly the same expression in Eq. (17.14) except that we now have $t_0^2 = (0.697285 a)^2$ instead of the former $t_0^2 = |a|^2$. Thus, we also have the same Eq. (17.15) but with the constant F_1^{spch} replaced by another universal constant F_1^{real} , where

$$F_1^{\text{real}} = 27\pi(0.697285)^2 \int_0^1 t' \mathcal{Im} z dt' = 27\pi(0.697285)^2(0.211765) = 8.734 , \quad (17.21)$$

which happens to be very close to F_1^{spch} . The integrated growth per harmonic S_-/n below transition is exactly equal to S_+/n .

When the condition that Z_0^{\parallel}/n is purely reactive or real is relaxed, the solution of the dispersion relation will not be so simple. The result can also be expressed in the form of Eq. (17.15). The numerical constant F_1 will deviate from F_1^{spch} and F_1^{real} . Also there will be a different F_1 for a different phase in Z_0^{\parallel}/n .

Here, we will apply these formulas to the Fermilab Booster, Main Ring, and Main Injector, as listed in Table 17.1. Since the total growth is exponential, it is very sensitive to the bunch area, impedance, number per bunch, and the growth harmonic. Even a factor of two decrease in the bunch area or a factor of two enhancement in one of the other quantities can increase the the total growth tremendously. Notice that some total growths are more than 10000 fold. But this is only the growth of a spectral component

and it is not easy to relate it to the growth of the bunch area. For this reason, the theory of growth at cutoff is not so enlightening. We will analyze all the shortcomings of the model and study the model of Hardt [6], which may provide a more reasonable criterion of beam blowup across transition.

Table 17.1: Growth-at-cutoff theory applied to the Fermilab Booster, Main Ring, and main Injector when the impedance is purely space charge or purely resistive.

	Booster	Main Ring	Main Injector	
95% Bunch Area S	0.025	0.15	0.15	eV-s
Number per bunch N_b	3×10^{10}	3×10^{10}	6×10^{10}	
Beam pipe radius	5.00	3.50	2.66	cm
Nonadiabatic time T_c	0.216	3.00	2.14	
Cutoff harmonic n	1510	28600	19900	
Cutoff frequency	0.938	1.36	1.79	GHz
<u>Purely Space Charge</u>				
$ Z_0^{\parallel} /n _{\text{spch}}$	30.0	2.63	1.72	Ohms
t_0	2.23	2.30	2.71	ms
σ_τ at t_0	0.463	0.342	0.251	ns
Growth rate per harmonic S_+/n	0.00619	7.40×10^{-6}	2.10×10^{-5}	
Growth index S_+	9.35	0.203	0.416	
Total growth exp(S_+)	11400	1.23	1.52	
<u>Resistive Impedance</u>				
Z_0^{\parallel}/n	15.0	10.0	1.6	Ohms
t_0	0.549	8.58	1.52	ms
σ_τ at t_0	0.326	0.475	0.217	ns
Growth rate per harmonic S_+/n	0.000125	1.66×10^{-5}	1.78×10^{-6}	
Growth index $S_+ + S_-$	3.30	8.31	0.619	
Total growth exp($S_+ + S_-$)	27.0	4060	1.86	

17.1.2 Shortcomings

In order to discuss the shortcomings of the Lee-Wang-Wei method, let us first review some theory of the negative-mass instability. If we ignore Landau damping, the growth

rate at peak current I_{pk} at the revolution harmonic n is given by

$$G(n, t) = n\omega_0 \left(\frac{|\eta|eI_{\text{pk}}|Z_0^{\parallel}/n|_{\text{spch}}}{2\pi\beta^2\gamma E_{\text{rest}}} \right)^{1/2}, \quad (17.22)$$

where E_{rest} is the particle rest energy, η the slippage factor, t the time measured from the moment of transition crossing, and the space charge impedance given by

$$\left[\frac{Z_0^{\parallel}}{n} \right]_{\text{spch}} = i \frac{Z_0 g}{2\beta\gamma^2}. \quad (17.23)$$

Here, $Z_0 \approx 377$ ohms is the free-space impedance, γ and β the relativistic parameters of the bunch particle at or near transition, and g the space charge geometric parameter, which has been derived in Sec. 3.2 at low frequencies as

$$g_0 = 1 + 2 \ln \frac{b}{a}, \quad (17.24)$$

where a is the beam radius and b the beam pipe radius. A more accurate derivation which is valid for high frequencies has been given by Keil and Zotter [7] in terms of Bessel functions. The result of Eq. (17.24) arrives from the expansion of the Bessel functions at zero frequency. At frequencies of the order $\gamma c/b$, $\gamma c/a$, or higher, the space charge geometric parameter g rolls off. When b/a is not too big, numerical fittings show that $g(n)$ can be approximated by

$$g(n) = \frac{g_0}{1 + (n/n_{\frac{1}{2}})^2}, \quad (17.25)$$

with the half-value revolution harmonic given roughly by

$$n_{\frac{1}{2}} = \gamma R \left(\frac{1.6}{b} + \frac{0.52}{a} \right), \quad (17.26)$$

where R is the radius of the accelerator ring. It is clear from Eq. (17.22) that at frequencies below the roll-off of the space charge impedance, the growth rate for negative-mass instability is directly proportional to the harmonic n . It will be shown later in Eq. (17.56) that, when Landau damping is taken into account, the growth rate will be modified and the integrated growth becomes

$$\int_0^{t_0} G(n, t) dt \propto n \sqrt{g(n)}, \quad (17.27)$$

where t_0 is the time after crossing transition when the slip factor η becomes large enough so that stability is restored. Thus, the integrated growth exhibits a maximum at $n_{\max} = n_{\frac{1}{2}}/\sqrt{3}$. Taking as an example the Fermilab Main Ring, which has a radius of 1 km and transition gamma $\gamma_t = 18.8$, this corresponds to 77.6 GHz when $a = 5$ mm and $b = 35$ mm. On the other hand, the cutoff frequency is only about 1.36 GHz. For a typical cycle at an intensity of 3×10^{10} per bunch and emittance 0.15 eV-s, the total growth across transition due to the space charge impedance for a spectral line is 1.74×10^5 times at the former frequency but only 1.23 at the latter frequency. Similarly, the maximum integrated negative-mass growths for the Fermilab Main Injector and the Fermilab Booster occur at 98.5 and 23.9 GHz, respectively. As a result, it is difficult to justify the correctness of the description of Lee-Wang-Wei. In addition, in Wei's simulation, the bunch was divided into bins with the bin width equal to the cutoff wavelength of the beam pipe. In other words, all large-growth-rate amplitudes at high frequencies had been neglected. Here, we want to point out that the first simulation across transition to exhibit negative-mass instability was done by Lee and Teng [4] on the Fermilab Booster, where they also divided the bunch up into cutoff wavelengths only. Later, similar simulations on the same booster were performed by Lucas and MacLachlan [5], and they also failed to include the high-frequency amplitudes.

Measurements were made near transition for the Fermilab Main Ring [8]. The top row of Fig. 17.3 displays the observed signals around transition at frequencies 4, 5, and 6 GHz for proton bunches with initial longitudinal emittance 0.07 eV-s and 2.3×10^{10} protons. The units on the vertical axis are 5 db per division and on the horizontal axis 2 ms per division. The transition time is marked with an arrow. As seen in the figure, the signals are getting stronger and more persistent with increasing frequency as expected from the negative-mass instability. In this case, the longitudinal emittance after transition was 0.25 eV-s corresponding to a blowup of 3.6. Next a phase mismatch at injection was introduced to blowup the longitudinal emittance from 0.06 to 0.10 eV-s. The lower row of Fig. 17.3 displays the signals observed at 5.0 GHz, with two different longitudinal emittances before transition. As expected, the 5.0 GHz signal is smaller for the bigger longitudinal emittance, and dies away faster compared to the signal in the case with the smaller emittance. The emittance blowup at transition is also much smaller for the bigger initial emittance, a factor of 2 compared with 3.7.

One may raise the question that a typical proton bunch which is usually much longer than the radius of the beam pipe will have a spectrum not much higher than the cutoff frequency. In order to have a growth at harmonic $n = n_{\max}$ or $n_{\frac{1}{2}}$, the original

amplitude or the seed of the growth has to be supplied by Schottky noise, which is extremely small, so that the growth effect to the bunch at such high frequencies may or may not be significant. This question will be discussed in Sec. 17.2.1 below, after we go over the Schottky-noise model of Hardt [6].

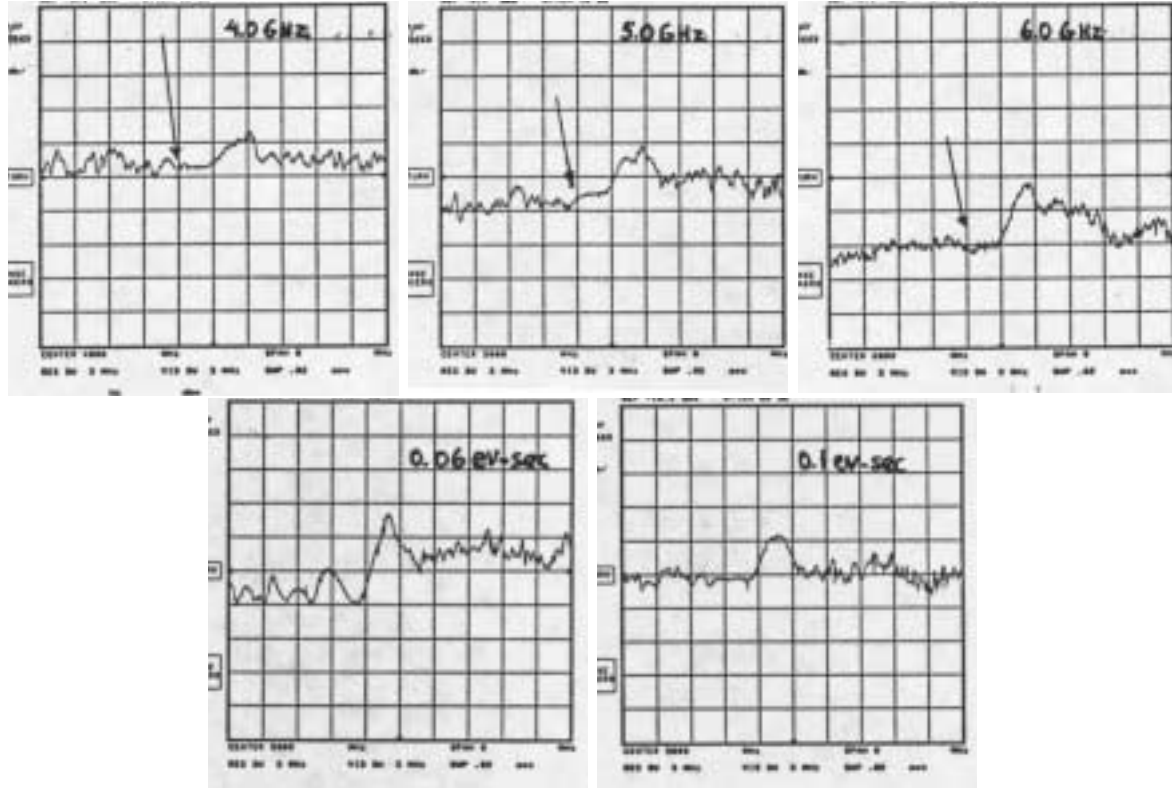


Figure 17.3: Top row: negative-mass signals at 4.0, 5.0, and 6.0 GHz for bunches with emittance of 0.07 eV-sec and 2.2×10^{10} protons. The signals are stronger and more persistent with increasing frequencies. The arrow marks the transition time. Lower row: negative-mass signals at 5.0 GHz for bunches with the same intensity but with longitudinal emittances 0.06 and 0.10 eV-s. The signals are smaller for the larger emittance.

17.2 Schottky-Noise Model

Hardt assumed that the seeds of the negative-mass growth are provided by the statistical fluctuations of the finite number of particles N_b within the bunch on top of a

smooth linear profile distribution $F(\Delta\phi)$, where $\Delta\phi$ is the rf phase offset measured from synchronous angle. The smooth distribution $F(\Delta\phi)$ has an average of unity but is normalized to $2\widehat{\Delta\phi}$, the total bunch length. The bunch is divided into M bins in the rf phase coordinate $\Delta\phi$. There are $N_b F(\Delta\phi)/M$ particles in the bin at $\Delta\phi$, and each bin has a width $2\widehat{\Delta\phi}/M$. Due to the statistical fluctuations, the m th bin contains δN_m extra particles. So a step function $f(\Delta\phi, t)$, which is a perturbation to $F(\Delta\phi)$, can be defined:

$$f(\Delta\phi, t) = \frac{\delta N_m}{\Delta N} \quad \text{if } \frac{m-1}{M} < \frac{\Delta\phi + \widehat{\Delta\phi}}{2\widehat{\Delta\phi}} < \frac{m}{M}, \quad (17.28)$$

where $\Delta N = N_b/M$ is the average number of particles in a bin. The function can be expanded in a Fourier series

$$f(\Delta\phi, t) = \sum_{k_b=-\infty}^{\infty} c_{k_b}(t) e^{i2\pi k_b \Delta\phi / (2\widehat{\Delta\phi})}, \quad (17.29)$$

where

$$c_{k_b}(t) = \frac{1}{2\widehat{\Delta\phi}} \int_{-\widehat{\Delta\phi}}^{\widehat{\Delta\phi}} f(\Delta\phi, t) e^{-i2\pi k_b \Delta\phi / (2\widehat{\Delta\phi})} d\Delta\phi, \quad (17.30)$$

and $c_0(t) = 0$ because of charge or particle conservation. Notice that the expansion has been made in bunch modes k_b , or the number of wavelengths in a wave that can reside in a bunch with periodic boundary condition at $\pm\widehat{\Delta\phi}$. It should not be confused with the revolution harmonic n , which is the number of wavelengths in a wave around the circumference of the accelerator ring. The two are, however, related to each other by

$$\frac{k_b}{n} = \frac{2\widehat{\Delta\phi}}{2\pi h}, \quad (17.31)$$

where h is the rf harmonic. If we work with waves that vanish at the ends of the bunch or $\pm\widehat{\Delta\phi}$, we need only to include positive integral k_b which represents the number of nodes in the waves across the bunch. However, we are working here with waves that satisfy periodic boundary conditions at $\pm\widehat{\Delta\phi}$; we need to include all integral k_b , positive and negative.

Let us compute the statistical expectation

$$E[|c_{k_b}(0)|^2] = \frac{1}{(2\widehat{\Delta\phi})^2} \int_{-\widehat{\Delta\phi}}^{\widehat{\Delta\phi}} d\Delta\phi \int_{-\widehat{\Delta\phi}}^{\widehat{\Delta\phi}} d\Delta\phi' E\left[\frac{\delta N_m \delta N_n}{(\Delta N)^2}\right] e^{i2\pi k_b (\Delta\phi - \Delta\phi') / (2\widehat{\Delta\phi})}. \quad (17.32)$$

Initially, without any contamination of instability, the statistical fluctuations in the bins are random, or

$$E[\delta N_m \delta N_n] = \delta_{mn} \Delta N F(\Delta\phi) , \quad (17.33)$$

where the right side is the expected number of particles in the m th bin, in which $F(\Delta\phi)$ is to be evaluated. This means that both $\Delta\phi$ and $\Delta\phi'$ have to be in the same bin in order to be nonvanishing. If we neglect the small fluctuation of the phase inside a bin, we can perform the integration over $d\Delta\phi'$, which just gives the width of the bin. What is left behind in Eq. (17.32) becomes trivial, and we readily get

$$E[|c_{k_b}(0)|^2] = \frac{1}{(2\widehat{\Delta\phi})^2} \int_{-\widehat{\Delta\phi}}^{\widehat{\Delta\phi}} \frac{F(\Delta\phi)}{\Delta N} \frac{2\widehat{\Delta\phi}}{M} d\Delta\phi = \frac{1}{N_b} . \quad (17.34)$$

This result is important because it is independent of mode number k_b and the number of bins M , otherwise the model will become meaningless. This also explains why $F(\Delta\phi)$ has been defined to have an average of unity. The evolution of each mode amplitude c_{k_b} is

$$|c_{k_b}(t_0)| \approx \frac{1}{\sqrt{N_b}} \exp \int_0^{t_0/T_c} G(n, x) dx , \quad (17.35)$$

where $G(n, x)$, the growth per unit $x = t/T_c$ with T_c being the nonadiabatic time. The following derivation will be very similar to what we did in the growth-at-cutoff model. The integration is up to time t_0 when the growth rate decreases to zero as the slippage factor η increases.

Hardt employed an elliptical initial particle distribution in the longitudinal phase space,[†]

$$\psi(\Delta\phi, \Delta E) = \frac{3}{2\pi\widehat{\Delta\phi}\widehat{\Delta E}} \sqrt{1 - \frac{\Delta\phi^2}{\widehat{\Delta\phi}^2} - \frac{\Delta E^2}{\widehat{\Delta E}^2}} , \quad (17.36)$$

so that the linear distribution

$$\rho(\Delta\phi) = \frac{3}{4\widehat{\Delta\phi}} \left(1 - \frac{\Delta\phi^2}{\widehat{\Delta\phi}^2} \right) \quad (17.37)$$

becomes parabolic. The offset of angular revolution frequency $\Delta\omega = \omega - \omega_0$ from that of the synchronous particle is related to the energy offset ΔE by

$$\Delta\omega = -\frac{\eta\omega_0}{\beta^2\gamma E_{\text{rest}}} \Delta E . \quad (17.38)$$

[†]We outline here our understanding of the original paper of Hardt, which is very condensed and is difficult to read.

Therefore, at a point $\Delta\phi_1$ along the bunch profile, the distribution in $\Delta\omega$ is

$$f(\Delta\omega) = \frac{2}{\pi\widehat{\Delta\omega}} \frac{\sqrt{1 - \frac{\Delta\phi_1^2}{\widehat{\Delta\phi}^2} - \frac{\Delta\omega^2}{\widehat{\Delta\omega}^2}}}{1 - \frac{\Delta\phi_1^2}{\widehat{\Delta\phi}^2}}. \quad (17.39)$$

Starting from the Vlasov equation, a dispersion relation is derived and is given by Eq. (6.19). For a perturbative wave with revolution harmonic n , the dispersion relation is

$$1 = - \left(\frac{\Delta\Omega_1}{n} \right)^2 \int \frac{df(\Delta\omega)/d\Delta\omega}{\Delta\Omega/n - \Delta\omega} d\Delta\omega, \quad (17.40)$$

where $\Delta\Omega$ is the deviation of coherent angular frequency Ω of the collective motion from $n\omega_0$. We are working with the revolution harmonic now and will go to bunch modes later. The factor before the integral can be written as [Eq. (6.19)]

$$\left(\frac{\Delta\Omega_1}{n} \right)^2 = \frac{ieI_{\text{local}}\eta\omega_0^2 \left[Z_0^{\parallel}(\Omega)/n \right]_{\text{spch}}}{2\pi\beta^2\gamma E_{\text{rest}}}, \quad (17.41)$$

where we substitute for the *local* current

$$I_{\text{local}} = \frac{3eN_b\omega_0}{4\widehat{\Delta\phi}} \left(1 - \frac{\Delta\phi_1^2}{\widehat{\Delta\phi}^2} \right), \quad (17.42)$$

and the space charge impedance

$$\left[\frac{Z_0^{\parallel}}{n} \right]_{\text{spch}} = i \frac{Z_0 g(n)}{2\beta\gamma^2} \quad (17.43)$$

with the geometric factor $g(n)$ given by Eq. (17.25). The result is

$$\left(\frac{\Delta\Omega_1}{n} \right)^2 = - \frac{3N_b r_p g \eta h \omega_0^2}{4\beta^2 \gamma^3 R \widehat{\Delta\phi}} \left(1 - \frac{\Delta\phi_1^2}{\widehat{\Delta\phi}^2} \right) = \left(\frac{\Delta\Omega_0}{n} \right)^2 \left(1 - \frac{\Delta\phi_1^2}{\widehat{\Delta\phi}^2} \right), \quad (17.44)$$

where R is the radius of the accelerator ring and r_p the classical radius of the beam particle. Notice that the last factor involving $\Delta\phi_1$ will cancel the same factor in the denominator of the distribution function $f(\Delta\omega)$ in the dispersion relation.

Changing the variable of integration from $\Delta\omega$ to

$$y = \frac{\Delta\omega}{\widehat{\Delta\omega} \sqrt{1 - \frac{\Delta\phi_1^2}{\widehat{\Delta\phi}^2}}} , \quad (17.45)$$

the dispersion relation simplifies to

$$1 = \frac{2}{\pi} \left(\frac{\Delta\Omega_0}{n\widehat{\Delta\omega}} \right)^2 \int_{-1}^1 \frac{y dy}{(\alpha - y) \sqrt{1 - y^2}} , \quad (17.46)$$

where

$$\alpha = \frac{\Delta\Omega}{n\widehat{\Delta\omega} \sqrt{1 - \frac{\Delta\phi_1^2}{\widehat{\Delta\phi}^2}}} . \quad (17.47)$$

The integral on the right side of Eq. (17.46) can be readily performed to give $-\pi + \pi\alpha/\sqrt{\alpha^2 - 1}$. We therefore obtain from the dispersion relation

$$\alpha = \pm \frac{a}{\sqrt{a^2 - 1}} , \quad \text{with } a = 1 + \left(\frac{n\widehat{\Delta\omega}}{\sqrt{2}\Delta\Omega_0} \right)^2 . \quad (17.48)$$

Now the dispersion relation has been solved. The imaginary part of Ω gives the growth rate if positive and damping rate if negative. It is clear from Eqs. (17.47) and (17.48) that the growth rate will be largest at the center of the bunch profile where $\Delta\phi_1 = 0$. From now on we are going to concentrate on the bunch center and drop $\Delta\phi_1$.

The maximum half spread in angular revolution frequency $\widehat{\Delta\omega}$ can be written in terms of the half bunch length $\widehat{\Delta\phi}$ via

$$\widehat{\Delta\omega} = \frac{|\eta|\omega_0 \widehat{\Delta E}}{\beta^2 \gamma E_{\text{rest}}} = \frac{|\eta|\omega_0 S_c}{\pi \beta \gamma \widehat{\Delta\phi}} , \quad (17.49)$$

where, for convenience, the dimensionless bunch area $S_c = \pi \widehat{\beta} \widehat{\gamma} \widehat{\Delta\phi}$ [Eq. (16.96)] has been used. Thus,

$$\left(\frac{n\widehat{\Delta\omega}}{\sqrt{2}\Delta\Omega_0} \right)^2 = - \frac{2\eta\gamma R S_c^2}{3\pi^2 r_p g N_b h \widehat{\Delta\phi}} . \quad (17.50)$$

Notice that this is essentially the inverse of the bunch length multiplied by the space charge force.

Since we are after the growth of each bunch mode component near transition, all quantities including the bunch length will be approximated by their values at transition. Recall that under the assumption of a linear time variation of η/E , we defined in Sec. 16.5 a normalized space charge parameter η_{N0} in Eq. (16.95) and a normalized half bunch length θ in Eq. (16.94). Here, we want to introduce η_N which is the same as η_{N0} with the exception that the space charge geometric parameter g_0 at zero frequency is replaced by the more general $g(n)$ which covers high frequencies. With the expression in Eq. (17.50), it just turns out that

$$\left(\frac{n\widehat{\Delta\omega}}{\sqrt{2}\Delta\Omega_0} \right)^2 = -\frac{x}{\eta_N\theta}, \quad (17.51)$$

where $x = t/T_c$ and T_c is the nonadiabatic time. The maximum half spread in angular revolution frequency can also be expressed in terms of θ via Eqs. (16.94) and (17.49) as

$$\widehat{\Delta\omega} = \frac{|\eta|\gamma_t}{\theta T_c} \sqrt{\frac{S_c\omega_0}{2\pi h\dot{\gamma}_t\beta_t}} = \frac{|x|}{\theta\gamma_t^2} \sqrt{\frac{2S_c\omega_0\dot{\gamma}_t}{\pi h\beta_t}}, \quad (17.52)$$

where the linear dependency of η near transition has been used.

With the help of Eqs. (17.47), (17.48), and (17.51), the growth rate (for $x > 0$) can be expressed as

$$\text{Im } \Omega = n\widehat{\Delta\omega} \text{Im } \alpha = n\widehat{\Delta\omega} \frac{\frac{\eta_N\theta}{x} - 1}{\sqrt{\frac{2\eta_N\theta}{x} - 1}}. \quad (17.53)$$

Now substitute for $\widehat{\Delta\omega}$ from Eq. (17.52) and the definition of the nonadiabatic time. We arrive at the growth per unit $x = t/T_c$,

$$G(n, x) = T_c \text{Im } \Omega = \frac{n\eta_N}{h} \sqrt{\frac{S_c |\tan \phi_s| \beta_t}{\pi \dot{\gamma}_t T_c}} \frac{1 - \frac{x}{\eta_N\theta}}{\sqrt{\frac{2\eta_N\theta}{x} - 1}}. \quad (17.54)$$

As a reminder, on the right side of the above equation, n is the revolution harmonic while η_N is the normalized space charge parameter. We see that this growth rate starts at zero right at transition ($x = 0$), increases to a maximum, and decreases to zero at $x = \eta_N\theta$. Thus the time when the beam regains stability is $t_0 = xT_c = \eta_N\theta T_c$. The accumulated or integrated growth E_{acc} is obtained by an integration over x from $x = 0$

to $x = \eta_N \theta$,

$$E_{\text{acc}}(n) = \int_0^{\eta_N \theta} G(n, x) dx . \quad (17.55)$$

The integration can be performed easily with the change of variable $u = x/(2\eta_N \theta)$, and the result is

$$E_{\text{acc}}(n) = \frac{n\eta_N^2 \theta}{h} \left(1 - \frac{\pi}{4}\right) \sqrt{\frac{S_c |\tan \phi_s| \beta_t}{\pi \dot{\gamma}_t T_c}} . \quad (17.56)$$

We have computed the accumulated growth of a spectral line with revolution harmonic n . Since the normalized space charge parameter η_N is linear in the geometric parameter $g(n)$ of the space charge impedance, the dependence on frequency is therefore

$$E_{\text{acc}}(n) \propto \frac{n}{\left(1 + \frac{n^2}{n_{\frac{1}{2}}^2}\right)^2} . \quad (17.57)$$

The maximum is denoted by

$$E_{\text{max}} = \frac{3\sqrt{3} n_{\frac{1}{2}} \eta_{N0}^2 \theta}{16h} \left(1 - \frac{\pi}{4}\right) \sqrt{\frac{S_c |\tan \phi_s| \beta_t}{\pi \dot{\gamma}_t T_c}} , \quad (17.58)$$

where η_{N0} is the same as η_N with the exception of the replacement of $g(n)$ by g_0 , and occurs when $n = n_{\text{max}} = n_{\frac{1}{2}}/\sqrt{3}$. The accumulated growth E_{acc} will be exponentiated to arrive at the total growth for a harmonic.

A criterion for negative-mass instability is required. Hardt made the assertion that there is no negative-mass blowup if

$$\sum_{k_b=-\infty}^{\infty} |c_{k_b}(t_0)|^2 \lesssim 1 , \quad (17.59)$$

where t_0 is the time when stability is regained. The meaning of this criterion will be explored later. From Eq. (17.35), such a criterion is equivalent to

$$\sum_{k_b=-\infty}^{\infty} \exp[2E_{\text{acc}}(k_b)] \lesssim N_b , \quad (17.60)$$

where N_b is the number of particles in the bunch and the summation is over all possible bunch modes. Because $\exp[E_{\text{acc}}]$ assumes a maximum at $n = n_{\text{max}}$ and falls off rapidly

later, the method of steepest decent will be employed. First, we find that[‡]

$$E_{\text{acc}}(n) \approx E_{\max} \left[1 - \left(\frac{3\Delta n}{2n_{\frac{1}{2}}} \right)^2 \right] , \quad (17.61)$$

with $\Delta n = n - n_{\max}$. Next, the summation over all the bunch modes is converted into an integral

$$\sum_{k_b=-\infty}^{\infty} \exp[2E_{\text{acc}}(k_b)] = \exp[2E_{\max}] \int_{-\infty}^{\infty} \exp \left[-2 \left(\frac{3\sqrt{E_{\max}}\Delta k_b}{2k_{b\frac{1}{2}}} \right)^2 \right] d\Delta k_b , \quad (17.62)$$

where the bunch mode number k_b has been used instead of the revolution harmonic n . The relation between the two are given by Eq. (17.31). In particular the half-value bunch mode is

$$k_{b\frac{1}{2}} = \frac{\widehat{\Delta\phi}}{\pi h} n_{\frac{1}{2}} . \quad (17.63)$$

The criterion of no blowup can be written as

$$E_{\max} \lesssim E_{\text{crit}} , \quad (17.64)$$

where the critical total growth E_{crit} is obtained through Eq. (17.60) by equating the right side of Eq. (17.62) to N_b ; or

$$\frac{k_{b\frac{1}{2}}}{3} \sqrt{\frac{2\pi}{E_{\text{crit}}}} \exp[2E_{\text{crit}}] = N_b , \quad (17.65)$$

after performing the Gaussian integration. This is a transcendental equation which can be solved by iteration, giving

$$E_{\text{crit}} \approx \frac{1}{2} \left[\ln N_b - \ln \left(\frac{2k_{b\frac{1}{2}}}{3} \sqrt{\frac{\pi}{\ln N_b}} \right) \right] . \quad (17.66)$$

The leading term, $\frac{1}{2} \ln N_b$, is usually an order of magnitude larger than the second term. Take for example the Fermilab Main Ring which has a radius of $R = 1$ km and transition gamma $\gamma_t = 18.8$. The beam has a radius of $a = 5$ mm and the beam pipe radius is

[‡]In Eq. (17.61), we obtain $[3\Delta n/(2n_{\frac{1}{2}})]^2$ for the second order term, while it is $[3\Delta n/(4n_{\frac{1}{2}})]^2$ in Ref. [6], which we think is incorrect. Therefore, we are getting slightly different results for Eqs. (17.62), (17.65), and (17.66).

$b = 3.5$ cm. The half-value harmonic number $n_{\frac{1}{2}} = 2.81 \times 10^6$ according to Eq. (17.26) and the half-value bunch mode is $k_{b\frac{1}{2}} = n_{\frac{1}{2}}\omega_0\widehat{\Delta\tau}/\pi = 268$ if we assume a half bunch length of $\widehat{\Delta\tau} = 1$ ns. For a bunch consisting of $N_b = 10^{11}$ particles the leading term is $\frac{1}{2}\ln N_b = 12.7$ and the second term is 0.57.

Finally, we will write out the criterion of no negative-mass blowup, Eq.(17.64), in terms of the more familiar parameters of the accelerator ring and the particle bunch. First, let us list the relevant expressions. They are the normalized space charge parameter at zero frequency

$$\eta_{N0} = \frac{3\pi^2 N_b r_p g_0 h}{2R S_c^{3/2}} \sqrt{\frac{h\omega_0}{2\pi\beta_t\dot{\gamma}_t}} = \frac{3\pi^2 N_b r_p g_0}{2R S_c^{3/2} \omega_0} \sqrt{\frac{E_{\text{rest}}^3 \beta_t^2}{2\pi\dot{\gamma}_t}}, \quad (17.67)$$

and the normalized half bunch length at transition

$$\theta = \sqrt{\frac{\pi\beta_t\gamma_t^4}{2h\omega_0\dot{\gamma}_t T_c^2 S_c}} \widehat{\Delta\phi} = \frac{2\sqrt{\pi}}{3^{1/3} \Gamma(\frac{1}{3})} = 0.91749. \quad (17.68)$$

where the conversion, $S_c/S = h\omega_0/(\beta_t E_{\text{rest}})$ has been used. Substituting into the expression for E_{max} in Eq. (17.58), the threshold for no negative-mass blowup [Eq. (17.64)] can be formulated by introducing a critical parameter c less than unity in the following expression:

$$\xi n_{\text{max}} \left(\frac{r_p}{R}\right)^2 \left(\frac{E_{\text{rest}}^{5/2} \beta_t^{7/6}}{h^{1/3} \omega_0^{4/3} \gamma_t^{2/3}}\right) \left(\frac{N_b^2 g_0^2 |\tan\phi_s|^{1/3}}{S^{5/2} \dot{\gamma}_t^{7/6}}\right) = c E_{\text{crit}}. \quad (17.69)$$

When the critical parameter $c < 1$, there is no blowup. In above, the coefficient ξ is

$$\xi = \frac{3^{25/6} \pi^2 \Gamma(\frac{2}{3})}{2^{41/6}} \left(1 - \frac{\pi}{4}\right) = 2.44656, \quad (17.70)$$

where $\Gamma(\frac{2}{3}) = 1.354118$ is the Gamma function, r_p the classical proton radius, E_{rest} the proton rest energy, R the ring radius, g_0 the geometric space charge parameter at zero frequency, S bunch area in eV-s, ϕ_s the synchronized rf phase, γ_t the transition gamma, $\dot{\gamma}_t$ the rate at which transition is crossed, n_{max} the revolution harmonic at which the accumulated growth is a maximum, which is related to the half-value revolution harmonic by $n_{\text{max}} = n_{\frac{1}{2}}/\sqrt{3}$, and $k_{b\frac{1}{2}}$ the half-value bunch mode which is given by $k_{b\frac{1}{2}} = n_{\frac{1}{2}}\widehat{\Delta\phi}/(\pi h)$. We have written Eq. (17.69) in such a way that the last factor on

the left side pertains to the properties of the beam while the two factors in front pertain to the properties of the accelerator ring.

Some comments are in order:

- (1) The critical condition $\sum_{k_b} |c_{k_b}(t_0)|^2 = 1$ implies, through Parseval theorem, that

$$\frac{1}{2\widehat{\Delta\phi}} \int |f(\Delta\phi, t_0)|^2 d\Delta\phi = 1. \quad (17.71)$$

From the definition of the function $f(\Delta\phi)$, the above integral can be re-written as summation over the M bins,

$$\sum_m \left(\frac{\delta N}{\Delta N} \right)_m^2 \frac{(\Delta\phi)_b}{2\widehat{\Delta\phi}} = \sum_m \left(\frac{\delta N}{\Delta N} \right)_m^2 \frac{1}{M}, \quad (17.72)$$

where ΔN is the average number of particles inside each bin and $(\Delta\phi)_b$ is the width of the bin. Then Eq. (17.71) becomes

$$\frac{\sum_m (\delta N)_m^2}{M} = (\Delta N)^2. \quad (17.73)$$

The assertion of a negative-mass blowup is equivalent to the situation when the rms fluctuation in each bin is comparable to the average number of particles in each bin, which is really a large particle fluctuation or a big blowup in the bunch. This blowup implies violent changes in the bunch, such as a total bunch breakup. However, the assertion of Eq. (17.59) is a bit hand-waving, because even when the rms fluctuation is much less than ΔN , there can be a big blowup of the bunch emittance already. Hardt's paper provides no recipe to compute the increase in bunch emittance in this regime.

- (2) The derivation so far has been a perturbative approach. Here, we want to examine its validity. The perturbation expansion is, in fact,

$$F(\Delta\phi) + f(\Delta\phi, t) = F(\Delta\phi) + \sum_{k_b=-\infty}^{\infty} c_{k_b}(t) e^{i2\pi k_b \Delta\phi / (2\widehat{\Delta\phi})}, \quad (17.74)$$

where $F(\Delta\phi)$ is the smooth linear profile distribution and $f(\Delta\phi, t)$ represents the fluctuation from the smooth distribution. Notice that the unperturbed distribution $F(\Delta\phi)$ has an average of unity. Since Hardt only studied the situation of no blowup or when the fluctuation function $f(\phi, t)$, as demonstrated in Eq. (17.71), has a rms of less than unity, the perturbation is therefore justified although the amount of growths of the c_{k_b} 's from $t = 0$ to $t = t_0$ are tremendous.

We are going to apply this Schottky-noise model to the Fermilab Main Ring, where many properties have been listed in Tables 16.1 and 17.1. Here, we want to study the negative-mass instability when the ramping rate across transition is $\dot{\gamma}_t = 90.0 \text{ s}^{-1}$. Table 17.2 lists and Fig. 17.4 plots the computed critical parameter c for bunches of $N_b = 2.2 \times 10^{10}$ and 4.0×10^{10} protons for various bunch areas according to Eq. (17.69). The half bunch length is evaluated right at transition. We see that the parameter c increases very rapidly as the bunch area shrinks to a certain size, $S \lesssim 0.11 \text{ eV-s}$ for the 4.0×10^{10} bunch and $S \lesssim 0.07 \text{ eV-s}$ for the 2.2×10^{10} bunch. In any case, there should not be any negative-mass blowup when the bunch area is around 0.15 eV-s , as demonstrated by experiment. For the Fermilab Main Injector, the ramp rate at transition has been increased to $\dot{\gamma}_t = 160.1 \text{ s}^{-1}$. Compared with the Main Ring at $N_b = 4 \times 10^{10}$ per bunch, the blowup across transition does not occur until the bunch area is about or smaller than $S = 0.07 \text{ eV-s}$ (Fig. 17.5). The Fermilab Booster ramps at $\dot{\gamma}_t = 406.7 \text{ s}^{-1}$ across transition and can therefore accommodate bunches at much smaller areas without blowup as indicated in Fig. 17.6.

Table 17.2: Critical parameter c for negative-mass instability for a proton bunch in the Fermilab Main Ring with $N_b = 2.2 \times 10^{10}$ or 4.0×10^{10} particles. The ramp rate across transition is $\dot{\gamma}_t = 90.0 \text{ s}^{-1}$. A value of $c \gtrsim 1$ implies negative-mass blowup.

Bunch area (eV-s)	Half bunch width (ns)	$N_b = 2.2 \times 10^{10}$		$N_b = 4.0 \times 10^{10}$	
		c	E_{crit}	c	E_{crit}
0.040	0.439	3.84	10.23	12.70	10.54
0.050	0.490	2.21	10.18	7.31	10.48
0.060	0.537	1.41	10.13	4.65	10.44
0.070	0.580	0.96	10.09	3.18	10.40
0.080	0.620	0.69	10.06	2.28	10.36
0.100	0.693	0.40	10.00	1.31	10.31
0.120	0.760	0.25	9.96	0.84	10.26
0.140	0.820	0.17	9.92	0.57	10.22
0.160	0.877	0.12	9.89	0.41	10.19
0.180	0.930	0.09	9.86	0.31	10.16
0.200	0.981	0.07	9.83	0.24	10.13
0.220	1.028	0.06	9.81	0.19	10.11
0.240	1.074	0.05	9.78	0.15	10.09

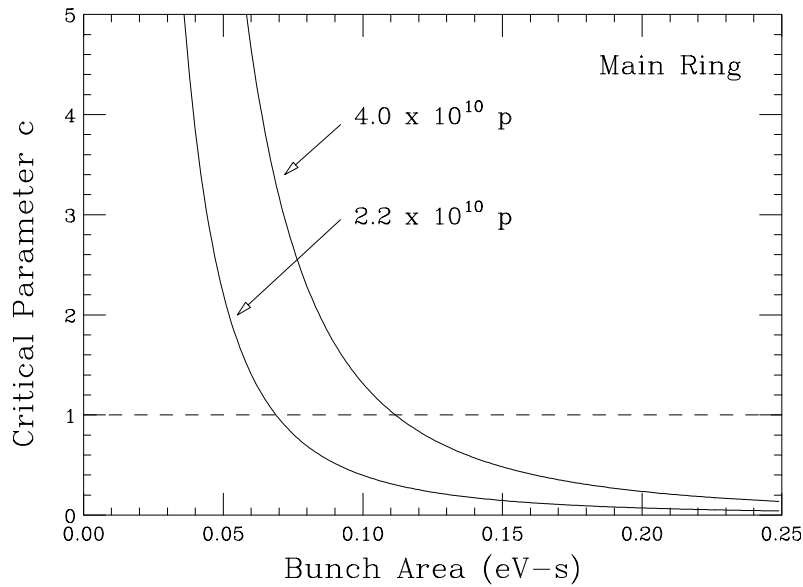


Figure 17.4: Plots showing the critical negative-mass parameter c as a function of the Fermilab Main Ring bunch area for bunches with $N_b = 2.2 \times 10^{10}$ and 4.0×10^{10} protons. The ramp rate across transition is $\dot{\gamma}_t = 90.0 \text{ s}^{-1}$. Negative-mass blowup occurs when $c \gtrsim 1$.

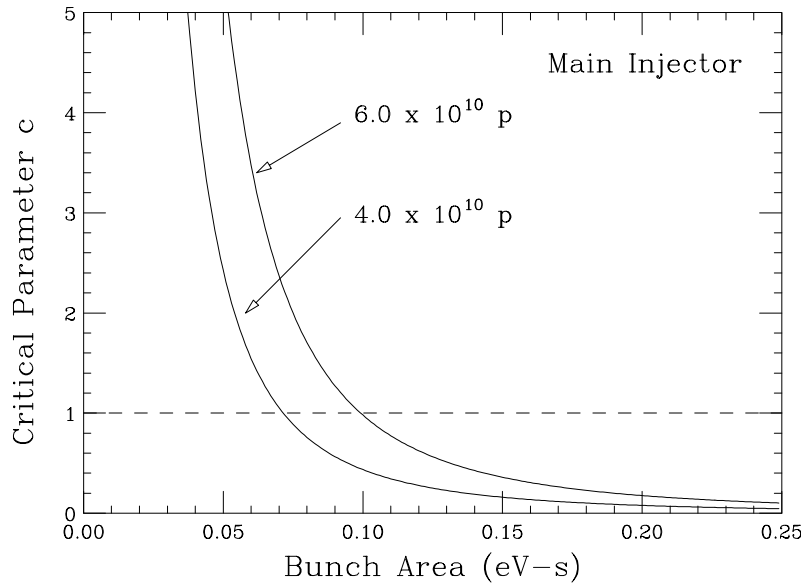


Figure 17.5: Plots showing the critical negative-mass parameter c as a function of the Fermilab Main Injector bunch area for bunches with $N_b = 4.0 \times 10^{10}$ and 6.0×10^{10} protons. The ramp rate across transition is $\dot{\gamma}_t = 160.1 \text{ s}^{-1}$. Negative-mass blowup occurs when $c \gtrsim 1$.

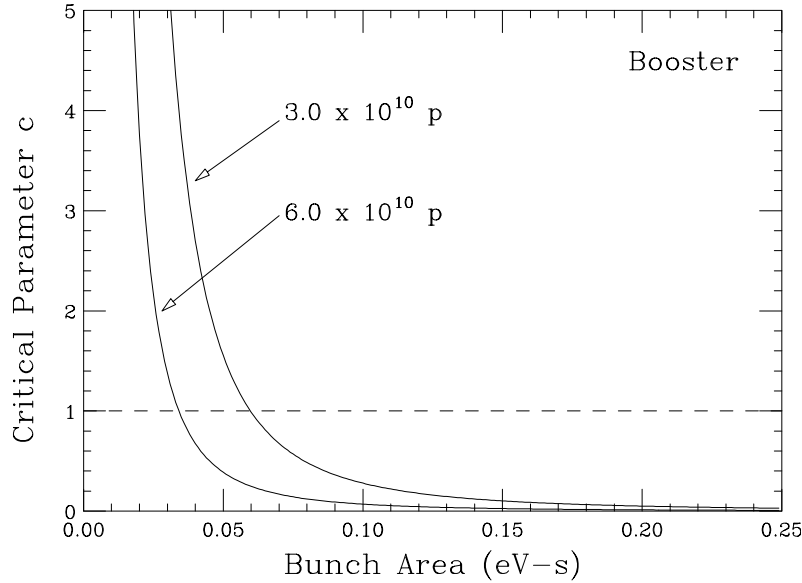


Figure 17.6: Plots showing the critical negative-mass parameter c as a function of the Fermilab Booster bunch area for bunches with $N_b = 3.0 \times 10^{10}$ and 6.0×10^{10} protons. The ramp rate across transition is $\dot{\gamma}_t = 406.7 \text{ s}^{-1}$. Negative-mass blowup occurs when $c \gtrsim 1$.

17.2.1 Comparison of Growths at Cutoff and High Frequencies

For a parabolic bunch, the unperturbed linear distribution is

$$F(\Delta\phi) = \frac{3}{2} \left(1 - \frac{\Delta\phi^2}{\widehat{\Delta\phi}^2} \right), \quad (17.75)$$

which is normalized to have an average of unity. It is expanded in a Fourier series at $t = 0$,

$$F(\Delta\phi) = \sum_{k_b=-\infty}^{\infty} \bar{a}_{k_b}(0) e^{i2\pi k_b \Delta\phi / (2\widehat{\Delta\phi})}, \quad (17.76)$$

where the mode amplitude is, for $k_b > 0$,

$$a_{k_b}(0) = \bar{a}_{k_b}(0) + \bar{a}_{-k_b}(0) = \frac{3}{\pi^2} \frac{(-1)^{k_b+1}}{k_b^2}. \quad (17.77)$$

The bunch mode number k_b which corresponds to the cutoff harmonic $n_{\text{cutoff}} = R/b$, with R and b being, respectively, the radii of the ring and the beam pipe, can be estimated

Table 17.3: Final fluctuation power spectra at cutoff and high-frequency Schottky harmonics.

$\dot{\gamma}_t$ (s^{-1})	N_b (10^{10})	Initial Bunch Emittance (eV-s)	Final Power Spectrum of Fluctuation at n_{cutoff}	at n_{max}	sum
90	2.2	0.05	3.70	1.50×10^9	4.03×10^{10}
90	2.2	0.06	2.21	1.08×10^2	3.97×10^3
90	2.2	0.07	1.67	1.19×10^{-2}	5.74×10^{-1}
90	2.2	0.08	1.41	4.86×10^{-5}	2.93×10^{-3}
90	2.2	0.09	1.26	1.41×10^{-6}	1.06×10^{-4}
120	4.0	0.06	7.44	4.37×10^{18}	1.00×10^{20}
120	4.0	0.07	3.80	1.94×10^9	5.83×10^{10}
120	4.0	0.08	2.54	4.40×10^3	1.67×10^5
120	4.0	0.09	1.95	1.02×10^0	4.76×10^1
120	4.0	0.10	1.64	3.57×10^{-3}	2.00×10^{-1}

using Eq. (17.31). Then, the final value of a power spectral line can be computed:

$$|a_{k_b}(t_0)|^2 = |a_{k_b}(0)|^2 \exp \left[\int_0^{t_0/T_c} 2G(n_{\text{cutoff}}, x) dx \right]. \quad (17.78)$$

The results are listed in Table 17.3 for various run cycles of the Fermilab Main Ring. The beam pipe radius and the beam radius are kept fixed at $b = 35$ mm and $a = 5$ mm, respectively. The synchronous phase is 60° . Alongside, we have also tabulated the final size of the Schottky power spectral line at the high harmonic n_{max} according to Eq. (17.35). The sum of all the Schottky power spectral modes has been derived in Eqs. (17.35), (17.62), and (17.65) to be

$$\sum_{k_b=-\infty}^{\infty} |c_{k_b}(t_0)|^2 \approx |c_{k_b}(t_0)|_{n=n_{\text{max}}}^2 \times \frac{k_b \frac{1}{2}}{3} \left(\frac{2\pi}{E_p} \right)^{\frac{1}{2}}, \quad (17.79)$$

where

$$E_p = \int_0^{t_0/T_c} G(n_{\text{max}}, x) dx \quad (17.80)$$

is the integrated growth at the peak harmonic n_{max} and $|c_{k_b}(t_0)|_{n=n_{\text{max}}}^2 = e^{2E_{\text{max}}}/N_b$ is just the absolute square of the component coefficient at $n = n_{\text{max}}$. This is also listed in the last column of the table.

We can see that the Hardt's blowup criterion of Eq. (17.59) appears to be critical, where the growth changes tremendously. When the criterion is exceeded, the Schottky modes are always larger than the mode at cutoff, showing that the inclusion up to cutoff frequency is inadequate. On the other hand, below the blowup limit, the mode at cutoff is larger than the high-frequency Schottky modes, implying that there should be modest emittance growth below the Hardt's blowup limit. However, this does not tell us how large the emittance growth is. It will be best if we can sum up the final power spectrum of the bunch distribution:

$$\sum_{k_b} |a_{k_b}(t_0)|^2 = \sum_{k_b} \frac{9}{\pi^4 k_b^4} \exp[\text{integrated growth}] . \quad (17.81)$$

Unfortunately, this sum is divergent because the integrated growth is directly proportional to k_b . Even when we take into account of the space charge roll-off, the sum still becomes unreasonably large. The reason behind this is the breakdown of the linear perturbation when the perturbed spectral mode becomes larger than the unperturbed one. As a result, it remains unclear whether the high-harmonic Schottky noise is dominating in the growth of the bunch emittance. A simulation seems to be the best solution.

17.2.2 Difficulties in Simulation

A simulation of the negative-mass instability is not trivial. There are two main difficulties:

(1) Inclusion of high-frequency components

The growth of the Schottky noise peaks at n_{\max} , which corresponds to roughly 78 GHz for the Fermilab Main Ring, while the half-value space charge roll-off harmonic $n_{\frac{1}{2}}$ corresponds to 134 GHz. Therefore, in simulations we need a bin size of about $1/(2 \times 134)$ or 0.00373 ns. The tracking code ESME [9] developed at Fermilab divides the whole rf wavelength or 18.8 ns up into 2^n bins where n is an integer, and the number of bins will have to be at least 4096 which is too large. As a rule of thumb, the bins should have a width less than a/γ , where a is the beam radius. Simulations of the Main Ring across transition had been performed using ESME. As we increase the bin number from 128 to 256 and 512, we do see self-bunching in the phase plot corresponding to the highest frequency of 3.40, 6.81, and 13.6 GHz, respectively, in each of the situations, as illustrated in Fig. 17.7. This suggests that the negative-mass growths at the high

Schottky frequencies do play a role across transition [10]. In an actual simulation, the space charge force is usually implemented by a differentiation of the bunch profile. To maintain the same numerical accuracy, we need to follow the “three-in-one rule” [11], which states that whenever the bin width is reduced by a factor of 2, the number of macro-particles needs to be increased by a factor of 2³. As a result, the tracking time will increase by a factor of 2⁴.

However, a typical Main Ring bunch has a full length of only 1 ns at transition. If we divide just two or three times the bunch region into bins, there will be only 256 or 512 bins, which will reduce the tracking time drastically. Sørensen [12] had successfully performed simulation with a bin width of a/γ . But he did not overcome the second difficulty that we are going to discuss next.

(2) The right amount of Schottky noise

In a simulation of microwave instability, there is usually ample time for the instability to develop to saturation. Therefore, we do not care so much about the size of the initial excitation or seed of the growth. Across transition, however, the bunch is negative-mass unstable only for a short time until the frequency-flip parameter η becomes large enough to provide enough Landau damping, and this time is typically of the order of the nonadiabatic time, which is about 3 ms for the Fermilab Main Ring. Therefore, the initial excitation amplitude needs to be tailored exactly. To have the exact Schottky noise level, we need to use in the simulation micro-particles instead of macro-particles. The Fermilab Main Ring bunch has typically $N_b = 2.2 \times 10^{10}$ particles, which is certainly unrealistically too many in a simulation.

A suggestion is to populate the bunch by N_M macro-particles according to a Hammersley sequence [13] instead of randomly. This is a population according to some pattern so that the statistical fluctuation will become much less. In fact, the number of particles in each bin in excess of the smooth distribution will become $\mathcal{O}(1)$ initially, or the fluctuation function defined in Eq. (17.28) starts from $f(\Delta\phi, 0) \approx 1/\Delta N_M = M/N_M$, where M is the number of bins and $\Delta N_M = N_M/M$ is the average number of macro-particles per bin. The expectation of the initial bunch mode amplitude turns out to be

$$E\left[|c_{k_b}(0)|^2\right] = \frac{M}{N_M^2}. \quad (17.82)$$

Comparing with Eq. (17.34) for a randomly distributed bunch, the required number of

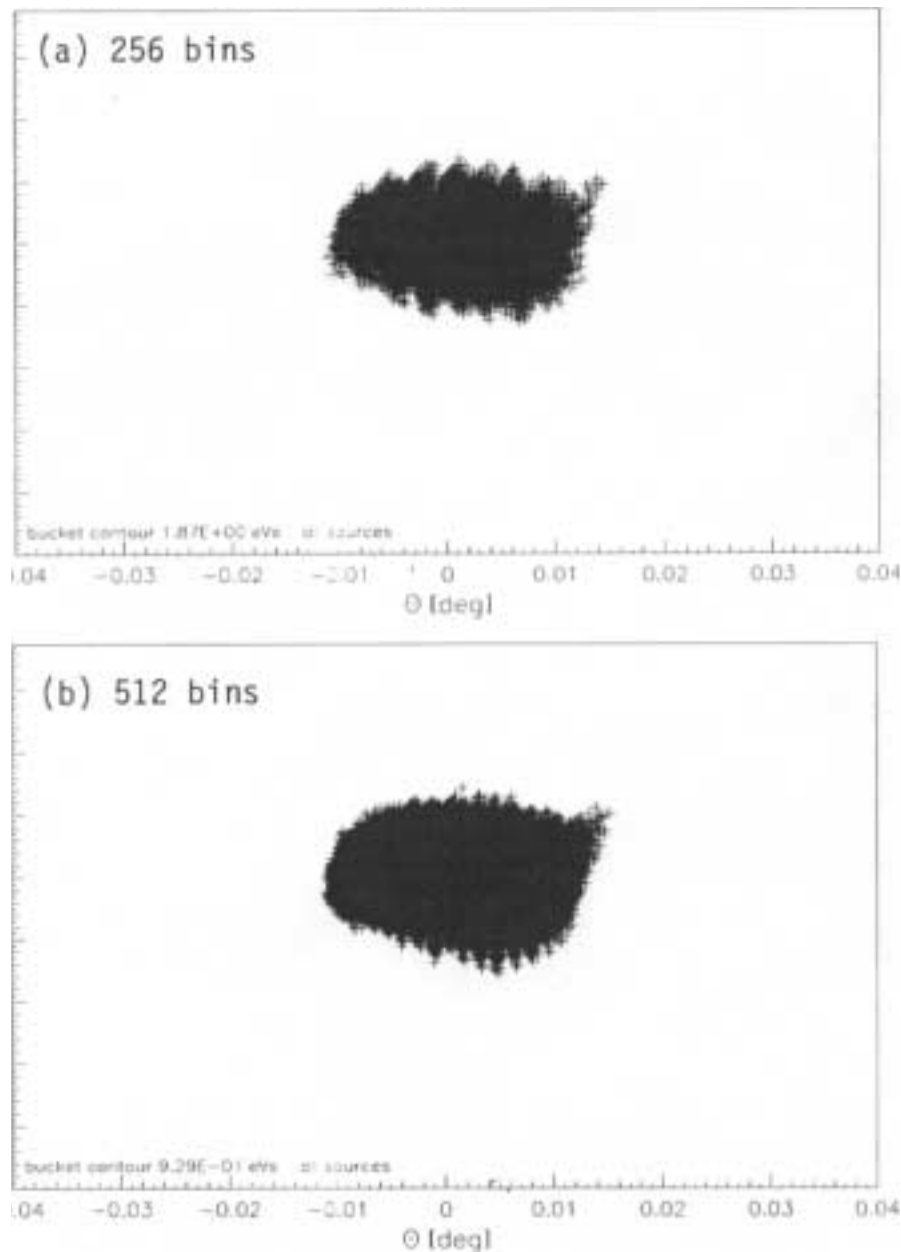


Figure 17.7: ESME simulations of a Fermilab Main Ring bunch containing 4×10^{10} particles with initial emittance of 0.1 eV-sec just after transition with (a) 256 bins and (b) 512 bins in an rf wavelength; 20,000 and 160,000 macro-particles have been used in the two cases. Excitations of 6.81 and 13.6 GHz corresponding to the respective bin widths are clearly seen in the two plots.

macro-particles becomes

$$N_M = (MN_b)^{\frac{1}{2}}, \quad (17.83)$$

which is more reasonable (~ 2.4 to 3.6×10^6), but may be still too large to be managed in a simulation.

There are, however, two other difficulties with the Hammersley-sequence method. In reality for a bunch containing N_b particles, at the m th bin, the step function $f(\Delta\phi_m, t)$ defined in Eq. (17.28) has an initial expectation of

$$E[f^2(\Delta\phi_m, 0)] = E\left[\frac{\delta N_m^2}{\Delta N^2}\right] = \frac{F(\Delta\phi_m)}{\Delta N} = \frac{M}{N_b} F(\Delta\phi_m), \quad (17.84)$$

which is proportional to the initial unperturbed bunch distribution $F(\Delta\phi)$. Here, $\Delta N = N_b/M$ is the average number of micro-particles in each bin and δN_m is the excess number of particle in the m th bin because of statistically fluctuation.. Now it changes to, for the Hammersley population, $E[f^2(\Delta\phi, 0)] = (M/N_M)^2$ which is independent of $F(\Delta\phi)$. Thus, the relative fluctuations in the bins cannot be made to resemble those in the randomly populated bunch, and the initial fluctuation spectrum would have been altered.

In order to have the bunch to fit the space charge modified rf bucket before transition, we usually switch on the space charge force adiabatically over many synchrotron periods so that the initial populated bunch emittance will be preserved. However, the favored Hammersley statistics can often be lost after several synchrotron oscillations. A test was performed with 2×10^5 particles in a truncated bi-Gaussian distribution. The bunch was projected onto one coordinate, where it was divided into 20 equal bins. To simulate synchrotron oscillation, the bunch was then rotated in phase space with an angular velocity which decreases linearly by 1% from the center to the edge of the bunch. The fluctuation or number of particles in excess of the smooth projected Gaussian distribution in each bin was recorded for every rotation, and the rms was computed. The results are plotted in Fig. 17.8 as a function of rotation number. We see that although the rms fluctuation starts from 7 initially, it increases rapidly to ~ 12 after 5 rotations, ~ 20 after 20 rotations, and will approach its statistical value of 100 eventually. This might have been an overestimation, because the actual decrease in synchrotron frequency is not linear and the decrease near the core of the bunch where most particles reside is very much slower. Nevertheless, this test gives us an illustration of restoration to randomness. To cope with the fast restoration to randomness, one possibility is to compute exactly the initial distribution of the bunch in the space charge modified rf bucket right at transition and populate the bunch according to a Hammersley sequence. In this way,

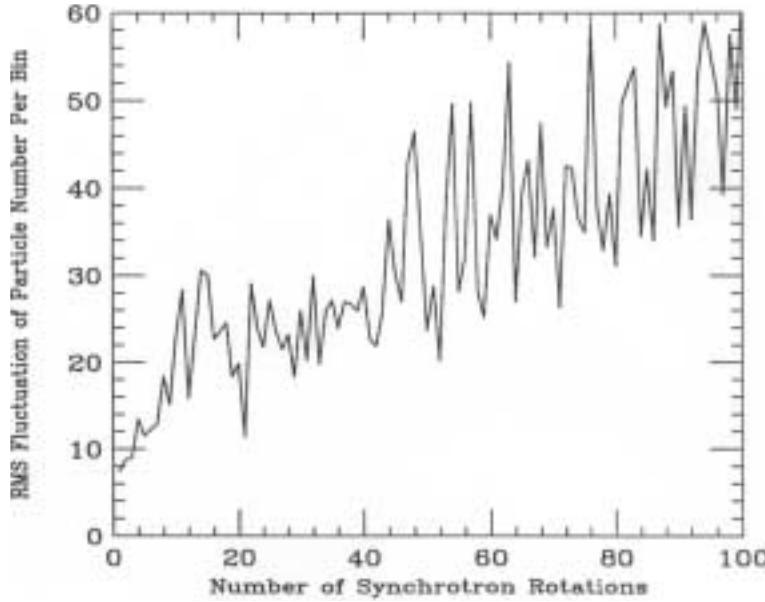


Figure 17.8: Plot of rms fluctuation of excess particles per bunch versus number of synchrotron rotations, showing the rapid loss of Hammersley statistics and restoration to randomness.

the tracking of the bunch particles across the negative-mass unstable period, which is usually of the order of one synchrotron period, may reveal the reliable growth from the correct Schottky noise level.

17.3 Self-Bunching Model

Microwave instability can be viewed as self-bunching. The beam current I_{pk} , seeing the impedance Z_I , gives rise to an rf voltage $I_{\text{pk}}Z_I$, and creates a self-bunching rf bucket with an energy half height

$$\frac{\Delta E}{E} = \left(\frac{2\beta^2 e I_{\text{pk}} Z_I}{\pi \eta n_z \gamma E_{\text{rest}}} \right)^{\frac{1}{2}}, \quad (17.85)$$

where n_z denotes the revolution harmonic of the impedance. If this bucket height is less than the energy spread of the bunch, there will not be any extra energy spread and the bunch will be stable. If the bucket height is larger than the energy spread of the bunch, the bunch particles will travel outside the original energy boundary of the bunch, giving rise to an emittance growth as a result of filamentation. In fact, this is just another way

of expressing the Keil-Schnell criterion [14].

Here, we want to make the conjecture that this self-bunching bucket height determines the final energy spread of the bunch. Inside this bucket, the angular synchrotron frequency is given by

$$\omega_s = \left(\frac{n_z \eta I_{\text{pk}} Z_I}{2\pi \beta^2 \gamma E_{\text{rest}}} \right)^{\frac{1}{2}} \omega_0. \quad (17.86)$$

Since the frequency-flip parameter η is changing rapidly at transition, we substitute

$$\frac{\eta}{\gamma} = \frac{2\dot{\gamma}_t}{\gamma_t^4} t. \quad (17.87)$$

If we denote by ϕ_{syn} the angle of rotation in the longitudinal phase space, we have $\omega_s = d\phi_{\text{syn}}/dt$. Integrating Eq. (17.86), we obtain the time to reach a quarter of a synchrotron oscillation ($\Delta\phi_{\text{syn}} = \pi/4$) from the moment of transition crossing as

$$T \approx \left(\frac{3\pi}{4} \right)^{\frac{2}{3}} \left(\frac{\pi E_{\text{rest}} \beta_t^2 \gamma_t^4}{n_z I_{\text{pk}} Z_I \dot{\gamma}_t \omega_0^2} \right)^{\frac{1}{3}}. \quad (17.88)$$

This will be the time required for some particles to reach the top of the bucket. Of course, the height of the self-bunching bucket is also changing, and the value of $\eta\gamma$ at this moment should be substituted in Eq. (17.85). At this moment, the unperturbed energy spread of an elliptical bunch with emittance S and without space charge distortion is, from Eq. (16.79),

$$\frac{\Delta E}{E} = \frac{\Gamma(\frac{1}{3})}{2^{1/2} 3^{1/6} \pi} \left(\frac{S \beta_t^2 \gamma_t^2}{E_{\text{rest}} T_c^2 \dot{\gamma}_t} \right)^{\frac{1}{2}} \left(1 - \frac{\pi}{3^{1/6} \Gamma^2(\frac{1}{3})} \frac{T}{T_c} \right), \quad (17.89)$$

where

$$T_c = \left(\frac{\beta_t^2 \gamma_t^4 |\tan \phi_s|}{2h\omega_0 \dot{\gamma}_t^2} \right)^{\frac{1}{3}}. \quad (17.90)$$

is the nonadiabatic time. The correction in the second term of Eq. (17.89) is usually small. Thus, the growth in energy spread can be computed easily, and assuming filamentation the growth in emittance can be obtained. This estimate will be valid if T is less than the time to regain stability. The growths for some situations of the Fermilab Main Ring are given in Table 17.4. The corresponding growths obtained from the growth-at-cutoff model are also listed for comparison.

There is at present no reliable simulation of emittance growth. Experimental measurements are also marred by other mechanisms, such as bunch tumbling due to bunch-length mismatch, particles with different momentum crossing transition at different time,

Table 17.4: Growth of emittance for the self-bunching and growth-at-cutoff models.

$\dot{\gamma}_t$ (s^{-1})	N_b (10^{10})	Initial Bunch Emittance (eV-s)	Fractional Emittance Growth	
			Self-Bunching Model	Cutoff Model
90	2.2	0.05	4.09	4.06
90	2.2	0.06	3.03	2.43
90	2.2	0.07	2.35	1.83
90	2.2	0.08	1.89	1.54
90	2.2	0.09	1.52	1.38
120	4.0	0.06	5.32	8.16
120	4.0	0.07	4.12	4.17
120	4.0	0.08	3.31	2.78
120	4.0	0.09	2.72	2.14
120	4.0	0.10	2.29	1.80

etc. Another example at the Fermilab Main Ring is that the bunch emittance usually grows to such a value that scraping occurs. Therefore, it is hard to judge at this moment the reliability of this crude model. On the other hand, this model can certainly be improved to a certain degree by including, for example, the space charge distortion of the bunch shape, the tilt effect in phase space near transition, as well as the mechanism of overshoot when stability is regained.

17.4 Exercise

- 17.1. The Alternating Gradient Synchrotron (AGS) at Brookhaven is a proton ring with a circumference of 807.11 m. The beam crosses transition at $\gamma_t = 8.8$ with $\dot{\gamma}_t = 63 \text{ s}^{-1}$. The rf harmonic is $h = 12$ and the synchronous phase is $\phi_s = 27.3^\circ$.
- (1) With beam pipe radius 2.356 cm and beam radius 0.5 cm, compute the space charge impedance at transition and the frequency at which the integrated negative-mass growth is at a maximum.
 - (2) For a bunch with[§] 1×10^{12} protons, compute the critical stability parameter c defined in Eq. (17.69) for various bunch areas. Determine the smallest bunch area to avoid negative-mass blowup. Repeat the computation with the intensity of 3×10^{12} protons.
- 17.2. It is possible that the AGS described in the previous problem is dominated by a broad-band impedance of $Z_0^{\parallel}/n \approx 20 \Omega$ at 1.5 GHz. Use the simplified model developed in Sec. 17.1.1 to compute the total growth across transition. The bunch area is assumed to be 6 eV-s.

[§]The AGS is currently running at the intensity of $\sim 1 \times 10^{13}$ particles per bunch with a transition jump. Here, we are estimating the growth without transition jump.

Bibliography

- [1] S.Y. Lee and J.M. Wang, *Microwave Instability Across the Transition Energy*, IEEE Trans. Nucl. Sc. **NS-32**, 2323 (1985).
- [2] J. Wei, *Longitudinal Dynamics of the Non-Adiabatic Regime on Alternating-Gradient Synchrotrons*, PhD Dissertation, SUNY, Stony Brook, 1990.
- [3] K.Y. Ng, *Microwave Stability Limits for the Main Ring and Growth across Transition*, Fermilab Report TM-1383, 1986.
- [4] W.W. Lee and L.C. Teng, *Beam-Bunch Length Matching at Transition Crossing*, Proc. 8th Int. Conf. High Energy Accel., Geneva, 1971, p.327.
- [5] P. Lucas and J. MacLachlan, *Simulation of Space Charge Effects and Transition Crossing in the Fermilab Booster*, Proc. 1987 IEEE Part. Accel. Conf., Washington, D.C., 1987, p.1114.
- [6] W. Hardt, *Gamma-Transition-Jump Scheme of the CPS*, Proc. 9th Int. Conf. High Energy Accel., SLAC, Stanford, 1974, p.434.
- [7] E. Keil and B. Zotter, Particle Accelerators **3**, 11 (1972).
- [8] I. Kourbanis and K.Y. Ng, *Transition Crossing in the Fermilab Main Ring, Past and Present*, Proc. 1993 IEEE Part. Accel. Conf., Washington, D.C., 1993, p.3630.
- [9] J.A. MacLachlan, *ESME: Longitudinal Phase-Space Particle Tracking—Program Documentation*, Fermilab Internal Report TM-1274, 1984.
- [10] I. Kourbanis and K.Y. Ng, unpublished.

- [11] See for example Ref. 3 or I. Kourbanis and K.Y. Ng, *Main Ring Transition Crossing Simulations*, Proc. Fermilab III Instabilities Workshop, Fermilab, Batavia, U.S., Ed. S. Peggs and M. Harvey, 1990, p.151.
- [12] A. Sørenssen, *What Happens Right After Phase Transition?* CERN/MPS/DL 72-14, 1972.
- [13] J.M. Hammersley and D.C. Handscomb, *Monte Carlo Methods*, Wiley, 1964.
- [14] E. Keil and W. Schnell, CERN Internal Report ISR-TH-RF/69-48, 1969.

Chapter 18

INSTABILITY OF ISOCHRONOUS RINGS

In a storage ring, sometimes there are advantages to work with a lattice having a smaller slippage factor η . One reason is the achievement of shorter bunch lengths. It can be shown easily that, in electron rings where the energy spread is determined by synchrotron radiation, the bunch length is proportional to $|\eta|^{1/2}$. For proton or muon storage rings where there is no synchrotron radiation, the bunch length at fixed rf voltage is proportional to $|\eta|^{1/4}$. Another reason for having a small slip factor is the possible reduction of the expensive rf system. To maintain a bunch at the required rms length σ_τ and momentum spread σ_δ , the synchrotron tune is

$$\nu_s = \frac{|\eta|\sigma_\delta}{\omega_0\sigma_\tau} , \quad (18.1)$$

and the rf voltage is therefore

$$V_{\text{rf}} = \frac{2\pi|\eta|\beta^2 E_0 \sigma_\delta^2}{e h \omega_0^2 \sigma_\tau^2 |\cos \phi_s|} \quad (18.2)$$

which decreases linearly as $|\eta|$. In above, h is the rf harmonic, ϕ_s is the synchronous phase angle, E_0 is the total energy of the synchronous particle which has angular revolution frequency ω_0 and velocity βc where c is the velocity of light. Ideally, when $\eta = 0$, no rf will be necessary, because there will not be any drift in phase. A ring with $\eta = 0$, i.e., operating right at transition energy, is called an *isochronous* ring. However, there is always a spread in energy in the beam particles. As a result, it is not possible

for every beam particle to see isochronicity. In addition, the slippage factor η is a nonlinear function of the momentum spread. Usually, isochronicity is defined when the slippage factor vanishes in the first order of the momentum spread. The higher-order contributions will provide a finite slippage. Thus, the ring is actually quasi-isochronous. For such a ring, the parameters of interest are (1) η for the synchronous particle and (2) the total spread in η seen by all the beam particles. It is necessary to design the lattice so that both η and the spread in η are small. When η is vanishing small, there will not be any Landau damping and collective instabilities will emerge as an important issue, which we are going to investigate in this chapter.

18.1 Higher-Order Momentum Compaction

Transition crossing is defined as the moment when the relativistic gamma of the particle is equal to γ_t of the accelerator ring. Let us recall that the transition gamma is defined as $\gamma_t = \alpha_0^{-1/2}$, where α_0 is the momentum-compaction factor which is the fractional increment of the circumferential orbit length of a particle with fractional momentum offset δ . Hence, if $C(\delta)$ is the length of the off-momentum orbit,

$$C(\delta) = C_0(1 + \alpha_0\delta) , \quad (18.3)$$

with $C_0 = C(0)$ being the length of the on-momentum orbit. Thus, the slippage factor η is exactly zero at transition. However, Eq. (18.3) only gives the linear dependence of the orbit length on momentum offset. In general, this is never the case for any accelerator lattice. Therefore, Eq. (18.3) should be extended to*

$$C(\delta) = C_0[1 + \alpha_0\delta(1 + \alpha_1\delta + \alpha_2\delta^2 + \dots)] , \quad (18.4)$$

where α_1 , α_2 , etc. are called the high-order components of the momentum-compaction factor. Now the slippage factor η also becomes momentum spread dependent. Its higher orders must be carefully defined so that it enters correctly into Eq. (16.3), the phase-slip equation of motion

$$\frac{d\Delta\phi}{dt} = \hbar\omega_0\eta\delta . \quad (18.5)$$

Here, we follow a derivation of Edwards and Syphers [1]. A particle with momentum offset δ_n sees an *accumulated* rf phase ϕ_n on its n th passage of the rf cavity, which is

*In Europe, α_0 , α_1 , α_2 , etc. are usually referred to as α_1 , α_2 , α_3 , etc. There is also another common definition, where $C(\delta) = C_0[1 + \alpha_0\delta + \alpha_1\delta^2 + \alpha_2\delta^3 + \dots]$.

considered to have an infinitesimal length. On its $(n+1)$ th passage, at a time $T_{n+1} + \Delta T_{n+1}$ later, the accumulated rf phase seen becomes

$$\phi_{n+1} = \phi_n + \omega_{\text{rf}}(T_{n+1} + \Delta T_{n+1}) , \quad (18.6)$$

where $\omega_{\text{rf}}/2\pi$ is the rf frequency, T_{n+1} is the revolution period of the synchronous particle during its $(n+1)$ th turn and ΔT_{n+1} is the extra time taken by the off-momentum particle to complete the revolution. On the other hand, the rf phase seen by the synchronous particle accumulates according to

$$\phi_n^s = \omega_{\text{rf}} t_n , \quad (18.7)$$

where t_n is the total accumulated time up to the n th passage of the cavity. Naturally, we like to measure the rf phase seen by the off-momentum particle relative to the synchronous particle. This leads to the introduction of the rf phase offset or rf phase slip $\Delta\phi_n$ defined by

$$\Delta\phi_n = \phi_n - \phi_n^s = \phi_n - \omega_{\text{rf}} t_n . \quad (18.8)$$

Substituting into Eq. (18.6) and noting that $T_{n+1} = t_{n+1} - t_n$, we arrive at

$$\Delta\phi_{n+1} = \Delta\phi_n + \omega_{\text{rf}} \Delta T_{n+1} . \quad (18.9)$$

In order for the synchronous particle to be synchronized, one must adjust the rf frequency so that $\omega_{\text{rf}} T_{n+1} = 2\pi h$ for all turns, where h is the rf harmonic number. Now, we can define the slippage factor as the slip in revolution period at the $(n+1)$ th passage of the cavity by

$$\frac{\Delta T_{n+1}}{T_{n+1}} = \eta_{n+1} \delta_{n+1} . \quad (18.10)$$

Here, the subscript of η implies its dependence on the momentum offset of the particle at the $(n+1)$ th passage and *not* its higher-order expansion terms. With this definition, Eq. (18.9) becomes

$$\frac{\Delta\phi_{n+1} - \Delta\phi_n}{T_{n+1}} = \eta_{n+1} \omega_{\text{rf}} \delta_{n+1} . \quad (18.11)$$

When smoothing is applied, we obtain the phase-slip equation of Eq. (16.10),

$$\frac{d\Delta\phi}{dt} = h\omega_0 \eta \delta . \quad (18.12)$$

Since the revolution period T can be expressed as

$$T = \frac{C}{\beta c} , \quad (18.13)$$

we can easily expand T as a Taylor series in δ , from which each higher-order of the slippage factor can be identified. For example, we have

$$\begin{aligned}\frac{T'_0}{T_0} &= \frac{C'_0}{C_0} - \frac{\beta'_0}{\beta_0}, \\ \frac{T''_0}{T_0} &= \frac{2C'^2_0}{C_0^2} - \frac{2\beta'_0 C'_0}{\beta_0 C_0} - \frac{\beta''_0}{\beta_0} + \frac{2\beta'^2_0}{\beta_0^2}, \\ \frac{T'''_0}{T_0} &= \frac{C'''_0}{C_0} - \frac{3\beta'_0 C''_0}{\beta_0 C_0} - \frac{3\beta''_0 C'_0}{\beta_0 C_0} + \frac{6\beta'^2_0 C'_0}{\beta_0^2 C_0} - \frac{\beta'''_0}{\beta_0} - \frac{\beta'_0 \beta''_0}{\beta_0^2} - \frac{6\beta'^3_0}{\beta_0^3},\end{aligned}\quad (18.14)$$

where the *prime* denotes differentiation with respect to δ and all variables are evaluated at the synchronous particle, which explains why all the variables above carry the subscripts zero, although these subscripts may have been suppressed in many occasions for the sake of convenience. The derivatives of C can be read off easily from Eq. (18.4). The derivatives of β can be computed straightforwardly. They are:

$$\begin{aligned}\frac{\beta'_0}{\beta_0} &= \frac{1}{\gamma_0^2}, \\ \frac{\beta''_0}{\beta_0} &= -\frac{3\beta_0^2}{\gamma_0^2}, \\ \frac{\beta'''_0}{\beta_0} &= -\frac{3\beta_0^2(1-5\beta_0^2)}{\gamma_0^2}.\end{aligned}\quad (18.15)$$

With the expansion of the slippage factor

$$\eta = \eta_0 + \eta_1 \delta + \eta_2 \delta^2 + \dots, \quad (18.16)$$

we obtain the expressions for the higher-order components of the slippage factor [Exercise 18.1]:

$$\eta_0 = \alpha_0 - \frac{1}{\gamma_0^2}, \quad (18.17)$$

$$\eta_1 = \alpha_0 \alpha_1 + \frac{3\beta_0^2}{2\gamma_0^2} - \frac{\eta_0}{\gamma_0^2}, \quad (18.18)$$

$$\eta_2 = \alpha_0 \alpha_2 + \frac{\alpha_0 \alpha_1}{\gamma_0^2} - \frac{2\beta_0^4}{\gamma_0^2} + \frac{3\alpha_0 \beta_0^2}{2\gamma_0^2} + \frac{\eta_0}{\gamma_0^4}. \quad (18.19)$$

Looking at the phase-slip equation above, one may be tempted to equate $d\Delta\phi/dt$ to $-\Delta\omega/h$, where $\Delta\omega$ is the slip in angular velocity of the off-momentum particle relative to the synchronous particle. However, this will translate the definition of η to

$$\frac{\Delta\omega}{\omega_0} = -\eta\delta , \quad (18.20)$$

which is different from Eq. (18.10) and therefore will lead to incorrect expressions for the higher-order terms of η . This misconception comes about in the smoothing procedure from Eq. (18.11) to Eq. (18.12), where we divide throughout by the revolution period of the *synchronous* particle. If $\Delta\omega$ of the off-momentum particle is desired, one should divide instead by $T_{n+1} + \Delta T_{n+1}$, the revolution period of the off-momentum particle. In other words, $d\Delta\phi/dt$ in the phase equation describing the motion of an off-momentum particle does not imply the rate of change of rf phase slip of the off-momentum particle according to the clock that registers the revolution period of that particle. Instead, it is referenced to the clock that registers the revolution period of the synchronous particle. Because of this easily-forgotten detail, it will be more convenient to use $s = v_0 t$ as the independent ‘time’ variable, where s is the distance measured along the closed orbit of the synchronous particle and v_0 is the velocity of the synchronous particle.

Another definition in the literature is [2]

$$\eta = -\frac{1}{\omega_0} \frac{d\omega}{d\delta} , \quad (18.21)$$

which is incompatible with the phase-slip equation in Eq. (18.12). This definition originates from the lowest order expansion in ω [2], and is therefore insufficient when higher-orders in η are studied. This is, in fact, a variation of the incorrect definition of Eq. (18.20).

18.2 η_1 -Dominated Bucket

To save the cost of rf power, suggestions have been made to make storage rings *isochronous* or *quasi-isochronous*, implying an operation when $\eta_0 \approx 0$. Since the drift of the longitudinal phase is small, a small rf system will be adequate. However, when η_0 is small enough, we need to include the next lowest nonlinear term of the slippage factor, namely η_1 . When the rf phase slip $\Delta\phi$ and the fractional momentum spread δ are used as canonical coordinates with time t being the independent variable, the Hamiltonian describing

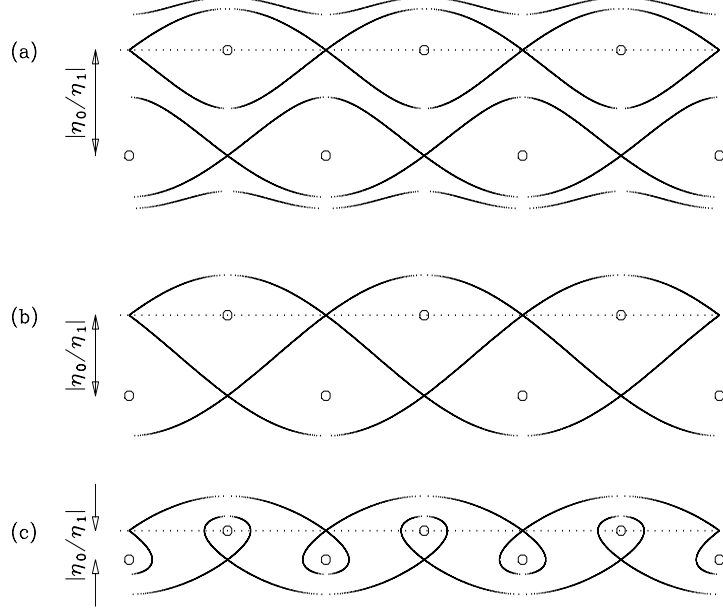


Figure 18.1: (a) When $|\eta_0/\eta_1|$ is not too small, the longitudinal phase space shows 2 series of distorted pendulum-like buckets. (b) As $|\eta_0/\eta_1|$ decreases to the critical value in Eq. (18.23), the 2 series merge. (c) Further reduction of $|\eta_0/\eta_1|$ leads to new pairing of stable and unstable fixed points and the buckets become α -like. In each case, the dotted line is the phase axis at zero momentum spread, and the small circles are the stable fixed points.

the motion of a particle in the longitudinal phase space becomes

$$H = \left(\frac{\eta_0 \delta^2}{2} + \frac{\eta_1 \delta^3}{3} \right) h\omega_0 + \frac{eV_{\text{rf}}\omega_0}{2\pi\beta^2 E_0} [\cos(\phi_s + \Delta\phi) + \Delta\phi \sin \phi_s], \quad (18.22)$$

where ϕ_s is the synchronous phase. With the presence of η_1 , the symmetry of the higher- and lower-momentum parts of the phase space is broken. As a result, the phase-space structure will be very much disturbed. This Hamiltonian gives stable fixed points at $(2n\pi, 0)$, $(2(n+1)\pi - 2\phi_s, -\eta_0/\eta_1)$ and unstable fixed points at $(2(n+1)\pi - 2\phi_s, 0)$, $(2n\pi, -\eta_0/\eta_1)$, where n is any integer. When the contribution of η_1 is much smaller than that of η_0 , the buckets are still roughly pendulum-like as shown in Fig. 18.1(a) for the case of $\phi_s = 0$. Note that there is another series of buckets at momentum spread $-\eta_0/\eta_1$. As $|\eta_0/\eta_1|$ decreases to a point when the values of the Hamiltonian through all unstable fixed points are equal, the two series merge as illustrated in Fig. 18.1(b). This

happens when

$$\left| \frac{\eta_0}{\eta_1} \right| = \left\{ \frac{6eV_{\text{rf}}}{\pi\beta^2 h\eta_0 E_0} \left[\left(\frac{\pi}{2} - \phi_s \right) \sin \phi_s - \cos \phi_s \right] \right\}^{1/2}. \quad (18.23)$$

The right side is just $\sqrt{3}$ times the half bucket height when the η_1 term in the Hamiltonian is absent. As $|\eta_0/\eta_1|$ is further reduced, the pairing of the stable and unstable fixed points is altered, and the buckets become α -like as illustrated in Fig. 18.1(c). The buckets in one series have heights given by

$$\hat{\delta} = \begin{cases} + \left| \frac{\eta_0}{2\eta_1} \right| & \delta > 0, \\ - \left| \frac{\eta_0}{\eta_1} \right| & \delta < 0. \end{cases} \quad (18.24)$$

For the other series, the buckets are just inverted and are centered at $\delta = -|\eta_0/\eta_1|$. Note that the heights of the buckets will vanish if the lattice approaches truly isochronous ($\eta_0 = 0$).

Let us now review some very peculiar properties of the α -like bucket.

(1) Since the height of the α -shape bucket is fixed, the bucket width ϕ is proportional to $V_{\text{rf}}^{-1/2}$ and so is the bucket area \mathcal{A} [3]. In fact,

$$\phi = \left(\frac{|\eta_0|^{3/2}}{|\eta_1|} \right) \left(\frac{2\pi\beta^2 h E_0}{3eV_{\text{rf}} |\cos \phi_s|} \right)^{1/2}, \quad (18.25)$$

$$\mathcal{A} = \frac{6}{5} \left(\frac{|\eta_0|^{5/2}}{\eta_1^2} \right) \left(\frac{2\pi\beta^2 h E_0}{eV_{\text{rf}} |\cos \phi_s|} \right)^{1/2}, \quad (18.26)$$

where the narrow width of the bucket has been assumed and its maximum momentum spreads of $|\eta_0/(2\eta_1)|$ and $-|\eta_0/\eta_1|$ have been used. Unlike the usual pendulum-like bucket where the bucket width is fixed and the bucket height and area increase with the rf voltage, here, this α -like bucket has fixed height while its width and area will be increased by *lowering* the rf voltage. As an example, set the bucket height to $|\eta_0/\eta_1| = k_\delta \delta_{\max}$ and the bucket half width to $\hat{\ell} = k_\ell \ell_{\max}$, where δ_{\max} and ℓ_{\max} are the maximum bunch momentum spread and length in m. The required rf voltage multiplied by the rf harmonic required to maintain the bunch in the bucket is, according to Eq. (18.25),

$$hV_{\text{rf}} = \frac{2\pi\beta^2 E_0 R^2 |\eta_0| k_\delta^2 \delta_{\max}^2}{3ek_\ell^2 \ell_{\max}^2 |\cos \phi_s|}. \quad (18.27)$$

The maximum momentum spread and bunch length are also related by the Hamiltonian,

$$\frac{V_{\text{rf}}}{h} = \frac{\pi\beta^2 E_0 |\eta_0| \delta_{\max}^2}{2e \sin^2 \frac{1}{2}\phi_{\max}} \left(1 + \frac{2}{3k_\delta}\right), \quad (18.28)$$

where we have set $\phi_s = 0$ or π . The maximum half phase spread is $\phi_{\max} = h\ell_{\max}/R$. Therefore, when the rf harmonic $h \ll 2R/\ell_{\max}$, Eqs. (18.27) and (18.28) give

$$\left(\frac{k_\delta}{k_\ell}\right)^2 = 3 + \frac{2}{k_\delta}, \quad (18.29)$$

which is universally true, independent of the bunch and lattice parameters.

(2) The asymmetry between positive and negative momentum spreads brought in by η_1 will lead to bunch length oscillations. Since the energy loss due to the resistive part of the impedance of the vacuum chamber is proportional to the bunch length, this may lead to a continuous growth of the synchrotron oscillation amplitude. This instability is called longitudinal head-tail, which had been observed in the CERN SPS [4]. The instability can become very strong here because η_0 has been made negligibly small.

(3) The synchrotron frequency as a function of oscillation amplitude can be computed easily [3]. As the oscillation amplitude increases, the synchrotron frequency inside the α -like bucket decreases much more slowly than that inside an ordinary pendulum-like bucket. However, it drops to zero very abruptly near the edge of the bucket. Thus, the α -like bucket resembles a resonance island more than the usual pendulum-like bucket. Because of the sudden drop of the synchrotron frequency near the separatrix, higher-order resonances due to small jitters or modulations of the rf phase or rf voltage overlap creating a thick stochastic layer thus further reducing the stable area inside the bucket.

(4) Although there are disadvantages of the α -like bucket, nevertheless, this bucket is intrinsically narrow in phase spread, as is depicted in Eq. (18.26). For a pendulum-like bucket, the bucket width is always equal to the rf wavelength, whereas for a α -like bucket, the bucket width is mostly much less than the rf wavelength. Moreover, for a bunch in an ordinary pendulum-like bucket, the bunch width varies as $(|\eta_0|/V_{\text{rf}})^{1/4}$; thus reducing the momentum-compaction factor or increasing the rf voltage is not very efficient in reducing the width of the bunch. On the other hand, a bunch in the α -like bucket has a width proportional to $|\eta|^{3/2}/V_{\text{rf}}^{1/2}$.

18.3 η_2 -Dominated Bucket

The η_1 term will lead to a small bucket area and possibly longitudinal head-tail instability, thus limiting the beam dynamic when the machine is near isochronous. The δ -asymmetric bucket can lead to unpleasant longitudinal head-tail instability. Furthermore, α_1 can destroy the isochronicity of the ring. For example, if we want to have a 2 TeV on 2 TeV isochronous ring for the muon collider with $|\eta| \lesssim 1 \times 10^{-6}$, the α_1 term can contribute a spread of γ_t^{-2} of $\sim 70 \times 10^{-6}$ at the momentum spread of $|\delta| < 0.3\%$ [5]. A large spread in γ_t^{-2} implies large slippage factors for some particles, so that an unusually large rf system will be required for bunching. Therefore, η_1 should be eliminated. Then, the Hamiltonian with the next nonlinear term η_2 included becomes

$$H = \left(\frac{\eta_0 \delta^2}{2} + \frac{\eta_2 \delta^4}{4} \right) h\omega_0 + \frac{eV_{\text{rf}}\omega_0}{2\pi\beta^2 E_0} [\cos(\phi_s + \Delta\phi) + \Delta\phi \sin \phi_s] . \quad (18.30)$$

A quadrupole bends particles with positive and negative off-momenta in opposite directions. To the lowest order, it contributes to α_0 of the momentum-compaction factor. On the other hand, a sextupole bends particles with positive and negative off-momenta in the same direction, and therefore contributes to α_1 . In fact, through first-order perturbation theory, one can show that α_2 can be corrected with octupoles, α_3 with decapoles, and so on [6, 7]. Having the ability to change α_2 with octupoles may be useful because it may be easier than adjusting α_2 with sextupoles since the latter also affect α_1 .

With the contribution of η_1 eliminated, it is possible to adjust η_0 to zero so that the Hamiltonian becomes

$$H = \frac{1}{4} h\omega_0 \eta_2 \delta^4 + \frac{eV_{\text{rf}}\omega_0}{2\pi\beta^2 E_0} [\cos(\phi_s + \Delta\phi) + \Delta\phi \sin \phi_s] , \quad (18.31)$$

Now for $\phi_s = 0$, the bucket looks pendulum-like with the usual width of $\Delta\phi = 2\pi$. The bucket half height is $\hat{\delta} = [4eV_{\text{rf}}/(\pi\beta^2 E_0 h |\eta_2|)]^{1/4}$. When the half bunch length ℓ_{max} is short, it is related to the half momentum spread δ_{max} by

$$\delta_{\text{max}}^4 = \left(\frac{eV_{\text{rf}} h}{\pi\beta^2 E_0 |\eta_2|} \right) \left(\frac{\ell_{\text{max}}}{R} \right)^2 . \quad (18.32)$$

If we let $\hat{\delta} = k\delta_{\text{max}}$, we can solve for the necessary rf voltage and rf harmonic:

$$V_{\text{rf}} = \frac{\pi\beta^2 E_0 R k^2 \Delta\eta \delta_{\text{max}}^2}{2\ell_{\text{max}}} , \quad h = \frac{2R}{\ell_{\text{max}} k^2} , \quad (18.33)$$

where $\Delta\eta = |\eta_2|\delta_{\max}^2$ is the desired spread of the slippage factor of the bunch. Note that the rf voltage is proportional to $\Delta\eta$, the desired spread in momentum-compaction, and δ_{\max}^2 , the momentum spread of the bunch squared. Thus, if we reduce the momentum-compaction spread, the rf voltage will be reduced by the same factor. On the other hand, the rf frequency is independent of the choice of $\Delta\eta$ and δ_{\max} .

For small phase spread, Eq. (18.31) describes a particle oscillating in a quartic potential (with $\Delta\phi$ and δ interchanged). This is a well-known situation when a higher harmonic cavity is present and the two cavity voltages are inversely proportional to the square of their respective harmonics (see Sec. 9.3.1). For such a system, the synchrotron frequency is zero at zero oscillating amplitude and increases linearly with respect to the momentum offset δ_{\max} , or the 4th root of the Hamiltonian. The synchrotron frequency increases to a maximum for larger oscillation amplitude and drops to zero again at the edge of the bucket. Simple derivation gives the synchrotron tune $\nu_s = \nu_{s0}F(H)$, where $\nu_{s0} = \sqrt{h\Delta\eta eV_{\text{rf}}/(2\pi\beta^2E_0)}$ with $\Delta\eta = |\eta_2|\delta_{\max}^2$ just the synchrotron tune of a synchronous particle in an ordinary single rf system with a slippage factor equal to $\Delta\eta$. For a constant η_2 , the ν_{s0} is directly proportional to the momentum-offset excursion δ_{\max} . The form factor $F(H)$ can be written as (Exercise 18.5)

$$F^{-1}(H) = \frac{2^{3/4}}{2\pi} \int_0^{\pi/2} \frac{dz}{\sqrt{\cos z} \sqrt{1 - \sin^2 \frac{\phi_{\max}}{2} \sin^2 z}} . \quad (18.34)$$

The form factor is evaluated at the Hamiltonian value,

$$H = \frac{eV_{\text{rf}}\omega_0}{\pi\beta^2E_0} \sin^2 \frac{\phi_{\max}}{2} = \frac{1}{4}h|\eta_2|\omega_0\delta_{\max}^4 , \quad (18.35)$$

where ϕ_{\max} and δ_{\max} are equal to, respectively, the phase and momentum-offset excursions of the beam particle under investigation. A large spread in synchrotron frequency can be advantageous in providing Landau damping to mode-coupling instabilities. For small ϕ_{\max} , from Eqs. (18.33) and (18.35), one obtains $\sin^2(\phi_{\max}/2) = k^{-4}$, where $k = \hat{\delta}/\delta_{\max}$. Thus, the form factor of Eq. (18.34) is almost a constant for any reasonable k , and is roughly equal to $F(H) = 1.45$.

18.4 Microwave Instability Near Transition

18.4.1 Analytic Solutions

In an operation near the transition energy ($\eta_0 \approx 0$), at least the next order, η_1 in Eq. (18.16), must be included for a meaningful discussion of the beam dynamics. Bogacz analyzed the stability of a coasting beam right at transition, $\eta_0 = 0$ [8], by including the η_1 term but neglecting other higher-order terms. For a Gaussian distribution with rms energy spread σ_E , he obtained an analytic expression for the growth rate at the revolution harmonic n :

$$\frac{1}{\tau_n} = -2\alpha_1 n\omega_0 \left(\frac{\sigma_E}{E_0} \right)^2 \phi_n \quad \text{with} \quad \tan \phi_n = \left[\frac{\operatorname{Im} Z_0^{\parallel}}{\operatorname{Re} Z_0^{\parallel}} \right]_n , \quad (18.36)$$

where $\operatorname{Im} Z_0^{\parallel} > 0$ implies capacitive and $\omega_0/(2\pi)$ is the revolution frequency of the on-energy particle which has energy E_0 . He drew the conclusion that the beam will be completely stable. However, when he made this conclusion, he had in mind the assumption of $\alpha_1 > 0$ and $\phi_n > 0$, which is not always true. As a result, there will be microwave growth in general.

Holt and Colestock studied the same problem with coasting beam and Gaussian energy distribution, but allowing $\eta_0 \neq 0$ [9]. The dispersion relation is expressed in terms of the complex error function. Their conclusion is that there is no unstable region in the complex Z_0^{\parallel} -plane below transition. On the other hand, there are both stable and unstable regions above transition. They also claimed that their conclusion was supported by simulations. However, they did not specify the values of η_0 and η_1 in the simulations they presented or in their stability plots in the complex Z_0^{\parallel} -plane. It is hard to understand at least the situation below transition. It is clear that when $|\eta_0|$ is not too small, the contribution of η_1 is irrelevant. Thus their claim as stated can be interpreted as *no microwave instability below transition*, no matter how far away it is from transition. For this reason, this claim is quite questionable. When we look into the stability plots of Holt and Colestock, Fig. 18.2, we can see something that resembles a stability curve below transition. The presence of a stability curve implies the existence of both stable and unstable regions, in contradiction to their conclusion.

We performed some simulations and got different results. A coasting beam at 100 GeV was considered in a hypothetical ring of circumference 50 m, with an initial rms

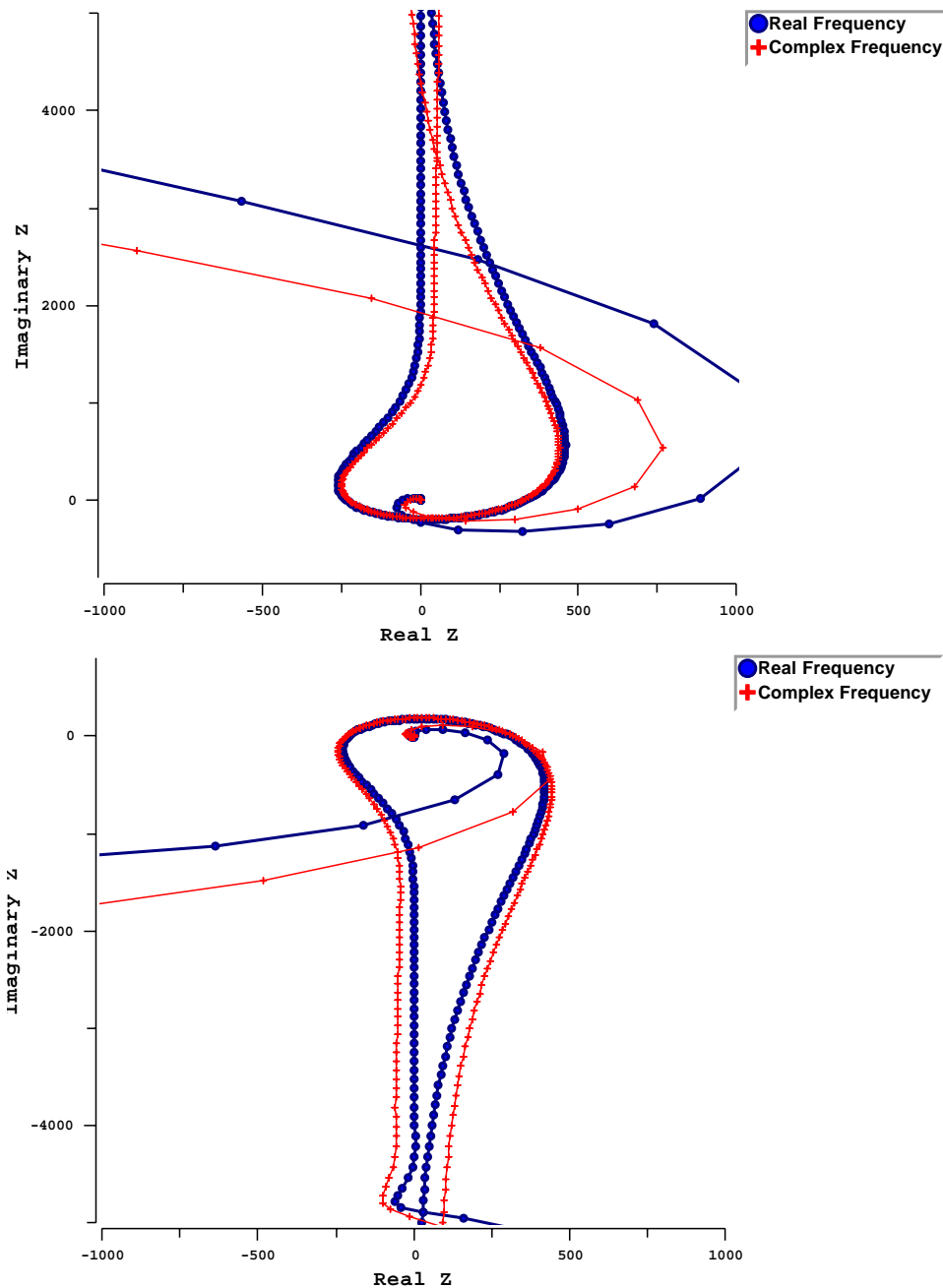


Figure 18.2: (color) Dispersion relation plots in the complex impedance plane. The thick blue curves with circles are for real frequencies and therefore should exhibit the stability boundaries. The red curves with +'s are for complex frequencies. Top plot is below transition and bottom plot is above transition.

parabolic fractional momentum spread of 0.001, interacting with a broadband impedance of $Z_0^{\parallel}/n = 3.00 \Omega$ at the resonance frequency of 600 MHz and quality factor $Q = 1$. This unrealistic small size of ring was chosen because we wanted to limit the number of longitudinal bins around the ring so that not so many macro-particles would be necessary. In the tracking, the bin size had been chosen to be 0.25 m, which was half the wavelength at 600 MHz. With the slip factor fixed at $|\eta| = 0.005$, the beam intensity was adjusted so that the Keil-Schnell circle-approximated criterion [10] gave a stability limit of $|Z_0^{\parallel}/n| = 1.00 \Omega$. All higher-order slip factors were set at zero. The tracking results are shown in Fig. 18.3: the top 4 plots for $\eta = -0.005$ (below transition) and the lower 4 plots for $\eta = +0.005$ (above transition) at 0, 1200, 2400, and 3600 turns. We see that below transition irregularities develop at the low-momentum edge. Ripples corresponding to the frequency of 600 MHz (wavelength = 0.5 m) are clearly seen. The momentum spread broadens at the low-momentum side until the total spread is about 1100 MeV, about 2.75 times the original total spread of about 400 MeV. This is partly because of the energy loss as a result of the resistive part of the impedance. The observation definitely confirms the occurrence of microwave instability below transition, and the eventual self-stabilization by overshooting. Above transition, irregularities also develop at the low-momentum edge and the momentum spread also broadens at the low-momentum edge. The total spread appears to be broader than the situation below transition. In addition, we see small bomb-like droplets launched at the low-momentum side, which are not observed below transition. Instability above transition appears to be more severe than below transition. We will come back to the simulations of coasting beam near transition later in Sec. 18.4.3.

18.4.2 Bunched Beam Simulations

In this section, we study the stability of a bunched beam very close to transition. As an example, take a muon bunch in the proposed 50×50 GeV muon collider, which has a slip factor of $|\eta| = 1 \times 10^{-6}$. Everything we discuss here will apply to a proton bunch also, with the exception that the muons decay while the protons are stable. We will first discuss the situation with the decay of the muons taken into consideration, and later push the lifetime to infinity. We assume that sextupoles and octupoles are installed and adjusted so that the contributions of η_1 and η_2 become insignificant compared with η_0 . The muon bunch we consider has an intensity of $N_b = 4 \times 10^{12}$ particles, rms width $\sigma_\ell = 13$ cm and rms fractional momentum spread $\sigma_\delta = 3 \times 10^{-5}$ or $\sigma_E = 1.5$ MeV.

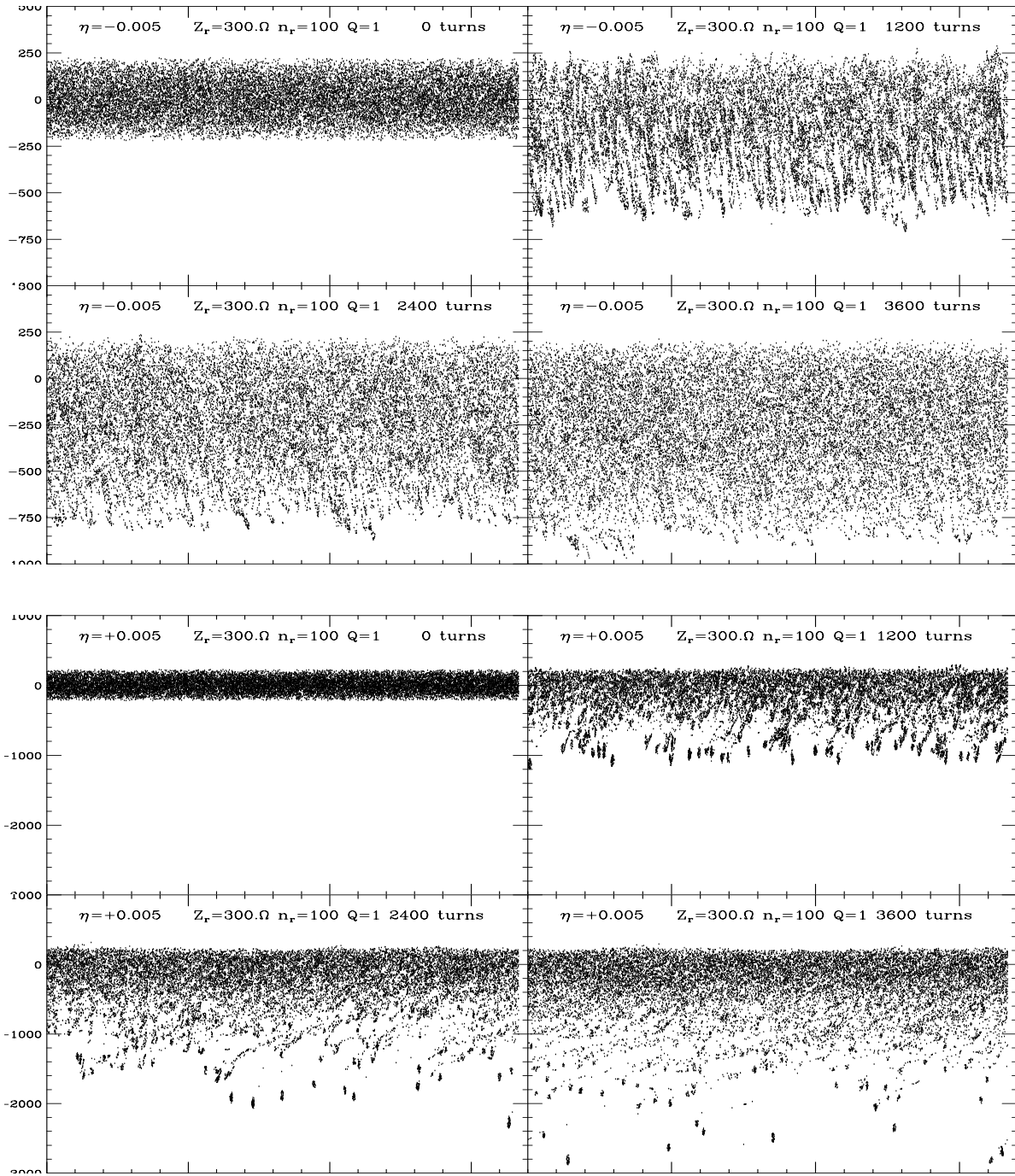


Figure 18.3: The top 4 plots and lower 4 plots are for $\eta = -0.005$ (below transition) and $\eta = +0.005$ (above transition), respectively, at 0, 12000, 24000, and 36000 turns. The impedance is a broadband with $Q = 1$, $Z_0^{\parallel}/n = 3.0 \Omega$ at the resonant frequency of 600 MHz.

The impedance is assumed to be broadband with $Z_0^{\parallel}/n = 0.5 \Omega$ at the angular resonant frequency of $\omega_r = 50$ GHz with quality factor $Q = 1$. The muons have an e -folding lifetime of 891 turns at 50 GeV in this collider ring. During the muon lifetime, there is negligible phase motion. Thus a bunching rf frequency system is not necessary. However, as will be explained below, rf systems are needed for the cancellation of potential-well distortion.

For bunched beams, there is the issue of potential-well distortion which must not be mixed up with the collective microwave instability. Potential-well distortion will change the shape of the bunch to something that looks like the plot of Fig. 18.4, with the difference that the distortion of the beam does not come from the space charge force, but mainly from the inductive part of the broadband impedance.

The wake potential seen by a particle inside a Gaussian bunch at a distance z behind the bunch center is shown in Fig. 18.5 and is given by

$$V(z) = e \int_{-\infty}^z dz' \rho(z') W_0(z - z') = -\frac{eN\omega_r R_{\parallel}}{2Q \cos \phi_0} \operatorname{Re} e^{i\phi_0 - z^2/(2\sigma_{\ell}^2)} w \left[\frac{\sigma_{\ell}\omega_r e^{i\phi_0}}{c\sqrt{2}} - \frac{iz}{\sqrt{2}\sigma_{\ell}} \right], \quad (18.37)$$

where $\rho(z)$ is the bunch distribution, $W_0(z)$ the longitudinal wake function, $\sin \phi_0 = 1/(2Q)$, and w is the complex error function. This distortion can be cancelled up to $\pm 3\sigma_{\ell}$ by 2 rf systems [11], which at injection are at frequencies $\omega_1/(2\pi) = 0.3854$ GHz and $\omega_2/(2\pi) = 0.7966$ GHz, with voltages $V_1 = 65.40$ kV and $V_2 = 24.74$ kV, and phases $\varphi_1 = 177.20^\circ$ and $\varphi_2 = 174.28^\circ$. This compensation is shown in Fig. 18.5. Since only 2 sinusoidal rf's are used, the cancellation is not complete; however, the error is less than 1% of the original wake potential and is considered to be not important. Because of the lifetime of the muons, we first performed tracking for only 1000 turns in the time domain using the broadband wake function $W_0(z)$. The initial and final bunch distributions are shown in Fig. 18.6. During the simulation the compensating rf voltages were lowered turn by turn to conform with the diminishing bunch intensity due to the decay of the muons.

We see from the right plot of Fig. 18.6 that the bunch distribution has been very much distorted after 1000 turns. This comes mostly from the fact that the original distribution of the bunch in the left plot is not exactly Gaussian. It consists of 2×10^6 macro-particles randomly distributed according to a bi-Gaussian distribution. As a result, the wake potential of the actual bunch shown as a red dotted curve in Fig. 18.7 deviates slightly from and wiggles around the ideal wake potential curve of a smooth

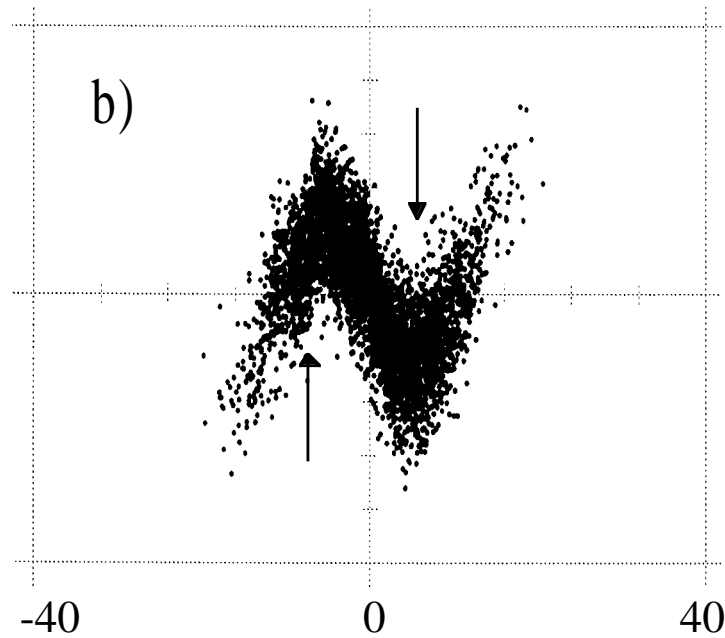


Figure 18.4: Effects of a strong space charge or potential-well distortion force result in a N -shape vertical shear on the bunch.

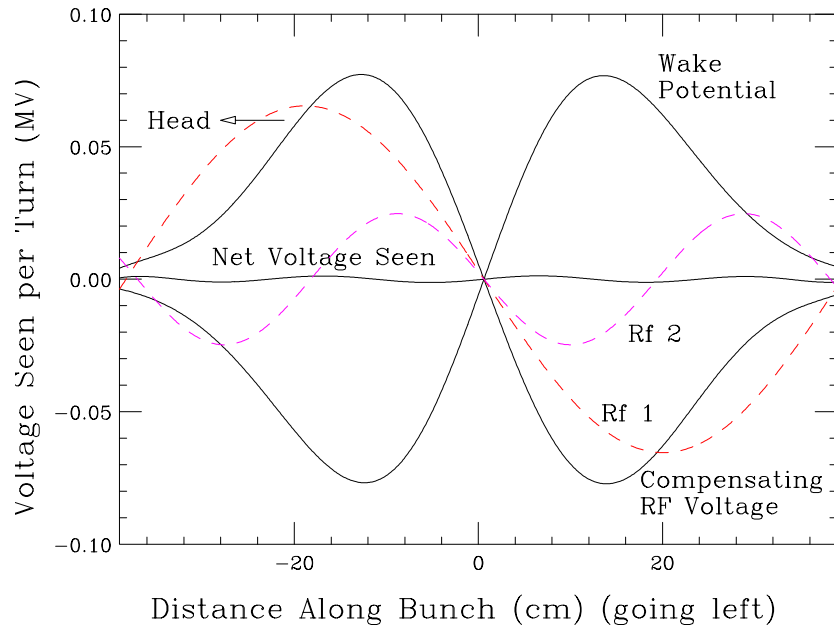


Figure 18.5: (color) Wake potential, compensating rf voltages, and net voltage seen by particles in the 13-cm bunch at injection. The compensating rf is the sum of two rf's represented by dashes.

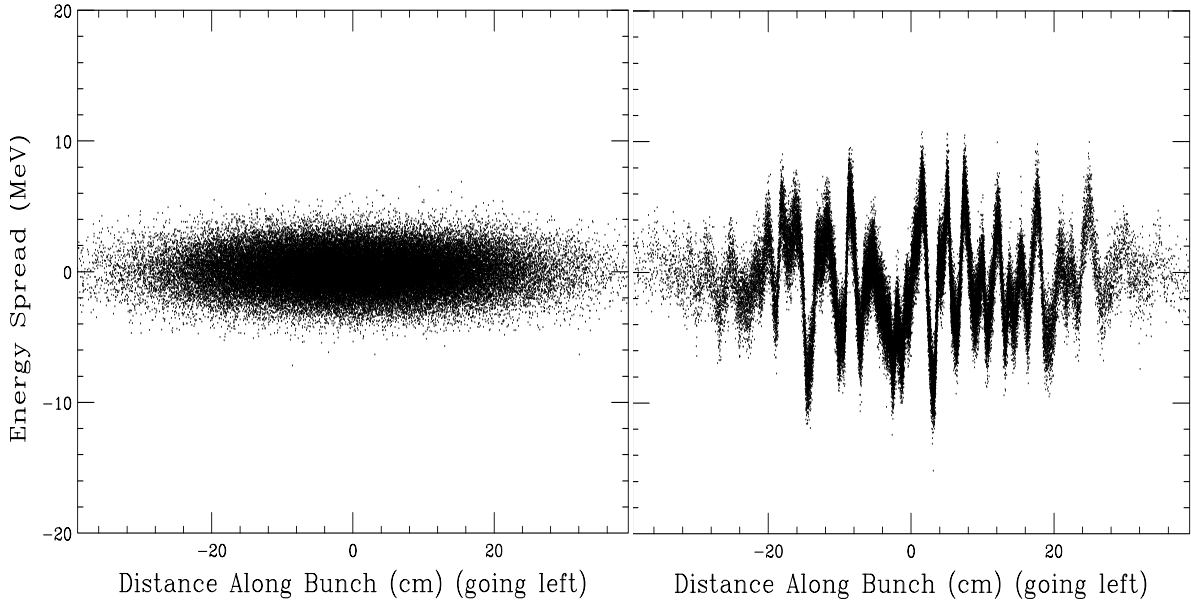


Figure 18.6: Simulation of the 13-cm bunch of 4×10^{12} muons subject to a broadband impedance with quality factor $Q=1$ and $Z_{\parallel}/n=0.5 \Omega$ at the resonant angular frequency $\omega_r = 50$ GHz. The half-triangular bin width is 15 ps (0.45 cm) and 2×10^6 macro-particles are used. Left plot shows initial distribution with $\sigma_E = 1.5$ MeV and $\sigma_\ell = 13$ cm. Right plot shows distribution after 1000 turns with compensating rf's depicted in Fig. 18.5.

Gaussian bunch shown in solid. The difference is the magenta dotted jitter curve in the center of the plot. The fluctuation seen in the right plot of Fig. 18.6 is the result of the accumulation of this dotted jitter curve in 1000 turns with muon decay taken into account. Although this tiny fluctuation leads to a small potential-well distortion in one turn (≤ 0.02 MeV), it is unfortunate that this distortion accumulates turn after turn and will never reach a steady state, since the beam is so close to transition[†]. (For an electron bunch, this growth will stop when it is balanced by radiation damping.) This accumulated distortion can be computed exactly from the the dotted jitter curve. Any growth in excess will come from collective microwave instability. Note that the uncompensated potential-well distortion is quite different from the growth due to microwave instability. For the former, the growth in energy fluctuations every turn will be exactly

[†]More exactly, a steady state will be reached when the momentum offset becomes so large that phase drift due to the small slip factor becomes significant. However, this will not happen in reality because of the finite momentum aperture of the storage ring.

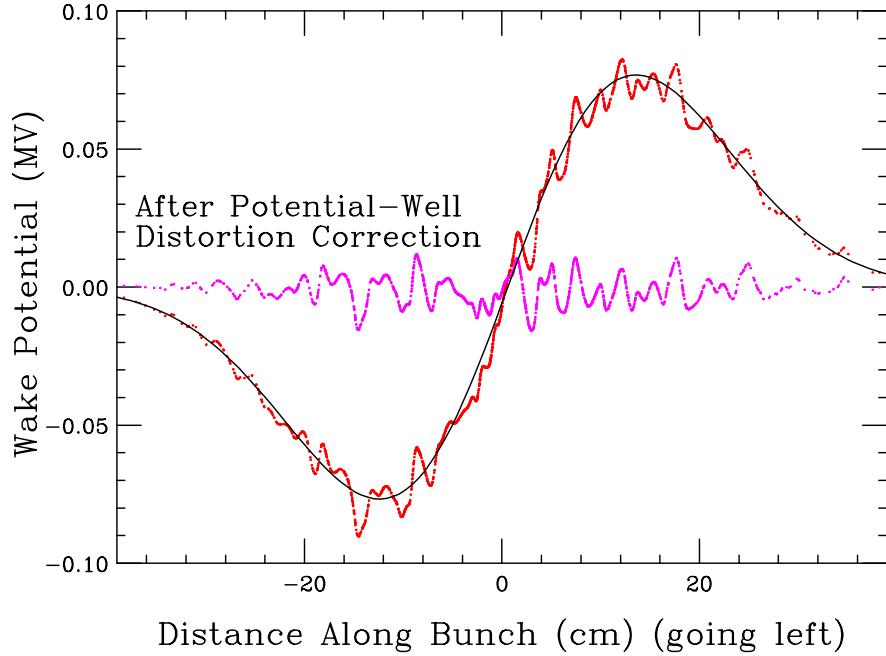


Figure 18.7: (color) Wake potential seen by the simulated bunch shown as red dots is interlaced with the wake potential of an ideal smooth Gaussian bunch shown in solid. The difference (center magenta curve) represents the random fluctuation of the finite number of macro-particles.

by the *same* amount as given by the dotted jitter curve in Fig. 18.7 (if muon decay is neglected). This is because the wake potential of particles along the bunch does not depend on the energy distribution of the bunch, but only on its linear density and the latter is essentially unchanged since the particles do not drift much during the first 1000 turns. On the other hand, the initial growth due to microwave instability at a particular turn is proportional to the actual energy fluctuation at that turn and the evolution of the growth is exponential. Thus, although the growth due to microwave instability is small at the beginning, it will be much faster later on when the accumulated energy fluctuations become larger. It is worth mentioning that even if the wake potential of the initial bunch with statistical fluctuations has been compensated exactly by the rf's, the bunch can still be unstable against microwave instability. An infinitesimal deviation from the bunch distribution can excite the collective modes of instability corresponding to some eigenfrequencies. In other words, the accumulated growth due to potential-well distortion is a static solution and this static solution converges very slowly close to

transition until the momentum spread is large enough for the small $|\eta|$ to smooth the distribution. Microwave instability, on the other hand, is a time dependent solution.

In Fig. 18.8, the 3 plots on the left are for a 4000-turn simulation of the same muon bunch using 2×10^6 macro-particles with the decay of the muons considered. The two compensating rf systems are turned on. The first plot is for $\eta = 0$ so that microwave instability cannot develop. All the fluctuations are due to the residual potential-well distortion or the accumulation of the uncompensated jitters. The second and third plots are for, respectively, $\eta = -1 \times 10^{-6}$ (below transition) and $\eta = +1 \times 10^{-6}$ (above transition). We see that they deviate from the first plot, showing that there are growths due to microwave instability although the effect is small. The 3 plots on the right are the same as on the left with the exception that the muons are considered stable, or, in other words, the particles can be protons. We see that the second and third plots differ from the first one by very much (note the change in energy scale), indicating that microwave instability does play an important role for proton bunches in a quasi-isochronous ring. We also see that microwave instability is more severe above transition than below transition even when the beam is so close to transition. In the simulations, the jitters, or the statistical fluctuation around the smooth distribution might have been very much exaggerated because of the small number of macro-particles included in the tracking. In a realistic beam, these statistical fluctuations should be very much smaller. However, these jitters can also come from other sources, such as electronic noises, rf acceleration, rf maneuvering, etc. These jitters will be very much larger than the Schottky noise. As a result, in the design of a quasi-isochronous ring, the sources of all jitters should be carefully considered in order to estimate the growth in energy offset due to potential-well distortion or microwave instability.

18.4.3 Coasting Beam Simulations

For coasting beams, we do not have the inverted tilted “N”-shape wake potential as in Fig. 18.5. Thus, no rf compensation will be required. However, the noise in the beam does result in a wake potential similar to the small residual wake-potential jitters in Fig. 18.5 after wake-potential compensation. Near transition where the phase motion is negligibly slow, these jitters will add up turn after turn without limit exactly in the same way as the bunched beam after having optimized the rf compensation. Thus, near transition, there is essentially no difference between a coasting beam and a bunched beam after the rf compensation. The only exception is that microwave instability develops

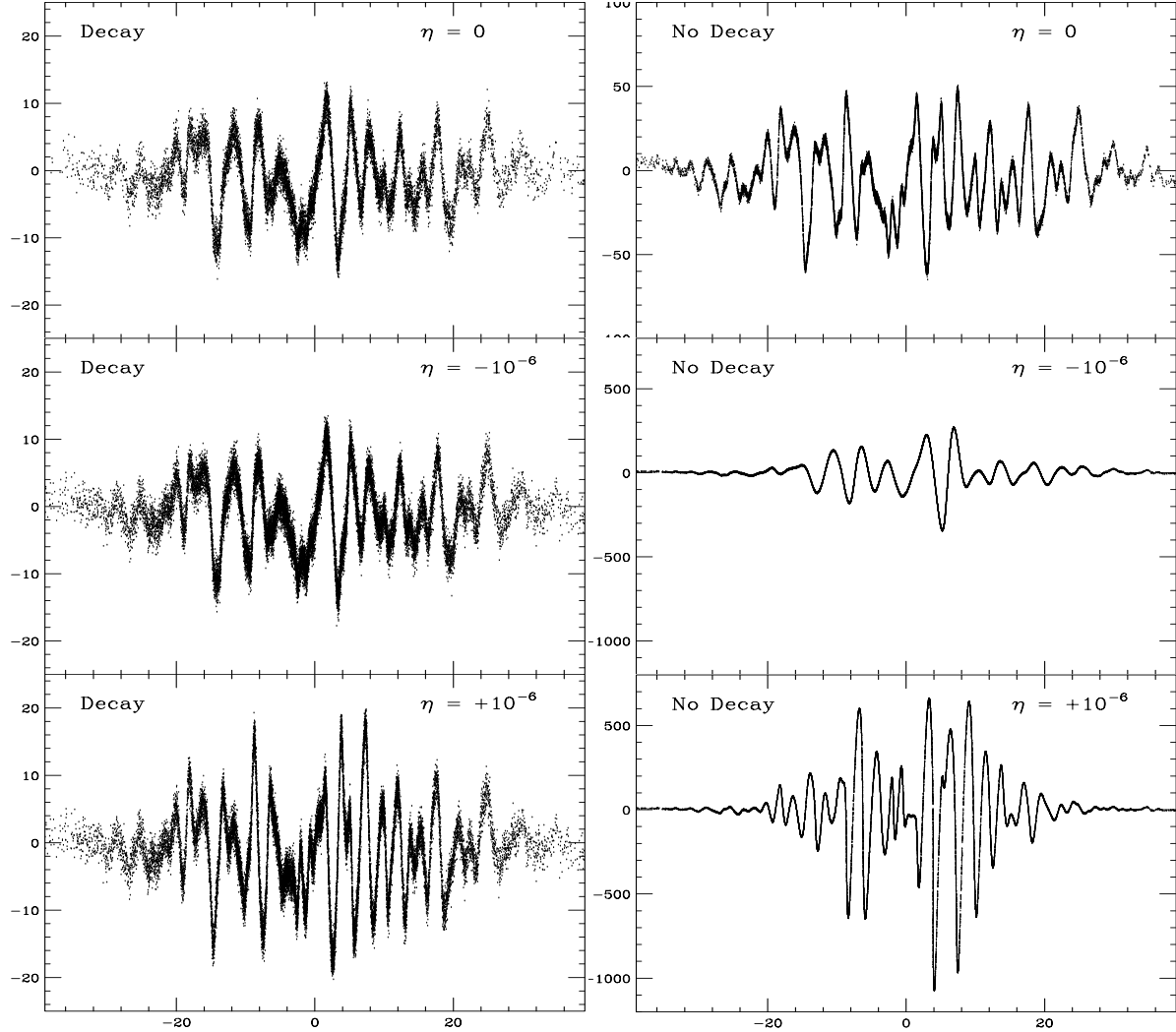


Figure 18.8: Phase-space plots of energy spread in MeV versus distance from bunch center in cm at the end of 4000 turns. All are simulating 4×10^{12} micro-particles with 2×10^6 macro-particles. In the left 3 plots, the decay of the muons has been taken into account. The first left plot is for $\eta = 0$ so that it just gives the amount of potential-well distortion. The second and third plots are for, respectively, $\eta = -1 \times 10^{-6}$ and $+1 \times 10^{-6}$. The small deviations from the first plot are results of microwave instability. The right 3 plots are the same as the left, except that the muons are considered stable. Here, large microwave growths develop (note the change of energy scale).

most rapidly near the center of the bunch where the local intensity is highest, whereas in a coasting beam, microwave instability develops with equal probability along the bunch depending on the statistical fluctuations in the macro-particles.

In Fig. 18.9, we show some coasting beam simulations near transition by having $\eta_0 = 0$ or $\pm 5 \times 10^{-5}$ and $\eta_1 = 0$ or ± 0.05 . The coasting beam consists of 3.27×10^{15} protons (or nondecaying muons) having an average energy of 100 GeV in a hypothetic ring with circumference 50 m. The initial momentum spread is Gaussian with rms fractional spread $\sigma_\delta = 0.001$ or $\sigma_E = 100$ MeV. Thus, at 1σ , the contribution of $|\eta_1| = 0.05$ is the same as the contribution of $|\eta_0| = 5 \times 10^{-5}$. The simulations are performed with 8×10^5 macro-particles in 400 triangular bins. The impedance is a broadband with $Q = 1$ and $Z_0^\parallel/n = 2 \Omega$ at the resonant frequency of $f_r = 300$ MHz.

All the plots in Fig 18.9 are illustrated with the same scale for easy comparison. The horizontal axes are longitudinal beam position from 0 to 166.7 ns, while the vertical axes are energy spread from -4000 to 3000 MeV. Plot (a) shows the initial particle distribution in the longitudinal phase space. All the other plots are simulation results at the end of 54,000 turns. Plot (b) is the result of having $\eta_0 = 0$ and $\eta_1 = 0$. It shows the accumulation of the wake-potential jitters over 54,000 turns. These jitters originate from the statistical fluctuation of the initial population of the macro-particles. Therefore, any deviation from Plot (b) implies microwave instability. Plots (c) and (d) are with $\eta_0 = 0$, but with $\eta_1 = +0.05$ and -0.05 , respectively. We see the growths curl towards opposite phase directions nonlinearly as expected. This is due to the nonlinearity in δ of the time slip given by Eq. (18.16), similar to the simulations in Fig. 18.4(a). It appears that Plot (c) with $\eta_1 = -0.05$ gives a larger growth. Plots (e), (g), and (i) are for $\eta_0 = -5 \times 10^{-5}$ (below transition), but with $\eta_1 = +0.05$, -0.05 , and 0 , respectively. We see that the microwave instability is most severe when $\eta_1 = 0$, indicating that η_1 has the ability to curb instability. This is, in fact, easy to understand. The phase drift driven by $|\eta_1| = 0.05$ is much faster than that driven by $|\eta_0| = 5.0 \times 10^{-5}$ at larger momentum spread; for example, it will be 4 times faster at $2\sigma_\delta$, 9 times faster at $3\sigma_\delta$, etc. As a result, a nonvanishing $|\eta_1|$ tends to move particles away from the clumps, thus lessening the growth due to microwave instability.

Plots (f), (h), and (j) are for $\eta_0 = +5 \times 10^{-5}$ (above transition), but with $\eta_1 = +0.05$, -0.05 , and 0 , respectively. Again microwave instability is most severe when $\eta_1 = 0$, and η_1 does curb instability to a certain extent. Comparing Plots (e), (g), and (i) with Plots (f), (h), and (j), it is evident that the beam is more unstable against microwave

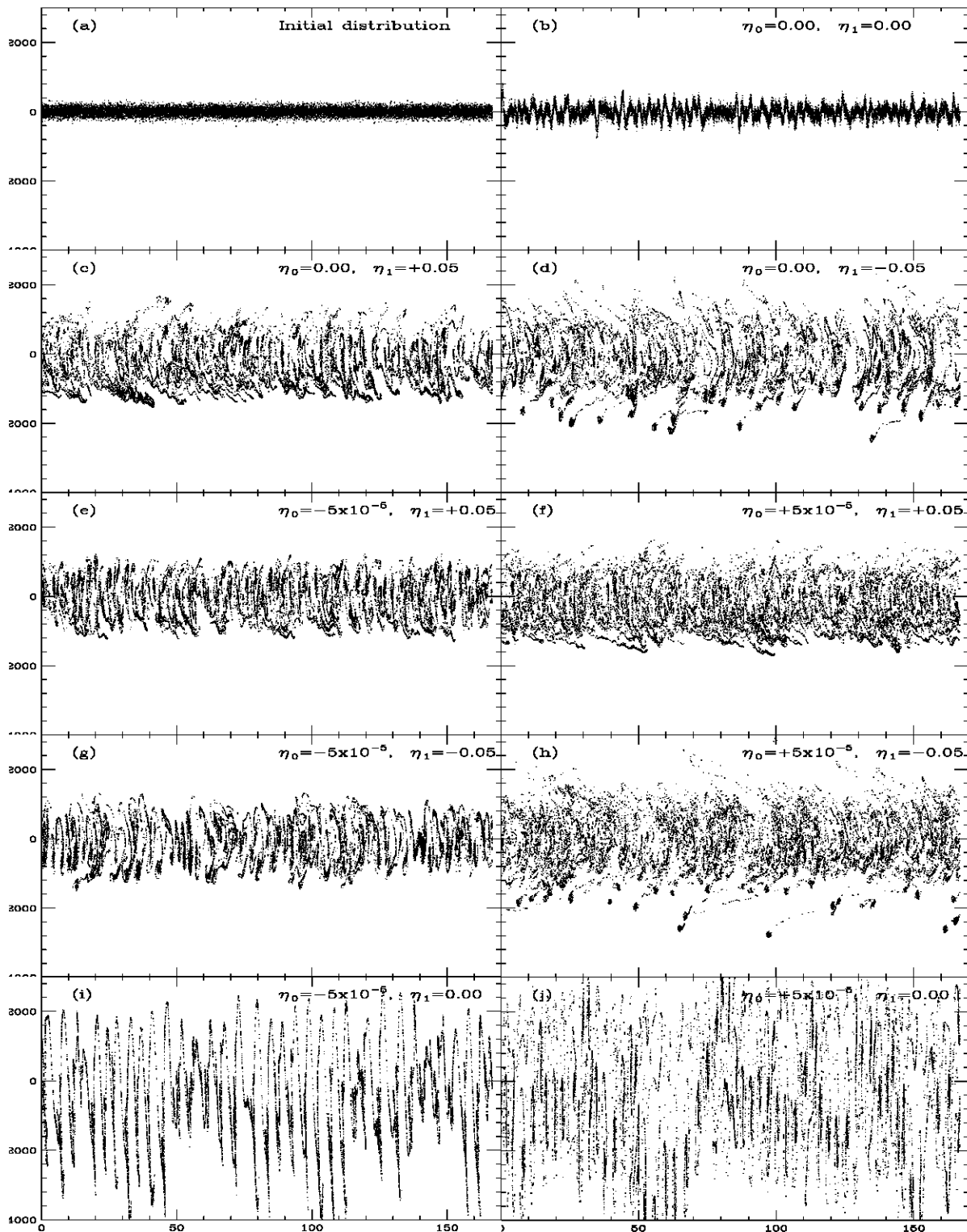


Figure 18.9: Energy spread (MeV) versus bunch position (ns) of coasting beam simulations. See text for explanation.

instability above transition ($\eta_0 > 0$) than below transition ($\eta_0 < 0$) independent of the sign of η_1 . For a fixed η_0 , we also notice that negative η_1 is more unstable than positive η_1 . The theoretical implications of these results are nontrivial and will be discussed in a future publication.

Now let us come back to the analytic investigations by Bogacz, Holt, and Colestock. Their results appear to contradict the simulations presented here. Analytic analysis often starts with the Vlasov equation. The time-dependent beam distribution $\psi(\phi, \Delta E; t)$ can be separated into two parts:

$$\psi(\phi, \Delta E; t) = \psi_0(\phi, \Delta E) + \psi_1(\phi, \Delta E) e^{-i\Omega t}. \quad (18.38)$$

Here, ψ_0 is the *steady-state* solution of the Hamiltonian and ψ_1 describes the collective motion of the beam with the collective frequency $\Omega/(2\pi)$. After linearization, the Vlasov equation becomes an eigenequation with ψ_1 as the eigenfunction and $\Omega/(2\pi)$ the eigenfrequency. The equation also depends on ψ_0 . Thus we must solve for the *steady-state* solution first before solving the eigenequation. The steady-state solution is the time-independent solution of the Hamiltonian which includes the contribution of the wake function. In other words, ψ_0 is the potential-well-distorted solution. Far away from transition, this distortion is mostly in the ϕ coordinate, for example, that brought about by the space charge or inductive forces. Therefore, for a coasting beam, there will not be any potential-well distortion at all. The situation, however, is quite different close to transition. As was pointed out in above, the potential-well distortion is now in the ΔE coordinate. For this reason, not only bunched beams, even coasting beams will suffer from potential-well distortion as a result of the nonuniformity of the beam. In simulations, the nonuniformity arrives from the statistical fluctuation of the distribution of the macro-particles. This nonuniformity will accumulate turn by turn until the momentum spread is so large that the small $|\eta|$ is able to smooth out all nonuniformity. In other words, the steady-state distribution ψ_0 that goes into the Vlasov equation will be completely different from the original distribution in the absence of the wake. In the analysis of Bogacz, Holt, and Colestock, the ideal smooth Gaussian distribution in energy was substituted for ψ_0 in the Vlasov equation. However, this is a very unstable static distribution; even a small perturbation will accumulate turn by turn with extremely slow convergence. For this reason, it is hard to understand what their results really represent.

18.5 Exercises

- 18.1. (1) Derive Eqs. (18.14) and (18.15), the expansions of the revolution period T and velocity β as powers of the momentum offset δ .
 (2) Derive Eq. (18.20), the expansion of the slippage factor.
- 18.2. Figure 18.1 indicates that there are two series of pendulum-like longitudinal buckets unless it is very close to the transition energy. Explain why we see only one series under most condition. Use the Fermilab Main Injector as an example. The Main Injector has a $\gamma_t = 21.8$ (20.45 GeV) and $\alpha_1 = 0.50$. Compute the distance between the two series of buckets in fractional momentum spread when it is in a coasting mode at the injection energy of 8 GeV and at 18.5 GeV.
- 18.3. For a proton storage ring with $\gamma_t = 21.8$ and $\alpha_1 = 0.50$. The rf voltage is 2.5 MV and the synchrotron phase is 0° . Compute the energy at which the two series of longitudinal buckets merge.
- 18.4. Keeping up to η_1 , for the α -like bucket,
 (1) derive the relation between width and height of the bucket [Eq. (18.25)],
 (2) derive the bucket area [Eq. (18.27)],
 (3) derive Eq. (18.29), the universal relation between width and height of a bunch fit to the bucket.
- 18.5. Derive the synchrotron tune of a η_2 -dominated bucket starting from the Hamiltonian of Eq. (18.31).
 Answer: $\nu_s = \nu_{s0}F$, where F is given by Eq. (18.34)

Bibliography

- [1] D.A. Edwards and M.J. Syphers, *An Introduction to the Physics of High Energy Accelerators*, Wiley and Sons, 1993.
- [2] See for example, E.D. Courant, R. Ruth, W. Weng, L. Michelotti, D. Neuffer, and L. Teng, AIP Conf. Proc. No. 87, 36 (1982).
- [3] A. Riabko, M. Bai, B. Brabson, C.M. Chu, X. Kang, D. Jeon, S.Y. Lee, and X. Zhao, Phys. Rev. **E54**, 815 (1996).
- [4] D. Boussard and T. Linnecar, Proc. 2nd European Particle Accelerator Conference, Nice, June 990, Ed. P. Martin and P. Mandrillon, p. 1560.
- [5] K.Y. Ng, Nucl. Instrum. Method **A404**, 199 (1998).
- [6] D. Robin, H. Hama, and A. Nadji, *Experimental Results on Low Alpha Electron-Storage Rings*, Proc. Micro Bunches Workshop, Upton, NY, Sep. 28-30, 1995, Ed. E.B. Blum, M. Dienes, and J.B. Murphy, (AIP Conf. Proc. 367), p. 150; D. Robin, R. Alvis, A. Jackson, R. Holtzapple, and B. Podobedov, *Low Alpha Experiments at the ALS*, *ibid* p. 181.
- [7] H. Hama, S. Takano, and G. Isoyama, Nucl. Inst. Meth. **A329**, 29 (1993).
- [8] A.S. Bogacz, *Microwave Instability at Transition—Stability Diagram Approach*, *Proceedings of IEEE Particle Accelerator Conference*, p.1815 (San Francisco, CA, 1991).
- [9] J.A. Holt, and P.I. Colestock, *Microwave Instability at Transition*, *Proceedings of IEEE Particle Accelerator Conference*, p.3067 (Dallas, TX, 1995).
- [10] E. Keil and W. Schnell, CERN Report TH-RF/69-48, 1969.

- [11] E.-S. Kim, A.M. Sessler, and J.S. Wurtele, *Phys. Rev. ST Accel. Beams*, **2**, 051001 (1999).
- [12] K.Y. Ng, *Phys. Rev. ST Accel. Beams*, **2**, 091001 (1999).

Chapter 19

TWO-STREAM INSTABILITY

19.1 Introduction

An intense particle beam forms a potential well for oppositely charged particles and will therefore trap particles of the opposite charge. These trapped particles can often accumulate to such an extent that they provide a potential well for particles of the original beam. Thus, the secondary beam can oscillate transversely in the potential well of the primary beam and the primary beam can oscillate transversely in the potential well of the secondary beam. This coupled-beam oscillation may grow in amplitude and lead to beam loss eventually. This is called *two-stream instability*. One way to eliminate the accumulation of particles of opposite charge is to leave a gap in the primary beam so that the secondary particles can be cleared. However, sometimes the accumulation of secondary particles produced by one single passage of the primary beam can be so intense that instability develops even before the clearing gap is reached.

19.2 Trapped Electrons

Proton beam trapping electrons was first observed in the Bevatron [1] and later in the CERN Intersecting Storage Ring (ISR) [2]. The ISR was a collider with an intense coasting proton beam in each of the intersecting vacuum chambers. It had been observed that electrons were trapped in the potential of the proton beams with oscillation frequency

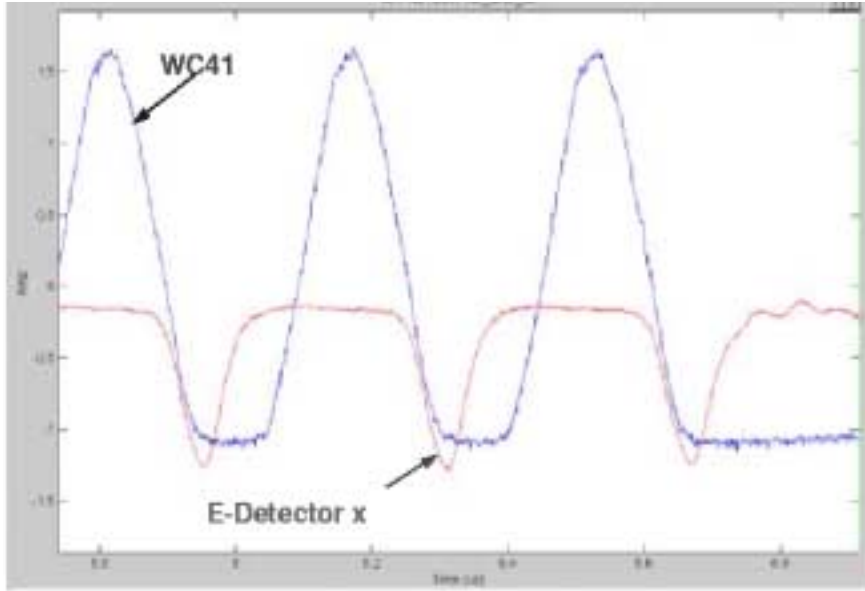


Figure 19.1: (color) Turn-by-turn electron signals are shown in relation to the proton beam pulse at PSR. Electrons start to appear at the back end of the beam pulse and are cleared in the bunch gap.

around 100 MHz. The instability was intermittent. It stopped when the electrons, driven to large amplitudes, were shaken out to the walls, or out of resonance with the protons. It restarted when a sufficient number of new electrons had been accumulated. Slow beam blowup and background problems were the result.

The Proton Storage Ring (PSR) at Los Alamos (LANL) running with $2.3 \text{ to } 4.2 \times 10^{13}$ protons has always been troubled by the electrons trapped inside the proton beam [3].

A turn-by-turn picture of the electron signal in relation to the circulating proton beam pulse at the end of a 500 ms store is shown in Fig. 19.1. The proton beam has a full width of about 240 ns. The timing between electrons and proton beam is good to a few ns. The electron detector was designed and built at Argonne National Laboratory (ANL). It has a repeller grid, so that it can decouple the electron energy analysis from collection. The repeller voltage of 5 volts means that the electrons have to have a kinetic energy above 5 eV in order to get through to the collector. Electrons start to appear after the peak of the beam pulse has passed and the peak of the electrons appears at the end of the beam pulse. Higher repeller voltage shows a smaller, and narrower pulse. The electron flux hitting the wall is sizeable, about 25 mA/cm^2 at the peak or about $2 \text{ pC/cm}^2/\text{pulse}$ or $60 \text{ pC/cm}/\text{pulse}$ integrated over the circumference of the beam pipe.

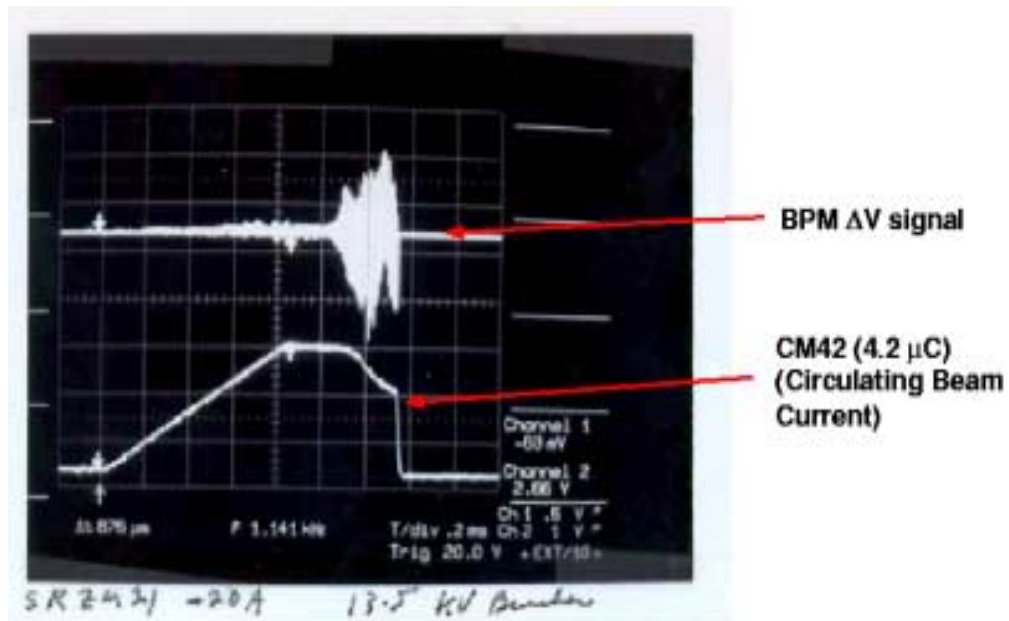


Figure 19.2: (color) Top trace: vertical difference signals of the beam reveal a growing instability about $300 \mu s$ after the end of injection. Lower trace: sum signals of the beam showing beam loss as the instability grows.

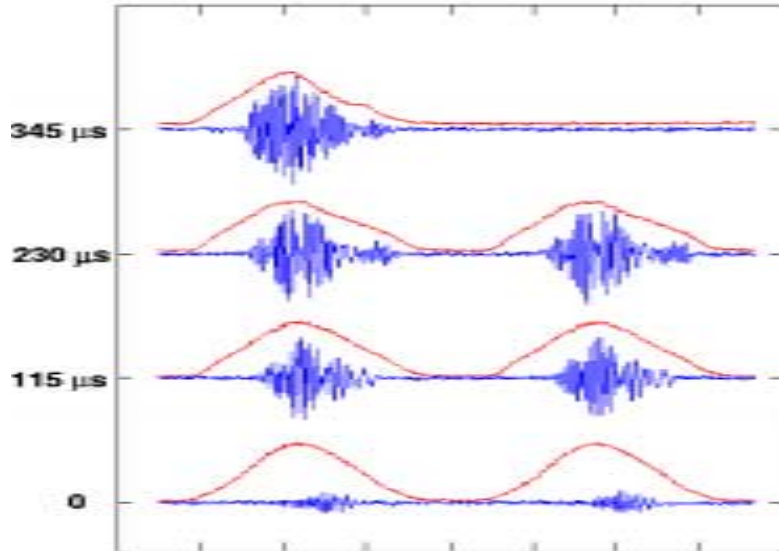


Figure 19.3: (color) Turn-by-turn vertical difference signals from a short stripline beam-position monitor at the final $300 \mu s$ of the store show a vertical instability starting at the back end of the bunch and spreading into the whole bunch with increasing amplitude. The bunch sum profiles from a wall current monitor are also shown revealing a beam loss as the instability develops.

It is interesting to compare this with the 420 pC/cm average line density of the proton beam. Unfortunately, one cannot deduce from this one picture alone how much electron multi-pactoring is occurring on the backside of the beam pulse without additional data and assumptions.

An instability is clearly seen in Fig. 19.2 when beam is stored for about 300 microseconds after the end of injection. A rapidly growing vertical difference signal (top trace) can be seen shortly before beam loss occurs (lower trace), indicating beam centroid oscillations. In Fig. 19.3, the growth of the instability can be seen turn by turn at the final $\sim 300 \mu\text{s}$ of the store. Here the vertical difference signal is compared to the wall current monitor trace. The beam transverse instability starts on the backside of the pulse and broadens out as it grows in strength. Some beam loss is evident at the last turn before extraction.

The Brookhaven booster running in the coasting beam mode suffers sudden beam loss due to a vertical instability [4], which cannot be identified with any reasonable amount of transverse impedance. This has been considered to be the result of two-stream instability between the proton beam and the electrons it traps.

The Fermilab antiproton ring traps positive ions and limits the intensity of the storage [5]. The newly built Advanced Photon Source (APS) at ANL is a synchrotron light source using a positron beam. It has been observed that electrons are trapped causing instability [6].

19.2.1 Single-Electron Mechanics

Coupled-centroid oscillation of the proton beam and the trapped electron beam will occur only when the amount of electrons becomes very intense. Therefore, to prevent such instability, we would like the electrons in the vacuum chamber not to accumulate. The electrons inside the vacuum chamber are supposed not to move longitudinally. As the proton bunch passes through them, they are attracted towards the central axis of the proton bunch with vertical electron *bounce frequency* $\Omega_e/(2\pi)$ given by [12]

$$\Omega_e^2 = \frac{4N_p r_e c^2}{a_v(a_v + a_H)L_b} . \quad (19.1)$$

Here, N_p is the number of protons in the bunch which has an elliptical cross section with vertical and horizontal radii a_v and a_H , L_b is the full bunch length, and r_e the

electron classical radius. In our derivation, we assume that the proton beam has uniform longitudinal and transverse distributions and has a cylindrical cross section with radius a inside a cylindrical beam pipe of radius b . Thus $a_V(a_V + a_H)$ can be replaced by $2a^2$. The images of the proton beam and the electron cloud in the walls of the vacuum chamber will modify the electron bounce frequency depicted in Eq. (19.1), but their effects are neglected in this study. Only linear focusing force acting on the electrons by the proton beam will be considered. The bounce frequency in Eq. (19.1) can be derived exactly as the space charge self-force tune shift in Chapter 4. In Eq. (4.24), for example, we make the replacement $2\nu_0^{V,H}\Delta\nu_0^{V,H}\omega_0^2 \rightarrow \Omega_e^2$ and $2a^2 \rightarrow a_V(a_V + a_H)$. We delete one factor of γ from the denominator because the trapped electrons are assumed to have no longitudinal motion. We delete the other factor of γ^2 from the denominator because the trapped electrons, having no longitudinal velocity, do not interact with the magnetic field of the proton beam.

An electron trapped inside the proton beam performs betatron oscillations with an equivalent betatron function* $\beta_b = \beta c / \Omega_e$ with a total betatron phase advance $\phi_b = \Omega_e L_b / v$, where βc is the velocity of the protons. After the passage of the proton bunch, the motion of the electron in the gap is equivalent to a drift of length $L_g = \lambda_{\text{rf}} - L_b$ with λ_{rf} being the rf wavelength or width of the stationary bucket. Here, we assume all rf buckets are filled. The transfer matrix for an rf wavelength is [7]

$$M = \begin{pmatrix} 1 & L_g \\ 0 & 1 \end{pmatrix} \begin{pmatrix} \cos \phi_b & \beta_b \sin \phi_b \\ -\frac{1}{\beta_b} \sin \phi_b & \cos \phi_b \end{pmatrix} = \begin{pmatrix} \cos \phi_b - \frac{L_g}{\beta_b} \sin \phi_b & \beta_b \sin \phi_b + L_g \cos \phi_b \\ -\frac{1}{\beta_b} \sin \phi_b & \cos \phi_b \end{pmatrix}. \quad (19.2)$$

In order that the electron will not be trapped inside the proton bunch, its motion has to be unstable or

$$\frac{1}{2} |\text{Tr} M| = \left| \cos \phi_b - \frac{L_g}{2\beta_b} \sin \phi_b \right| > 1. \quad (19.3)$$

If the electron is unstable, we can write

$$\frac{1}{2} |\text{Tr} M| = \cosh \mu, \quad (19.4)$$

where μ^{-1} is the growth of the electron oscillation amplitude in one rf bucket, and the growth rate is $\mu \beta c / \lambda_{\text{rf}}$. Here, we study the effect of trapped electrons in three

*The electron bounce tune is $Q_e \Omega_e / \omega_0$ and the equivalent betatron function is $\beta_b = R / Q_e$, where R is the mean radius of the accelerator ring.

synchrotron rings: the storage ring of the Spallation Neutron Source (SNS) to be built at Oak Ridge National Laboratory (ORNL), the Los Alamos PSR, and the booster at Brookhaven (BNL). Some information of the three rings are listed in Table 19.1.

Table 19.1: Some data of the Oak Ridge SNS, the Los Alamos PSR, and the Brookhaven booster at injection.

	Oak Ridge SNS	Los Alamos PSR	Brookhaven Booster
Circumference C (m)	220.6880	90.2000	201.769
Injection kinetic energy (GeV)	1.000	0.797	0.200
γ	2.0658	1.8494	1.2132
β	0.8750	0.8412	0.5662
Revolution frequency f_0 (MHz)	1.1887	2.7959	0.8412
Revolution period T_0 (ns)	841.3	357.7	1189
Total number of protons N_p	2.1×10^{14}	4.2×10^{13}	2.4×10^{13}
Rf harmonic (no. of bunches) h	1	1	1
Number of injection turns	1225	2000	300
Repetition rate (Hz)	60	12	7.5

Equation (19.3) appears to be a simple criterion. In fact, it is much more complex in application, because the electron bounce frequency turns out to be usually very high. Take for example the PSR, we find $\Omega_e = 1.254$ GHz, which gives an equivalent betatron function $\beta_b = \beta c / \Omega_e = 0.201$ m. With the gap length 30.07 m, $L_g / \beta_b = 150$. Although Ω_e is not sensitive to L_g / β_b , it is very sensitive to the phase $\phi_b = \Omega_e L_g / v \approx 299$ rad and therefore to $\sin \phi_b$ and $\cos \phi_b$. Thus, a very slight change in the number of protons in the beam will alter the electron bounce frequency, the betatron phase, and give rise to a large change in the trace. Since the electron bounce frequency usually has a large spread, it is more reasonable to consider the rms value of the trace instead.

The results of $\frac{1}{2}|\text{Tr}M|$ are listed in Table 19.2. We see that for all the 3 rings, the electrons trapped should be able to escape to the walls of the beam pipe in the beam gap. In fact, with such high electron bounce frequency, L_g / β_b will be large and it will not be easy to trap electrons if the gap is clean. When the intensity of the proton beam is raised, the electron bounce frequency will increase, making the electrons easier to escape at the gap.

Table 19.2: Instability and escape time through the bunch gap of a single electron trapped inside the proton bunches of the ORNL SNS, LANL PSR, and BNL booster.

	Oak Ridge SNS	Los Alamos PSR	Brookhaven Booster
Injection full bunch length (m)	143.39	60.13	100.89
Gap length (m)	77.30	30.07	100.89
Proton beam radius a (m)	0.0380	0.0150	0.0150
Bounce angular frequency Ω_e (MHz)	713.3	1253.9	462.6
Bounce betatron phase ϕ_b (rad)	309.9	299.0	435.2
$\frac{1}{2} \text{Tr}M $ (rms)	52.55	37.38	108.8
Escape time in no. of rf buckets	0.2148	0.2318	0.1858

Sometimes, the gap is not totally free of protons. The space charge effect of the protons will distort the rf bucket reducing its momentum acceptance. As a result, some protons may leak out of the bucket and end up in the bunch gap. If a fraction η of the protons leaks into the gap, the electron will oscillate with bounce frequency $\Omega_{eb}/(2\pi)$ inside the proton beam and bounce frequency $\Omega_{eg}/(2\pi)$ in the bunch gap. These frequencies are given by [7, 10]

$$\Omega_{eb}^2 = \Omega_e^2(1 - \eta) \quad \text{and} \quad \Omega_{eg}^2 = \Omega_e^2\eta \frac{L_b}{L_g}. \quad (19.5)$$

Again, only linear focusing force by the proton beam is considered. The betatron phase advances in the beam and in the gap are, respectively, $\phi_b = \Omega_{eb}L_b/(\beta c)$ and $\phi_g = \Omega_{eb}L_g/(\beta c)$. The transfer matrix is therefore

$$M = \begin{pmatrix} \cos \phi_g & \beta_g \sin \phi_g \\ -\frac{1}{\beta_g} \sin \phi_g & \cos \phi_g \end{pmatrix} \begin{pmatrix} \cos \phi_b & \beta_b \sin \phi_b \\ -\frac{1}{\beta_b} \sin \phi_b & \cos \phi_b \end{pmatrix}$$

$$= \begin{pmatrix} \cos \phi_g \cos \phi_b - \frac{\beta_g}{\beta_b} \sin \phi_g \sin \phi_b & \beta_b \cos \phi_g \sin \phi_b + \beta_g \cos \phi_b \sin \phi_g \\ -\frac{1}{\beta_g} \cos \phi_b \sin \phi_g - \frac{1}{\beta_b} \cos \phi_g \sin \phi_b & -\frac{\beta_b}{\beta_g} \sin \phi_b \sin \phi_g + \cos \phi_g \cos \phi_b \end{pmatrix}, \quad (19.6)$$

where the equivalent betatron functions in the bunch and in the gap are, respectively,

$$\beta_b = \frac{\beta c}{\Omega_{eb}} \quad \text{and} \quad \beta_g = \frac{\beta c}{\Omega_{eg}}. \quad (19.7)$$

The condition for the electrons to escape is therefore

$$\frac{1}{2}|\text{Tr}M| = \left| \cos \phi_g \cos \phi_b - \frac{1}{2} \left(\frac{\Omega_{eb}}{\Omega_{eg}} + \frac{\Omega_{eg}}{\Omega_{eb}} \right) \sin \phi_g \sin \phi_b \right| > 1 . \quad (19.8)$$

It is easy to demonstrate that Eq. (19.8) reduces to Eq. (19.3) when $\eta \rightarrow 0$.

Figure 19.4 show $\frac{1}{2}\text{Tr}M$ as a function of the fractional proton leakage η into the gap, respectively, for the ORNL SNS, LANL PSR, and BNL booster. The plots for the ORNL SNS and LANL PSR are very similar; $\frac{1}{2}\text{Tr}M$ oscillates rapidly with the fractional leakage and becomes bounded by ± 1 or electrons will be trapped when $\eta \lesssim 0.05$. The situation for the BNL booster is different. Even up to $\eta = 0.20$, the oscillation of $\frac{1}{2}\text{Tr}M$ still has an amplitude larger than 1. This is mainly due to the fact of a larger gap-to-bunch-length ratio in the BNL booster. Thus, we may conclude that electrons are not so easily trapped in BNL booster as in the ORNL SNS and LANL PSR when protons are spilled into the bunch gaps. We also try to vary the electron bounce frequency in each case and find that the results remain relatively the same. The only changes in the plots are faster oscillations when the bounce frequency is increased.

19.2.2 Centroid-Oscillation Instability

Consider coupled oscillation of the proton beam and the electron ‘beam’ in the vertical direction. The displacements of a proton and electron from the central axis of the vacuum chamber are denoted, respectively, by y_p and y_e . Here, we assume both the proton and electron beams are coasting beams having the same transverse sizes and uniform distribution longitudinally and transversely. The coupled equations of motion are [12, 7, 4, 14]

$$\left(\frac{\partial}{\partial t} + \omega_0 \frac{\partial}{\partial \theta} \right)^2 y_p + Q_\beta^2 \omega_0^2 y_p = -Q_p^2 \omega_0^2 (y_p - \bar{y}_e) + Q_{ps}^2 \omega_0^2 (y_p - \bar{y}_p) , \quad (19.9)$$

$$\frac{d^2 y_e}{dt^2} = -Q_e^2 \omega_0^2 (y_e - \bar{y}_p) + Q_{es}^2 \omega_0^2 (y_e - \bar{y}_e) , \quad (19.10)$$

where \bar{y}_p and \bar{y}_e are the vertical displacements of the centroids of, respectively, the proton and electron beams from the axis of the vacuum chamber, ω_0 is the angular revolution frequency, θ is the azimuthal angle around the ring, Q_β is the betatron tune, and Q_p and Q_e are, respectively, the oscillation tune of the electrons inside the proton beam and

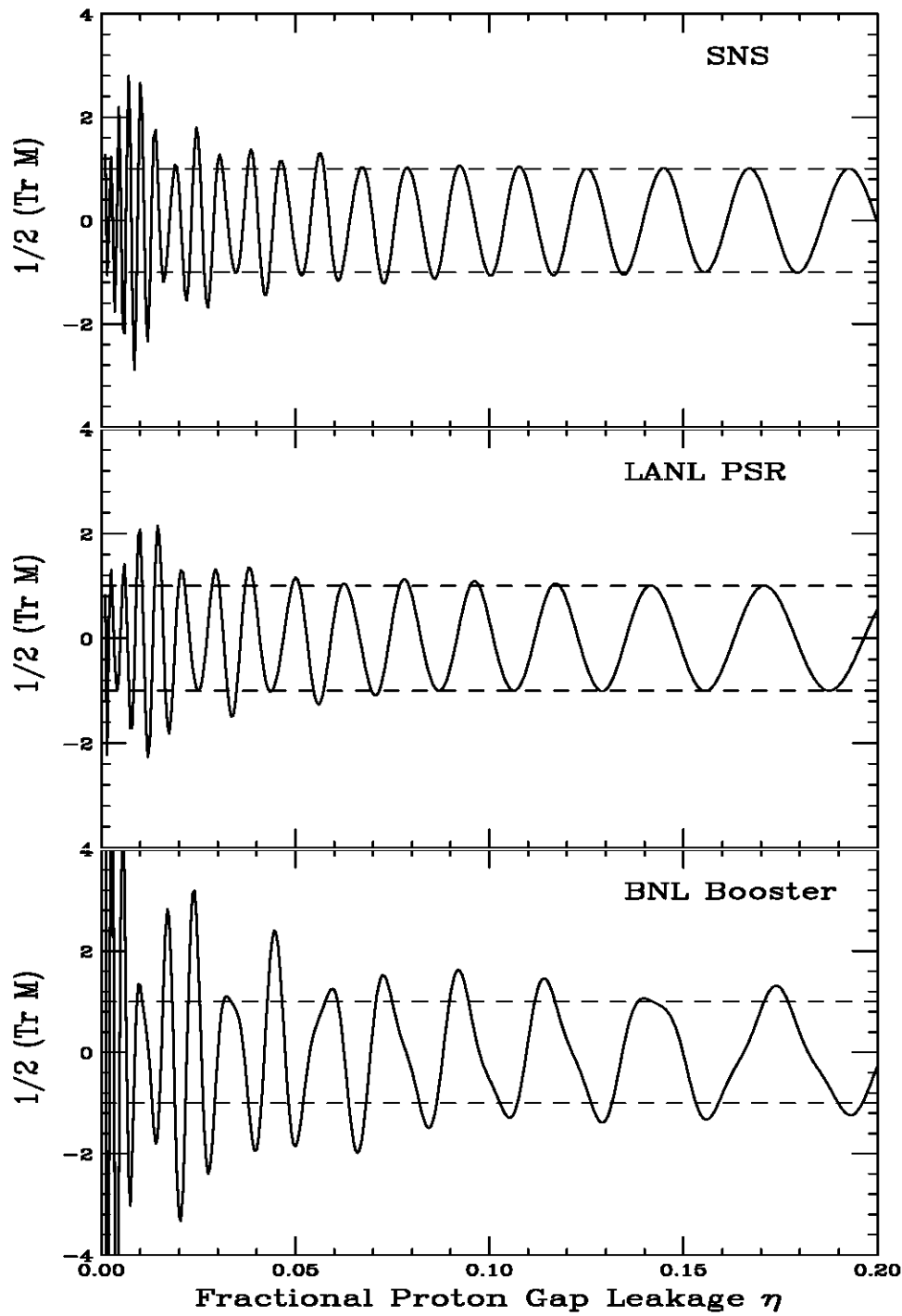


Figure 19.4: The ORNL SNS: Electrons will be trapped if $\frac{1}{2}\text{Tr}M$ falls between the ± 1 dashed lines. The 3 plots are, from top down, for the ORNL SNS, LANL PSR, and BNL booster.

the oscillation tune of the protons inside the electron beam. We have

$$\Omega_e^2 = (Q_e \omega_0)^2 = \frac{4N_p r_e c^2}{a_v(a_H + a_V)C}, \quad (19.11)$$

$$\Omega_p^2 = (Q_p \omega_0)^2 = \frac{4N_p r_p c^2 \chi_e}{a_v(a_H + a_V)\gamma C}, \quad (19.12)$$

where χ_e is the neutralization factor, or the ratio of the electron distribution to the proton distribution. In above, r_p is the classical proton radius, r_e the classical electron radius, and C the circumference of the accelerator ring. The negative signs on first terms on the right hand sides of Eqs. (19.9) and (19.10) indicate that the protons are focused by the electron beam and the electrons are focused by the proton beam. The factor γ in the denominator of Ω_p^2 comes about because the protons are circulating around the ring while the electrons do not. Notice that there are no magnetic force contributions. For Ω_e , the electron has no velocity although it sees a magnetic field from the proton beam. For Ω_p , the proton, although at a high velocity, does not see a magnetic field in the stationary electron beam. Again, we are considering uniformly and cylindrically-symmetrically distributed proton and electron beams of radius a ; or $a_v(a_H + a_V) \rightarrow 2a^2$. Image effects in the walls of the vacuum chamber as well as nonlinear focusing forces are neglected.

The last term in the proton equation denotes the oscillations of the proton under the self-field of the proton beam. Here,

$$(Q_{ps} \omega_0)^2 = \frac{4N_p r_p c^2}{a_v(a_H + a_V)\gamma^3 C} \quad (19.13)$$

is proportional to the linear space charge tune shift of the proton beam. Similarly the last term in the electron equation, with

$$Q_{es}^2 = Q_e^2 \chi_e \quad (19.14)$$

denoting the space charge tune shift of the electron beam, depicts the corresponding oscillations of the electron in the self-field of the electron beam.

Averaging over the proton displacements and electron displacements, we obtain the equations for the coupled motion of the proton-beam centroid \bar{y}_p and the electron-beam centroid \bar{y}_e . Notice that the space charge terms, Q_{ps}^2 and Q_{es}^2 , drop out. If there is a coherent instability occurring at the angular frequency $\Omega = Q\omega_0$, we can write

$$\bar{y}_p \sim e^{i(n\theta - \Omega t)} \quad \text{and} \quad \bar{y}_e \sim e^{i(n\theta - \Omega t)}, \quad (19.15)$$

where n is the longitudinal harmonic number. The coupled equations can be readily solved to give

$$(Q^2 - Q_e^2)[(n - Q)^2 - Q_\beta^2 - Q_p^2] - Q_e^2 Q_p^2 = 0 , \quad (19.16)$$

which is a quartic. For a solution when Q is near Q_e , we can expand Q around Q_e . When Q_p or the neutralization factor χ_e is large enough, the solution becomes complex and an instability occurs. The limiting Q_p for stability is given by

$$Q_p \lesssim \frac{|(n - Q_e)^2 - Q_\beta^2 - Q_p^2|}{2\sqrt{Q_e|n - Q_e|}} , \quad (19.17)$$

from which the limiting neutralization factor χ_e can be obtained. Once above threshold, the growth rate, given by

$$\frac{1}{\tau} \approx \frac{Q_p \omega_0}{2} \sqrt{\frac{Q_e}{|n - Q_e|}} , \quad (19.18)$$

is very fast. Notice that Q_p^2 on the right side of Eq. (19.17) in the numerator can be neglected because usually $Q_p^2 \ll Q_\beta^2$.

A proper employment of Eq. (19.17) is important, because it can give meaningless result. For example, in the situation:

$$[Q_e] = [Q_\beta] \quad \text{or} \quad [Q_e] + [Q_\beta] = 1 , \quad (19.19)$$

where $[Q_e]$ and $[Q_\beta]$ are, respectively, the residual betatron tune and the residual electron bounce tune, there will always exist a harmonic n which leads to instability for $Q_p \rightarrow 0$ or neutralization $\chi_e \rightarrow 0$. However, the growth rate will go to zero also. In reality, there is always a variation in the proton linear density or the electron bounce tune Q_e usually has a spread. Furthermore, the betatron tune can be suitably adjusted. To obtain something meaningful, first let us separate the numerator of the right side of Eq. (19.17) into the fast and slow waves and keep only the dangerous slow wave:

$$|(n - Q_e)^2 - Q_\beta^2 - Q_p^2| \approx 2Q_\beta|n - Q_e - Q_\beta| \quad (19.20)$$

Compute Q_e from Eq. (19.11). Then the most offending harmonic n is determined as the integer closest to $Q_e + Q_\beta$. We next modify Q_e slightly so that

$$n - Q_e - Q_\beta = \frac{1}{2} . \quad (19.21)$$

Table 19.3: Coherent centroid-oscillation instability for proton-electron coasting beams.

	Oak Ridge SNS	Los Alamos PSR	Brookhaven Booster
Total number of protons N_p	2.10×10^{14}	4.2×10^{13}	4.42×10^{13}
Betatron tune Q_β	5.82	2.14	4.80
Proton beam radius a (m)	0.0380	0.0150	0.0150
$Q_p/\sqrt{\chi_e}$	1.2501	1.000	1.070
Most offending harmonic n	83	61	67
$Q_e = n - Q_\beta - \frac{1}{2}$	76.68	58.36	79.70
Limiting Q_p	0.1378	0.0957	0.1227
Limiting neutralization χ_e	0.0122	0.0093	0.0132
Growth rate in number of turns	0.637	0.637	0.637
Landau damping with $(\Delta Q_\beta - 2\Delta Q_{sc})/Q_\beta = 0.03$ and $\Delta Q_e/Q_e - \chi_e = 0.25$			
Limiting Q_p	0.5040	0.1853	0.4157
Limiting neutralization χ_e	0.1626	0.0343	0.151
Growth rate in number of turns	0.176	0.340	0.386

As a result, the stability condition of Eq. (19.17) reduces to

$$Q_p \lesssim \frac{1}{2} \sqrt{\frac{Q_\beta}{Q_e}}, \quad (19.22)$$

and the growth rate of Eq. (19.18) reduces to

$$\frac{1}{\tau} \approx \frac{Q_p \omega_0}{2} \sqrt{\frac{Q_e}{Q_\beta}}. \quad (19.23)$$

The latter becomes $\tau^{-1} \approx \omega_0/4$ when the threshold values in Eq. (19.22) are substituted.

With this consideration, the results are listed in Table 19.3. Here, the intensity of 4.42×10^{13} protons is used for the Brookhaven booster, where coasting beam experiments with possible e-p instabilities have been observed. We notice that the neutralization threshold is about 1.2% for the ORNL SNS, 0.9% for the LANL PSR, and 1.3% for the BNL booster. Once the thresholds are reached, the growth rates are very fast and the corresponding growth times are less than one turn for all the 4 machines.

There is another consideration of the stability of the two beam centroids, since the coherent oscillation can be stabilized by Landau damping. The equation of motion of the electron, Eq. (19.10), can be viewed as an undamped oscillator driven by \bar{y}_p , the centroid of the proton beam. Thus, spreads in the proton betatron tune Q_β and/or proton bounce tune Q_p alone will not be able to damp the electron oscillations. To damp the electron oscillation, there must be a spread in the electron bounce tune Q_e . The same applies to the equation of motion of the proton, Eq. (19.9), driven by the centroid of the electron beam. Therefore, to provide Landau damping to the coupled-centroid oscillation, there must exist large enough spreads in both the betatron tune ΔQ_β and the electron bounce tune ΔQ_e .

First, we rewrite Eqs. (19.9) and (19.10) as

$$\left(\frac{\partial}{\partial t} + \dot{\theta} \frac{\partial}{\partial \theta} \right)^2 y_p + Q_p'^2 \omega_0^2 y_p = Q_p^2 \omega_0^2 \bar{y}_e - Q_{ps}^2 \omega_0^2 \bar{y}_p , \quad (19.24)$$

$$\frac{d^2 y_e}{dt^2} + Q_e'^2 \omega_0^2 y_e = Q_e^2 \omega_0^2 \bar{y}_p - Q_{es}^2 \omega_0^2 \bar{y}_e , \quad (19.25)$$

where we have denoted

$$Q_p'^2 = Q_\beta^2 + Q_p^2 - Q_{ps}^2 \quad \text{and} \quad Q_e'^2 = Q_e^2 - Q_{es}^2 . \quad (19.26)$$

Second, with the ansatz in Eq. (19.15), the coupled differential equations becomes

$$y_p = \frac{Q_p^2 \bar{y}_e - Q_{ps}^2 \bar{y}_p}{Q_p'^2 - \left(Q - \frac{n\dot{\theta}}{\omega_0} \right)^2} , \quad (19.27)$$

$$y_e = \frac{Q_e^2 \bar{y}_p - Q_{es}^2 \bar{y}_e}{Q_e'^2 - Q^2} . \quad (19.28)$$

Third, we need to integrate both sides with the suitable distribution functions. In doing so, two approximations are to be made: (1) only the denominators of Eqs. (19.27) and (19.28) depend on the distributions which appear in differences of squares but not the numerator, and (2) only the *slow wave* will be included. It is then easy to obtain

$$\bar{y}_p = \frac{Q_p^2}{2Q_p' \delta Q_p'} \bar{y}_e - \frac{Q_{ps}^2}{2Q_p' \delta Q_p'} \bar{y}_p , \quad (19.29)$$

$$\bar{y}_e = \frac{Q_e^2}{2Q_e' \delta Q_e'} \bar{y}_p - \frac{Q_{es}^2}{2Q_e' \delta Q_e'} \bar{y}_e , \quad (19.30)$$

where

$$\frac{1}{\delta Q'_p} = \int \frac{F_p(s)ds}{Q'_p - n + Q + \delta_p s}, \quad (19.31)$$

$$\frac{1}{\delta Q'_e} = \int \frac{F_e(s)ds}{Q'_e - Q + \delta_e s}, \quad (19.32)$$

$$\delta_p = \frac{\partial}{\partial s} \left(Q'_p(s) - \frac{n\dot{\theta}(s)}{\omega_0} \right)_{s=0}, \quad (19.33)$$

$$\delta_e = \left(\frac{\partial Q'_e(s)}{\partial s} \right)_{s=0}, \quad (19.34)$$

and $Q_p, Q'_p, Q_{ps}, Q_e, Q'_e, Q_{es}$ in Eqs. (19.29) to (19.32) are all evaluated at $s = 0$. Here, s being a generic variable, which can represent amplitude, momentum spread, etc, while $F_p(s)$ and $F_e(s)$ are distributions normalized to unity for the protons and electrons. From Eqs. (19.29) and (19.30), it is easy to get

$$\left(2\delta Q'_p + \frac{Q_{ps}^2}{Q'_p} \right) \left(2\delta Q'_e + \frac{Q_{es}^2}{Q'_e} \right) - \frac{Q_p^2 Q_e^2}{Q'_p Q'_e} = 0. \quad (19.35)$$

Now following Laslett, *et al.*, semi-circular distributions,

$$F_p(s) = \frac{2}{\pi \hat{s}_p^2} \sqrt{\hat{s}_p^2 - s^2} \quad \text{and} \quad F_e(s) = \frac{2}{\pi \hat{s}_e^2} \sqrt{\hat{s}_e^2 - s^2}, \quad (19.36)$$

are assumed for both the protons and electrons. One obtains

$$\begin{cases} 2\delta Q'_p = Q'_p - n + Q + i\bar{\Delta}_p, \\ 2\delta Q'_e = Q'_e - Q - i\bar{\Delta}_e, \end{cases} \quad (19.37)$$

where

$$\begin{cases} \bar{\Delta}_p = \sqrt{\Delta Q_p^2 - (Q - n + Q'_p)^2}, \\ \bar{\Delta}_e = \sqrt{\Delta Q_e^2 - (Q - Q'_e)^2}, \end{cases} \quad (19.38)$$

while ΔQ_p and ΔQ_e are the actual half spread of Q'_p and Q'_e in these distributions and are related to δ_p and δ_e in Eqs. (19.33) and (19.34) by

$$\Delta Q_p = \hat{s}_p \delta_p = \hat{s}_p \frac{\partial}{\partial s} \left(Q'_p(s) - \frac{n\dot{\theta}(s)}{\omega_0} \right)_{s=0}, \quad (19.39)$$

$$\Delta Q_e = \hat{s}_e \delta_e = \hat{s}_e \left(\frac{\partial Q'_e(s)}{\partial s} \right)_{s=0}. \quad (19.40)$$

Equation (19.35) is obtained via the integral [9]

$$\int_{-1}^1 \frac{\sqrt{1-x^2} dx}{x+x_1-i\epsilon} = \pi \left[x_1 + i\sqrt{1-x_1^2} \right] . \quad (19.41)$$

Substitution into Eq. (19.35) leads to a quadratic equation in the coherent coupled-oscillation tune Q , the solution of which is

$$Q = Q'_e + \frac{Q_{es}^2}{Q'_e} + d_1 - \frac{i}{2} (\bar{\Delta}_e + \bar{\Delta}_p) \pm i \left\{ \frac{Q_p^2 Q_e^2}{Q'_p Q'_e} - \left[d_1 + \frac{i}{2} (\bar{\Delta}_e - \bar{\Delta}_p) \right]^2 \right\}^{1/2} , \quad (19.42)$$

where

$$d_1 = \frac{1}{2} \left[\left(n - Q'_p - \frac{Q_{ps}^2}{Q'_p} \right) - \left(Q'_e + \frac{Q_{es}^2}{Q'_e} \right) \right] . \quad (19.43)$$

It is clear that stability requires in Eq. (19.42)

$$\Re e \left\{ \frac{Q_p^2 Q_e^2}{Q'_p Q'_e} - \left[d_1 + \frac{i}{2} (\bar{\Delta}_e - \bar{\Delta}_p) \right]^2 \right\}^{1/2} \leq \frac{1}{2} (\bar{\Delta}_e + \bar{\Delta}_p) . \quad (19.44)$$

This criterion is equivalent to, after considerable amount of algebra,

$$\bar{\Delta}_p \bar{\Delta}_e \geq \frac{Q_p^2 Q_e^2}{Q'_p Q'_e} \left[1 + \left(\frac{2d_1}{\bar{\Delta}_p + \bar{\Delta}_e} \right)^2 \right]^{-1} . \quad (19.45)$$

Within a narrow band of instability, associated with the resonance $d_1 \approx 0$, or $n - Q'_p - Q \approx Q_{ps}^2/Q'_p$ and $|Q'_e - Q| \approx Q_{es}^2/Q'_e$, the stability limit can be simplified. With the substitution of Eq. (19.38), we finally arrive at

$$\left[\Delta Q_p^2 - \left(\frac{Q_{ps}^2}{Q'_p} \right)^2 \right]^{1/2} \left[\Delta Q_e^2 - \left(\frac{Q_{es}^2}{Q'_e} \right)^2 \right]^{1/2} \geq \frac{Q_p^2 Q_e^2}{Q'_p Q'_e} . \quad (19.46)$$

Because square roots are involved, we also require

$$\Delta Q_p > \left| \frac{Q_{ps}^2}{Q'_p} \right| \quad \text{and} \quad \Delta Q_e > \left| \frac{Q_{es}^2}{Q'_e} \right| . \quad (19.47)$$

It is important to point out that the space charge self-force terms of Eqs. (19.9) and (19.10) do not drop out when averaged over the distributions. As an approximation,

$Q'_p \sim Q_\beta$ implying that $Q_{ps}^2/Q'_p \sim 2\Delta Q_{sc}$, where ΔQ_{sc} is the linear space charge tune shift of the proton beam. Similarly, we can write $Q_{es}^2/Q'_e \sim Q_e \chi_e$, which is twice the linear space charge tune shift of the electron beam. The stability condition then simplifies to

$$[\Delta Q_\beta^2 - 4\Delta Q_{sc}^2]^{1/2} [\Delta Q_e^2 - \chi_e^2 Q_e^2]^{1/2} \gtrsim \frac{Q_p^2 Q_e}{Q_\beta} . \quad (19.48)$$

Because of the square roots on the left side of Eq. (19.48), we also require for stability,

$$\Delta Q_\beta \geq 2Q_{sc} \quad \text{and} \quad \frac{\Delta Q_e}{Q_e} \geq \chi_e . \quad (19.49)$$

The spread in the electron bounce frequency is difficult to measure. However, when instability occurs, the electron bounce frequency is very close to the coherent instability frequency, which is the same for the proton beam and the electron. Thus measuring the coherent transverse oscillation frequency of the proton beam, we can infer the electron bounce frequency. According to the measurement at PSR, $\Delta Q_e/Q_e \sim 0.25$. Assuming that the neutralization factor is small, we may set the half maximum fractional spread of the electron bounce tune to be $\Delta Q_e/Q_e - \chi_e \sim 0.1$, and the half maximum fractional spread of the betatron tune in excess of twice the space charge tune shift is $(\Delta Q_\beta - 2\Delta Q_{sc})/Q_\beta \sim 0.03$. The limiting Q_p and neutralization factor χ_e can now be computed and are also listed in Table 19.3. For the ORNL SNS and the Brookhaven booster, the threshold neutralization factors have been increased to 16.3% and 15.1%, respectively, which are more than 10 times. For the LANL PSR, however, the neutralization threshold χ_e becomes $\sim 3.4\%$, an increase of less than 4 times. Further increase in threshold requires larger spreads in Q_e and Q_β . In fact, it has been demonstrated that anti-damping can even happen unless there is a large enough overlap between ΔQ_β and ΔQ_e [12]. Notice that these stability limits of the neutralization factor can be sensitive to the distributions of the betatron tune and the electron bounce tune.

A stability condition has also been derived by Schnell and Zotter [12] assuming parabolic distributions for the betatron tune and the electron bounce tune, but without consideration of the space charge self-forces. They obtain

$$\frac{\Delta Q_\beta}{Q_\beta} \frac{\Delta Q_e}{Q_e} \gtrsim \frac{9\pi^2}{64} \frac{Q_p^2}{Q_\beta^2} . \quad (19.50)$$

Notice that the Schnell-Zotter criterion is essentially the same as the Laslett-Sessler-Möhl criterion, if we interpret ΔQ_β of the former as the half tune spread of the betatron tune *in excess* of twice the space charge tune spread of the proton beam, and ΔQ_e as

the half tune spread of the electron bounce tune *in excess* of twice the space charge tune spread of the electron beam. The factor $9\pi^2/64$ in Eq. (19.50) is probably a form factor of the parabolic distributions. Our discussion can be generalized when we notice that both Q_{ps}^2/Q_p' and Q_{es}^2/Q_e' in Eq. (19.46) come from, respectively, the \bar{y}_e term in Eq. (19.9) and the \bar{y}_p term in Eq. (19.10). Thus, Q_{ps}^2 and Q_{es}^2 can be extended to include the perturbations of oscillations coming from all types of impedances of the accelerator ring. In that case, the Schnell-Zotter stability criterion should be valid if we interpret ΔQ_β as the half tune spread of the betatron tune in excess of what is necessary to cope with the instabilities of the single proton beam, and ΔQ_e as the half tune spread of the electron bounce tune in excess of what is necessary to cope with the instabilities of the single electron beam.

19.2.3 Production of Electrons

As seen in the previous section, the e-p coherent centroid-oscillation instability depends strongly on the neutralization factor, or the amount of electrons trapped inside the proton bunch.

One source of electron production is through collision of the protons with the residual gas in the vacuum chamber. At a vacuum pressure of 1×10^{-7} Torr (1 atm = 760 Torr) and room temperature ($T = 300^\circ\text{K}$), there is a residual gas density of

$$n_{\text{res}} = \frac{N_A p}{RT} = 3.2 \times 10^{15} \text{ molecules/m}^3 , \quad (19.51)$$

where the ideal gas law has been used, with $N_A = 6.022 \times 10^{23}$ being the Avogadro number and $R = 82.55 \times 10^{-6}$ Atm-m³K⁻¹ the gas constant. The expected average ionization cross section is $\sigma_i = 1.2 \times 10^{-18}$ cm² (or 1.2 Mb). If the residual gas is mostly bi-atomic molecules, each contributing two electrons, the rate of electron production is [10]

$$\frac{dN_e}{dt} = 2\beta c n_{\text{res}} \sigma_i N(t) , \quad (19.52)$$

where $N(t)$ is the number of protons accumulated from injection at time t . If t_{inj} is the total injection time, $N(t) = N_p t / t_{\text{inj}}$, where N_p is the total number of protons at the end of the injection. The neutralization due to ionization collision at the end of injection is therefore

$$\chi_e = \frac{N_e}{N_p} = \beta c n_{\text{res}} \sigma_i t_{\text{inj}} . \quad (19.53)$$

The vacuum pressure for the ORNL SNS is designed to be 1×10^{-9} Torr and that for the LANL PSR is 2×10^{-8} Torr, while the other ring is with vacuum pressure 1×10^{-7} Torr. The neutralization due to ionization collision turns out to be 0.104%, 1.39%, and 2.33%, respectively, for the ORNL SNS, LANL PSR, and BNL booster. The neutralization factors are large for PSR and the BNL booster because of their relatively low vacuum and long injection times of, respectively, ~ 2000 and 300 turns. The maximum neutralization of the ORNL SNS is small because of the very high vacuum.

Another source of electron production is through the multi-traversing of the stripping foil by the proton beam. For example, a proton in the LANL PSR can generate on the average two electrons because of the presence of the stripping foil.

A more important source of electron production is when an electron hitting the walls of the beam pipe releases secondary electrons. These secondary electrons can cause multi-pactoring and generate a large amount of electrons. Here, we would like to compute the energy of an electron hitting the beam pipe and estimate the efficiency of secondary emission [11].

An electron is oscillating with bounce frequency $\Omega_e/(2\pi)$ with amplitude increasing exponentially with an e-folding growth rate ω_I . Assume that the electron just grazes the wall of the beam pipe at time $t = 0$. Its amplitude is given by

$$y = b e^{\omega_I t} \cos \Omega_e t , \quad (19.54)$$

where b is the beam pipe radius. It will hit the other side of the wall at time $t_1 = (\pi - \Delta)/\Omega_e$, where

$$-b = b e^{\omega_I t_1} \cos \Omega_e t_1 = b e^{(\pi - \Delta)\omega_I/\Omega_e} \cos(\pi - \Delta) . \quad (19.55)$$

Assuming $\Delta \ll 1$ and $\pi\omega_I/\Omega_e \ll 1$, the solution is

$$\Delta = \sqrt{\frac{2\pi\omega_I}{\Omega_e}} \left[1 + \mathcal{O}\left(\sqrt{\frac{\omega_I}{\Omega_e}}\right) \right] . \quad (19.56)$$

The velocity of the electron hitting the other side of the wall can be obtained by differentiating Eq. (19.54) and is given by

$$\dot{y} = -b \sqrt{2\pi\omega_I\Omega_e} \left[1 + \mathcal{O}\left(\sqrt{\frac{\omega_I}{\Omega_e}}\right) \right] . \quad (19.57)$$

The kinetic energy is therefore

$$E_{\text{kin}} = \pi m_e \omega_I \Omega_e b^2 , \quad (19.58)$$

where m_e is the electron mass.

For single-electron motion, we can identify the growth rate $\omega_I = \mu\beta c/\lambda_{\text{rf}}$, where μ is given by Eq. (19.4). The velocities and kinetic energies of the electrons hitting the wall on the other side of the beam pipe are listed in Table 19.4. We see that when hitting the beam pipe wall, the electrons possess kinetic energies of 198.6, 775.4, and 139.5 eV, respectively, for the three rings. For the BNL booster, the bunched mode intensity has been used. It is a known fact that an electron in excess of 100 eV hitting a metallic wall will result in a secondary-emission coefficient greater than unity. This implies that multi-pactoring will occur in these three rings. This consideration is for the motion of a single electron and is independent of the amount of electrons present inside the vacuum chamber of the ring. In the design of the ORNL SNS, the beam pipe will be made of stainless steel with a titanium coating, which will reduce the secondary-emission efficiency and thus prevent multi-pactoring to occur. An experiment had been performed at the LANL PSR by coating part of the walls of the vacuum chamber with TiN. The electron flux was found to have been suppressed about 1000 times [15]. However, it was reported at the SLAC PEP low energy positron ring that TiN coating did not help much in reducing electron secondary emission. In passing, it is worth mentioning that aluminum has a much higher second-emission coefficient than stainless steel. Thus, an aluminum vacuum chamber should be avoided if one wish to limit the amount of trapped electrons.

We can also identify ω_I with the growth rate τ^{-1} of the coherent centroid oscillation in Eq. (19.18). The kinetic energy of an electron hitting the other side of the beam pipe wall becomes

$$E_{\text{kin}} = \frac{\pi m_e Q_p Q_e^{3/2} \omega_0^2 b^2}{2 \sqrt{|n - Q_e|}} . \quad (19.59)$$

The kinetic energy of the electron hitting the pipe wall is now proportional to Q_p and therefore $\sqrt{\chi_e}$, the amount of trapped electrons. These results for the three rings are listed in Table 19.4 at the threshold neutralization. Actually, Eq. (19.59) becomes $E_{\text{kin}} \approx \pi m_e Q_e \omega_0^2 b^2 / 4$ when the threshold values in Eq. (19.22) are substituted. Notice that the kinetic energies of the electrons hitting the beam pipe walls at the onset of coupled-centroid instability are less than 100 eV for the ORNL SNS and the BNL booster in the bunched mode. Thus multi-pactoring will occur only if the neutralization factor is much larger than $\sim 1\%$. On the other hand, the electron kinetic energy is 201 eV for the Los Alamos PSR. Thus, multi-pactoring will occur near the onset of coherent centroid instability.

Table 19.4: Kinetic energy of electron hitting the wall of the beam pipe.

	Oak Ridge SNS	Los Alamos PSR	Brookhaven Booster
Total number of protons N_p	2.1×10^{14}	4.2×10^{13}	2.4×10^{13}
Beam pipe radius b (m)	0.0500	0.0500	0.0600
<u>Single-electron consideration</u>			
Electron escaping rate ω_I (MHz)	6.24	13.9	4.69
Ω_e (MHz)	713.3	1253.9	462.6
Velocity hitting wall \dot{y}/c	0.0279	0.0551	0.0234
Kinetic energy hitting wall (eV)	198.6	775.4	139.5
<u>Coherent-centroid-oscillation consideration</u>			
Threshold neutralization χ_e	0.0122	0.0093	0.0132
Growth rate ω_I (MHz)	1.867	4.392	1.320
Ω_e (MHz)	572.7	1025.2	325.8
Velocity hitting wall \dot{y}/c	0.0137	0.0281	0.0104
Kinetic energy hitting wall (eV)	47.8	201.1	27.6

19.2.4 Electron Bounce Frequency

Electron-proton instability is different from other transverse instability in that the bounce frequency of the electrons inside the proton bunch is very broad. Recall that the angular bounce frequency is defined as

$$\Omega_e = \sqrt{\frac{4\lambda r_e c^2}{a_v(a_v + a_H)}} . \quad (19.60)$$

where λ is the linear particle density of the proton bunch. Thus, the bounce frequency of the electrons depends on where they are inside the proton bunch. For example, if the electrons are trapped within the proton FWHM bunch profile, the spread of the bounce frequency will be $1/\sqrt{2}$ its mean value, which is certainly a wide spread. Another test of the e-p bounce oscillation is to measure the dependency of the bounce frequency on the proton beam intensity. As is given by Eq. (19.60), the bounce frequency should be proportional to the square root of the proton intensity. Such a measurement has been performed at the Los Alamos PSR and is shown in Fig. 19.5. At countdown 1 (CD 1), the longest chopped proton beam is injected from the linac. At $6.1 \mu\text{C}$ or 3.81×10^{13} proton injected, the electron bounce frequency observed is ~ 200 MHz, very close to

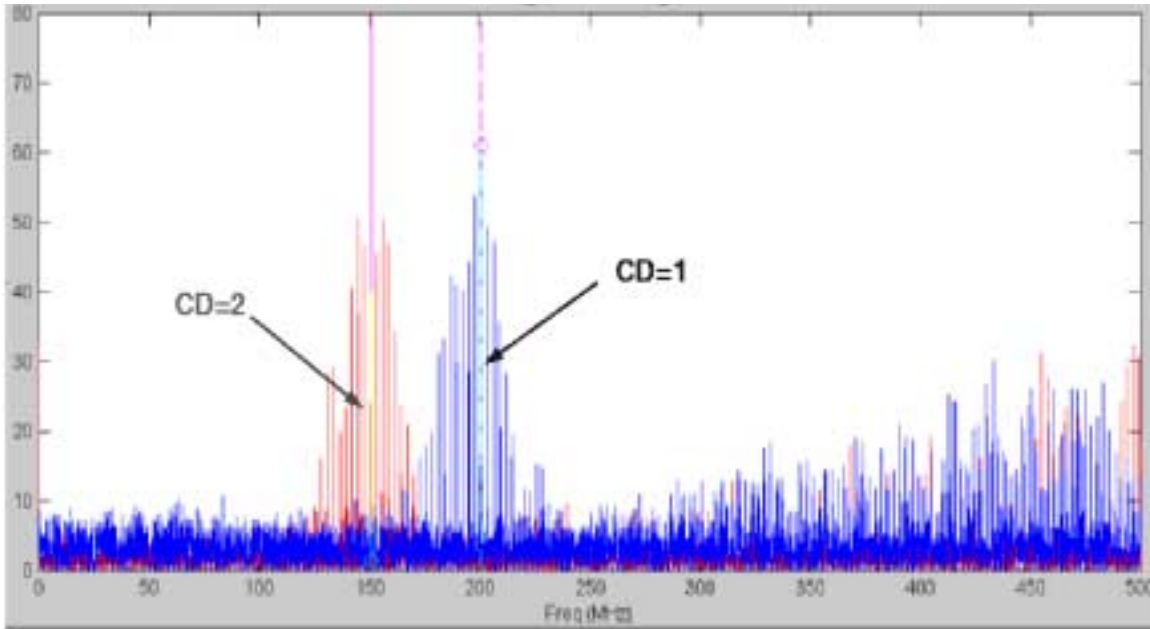


Figure 19.5: (color) The PSR is run at CD 1 with $6.1 \mu\text{C}$. The electron bounce frequency is measured to be centered at ~ 200 MHz, close to the theoretical prediction. The total spread of the bounce frequency is roughly 100 MHz, the same order of magnitude as its center value. Operated at CD 2 with $3.0 \mu\text{C}$, the bounce frequency reduces to ~ 140 MHz, roughly by $\sqrt{2}$ times as expected.

the prediction of Eq. (19.60). Next the injection is at countdown 2 (CD 2), where the chopped beam from the linac is injected into the PSR on alternate turns, thus reducing the total injection intensity by half to $3.0 \mu\text{C}$. The bounce frequency is found to peak at ~ 140 MHz, very close to a reduction of $\sqrt{2}$ as predicted. The total spread of the bounce frequency at CD 1 is about 100 MHz, which is also the same order of magnitude as predicted above.

19.2.5 Discussion and Conclusion

- (1) In the above single-electron analysis, it appears that electrons will be cleared in the bunch gap within one rf wavelength for all the 3 proton rings under consideration. However, if more than $\eta \sim 4\%$ of the protons are spilled into the bunch gap, electrons will be trapped inside the proton beam in the ORNL SNS and LANL PSR. For the BNL booster, on the other hand, electrons are relatively more difficult to be trapped when

there are spilled protons in the bunch gaps even if $\eta > 20\%$. This is probably due to its much larger gap-to-bunch-length ratio.

(2) For coherent centroid oscillation to become unstable, neutralization factors of $\chi_e \sim 1.2\%$, 0.9%, and 1.1% are required, respectively, for the three machines. However, spreads in the betatron frequencies and the electron bounce frequencies can provide Landau damping.

(3) The LANL PSR may accumulate protons through an injection in ~ 2000 turns and the BNL booster in 300 turns. The vacuum pressures of both rings are relatively high, $\sim 1 \times 10^{-8}$ Torr for the former and $\sim 1 \times 10^{-7}$ Torr for the latter. As a result, the amount of electrons per proton produced by collision with residual gases can be as high as 1.39 and 2.33%, respectively, for the two rings. However, the electron production for the ORNL SNS via proton-ion collision is less than 1%, which is the result of a high vacuum of 1×10^{-9} Torr in the vacuum chamber.

(4) Multi-pactoring as a result of secondary emission will be possible for all the three rings when single electron escapes from the trapping proton beam and hits the metallic beam pipe. For the LANL PSR, multi-pactoring will occur near the onset of coherent centroid instability. However, for the other two rings, multi-pactoring will not occur as soon as centroid oscillations become unstable.

(5) There is a similar proton ring called ISIS at the Rutherford Appleton Laboratory. At the injection energy of 70.4 MeV, about 2.5×10^{13} protons are stored as a continuous coasting beam, which is then captured adiabatically into 2 rf buckets. The protons are ramped to 0.8 GeV when they are extracted. No e-p instabilities have ever been observed at ISIS either running in the bunched mode or the coasting-beam mode. This has always been a puzzle. However, when we compare ISIS with the LANL PSR, we do find some important differences. First, ISIS has a repetition rate of 50 Hz. The injection is fast, about 200 turns. On the other hand, it usually takes about 200 turns for the e-p instability of the PSR to develop to a point when it can be monitored. Second, ISIS has a much larger vacuum chamber, 7 cm in radius. Also the ISIS vacuum chamber is made of ceramic to limit eddy current because of the high repetition rate of 50 Hz. A wire cage is installed inside the ceramic beam pipe to carry the longitudinal return current. The wire cage does not allow transverse image current to flow, thus alleviating in some way the transverse instability. Also the cage wires have much less surface area than the walls of an ordinary metallic beam pipe. As a result, secondary emission will be reduced. The secondary emitted electrons will come out in all directions from the cage

wires. The probability for them to hit another cage wire will be small, thus preventing multi-pactoring to occur. These may be the reasons why e-p instabilities have never been observed at ISIS.

19.3 Fast Beam-Ion Instability

In the above sections, we discuss ions trapped in an electron beam (or electrons trapped in a proton beam) causing coherent coupled ion-electron oscillation once the intensity of the trapped ions is high enough. The best cure appears to be a gap between the consecutive bunches. The ions will be cleared in the gap. They will not accumulate inside the potential of the electron beam turn after turn and their intensity will not reach the threshold of coupled-beam instability.

However, if the linear density of the electron beam is large enough and the electron bunch is long enough, even in one pass through a region in the vacuum chamber the electron beam is able to generate and trap so many ions that coupled ion-electron occurs resulting in the emittance growth of the electron beam. This instability, called *fast ion instability*, was first investigated by Raubenheimer and Zimmermann [16]. Instead of a long electron bunch, fast ion instability can also occur for a long train of short electron bunches, because the gaps between consecutive bunches may not be long enough to clear all the ions. This instability is important because of its one pass nature and is not curable by clearing gap. For this reason, this instability can also happen inside a linac.

19.3.1 The Linear Theory

In this section, we derive the linear theory of fast ion instability. We will follow the approach of Chao [17]. The only difference is that we need to keep tract of the gradual accumulation of ions generated.

Let $y_e(s|z)$ denotes the vertical displacement of the centroid of a slice of the electron bunch, where z is the distance of the slice from the head of the electron bunch and s is the distance along the accelerator. If the head of the bunch passes position $s = 0$ at time $t = 0$, $s = vt - z$, where v is the beam velocity. We assume that the electron beam contains N_e electrons, uniformly distribution longitudinally and transversely, has

a length ℓ and horizontal and vertical radii a_H and a_V .

Let $y_I(s, t|z)$ denotes the vertical displacement of the centroid of a slice of the ions at time t position s along the accelerator. These ions are generated by the electron slice at a distance z behind the head of the electron bunch. Since the ions are assumed to have no longitudinal velocity, s and t are not related.

19.3.1.1 The Ion Equation of motion

Because the focusing force experienced by the ion is relative to the centroid of the electron beam, the equation of motion of the ion is just

$$\frac{\partial^2}{\partial t^2} y_I(s, t|z') + \omega_I^2 [y_I(s, t|z') - y_e(s|vt-s)] = 0 . \quad (19.61)$$

The second argument of the electron displacement has been substituted with $z = vt - s$ because it is the electron slice at $z = vt - s$ which are interacting with the ions at location s and time t . Here, only the linear force has been included for the linear theory and all image and space charge forces are neglected. The ion bounce angular frequency ω_I is given by

$$\omega_I = \sqrt{\frac{4N_e r_p c^2}{\ell a_V (a_V + a_H) A}} , \quad (19.62)$$

where r_p is the proton classical radius and A is the atomic mass of the ions. This is exactly the same as the electron bounce frequency we derived in Eq. (19.1) with the electron mass replaced by the ion mass. Although the ion is very much heavier than the electron, the electron beam size is usually very much smaller than the proton beam size. Therefore this ion bounce frequency can be very large also. For a nitrogen ion of $A = 14$ in an electron bunch containing 10^{11} particles, of total length $\ell = 1$ cm, and radius $a = 1$ mm, we find $\omega_I/(2\pi) = 70$ MHz. In case the beam transverse distribution is bi-Gaussian with rms spreads σ_H and σ_V , the following substituting should be made [16] in Eq. (19.62):

$$a_V (a_V + a_H) \longrightarrow 3\sigma_V (\sigma_V + \sigma_H) . \quad (19.63)$$

The ions described in Eq. (19.61) were produced by proton at location s (the head is at $s + z'$) at time $t = (s + z')/v$, and should have the same distribution as the proton

and has no transverse velocity. Therefore, Eq. (19.61) has the initial conditions

$$\begin{aligned} y_I\left(s, \frac{s+z'}{v} \middle| z'\right) &= y_e(s, z') , \\ \frac{\partial}{\partial t} y_I(s, t | z') \Big|_{t=\frac{s+z'}{v}} &= 0 . \end{aligned} \quad (19.64)$$

These initial conditions offer a way to determine the ion distribution. A slice of ions, when produced at time t_0 , have exactly same transverse distribution as the slice of electrons. These ions have no initial transverse velocity, but they will start their oscillation about the centroid of the electron slice according to $r \cos \omega_I(t - t_0)/v$, with r being the initial distance of a particular ion from the centroid of the electron slice. This implies that this slice will first contract to zero in one quarter of a betatron oscillation and expand again. Of course, we will not find the ions contract to zero at a location at any time, because at the same location there are other slices of ions produced by other slices of electrons. These ion slice will have different betatron phases than the one that we are talking about, because the electron slice producing them are at different z from the head of the beam. Because of the betatron oscillation (even in the absence of couple ion-beam oscillation), the average horizontal and vertical radii of the ion slice will be smaller than those of the electron beam. They are just $a_H/\sqrt{2}$ and $a_V/\sqrt{2}$ if the distribution of the ions is assumed to be uniform.

A derivation of the ion distribution is as follow. For simplicity, in this derivation a round electron beam with $a = a_H = a_V$ is assumed. If Σ is the ionization cross section and n_g is the residual gas density in the vacuum chamber, the linear density of ions

$$\lambda_I = \Sigma n_g N_e \quad (19.65)$$

is produced near the tail of the electron beam, after a total of N_e electrons have passed through. Now an electron slice of width dz' at distance z' behind the head of the electron beam will produce a slice of ions with linear density $\Sigma n_g N_e dz' / \ell$. This slice of ions will have radius a when born. These ions do not move longitudinally. When the electron slice at distance z behind the head reaches these ions, this ion slice shrinks to the radius $a \cos \omega_I(z-z')/v$. Summing up the ions produced by all the electron slices up to the slice at z , the transverse ion density within a circle of radius r is

$$\begin{aligned} n_I(r|z) &= \frac{\Sigma n_g N_e}{\pi a^2 \ell} \int_{0, \left(|\cos \frac{\omega_I(z-z')}{v}| < \frac{r}{a} \right)}^z \frac{dz'}{\cos^2 \frac{\omega_I(z-z')}{v}} \\ &= \frac{\Sigma n_g N_e v}{\pi a^2 \ell \omega_I} \tan \frac{\omega_I z}{v} \Big|_{0, \left(|\cos \frac{\omega_I(z-z')}{v}| < \frac{r}{a} \right)} . \end{aligned} \quad (19.66)$$

Now

$$\left| \cos \frac{\omega_I(z')}{v} \right| < \frac{r}{a} \longrightarrow \left| \tan \frac{\omega_I(z')}{v} \right| < \frac{\sqrt{a^2 - r^2}}{r}. \quad (19.67)$$

Thus, in each π period, $\left| \tan \frac{\omega_I z'}{v} \right|$ receives the contribution of $\frac{2\sqrt{a^2 - r^2}}{r}$. When $\omega_I z/c \gg 1$, from $z' = 0$ to z there are $\omega_I z/(v\pi)$ such periods. The transverse ion distribution is therefore

$$n_I(r|z) \approx \frac{2\Sigma n_g N_e z}{\pi^2 a^2 \ell} \frac{\sqrt{a^2 - r^2}}{r}. \quad (19.68)$$

This distribution has rms radius $a/2$. However, a uniform beam of radius a has rms radius $a/\sqrt{2}$. If we approximate the ion distribution to be uniform, it corresponds to a radius of $a/\sqrt{2}$.

19.3.1.2 The Electron Equation of Motion

Similar to the ion oscillation in the electron beam, the electron beam also oscillates in the ions. Near the very end of the electron beam, the ions generated by the passage of the whole beam has linear density $\lambda_I = \Sigma n_g N_e$. The bounce angular frequency of the last slice of the electron beam in the ions is therefore

$$\omega_e = \sqrt{\frac{8\Sigma n_g N_e r_e c^2}{\gamma a_V (a_V + a_H)}}. \quad (19.69)$$

Comparing with the ion bounce frequency ω_I in Eq. (19.62), the γ in the denominator indicates the longitudinal motion of the electron, and the extra factor of 2 in the numerator reminds us that the radii of the ions are smaller than those of the electron beam by $\sqrt{2}$. For bi-Gaussian distribution, the substitution $a_V(a_V + a_H) \rightarrow 6\sigma_V(\sigma_V + \sigma_H)$ should be made. If the residual pressure inside the vacuum chamber is low, this electron bounce frequency is usually small. Take our previous example. If the residual pressure is $p = 10^{-9}$ Torr, the residual gas density is $n_g = 3.2 \times 10^{13}$ molecules/m³ according to Eq. (19.51). For carbon monoxide, the ionization cross section is $\Sigma = 2.0$ Mb, ion linear density at the tail of the electron bunch is $\lambda_I = 640$ m⁻¹, and the electron bounce frequency is $\omega_e/(2\pi) = 1.3$ kHz. For an electron slice at distance $z < \ell$ behind the head of the electron beam, the bounce frequency becomes $\omega_e \sqrt{z/\ell}$ because only $N_e z/\ell$ electrons have participated in the ion production. The equation of motion for the centroid of a slice of the electron beam can therefore be written as

$$v^2 \frac{\partial^2}{\partial s^2} y_e(s|z) + \omega_\beta^2 y_e(s|z) + \frac{\omega_e^2 z}{\ell} \left[y_e(s|z) - \frac{1}{z} \int_0^z dz' y_I\left(s, \frac{s+z'}{v} | z'\right) \right] = 0, \quad (19.70)$$

where ω_β is the angular betatron frequency due to external focusing. The last term in the square brackets denotes the centroid of the ion slice produced by those electrons electron beam from the head to the length ℓ of the electron beam, where a uniform longitudinal distribution of the electron beam has been assumed.

19.3.1.3 Coupled-Ion-Beam Solution

The coupled ion-beam motion, Eqs. (19.61) and (19.70), is solved by separating the fast oscillating part and slow amplitude evolution part. We would like to obtain the asymptotic behavior of the beam-ion system. Let us make our observation at a fixed location s when there is a resonance between the beam and ions. the electron slice z behind the head of the electron bunch passes this location, it should have the same fast oscillating frequency as the ions at the same location. The fast oscillating part of the electron slice is

$$y_e(s|z) \sim e^{-i\omega_\beta s/v + ikz} \sim e^{-i\omega_\beta s/v + ikvt - iks}, \quad (19.71)$$

where k is to be determined and $z = vt - s$ has been substituted. The ions execute simple harmonic motion like

$$y_I(s, t|z') \sim y_I(s, t_0|z')e^{\pm i\omega_I(t-t_0)}. \quad (19.72)$$

At the time $t_0 = (s + z')/v$ when the ions are born (for any $z' < \ell$), since they should have the same displacement as the electrons that produce them, therefore

$$\begin{aligned} y_I(s, t|z') &\sim y_e(s|z')e^{\pm i\omega_I(t-t_0)} \\ &\sim e^{-i\omega_\beta s/v + ikz'} e^{\pm i\omega_I t \mp i\omega_I(s+z')/v}. \end{aligned} \quad (19.73)$$

Comparing the time dependency of Eqs (19.71) and (19.73), for a resonance to occur we must have

$$k = \omega_I v. \quad (19.74)$$

The other solution, $k = -\omega_I v$, will lead to a decaying oscillatory solution which is of no interest to us (see below).

After determining the fast oscillating part at a resonance, now let

$$\begin{aligned} y_e(s|z) &\sim \tilde{y}_e(s|z)e^{-i\omega_\beta s/v + i\omega_I z/v}, \\ y_I(s, t|z') &\sim \tilde{y}_I(s, t|z')e^{-i(\omega_\beta + \omega_I)s/v + i\omega_I t}, \end{aligned} \quad (19.75)$$

where $\tilde{y}_e(s|z)$ and $\tilde{y}_I(s,t|z')$ are slowly varying in s and t , respectively. Substitute Eq. (19.75) into Eqs. (19.61) and (19.70), and neglecting second order derivatives of $\tilde{y}_e(s|z)$ and $\tilde{y}_I(s,t|z')$, we obtain

$$\frac{\partial}{\partial t} \tilde{y}_I(s,t|z') + \frac{i\omega_I}{2} \tilde{y}_e(s|vt-s) = 0 , \quad (19.76)$$

$$\frac{\partial}{\partial s} \tilde{y}_e(s|z) + \frac{i\omega_e^2}{2\omega_\beta v \ell} \left[z \tilde{y}_e(s|z) - \int_0^z dz' \tilde{y}_I\left(s, \frac{s+z}{v} | z'\right) \right] = 0 , \quad (19.77)$$

with the initial condition

$$\tilde{y}_I\left(s, \frac{s+z'}{v} | z'\right) = \tilde{y}_e(s|z') . \quad (19.78)$$

The first equation can be integrated to give

$$\begin{aligned} \tilde{y}_I(s,t|z') &= \tilde{y}_I\left(s, \frac{s+z'}{v} | z'\right) - \frac{i\omega_e}{2} \int_{\frac{s+z}{v}}^t dt' y_e(s|vt'-s) \\ &= \tilde{y}_e(s|z') - \frac{i\omega_e}{2v} \int_{z'}^{vt-s} dz'' y_e(s|z'') . \end{aligned} \quad (19.79)$$

Substituting into the second equation, we get

$$\frac{\partial}{\partial s} \tilde{y}_e(s|z) + \frac{i\omega_e^2}{2\omega_\beta v \ell} \left[z \tilde{y}_e(s|z) - \int_0^z dz' y_e(s|z') \right] + \frac{i\omega_e^2}{2\omega_\beta v \ell} \frac{i\omega_I}{2v} \int_0^z dz' \int_{z'}^z dz'' \tilde{y}_e(s|z'') = 0 . \quad (19.80)$$

Integrating by part, it is easy to show that

$$\begin{aligned} z \tilde{y}_e(s|z) - \int_0^z dz' \tilde{y}_e(s|z') &= \int_0^z dz' z' \frac{\partial}{\partial z'} \tilde{y}_e(s|z') , \\ \int_0^z dz' \int_{z'}^z dz'' \tilde{y}_e(s|z'') &= \int_0^z dz' z' \tilde{y}_e(s|z') . \end{aligned}$$

Then we arrive at

$$\frac{\partial}{\partial s} \tilde{y}_e(s|z) + \frac{i\omega_e^2}{2\omega_\beta v \ell} \left[\int_0^z dz' z' \frac{\partial}{\partial z'} \tilde{y}_e(s|z') + \frac{i\omega_I}{2v} \int_0^z dz' z' \tilde{y}_e(s|z') \right] . \quad (19.81)$$

Another differentiating with transform the differential-integral equation into a differential equation:

$$\frac{\partial^2}{\partial s \partial z} \tilde{y}_e(s|z) + \frac{i\omega_e^2}{2\omega_\beta v \ell} z \left[\frac{\partial}{\partial z} \tilde{y}_e(s|z) + \frac{i\omega_I}{2v} \tilde{y}_e(s|z) \right] . \quad (19.82)$$

Earlier, we have estimated that the ion bounce frequency is usually very high. If the growth rate of the electron beam envelope is small, we can neglect the first term in the square brackets. Then, Eq. (19.82) will be very much simplified to

$$\frac{\partial^2}{\partial s \partial z} \tilde{y}_e(s|z) + \frac{i\omega_e^2 \omega_I}{4\omega_\beta v^2 \ell} z \tilde{y}_e(s|z) = 0 . \quad (19.83)$$

The solution is that $\tilde{y}_e(s|z)$ depends on s and z through one dimensionless variable

$$\eta = \frac{z}{\ell} \sqrt{\frac{\omega_e^2 \omega_I \ell s}{2\omega_\beta v^2}} , \quad (19.84)$$

and Eq. (19.83) becomes

$$\eta \frac{d^2 \tilde{y}_e}{d\eta^2} + \frac{d\tilde{y}_e}{d\eta} - \eta \tilde{y}_e = 0 . \quad (19.85)$$

which is just the modified Bessel equation. Thus, we obtain the simple solution

$$\tilde{y}_e(s, z) = y_0 I_0(\eta) , \quad (19.86)$$

where I_0 is the modified Bessel function of order zero, while $y_0 = \tilde{y}_e(s|0)$ is the amplitude of oscillation of the head of the bunch if we make observation at a fixed location s , or $y_0 = \tilde{y}_e(0|z)$ is the initial amplitude of the centroid of a slice in the electron beam. In the asymptotic regime with $\eta \gg 1$, we have

$$\tilde{y}_e(s, z) = y_0 \frac{e^\eta}{\sqrt{2\pi\eta}} . \quad (19.87)$$

Thus the asymptotic growth of the oscillating amplitude is exponential in z along the electron beam. However, for a fixed slice (fixed z), the growth of the amplitude is exponential in \sqrt{s} . If we have chosen $k = -\omega_I v$ as the resonance condition in Eq. (19.74), the solution of Eq. (19.87) would have become

$$\tilde{y}_e(s, z) \sim \frac{e^{\pm i|\eta|}}{\sqrt{2\pi|\eta|}} , \quad (19.88)$$

which is oscillatory and slowing decreasing. In fact, Eq. (19.85) becomes the Bessel equation and the solution becomes $J_0(|\eta|)$.

Observing at a fixed location s , we can define a growth length (in time) along the bunch

$$\tau_0 = \sqrt{\frac{2\omega_\beta \ell}{\omega_e^2 \omega_I s}} . \quad (19.89)$$

One may expect this growth time not dependent on the total length of the bunch. In fact, this is true, because from Eq. (19.69) ω_e^2/τ_L depends only on the linear density of the electron beam. If we are monitoring a specific slice of the electron beam (at fixed z or $\tau = z/v$ in time behind the head) as a function of time t or $s = vt$ along the accelerator, we can define a growth time for a roughly e -folding,

$$t_0 = \frac{2\omega_\beta\tau_L}{\omega_e^2\omega_I\tau^2}, \quad (19.90)$$

which is also independent of the electron bunch length $\tau_L = \ell/v$.

Knowing the asymptotic behavior of the amplitude of the electron bunch, we can compute the same for the ions. Substituting Eq. (19.87) into the second term on the right side of Eq. (19.79), we obtain

$$\tilde{y}_I(s, t|z') \approx -iy_0 \sqrt{\frac{\omega_\beta\omega_I\ell}{2\omega_e^2 s}} \frac{e^\eta}{\sqrt{2\pi\eta}} \Big|_{z=vt-s}. \quad (19.91)$$

This tells us that the first term on the right side of Eq. (19.79) can be neglected because it is $\sqrt{\omega_\beta\omega_I\ell/(2\omega_e^2 s)}$ smaller. Therefore when the ions meet the electron slide z behind the head of the electron bunch at location s , the ratio of the ion displacement to the beam displacement is

$$\frac{y_I(s, t|z')}{y_e(s|z)} \Big|_{z=vt-s} = \frac{\tilde{y}_I(s, t|z')}{\tilde{y}_e(s|z)} \Big|_{z=vt-s} \approx -i \sqrt{\frac{\omega_\beta\omega_I\ell}{2\omega_e^2 s}}. \quad (19.92)$$

Thus the ion oscillation is 90° out of phase relative to the electrons, and the ion amplitude is very much larger according to the example we demonstrated earlier.

We can now check the validity of a previous approximation of neglecting the first term in the square brackets of Eq. (19.82), which implies the necessity of

$$\left| \frac{\partial}{\partial z} \tilde{y}_e(s|z) \right| \ll \left| \frac{\omega_I}{2v} \tilde{y}_e(s|z) \right|. \quad (19.93)$$

Knowing the asymptotic behavior of the electron beam, this is equivalent to requiring

$$\frac{\eta}{z} = \sqrt{\frac{\omega_e^2\omega_I s}{2\omega_\beta\ell}} \ll \frac{\omega_I}{2}. \quad (19.94)$$

Using the definition of the growth time τ_0 [Eq. (19.89)] along the electron beam, this requirement is just

$$\frac{\omega_I \tau_0}{2} \gg 1 . \quad (19.95)$$

In other words, the beam makes many oscillations within one growth length along the beam.

19.3.2 Spectrum of Electron Beam

Observing at location $s = 0$, the spectrum $\tilde{\rho}\Omega$ of the electron beam is given by

$$\tilde{\rho}(\Omega) \propto \int_0^\infty dt e^{-i\Omega t} \sum_{k=0}^{\infty} y_e(kC|vt - kC) \Big|_{0 < vt - kC < \ell} , \quad (19.96)$$

where $C = 2\pi R = vT_0$ is the ring circumference and k sums over multiple turns. We next transform the integration to t within one turn only. Thus

$$\begin{aligned} \tilde{\rho}(\Omega) &\propto \sum_{k=0}^{\infty} \int_0^{\ell/v} dt e^{-i\Omega(t+kT_0)} y_e(kC|vt) \\ &= \sum_{k=0}^{\infty} e^{-i(\Omega+\omega_\beta)kT_0} \int_0^{\ell/v} dt e^{-i(\Omega-\omega_I)t} \tilde{y}_e(kC|vt) \\ &= \sum_{k=0}^{\infty} e^{-i(\Omega+\omega_\beta)kT_0} \int_0^{\ell/v} dt e^{-i(\Omega-\omega_I)t} \frac{y_0 e^{\eta'}}{\sqrt{2\pi\eta'}} , \end{aligned} \quad (19.97)$$

with

$$\eta' = t \sqrt{\frac{\omega_e^2 \omega_I k C}{2\omega_\beta \ell}} . \quad (19.98)$$

The integral, denoted by I , can be performed exactly in terms of the incomplete gamma function γ . We obtain

$$I = \int_0^{\ell/v} dt \frac{e(B - ia)t}{\sqrt{2\pi Bt}} = \frac{1}{\sqrt{2\pi B}} (-B + iA)^{-1/2} \gamma \left[\frac{1}{2}, \frac{(-B + iA)\ell}{v} \right] , \quad (19.99)$$

where $A = \Omega - \omega_I$ and $B = \eta'/t'$. When $|x| \gg 1$, we have $\gamma(\alpha, x) \approx -x^{\alpha-1} e^{-x}$, and

$$I \approx e^{B\ell/v} \sqrt{\frac{\ell}{2\pi Bv}} \left(\frac{e^{-iA\ell/(2v)} \sin \frac{A\ell}{2v}}{\frac{A\ell}{v}} \right) , \quad (19.100)$$

where $|A|\ell/v \gg B\ell/v \gg 1$ has been used. The summation over k diverges because the signal itself diverges. However, if we measure in a small window around some large $k = \bar{k}$, we obtain the spectrum

$$|\tilde{\rho}(\Omega)| \propto y_0 e^{\bar{B}\ell/v} \sqrt{\frac{\ell}{2\pi\bar{B}v}} \left| \frac{\sin \frac{(\Omega - \omega_I)\ell}{2v}}{\frac{(\Omega - \omega_I)\ell}{2v}} \right| \sum_{p=-\infty}^{\infty} \delta(\Omega - p\omega_0 + \omega_\beta) , \quad (19.101)$$

where ω_0 is the revolution angular frequency and \bar{B} is the former B when k replaced by \bar{k} . The spectrum observed is therefore all the lower betatron sidebands modulated by the sinc function which peaks at ω_I with a width equals to the inverse length of the electron beam.

19.3.3 Possible Cures

There are several methods to overcome this fast beam-ion instability. Simulations shows that the oscillation amplitude of the trailing beam particles saturates at about one σ_v due to nonlinear character of the coupling force. Thus, if we can reduce the original vertical emittance by a factor of two, the saturated emittance will be approximately what is desired. Another method is to have a lattice of the accelerator ring in which the product of the horizontal and vertical betatron functions changes substantially as a function of position along the ring. The transverse beam size of the beam will have such large variation accordingly. As a result, the ion bounce frequency ω_I will vary significantly with time and no coherent oscillation can therefore develop. A third remedy is to introduce gaps within the beam if it is very long. In case of a bunch train, the introduction of additional longer bunch gaps will certainly help. As an example, additional 10 bunch gaps in PEP-II increase the instability rise time from $0.5 \mu\text{s}$ to 0.5 ms , which is inside the bandwidth of the feedback system. For linacs, the trailing bunches of a long train may be realigned by use of fast kickers and feedback.

19.3.4 Applications

Raubenheimer and Zimmermann applied the linear theory of fast beam-ion instability to some existing accelerators like the SLAC Linear Collider (SLC) arc, the SLC positron Damping Rings (DR), the LBL Advanced Light Source (ALS), the DESY HERA, the

Table 19.5: Parameters and oscillation growth rates for some existing accelerators.

Accelerator	SLC arc	SLC e ⁺ DR	ALS	HERA e ⁻	CESR	ESRF
ϵ_x^N (m)	5×10^{-5}	3×10^{-5}	1.2×10^{-5}	2×10^{-3}	2.7×10^{-3}	7.5×10^{-5}
ϵ_y^N (m)	5×10^{-6}	3×10^{-6}	2×10^{-7}	1.1×10^{-4}	1.2×10^{-4}	7.5×10^{-6}
n_b	1	1	328	210	7	330
N_b	3.5×10^{10}	4×10^{10}	7×10^9	3.7×10^{10}	4.6×10^{11}	5×10^9
$\beta_{x,y}$	4	1, 3	2.5, 4	25	14, 13	8, 8
$\bar{\beta}_y$	4	3	4	25	13	8
σ_x (μm)	47	113	101	991	1965	226
σ_y (μm)	15	62	17	232	399	71
ℓ or σ_z	1 mm	5.9 mm	200 m	6048 m	670 m	280 m
E (GeV)	46	1.2	1.5	26	5	6
p (Torr)	10^{-5}	10^{-8}	10^{-9}	10^{-9}	5×10^{-9}	2×10^{-9}
particle	e ⁺	e ⁺	e ⁻	e ⁻	e ⁻	e ⁻
$\omega_I/(2\pi)$ (MHz)	3.6×10^5	4.6×10^4	31	0.87	0.92	6.8
$\omega_\beta/(2\pi)$ (MHz)	11.9	15.9	11.9	1.91	3.67	5.96
$\omega_e/(2\pi)$ (MHz)	0.481	0.029	0.149	0.0054	0.0098	0.027
Single or multibunch	single	single	multi	multi	multi	multi
t_0 ($z \approx \ell$)	1.09 μs	511 μs	1.30 μs	187 μs	942 μs	65 μs

Cornell Electron Storage Ring (CESR), and the European Synchrotron Radiation Facility (ESRF). The results[†] are shown in Table 19.5. Applications are also made to some future accelerators, like the Next Linear Collider (NLC) electron and positron Damping Rings (DR), the NLC Main Linac, the NLC Pre-Linac, the PEP-II Higher Energy Ring[‡] (HER), the KEK Accelerator Test Facility (ATF) Damping Ring. The results are shown in Table 19.6. In the tables, some are data for the accelerators and some are computed numbers. For example, the beam transverse rms sizes, $\sigma_{x,y}$, are computed from the given normalized rms emittances $\epsilon_{x,y}^N$ and betatron functions $\beta_{x,y}$. In computing the ion bounce frequency $\omega_I/(2\pi)$, the beam linear density is taken at the peak density in case the beam considered is a single bunch, and as an average in case the beam considered is a train of bunches. In computing the beam particle bounce frequency $\omega_e/(2\pi)$, an ionization cross section of 2 Mb has been assumed. In computing the growth time t_0 ,

[†]In some cases, our computed numbers are different from what are given in Ref. [16].

[‡]This ring is in operation now. But it was under construction at the time Ref. [16] was written.

Table 19.6: Parameters and oscillation growth rates for some future accelerators.

Accelerator	NLC e ⁻ DR	NLC e ⁺ DR	NLC Pre-linac	NLC Main linac	PEP-II HER	ATF DR
ϵ_x^N (m)	3×10^{-6}	3×10^{-6}	3×10^{-6}	3×10^{-6}	5×10^{-4}	3×10^{-6}
ϵ_y^N (m)	3×10^{-8}	3×10^{-8}	3×10^{-8}	3×10^{-8}	2.5×10^{-5}	3×10^{-8}
n_b	90	90	90	90	1658	60
N_b	1.5×10^{10}	1.5×10^{10}	1.5×10^{10}	1.5×10^{10}	3×10^{10}	1×10^{10}
$\beta_{x,y}$	0.5, 5	0.5, 5	6	8	15	0.5, 5
$\bar{\beta}_y$	2	2	6	8	15	2.5
σ_x (μm)	62	62	68	35	1060	22
σ_y (μm)	3.9	3.9	6.8	3.5	169	7.1
ℓ or σ_z	38 m	4 mm	38 m	38 m	2000 m	50 m
E (GeV)	2	2	2	10	9	1.54
p (Torr)	10^{-9}	10^{-9}	10^{-8}	10^{-8}	10^{-9}	6×10^{-8}
particle	e ⁻	e ⁺	e ⁻	e ⁻	e ⁻	e ⁻
$\omega_I/(2\pi)$ (MHz)	151	2.23×10^5	108	209	4.46	98.2
$\omega_\beta/(2\pi)$ (MHz)	23.9	23.9	7.95	5.96	3.18	19.1
$\omega_e/(2\pi)$ (MHz)	0.271	0.029	0.613	0.531	0.027	1.78
Single or multibunch	multi	single	multi	multi	multi	multi
t_0 ($z \approx \ell$)	856 ns	124 μs	78 ns	40 ns	7.2 μs	19 ns

the bunch length is taken as $\ell = 2\sigma_z$ in case the beam considered is a single bunch. With the exception of HERA and PEP-II HER, we find

$$\omega_e \ll \omega_\beta \ll \omega_I . \quad (19.102)$$

But in all cases, we do have

$$\omega_e \ll \omega_I . \quad (19.103)$$

For the existing accelerators, all the rise times are longer than the synchrotron damping times, except for the ALS and ESRF. Transverse instabilities have been reported in the ALS; but they are not necessarily caused by ions. For the ESRF, the expected fast beam-ion instability growth time is about a factor 150 smaller than the radiation damping time. But so far there is no evidence for ion-related effects or multibunch instability at the ESRF. One possible explanation for the observed stability pertains to the distinct focusing optics: a Chasman-Green lattice, in which the product of the horizontal and

vertical betatron functions varies by more than a factor of 100 around the ring. This will lead to a variation of the ion bounce frequency by an order of magnitude. The decoherence of the ion motion due to this large frequency variation could effectively suppress the instability. On the other hand, this source of decoherence does not exist in a FODO lattice where the product of the transverse beam sizes is nearly constant. It is fortunate that the fast beam-ion instability was discovered when the B-factories at SLAC and KEK were still under construction. Theoretical and experimental analyses had been performed to make sure that this instability would be avoided.

19.3.4.1 Observation at ALS

The fast beam-ion instability had been demonstrated experimentally at the LBL ALS, the Pohang Light Source (PLS), and the KEK TRISTAN [18, 19, 20]. The ALS has 328 rf buckets. In the experiment, only up to 240 consecutive buckets were filled so that there was a large gap to make sure that ions would not be trapped turn after turn. Unlike the experiment at the PLS, the feedback damping was turned on to suppress any coupled-bunch instabilities. Thus if any beam-ion instabilities developed, they would be due to single-pass generated ions. The pressure in the vacuum chamber was elevated to $\sim 80 \times 10^{-9}$ Torr by injected He. The onset of instability was carefully monitored by increasing the length of the bunch train slowly. Starting with a single bunch at 0.5 mA, consecutive bunches were filled slowly and the vertical beam size was measured. Figure 19.6 plots the rms beam size as a function of number of bunches in the train. We see that at elevated pressure with He added, the beam size increases strongly with number of bunches and becomes saturated when number of bunches exceed 8. We also see that at normal operating vacuum pressure, the beam size does not vary with the number of bunches in the train. The spectrum of the bunch train was also measured when the train contained 240 bunches, but with the total bunch intensity varied. The results in the left plots of Fig. 19.7 show the vertical betatron sidebands (the difference of the upper-sideband amplitude and the lower-sideband amplitude) clustered about 10 MHz when the total bunch current is 82 mA. As the current was raised to 142 mA and 212 mA, we see that the cluster of sidebands move to higher frequencies. If this is the fast beam-ion instability, these sideband frequencies are just the ion bounce frequencies. Figure 19.7 plots the measured ion bounce frequency as a function of beam current along with the theoretical prediction given by Eq. (19.62). We see that the theory fits the experimental data rather well.

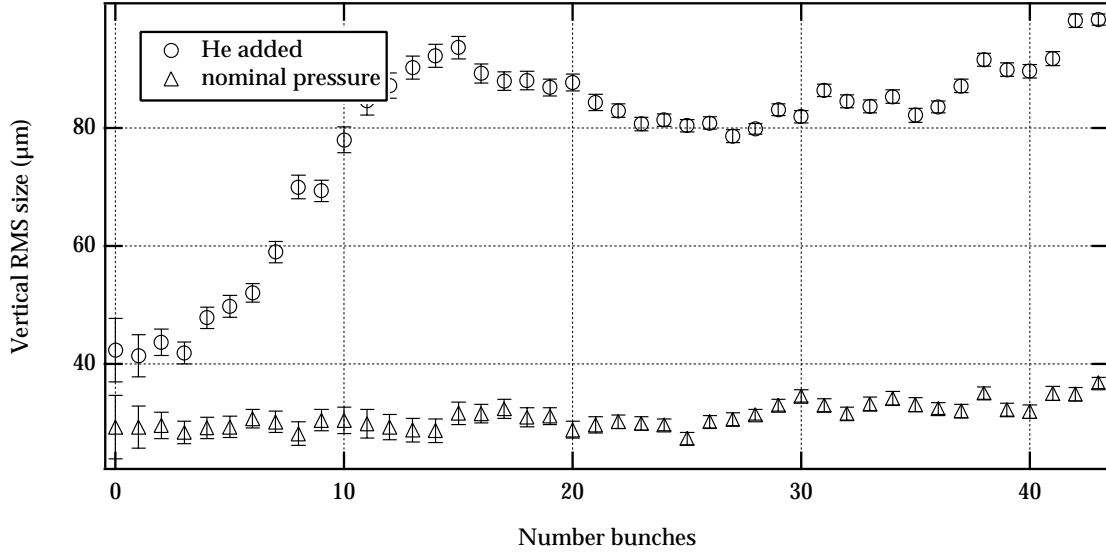


Figure 19.6: Rms vertical beam size versus the number of bunches for nominal and elevated pressure conditions.

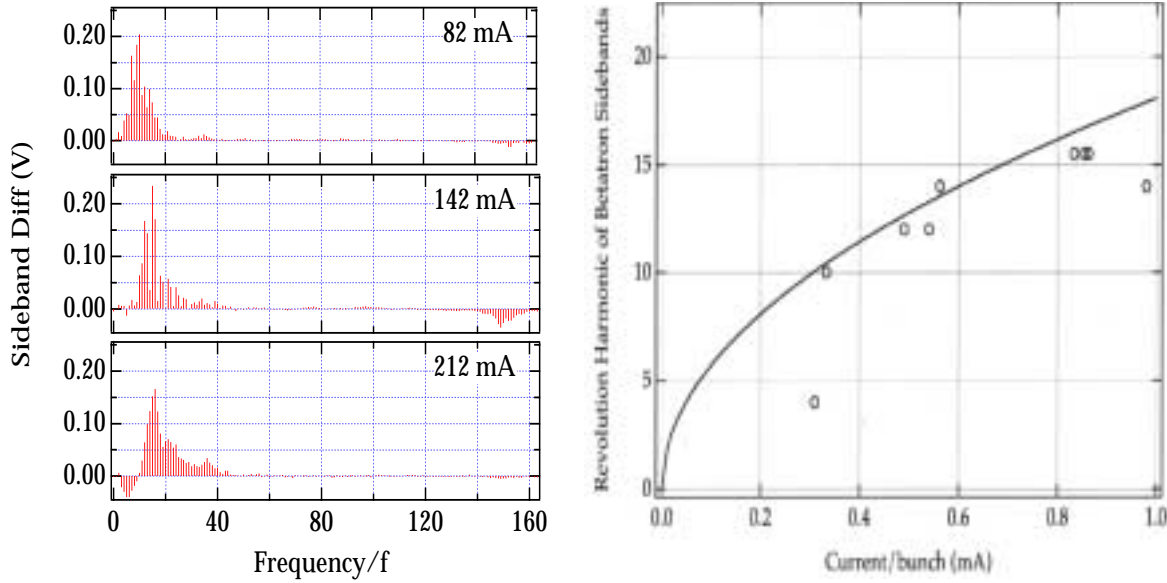


Figure 19.7: (color) Left: Vertical betatron sidebands measured in the 240/328 fill pattern for three different total currents of the bunch train. Right: Comparison between the measured and predicted frequency of coherent beam oscillations as a function of current per bunch for the 240/328 fill pattern.

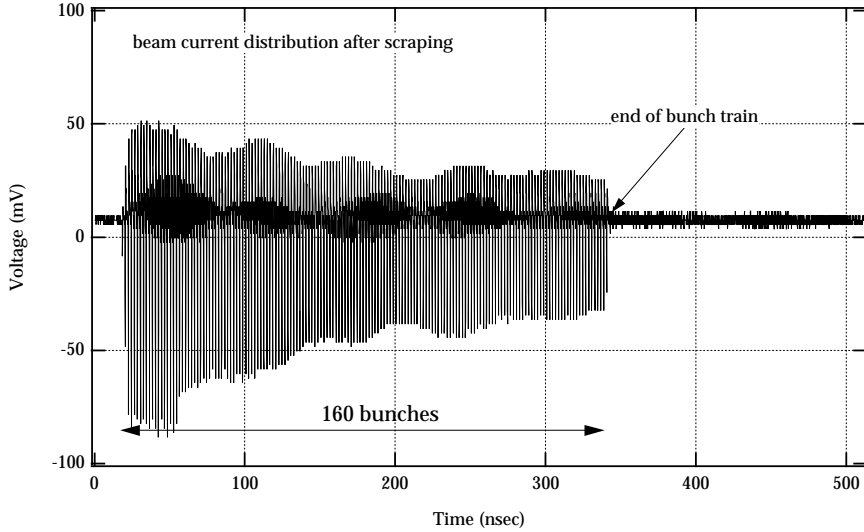


Figure 19.8: Beam current along the bunch train for 160 bunches after scraping a vertical aperture close to the beam. The decreasing bunch current shows the increasing vertical oscillation amplitude along the bunch train (before scraping).

The relative amplitude of oscillations along the bunch train was also measured indirectly. A collimator was used to scrape a train consisting of 160 bunches. After scraping, the bunch intensity was found to be decreasing from the head of the train to the tail. In fact, the scraper reduced the bunch population in the tail about 2.5 times more than that of the leading bunches. This indicates that, before the scraping, the bunch vertical oscillating amplitudes increase along the bunch train.

The growth rate was also estimated and it agreed with the prediction of the linear theory. Thus, all evidence accumulated is qualitatively consistent with the assumption that the observed instability is the fast beam-ion instability.

19.3.4.2 Observation at the Fermilab Linac

Fast transverse oscillations with large amplitudes were observed [21] in the H^- beam in the 750 keV transfer line of the Fermilab linac in 1988 when the vacuum pressure was raised to 7×10^{-6} Torr to reduce the effect of space charge on the beam [22, 23] and thereby reduce the effective emittance entering the linac. In order not to degrade the performance of the 8 GeV booster, into which the linac injects, this transverse instability

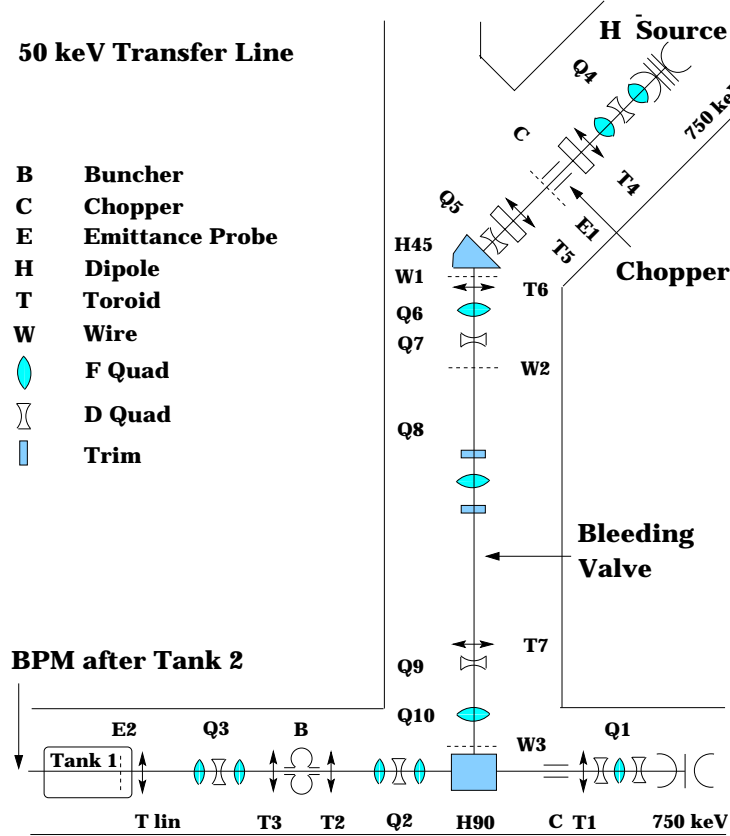


Figure 19.9: The 750 keV transfer line of the Fermilab linac. The length is ~ 10 m from the chopper C to the entry into the linac. Beam current measurements are made by a toroid monitor between Tank 1 and Tank 2, and again further downstream.

has been avoided by choosing the operating vacuum pressure to be 2.65×10^{-6} Torr. The observation resembles the fast beam-ion instability, where individual ions last only for a single passage of the particle beam and need not be trapped. An experiment was performed at the 750 keV transfer line in 2000 in order to further understand the instability previously observed [24].

Figure 19.9 shows the 750 keV transfer line into the main linac. Different gases like hydrogen, helium, nitrogen, argon, and krypton, were injected through the bleeding valve. The gas pressure was controlled by adjusting the rate of flow of gas at the bleeding valve while vigorously pumping at the large ion pumps near the chopper C and the entrance into Tank 1 as well as a small ion pump near the bleeding valve. The

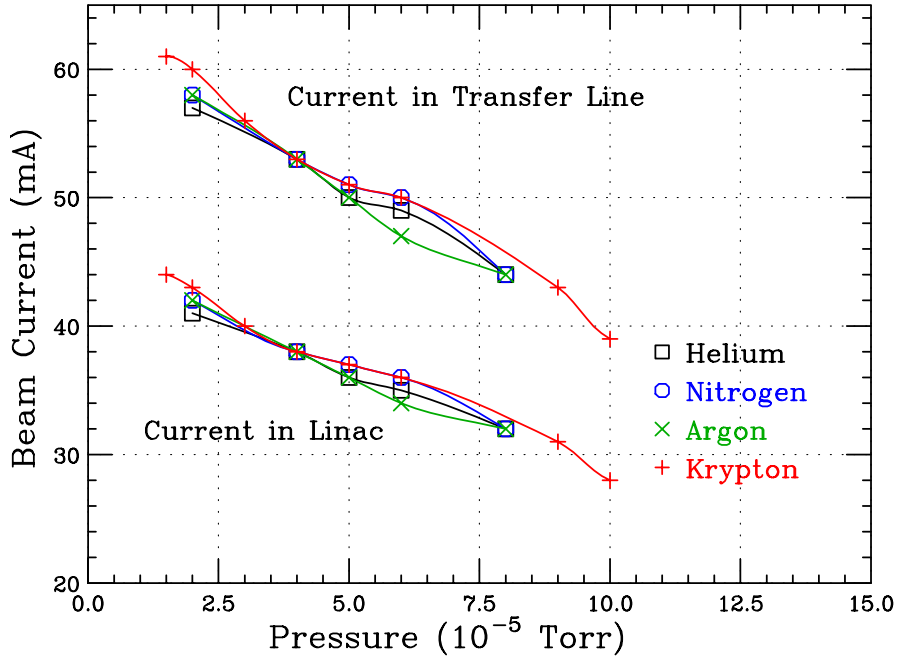


Figure 19.10: (color) Beam current in the transfer line (top) measured by toroids between Tank 1 and Tank 2, and further downstream in the linac (bottom). The drop in beam current at higher vacuum pressure is probably due to the stripping of the electron on the H^- by the gases injected.

pressure monitored near the three ion pumps showed steady readings. In this way the vacuum pressure could be varied between 1×10^{-5} and 1×10^{-4} Torr, while the normal operating vacuum pressure has been 2.65×10^{-6} Torr. A toroidal monitor near the exit of Tank 1 and entrance of Tank 2 measured the beam current. We see in Fig. 19.10 that the beam current in the transfer line (top) decreases with pressure. This is mostly due to the stripping of the electron on H^- by collision with the gas particles so that the resulting neutral H particles could not follow the dipole bend H90 into the current monitor. Another current monitor downstream measured the beam current in the linac downstream (bottom). The smaller values observed represent beam loss.

A 750 keV H^- beam chopped to the length of $\tau_b = 35 \mu s$ entered the transfer line. Its center position was picked up by the beam-position monitor (BPM) after Tank 2. The signals were recorded using a LeCroy scope and the spectral content was obtained numerically using FFT. To lower the noise level, measurements were averaged over approximately 20 beam pulses. To avoid any signal not related with the beam oscillation, only the last $20 \mu s$ of the beam pulse were Fourier analyzed. There was no

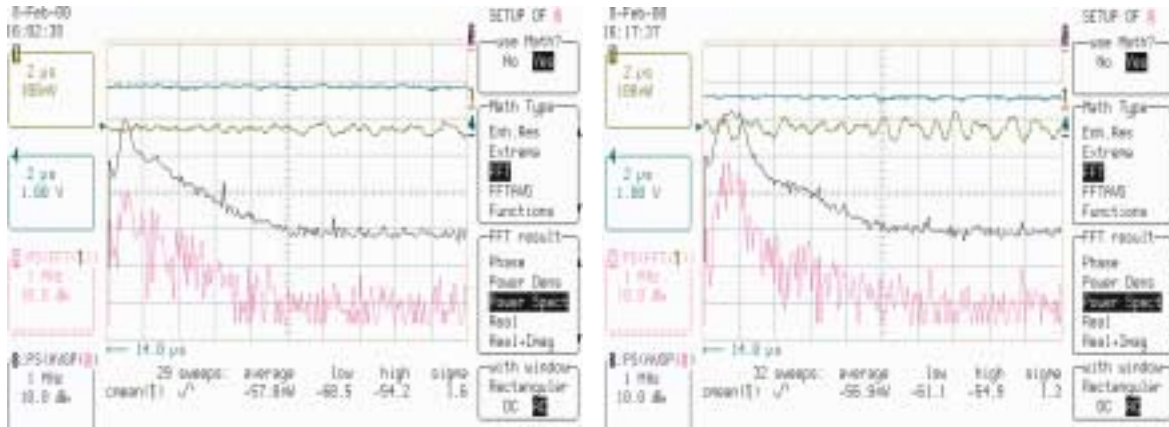


Figure 19.11: (color) Beam intensity (1st trace) and beam horizontal displacement (2nd trace) from the 14th μ s at 2 μ s per division, when the injected gas is nitrogen at 3×10^{-5} Torr (left) and 8×10^{-5} Torr (right). The 4th trace is the FFT at 1 MHz per division of the last 20 μ s of the beam horizontal displacement. The third trace is the FFT averaged over 20 beam pulses. As pressure increases, the resonant peak becomes broadened and moves towards higher frequencies.

noticeable difference between displacement signals in the horizontal and vertical planes, so all data were taken in the horizontal plane only.

A typical set of results for nitrogen at 3×10^{-5} Torr is shown in the left plot of Fig. 19.11, where the first two traces correspond to the beam intensity and the horizontal beam position, respectively. The 4th trace is the FFT of the beam position for the last 20 μ s of the beam, while the 3rd trace depicts the average of 23 FFT beam pulses. We can clearly see a resonant frequency of ~ 0.5 MHz. As the gas pressure was increased to 8×10^{-5} Torr in the right plot of Fig. 19.11, the resonant signal is broadened and spreads out to higher frequencies. Figure 19.12 shows the BPM signals for the horizontal oscillations of the H⁻ beam when argon is introduced. We see rapid growth in oscillation amplitude along the beam. The growth becomes much faster as the gas pressure is increased from 3×10^{-5} to 1×10^{-4} Torr. We also notice that saturation is reached very soon and the growth stops.

19.3.4.3 Ionization Cross section

When the velocity of the incident particle is much larger than the velocity of the electron inside the target atom about to be ionized, the impulse approximation can be used. Our

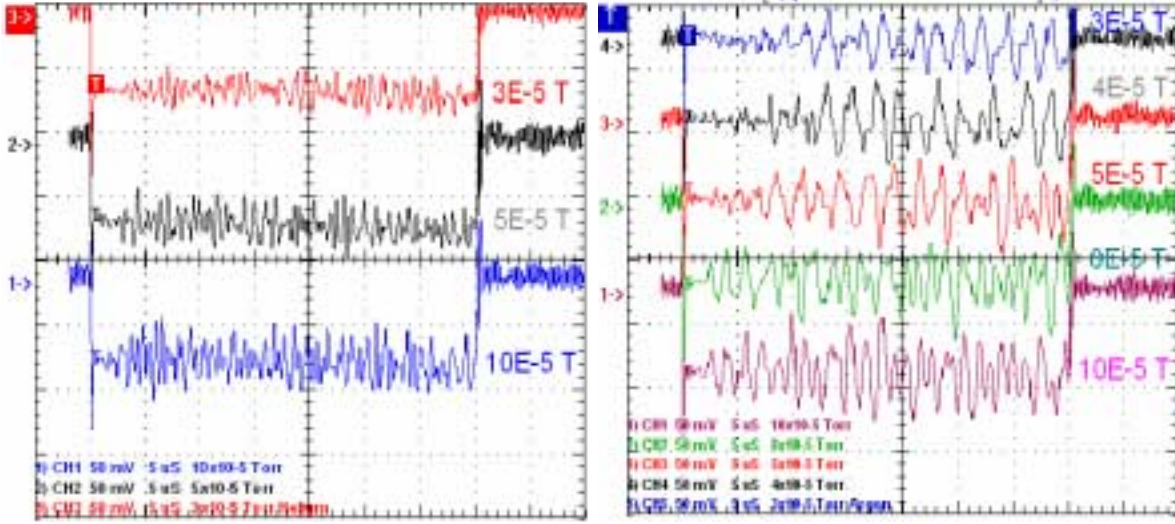


Figure 19.12: (color) Horizontal displacements of the $35 \mu\text{s}$ H^- beam in helium (left) and (right) argon gas environments at various pressures. An instability is observed and the beam displacements become saturated. The growth rate increases with gas pressure.

experiment condition satisfies this criterion. The ionization energy of the electron in the outermost shell is given by

$$U = U_0 \left(\frac{Z}{n} \right)_{\text{eff}}^2 \quad (19.104)$$

where Z is the atomic number of the gas element and n is the principal quantum number of the outermost shell of the gas atom. Here, $U_0 = hcR_\infty = 13.605 \text{ eV}$ is Rydberg energy or the ionization energy of hydrogen, $h = 6.582 \times 10^{-22} \text{ MeV-s}$ is the Planck constant, and c is the velocity of light. Since the electrons in the inner shells shield the electric charges of the nucleus, the effective ratio $(Z/n)_{\text{eff}}^2$ is less than the actual $(Z/n)^2$. The effective ratios for the various gases estimated from Eq. (19.104) are listed in Table 19.7. The velocity v_e of the electron in the outermost shell is

$$v_e = v_0 \left(\frac{Z}{n} \right)_{\text{eff}} \quad (19.105)$$

where $v_0 = r_e c / \lambda_e = 0.0073$ is the velocity of the electron in the hydrogen atom, $r_e = 2.818 \times 10^{-18} \text{ m}$ is the electron classical radius, and $\lambda_e = \hbar / (m_e c) = 3.86159323 \times 10^{-13} \text{ m}$ is the reduced electron Compton wavelength. We see that the velocities of the electron in the outermost cells of the gas atoms in this experiment are roughly $0.0073c$ to $0.0098c$, which are indeed much less than the velocity $\beta c = 0.040c$ of the 750 keV H^- .

Table 19.7: Ionization cross sections of various gases by 750 keV H⁻. Velocities of electrons in the outermost shells of the gas atoms are estimated by an effective value of Z/n due to screening, where Z is the atomic number of the gas element and n the principal quantum number of the electron. Values of M^2 and C are from experiments [27].

	H	He	N	Ar	Kr
Atomic number Z	1	2	7	18	36
Atomic mass number A	1	4	14	40	84
Ionization energy U (eV)	13.6	24.6	14.5	15.6	14.0
Effective ratio $(Z/n)_{\text{eff}}^2$	1.00	1.8088	1.0662	1.1618	1.029
Electron velocity in outermost shell v_e/c	0.0073	0.0098	0.0075	0.0079	0.0074
Target variable in Eq. (19.106) M^2	0.695	0.738	3.73	4.22	6.09
Target variable in Eq. (19.106) C	8.115	7.056	34.84	37.93	52.38
Ionization cross section Σ (Mb)	42.71	27.03	126.2	126.2	154.5

In the impulse approximation, the bound electrons are knocked out by a sudden transfer of energy from the incident particle. Therefore, the ionization cross section does not depend very much on the ionization energy of the target atom. From the work of Bethe [25, 26], the ionization cross section in the first Born approximation can be written as

$$\Sigma = 4\pi \chi_e^2 \left[M^2 \left(\frac{\ln \beta^2 \gamma^2}{\beta^2} - 1 \right) + \frac{C}{\beta^2} \right], \quad (19.106)$$

where β and γ are the Lorentz factors of the incident particle with the target at rest. The two variables M^2 and C depend on the generalized oscillator strength inside the target atom for all the transitions involved. Notice that this expression depends on the incident particle only through its *velocity*, which is an important consequence of the Born approximation and has been verified by many experiments [27]. The experimental values of M^2 and C as well as the cross sections of the gases involved are listed in Table 19.7.

19.3.4.4 Ion Bounce Frequencies

At the vacuum pressure of 3×10^{-5} Torr, the beam current in the transfer line is $I \sim 56.1$ mA (see Fig. 19.10). Thus the $\tau_b = 35 \mu\text{s}$ H⁻ beam corresponds to a linear density of $\lambda_b = I/(e\beta c) = 2.92 \times 10^{10} \text{ m}^{-1}$. The H⁻ beam has a round cross section of radius

Table 19.8: Ion-beam resonant frequencies according to Ref. [16] for gases at various vacuum pressures or beam currents.

Gas	H	He	N	Ar	Kr
Mass number A	1	4	14	39	84
Resonant frequency (MHz)					
at 1×10^{-5} Torr (61.0 mA)	1.490	0.745	0.398	0.236	0.163
at 2×10^{-5} Torr (58.6 mA)	1.460	0.730	0.390	0.231	0.159
at 3×10^{-5} Torr (56.1 mA)	1.429	0.715	0.382	0.226	0.156
at 4×10^{-5} Torr (53.7 mA)	1.398	0.699	0.374	0.221	0.153
at 5×10^{-5} Torr (51.2 mA)	1.366	0.683	0.365	0.216	0.149
at 6×10^{-5} Torr (48.8 mA)	1.333	0.666	0.356	0.211	0.145
at 7×10^{-5} Torr (46.3 mA)	1.299	0.649	0.347	0.205	0.142
at 8×10^{-5} Torr (43.9 mA)	1.264	0.632	0.338	0.200	0.138
at 9×10^{-5} Torr (41.4 mA)	1.228	0.614	0.328	0.194	0.134
at 1×10^{-4} Torr (39.0 mA)	1.192	0.596	0.319	0.188	0.130

$a_h = a_v = 1.0$ cm. This gives the resonant frequency of $\omega_i/(2\pi) = 1.43/\sqrt{A}$ MHz as tabulated in Table 19.8.

The resonant frequencies computed in Table 19.8 are in the neighborhood of 1 MHz, in qualitative agreement with the experimental resonant frequencies depicted in, for example, Figs. 19.11 and 19.13. The observed resonant peaks in general have wide spreads. This may be because of the nonuniformity of the linear distribution of the H^- beam as well as the variation of its transverse radius. On the other hand, there are also disagreements with theory. Definitely, we do not see the $A^{-1/2}$ dependency given by Eq. (19.62). However, in computing the resonant frequencies in Table 19.8, we have assumed only singly charged ions. Because the velocity of the incident H^- are much greater than those of the electrons in the outermost shells of the various gases, the ionization cross sections do not depend much on the ionization energy. There are, for example, 6 electrons in the outermost shell of an argon atom or krypton atom, it will be as easy for two or more electrons to be knocked off as for one. If there were doubly or triply charged ions produced, the resonant frequency would have been $\sqrt{2}$ and $\sqrt{3}$ times larger. It is very plausible that the deviation of the $A^{-1/2}$ dependency for argon and krypton is due to the production of multi-charged ions. The expression, Eq. (19.62), is independent of the gas pressure. The slight decrease of the resonant frequency with

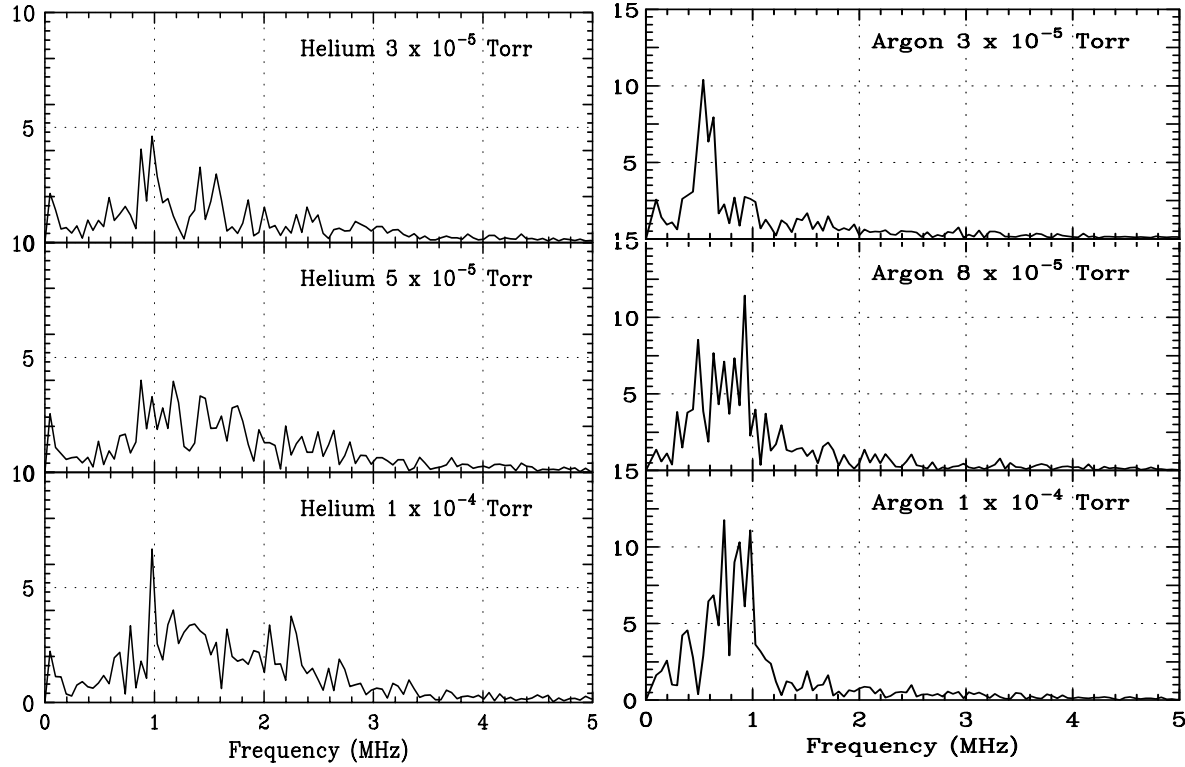


Figure 19.13: FFT of H^- beam horizontal displacement averaged over many beam pulses. The gas environments are helium (left) and argon (right). The frequency spread does not depend much on gas pressure for helium, but does depend on pressure for argon.

rising pressure tabulated in Table 19.8 is just a reflection of the H^- current or linear density as a result of possible stripping by the gas particles.

In summary, we find that the resonant frequency is not sensitive to pressure for light gases like helium and nitrogen. However, for the heavier gases such as argon and krypton, the resonant peaks are broadened and move towards higher frequencies when the pressure is larger than $\sim 5 \times 10^{-5}$ Torr. To conclude, we plot the spreads of the experimental resonant frequencies of the different gases for all the pressures studied in Fig. 19.14. On the same plot we also include the resonant frequencies computed in Table 19.8 from 1×10^{-5} Torr (top trace) to 1×10^{-4} Torr (bottom trace). From the figure, it is evident that the theoretical predictions, as a whole, underestimate the experimental results.

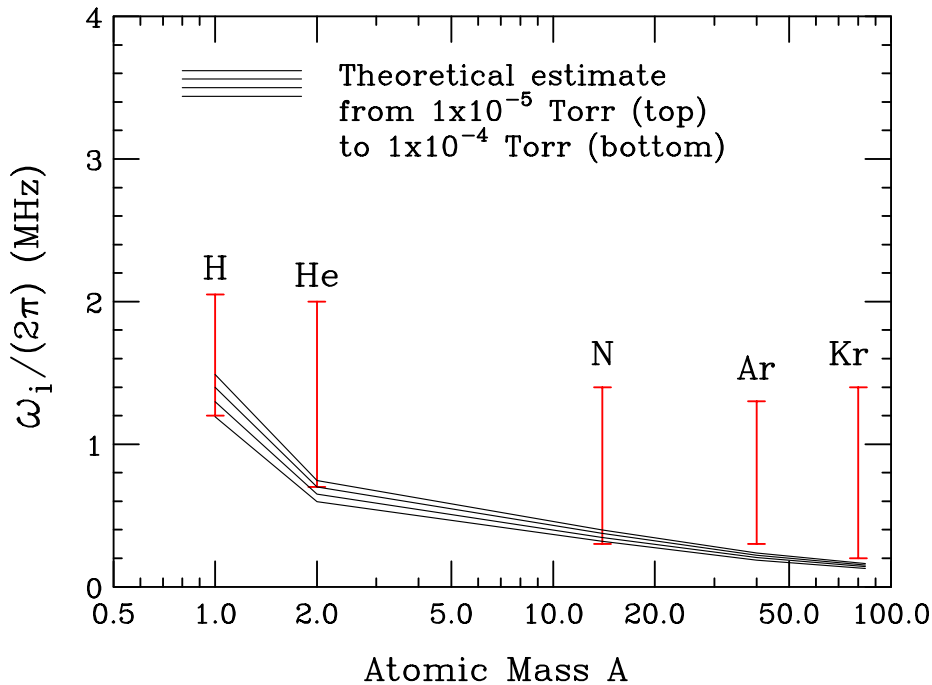


Figure 19.14: Spreads of measured resonant frequencies of different gases at all the pressures studied. The theoretical predictions from 1×10^{-5} Torr (top trace) to 1×10^{-4} Torr (bottom trace) are also shown.

19.3.4.5 Growth Times

The transverse displacement of the H^- beam was measured by the BPM after Tank 2 in the linac. The excitation of transverse oscillation had been going on in the $\ell_t \sim 10$ m of the 750 keV transfer line from the chopper to the big ion pump near the entrance into the linac. Thus the time for which the beam can actually generate and interact with the ions is $t \sim \ell_t/(\beta c) = 0.835 \mu s$. The growth time along the beam τ_0 in Eq. (19.89) should be derived and compared with theory. These growth times along the beam, τ_0 , at the pressure of 1×10^{-5} Torr are listed in the last row of Table 19.9.

Table 19.9: Computation of growth time along the H^- beam at 1×10^{-5} Torr. The growth time at other pressure p scales with $p^{-1/2}$.

	H	He	N	Ar	Kr
ω_b (MHz)	10.1	8.00	20.2	17.3	19.1
Growth time along beam τ_0 (μs)	0.91	1.61	0.87	1.33	1.44

19.3.4.6 Comments

The beam-ion environment here is very different from that in an electron ring. Some relevant quantities are listed in Table 19.10. We see a huge difference:

Table 19.10: Comparison of some beam and ion parameters in a typical electron ring and in the Fermilab linac, assuming that CO is the residual gas.

	Electron Ring	Fermilab Linac Experiment
Number per bunch N_b	10^{11}	1.3×10^{13}
Bunch length ℓ_b	0.010	419 m
Beam radius	0.001	0.010 m
Beam linear density λ_b	10^{13}	$3.2 \times 10^{10} \text{ m}^{-1}$
Residual gas pressure	10^{-9}	1×10^{-5} Torr
Gas-in-beam linear density λ_{gas}	1×10^8	$1.0 \times 10^{14} \text{ m}^{-1}$
Ionization cross section for CO Σ	2	133 Mb
Maximum ion linear density λ_i	640	$5.7 \times 10^{10} \text{ m}^{-1}$
CO^+ ion bounce frequency $\omega_i/(2\pi)$	64	0.40 MHz
Beam bounce frequency [†] $\omega_b/(2\pi)$	0.00092	2.82 MHz

[†]10 GeV electrons are assumed for electron ring.

ω_b is the same as ω_e referenced earlier in Eq. (19.69).

1. The ion bounce frequency in an electron ring is very much larger because of much higher electron linear density and the much smaller transverse electron beam size.
2. There are very much more ions produced in the Fermilab linac than in an electron ring. The ion linear density in an electron ring is negligibly small compared with the beam linear density, while in the Fermilab linac the ion linear density is of the same order as the beam linear density. This is due to the much higher residual gas pressure and larger ionization cross section in the transfer line where the H^- are traveling with a small velocity. As a result, the beam bounce frequency in the ions becomes very much smaller in an electron ring.
3. There are 3 frequencies in the fast beam-ion instability theory, the ion bounce frequency $\omega_i/(2\pi)$, the beam bounce frequency $\omega_b/(2\pi)$ [same as ω_e referenced

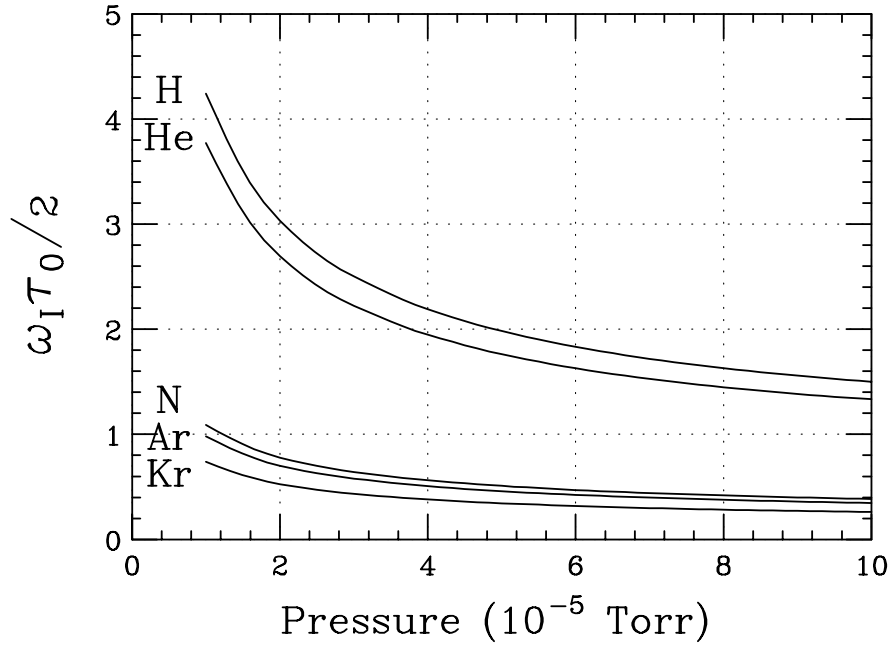


Figure 19.15: Plot of $\frac{1}{2}\omega_i\tau_0$ versus gas pressure for various gases. When $\frac{1}{2}\omega_i\tau_0 \gg 1$, the neglect of the first term inside the square brackets of Eq. (19.82) is justified leading to the exponential asymptotic solution of Eq. (19.87). Since the requirement is not satisfied for nitrogen, argon, and krypton, the concept of the growth time given by Eq. (19.89) may not be correct.

earlier in Eq. (19.69)], and the betatron frequency $\omega_\beta/(2\pi)$. For the two situations,

$$\begin{aligned} \text{Electron ring} \quad & \omega_I \gg \omega_\beta \gg \omega_b \\ \text{Fermilab linac} \quad & \omega_b \gtrsim \omega_\beta \gtrsim \omega_I . \end{aligned} \quad (19.107)$$

Now let us examine whether the above approximation can be made in our situation. When we are talking about growth time, we are looking in the asymptotic behavior, like Eq. (19.4), or when $\eta \gg 1$, which is well satisfied when we are considering a position along the beam which is a few growth times behind the head. The neglect of the first term in the square brackets therefore requires the satisfaction of

$$\frac{\omega_I\tau_0}{2} \gg 1 . \quad (19.108)$$

In Fig. 19.15, we plot $\frac{1}{2}\omega_i\tau_0$ as a function of pressure for the different gases. It is clear that criterion in Eq. (19.95) is satisfied for hydrogen and helium when the pressure is

low and becomes marginal when the pressure is higher than 5×10^{-5} Torr. For nitrogen, argon, and krypton, the criterion fails. This implies that the concept of a growth time τ_0 given by Eq. (19.89) may not be valid for these heavier gases. Therefore, we cannot say whether the results for nitrogen, argon, and krypton agree with the linear theory of fast beam-ion instability or not. A more sophisticated solution of Eqs. (19.76) and (19.77) must be obtained without the deletion of the first term in the square brackets before further comparison with experiment can be made for these heavier gases. Even the approximation of neglecting the second derivatives in obtaining Eqs. (19.76) and (19.77) should be re-examined.

Even for hydrogen and helium, the resonant frequency is around 1 MHz and less, and the passage time through the 10 m transfer line is 0.835 μs . This implies that the beam and the ion made less than one oscillation about each other. It is hard to visualize how a coherent instability can be established within such a short time. This is another reason why we are skeptical whether the expression for growth time could be applied to this experiment.

19.4 Exercises

- 19.1. Modify the coupled proton and electron equations of motion [Eqs. (19.9) and (19.10)] by including the influence of an infinitely conducting cylindrical beam pipe of radius b . Without taking into account the distributions of the various tunes, solve the equations for the threshold of coupled-centroid instability [similar to Eq. (19.17)] and the initial growth rate [similar to Eqs. (19.17) and (19.18)].
- 19.2. Derive in detail Eq. (19.59) for the kinetic energy of an electron hitting the wall of the beam pipe after it grazes the opposite wall.
- 19.3. In the experiment for measuring coupled-centroid instability at the Los Alamos PSR, the bunch occupies $2/3$ of the circumference of the storage ring. The coherent frequency which is close to the electron bounce frequency at CD 1 or $6.1 \mu\text{C}$ is shown in Fig. 19.5. Other information of the PSR are listed in Table 19.1.
 - (1) Assuming a parabolic linear distribution of the proton bunch, and the maximum coherent or bounce frequency of 240 MHz, estimate the transverse size of the proton beam.
 - (2) From the peak value of the bounce frequency, estimate the location along the proton beam where the electron density is at a maximum.
- 19.4. Fermilab is proposing a new high intensity booster having circumference 711.304 m with rf harmonic 4. Protons are injected at the kinetic energy of 400 MeV to an intensity of 8.6×10^{12} per bunch. At the end of injection, each proton bunch has a uniform linear density but is occupying $2/3$ of the rf bucket. The transverse cross section of the beam is circular with a radius of 2.35 cm.
 - (1) Assuming the bunch gap is totally clean, show that electrons will not be trapped inside the proton beam.
 - (2) If a fraction η of protons is spilled into the bunch gaps, compute the minimum η that will lead to electron trapping.
- 19.5. Starting from the equations of coupled transverse motion, Eqs (19.9) and (19.10), assuming circular distributions for the protons and electrons, derive the Laslett-Sessler-Möhl stability criterion, Eq. (19.46).
- 19.6. In Tables 19.5 and 19.6, rows 1-6, 9-12, and 16 are inputs. Compute the output rows 7-8 and 13-15.

Bibliography

- [1] H. Grunder, G. Lambertson, Proc. VIII Int. Conf. on High Energy Accel., p.308 (1971).
- [2] H.G. Herewards, CERN Report CERN-71-15, (1971).
- [3] R. Macek, *Overview of New Developments on the PSR Instability*, Proceedings of 8th Advanced Beam Dynamics Mini-Workshop on Two-Stream Instabilities in Particle Accelerators and Storage Rings, Santa Fe, Feb. 16-18, 2000, web site: <http://www.aps.anl.gov/conferences/icfa/proceedings.html>.
- [4] M. Blaskiewicz, *The Fast Loss Electron Proton Instability*, Proceedings of the Workshop on Instabilities of High Intensity Hadron Beams in Rings, ed. T. Roser and S.Y. Zhang, Upton, N.Y., 1999, p. 321; *Estimating Electron Proton Instability Thresholds*, Proceedings of 8th Advanced Beam Dynamics Mini-Workshop on Two-Stream Instabilities in Particle Accelerators and Storage Rings, Santa Fe, Feb. 16-18, 2000, web site: <http://www.aps.anl.gov/conferences/icfa/proceedings.html>.
- [5] J. Rosenzweig and P. Zhou, *Coherent Beam-ion Instabilities in the Fermilab Antiproton Accumulator, Ion Trapping in the Tevatron with Separated Orbits, Ion Clearing Using Cyclotron Shaking*, Proceedings of Fermilab III Instabilities Workshop, Fermilab, Batavia, Ed. S. Peggs and M. Harvey, June 25-29, 1990, p. 9, 26, and 39.
- [6] K. Harkay, *Electron Cloud Effects at APS*, Proceedings of 8th Advanced Beam Dynamics Mini-Workshop on Two-Stream Instabilities in Particle Accelerators and Storage Rings, Santa Fe, Feb. 16-18, 2000, web site: <http://www.aps.anl.gov/conferences/icfa/proceedings.html>.
- [7] D. Neuffer, E. Colton, D. Fitzgerald, T. Hardek, R. Hutson, R. Macek, M. Plum, H. Thiessen, and T.-S.Wang, Nucl. Instr. Meth. **A321**, 1 (1992).

- [8] In the reference below, aluminum pipe with titanium coating is mentioned:
<http://www.ornl.gov/~nsns/CDRDocuments/CDRSections/CDRSections.html>. In the more recent design, however, stainless steel beam pipe with TiN coating is used.
- [9] Obtainable by contour integration or see for example, I.S. Gradshteyn and I.M. Ryzhik, *Table of Integrals, Series, and Products*, Academic Press, Inc., Formula 3.644-4.
- [10] A. Ruggiero and M. Blaskiewicz, *e-p Instabilities in the NSNS Accumulator Ring*, Proceedings of the 1999 Particle Accelerator Conference, New York, 1999, p.1581.
- [11] M. Blaskiewicz, *Instabilities in the SNS*, Proceedings of the 1999 Particle Accelerator Conference, New York, 1999, p.1611.
- [12] W. Schnell and B. Zotter, CERN Report ISR-GS-RF/76-26 (1976).
- [13] L.J. Laslett, A.M. Sessler and D. Möhl, Nucl. Inst. Meth. **121** 517 (1974).
- [14] Tai-Sen F. Wang, *A Theoretical Study of Electron-Proton Instability I and II*, LANL Report PSR-96-004 and PSR-96-004 (1996).
- [15] R. Macek, talk given at the 8th Advanced Beam Dynamics Mini-Workshop on Two-Stream Instabilities in Particle Accelerators and Storage Rings, Santa Fe, New Mexico, February 16-18, 2000
- [16] T.O. Raubenheimer and F. Zimmermann, Phys. Rev. **E52**, 5487 (1995).
- [17] A.W. Chao, *Lecture Notes on Topics in Accelerator Physics*, US Particle Accelerator School, 5-16 June 2000, SUNY Stony Brook, New York, available at <http://www.slac.stanford.edu/~achao/lecturenotes.html>.
- [18] J. Byrd *et al.*, Phys. Rev. Lett. **79**, 79 (1997).
- [19] H. Fukuma *et al.*, (unpublished).
- [20] M. Kwon *et al.*, Phys. Rev. **E57**, 6016 (1998).
- [21] E. McCrory, G. Lee, and R. Webber, *Observation of Transverse Instabilities in FNAL 200 MeV Linac*, Proceedings of 1988 Int. Linac Conf. 3-7 October 1988, Williamsburg, VA.

- [22] I.A. Soloshenko, *Space Charge Compensation and Collective Processes in the Intense Beams of H⁻ Ions*, AIP Conf. Proceedings **380**, 1995, pp 345.
- [23] M.D. Gabovich, V.P. Goretsky, D.G. Dzhabbarov, and A.P. Naïda, Institute of Physics of Ukrainian Science Academy **N 9**, Kiev, 1979, pp 18.
- [24] M. Popovic and T. Sullivan, *Observation of a H⁻ Beam Ion Instability*, Proceedings of XX Int. Linac Conf. 21-25 August 2000, Monterey, CA.
- [25] H. Bethe, Ann. Physik **5**, 325 (1930).
- [26] M. Inokuti, Rev. Mod. Phys. **43**, 297 (1971).
- [27] F.F. Rieke and W. Prepejcjal, Phys. Rew. **A6**, 1507 (1972).

